

**UC Davis**

**UC Davis Previously Published Works**

**Title**

Chapter Four Oxygen-Isotope Exchange and Metastable Dissociation in Oxides

**Permalink**

<https://escholarship.org/uc/item/8qf6n848>

**Author**

Casey, WH

**Publication Date**

2017

**DOI**

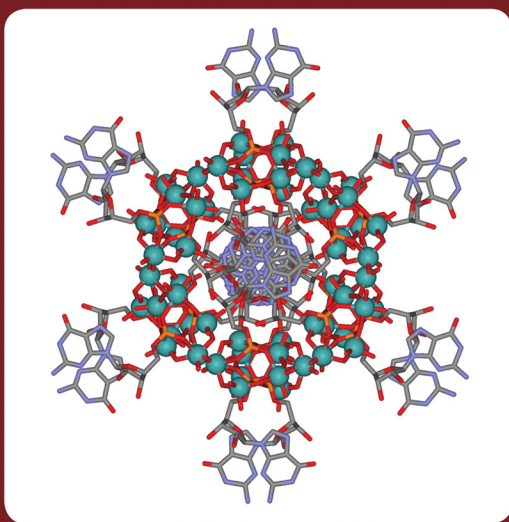
10.1016/bs.adioch.2016.12.007

Peer reviewed

VOLUME

69

Advances in  
**Inorganic  
Chemistry**



Polyoxometalate Chemistry





VOLUME SIXTY NINE

ADVANCES IN  
**INORGANIC CHEMISTRY**

Polyoxometalate Chemistry

## ADVISORY BOARD

**L. H. Gade**

*Universität Heidelberg  
Germany*

**M. L. H. Green**

*University of Oxford  
Oxford, United Kingdom*

**A. E. Merbach**

*Laboratoire de Chimie et Bioanorganique EFPL,  
Lausanne, Switzerland*

**P. J. Sadler**

*University of Warwick  
Warwick, England*

**K. Wieghardt**

*Max-Planck-Institut  
Mülheim, Germany*

**D. Darensbourg**

*Texas A & M University  
College Station, Texas, USA*

**H. B. Gray**

*California Institute of Technology  
Pasadena, California, USA*

**P. A. Lay**

*University of Sydney  
Sydney, Australia*

**J. Reedijk**

*Leiden University  
Leiden, The Netherlands*

**Y. Sasaki**

*Hokkaido University  
Sapporo, Japan*

VOLUME SIXTY NINE

# ADVANCES IN INORGANIC CHEMISTRY

## Polyoxometalate Chemistry

Edited by

**RUDI van ELDIK**

*University of Erlangen–Nuremberg, Germany  
Jagiellonian University, Krakow, Poland*

**LEROY CRONIN**

*University of Glasgow, United Kingdom*



**ACADEMIC PRESS**

An imprint of Elsevier  
elsevier.com

Academic Press is an imprint of Elsevier  
50 Hampshire Street, 5th Floor, Cambridge, MA 02139, United States  
525 B Street, Suite 1800, San Diego, CA 92101-4495, United States  
The Boulevard, Langford Lane, Kidlington, Oxford, OX5 1GB, United Kingdom  
125 London Wall, London, EC2Y 5AS, United Kingdom

First edition 2017

Copyright © 2017, Elsevier Inc. All rights reserved

No part of this publication may be reproduced or transmitted in any form or by any means, electronic or mechanical, including photocopying, recording, or any information storage and retrieval system, without permission in writing from the publisher. Details on how to seek permission, further information about the Publisher's permissions policies and our arrangements with organizations such as the Copyright Clearance Center and the Copyright Licensing Agency, can be found at our website: [www.elsevier.com/permissions](http://www.elsevier.com/permissions).

This book and the individual contributions contained in it are protected under copyright by the Publisher (other than as may be noted herein).

### Notices

Knowledge and best practice in this field are constantly changing. As new research and experience broaden our understanding, changes in research methods, professional practices, or medical treatment may become necessary.

Practitioners and researchers must always rely on their own experience and knowledge in evaluating and using any information, methods, compounds, or experiments described herein. In using such information or methods they should be mindful of their own safety and the safety of others, including parties for whom they have a professional responsibility.

To the fullest extent of the law, neither the Publisher nor the authors, contributors, or editors, assume any liability for any injury and/or damage to persons or property as a matter of products liability, negligence or otherwise, or from any use or operation of any methods, products, instructions, or ideas contained in the material herein.

ISBN: 978-0-12-811105-5

ISSN: 0898-8838

For information on all Academic Press publications  
visit our website at <https://www.elsevier.com/books-and-journals>



Working together  
to grow libraries in  
developing countries

[www.elsevier.com](http://www.elsevier.com) • [www.bookaid.org](http://www.bookaid.org)

*Publisher:* Zoe Kruze

*Acquisition Editor:* Poppy Garraway

*Editorial Project Manager:* Shellie Bryant

*Production Project Manager:* Vignesh Tamil

*Cover Designer:* Greg Harris

Typeset by SPi Global, India

# CONTENTS

<i>Contributors</i>	<i>ix</i>
<i>Preface</i>	<i>xi</i>
<b>1. Exploring Self-Assembly and the Self-Organization of Nanoscale Inorganic Polyoxometalate Clusters</b>	<b>1</b>
H.N. Miras, D.-L. Long, and L. Cronin	
1. Introduction to Polyoxometalate Chemistry	2
2. From Serendipity to Directed Assembly	4
3. Synthetic Methodologies	6
4. POM-Based Supramolecular Structures	18
5. From Self-Assembled to Self-Organizing Cluster Systems	21
6. Conclusions	24
References	25
<b>2. Supramolecular Structures Formation of Polyoxometalates in Solution Driven by Counterion–Macroion Interaction</b>	<b>29</b>
Y. Gao, S.A. Eghtesadi, and T. Liu	
1. Introduction	30
2. Self-Assembly of POM Macroions Into “Blackberries”	33
3. Counterion-Mediated Self-Assembly of POM Macroions	35
4. The Kinetic Properties and Lag Phase of POM Assembly	42
5. POM–Counterion Ion Pairing in Solution	45
6. Dynamic of Alkali Counterions in POM Solution	47
7. Cation Transportation Through Blackberry “Membrane”	49
8. Selective Permeability of Uranyl Peroxide Nanocage	51
9. Self-Recognition Behaviors During Their Self-Assembly	56
10. Simulation Studies on Self-Assembly of POM Macroions	60
11. Conclusions	62
Acknowledgments	63
Reference	63
<b>3. Electron Transfer–Oxygen Transfer Reactions and Beyond With Polyoxometalates</b>	<b>67</b>
R. Neumann	
1. Mechanisms for the Aerobic Oxidation of Organic Compounds	68
2. The H <sub>5</sub> PV <sub>2</sub> Mo <sub>10</sub> O <sub>40</sub> Polyoxometalate and Electron Transfer Oxidations	70

3. The First Example of Electron Transfer–Oxygen Transfer Catalyzed by $\text{H}_5\text{PV}_2\text{Mo}_{10}\text{O}_{40}$	72
4. Oxidation of Sulfides	73
5. Oxidation of Primary and Vicinal Alcohols	76
6. Oxidation of via Activation of C–H Bonds Revisited	79
7. Insertion of Oxygen Into a Carbon–Metal Bond	84
8. The Structure of $\text{H}_5\text{PV}_2\text{Mo}_{10}\text{O}_{40}$ During the Catalytic Reaction	85
9. Conclusions	87
Acknowledgments	89
References	89
<b>4. Oxygen–Isotope Exchange and Metastable Dissociation in Oxides</b>	<b>91</b>
W.H. Casey	
1. Introduction	92
2. Broad Reactivity Trends for Dissolving Materials and Glasses	94
3. Acid–Base Chemistry and Reactivity in Niobates	98
4. The Transition to a Partly Detached Structure in $\text{MAI}_{12}$ Cations	102
5. Metastable Intermediates	105
6. Conclusions	112
Acknowledgments	113
References	113
<b>5. Polyoxometalate Multielectron Catalysts in Solar Fuel Production</b>	<b>117</b>
S.M. Lauinger, Q. Yin, Y.V. Geletii, and C.L. Hill	
1. Introduction	118
2. Definitions	119
3. Water Splitting Overview	123
4. Water Oxidation Catalysts	124
5. Water Reduction Catalysts	134
6. Immobilization of Polyoxometalate WOCs	137
7. Assessment of Catalytic Activity	143
8. Stability in POM Catalytic Systems	145
9. Conclusions	148
Acknowledgments	149
References	149



<b>6. <math>[\text{Co}_9(\text{H}_2\text{O})_6(\text{OH})_3(\text{HPO}_4)_2(\text{PW}_9\text{O}_{34})_3]^{16-}</math>: A Highly Efficient Catalyst for Water Oxidation</b>	<b>155</b>
J. Soriano-López, S. Goberna-Ferrón, J.J. Carbó, J.M. Poblet, and J.R. Galán-Mascarós	
1. Introduction	156
2. Homogeneous Electrocatalytic Water Oxidation Activity of $\text{Co}_9$	158
3. Characterization of the Catalytic Activity of $\text{Co}_9$ With $\text{NaClO}$	161
4. Stability and Solution Speciation Under Catalytic Water Oxidation Conditions	166
5. Heterogeneous WOC With Modified $\text{Co}_9$ /Carbon Paste Electrodes	171
6. Conclusions	177
References	178
<b>7. Polyoxometalate-Functionalized Nanocarbon Materials for Energy Conversion, Energy Storage, and Sensor Systems</b>	<b>181</b>
C.-G. Lin, J. Hu, and Y.-F. Song	
1. Introduction	182
2. Synthesis of the POM/Nanocarbon Composites	183
3. Applications of the POM/Nanocarbon Composites	185
4. Conclusions	208
References	209
<b>8. Design of Magnetic Polyoxometalates for Molecular Spintronics and as Spin Qubits</b>	<b>213</b>
J.J. Baldoví, S. Cardona-Serra, A. Gaita-Ariño, and E. Coronado	
1. Introduction	213
2. Relevant Precedent Studies of POMs in Molecular Magnetism	217
3. Relevance of POMs in Molecular Spintronics	232
4. Recent Advances on the Use of POMs for Quantum Computing	236
5. Concluding Remarks	243
Acknowledgments	245
References	245
<b>9. Perspectives for Polyoxometalates in Single-Molecule Electronics and Spintronics</b>	<b>251</b>
K.Y. Monakhov, M. Moors, and P. Kögerler	
1. Introduction	252
2. Basics of Molecular Spin Electronics	255

---

3. Material Requirements for Molecular Spintronics	258
4. Advantages of Magnetic Polyoxometalates	260
5. Polyoxometalates in Redox-Based Resistive Switching	277
6. Conclusions	282
Acknowledgments	283
References	283
<b>10. Nonaqueous Polyoxometalate Synthesis for Systematic Studies of Hydrolysis, Protonation, and Reduction</b>	<b>287</b>
R.J. Errington	
1. Introduction	288
2. Synthesis of Lindqvist-Type Heterometalates	289
3. Synthesis of Keggin-Type Heterometalates	299
4. Protonolysis of M–OR Bonds and Condensation	303
5. Synthesis and Reactivity of Chlorido {ClM <sub>W</sub> } Lindqvist Anions	315
6. Studies of {M <sub>W</sub> } Lindqvist Anion Protonation	319
7. Ligand Behavior of [(μ-O)(TiW <sub>5</sub> O <sub>18</sub> ) <sub>2</sub> ] <sup>6-</sup>	324
8. Reductive Transformations	327
9. Summary	332
Acknowledgments	333
References	333
<i>Index</i>	<b>337</b>
<i>Errata: Catalytic Hydrogenation of Carbon Dioxide to Formic Acid</i>	<b>345</b>

# CONTRIBUTORS

**J.J. Baldoví**

Instituto de Ciencia Molecular (ICMol), Universidad de Valencia, Paterna, Spain

**J.J. Carbó**

Universitat Rovira i Virgili, Tarragona, Spain

**S. Cardona-Serra**

Instituto de Ciencia Molecular (ICMol), Universidad de Valencia, Paterna, Spain

**W.H. Casey**

University of California, Davis, CA, United States

**E. Coronado**

Instituto de Ciencia Molecular (ICMol), Universidad de Valencia, Paterna, Spain

**L. Cronin**

WestCHEM, School of Chemistry, The University of Glasgow, Glasgow, United Kingdom

**S.A. Eghetesadi**

The University of Akron, Akron, OH, United States

**R.J. Errington**

School of Chemistry, Newcastle University, Newcastle upon Tyne, United Kingdom

**A. Gaita-Ariño**

Instituto de Ciencia Molecular (ICMol), Universidad de Valencia, Paterna, Spain

**J.R. Galán-Mascarós**

Institute of Chemical Research of Catalonia (ICIQ), Tarragona; ICREA, Passeig Lluís Companys, Barcelona, Spain

**Y. Gao**

The University of Akron, Akron, OH, United States

**Y.V. Geletii**

Emory University, Atlanta, GA, United States

**S. Goberna-Ferrón**

Institute of Chemical Research of Catalonia (ICIQ), Tarragona, Spain

**C.L. Hill**

Emory University, Atlanta, GA, United States

**J. Hu**

State Key Laboratory of Chemical Resource Engineering, Beijing University of Chemical Technology, Beijing, PR China

**P. Kögerler**

Institute of Inorganic Chemistry, RWTH Aachen University, Aachen; Peter Grünberg Institute (PGI-6), Research Centre Jülich, Jülich, Germany

**S.M. Lauinger**

Emory University, Atlanta, GA, United States

**C.-G. Lin**

State Key Laboratory of Chemical Resource Engineering, Beijing University of Chemical Technology, Beijing, PR China

**T. Liu**

The University of Akron, Akron, OH, United States

**D.-L. Long**

WestCHEM, School of Chemistry, The University of Glasgow, Glasgow, United Kingdom

**H.N. Miras**

WestCHEM, School of Chemistry, The University of Glasgow, Glasgow, United Kingdom

**K.Y. Monakhov**

Institute of Inorganic Chemistry, RWTH Aachen University, Aachen; Peter Grünberg Institute (PGI-6), Research Centre Jülich, Jülich, Germany

**M. Moors**

Peter Grünberg Institute (PGI-7), Research Centre Jülich, Jülich, Germany

**R. Neumann**

Weizmann Institute of Science, Rehovot, Israel

**J.M. Poblet**

Universitat Rovira i Virgili, Tarragona, Spain

**Y.-F. Song**

State Key Laboratory of Chemical Resource Engineering, Beijing University of Chemical Technology, Beijing, PR China

**J. Soriano-López**

Institute of Chemical Research of Catalonia (ICIQ); Universitat Rovira i Virgili, Tarragona, Spain

**Q. Yin**

Emory University, Atlanta, GA, United States

## PREFACE

Volume 69 of *Advances in Inorganic Chemistry* explores the latest trends and research results in the versatile and expanding area of Polyoxometalate Chemistry. Polyoxometalates are not only an extraordinary class of inorganic molecules with a vast range of structures, they have a seemingly never ending set of possible applications and yet still challenge our fundamental ideas of structure and bonding in inorganic chemistry. Their extraordinary potential today is matched by their history, and the growth of polyoxometalate cluster science has been made possible by advances in crystallography, mass spectroscopy, and NMR.

In [Chapter 1](#), Cronin and coworkers give an overview of the state of the art in understanding the assembly of polyoxometalate clusters. Given that polyoxometalate clusters span a large range of metal ion nuclearity and size, understanding the mechanism of assembly is a really big challenge. Indeed, how do local structure and bonding rules translate beyond a few atoms to the hundreds of heavy atoms found in a molybdenum cluster ring? Insight to this process is given along with an overview of how dynamic assembly and the self-organization of clusters across length scales is now being investigated. In [Chapter 2](#), the theme of assembly is continued beyond the supermolecule by Liu whereby the formation of polyoxometalate blackberries, i.e., super macroion interactions, is explored. This contribution shows how polyoxometalate colloids with extraordinary properties and functions can be fashioned and also demonstrates that there are new guiding principles responsible for the structuring of gigantic macroanions. In [Chapter 3](#), Neumann explores electron transfer reactions of metal oxide clusters and shows how molecular design can lead to reactivity control and small-molecule activation. The design of metal oxide catalysts and photo- and electrosystems is a very important emerging area in this context. In [Chapter 4](#), Casey summarizes recent work exploring oxygen-isotope exchange and metastable dissociation in oxides. The kinetics here provides a great insight into how metal oxides can form clusters across the periodic table not only Mo, W, but also of Nb. In [Chapter 5](#), Hill and coworkers concentrate on the explosion of work exploring polyoxometalate-based water oxidation catalysts (WOCs) and describe the synthesis, structure, and kinetic properties of a range of extremely good WOCs and also explain the prospects that understanding WOC might be important in the development of earth-abundant

development of polyoxometalates as active components in solar-fuel production. This theme is continued in [Chapter 6](#) by Poblet and coworkers who describe the detailed behavior of a specific POM-cobalt oxide WOC system. In [Chapter 7](#), Song and colleagues broaden the catalyst for energy theme to energy storage and sensors describing how POMs are being used as active components in electrode materials for batteries and electrochemical sensors. In [Chapter 8](#), Coronado and coworkers outline an ambitious plan for the use of magnetic polyoxometalate clusters as spin qubits. Driven by the discovery of POM-based single ion magnets, this is likely to become a major area of electronic nanotechnology, and [Chapter 9](#) by Kögerler and coworkers expand this to both spintronics and single-molecule electronics explaining how new types of switching behavior could lead to fundamentally new types of computing systems. Finally in [Chapter 10](#), Errington describes the fascinating developments in nonaqueous polyoxometalate synthesis and shows that hydrolysis, protonation, and reduction can be explored in organic solvents. Here, again POMs have something unique to offer both in terms of structure, mechanism, and reactivity.

We Editors are very excited by this collection of important research chapters and are grateful to the authors for their effort in producing such engaging, exciting, and cutting-edge chapters. This surely will be an important resource for the expanding number of researchers tempted to explore the riches of polyoxometalate cluster science.

R. VAN ELDIK

Editor of *Advances in Inorganic Chemistry*  
Emeritus Professor of Inorganic Chemistry,  
University of Erlangen–Nuremberg, Germany  
Professor of Inorganic Chemistry,  
Jagiellonian University, Krakow, Poland

L. CRONIN

Co-Editor of this volume  
Regius Professor of Chemistry,  
University of Glasgow, United Kingdom  
December 2016



# Exploring Self-Assembly and the Self-Organization of Nanoscale Inorganic Polyoxometalate Clusters

H.N. Miras, D.-L. Long, L. Cronin<sup>1</sup>

WestCHEM, School of Chemistry, The University of Glasgow, Glasgow, United Kingdom

<sup>1</sup>Corresponding author: e-mail address: lee.cronin@glasgow.ac.uk

## Contents

1. Introduction to Polyoxometalate Chemistry	2
1.1 Background	2
1.2 Classification of the Polyoxometalate Family	2
2. From Serendipity to Directed Assembly	4
3. Synthetic Methodologies	6
3.1 Ligands and Metal Cations as Assembly Directing Motifs	6
3.2 Templated Assembly	10
3.3 Reductively Triggered Assembly	17
4. POM-Based Supramolecular Structures	18
4.1 POM Nanostructures	18
5. From Self-Assembled to Self-Organizing Cluster Systems	21
6. Conclusions	24
References	25

## Abstract

Polyoxometalates (POMs) are a family of self-assembled molecular clusters with an unmatched range of physical properties, structural features, and sizes. The development of appropriate synthetic methodologies, analytical techniques, and approaches which allow the constructive exploration of the vast parameter space of POM chemistry is crucial for the understanding and control of the underlying complex reactions masked by the self-assembly. This chapter discusses the main aspects of the self-assembly that govern the POM-based chemical systems and the methodologies used for the generation of libraries of molecular synthons that can be used for the construction of large molecular moieties. We will illustrate how the effective combination of synthetic approaches in this area contributed to our deeper understanding of the self-assembly by revealing important mechanistic information. The final sections are devoted to discussing the self-organization of the preassembled molecular components into complex functional macrostructures.



## 1. INTRODUCTION TO POLYOXOMETALATE CHEMISTRY

### 1.1 Background

Polyoxoanions or polyoxometalates (POMs) (1) are a diverse class of anionic metal–oxo clusters constructed mainly by early transition metals (V, Nb, Ta, Mo, W) in high oxidation states. Almost two centuries have passed since the discovery of the first POM species by Berzelius in 1826 (2), and this was followed by the first detailed crystallographic characterization by Keggin (3). POMs continue to attract the attention of research groups due to their remarkable molecular and electronic structural diversity, unexpected functionalities, and their application in diverse scientific fields, e.g., catalysis, medicine, and materials science (4–6). More specifically, in the last two decades (7,8), a dramatic increase in the number of structurally characterized POM compounds due to developments in instrumentation and novel synthetic approaches has occurred. This has been driven by the development of fast and routine single crystal data collection of large and complex POM architectures in combination with advances in spectroscopic techniques such as electrospray-ionization mass spectrometry and heteronuclear NMR. As such these studies have allowed researchers to bridge the gap between solution and solid state of self-assembled chemical systems and gain insight into mechanistic aspects of the complex underlying chemical occurrences (9,10). Additionally, research has also explored the supramolecular aspects of polyoxometalate chemistry, i.e., the organization of small fragments to larger species via weak interactions (11). This idea has been driven by the thesis that even the molecular clusters can be treated as having a set of transferable building blocks that can be reliably utilized in the formation of new gigantic structures, materials, and functional supramolecular formations, triggered the rapid development of synthetic approaches in an effort to better understand the parameters that affect and control the self-assembly-governed processes.

### 1.2 Classification of the Polyoxometalate Family

There is a vast number of anionic multinuclear species which fall into the polyoxometalate category and exhibit a plethora of structural features, compositions, and sizes ranging from 1 to 5.6 nm (12). Thus, their organization in an informative manner in terms of either their reactivity, composition, or structure can be confusing or even meaningless. However, a very general



approach has been adopted in order to help the researchers make the necessary connections between the different building block types, archetypes, and physical properties. Fig. 1 presents a very broad classification of the polyoxometalate family which structurally and compositionally can be broken into three subcategories.

- (a) The first general category consists of the heteropolyanionic species which are constructed by a vanadium-, tungsten-, or molybdenum-based metal oxide framework and incorporates heteroanions such as  $\text{PO}_4^{3-}$ ,  $\text{SO}_4^{2-}$ ,  $\text{SiO}_4^{2-}$ , etc. This subgroup is by far the most explored subset of POM clusters with a wide range of structural archetypes due to the inherent stability of the generated building block libraries which arises by the incorporation of heteroanions. This is the main reason that a lot of previous research focused on the modulation of catalytic, electronic, and acidic properties of these species with great emphasis on the Keggin  $[\text{XM}_{12}\text{O}_{40}]^{n-}$  and the Wells–Dawson  $[\text{X}_2\text{M}_{18}\text{O}_{62}]^{n-}$  (where  $\text{M}=\text{W}$  or  $\text{Mo}$  and  $\text{X}=\text{PO}_4^{3-}$ ,  $\text{SO}_4^{2-}$ ,  $\text{SiO}_4^{2-}$ , etc.) anions. Moreover, the kinetic inertness of tungsten-based POMs has given the opportunity for the development of Keggin- and Dawson-based

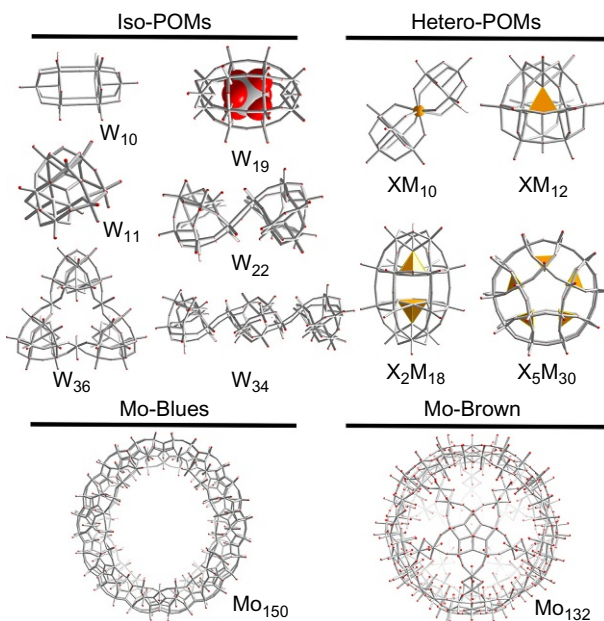


**Fig. 1** Classification of polyoxometalate clusters. The metal oxygen framework is shown in gray sticks (M, gray; O, red). The heteroatoms are shown as orange tetrahedra.

derivatives (most common are mono-, di-, and trilacunary clusters) that can be used as stable building blocks for the construction of larger aggregates in a controllable fashion (13). The development of lacunary  $\{M_{12-n}\}$  and Dawson  $\{M_{18-n}\}$ , tungsten-based polyoxometalates is a large area; however, some guiding principles will be discussed to allow the critical evaluation of the literature.

- (b) The second subset of the POM family consists of the isopolyanions where they are composed of a metal oxide framework without the incorporation of heteroatoms or heteroanions. Consequently, the members of this subset are much smaller due to the less robust structural motifs than their heteropolyanion counterparts. However, they also have interesting physical properties, while they can also be used as cluster-based building blocks in a similar manner (14).
- (c) Finally there is a third category which consists of molybdenum-based reduced POM nanosized clusters, namely, Mo-blue and Mo-brown species. These clusters have been reported for the first time in 1783 by Scheele. However, due to their gigantic size, their composition and complex structural features were extremely challenging back then to be determined by the available X-ray diffraction instruments. Thus, their exceptional size and structural complexity remained unknown until Müller *et al.* reported, in 1995, the synthesis and structural characterization of the first member of this subset which exhibited a ring topology and high nuclearity  $\{Mo_{154}\}$  (15). Following careful exploration of the experimental variables of these systems led to the discovery and proper characterization of the first member of the Mo-brown species which exhibited a porous spherical topology  $\{Mo_{132}\}$  constructed by 132 molybdenum centers and higher extend of reduction comparing to their Mo-blue counterparts (16).



## 2. FROM SERENDIPITY TO DIRECTED ASSEMBLY

The synthesis of polyoxometalate species is usually described by a series of ill-defined and confusing terms such as “one-pot” or self-assembly regarding the synthetic approach. These terms usually describe only the final outcome of a quite complicated network of interactive chemical processes giving the false impression of systems governed by simplicity, while the result is directed entirely by serendipitous and seemingly arbitrary events at the molecular level. The development in instrumentation and advances

in analytical techniques which have been discussed earlier have allowed the isolation of a huge number of structures and yielded a range of important mechanistic information which has started to contribute to our understanding of the so-called self-assembly process (17). Based on the information obtained over the years, it has become clear that the self-assembly processes often conceals very complicated networks of chemical reactions which can influence each other by acting upon the existing equilibria states via a long list of experimental variables. Indeed, these reaction equilibria will generate the pool of available building blocks to assemble into successively more complex architectures and appear to be controlled by a long list of experimental variables. It is necessary to take these variables into consideration in an effort gain insight into the assembly process, such as: (1) concentration/type of metal oxide anion, (2) pH, (3) ionic strength, (4) heteroatom type/concentration, (5) presence of additional ligands, (6) reducing environment, (7) temperature and pressure of reaction (e.g., microwave, hydrothermal, refluxing), (8) counterion and metal ion effect, and (9) processing methodology (one-pot, continuous flow conditions, 3D printing of reactionware) (6, 18–20). Thus, the careful consideration of the above experimental variables in combination with the observations from the “serendipitous” outcome of the experimental efforts led not only to discoveries of new clusters and emergence of new functionalities but also to understanding the relationship between the starting materials (metallic salts of tungsten, molybdenum, etc.), the library of building blocks generated, the architecture of the isolable POM-based compounds, and finally the potential functionality of the POM-based material.

Furthermore, knowledge so far obtained has prompted researchers to adopt a better defined synthetic approach, which utilizes preformed POM clusters as a set of transferable building blocks that can be reliably used in the formation of new materials under a given set of experimental conditions (21). In this way, POM building blocks are assembled either through M–O–M oxo bridges or by the use of metal–organic complexes as linkers. In fact, vast numbers of molybdenum- and tungsten oxide-based organic–inorganic hybrid materials are reported by various groups using metal–organic complexes/coordination polymers as linkers between POM clusters, and the number of examples is expanding seemingly at an exponential rate (22). However, the quest for a deeper understanding of the assembly of POM-based chemical systems should not be confined to the predictability of a “fully controlled” assembly process which could limit our horizons and minimize the chances of ground-breaking discoveries. The following

sections will be devoted in discussing the various synthetic methodologies which have been developed in order to improve our understanding and achieve greater control over the assembly process, while the element of “serendipity,” which leads to unexpected discoveries, feeds back into our further understanding of the assembly mechanism. Ultimately, these frameworks might even lead to predictive powers.



### 3. SYNTHETIC METHODOLOGIES

#### 3.1 Ligands and Metal Cations as Assembly Directing Motifs

One important factor that triggers the assembly of a set of building blocks into a particular POM species out of a vast number of possible candidates relates to the preferential stabilization of a specific building block library which can be used for the construction of larger aggregates. This point is brought into sharp focus when one realizes that, even though the POM's structural features usually becomes the center of the researchers' attention, these POMs are still polyanions and cannot exist without the charge balancing cations, which often define the network into which the anion is “complexed” and charge balance is achieved. In this way, the cations themselves are able to influence the existing equilibria in solution, stabilize certain building blocks, and direct the linkage of the assemblies toward the formation and crystallization of a specific compound (see Fig. 2).

Extensive research efforts over the last decade has contributed toward a better understanding regarding the counterions' crucial effect on the self-assembly process, and this goes beyond than simply maintaining the charge neutrality in the reaction mixture. Since the properties of the cations such as size, charge, coordination modes, symmetry, solubility, etc., are found to affect the reactivity, as well as the intrinsic stability of the POM building blocks, these cations can clearly affect the nature of the product obtained from a POM synthesis (23). In using a counterion-directed self-assembly approach for the construction of novel POM species, there are two important points that needs to be taken into consideration: (a) the generation of novel POM-based building block libraries and (b) promotion of their self-assembly in a controlled fashion to form novel architectures with potentially useful functionality (19a). One approach to achieve these targets is based on the use of bulky positively charged organic cations as counterions in the synthetic procedure (24–26). For instance, it has been shown that the use of bulky cations such as hexamethylene

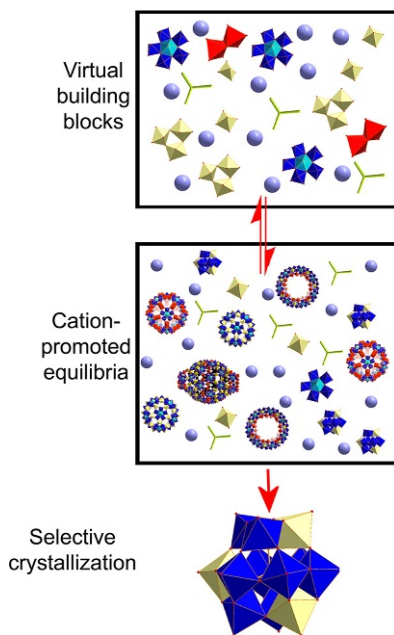


**Fig. 2** Schematic representation of the traditional “one-pot” synthesis of POM clusters leading to the formation of various structural archetypes in solution highlighting the role of counterions in selective stabilization, formation, and crystallization of a specific POM cluster.

tetramine, triethanol amine, *N,N*-bis-(2-hydroxyethyl)-piperazine, morpholine, etc., prevents the rapid aggregation of POM-based synthons into clusters of stable and uniform spherical topology. Also the use of cations in combination with transition metals as linker units is found to be capable of diversifying the population of the available constituents by stabilizing reactive secondary building units and also directing their self-assembly into novel archetypes. The second option is based on the combined use of organic ligands and additional transition metals not only as counterions but also as ligands, metal linkers, buffers, and even as redox reagents in some cases, in order to direct the self-assembly process in a completely new direction (27–29).

Extensive use of the above approach gave researchers the opportunity to isolate a number of discrete iso- and heteropolyoxometalate clusters as well as many extended architectures using this simple but efficient concept. For example, the assembly of one of the largest tungsten-based clusters,  $[\text{H}_{12}\text{W}_{92}\text{O}_{311}]^{58-}$ , was promoted by the cooperative effect of transition

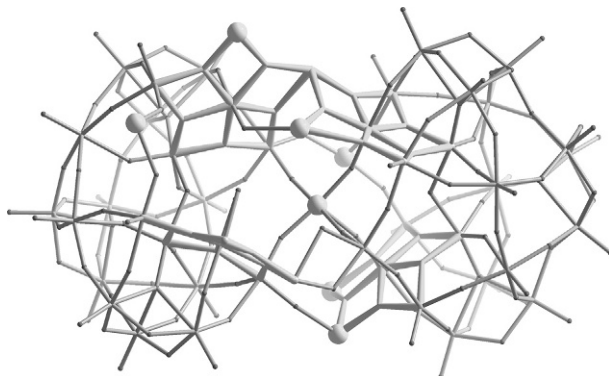


**Fig. 3** Representation of the W-only framework of the  $[H_{12}W_{92}O_{311}]^{58-}$  anion possessing  $\{W(W_5)\}$  (green) pentagonal-based synthons, shown by the *thick lines*. The  $Cu^{2+}$  metal linkers are shown as *gray spheres*. The counterions are omitted for clarity.

metal ions,  $Cu^{2+}$  and ethylenediamine molecules (Fig. 3) (30). The organic ligand was partially coordinated to some of the available  $Cu^{2+}$ -based coordination sites and triggered the formation of soluble molecular species instead of infinite frameworks. Sixteen  $Cu^{2+}$  ions per cluster which were identified by X-ray diffraction analysis were located on key positions to support the self-assembly of the metal oxide framework. The cluster is the first known example of an inorganic architecture that constructed by three types of complete and incomplete pentagonal units:  $\{W(W_5)\}$ ,  $\{W(W_4)\}$ , and  $\{W(W_3)\}$ , respectively.

Another interesting example involves the entrapment of the necessary building blocks via ligand coordination which led to the isolation of the elusive  $\delta$ -Keggin isomer which in the absence of coordinating ligands exhibits the tendency to transform into other thermodynamically stable isomers (either  $\alpha$ ,  $\beta$ ,  $\gamma$ , or  $\epsilon$ ) with similar energy activation barriers (27). In another case, utilization of acetate ligands induced the stabilization of a  $[Mn^{III}_2Mn^{IV}_2O_4]^{6+}$  cubane core grafted on a vanadium oxide fragment, giving rise to the formation of a molecular manganese vanadium oxide water-oxidation catalyst,  $[Mn_4V_4O_{17}(OAc)_3]^{3-}$  (31). Moreover, utilization of the same approach led to the formation of the gigantic  $[H_{34}W_{119}Se_8Fe_2O_{420}]^{54-}$  (30 kDa) cluster by precise control of the “one-pot” reaction conditions for the assembly a nanosized 2.8 nm POM, where Fe centers were used as appropriate linkers (32). Further exploration of the effect of the transition metal cations on the assembly process of this system led to the isolation of a whole family of nanoscaled clusters with the general

formula  $\{M_2W_nO_m(H_2O)_m(Se_2W_{29}O_{102})_4\}$ , where  $M = Mn, Co, Ni,$  or  $Zn, n = 2, m = 4;$   $M = Cu, n = 3, m = 5.$  The incorporation of additional transition metals not only generated and stabilized a novel building unit,  $\{W_{29}\},$  but also triggered its assembly into gigantic architectures up to a nuclearity of  $\{W_{174}\}$  and a mass of  $\sim 50$  kDa (Fig. 4) (33).

In addition, researchers have also exploited the effect of lanthanide cations on the assembly of POM-based systems. It was hypothesized that their high coordination numbers could generate and stabilize new building block libraries, diversify their topology, and potentially induce interesting optical and/or magnetic behavior. One of the first examples was reported in the 1990s, where Pope *et al.* discussed the synthesis and characterization of the  $[As_{12}Ce_{16}(H_2O)_{36}W_{148}O_{524}]^{76-}$  cluster. The folded cyclic structure incorporates 12  $\{AsW_9O_{33}\}$  and 4  $\{W_5O_{18}\}$  anionic subunits (34).

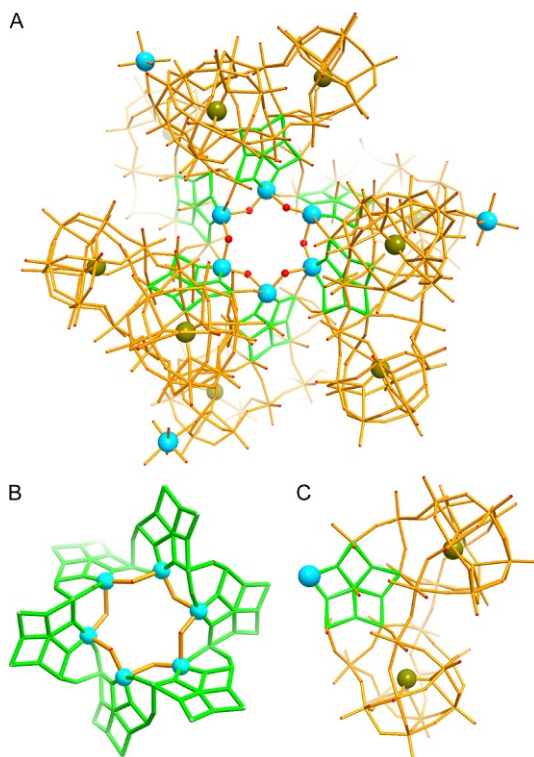


**Fig. 4** Wireframe representation of the gigantic (A)  $\{W_{174}\}$  anion exhibiting a (B) crown ether-type formation, and (C) six  $\{W_{29}\}$  building blocks assembled orthogonally on the periphery of the Cu-based crown ether formation. Se, dark yellow;  $Cu^{2+}$ , cyan; Pentagonal  $\{W(W_5)\}$  units are highlighted as green wireframe.

A few years later the same group reported the second largest tungstogermanate  $[\text{Ce}_{20}\text{Ge}_{10}\text{W}_{100}\text{O}_{376}(\text{OH})_4(\text{H}_2\text{O})_{30}]^{56-}$  which contains 20 cerium(III) centers and was synthesized by the interaction of  $\text{Ce}^{\text{III}}$  ions and  $[\alpha\text{-GeW}_9\text{O}_{34}]^{10-}$  preformed building blocks in aqueous acidic medium at pH 5.0. This can be described as a dimer that is linked through long Ce–O (W) bridges (35). The influence of the high coordination number on the generation of new building blocks and their consecutive assembly into large structures becomes obvious also from the fact that in the absence of lanthanide ions, replacement of  $\text{Ce}^{\text{III}}$  with  $\text{As}^{\text{III}}$  or  $\text{Sb}^{\text{III}}$  ions led to the formation of smaller metal oxide frameworks,  $[\text{X}_6^{\text{III}}\text{W}_{65}\text{O}_{217}(\text{H}_2\text{O})_7]^{26-}$ , where  $\text{X} = \text{As}^{\text{III}}$  or  $\text{Sb}^{\text{III}}$  constructed by  $\{\beta\text{-AsW}_9\text{O}_{33}\}$  units assembled in a different fashion (36).

### 3.2 Templated Assembly

The utilization of small inorganic anions as templates had been exploited by the research groups from the very early development stages of POM chemistry. Berzelius reported for the first time in 1826 the Keggin species,  $(\text{NH}_4)_3[\text{PMo}_{12}\text{O}_{40}]$ , followed by the structural determination of the Keggin (3). This ion has a tetrahedral symmetry with the general formula  $[\text{XM}_{12}\text{O}_{40}]^{n-}$ , where X is a heteroatom (P, Si, S, Ge, As, Co, Fe) (37) with four O atoms completing the tetrahedral geometry which templates the formation of the Keggin archetype. Later on, researchers exploited the template-based synthetic approach for the stabilization of new clusters and generate isolable building blocks deriving from the partial hydrolysis of archetype structures (Lindqvist, Keggin, Dawson) which can be assembled into more complex architectures (33,35,36). The generation of isolable lacunary-based building blocks gave the opportunity not only to direct the assembly of complex architectures but also to engineer-specific functionality to final product by stabilizing interesting metallic cores which exhibit interesting catalytic (31,38,39,[39]a,[39]b,40–42) and magnetic (20,43–45) properties, for example. In 2008, our group reported the first example of POM-based single molecule magnet (SMM) based on the trivalent lacunary  $\{\text{B-a-X}^{\text{IV}}\text{W}_9^{\text{VI}}\text{O}_{34}\}^{10-}$  polyanion. This is a representative example of effective utilization of two  $\{\text{B-a-XW}_9\text{O}_{34}\}^{10-}$  ( $\text{X} = \text{Si}$  or  $\text{Ge}$ ) polyanions to “trap” a novel mixed-valence double-cubane hexanuclear  $\{\text{Mn}_6\} = [\text{Mn}^{\text{III}}_4(\text{H}_2\text{O})_2\text{Mn}^{\text{II}}_2\text{O}_4(\text{H}_2\text{O})_2]^{8+}$  magnetic core (Fig. 5) giving rise to interesting SMM behavior.

A couple of years later, in 2011, Kortz and coworkers reported the synthesis and characterization of the tetrameric  $[\{\text{Co}_4(\text{OH})_3\text{PO}_4\}_4$



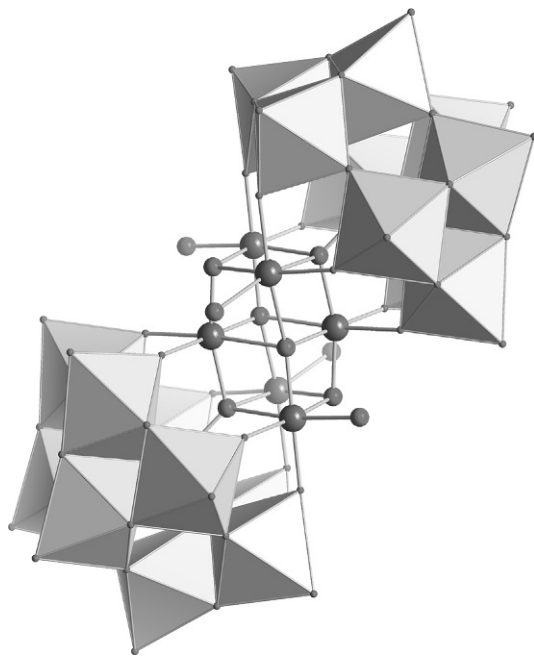


**Fig. 5** Representation of the  $[\{XW_9\}_2\{Mn_6\}]^{12-}$  SMM polyanion. The polyoxotungstate fragments are shown in polyhedral representation, and the central  $\{Mn_6O_4(OH_2)_4\}$  double-cubane cores are shown as *ball-and-stick*. Code: W, *gray polyhedra*; O, *small spheres*; Mn, *large spheres*. Counterions and protons are omitted for clarity.

$(PW_9O_{34})_4]^{28-}$  nanosized cluster which encapsulates a  $\{Co_{16}\}$  magnetic core (12). The cluster synthesized under mild conditions and comprises a central  $\{Co_4O_4\}$  cubane unit which is capped by four tricobalt(II)-substituted Keggin fragments  $[\{Co(OH)\}_3(A-\alpha-PW_9O_{34})]^{6-}$  and four phosphate linkers, resulting in an assembly with idealized  $T_d$  symmetry and is the first example of a cobalt-core-based POM with SMM behavior.

In terms of POM-based clusters which exhibit catalytic functionality, the groups of Hill *et al.* (46,47) and Bonchio *et al.* (48,49) reported their investigations into the assembly of a tetraruthenium(IV)-POM-based homogeneous catalyst for the rapid oxidation of the water. Also in this case, the POM-based lacunary building blocks allowed the incorporation and stabilization of a polynuclear ruthenium core with remarkable consequences on the cluster's catalytic activity. These studies from the two groups demonstrated that the tetra-Ru cluster  $[\{Ru_4O_4(OH)_2(H_2O)_4\}(\gamma-SiW_{10}O_{36})_2]^{10-}$  is a robust homogeneous catalyst (500 turnovers based on the evolved oxygen) which showed a remarkable rate (maximum TOF  $> 450 \text{ h}^{-1}$ ).

The effective use of “traditional” tetrahedral inorganic anions as templates has not only helped the researchers to generate useful building blocks and engineer-specific functionality but also to demonstrate the versatility offered by these libraries. This is especially true when their constituents can be assembled into gigantic structures and interconvert dynamically depending on an external chemical stimulus. This responsive nature of the POM-based libraries is an additional indication of the complex equilibria networks that coexist in solution where depending on the conditions of the chemical environment only the fittest species will prevail or will be transformed into another in order to adapt to the chemical changes that occurred. Mizuno *et al.* recently reported the disassembly and reassembly of a giant ring-shaped polyoxometalate species without isomerization of the monomeric building blocks. The reaction of a hexavacant lacunary POM-based synthon that is soluble in organic solvents,  $[P_2W_{12}O_{48}]^{14-}$ , in the presence of manganese cations as linkers led initially to the formation of a giant ring-shaped POM  $\{[\gamma-P_2W_{12}O_{48}Mn_4(C_5H_7O_2)_2(CH_3CO_2)]_6\}^{42-}$ . This POM is a hexamer of manganese-substituted  $\{P_2W_{12}O_{48}Mn_4\}$  units, which exhibits the larger reported cavity reported so far for ring-shaped polyoxotungstates. It was disassembled into monomeric units in organic medium, and the removal of the capping organic ligands on the manganese cations led to reassembly into a tetrameric ring-shaped POM,  $\{[\gamma-P_2W_{12}O_{48}Mn_4(H_2O)_6]_4(H_2O)_4\}^{24-}$  (Fig. 6) (50).

The small inorganic templates discussed earlier helped the research group generate sets of building block libraries which have used constructively for

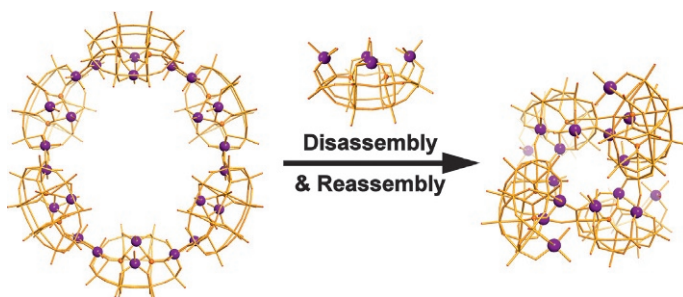


**Fig. 6** Wireframe representation of a gigantic ring made of hexameric  $\{P_2W_{12}O_{48}Mn_4\}$  units which can be disassembled into the hexavacant lacunary synthons and reassembled into a tetrameric “twisted” architecture. Mn, violet; P, orange; O, red; W, wireframe structure. The counterions and organic capping ligands (acac and acetate) are omitted for clarity.

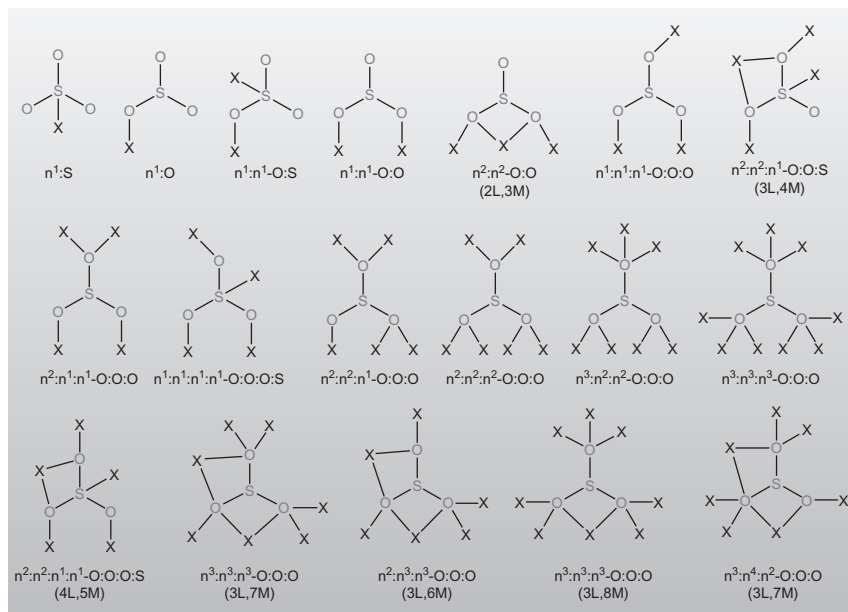


**Fig. 7** Representation of the observed coordination modes for the sulfite anion (X: transition metal and/or alkali metal).

the assembly of a vast number of POM clusters with very interesting properties. It worth noting that the templated approach so far involved small inorganic templates of tetrahedral geometry with the general formula  $\{XO_4\}$ . In an effort to generate new set of building blocks which will give rise to new clusters, Kabanos *et al.* reported (51) the use of sulfite anions as small inorganic templates for the generation of new POM species, and this was partly due to the diverse range of coordination modes (see Fig. 7).

The main advantages of the  $SO_3^{2-}$  anion are mainly focused on its ability to act as mild reducing agent, exhibit a wide range of coordination modes (Fig. 7), and could act either as ligand or linker or template and a structure directing agent (due to the lone pair of electrons). All the above attributes could introduce the necessary diversity to the POM systems which could generate new libraries of building units, as well as allow the control of the associated assembly process and engineering of functionality.

Thus, in 2002, the group reported initially a series of  $Mo - SO_3^{2-}$  compounds (52). In this work, reported the isolation and crystallographic characterization of the dodecanuclear Keggin type,  $[(Mo^V_2O_4)_6(\mu_2 - SO_3)_{12}(\mu_3 - SO_3)_4]^{20-}$  species and the  $\{Na[(Mo^V_2O_4)_3(\mu_2 - O)_3(\mu_2 - SO_3)_3$

$(\mu_6 - \text{SO}_3)_2\}^{15-}$  anion consisting of two identical hexanuclear polyoxomolybdenum(V)-sulfite anions  $[(\text{Mo}^{\text{V}}_2\text{O}_4)_3(\mu_2 - \text{O})_3(\mu_2 - \text{SO}_3)_3(\mu_6 - \text{SO}_3)]^{8-}$  linked by a sodium cation and of a dinuclear molybdenum(V) species decorated by five  $\text{SO}_3^{2-}$  anions. Further on, the same synthetic approach has been employed by the same group during for their investigations of the effect of the sulfite anion on the assembly of a vanadium-based system. The group reported a series of V-based archetypes ranging from hexanuclear cluster,  $[(\text{V}^{\text{IV}}\text{O})_6(\mu_4 - \text{O})_2(\mu_3 - \text{OH})_2(\mu_3 - \text{SO}_3)_4(\text{H}_2\text{O})_2]^{2-}$ , to open-framework 2D material  $[(\text{V}^{\text{IV}}\text{O})(\text{SO}_3)_{1.5}(\text{H}_2\text{O})]^-$ , and the 1D chain  $(4,4' - \text{Hbpy})[(\text{V}^{\text{IV}}\text{O})_6(\mu_4 - \text{O})_2(\mu_3 - \text{OH})_2(\mu_3 - \text{SO}_3)_4(\mu - \text{SO}_3)]^{3-}$  with interesting magnetic properties (Fig. 8) (53).

After the initial reports of the first members of POM-based clusters that incorporate the sulfite anion, it seemed reasonable to explore the effect of other versatile anions of pyramidal geometry such as sulfite, selenite, and tellurite or even anions with octahedral geometry such as periodate or tellurate as templates. For example, we have reported several new types of redox active anion-based hetero-POMs, where these POMs exhibit interesting thermochromic behavior or electrochemical properties related to the electron transfer reactions within the molecular cages (54). Further, it has been shown that the POM cluster  $[\text{Mo}_{18}\text{O}_{54}(\text{SO}_3)_2]^{4-}$ , which contains two embedded redox active sulfite templates, can be electronically activated by a metallic surface and can reversibly interconvert between two

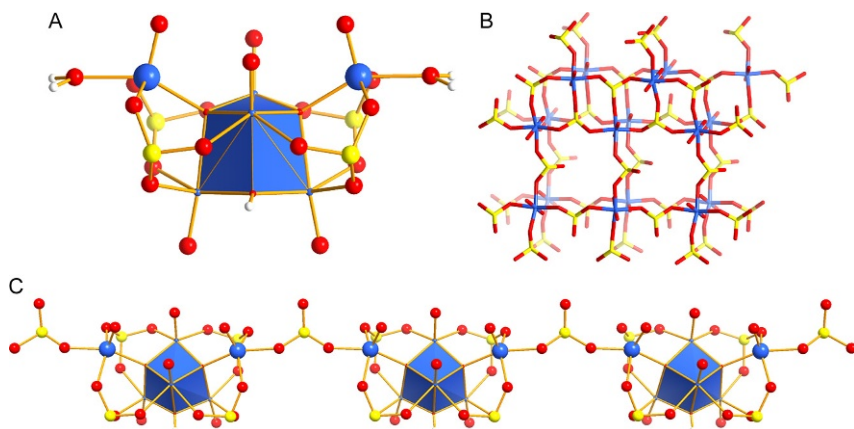


**Fig. 8** Ball-and-stick representations of: (A)  $[(\text{V}^{\text{IV}}\text{O})_6(\mu_4 - \text{O})_2(\mu_3 - \text{OH})_2(\mu_3 - \text{SO}_3)_4(\text{H}_2\text{O})_2]^{2-}$  and (B)  $[(\text{V}^{\text{IV}}\text{O})(\text{SO}_3)_{1.5}(\text{H}_2\text{O})]^-$  sulfite POMs. (C) Assembly of  $[(\text{V}^{\text{IV}}\text{O})_6(\mu_4 - \text{O})_2(\mu_3 - \text{OH})_2(\mu_3 - \text{SO}_3)_4(\text{H}_2\text{O})_2]^{2-}$  synthons into 1D chains. Color code: V, light blue; O, red; S, yellow; H, white.

electronic states (55). Recently, we extended this by the design and fabrication of flash memory devices based on Dawson-type molecular capsules templated by the redox active selenite anions (Fig. 9) (56).

The constructive use of heteroanions which exhibit pyramidal geometry has been demonstrated successfully in a number of cases recently. For example, the assembly of gigantic heteropolyoxotungstates such as  $[\text{H}_2\text{W}_{43}\text{Se}_3\text{O}_{148}]^{24-}$ ,  $[\text{H}_4\text{W}_{77}\text{Se}_5\text{O}_{265}]^{44-}$ ,  $[\text{H}_6\text{W}_{63}\text{Se}_6\text{O}_{221}]^{34-}$ , and  $[\text{H}_8\text{W}_{100}\text{Se}_{16}\text{O}_{364}]^{56-}$  was accomplished by using  $\text{SeO}_3^{2-}$  to generate in situ a new building block,  $\{\text{W}_{25}\text{Se}_3\}$ , which has been used to assemble nanosized architectures (57). Further systematic studies on the  $\text{TeO}_3^{2-}$ -based POMs have shown that the tellurite-based template gave rise to high nuclearity clusters in a similar manner. Using a time-dependent synthetic

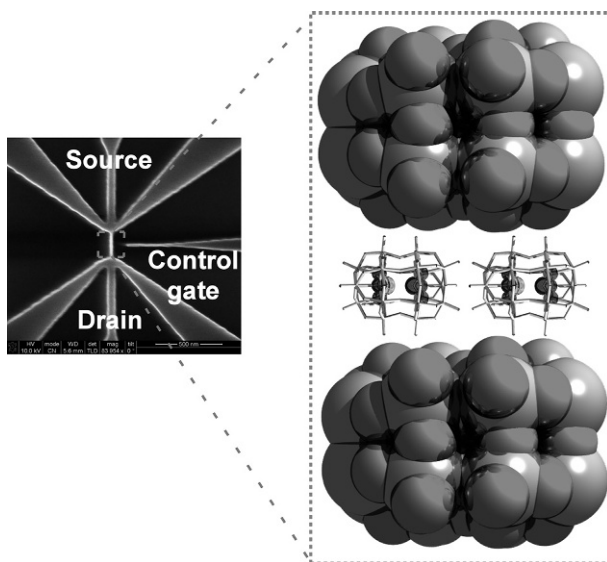


**Fig. 9** Representation of an SEM image (*left*) of the, 5-nm Si nanowire channel with side control gate. Schematic diagram representation (*right*) of a single-transistor nonvolatile memory cell, indicating the aimed substitution of the poly-Si floating gate with an array of POM clusters. Crystal structure of the core-shell cluster  $[\text{W}_{18}\text{O}_{54}(\text{SeO}_3)_2]^{4-}$  with the  $\{\text{W}_{18}\text{O}_{54}\}$  cage shown in gray colored wire representation. The two Se core dopants are shown as large spheres. In this work, it was demonstrated for the first time the use of POM-based molecular capsules could be used as an effective candidate for the storage node for a nonvolatile MOS flash memory. More specifically, it is highlighted that embedding  $\{(\text{Se}^{\text{IV}}\text{O}_3)_2\}^{4-}$  as oxidizable dopant in the molecular cage allows the oxidation of the molecule to a  $\{\text{Se}^{\text{V}}_2\text{O}_6\}^{2-}$  moiety containing a  $\{\text{Se}^{\text{V}}-\text{Se}^{\text{V}}\}$  bond and a new 5+ oxidation state for selenium, which can be observed at the device-level, resulting in a new type of “write-once-erase” memory.

approach, the construction of a new class of tungsten-based macrocyclic structures:  $[\text{W}_{28}\text{Te}_8\text{O}_{112}]^{24-}$ ,  $[\text{W}_{28}\text{Te}_9\text{O}_{115}]^{26-}$ , and  $[\text{W}_{28}\text{Te}_{10}\text{O}_{118}]^{28-}$  has been reported (58). A similar behavior has been observed in the case of mixed-metal, mixed-valence polyoxomolybdenum/vanadium-tellurite clusters such as  $[\text{Mo}^{\text{VI}}_{12}\text{V}^{\text{V}}_8\text{V}^{\text{IV}}_4\text{Te}^{\text{IV}}\text{O}_{69}(\text{Te}^{\text{IV}}\text{O}_3)_2]^{10-}$ , where it was demonstrated the cooperative effect of the counterion, along with the size of the heteroion, which allowed the discovery and isolation of this novel family of POMs (59).

The characterization of Dawson-based clusters incorporating templates of octahedral geometry  $\{\text{XO}_6\}$  was reported by our group. Following the same approach and based on the analogy of the tungstatoperiodate and tungstatotellurate compounds,  $[\text{H}_n\text{W}_{18}\text{O}_{56}(\text{XO}_6)]^{m-}$  ( $\text{X} = \text{I}^{\text{VI}}$  or  $\text{Te}^{\text{VI}}$ ), we reported the discovery of Dawson capsules which incorporate either high-valent  $\text{I}^{\text{VII}}\text{O}_6$  or the  $\text{Te}^{\text{VI}}\text{O}_6$  (60, 61). The  $[\text{H}_3\text{W}_{18}\text{O}_{56}(\text{IO}_6)]^{6-}$  anion is the first example of a  $\beta^*$ -Dawson isomer, and its electrochemical, catalytic, and DFT studies show significant differences compared with the ones observed for the conventional Dawson-type polyoxotungstates (62). Additionally, the selective reduction of the  $\gamma^*$ - $[\text{H}_3\text{W}_{18}\text{O}_{56}(\text{TeO}_6)]^{7-}$  yielded the  $[\text{H}_3\text{W}_{18}\text{Te}^{\text{IV}}\text{O}_{60}]^{5-}$  cluster, which resulted in both electronic and structural reorganizations of the Te-based anionic templates within the cluster shell. Control of the solution's pH allowed us to isolate a nanosized high-nuclearity POM polytungstate  $[\text{H}_{10}\text{Te}^{\text{VI}}_2\text{W}_{58}\text{O}_{198}]^{26-}$  anion (Fig. 10) without using additional electrophilic linkers (61).

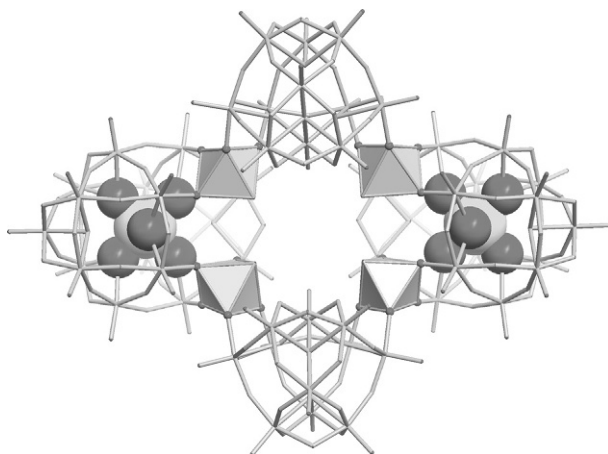


**Fig. 10** Structure of  $[\text{H}_{10}\text{Te}^{\text{VI}}_2\text{W}_{58}\text{O}_{198}]^{26-}$ . The structures are shown as *stick models* with the linking  $\{\text{WO}_6\}$  units and the embedded  $\{\text{TeO}_6\}$  groups in space-filling mode. W, gray polyhedra; O, small gray spheres; Te, large gray spheres. H atoms are omitted for clarity.

### 3.3 Reductively Triggered Assembly

The reducing environment is another approach which has been exploited by the research groups in order to promote the assembly of new POM species in solution. The main reason the reported efficacy is that the presence of vanadium(V), molybdenum(VI), or tungsten(VI) centers in acidified reducing environment has the tendency to form libraries of virtual mainly building blocks that can be used to construct large architectures. Specifically, in the case of molybdenum/tungsten(VI), demonstrated a tendency to form pentagonal building blocks which are necessary to produce curved and spherical architectures, similar to the architectures of carbon nanostructures. This structural requirement is well reported for the molybdenum blue wheels (15)  $[\text{Mo}_{154}\text{O}_{462}\text{H}_{14}(\text{H}_2\text{O})_{70}]^{14-}$  and molybdenum brown,  $[\text{Mo}_{132}\text{O}_{372}(\text{CH}_3\text{COO})_{30}(\text{H}_2\text{O})_{72}]^{42-}$ , clusters (16). The discovery of the Mo-based pentagonal units gave the opportunity for researchers to vastly expand the Mo-blue family of gigantic clusters with nuclearities up to 368 molybdenum centers and sizes comparable to the ones observed in small proteins, 5.6 nm (Fig. 11). On the other hand, the W-based pentagonal

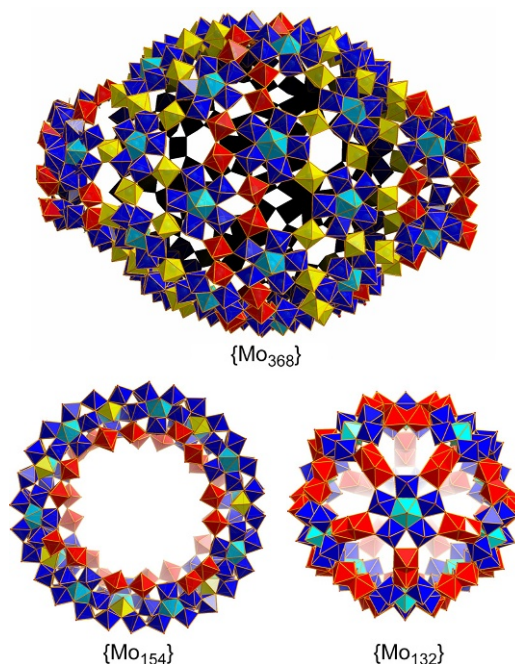


**Fig. 11** Polyhedral representation of typical archetypes observed in molybdenum blue (MB) chemistry. The sizes range from 2.9  $\{\text{Mo}_{132}\}$  and 3.6  $\{\text{Mo}_{154}\}$  to 5.6 nm  $\{\text{Mo}_{368}\}$ , respectively. The common MB virtual building blocks are highlighted as follows:  $\{\text{Mo}_2\}$ , red;  $\{\text{Mo}_1\}$ , yellow;  $\{\text{Mo}(\text{Mo}_5)\}$ , blue/cyan.

building block analog,  $\{W_6\}$ , has only recently been observed in a  $\{W_{72}Mo_{60}\}$ -type species constructed by 30  $\{Mo^V_2\}$  dimeric and 12 pentagonal  $\{W_6\}$  subunits, which represent the first examples of pentagonal  $\{W_6\}$  moiety ever discovered in polyoxometalate chemistry. These units are necessary for the formation of the spherical cluster like those of Mo analogs (63). Also, the recognition that pentagonal units can generate curved structures allows the design principles to be extended. For instance, elements like uranium should be able to form structures that can incorporate hexagonal and pentagonal units, i.e., the uranyl ion  $\{UO_2\}^{2+}$  is able to coordinate to up to six additional ligands. This idea was recently demonstrated whereby a series of ball shaped uranyl complexes, with peroxo ligands, can be obtained (64). Even though the vanadium(V) does not meet the size requirement to form a V-based pentagonal unit, still has the tendency as well to generate smaller building blocks in reducing environment which can be further assembled in smaller spherical structures and molecular cages with nuclearities up to 34 metal centers (65).

Further examples of tungsten oxide frameworks constructed by W-based building blocks have been reported recently by us. A representative example is the preparation of a gigantic isoPOM species,  $[H_{12}W_{48}O_{164}]^{28-}$ , obtained at pH 1.7 in the presence of dimethylamine hydrochloride. The solution was reduced initially to a dark blue solution by addition of sodium dithionite. The solution was stored at 4°C for a period of time, during which the tungsten centers gradually oxidized back to  $W^{6+}$ , with an associated discoloration of the solution. The initial chemical reduction step appears to be necessary for the generation of W-based pentagonal units in solution which can then be assembled further into a large iso-POM architecture (30).



## 4. POM-BASED SUPRAMOLECULAR STRUCTURES

### 4.1 POM Nanostructures

Earlier we described that polyoxometalate species are multinuclear clusters with high negative charge and usually are associated with positively charged counterions due to charge neutrality requirements, but these objects themselves can undergo several layers of assembly. This is because the associated counterions can influence the way the available building blocks are involved in various equilibria and direct their assembly toward the formation of specific large structures due to counterions'-induced electrostatic interactions and/or coordination ability.



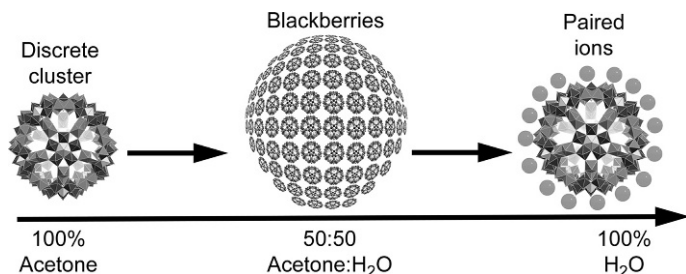


**Fig. 12** Controlled supramolecular assembly from discrete clusters to blackberry formations achieved via adjustment of the dielectric constant of the H<sub>2</sub>O/acetone solvent system.

However, as soon as the charge balanced species form into solution, the system remains in a dynamic equilibrium which can be influenced either by any potential changes of the existing chemical environment (pH, temperature, etc.) or proceed to further assembly stages which involves the molecular moieties and the solvent system to form vesicle structures (Fig. 12) (66). The combination of the large size and charges of POMs compared to usually smaller solvent molecules and the moderate amount of charges on them are crucial factors for the formation of stable supramolecular structures. In contrast to heavily charged colloidal particles which they tend to aggregate into large aggregates and precipitate, macroions (2–10 nm) behave quite differently and they tend to slowly self-assemble into a single-layered, spherical, hollow, “blackberry” type structures. The investigation of this type of macroionic “blackberry” formations along with their functionalized with organic ligands hybrids offer a great opportunity for the development of materials for catalysis, polymerization, drug delivery, and medicines.

For example, during the last few years Liu *et al.* (67) has investigated this type of dynamic assembly which has governed formation of nanoscale superstructures, so-called blackberry moieties. The responsiveness of these supramolecular structures by monitoring the continuous transition from discrete anionic clusters to blackberry structures has also been reported, and then back to discrete anionic clusters by dynamic light scattering (DLS), using a system of Keplerate-type Mo-brown clusters with the formula  $(\text{NH}_4)_{42}[\text{Mo}_{132}\text{O}_{372}(\text{CH}_3\text{COO})_{30}(\text{H}_2\text{O})_{72}] \cdot \text{ca. } 300\text{H}_2\text{O} \cdot \text{ca. } 10\text{CH}_3\text{COONH}_4 \{ \text{Mo}_{132} \}$ , in a solvent mixture of water/acetone. Fine control of the polarity of the solvent system defined by the water:acetone ratio led to the formation of blackberry type moieties with average hydrodynamic

radius ( $R_h$ ) ranging from 45 to 100 nm. Investigation of the anionic cluster—blackberry—anionic cluster transitions shed light upon the underlying driving forces behind this interesting process.

Depending on the structure of the polyanion, it could be possible to control the functionality of the either of the surface or the blackberry's interior area or even both. For example, Liu *et al.* (68) demonstrated that the microenvironment inside the self-assembled supramolecular formations made of Keplerate-based structures,  $[\text{Mo}^{\text{VI}}_{72}\text{Fe}^{\text{III}}_{30}\text{O}_{252}(\text{CH}_3\text{COO})_{12}\{\text{Mo}_2\text{O}_7(\text{H}_2\text{O})\}_2\{\text{H}_2\text{Mo}_2\text{O}_8(\text{H}_2\text{O})\}(\text{H}_2\text{O})_{91}] \{\text{Mo}_{72}\text{Fe}_{30}\}$  (69), is different from that in bulk aqueous solutions. It was also showed that the membrane-like blackberry shell allows ion transfer of small cations to the interior. If the structural features of the cluster-based synthon are modified, e.g., use of 3.6 nm size  $\{\text{Mo}_{154}\}$ -type nanowheel instead, it was observed the assembly of up to 19,000 nanowheels homogeneously distributed flat on the surface of a spherical vesicle formation with a hydrodynamic radius of  $R_h \approx 130$  nm (70).

Shortly after the first discovery and series of studies exploiting the fact that POM-based clusters can be used further as a set of transferable building blocks for the construction of nanosized and soluble supramolecular assemblies, many researchers have tried to explore the potential of hybrid POM adducts to form amphiphilic supramolecular assemblies. In this approach, inorganic–organic molecular hybrids are expected to render amphiphilic properties to the POMs and consequently improve their applications by expanding their compatibility in organic media. Furthermore, these organic ligands grafted on the metal oxide framework provide an excellent opportunity for modulating the functionality of POM-based component of the vesicle, including electronic, catalytic, and optical properties (71). An interesting example of hybrid POM clusters was reported a few years ago by us where we reported the preparation and structural characterization of two members of a new class of “inorganic–organic–inorganic” hybrid molecules synthesized by grafting the linear bis-(tris) ligands onto the  $V_3$ -capped of a Wells–Dawson-type cluster  $\text{TBA}_5\text{H}_4[\text{P}_2\text{V}_3\text{W}_{15}\text{O}_{62}]$ , ( $\text{TBA} = n\text{Bu}_4\text{N}^+$ ). These inorganic–organic–inorganic “dumb-bell” hybrids are approximately 3.4-nm long and have the ability to self-assemble into vesicles in acetone/water solutions (72). DLS studies provided the initial evidence that the formed vesicles are hollow a fact which was supported further by the TEM studies. Also in this case, the formed vesicles showed dynamic behavior in relation to the dielectric constant of the solvent medium. Varying the acetone:water ratio, it has

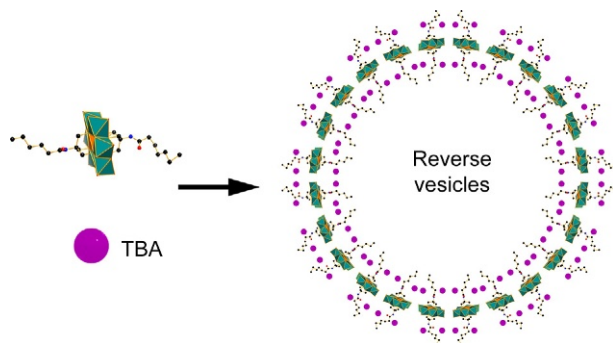


**Fig. 13** Representation of the symmetrically derivatized hybrid Mn-Anderson-Cn ( $n=6, 16$ ) and their supramolecular organization into reverse vesicles (Mn, orange; Mo, teal; O, red; C, black; N, blue; TBA =  $n\text{Bu}_4\text{N}^+$ , pink).

been observed a variation of the vesicles' size ranging from 61 to 83 nm. In another example, it was demonstrated the possibility to form reverse-vesicular structures using this time “organic–inorganic–organic” hybrid molecules synthesized by the symmetrical grafting of long alkyl chain ligands on both sides of the Mn-Anderson polyoxometalate structure leading to the formation of hybrid surfactants,  $[\text{nBu}_4\text{N}]_3[\text{MnMo}_6\text{O}_{18}\{(\text{OCH}_2)_3\text{CNHCO}(\text{CH}_2)_{n-2}\text{CH}_3\}_2]$  (Mn-Anderson-Cn,  $n=6, 16$ ), in nonpolar medium (toluene:acetonitrile). Gradual change of the solvent polarity induces self-assembly of the hydrophilic Mn-Anderson cluster on the hybrid amphiphiles (73). Moreover, it was observed that the length of the grafted alkyl chains on the hybrid surfactants had minimum effect on the vesicle sizes. It was shown that the reverse-vesicle formation process is mainly dominated by the intermolecular interactions between the polyoxometalate components (Fig. 13).

## 5. FROM SELF-ASSEMBLED TO SELF-ORGANIZING CLUSTER SYSTEMS

The intrinsic anionic nature of molecular metal oxides along with their diverse architectures, modular redox activity, as well as their multiple functionalities mean that they can reveal new and unexpected properties. In 2009, we reported a new inherent behavior for the molecular metal oxide species which involves the self-organization of cluster systems into microscaled structures with morphologies and properties that deviate from the “blackberry” and vesicle-type formations. Initially, it was demonstrated

that it is possible to fabricate POM-based tubular structures via an osmotic process resembling a type of material morphogenesis process (74). The self-assembly of these cluster anions into a molecular tube via a “chemical garden” (75) type mechanism is the first step toward constructing a molecule-based metal oxide network. Further detailed work shown that this is a general phenomenon for POMs within a critical solubility range (76). The fabrication process is promoted by an ion exchange upon slow dissolution of single crystals of POM immersed into a solution containing large organocations including several dihydroimidazo-phenanthridinium (DIP) compounds, 3,7-bis(dimethylamino)-phenothiazin-5-ium chloride (methylene blue), polymeric poly(*N*-[3-(dimethylamino)propyl]metacrylamide), and even the complex  $\text{Ru}^{\text{II}}(\text{bipy})_3(\text{BF}_4)_2$  (bipy = 2,2'-bipyridyl) followed by self-organization of the cluster-based species on a supporting surface. Moreover, we showed that microtubes can be spontaneously grow from crystals of POM-based materials with variable growth rates (1–100  $\mu\text{m/s}$ ) and with high aspect ratios ( $>10,000$ ). Interestingly, it was also demonstrated that the self-organization can be controlled utilizing “optical tweezers.” The flow patterns are generated via a laser heating process, which can easily be reconfigured in real time either by direct user input or autonomous computer controlled process, and produce a variety of architectures and patterns. The controllable micronetworks naturally form hollow tubes, allowing material to flow through them during and after fabrication (Fig. 14). This discovery opens up exciting prospects for macroscopic control of surface patterning as well as the development of multicomponent composite materials with predefined device functionality.

Building on this, it was demonstrated that the fabrication of POM-based membrane type structures with well-defined boundaries could be possible. More specifically, when the POM solution is very concentrated or the aperture is large (200  $\mu\text{m}$  or greater), the injection of POM into a cation solution does not produce microtubular formations but instead produces large membranous vesicles. In this case, the formation of membrane material can be achieved via an “extrusion/exchange” mechanism of a solution containing large metal oxide anions along with small cations into a solution containing the organic cations accompanied by small anions (77). The use of POM building blocks is very interesting since these can induce functionality to the formed inorganic chemical cells (iCHELLs), including redox, catalytic, photochemical, and magnetic properties (6). The above methodology can produce robust, spontaneously repairing membranous iCHELLs with diameters that range from 50  $\mu\text{m}$  to cell-like compartments of several millimeters. The membranous structures exhibit physical properties “inherited” by



**Fig. 14** Picture representing the transformation of crystals from their crystalline form to tubular formations upon addition of large cations to the aqueous solution in which the tubes are immersed.

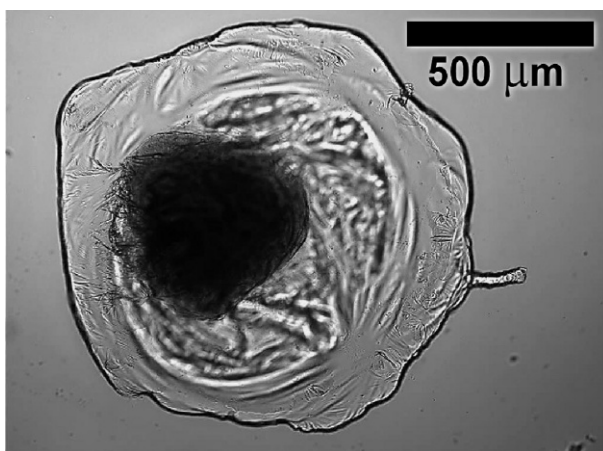


**Fig. 15** Formation of a nested membranous system. A membrane sack was first produced by injecting DIP-Me into a droplet of  $\{PMo_{12}\}$ . A second manipulator was then used to inject a solution of  $\{PW_{12}\}$ , containing a little potassium permanganate as a marker, into the DIP-Me containing sack, thus producing another compartment inside.

their molecular building blocks, such as redox activity or chiral structure. Moreover, there is the potential to partition chemical components within a system by injecting an aqueous solution of one component through a nozzle into an aqueous solution of the other, forming a closed compartment. Interestingly, they can even be nested within one another to produce clearly separated domains within a single structure (Fig. 15). Considering the vast

number and diversity of POM-cation starting materials that can be used to produce iCHELLs, there is a great opportunity for the design of functional minireactors with various in-built functionalities. This is an exciting finding which paves the way for the fabrication of diverse and easily configurable functional structures which allow designing and building membrane-based devices for future applications in energy storage, microfluidics, electronics, and catalysis.



## 6. CONCLUSIONS

There is no doubt that POMs are extremely diverse, and their dynamic nature associated with their unique chemistry often leads to new discoveries and novel phenomena. After decades of thorough investigations, it seems that the field of molecular metal oxides is now entering into a new period whereby it is possible to design and control both the structure and the function of the systems. The obvious endless structural diversity coupled with the adaptive nature of the molecular metal oxides paves the way for further development of synthetic approaches that deviate substantially from the traditional methodologies and take into consideration the adaptability of the systems. These new approaches are currently exploited in order to access new building block libraries which will lead to the formation of novel architectures and nanostructured materials possessing functionalities which are not accessible using traditional synthetic and processing techniques. Moreover, it is worth noting that polyoxometalate-based systems are ideal candidates which could help define the new field of inorganic complex synthetic systems that involves the investigation of complex equilibria networks and supramolecular organization behavior which demonstrate emergent self-organizing functionalities. Additionally, the control of the molecular assembly and the correlation of the structure with the function is the key point which will allow not only the engineering of functionality utilizing a design approach at molecular level but also the design of adaptive inorganic chemical systems which will promote the emergence of new types of inorganic matter which possess complex functionality. Finally, the ultimate challenge will be the fundamental understanding of the underlying processes and control of the dynamic changes of inorganic matter which will lead toward the development of functional molecule-based systems.

## REFERENCES

1. Pope, M. T.; Müller, A. *Angew. Chem. Int. Ed. Engl.* **1991**, *30*, 34.
2. Berzelius, J. "Poggendorff's". *Ann. Phys.* **1826**, *6*, 369–380.
3. Keggin, J. F. *Proc. Roy. Soc. A.* **1934**, *144* (851), 75.
4. Pope, M. T. *Heteropoly and Isopoly Oxometalates*, Springer-Verlag: New York, 1983.
5. Pope, M. T.; Müller, A., Eds. *Polyoxometalates: From Platonic Solids to Anti-Retroviral Activity*; Kluwer Academic Publishers: Dordrecht, The Netherlands, 1994.
6. Miras, H. N.; Yan, J.; Long, D.-L.; Cronin, L. *Chem. Soc. Rev.* **2012**, *41*, 7403.
7. Müller, A.; Roy, S. In *The Chemistry of Nanomaterials: Synthesis, Properties and Applications*; Rao, C. N. R., Müller, A., Cheetham, A. K., Eds.; Wiley-VCH: Weinheim, 2004; pp. 452–475.
8. Hill, C. L. *Chem. Rev.* **1998**, *98*, 1.
9. (a) Miras, H. N.; Wilson, E. F.; Cronin, L. *Chem. Commun.* **2009**, 1297; (b) Wilson, E. F.; Miras, H. N.; Rosnes, M. H.; Cronin, L. *Angew. Chem. Int. Ed.* **2011**, *50*, 3720.
10. Zheng, Q.; Vilà-Nadal, L.; Busche, C.; Mathieson, J. S.; Long, D.-L.; Cronin, L. *Angew. Chem. Int. Ed.* **2015**, *54*, 7895.
11. Müller, A.; Reuter, H.; Dillinger, S. *Angew. Chem. Int. Ed. Engl.* **1995**, *34*, 2328.
12. Müller, A.; Beckmann, E.; Bögge, H.; Schmidtmann, M.; Dress, A. *Angew. Chem. Int. Ed.* **2002**, *114*, 1210–1215.
13. Cronin, L. In *High Nuclearity Clusters: Iso and Heteropolyoxoanions and Relatives*; McCleverty, J. A., Meyer, T. J., Eds.; Comprehensive Coordination Chemistry II; Vol. 7, ;Elsevier: Amsterdam, 2004; pp 1–56.
14. Miras, H. N.; Yan, J.; Long, D.-L.; Cronin, L. *Angew. Chem. Int. Ed.* **2008**, *47*, 8420.
15. Müller, A.; Krickemeyer, E.; Meyer, J.; Bögge, H.; Peters, F.; Plass, W.; Diemann, E.; Nonnenbruch, F.; Randerath, M.; Menke, C. *Angew. Chem. Int. Ed.* **1995**, *34*, 2122.
16. Müller, A.; Krickemeyer, E.; Bögge, H.; Schmidtmann, M.; Peters, F. *Angew. Chem. Int. Ed.* **1998**, *37*, 3360.
17. (a) Miras, H. N.; Cooper, G. J. T.; Long, D.-L.; Bögge, H.; Müller, A.; Streb, C.; Cronin, L. *Science* **2010**, *327*, 72; (b) Miras, H. N.; Richmond, C. J.; Long, D.-L.; Cronin, L. *J. Am. Chem. Soc.* **2012**, *134*, 3816.
18. Symes, M. D.; Kitson, P. J.; Yan, J.; Richmond, C. J.; Cooper, G. J. T.; Bowman, R. W.; Vilbrandt, T.; Cronin, L. *Nature Chem.* **2012**, *4*, 349.
19. (a) Long, D.-L.; Tsunashima, R.; Cronin, L. *Angew. Chem. Int. Ed.* **2010**, *49*, 1736; (b) Pradeep, C. P.; Long, D.-L.; Cronin, L. *Dalton Trans.* **2010**, *39*, 9443.
20. (a) Ibrahim, M.; Lan, Y.; Bassil, B. S.; Xiang, Y.; Suchopar, A.; Powell, A. K.; Kortz, U. *Angew. Chem. Int. Ed.* **2011**, *50*, 4708; (b) Bassil, B. S.; Ibrahim, M.; Al-Oweini, R.; Asano, M.; Wang, Z.; van Tol, J.; Dalal, N. S.; Choi, K.-Y.; Ngo Biboum, R.; Keita, B.; Nadjjo, L.; Kortz, U. *Angew. Chem. Int. Ed.* **2011**, *50*, 5961.
21. (a) Long, D.-L.; Burkholder, E.; Cronin, L. *Chem. Soc. Rev.* **2007**, *36*, 105; (b) Long, D.-L.; Cronin, L. *Chem. Eur. J.* **2006**, *12*, 3699; (c) Kögerler, P.; Cronin, L. *Angew. Chem. Int. Ed.* **2005**, *44*, 844.
22. (a) Hargman, P. J.; Hargman, D.; Zubieta, J. *Angew. Chem. Int. Ed.* **1999**, *38*, 2638; (b) Fang, X.; Anderson, T. M.; Hill, C. L. *Angew. Chem. Int. Ed.* **2005**, *44*, 3540; (c) Wang, X.-L.; Qin, C.; Wang, E.-B.; Su, Z.-M.; Li, Y.-G.; Xu, L. *Angew. Chem. Int. Ed.* **2006**, *45*, 7411; (d) Lan, Y. Q.; Li, S. L.; Su, Z. M.; Shao, K. Z.; Ma, J. F.; Wang, X. L.; Wang, E. B. *Chem. Commun.* **2008**, 58.
23. (a) Contant, R. *Inorg. Synth.* **1990**, *27*, 109; (b) Contant, R.; Ciabrini, J.-P. *J. Chem. Res. Synop.* **1977**, *1*, 222; (c) Knoth, W. H.; Harlow, R. L. *J. Am. Chem. Soc.* **1981**, *103*, 1865; (d) Canny, J.; Tézé, A.; Thouvenot, R.; Hervé, G. *Inorg. Chem.* **1986**, *25*, 2114; (e) Kirby, J. F.; Baker, L. C. W. *Inorg. Chem.* **1998**, *37*, 5537.

24. Yan, J.; Long, D.-L.; Miras, H. N.; Cronin, L. *Inorg. Chem.* **2010**, *49*, 1819–1825.
25. Miras, H. N.; Stone, D. J.; McInnes, E. J. L.; Raptis, R. G.; Baran, P.; Chilas, G. I.; Sigalas, M. P.; Kabanos, T. A.; Cronin, L. *Chem. Commun.* **2008**, 4703.
26. Miras, H. N.; Ochoa, M. N. C.; Long, D.-L.; Cronin, L. *Chem. Commun.* **2010**, *46*, 8148.
27. Sartzi, C.; Miras, H. N.; Vilà-Nadal, L.; Long, D.-L.; Cronin, L. *Angew. Chem. Int. Ed.* **2015**, *54*, 15488.
28. Miras, H. N.; Sorus, M.; Hawckett, J.; Sells, D. O.; McInnes, E. J. L.; Cronin, L. *J. Am. Chem. Soc.* **2012**, *134*, 6980.
29. Ritchie, C.; Streb, C.; Thiel, J.; Mitchell, S. G.; Miras, H. N.; Long, D.-L.; Peacock, R. D.; McGlone, T.; Cronin, L. *Angew. Chem. Int. Ed.* **2008**, *47*, 6881.
30. Zhan, C.-H.; Winter, R. S.; Zheng, Q.; Yan, J.; Cameron, J. M.; Long, D.-L.; Cronin, L. *Angew. Chem. Int. Ed.* **2015**, *54*, 14308.
31. Schwarz, B.; Forster, J.; Goetz, M. K.; Yücel, D.; Berger, C.; Jacob, T.; Streb, C. *Angew. Chem. Int. Ed.* **2016**, *55*, 6329.
32. Yan, J.; Gao, J.; Long, D.-L.; Miras, H. N.; Cronin, L. *J. Am. Chem. Soc.* **2010**, *132*, 11410.
33. Gao, J.; Yan, J.; Beeg, S.; Long, D.-L.; Cronin, L. *J. Am. Chem. Soc.* **2013**, *135*, 1796.
34. Wassermann, K.; Dickman, M. H.; Pope, M. T. *Angew. Chem. Int. Ed. Engl.* **1997**, *36*, 1445.
35. Bassil, B. S.; Dickman, M. H.; Römer, I.; von der Kammer, B.; Kortz, U. *Angew. Chem. Int. Ed.* **2007**, *46*, 6192.
36. Kortz, U.; Savelieff, M. G.; Bassil, B. S.; Dickman, M. H. *Angew. Chem. Int. Ed.* **2001**, *40*, 3384.
37. Server-Carrió, J.; Bas-Serra, J.; González-Núñez, M. E.; García-Gastaldi, A.; Jameson, G. B.; Baker, L. C. W.; Acerete, R. *J. Am. Chem. Soc.* **1999**, *121*, 977.
38. Dzhumakaeva, B. S.; Golodov, W. A. *J. Mol. Catal.* **1986**, *35*, 303.
39. (a) Harrup, M. K.; Hill, C. L. *Inorg. Chem.* **1994**, *33*, 5448; (b) Harrup, M. K.; Hill, C. L. *J. Mol. Catal. A Chem.* **1996**, *106*, 57.
40. Neumann, R.; Levin, M.; Simandi, L. I., Eds. *Dioxygen Activation and Homogeneous Catalytic Oxidation*; Elsevier: Amsterdam, 1991; p 121.
41. Mizuno, N.; Suh, D. J.; Han, W.; Kudo, T. *J. Mol. Catal. A Chem.* **1996**, *114*, 309.
42. Khenkin, A. M.; Neumann, R. *J. Am. Chem. Soc.* **2004**, *126*, 6356.
43. Compain, J.-D.; Mialane, P.; Dolbecq, A.; Mbomekalle, I. M.; Marrot, J.; Sécheresse, F.; Rivière, E.; Rogez, G.; Wernsdorfer, W. *Angew. Chem. Int. Ed.* **2009**, *48*, 3077.
44. Fang, X.; Kögerler, P.; Speldrich, M.; Schilder, H.; Luban, M. *Chem. Commun.* **2012**, *48*, 1218.
45. Ritchie, C.; Ferguson, A.; Nojiri, H.; Miras, H. N.; Song, Y.-F.; Long, D.-L.; Burkholder, E.; Murrie, M.; Kögerler, P.; Brechin, E. K.; Cronin, L. *Angew. Chem. Int. Ed.* **2008**, *47*, 5609.
46. Botar, B.; Kögerler, P.; Hillesheim, D. A.; Musaev, D. G.; Hill, C. L. *Angew. Chem. Int. Ed.* **2008**, *47*, 3896.
47. Geletii, Y. V.; Besson, C.; Hou, Y.; Yin, Q. S.; Musaev, D. G.; Quinonero, D.; Cao, R.; Hardcastle, K. I.; Proust, A.; Kögerler, P.; Hill, C. L. *J. Am. Chem. Soc.* **2009**, *131*, 17360.
48. Sartorel, A.; Carraro, M.; Scorrano, G.; De Zorzi, R.; Geremia, S.; McDaniel, N. D.; Bernhard, S.; Bonchio, M. *J. Am. Chem. Soc.* **2008**, *130*, 5006.
49. Sartorel, A.; Miró, P.; Salvadori, E.; Romain, S.; Carraro, M.; Scorrano, G.; Di Valentin, M.; Llobet, A.; Bo, C.; Bonchio, M. *J. Am. Chem. Soc.* **2009**, *131*, 16051.



50. Minato, T.; Suzuki, K.; Yamaguchi, K.; Mizuno, N. *Angew. Chem. Int. Ed.* **2016**, *55*, 9630.
51. Miras, H. N.; Chilas, G.; Cronin, L.; Kabanos, T. A. *Eur. J. Inorg. Chem.* **2013**, 1620.
52. Manos, M. J.; Woollins, J. D.; Slawin, A. M. Z.; Kabanos, T. A. *Angew. Chem. Int. Ed.* **2002**, *41*, 2801.
53. (a) Manos, M. J.; Miras, H. N.; Tangoulis, V.; Woollins, J. D.; Slawin, A. M. Z.; Kabanos, T. A. *Angew. Chem. Int. Ed.* **2003**, *42*, 425; (b) Chilas, G. I.; Miras, H. N.; Manos, M. J.; Woollins, J. D.; Slawin, A. M. Z.; Stylianou, M.; Keramidis, A. D.; Kabanos, T. A. *Pure Appl. Chem.* **2005**, *77*, 1529; (c) Miras, H. N.; Raptis, R. G.; Lalioti, N.; Sigalas, M. P.; Baran, P.; Kabanos, T. A. *Chem. Eur. J.* **2005**, *11*, 2295.
54. Long, D.-L.; Kögerler, P.; Cronin, L. *Angew. Chem. Int. Ed.* **2004**, *43*, 1817.
55. Fleming, C.; McMillan, N.; Johnston, J.; Bovet, N.; Dhanak, V.; Gadegaard, N.; Kögerler, P.; Kadodwala, M. *Nat. Nanotech.* **2008**, *3*, 229.
56. Busche, C.; Vilà-Nadal, L.; Yan, J.; Miras, H. N.; Long, D.-L.; Georgiev, V. P.; Asenov, A.; Pedersen, R. H.; Gadegaard, N.; Mirza, M. M.; Paul, D. J.; Poblet, J. M.; Cronin, L. *Nature* **2014**, *515*, 545.
57. Yan, J.; Long, D.-L.; Cronin, L. *Angew. Chem. Int. Ed.* **2010**, *49*, 4117.
58. Gao, J.; Yan, J.; Mitchell, S. G.; Miras, H. N.; Boulay, A. G.; Long, D.-L.; Cronin, L. *Chem. Sci.* **2011**, *2*, 1502.
59. Corella-Ochoa, M. N.; Miras, H. N.; Kidd, A.; Long, D.-L.; Cronin, L. *Chem. Commun.* **2011**, *47*, 8799.
60. Long, D.-L.; Song, Y.-F.; Wilson, E. F.; Kögerler, P.; Guo, S. X.; Bond, A. M.; Hargreaves, J. S. J.; Cronin, L. *Angew. Chem. Int. Ed.* **2008**, *47*, 4384.
61. Yan, J.; Long, D.-L.; Wilson, E. F.; Cronin, L. *Angew. Chem. Int. Ed.* **2009**, *48*, 4376.
62. Vila-Nadal, L.; Mitchell, S. G.; Long, D.-L.; Rodriguez-Fortea, A.; Lopez, X.; Poblet, J. M.; Cronin, L. *Dalton Trans.* **2012**, *41*, 2264.
63. Schäffer, C.; Merca, A.; Bögge, H.; Todea, A. M.; Kistler, M. L.; Liu, T. B.; Thouvenot, R.; Gouzerh, P.; Müller, A. *Angew. Chem. Int. Ed.* **2009**, *48*, 149.
64. Simon, G. E.; Unruh, D. K.; Ling, J.; Weaver, B.; Ward, M.; Pressprich, L.; Simonetti, A.; Burns, P. C. *Angew. Chem. Int. Ed.* **2009**, *48*, 2737.
65. Müller, A.; Rohlfing, R.; Doring, J.; Penk, M. *Angew. Chem. Int. Ed. Engl.* **1991**, *30*, 588.
66. Liu, T. *J. Am. Chem. Soc.* **2002**, *124*, 10942.
67. Kistler, M. L.; Bhatt, A.; Liu, G.; Casa, D.; Liu, T. *J. Am. Chem. Soc.* **2007**, *129*, 6453.
68. Mishra, P. P.; Pigga, J.; Liu, T. *J. Am. Chem. Soc.* **2008**, *130*, 1548.
69. Müller, A.; Sarkar, S.; Shah, S. Q. N.; Bögge, H.; Schmidtmann, M.; Sarkar, S.; Kögerler, P.; Hauptfleisch, B.; Trautwein, A. X.; Schünemann, V. *Angew. Chem. Int. Ed.* **1999**, *38*, 3238.
70. Liu, T.; Diemann, E.; Li, H.; Dress, A. W. M.; Müller, A. *Nature* **2003**, *426*, 59.
71. Yamase, T. *Mol. Eng.* **1993**, *3*, 241.
72. Pradeep, C. P.; Misrahi, M. F.; Li, F.-Y.; Zhang, J.; Xu, L.; Long, D.-L.; Liu, T.; Cronin, L. *Angew. Chem. Int. Ed.* **2009**, *48*, 8309.
73. Zhang, J.; Song, Y.-F.; Cronin, L.; Liu, T. *Chem. Eur. J.* **2010**, *16*, 11320.
74. Ritchie, C.; Cooper, G. J. T.; Song, Y.-F.; Streb, C.; Yin, H.; Parenty, A. D. C.; MacLaren, D. A.; Cronin, L. *Nature Chem.* **2009**, *1*, 47.
75. (a) Collins, C.; Zhou, W.; Mackay, A. K.; Klinowski, J. *Chem. Phys. Lett.* **1998**, *286*, 88; (b) Cartwright, J. H. E.; Garci-Ruiz, J. M.; Novella, M. L.; Otálora, F. J. *Colloid Interface Sci.* **2002**, *256*, 351; (c) Barge, L. M.; Cardoso, S. S. S.; Cartwright, J. H. E.; Cooper, G. J. T.; Cronin, L.; De Wit, A.; Dolobo, I. J.; Escribano, B.; Goldstein, R. E.; Haudin, F.; Jones, D. E. H.; Mackay, A. L.; Maselko, J.;

- Pagano, J. J.; Pantaleone, J.; Russell, M. J.; Sainz-Díaz, C. I.; Steinbock, O.; Stone, D. A.; Tanimoto, Y.; Thomas, N. L. *Chem. Rev.* **2015**, *115*, 8652.
76. (a) Cooper, G. J. T.; Boulay, A. G.; Kitson, P. J.; Ritchie, C.; Richmond, C. J.; Thiel, J.; Gabb, D.; Eadie, R.; Long, D.-L.; Cronin, L. J. *Am. Chem. Soc.* **2011**, *133*, 5947;  
(b) Points, L. J.; Cooper, G. J. T.; Dolbecq, A.; Mialane, P.; Cronin, L. *Chem. Commun.* **2016**, *52*, 1911.
77. Cooper, G. J. T.; Kitson, P. J.; Winter, R. S.; Zagnoni, M.; Long, D.-L.; Cronin, L. *Angew. Chem. Int. Ed.* **2011**, *50*, 10373.



# Supramolecular Structures Formation of Polyoxometalates in Solution Driven by Counterion–Macroion Interaction

Y. Gao, S.A. Eghtesadi, T. Liu<sup>1</sup>

The University of Akron, Akron, OH, United States

<sup>1</sup>Corresponding author: e-mail address: tliu@uakron.edu

## Contents

1. Introduction	30
2. Self-Assembly of POM Macroions Into “Blackberries”	33
3. Counterion-Mediated Self-Assembly of POM Macroions	35
3.1 Driving Force for Blackberry Formation	35
3.2 Counterion Distribution in POM Solutions	37
3.3 Counterion Exchange Around POMs	39
3.4 Self-Assembly With Anisotropic Surface Charge Density Distribution	41
4. The Kinetic Properties and Lag Phase of POM Assembly	42
5. POM–Counterion Ion Pairing in Solution	45
6. Dynamic of Alkali Counterions in POM Solution	47
7. Cation Transportation Through Blackberry “Membrane”	49
8. Selective Permeability of Uranyl Peroxide Nanocage	51
8.1 Role of Hydration Layer in Selective Permeability of U <sub>60</sub>	51
8.2 Controlling the Ion Selectivity of U <sub>60</sub>	53
9. Self-Recognition Behaviors During Their Self-Assembly	56
10. Simulation Studies on Self-Assembly of POM Macroions	60
11. Conclusions	62
Acknowledgments	63
Reference	63

## Abstract

Hydrophilic macroions, represented by polyoxometalate (POM) clusters, demonstrate unique solution behaviors that are clearly different from simple ions or colloids. Almost all their special features are related to the interaction between the macroions and their counterions, such as their self-assembly into single-layered, hollow, spherical “blackberry” structures in solution due to the counterion-mediated attraction based upon the moderate counterion association around the POM macroions. The delicate

macroion-counterion interaction, including the related partial or complete breakage of the water ligands around both parties, enables the macroions to accurately distinguish different types of counterions based on their valence and hydrated size. POM macroions show many amazing properties shared with biological macromolecules, such as ion selectivity, similar kinetic features with the virus capsid formation and the strict self-recognition phenomenon. Understanding and controlling the POM-counterion interactions, such as the distribution of the counterions around and inside the POMs, the counterion exchange near the POMs, as well as the POM-POM interaction in the presence of counterions, is the key to understand the POM solutions and consequently to rationally design functional systems.



## 1. INTRODUCTION

Macroions are a large group of soluble species with sizes vary between simple ions and large colloids that demonstrate different solution properties from the other two types, represented by polyoxometalate (POM) molecular clusters, metal organic nanocages, dendrimers, and biomacromolecules. Macroions show promising technological and biological properties in both scientific and industrial realms such as electronics (1,2), drug delivery (3,4), water treatment (5), and catalysis (6). The size of macroions are too big to be treated as point charges like simple ions, whose solution behaviors can be described by well-known Debye-Huckel theory. Meanwhile, as most macroions are highly soluble in solution due to their inherent charges, they can form homogeneous “real solutions,” which distinguish them from those large, thermodynamically unstable colloidal particles that are guided by the Derjaguin-Landau-Verwey-Overbeek (DLVO) theory (7,8). How to precisely describe the behaviors of complex solutions such as proteins, DNA, RNA, or polyelectrolytes in a systematical way has always been challenging, due to the complicated intermolecular and intramolecular interactions caused by chain entanglements, sample polydispersity, poor stability, and so on (7,8).

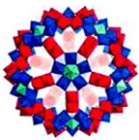
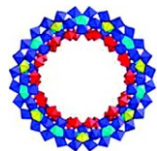
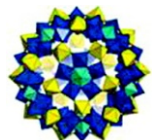
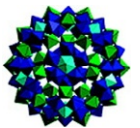
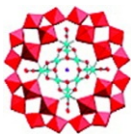
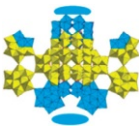
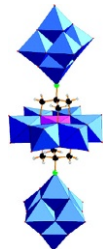
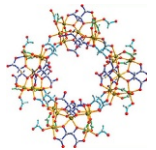
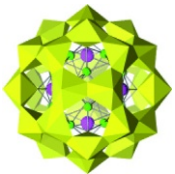
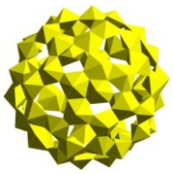
Among the above-mentioned macroions, POMs can serve as a perfect model for the macroion solution study. POMs are a large group of metal oxide clusters with covalently linked metal oxide polyhedra as building blocks (9). In the past decades, extensive synthesis efforts have provided substantial traditional transition-metal POMs macroions with different size, shape, and charges (10–17). Moreover, the discovery and development of actinyl peroxide POMs chemistry also demonstrate promising future applications (18) (Table 1). They are usually highly stable and monodispersed in

**Table 1** Formulas of POM Macroions

Abbreviation	Formula	Refs.
{Mo <sub>132</sub> }	(NH <sub>4</sub> ) <sub>42</sub> [ { (Mo <sup>VI</sup> )Mo <sup>V</sup> <sub>15</sub> O <sub>21</sub> (H <sub>2</sub> O) <sub>6</sub> } <sub>12</sub> { Mo <sub>2</sub> O <sub>4</sub> (CH <sub>3</sub> COOH) } <sub>30</sub> ] · ca. 300H <sub>2</sub> O · ca. 10CH <sub>3</sub> COONH <sub>4</sub>	(15)
{Mo <sub>154</sub> }	Na <sub>15</sub> [ Mo <sub>154</sub> O <sub>462</sub> H <sub>14</sub> (H <sub>2</sub> O) <sub>70</sub> ] <sub>0.5</sub> [ Mo <sub>152</sub> O <sub>457</sub> H <sub>14</sub> (H <sub>2</sub> O) <sub>68</sub> ] <sub>0.5</sub> · ca. 400H <sub>2</sub> O	(12)
{Mo <sub>72</sub> Fe <sub>30</sub> }	[ Mo <sup>VI</sup> <sub>72</sub> Fe <sup>III</sup> <sub>30</sub> O <sub>252</sub> (CH <sub>3</sub> COO) <sub>12</sub> { Mo <sub>2</sub> O <sub>7</sub> (H <sub>2</sub> O) } <sub>2</sub> { H <sub>2</sub> Mo <sub>2</sub> O <sub>8</sub> (H <sub>2</sub> O) } (H <sub>2</sub> O) <sub>91</sub> ] · ca. 150H <sub>2</sub> O	(10)
{Mo <sub>72</sub> V <sub>30</sub> }	Na <sub>8</sub> K <sub>14</sub> (VO) <sub>2</sub> [ { (Mo <sup>VI</sup> )Mo <sup>VI</sup> <sub>5</sub> O <sub>21</sub> (H <sub>2</sub> O) <sub>3</sub> } <sub>10</sub> { (Mo <sup>VI</sup> )Mo <sup>VI</sup> <sub>5</sub> O <sub>21</sub> (H <sub>2</sub> O) <sub>3</sub> (SO <sub>4</sub> ) } <sub>2</sub> { V <sup>IV</sup> O(H <sub>2</sub> O) } <sub>20</sub> { V <sup>IV</sup> O } <sub>10</sub> ( { KSO <sub>4</sub> } <sub>5</sub> ) <sub>2</sub> ] · ca. 150H <sub>2</sub> O	(16)
{Cu <sub>20</sub> P <sub>8</sub> W <sub>48</sub> }	K <sub>12</sub> Li <sub>13</sub> [ Cu <sub>20</sub> Cl(OH) <sub>24</sub> (H <sub>2</sub> O) <sub>12</sub> (P <sub>8</sub> W <sub>48</sub> O <sub>184</sub> ) ] · 22H <sub>2</sub> O	(13)
{Mn <sub>40</sub> P <sub>32</sub> W <sub>224</sub> }	K <sub>56</sub> Li <sub>74</sub> H <sub>22</sub> [Mn <sub>40</sub> <sup>III</sup> P <sub>32</sub> W <sub>224</sub> <sup>VI</sup> O <sub>888</sub> ] <sup>152-</sup> · ca. 680H <sub>2</sub> O	(19)
LAL(X)	((C <sub>4</sub> H <sub>9</sub> ) <sub>4</sub> N) <sub>7</sub> <sup>-</sup> [ Mo <sub>6</sub> O <sub>18</sub> NC(OCH <sub>2</sub> ) <sub>3</sub> XMo <sub>6</sub> O <sub>18</sub> (OCH <sub>2</sub> ) <sub>3</sub> CNMo <sub>6</sub> O <sub>18</sub> ] (X = Mn <sup>III</sup> or Fe <sup>III</sup> )	(20)
L/D-Fe <sub>28</sub>	[ Fe <sub>28</sub> (μ <sub>3</sub> -O) <sub>8</sub> (Tart) <sub>16</sub> (HCOO) <sub>24</sub> ] <sup>20-</sup> (Tart = D-(S,S)-(-)-tartaric acid tetra-anion or Tart = L-(R,R)-(+)-tartaric acid tetra-anion)	(21)
U <sub>28</sub>	Cs <sub>15</sub> [ (Ta(O <sub>2</sub> ) <sub>4</sub> )Cs <sub>4</sub> K <sub>12</sub> (UO <sub>2</sub> (O <sub>2</sub> ) <sub>1.5</sub> ) <sub>28</sub> ] · 20H <sub>2</sub> O (CsKU <sub>28</sub> ) Na <sub>6</sub> K <sub>9</sub> [ (Ta(O <sub>2</sub> ) <sub>4</sub> )Rb <sub>4</sub> Na <sub>12</sub> (UO <sub>2</sub> (O <sub>2</sub> ) <sub>1.5</sub> ) <sub>28</sub> ] · 20H <sub>2</sub> O (RbNaU <sub>28</sub> )	(22)
U <sub>60</sub>	Li <sub>48+m</sub> K <sub>12</sub> (OH) <sub>m</sub> [ UO <sub>2</sub> (O <sub>2</sub> )(OH) ] <sub>60</sub> -(H <sub>2</sub> O) <sub>n</sub> (m ≈ 20 and n ≈ 310)	(23)

Continued

Table 1 Formulas of POM Macroions—cont'd

Abbreviation	Formula	Refs.		
<b>Molecular structure</b>				
				
{Mo <sub>132</sub> }	{Mo <sub>154</sub> }	{Mo <sub>72</sub> Fe <sub>30</sub> }	{Mo <sub>72</sub> V <sub>30</sub> }	{Cu <sub>20</sub> P <sub>8</sub> W <sub>48</sub> }
				
{Mn <sub>40</sub> P <sub>32</sub> W <sub>224</sub> }	LAL(X)	L(D)-Fe <sub>28</sub>	U <sub>28</sub>	U <sub>60</sub>

solution with rigid structure, tunable charges, and no intermolecular interaction. Counterions have been proved to play a vital role in directing the solution behaviors of POM macroions by regulating POMs' charge density and surface properties (7,8). Understanding the POM-counterion interaction is crucial for exploring and predicting the solution behaviors of the entire family of macroions.

## 2. SELF-ASSEMBLY OF POM MACROIONS INTO "BLACKBERRIES"

The self-assembly behaviors of POMs molecules in solution are directly related to the POM-counterion interaction. POM macroions can strongly attract each other and form large supramolecular structures when dissolved in aqueous solution, although the solubility of those POMs can be quite high (24). Those large assemblies in solution can be characterized by laser light scattering. Properties like radius of gyration ( $R_g$ ) and molecular weight ( $M_w$ ) can be determined by static light scattering (SLS) through measuring the angular dependence of scattering intensity of the supramolecular assemblies in solution. By analyzing the intensity-intensity time correlation function, the hydrodynamic radius ( $R_h$ ), and particle size distribution will be obtained by dynamic light scattering (DLS) measurements.

It was discovered that many large assemblies form in a 0.010 mg/mL  $\{\text{Mo}_{154}\}$  aqueous solution when pH 3.0 at room temperature (25). As shown in Fig. 1A, transmission electron microscopy (TEM) images demonstrated that the assemblies were spherical and their sizes are relatively uniform (ca. 90 nm). In addition, an atomic force microscopy study showed that those spherical assemblies will suddenly burst shifting from normal mode to vacuum mode, indicating that they might be hollow. As the solubility of  $\{\text{Mo}_{154}\}$  clusters in aqueous solution can be as high as 100 mg/mL at room temperature, those large "aggregates" were not expected.

To further understand the nature of those structures, DLS and SLS measurements were applied. A CONTIN analysis of the DLS results suggested that  $R_h$  of those assemblies is around 45 nm, and the size distribution is very narrow, which is consistent with the previous TEM images. The SLS result, analyzed by Zimm plot, showed that the  $R_g$  of assembled structures is about 45 nm (Fig. 1B). The ratio of  $R_g/R_h \sim 1$  suggests that those spheres should be hollow ( $R_g/R_h \sim 0.77$  if they are solid). An average  $M_w$  of

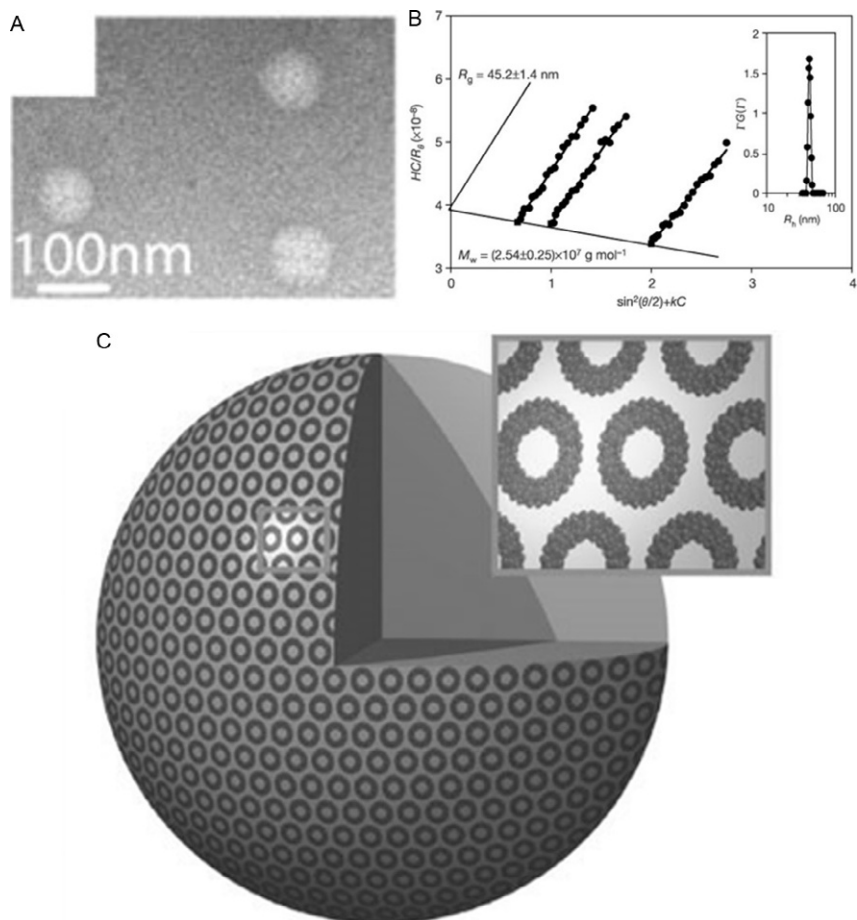


**Fig. 1** (A) TEM image on dilute aqueous solution of  $\{\text{Mo}_{154}\}$  macroions showing the existence of spherical assemblies. (B) Zimm plot based on the SLS study of the  $\{\text{Mo}_{154}\}$  aqueous solutions at pH 3; (*inset*) CONTIN analysis on the DLS study of the same solution. (C) Proposed model for blackberry structure formed by  $\{\text{Mo}_{154}\}$  macroions in aqueous solution.

$\sim(2.54 \pm 0.25) \times 10^7$  g/mol was also obtained using Zimm plot, which is equivalent to around 1150  $\{\text{Mo}_{154}\}$  clusters. It was calculated by comparing this value to the overall size of these assemblies that the  $\{\text{Mo}_{154}\}$  clusters can only cover one layer of the sphere while the neighboring  $\{\text{Mo}_{154}\}$  are not touching each other. Summarized from earlier, the proposed model for these assemblies is shown in Fig. 1C. For these spherical, single-layered, hollow structures, a nickname “blackberry” was given. Although the blackberry



structures looks very similar to vesicles, these two structures are fundamentally different: the blackberries are single layered rather than double layered, and the shell is composed of pure hydrophilic molecules instead of amphiphilic surfactants.



### 3. COUNTERION-MEDIATED SELF-ASSEMBLY OF POM MACROIONS

Debye–Hückel theory successfully describes the dilute solutions of simple ions by assuming both cations and anions are point charges. In colloidal solutions, the counterions are too small compared to colloidal particles so that they can also be treated as point charges, as reflected by the DLVO Theory. In macroion systems, although the size disparity between POMs and simple ions still exist, their sizes are more comparable, and the significance of electrostatic interaction should be reconsidered when investigating their solution behaviors. For colloidal systems, the interparticle interaction is expected to be achieved by a balance of attractive van der Waals forces and the repulsive electrical double-layer forces according to the DLVO theory. However, in macroion systems, interactions between those giant charged particles show substantial deviations from DLVO expectation. Due to the obvious charge-regulated self-assembly behaviors of POM macroions (26–28), the counterion-mediated attraction is believed to be potential driving force. Sogami and Ise developed a general theory on the electrostatic interaction in macroionic solution and proposed the existence of long-range weak attractions introduced by counterions in the colloidal systems (29).

#### 3.1 Driving Force for Blackberry Formation

One of the most crucial issue need to be addressed for the blackberry formation process is that what is the driving force to bring the purely hydrophilic, negatively charged POM macroions together in aqueous solution. An experiment with  $\{\text{Mo}_{132}\}$  can help to explain this issue (28).  $\{\text{Mo}_{132}\}$  is a type of molybdenum brown “Keplerate” anions with 42 negative charges and a diameter of around 2.9 nm. Each  $\{\text{Mo}_{132}\}$  is composed of 12 pentagonal  $\{(\text{Mo}^{\text{VI}})\text{Mo}^{\text{VI}}_5\}$ , which are connected by 30  $\text{Mo}^{\text{V}}_2$  linkers (15).  $\{\text{Mo}_{132}\}$  are highly soluble in water. Both SLS and DLS study reveal that no large assemblies will form in dilute  $\{\text{Mo}_{132}\}$  solution. However, when 1.0 mg/mL  $\{\text{Mo}_{132}\}$  macroions are dissolved in water/acetone mixture, blackberries can be observed. The size of blackberries will increase from

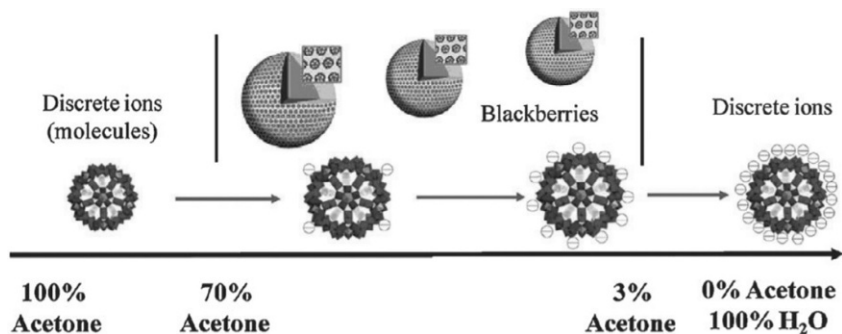


**Fig. 2** Transition between discrete macroions (molecules) to blackberries achieved by tuning solvent quality.

40 to 100 nm when the acetone content change from 3 to 70 vol%, while the  $\{\text{Mo}_{132}\}$  clusters stay as discrete molecules when the acetone content  $<3\%$  or  $>70\%$ , as shown in Fig. 2 (28).

Changing the quality of solvent will obviously alter the charge density of  $\{\text{Mo}_{132}\}$  in solution. When dissolved in  $<3\%$  vol% acetone/water mixture, the  $\{\text{Mo}_{132}\}$  macroions are highly negative charged so that the strong repulsive forces will prevent them from staying close. While in  $>70\%$  vol% acetone/water solutions, the negative charges on  $\{\text{Mo}_{132}\}$  macroions are mostly balanced so the clusters are almost neutral. Besides, the solubility of  $\{\text{Mo}_{132}\}$  will become lower as acetone content increase (1 mg/mL  $\{\text{Mo}_{132}\}$  can be soluble when acetone content  $<90\%$ ). The fact that no blackberry will form when the charge density of POM clusters are too high or too low suggests that electro static interaction play an essential role in the self-assembly of POM macroions. In colloidal system, van der Waals attractions are believed to be one of the dominant forces that bring the colloids together. In the above mentioned  $\{\text{Mo}_{132}\}$  case, while the strength of van der Waals forces does not varies much during the whole acetone content range, the assembly behavior of  $\{\text{Mo}_{132}\}$  clusters undergoes obvious change. The  $\{\text{Mo}_{132}\}$  system should experience more serious aggregation with higher acetone content if van der Waals are the dominant driving forces responsible, as the lower charge density shall lead to a weaker repulsive forces while the strength of van der Waals attractions remain the unchanged. Additionally, the estimated distance between neighboring POMs of blackberry should be around 1 nm, upon which the van der Waals attraction is supposed to be weak. These evidences suggest that van der Waals forces are not the major driving forces for the blackberry assembly. Moreover, the size of

blackberry structures demonstrates linear relationship with the inverse of dielectric constant of solvent, indicating that the POM self-assembly process is a charge regulated (26).

The assumption of charge-regulated process can be further confirmed by the self-assembly behaviors of  $\{\text{Mo}_{72}\text{Fe}_{30}\}$ .  $\{\text{Mo}_{72}\text{Fe}_{30}\}$  is a weak acid-type POM with 30 potential deprotonation sites when dissolved in water (10). The equilibrium between protonation and deprotonation can be regulated by solution pH, which will lead to charge the density change of  $\{\text{Mo}_{72}\text{Fe}_{30}\}$  (27). The natural pH of 1.0 mg/mL  $\{\text{Mo}_{72}\text{Fe}_{30}\}$  aqueous solution is 3.4 while about 7 or 8 protons are released from one  $\{\text{Mo}_{72}\text{Fe}_{30}\}$  molecule. When  $\text{pH} < 2.9$ , no self-assembly or aggregation of  $\{\text{Mo}_{72}\text{Fe}_{30}\}$  can be observed, they stay as discrete macroions in solution due to its low charge density. When solution pH reaches 3.0, blackberries start to form in solution. The  $R_h$  of  $\{\text{Mo}_{72}\text{Fe}_{30}\}$  blackberry drops linearly with increasing pH. The transition from single cluster to blackberry verifies that the major driving force for the blackberry formation is electro static interaction rather than van der Waals forces.

### 3.2 Counterion Distribution in POM Solutions

The distribution of counterions in POM solutions should be clarified before POM-counterion interaction can be investigated. Small-angle X-ray scattering (SAXS) is a powerful technique to characterize the molecule morphology, distribution, ion-pairing state, etc. (30). Due to the well-defined and rigid structure of POMs, their scattering curves can be fitted with a proper form factor. These curves respond to the states of counterion-POM association, and the  $R_g$  value and the distance pair distribution function of POMs in solution can be further calculated (31).

$\{\text{Mo}_{72}\text{V}_{30}\}$  is a hollow, spherical Keplerate-type POM with a diameter of 2.5 nm (32). Each  $\{\text{Mo}_{72}\text{V}_{30}\}$  carries 31 negative charges, which are balanced by 8  $\text{Na}^+$ , 14  $\text{K}^+$ , 2  $\text{VO}^{2+}$ , and 5  $\text{H}^+$ . It was observed that they can form blackberry structures upon introduction of acetone into water, and self-assembly process is quite slow at room temperature, which makes the SAXS a proper tool for monitoring the state of  $\{\text{Mo}_{72}\text{V}_{30}\}$  in mixed solvents (Fig. 3) (31). SAXS results demonstrated that  $R_g$  of  $\{\text{Mo}_{72}\text{V}_{30}\}$  remained 10.8 (5) Å at different concentrations, which proves that  $\{\text{Mo}_{72}\text{V}_{30}\}$  clusters indeed stay as discrete ions and no significant counterion association when their concentrations are relatively low (counterion association will result in an increase of  $R_g$ ) (31). The curve clearly showed that there is no counterion

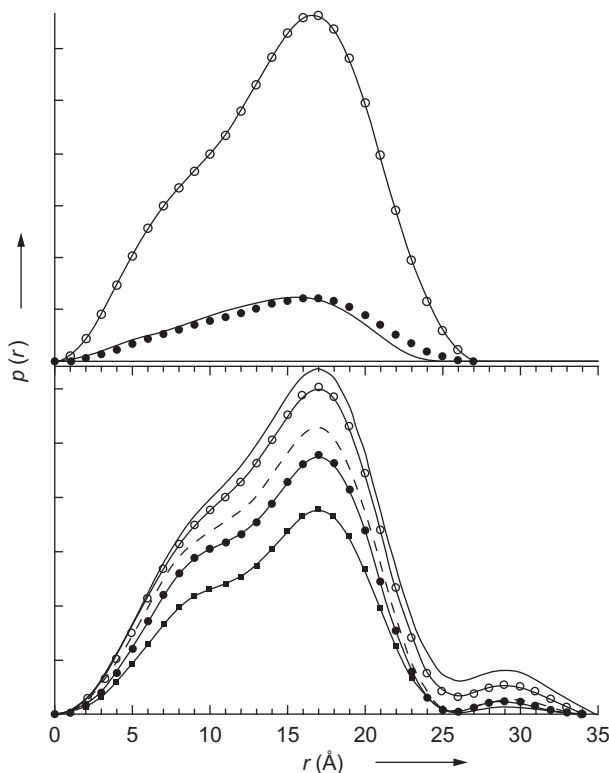


**Fig. 3** The distance distribution  $p(r)$  describes the probability of finding the vector length  $r$  in the molecule. Its value will drop to zero when the vector length reaches the maximum. *Top*: Distance distribution functions based on calculated and experimental scattering data for  $\{\text{Mo}_{72}\text{V}_{30}\}$  obtained by using an indirect Fourier transform of the primary SAXS data. ( $\circ$ ), 0.052 mM  $\{\text{Mo}_{72}\text{V}_{30}\}$ ; ( $\bullet$ ), 0.013 mM  $\{\text{Mo}_{72}\text{V}_{30}\}$ ; (—),  $\{\text{Mo}_{72}\text{V}_{30}\}$  calculated. *Bottom*: Experimental distance distributions for 0.26 mM  $\{\text{Mo}_{72}\text{V}_{30}\}$  in water and acetone/water mixed solvents with various acetone content (in vol%). (—), 75% acetone/water; ( $\circ$ ), 65% acetone/water; (---), 45% acetone/water; ( $\bullet\bullet\bullet$ ), 10% acetone/water; ( $\square$ ), in pure water.

association in  $\{\text{Mo}_{72}\text{V}_{30}\}$  solution when the concentration is low. However, when the concentration of  $\{\text{Mo}_{72}\text{V}_{30}\}$  went above 0.052 mM, a new peak at about 30 Å appeared which made the effective distribution to about 34 Å, while the original peaks for  $\{\text{Mo}_{72}\text{V}_{30}\}$  remained. The new peak indicated the existence of additional species around  $\{\text{Mo}_{72}\text{V}_{30}\}$  clusters that will contribute to the electro density. The only available solute was the counterions. It can be concluded that the close counterion–macroion association should be responsible for the high- $r$  distribution. Similar pattern

can be observed when additional acetone (10–75 vol%) was introduced into the solution. The Guinier plot demonstrated the  $R_g$  value goes up with increasing acetone content, which suggests the degree of association increases accordingly. The  $p(r)$  data revealed that the associated counterions around  $\{\text{Mo}_{72}\text{V}_{30}\}$  were distributed within 2–9 Å around the cluster surface.

The counterion distribution measured by SAXS suggests that those associated counterions can stay in between POMs when they self-assembled. It shows that the neighboring POMs are not in direct contact with each other. The close counterion–macroion association will decrease the surface charge density of POMs, which will lead to an increase in the attraction forces between POMs, so they will stay closer in solutions. Correspondingly, larger blackberries will form.

### 3.3 Counterion Exchange Around POMs

An essential feature of the POM macroionic solutions is that when additional counterions are present in solution, they may replace the original ones. Different counterions can be accurately recognized and selected by macroions in a specific order, depending on their hydrated sizes and valance. Counterions with higher valence (major effect) and/or smaller hydrated size (minor effect) are preferred by the macroions and are able to replace the macroions' original counterions which are lower on the preference list. This phenomenon can be observed by monitoring the blackberry sizes when different amount of counterions are added into the POM solution (33).  $\{\text{Mo}_{72}\text{Fe}_{30}\}$  clusters, with protons as their original counterions, are known to form blackberries of  $R_h \sim 25$  nm without any additional electrolytes at 40°C. When 1–20 mM LiCl or NaCl was introduced, blackberry sizes did not have obvious change. However, 0.1–10 mM KCl or RbCl will make the blackberry sizes considerably larger (Fig. 4). This phenomenon can be explained through a counterion replacement model. The affinity of  $\{\text{Mo}_{72}\text{Fe}_{30}\}$  to its original counterions (protons) is stronger than that of  $\text{Li}^+$  and  $\text{Na}^+$ , but weaker than  $\text{K}^+$  and  $\text{Rb}^+$ . In other words, additional  $\text{K}^+$  or  $\text{Rb}^+$  in solution are able to replace the original protons and decrease the surface charge density of  $\{\text{Mo}_{72}\text{Fe}_{30}\}$ , leading to a stronger attractive forces between  $\{\text{Mo}_{72}\text{Fe}_{30}\}$  clusters. Consequently, larger blackberry sizes are obtained.

This hypothesis can be further confirmed by isothermal titration calorimetry (ITC) studies. ITC results demonstrated that no measurable binding strength exists between  $\text{Na}^+$  and 2.0 mg/mL  $\{\text{Mo}_{72}\text{Fe}_{30}\}$  even with a

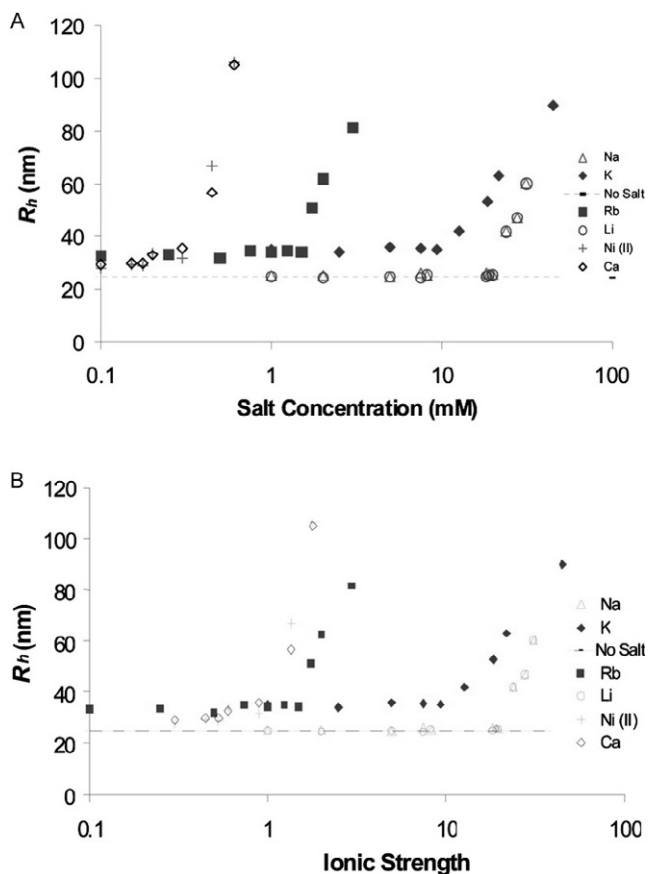


**Fig. 4** Change of blackberry size (in  $R_h$ ) with added chloride salt concentration (A) and total ionic strength (B) for 0.5 mg/mL  $\{\text{Mo}_{72}\text{Fe}_{30}\}$  solutions. For each added cation salt, there is a CSC (critical salt concentration), above which the blackberry size increases with increasing salt concentration.

molar ratio of  $\text{Na}^+/\text{POM} = 1000$ . The binding constant between  $\text{K}^+$  and  $\{\text{Mo}_{72}\text{Fe}_{30}\}$  was improved ( $k = 75$ ). Calculations showed that about 10  $\text{K}^+$  per POM charge are needed to saturate the binding sites of  $\{\text{Mo}_{72}\text{Fe}_{30}\}$ . The binding constant ( $k$ ) between  $\text{Rb}^+$  and  $\{\text{Mo}_{72}\text{Fe}_{30}\}$  was measured to be 773, which is about one order of magnitude larger than that of  $\text{K}^+$ . In addition, less than 10  $\text{Rb}^+$  were needed to saturate the binding sites per POM charge. The introduction of  $\text{CsCl}$  into solution will result in precipitation, as the interaction between  $\text{Cs}^+$  and  $\{\text{Mo}_{72}\text{Fe}_{30}\}$  cluster were believed to be stronger than all other monovalent counterions. The binding strength between  $\{\text{Mo}_{72}\text{Fe}_{30}\}$  and monovalent counterions

follows an order of  $(\text{Li}^+, \text{Na}^+) < \text{H}_3\text{O}^+ < \text{K}^+ < \text{Rb}^+ < \text{Cs}^+$ , which was consistent with the previous observations of blackberry size change upon different counterions.

### 3.4 Self-Assembly With Anisotropic Surface Charge Density Distribution

Most POM macroions in previous studies are highly isotropic in charge distribution. The blackberry formation from POM macroions is driven by counterion-mediated attraction thus isotropic charge density will lead to nondirectional assemblies (spherical). One question that worth further exploration is that whether the situation will be different if the charges around the macroions are anisotropic, e.g., oriented. A study on  $\{\text{Mn}_{40}\text{P}_{32}\text{W}_{224}\}$ , the largest polyoxotungstate cluster known so far, helps to answer this question. Four Dawson trimers are connected to one  $\text{P}_8\text{W}_{48}$  wheel by Mn–O bonds, creating an S4 symmetrical structure. The 152 negative charges are balanced by 22 protons, 74  $\text{Li}^+$  and 56  $\text{K}^+$  (19). The weak SLS intensity revealed that the clusters did not self assemble in aqueous solution as a result of their high charge density. Blackberry structures were found when the clusters are dissolved in water methanol mixture containing 50–100 vol% of methanol, confirmed by DLS, SLS ( $R_h \sim R_g$ ), and TEM studies. However, when dissolved in acetone–water mixture with 40–80 vol% of acetone, they formed a rod-like structure (Fig. 5). Unlike the blackberry structures, the  $R_h$  of such assemblies were lower than their corresponding  $R_g$ . Although the solvent polarity have been proved to

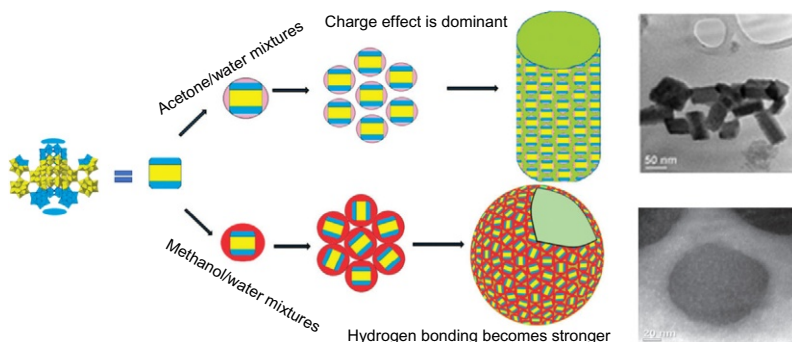


**Fig. 5** The structure of  $\{\text{Mn}_{40}\text{P}_{32}\text{W}_{224}\}$  highlighting the areas of the high charge density (blue) along with a model that proposes its solution behavior. The red color highlights the strength of hydrogen bonding.

significantly influence self-assembly of POM macroions by tuning their surface charge densities, the polarities of acetone–water and methanol–water mixtures are quite similar (34).

It is believed that hydrogen bonding, along with counterion-mediated attraction, is playing an essential role in controlling the assemble direction (34,35). In acetone–water mixed solvent, the charge effect is dominant. POM macroions will favors to interact with the areas of high charge density. The anisotropic charge distribution of  $\{\text{Mn}_{40}\text{P}_{32}\text{W}_{224}\}$  clusters leads to a directional growth, resulting in the rod-like structures. However, in methanol–water mixtures, hydrogen bonding effect is much stronger than it in the acetone–water mixture. The oxo and water ligands of POMs facilitate the formation of hydrogen bonding with the solvent. The strong, isotropic hydrogen bonding weakens the orientation effect caused by the counterion-mediated attraction. Consequently,  $\{\text{Mn}_{40}\text{P}_{32}\text{W}_{224}\}$  macroions behave more like the POMs with isotropic charge distribution. To confirm this speculation,  $\{\text{Mn}_{40}\text{P}_{32}\text{W}_{224}\}$  was dissolved in deuterated solvent and regular nondeuterated solvent. The clusters in 50 vol% D-methanol–D<sub>2</sub>O mixtures self-assembled into rod-like structure while in 50 vol% methanol–H<sub>2</sub>O mixed solvent blackberries formed, confirming the role of hydrogen bonding in macroionic self-assembly.



#### 4. THE KINETIC PROPERTIES AND LAG PHASE OF POM ASSEMBLY

Unlike colloidal systems, the blackberries in solution are thermodynamically stable (36–39). Depending on the properties of the macroions, the blackberry formation process may take a long period of time (up to several months) (40,41), which will facilitate the detailed investigation of the mechanism of the self-assembly. It was speculated that the possible mechanism of blackberry formation should follow the route in Fig. 6 (41). After dissolving POM macroions in solution, they will first assemble into oligomers. Once the amount of oligomers reaches a critical point, they will quickly associate into blackberries of specific size. The SLS results demonstrate that there is no overlap between the monomer and blackberry peak, indicating that the formation of oligomers should be the rate-determining step.

The self-assembly process of  $\{\text{Mo}_{72}\text{Fe}_{30}\}$  monitored by SLS, demonstrated a linear time-resolved intensity increase vs time in aqueous solution in the presence of no or small amount of additional counterions (e.g., NaCl,



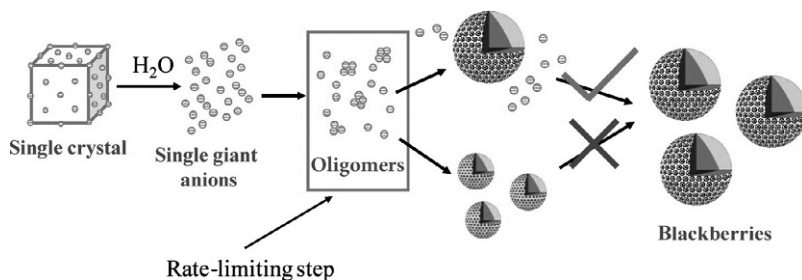


**Fig. 6** Possible mechanisms of  $\{\text{Mo}_{72}\text{Fe}_{30}\}$  blackberry formation in dilute aqueous solution. The *upper* mechanism has been proven to be correct based on SLS and DLS results, while the *bottom* mechanism can be ruled out.

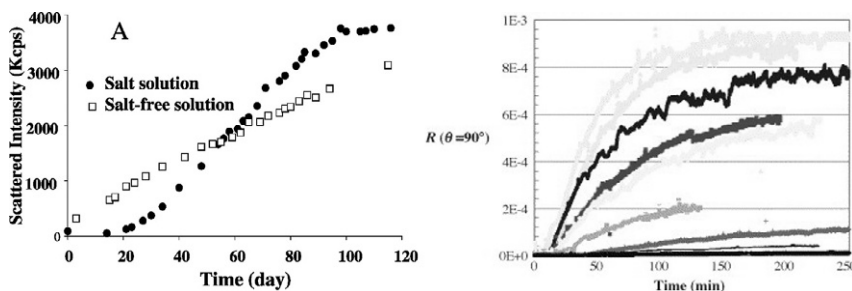


**Fig. 7** (Left) Comparison of scattered intensity increment (A) and  $R_h$  change (B) of two  $\{\text{Mo}_{72}\text{Fe}_{30}\}$  samples along reaction time in 0.9 wt% NaCl and salt-free solutions. (Right) Light scattering study of the assembly of HPV capsid proteins at various HPV concentrations. The lag time, reaction slope, and extent of assembly were dependent upon the initial protein concentration. Changes in scattered light were not observed until minutes later.

NaBr, NaI, and  $\text{Na}_2\text{SO}_4$  at the concentration of 0.017 mol/L), which is very similar to a first order reaction (40). However, there actually existed a very short lag period at the beginning of the assembly (in min). Similar lag phase can also be observed with  $\{\text{Cu}_{20}\text{P}_8\text{W}_{48}\}$  (41). The lag phase became more significant when higher amount of additional electrolytes were introduced (Fig. 7), and the overall intensity growth is shown as a sigmoidal curve (42). It is believed that the POM macroion association is a thermodynamically unfavorable step, while the blackberry formation from oligomers is thermodynamically favorable as the system can reach a much lower free energy level with the blackberry state. When additional salts are introduced, the activation energy of the blackberry formation will be increased. The surface charge density is reduced due to the addition of salts. The attractive force

between neighboring  $\{\text{Mo}_{72}\text{Fe}_{30}\}$  clusters becomes weaker due to the enhanced screening effect.  $\{\text{Mo}_{72}\text{Fe}_{30}\}$  clusters are in general getting stabilized with increasing concentration of counterions and coions. As a result, both steps of self-assembly are prolonged (42).

$\text{U}_{28}$  is a member of the actinyl peroxide cluster family. The assembly and lag period behaviors of  $\text{U}_{28}$  are different from the case of  $\{\text{Mo}_{72}\text{Fe}_{30}\}$  due to its extreme high surface charge density. Each  $\text{U}_{28}$  cluster carries 15 negative charges, which are balanced by 15  $\text{Cs}^+$ , or 6  $\text{Na}^+$  and 9  $\text{K}^+$  (22,43–45). With a diameter of 1.8 nm,  $\text{U}_{28}$  is the smallest POM macroions reported so far that can self-assemble into blackberries (46). However, due to the very high surface charge density, the  $\text{U}_{28}$  clusters cannot directly self-assemble at room temperature, indicated by the constant low SLS intensity. Additional counterions are needed to bring down the surface charge density to a proper level in order to reduce the strong repulsive force between the clusters. Counterions will affect the lag phase in two ways: by forming specific ion pairing and by increasing the total ionic strength. It was observed that when the counterion concentration was low, the specific ion-pairing effect dominated. Therefore, when the counterion concentration was smaller than 0.6 mol/L,  $\text{Na}^+$  and  $\text{K}^+$  were always more efficient in reducing the length of lag period as they can bridge the clusters in blackberries, while larger amphiphilic counterions like tetraethylammonium ( $\text{TEA}^+$ ), tetrapropylammonium ( $\text{TPA}^+$ ), and tetrabutylammonium ( $\text{TBA}^+$ ) are generally less effective. When the counterion concentrations were relatively high ( $>0.6$  mol/L), the ionic strength effect took over so the difference between various counterions in reducing lag period vanishes (Fig. 8).

An interesting analogy of the POM macroionic self-assembly process is the virus capsid formation. Similar to blackberries, the virus capsid shells, assembled by virus capsid proteins, are also single-layered, hollow, and spherical. Both assembly processes demonstrate similar kinetic features by displaying sigmoidal growth curve (Fig. 7), suggesting that they may share similar mechanisms (7,8,47). For example, the lag phase of human papilloma virus (HPV) is found to be sensitive to the protein concentration and ionic strength (48). Similar cases have been reported with *in vitro* hepatitis B virus capsids and cowpea chlorotic mottle virus capsids (49–51). It is worth mentioning that although the hydrophobic interaction is believed to be the dominant driving force for the virus capsid assembly, there exist no hydrophobic region for POMs so the hydrophobic interaction must not be responsible for the blackberry formation. Whether the role of charges is being underestimated in virus capsid formation remains a question that

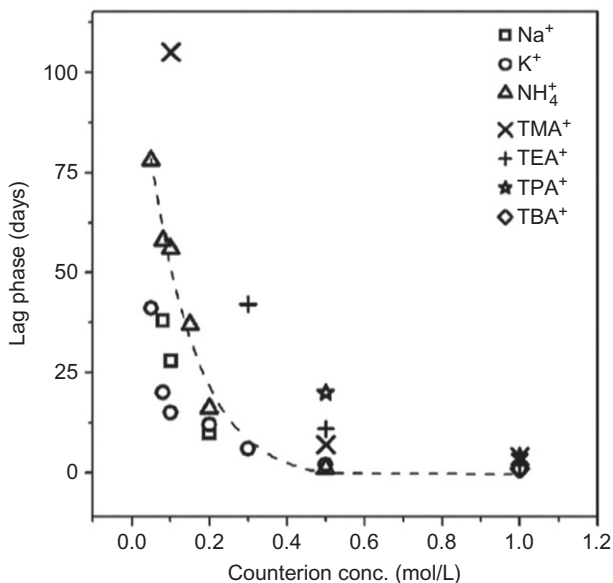


**Fig. 8** Influence of the addition of different electrolytes on the lag period of the blackberry-structure formation in 0.5 mg/mL CsKU<sub>28</sub> solution. Although the anion is chlorine in common, the cations were systematically varied. The *dashed line* is used to guide the eyes for the general trend of the change of the lag phase.

may worth further exploration. Considering the similarities between POMs and other charged biomacromolecules, POMs can serve as a simplified model for investigating the solution behaviors of such complicated biomacromolecules (7,8).

## 5. POM-COUNTERION ION PAIRING IN SOLUTION

The hydration of ions must be considered when studying their interactions in solution. There are three different ion pairs based on different states of hydration between cations and anions: solvent separated ion pair, solvent-shared ion pair, and contact ion pair (52).

Antonio, Nyman, and their colleagues have applied SAXS to directly investigate the ion-pairing phenomenon between Lindquist type [Nb<sub>6</sub>O<sub>19</sub>]<sup>8-</sup> POM and different alkali counterions (53). The solubility of [Nb<sub>6</sub>O<sub>19</sub>]<sup>8-</sup> with alkali ions follows the trend: Cs<sup>+</sup> > Rb<sup>+</sup> > K<sup>+</sup> > Na<sup>+</sup> > Li<sup>+</sup> (Cs<sup>+</sup> salt is most soluble while Li<sup>+</sup> salt is least soluble), which is known to be opposite to that of classical POMs. Because of the good solubility of Rb<sup>+</sup> or Cs<sup>+</sup> salt

of  $[\text{Nb}_6\text{O}_{19}]^{8-}$ , and more importantly,  $\text{Rb}^+$  or  $\text{Cs}^+$  ions can be easily detected using X-ray scattering due to their higher electron density compared to light ions ( $\text{Li}^+$  or  $\text{Na}^+$ ),  $[\text{Nb}_6\text{O}_{19}]^{8-}$  represents an excellent paradigm to study the macroion-counterion ion-pairing phenomenon (Fig. 9). It was shown that when different concentrations of the alkali metal salts of  $[\text{Nb}_6\text{O}_{19}]^{8-}$  were dissolved in solutions containing 3 M of tetramethylammonium hydroxide (TMAOH), the average  $R_g$  does not change and is consistent with the calculated value for the  $[\text{Nb}_6\text{O}_{19}]^{8-}$  (3.1 Å), suggesting a somewhat loose interaction between the macroion and its counterions. Interestingly, the physical radius of the Lindqvist sphere ( $R_s$ ) increases as the ionic radii of the alkali metal counterion increases. For instance, the average  $R_s$  values were calculated to be 4.1, 4.3, and 4.6 Å for the potassium, rubidium, and cesium salts, respectively. As a result of the relatively small number of alkali metal counterions in solutions of TMAOH, studies of these alkali metal salts of  $[\text{Nb}_6\text{O}_{19}]^{8-}$  were done in solutions of their corresponding alkali metal base to ensure the presence of

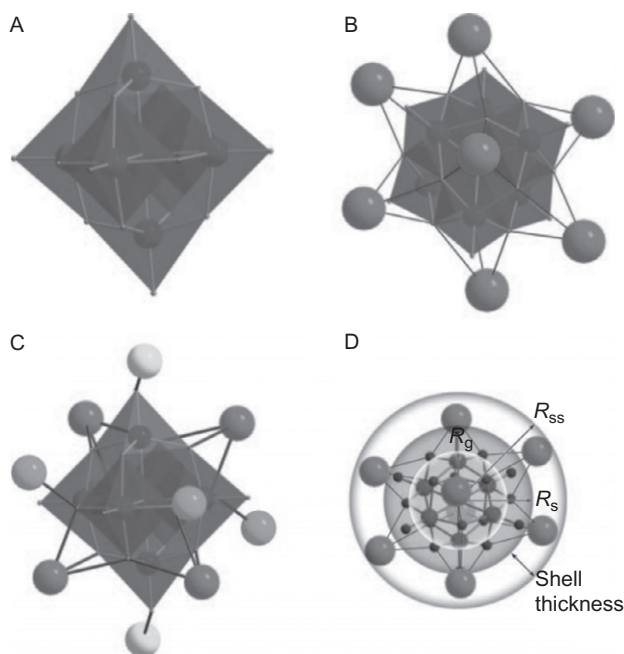


**Fig. 9** (A) The bare  $[\text{Nb}_6\text{O}_{19}]^{8-}$  Lindqvist ion. *Octahedra* are  $\text{NbO}_6$ . (B) The neutral  $A_8[\text{Nb}_6\text{O}_{19}]$  species ( $A = \text{Rb}, \text{Cs}$ ). *The spheres* are face-bonded  $\text{Rb}/\text{Cs}^+$ . (C)  $\text{K}^+ - [\text{Nb}_6\text{O}_{19}]^{8-}$  association observed in the crystal structure. *Spheres* indicate  $\text{K}^+$  associated on the cluster face, cluster edge, and cluster apices. (D) Representation of the three particle radii ( $R_g$ ,  $R_s$ , and  $R_{ss}$ ).

many counterions. It is shown that the  $R_g$  of  $A_8[Nb_6O_{19}]$  in 3 M solutions of AOH ( $A = K, Rb, \text{ or } Cs$ ) is 0.6–0.8 Å larger than the calculated for the bare  $[Nb_6O_{19}]^{8-}$  anion, suggesting the presence of extra alkali metal counterion enhances the ion-pairing process in solution. Furthermore, the average spherical shell radius ( $R_{ss}$ ) was shown to be 7.6, 6.1, and 5.9 for the solutions of  $A_8[Nb_6O_{19}]$  in 3 M solutions of AOH, where  $A = K, Rb, \text{ or } Cs$ , respectively. This is an opposite trend compared to the TMAOH solutions suggesting that when extra alkali metal counterions present in the solution, the effect of the hydrated size of the counterion is more dominant than the effect of ionic radius; thus, in this system, it is highly likely that only contact ion pairs are present.

To further understand the ion-pairing in POM systems, Nyman's group further investigated the solution behaviors of  $[Ta_6O_{19}]^{8-}$ , another POM with almost identical solid-state structure as  $[Nb_6O_{19}]^{8-}$  in TMAOH and AOH ( $A = Rb, Cs$ ) (54). The pair distance distribution functions are compared. It is discovered that for  $[Ta_6O_{19}]^{8-}$ , solvent-separated or solvent-shared ion-pairing dominates when alkalinity is high, while  $[Nb_6O_{19}]^{8-}$  shows only contact ion pairing. This phenomenon is a result of the strong protonation of  $[Ta_6O_{19}]^{8-}$  in solution, which will not only decrease the cluster's overall charge density and reduce the attractive force to alkali ions but also occupy the potential coordination sites from alkali ions. Besides, this work also partially helps explain the solubility difference between  $[Ta_6O_{19}]^{8-}$  and  $[Nb_6O_{19}]^{8-}$ . The high solubility of  $Cs_8[Nb_6O_{19}]^{8-}$  is a result of low attractions between two neutral clusters. For  $[Ta_6O_{19}]^{8-}$ , the alkali ions, while not being directly bonded with the cluster, can form bridges between clusters to saturate the bond valence, which may lead to precipitation.



## 6. DYNAMIC OF ALKALI COUNTERIONS IN POM SOLUTION

The counterions are essential for the solubility, crystallization, assembly, and even templating cluster formation of macroions. Understanding and controlling the dynamic behaviors of counterions is imperative for the further applications of those macroions.

The dynamic counterion behaviors of two actinyl peroxide clusters,  $U_{28}$  and  $U_{24}$ , are revealed via NMR studies by Nyman and Alam (44). It is discovered that those clusters are not rigid entities and the internal counterions

can exchange with the external ions in solution. The ratio between external and internal  $\text{Na}^+$  of  $\text{U}_{28}$  and  $\text{U}_{24}$  via solid state  $^{23}\text{Na}$  NMR agreed well with the ratio determined by compositional analysis and X-ray studies. Temperature also plays a critical role in the dynamic exchange process of counterions. As shown in Fig. 10, when the solution of Ta-BaRb $\text{U}_{28}$  was heated from 25°C to 90°C, the external Na peak became border while the chemical shift difference between the two species were reduced. The broadening, rather than narrowing as expected with nonexchanging Na environment, of external Na resonance at higher temperature demonstrated that the exchange behaviors were undergoing. In addition, the ratio of internal/external Na will be significantly reduced after dissolved in water, indicating that some of internal  $\text{Na}^+$  will exit the cluster. It is expected that the dissolved species moves from high concentration area to the low concentration area while the system gains entropy. For  $\text{U}_{24}$  clusters, the solution NMR results showed that the resonances of encapsulated and free  $\text{Na}^+$  gradually with each other when temperature increased, which suggests that the

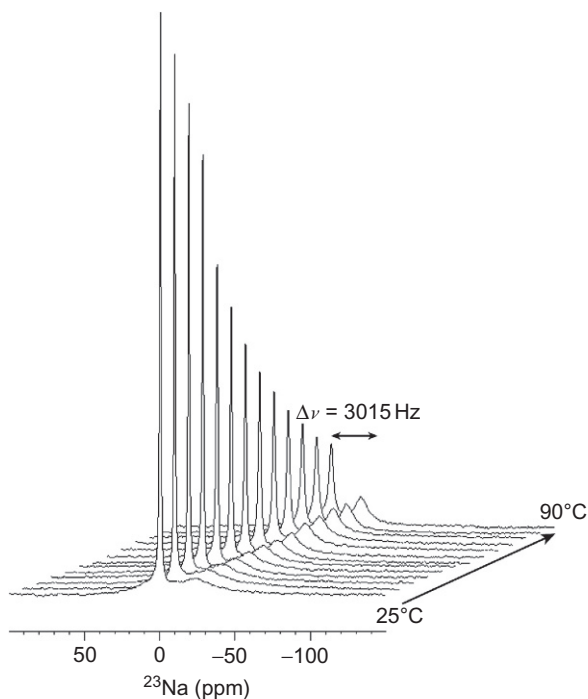


**Fig. 10** Variable-temperature solution  $^{23}\text{Na}$  NMR spectra of Ta-NaCs $\text{U}_{28}$ .

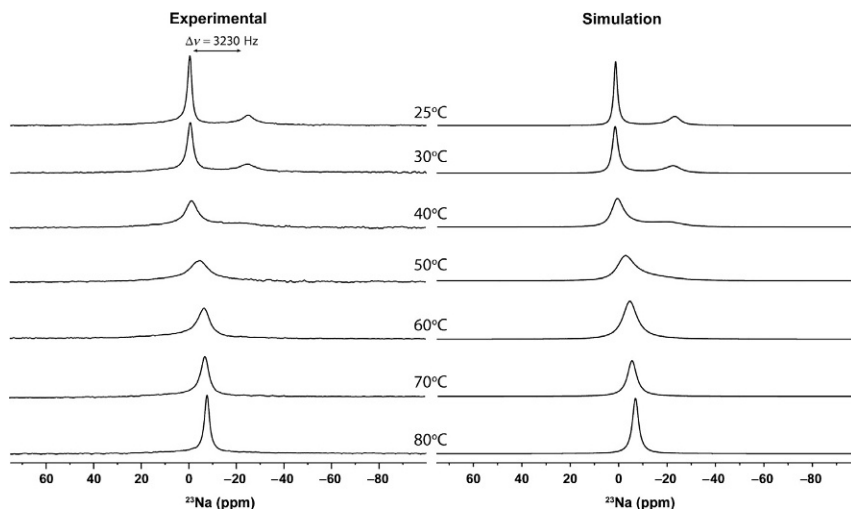


**Fig. 11** Variable-temperature solution  $^{23}\text{Na}$  NMR spectra and dynamic line shape simulations for the  $\text{Na-U}_{24}$  capsule.

exchange between external/internal  $\text{Na}^+$  is faster than peak separation (Fig. 11). The  $\text{Na}$  exchange rate of  $\text{U}_{24}$  was obviously more rapid than  $\text{U}_{28}$ . It was speculated that the higher  $\text{Na}^+$  exchange rate of  $\text{U}_{24}$  may be results of: (1) the absence of larger alkali ions, which may lead to the decrease of overall mobility inside, rather than higher free volume inside  $\text{U}_{24}$ ; (2) the fact that  $\text{U}_{24}$  has more of the large hexagonal windows than  $\text{U}_{28}$ , assuming  $\text{Na}^+$  can exit from the cluster through any capsule faces; and (3) the difference between the water molecules inside  $\text{U}_{24}$ , which can be influenced by hydrogen bonding, proton transfer, bonding between alkali ions, water, etc.

## 7. CATION TRANSPORTATION THROUGH BLACKBERRY “MEMBRANE”

The surface of blackberry structure is soft, “porous,” and membrane like. The fact that there are no hydrophobic regions in blackberries makes those blackberry membranes different from the cell membranes in nature. The space between neighboring POMs is large enough to serve as channels for simple ions to pass through. The stable and robust nature of blackberry structure make it suitable for ion transport study.

A typical experiment was conducted with  $\{\text{Mo}_{72}\text{Fe}_{30}\}$ . Fluorescence spectroscopy was applied for tracking the transport of small ions through the blackberry membrane. Three different water soluble dyes were added into the  $\{\text{Mo}_{72}\text{Fe}_{30}\}$  solution: chlorotetracycline (CTC) for  $\text{Ca}^{2+}$  and  $\text{Mg}^{2+}$ ; 6-methoxyquinoline (6-MQ) for  $\text{Cl}^-$  and Coumarin-1 for  $\text{Br}^-$ . The dyes were captured and stayed inside the blackberries, which was proved by an 18 nm shift of the fluorescence signal. Once the blackberry formation was complete, no further changes were observed. The results suggested that the solution environment inside the blackberry was different from the bulk solution. The higher viscosity may be a result of strong hydrogen bonding effect of  $\{\text{Mo}_{72}\text{Fe}_{30}\}$  (55).

Additional electrolytes were added into the solution upon the completion of the fluorophore-containing blackberry formation. For cations, except for the immediate intensity increase upon the titration of  $\text{Ca}^{2+}$  and  $\text{Mg}^{2+}$ , a slow and continuous increase of fluorescence signal reveals that the continuous binding between  $\text{Ca}^{2+}/\text{Mg}^{2+}$  and CTC. This is an indication of slow transportation of  $\text{Ca}^{2+}/\text{Mg}^{2+}$  through the blackberry membrane (Fig. 12). In that way, the cations can interact with the fluorophores inside blackberry. The results confirm that small cations are able to pass through the blackberry membrane. However, anions like  $\text{Cl}^-$  and  $\text{Br}^-$  show no evidences that they can move across the membrane. A reasonable explanation is that the highly negatively charged blackberries will repel those anions (55).

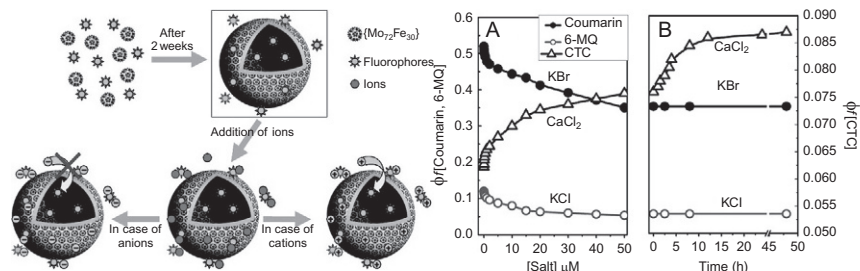


**Fig. 12** (Left) Formation of fluorophore-containing  $\{\text{Mo}_{72}\text{Fe}_{30}\}$  blackberries in solution. The additional cations, once added into solution, instantly interact with fluorophores in bulk solution and on blackberry surfaces, subsequently enter into the blackberries, and interact with the fluorophores inside. The anions could not cross the membrane. (Right) Change in fluorescence quantum yield of Coumarin 1, 6-MQ, and CTC with addition of KBr, KCl, and  $\text{CaCl}_2$ , respectively; (a) instantaneous change occurs with the addition of salts; (b) change in fluorescence quantum yield with time, once the addition of salt is stopped.





## 8. SELECTIVE PERMEABILITY OF URANYL PEROXIDE NANOCAGE

The precise guidance toward different ions across biological channels is essential for many biological processes. Given the broad application of ion channels, considerable efforts have been dedicated to investigating ion transport and ion selectivity behaviors (56,57). Example of ion channels in nature are proteins embedded in the cell membrane. However, due to the fragility of protein molecules, their bioactivities can be greatly reduced in non-biological environments where they are expected to function (58,59). Therefore, artificial ion channels built from inorganic materials might be a way out. POM macroions, with rigid structures and porous surfaces, can serve as perfect candidates of pure inorganic ion channels to allow selective transmembrane transport of cation in aqueous environments (60,61).

The change of blackberry size can serve as an accurate indicator to detect the ion-transport process in aqueous solution. The blackberry formation process is mediated by electrostatic interaction, and it is sensitive to the environmental stimuli that may cause a minor change in charge density such as pH, solvent polarity, or extra electrolytes. The distance between two POM macroions in blackberry will be mainly determined by two factors: counterion density between the two macroions and the net effective charge of each macroion. As explained in Section 3.3, cations with smaller hydrated sizes will usually be more effective in increasing the counterion density and decreasing their net surface charge between two neighboring macroions to attract them together, leading to a larger blackberry size (7,8).

### 8.1 Role of Hydration Layer in Selective Permeability of $U_{60}$

$U_{60}$  is a 2.5-nm sized, C<sub>60</sub>-like uranyl peroxide nanocage. The 60 negative charges of  $U_{60}$  are balanced by 48  $Li^+$  and 12  $K^+$ . Each  $U_{60}$  cluster contains 60 uranyl polyhedral, which are arranged into 20 hexagons and 12 pentagons (23,62,63). Similar to  $U_{28}$ ,  $U_{60}$  cannot self-assemble into blackberries due to its high surface charge density. Addition of salt into the  $U_{60}$  solution would help to trigger the self-assembly. When NaCl, KCl, RbCl, and CsCl were added into 1 mg/mL  $U_{60}$  solution, different phenomenon were observed. With 3 mM NaCl,  $U_{60}$  clusters precipitated, indicating an extremely strong interaction between  $U_{60}$  and  $Na^+$ . Although same amount of KCl, RbCl, and CsCl in separate experiments can self-assemble  $U_{60}$  into blackberry structure. Interestingly, the  $R_h$  of  $U_{60}$  blackberry in the presence of RbCl

or CsCl is similar, however, smaller than the  $R_h$  with KCl (64). This result revealed a sequence of  $\text{Na}^+$ ,  $\text{K}^+ > \text{Rb}^+/\text{Cs}^+$  in terms of the strength of interaction to  $\text{U}_{60}$ , which was at odds with our previous results for  $\{\text{Mo}_{72}\text{Fe}_{30}\}$ . In Section 2, a “normal” interaction strength trend of  $\text{Cs}^+ > \text{Rb}^+ > \text{K}^+ > \text{Na}^+$ ,  $\text{Li}^+$  was obtained, summarizing from their corresponding blackberry sizes (33).

This trend was confirmed by a series of ITC studies (64). Consistent with the previous results, the binding constants between  $\text{U}_{60}$  and  $\text{Na}^+/\text{K}^+$  were indeed larger than that of  $\text{Rb}^+/\text{Cs}^+$ , suggesting that the system can reach a lower free energy level when binding with  $\text{Na}^+/\text{K}^+$  rather than  $\text{Rb}^+/\text{Cs}^+$ . The unusual strong binding strength of  $\text{Na}^+$  and  $\text{K}^+$  can be clarified by examining the thermodynamic parameters when  $\text{U}_{60}$  clusters bind with different counterions. When binding with  $\text{Rb}^+$  and  $\text{Cs}^+$ , the  $\text{U}_{60}$  solution showed more entropy loss comparing with the situation of binding with  $\text{K}^+$ , and the system even demonstrated an entropy gain when interacting with  $\text{Na}^+$ .

The abnormal binding strength of  $\text{Na}^+/\text{K}^+$  is due to the fact that  $\text{Na}^+/\text{K}^+$  can pass through the surface pores of  $\text{U}_{60}$ , while  $\text{Rb}^+/\text{Cs}^+$  are unable to do that (Fig. 13) (64). On one hand, the self-assembly results proved this conclusion. When  $\text{Na}^+/\text{K}^+$  is inside the  $\text{U}_{60}$  cage, the charge density of  $\text{U}_{60}$  is reduced so the repulsive forces between neighboring  $\text{U}_{60}$  clusters become smaller. Therefore, the distance between  $\text{U}_{60}$  becomes smaller, resulting in a larger blackberry size. On the other hand, this conclusion is also supported by the ITC results. While the bare ionic radii of  $\text{Li}^+$ ,  $\text{Na}^+$ ,  $\text{K}^+$ ,  $\text{Rb}^+$ , and  $\text{Cs}^+$  increase from 0.094, 0.117, 0.149, 0.163 to 0.186 nm, their hydrated radii follow the opposite trend as 0.382, 0.358, 0.331, 0.329, and 0.329 nm, respectively. By comparing the sizes of  $\text{U}_{60}$  surface pores and the hydrated sizes of those counterions, it is obvious that both  $\text{U}_{60}$  and counterions need to lose part of their hydration layer to fit each other. It is believed the entropy gain during the binding process mainly arise

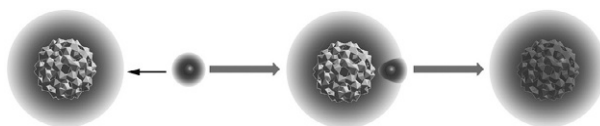


**Fig. 13** Possible mechanism for  $\text{Na}^+/\text{K}^+$  counterions interacting with  $\text{U}_{60}$ . The *small sphere* represents  $\text{Na}^+/\text{K}^+$  ions. The *corona* represents the hydration layers of  $\text{U}_{60}$  or counterions. Destruction of hydration layers of  $\text{U}_{60}$  and  $\text{Na}^+/\text{K}^+$  will lead to an entropy increase. A fusion of hydration layers may be achieved finally.

from the destruction of hydration shells from both  $U_{60}$  and counterions. For  $Na^+$  and  $K^+$ , the entropy gain they obtained from losing the hydration layer when they pass through the  $U_{60}$  surface pore are large enough to compensate for the energy needed for dragging them out of their hydration layers. As a comparison, the hydration shells of  $Rb^+$  and  $Cs^+$  are thinner than  $Na^+$  and  $K^+$  so less entropy gain can be obtained for them the move across the surface pores. Besides, more energy needed for  $Rb^+$  and  $Cs^+$  to get rid of their hydration layers. In general, the  $U_{60}$  solution system reaches a lower free energy level with  $Na^+$  or  $K^+$  inside the cage.

## 8.2 Controlling the Ion Selectivity of $U_{60}$

Although  $U_{60}$  demonstrate selective permeability for  $Na^+$  and  $K^+$ , making it further differentiate between  $Na^+$  and  $K^+$ , which are almost identical in size, remains challenging. As the shape and size of the  $U_{60}$  surface pore are fixed, the possibility of tuning its selective permeability may only come from controlling the hydration shell, which can be simply achieved though regulating the solution temperature.

Small amounts of  $NaCl/KCl/RbCl/CsCl$  (5 mM) were titrated into  $U_{60}$  solution (1 mg/mL, 3 mL, same volume, and concentration were used in all groups) at room temperature. DLS and SLS confirmed the formation of blackberry, and the trend of blackberry size was consistent with the previous results.  $U_{60}/NaCl$  and  $U_{60}/CsCl$  precipitate in solution, while the blackberry size of  $U_{60}/KCl$  (ca. 36 nm) is larger than  $U_{60}/RbCl$  (ca. 15 nm), as shown in Fig. 15, group 1. Subsequent to the completion of blackberry formation, the group 1 solutions were kept at 70°C. Two weeks later, the following phenomenon can be observed. (1) The precipitates in both  $U_{60}/NaCl$  and  $U_{60}/CsCl$  solution were disappeared. While the scattering intensity level of  $U_{60}/CsCl$  solution remained high, the  $U_{60}/NaCl$  solution demonstrated a very low scattering intensity. (2) The blackberry size of  $U_{60}/KCl$  had an obvious drop however the blackberry size of  $U_{60}/RbCl$  remained stable. From the above observations, several conclusions can be drawn. First, the precipitation in  $U_{60}/NaCl$  solution is due to the aggregation of discrete  $U_{60}$  clusters, while the precipitation of  $U_{60}/CsCl$  solution is a result of blackberry aggregation. The  $U_{60}/CsCl$  blackberry aggregations redissolved when heated up to 70°C. Second,  $K^+$  ions migrate out of  $U_{60}$  cage after incubating at 70°C, leading to a higher surface charge density of  $U_{60}$  thus a smaller blackberry size. This is due to two reasons: (1) the higher kinetic energy makes the trapped

$K^+$  ions less willingly to stay inside the cage and (2) the thinner hydration layer of  $U_{60}$  facilitates the escape of  $K^+$  ions (65).

To clarify the role of hydration layer, another three sets of experiments were conducted (Fig. 14). Group 2 solutions were titrated directly with different counterions at room temperature, and group 3 solutions were pre-incubated at  $50^\circ\text{C}$  before titration. Both groups 2 and 3 were held at  $50^\circ\text{C}$  to form blackberries. For  $U_{60}/\text{NaCl}$ , the solution intensities in both groups 2 and 3 remained relatively low indicating the  $\text{Na}^+$  cannot enter the  $U_{60}$  cage at this temperature due to the change of hydration shells. Blackberry sizes of  $U_{60}/\text{RbCl}$  and  $U_{60}/\text{CsCl}$  in groups 2 and 3 did not vary a lot from group 1. However, while  $U_{60}/\text{KCl}$  blackberry sizes of group 2 were still

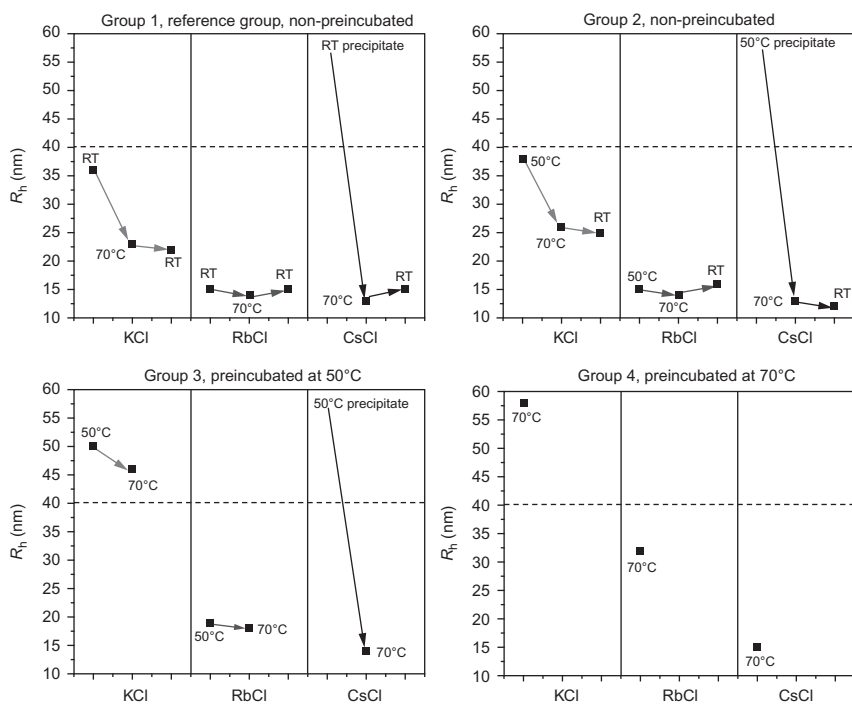


**Fig. 14** Change of  $U_{60}$  assembly sizes ( $R_h$ ) with additional counterions (molar ratio of  $U_{60}:\text{K}^+/\text{Rb}^+/\text{Cs}^+$ , ca. 1:130) upon heating at different temperatures. For group 1, the solutions were initially titrated and held at room to allow blackberry formation. Subsequently, the solutions were heated to  $70^\circ\text{C}$  and then returned to room temperature. For group 2, the solutions were initially titrated at room temperature and held at  $50^\circ\text{C}$  for blackberry formation, followed by the same thermal sequence conducted for group 1. In groups 3 and 4, the  $U_{60}$  solutions were preincubated at  $50^\circ\text{C}/70^\circ\text{C}$  for 3 days before titration.

similar to group 1, the initial blackberry sizes in group 3 demonstrated a noticeable increase comparing to group 1. Those results clearly showed the effect of hydration layers in self-assembly process.  $U_{60}$  clusters in group 3 were preincubated in  $50^{\circ}\text{C}$  in order to have a thinner hydration shell before contacting with the additional counterions. Therefore, they were more permeable to the diffusion of  $\text{K}^+$  ions thus more  $\text{K}^+$  ions will enter the cage after preincubation, which will make the blackberries larger (Fig. 15). Moreover, compared to group 3, group 2 was immediately placed at  $50^{\circ}\text{C}$  after titration. However, the blackberry size did not vary from group 1. This suggested that the transport of  $\text{K}^+$  ions had already been finished before blackberry formation. Combined with the fact that the self-assembly process of  $U_{60}$  happened immediately after salts titration, it was obvious that the  $\text{K}^+$  diffusion must be extremely fast, so that the transport can finish even before the hydration shells being impaired by high temperature. This is another important feature  $U_{60}$  clusters shared with  $\text{K}^+$  ion channels. Groups 2 and 3 were then heated up to  $70^{\circ}\text{C}$ .  $U_{60}/\text{KCl}$  solution in both groups 2 and 3 showed an obvious blackberry size drop at  $70^{\circ}\text{C}$ , while  $U_{60}/\text{RbCl}$

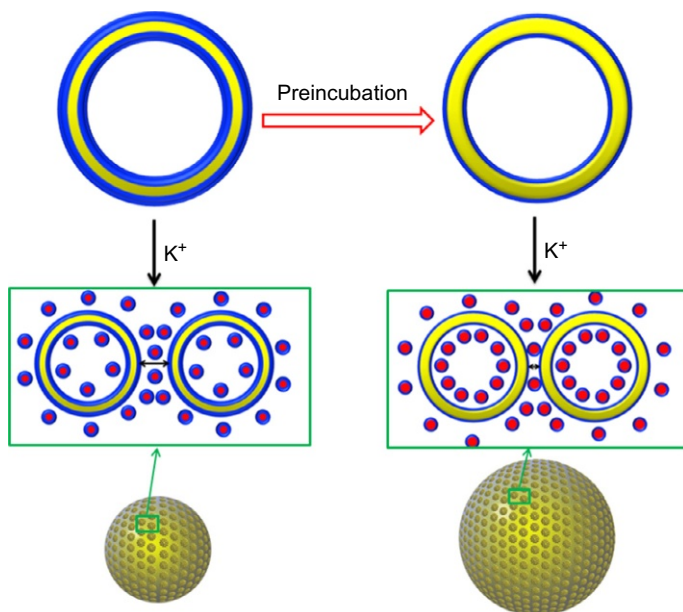


**Fig. 15** After preincubation, the hydration shell (blue corona) of  $U_{60}$  clusters (yellow circle) is reduced so that more  $\text{K}^+$  ions are able to enter the inner cage of  $U_{60}$ . The diffusion of  $\text{K}^+$  ions is extremely fast and goes to completion before blackberry are formed.

and  $U_{60}/CsCl$  blackberry sizes remained, which confirmed our previous conclusion (65).

Those conclusions were further proved by ITC studies. One set of  $U_{60}$  solutions were titrated directly at  $50^{\circ}C$ , while the other set of solutions were preincubated at  $50^{\circ}C$  for 3 days, before ITC measurements. First, the results showed that no noticeable interaction between  $U_{60}$  and  $Na^{+}$  existed after preincubation, while the binding strength between  $U_{60}$  and  $K^{+}$  were still strong, suggesting that indeed  $U_{60}$  can distinguish between  $Na^{+}$  and  $K^{+}$  at  $50^{\circ}C$ . Second, the entropy change ( $\Delta S$ ) became much more positive after preincubation. Although the thicknesses of hydration shells were reduced after preincubation, the entropy loss can be compensated by the excess  $K^{+}$  ions migrating out of  $U_{60}$  cages (65).

In group 4, the preincubation temperature was further increased to  $70^{\circ}C$  in order to further dehydrate  $U_{60}$  clusters. The  $U_{60}/NaCl$  solution still showed a low scattered intensity. While the  $U_{60}/CsCl$  blackberry size remained similar as in group 1, the sizes of both  $U_{60}/KCl$  and  $U_{60}/RbCl$  blackberries clearly increased comparing to group 1, suggesting that both  $K^{+}$  and  $Rb^{+}$  entered the cage of  $U_{60}$  clusters after a  $70^{\circ}C$  preincubation because of a thinner hydration shell (65).

In general,  $U_{60}$  clusters show tunable ion selectivity in respond to different temperatures.  $U_{60}$  allowed  $Na^{+}$  and  $K^{+}$  to enter the cage at room temperature. After preincubation at  $50^{\circ}C$ , only  $K^{+}$  can migrate across the surface pores. When the preincubation temperature reaches  $70^{\circ}C$ , both  $K^{+}$  and  $Rb^{+}$  can diffuse into  $U_{60}$  cages (65).



## 9. SELF-RECOGNITION BEHAVIORS DURING THEIR SELF-ASSEMBLY

Following the understanding of the mechanism and conditions of charge-mediated Blackberry-type assembly of POMs, it is also interesting to investigate their behavior in more complex environments. One important question that could be asked is if POM molecules of different nature can recognize each other in solution. This phenomenon is even more interesting in biological systems where it can be used as a model to explain their complicated and unknown behavior in solutions.

The self-recognition behavior of spherical polyprotic macroions of  $\{Mo_{72}Fe_{30}\}$  and  $\{Mo_{72}Cr_{30}\}$  was studied in dilute, homogenous solutions

(66). DLS study indicated the presence of two separate large species in solution which could represent the formation of two types of blackberries. This could be rationalized with previous understanding about the charge regulated nature of these assemblies which directly related to charge density of macroions. In addition, it was believed that different hydrogen bonding network and lability of water ligands in  $\text{Cr}^{\text{III}}(\text{H}_2\text{O})$  and  $\text{Fe}^{\text{III}}(\text{H}_2\text{O})$  groups of two macroions also contribute to the self-recognition in solution. Time-resolved SLS at early stage of self-assembly showed that dimer/oligomer formation processes in the solutions of two macroions were kinetically similar. This was suggested by almost identical slope and minor lag periods of both  $\{\text{Mo}_{72}\text{Cr}_{30}\}$  and  $\{\text{Mo}_{72}\text{Fe}_{30}\}$ . SLS study over long period of time also indicated that each macroion had faster assembly rate while they were alone compared to their mix solutions at a fixed total cluster concentration. This suggested that self-recognition started at very early stage when oligomers are forming (Fig. 16). Moreover, the self-recognition behavior remained when the pH or temperature of the solution were changed. That was however against what was expected that changing the pH or temperature would make the self-recognition more difficult by making the charge densities of the two clusters closer, or by decreasing the activation energy barrier for the blackberry formation, respectively (67).

In another study, the self-recognition of two rod-shape clusters  $((\text{C}_4\text{H}_9)_4\text{N})_7^- [\text{Mo}_6\text{O}_{18}\text{NC}(\text{OCH}_2)_3\text{XMo}_6\text{O}_{18}(\text{OCH}_2)_3\text{CNMo}_6\text{O}_{18}]$  ( $\text{X} = \text{Mn}^{\text{III}}$  (1),  $\text{Fe}^{\text{III}}$  (2)) was reported (68). These two POMs have identical morphology (lengths and diameters of  $\sim 2.77$  and  $0.88$  nm confirmed with SAXS) except for their different central metal atoms (20). Each macroion could self-assemble into blackberry structure in their dilute solutions in acetonitrile with  $\text{Zn}^{2+}$  as counterions. The mixed solution of two very similar macroions showed self-recognition behavior, as confirmed by DLS, SLS, and TEM/EDS. The difference in the blackberry size, and also the self-recognition behavior of macroions came from their different charge distribution while the overall charges were similar. DFT calculation on Milliken charge distribution showed that the central Mn atom is more positively charged than the central Fe atom, while the perimeter of the planar molecular unit of macroion containing Mn is more negative compared to the one with Fe, making their net charges still identical. This difference in charge distribution affected the interaction of two macroions with the surrounding counterions and led to the formation of Blackberries of different sizes and

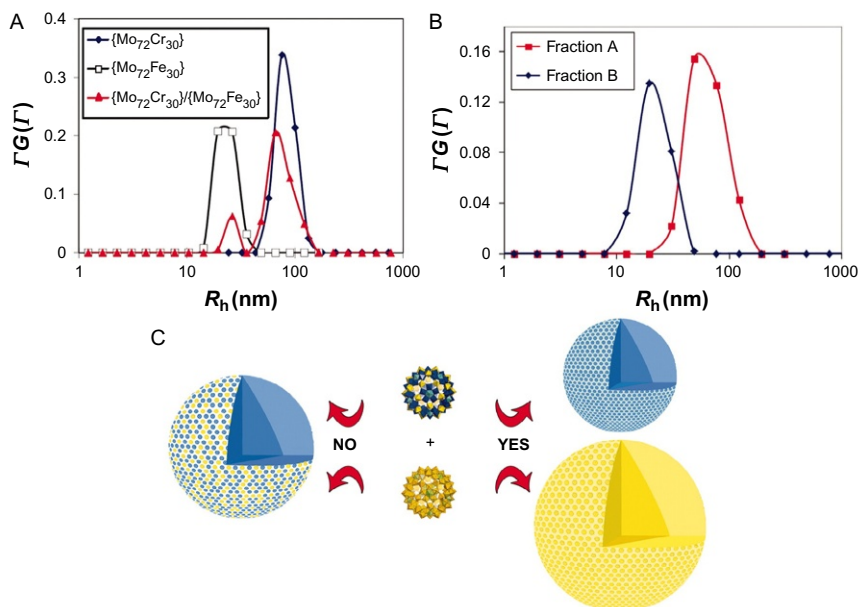


**Fig. 16** (A) CONTIN analysis of the DLS studies at 90 degree scattering angle measured for aqueous solutions containing  $\{Mo_{72}Cr_{30}\}$  or  $\{Mo_{72}Fe_{30}\}$  (0.1 mg/mL each), as well as for a solution containing both species (0.1 mg/mL of each) (pH 4.2). (B) CONTIN analysis of the DLS experiment carried out on the two components after ultrafiltration of the aqueous solution originally containing both  $\{Mo_{72}Cr_{30}\}$  and  $\{Mo_{72}Fe_{30}\}$  (0.1 mg/mL of each). (C) (Middle) In mixed dilute aqueous solutions, the clusters (polyhedral representation)  $\{Mo_{72}Fe_{30}\}$  (Top) and  $\{Mo_{72}Cr_{30}\}$  (Bottom) self-assemble into different (i.e., individual) blackberry structures of the  $Cr_{30}$  (yellow) and  $Fe_{30}$  type (blue)—with interfacial water between the macroions (Right)—and do not form mixed species (such as the hypothetical structure shown in the left).

also self-recognition in the mixture. This observation proved that beside difference in charge density, dissimilarity in charge distribution could also make a difference in solution behavior of macroions.

To further push the limit, self-recognition and chiral selection of racemic mixture of two wheel-shaped enantiomer macroions ( $[Fe_{28}(\mu_3-O)_8(Tart)_{16}(HCOO)_{24}]^{20-}$  (Tart  $\frac{1}{4}$  D- or L-tartaric acid tetra-anion)) (21) were studied (69). It was observed that enantiomers remained self-sorted and self-assembled into two different assemblies in their racemic mixture solution (Fig. 17). It was also shown that the addition of chiral coions could suppress the self-assembly of one type of macroionic enantiomers into blackberry structures while promoting the self-assembly of the other type. As a result, blackberries formed in



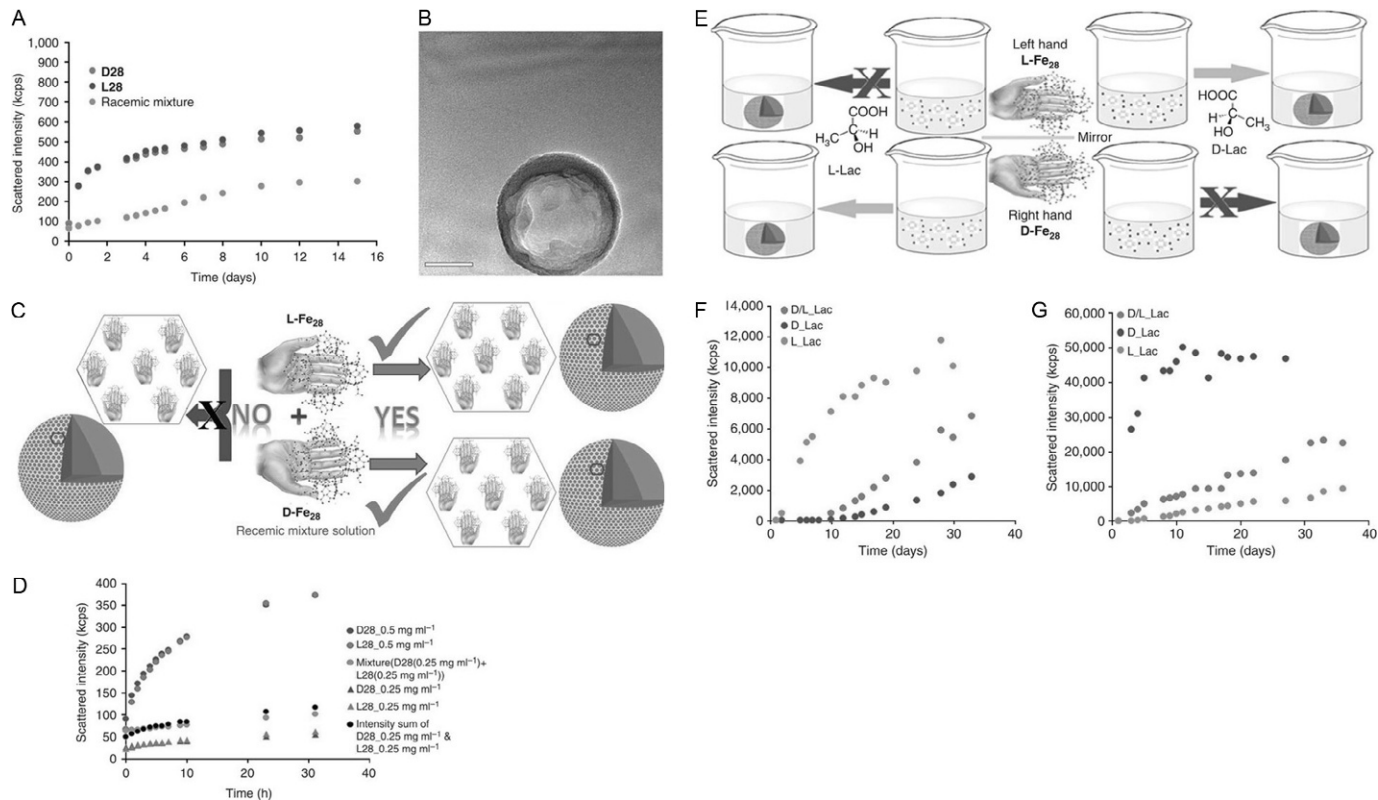


**Fig. 17** (Left) (A) SLS results of Ba-D-Fe<sub>28</sub>, Ba-L-Fe<sub>28</sub> and their racemic mixture solutions. (B) TEM image of the assembly in the aged solution of Ba-D-Fe<sub>28</sub> (0.5 mg/mL). Scale bar, 50 nm. (C) Graphical representation of the chiral recognition behavior. (D) SLS monitoring of different solutions for 31 h (Right). (E) Graphical representation of the chiral selection experiments by the introduction of lactic acid molecules. (F,G) SLS results of Ba-D-Fe<sub>28</sub> (0.5 mg/mL) and Ba-L-Fe<sub>28</sub> (0.5 mg/mL) in three different buffers, respectively.

solution only contained one type of enantiomer while the other type remained as single clusters. This property could be used to separate enantiomers from their mixture due to self-assembly of one type to larger blackberry structure and the other one remain unaffected in solution. This study suggested that long-range, charge-mediated electrostatic interactions is essential in chiral recognition of chiral macroions in solution.



## 10. SIMULATION STUDIES ON SELF-ASSEMBLY OF POM MACROIONS

Various simulation approaches were applied to help finding better understanding over solution behavior and blackberry type assembly process of hydrophilic macroions in solution.

Chaumont and Wipff studied the interaction of Keggin clusters with different counterions, e.g.,  $\text{Cs}^+$ ,  $\text{NBu}_4^+$ ,  $\text{UO}_2^{2+}$ ,  $\text{Eu}^{3+}$ ,  $\text{H}_3\text{O}^+$ , and  $\text{H}_5\text{O}_2^+$  in water and methanol solutions. They found that POMs, mostly aggregate not only into dimers with short distances between them but also into oligomers in concentrated solutions. They showed that dynamic behavior of POMs which affects their solution behavior is dependent on the charge, the thickness of hydration layer, and size of the surrounding counterions (70). Wipff's other study also confirmed the counterion-mediated attraction and hydrogen bonding as driving forces between Keggin POMs (71). They used potential of mean force to calculate the free energy change  $\Delta G$  as a function of distance between Keggin anions. They found that the free energy profile is quite flat with tiny minimum at 11 Å and suggested that anions could form contact ion pairs in the presence of their counterions. Same results (minimum around 10 Å and contact ion pairs) were observed with different methodologies which supported their results. Above findings helped to understand the role of counterions in bridging the Keggin-type POMs in solution and suggested that they basically act like "cationic glue."

Verhoeff *et al.* proposed a semiempirical model through a thermodynamic study over blackberry structures to describe the relation between equilibrium size of single layer shell and dielectric constant of the medium (26). They suggested that the cohesive bond energy between POMs on the shell was in agreement with critical aggregation concentration which was independent of the model. Their model was based on the assumption that equilibrium size is determined by their renormalized charge density regulated by condensation of counterions. Their simplified model based on free

energy of the shell showed that the size of the shells is linearly dependent on the inverse of the dielectric constant ( $R \sim -48\lambda_{Bu}/\psi^2$ ).

Liu *et al.* recently applied coarse-grained molecular dynamic model to study the interactions of charge macroions in the presence of their counterions in solution (72). They neglected the atomic details of the macroions so that it could be generalized to other macroions. The macroions were mimicked as hollow spheres comprise charged and uncharged beads as depicted in Fig. 18. In this model, the van der Waals and electrostatic forces were emphasized as main interactions between macroions and their surroundings. With all above assumptions, it was shown that the role of van der Waals forces in the self-assembly of macroions should be minimal and electrostatic interactions play a major part instead.

It was suggested that the counterion mediation between macroions is essential in dimer and eventually blackberry formation. It was shown that like charge macroions attract each other to form aggregates while counterions are among them and also the absence of charge would result in minimal attraction of macroions in solution (Fig. 19E). The reverse simulation was designed and started with aggregated configuration (Fig. 19B) but in the absence of all electrostatic interactions; disassembly of all aggregates was observed within a few picoseconds. It was claimed that electrostatic force rather than van der Waals forces are responsible for the self-assembly of macroions in solution (Fig. 19B and C). To study the effect of surface charge

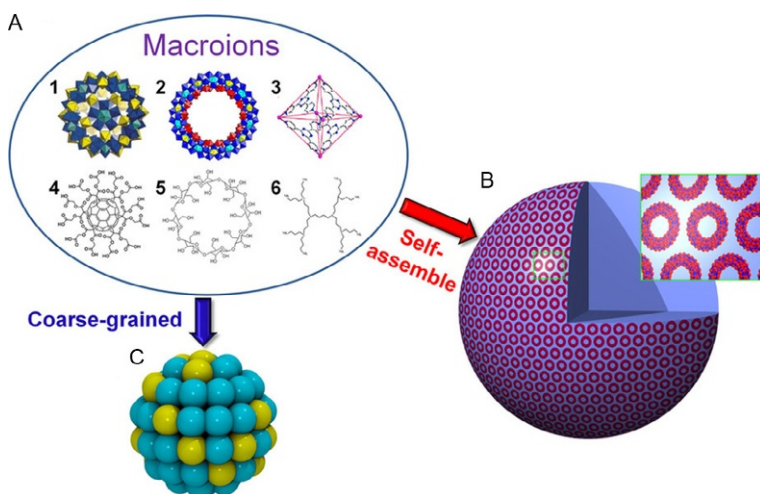


**Fig. 18** A coarse-grained model designed for general spherical macroions that form blackberries in solution.

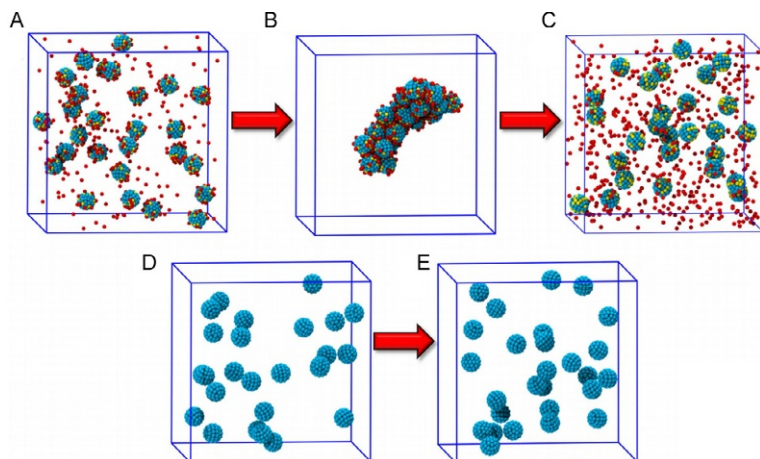


**Fig. 19** (A,D) at the beginning and (B,E) at the end of the simulations, respectively. Coloring: charged beads on macroions are given in *yellow*, uncharged beads on macroions are *cyan*, and charged counterions are *red*. Turning off the charges on the macroions and counterions after aggregate formation and running the simulation further results in a disassembled state (C).

of macroions on their aggregation, the number of charged beads was changed from 2 to 64 and observed that the moderate amount of charge resulted in the most number of nearest neighbors which was in good agreement with the experimental results.



## 11. CONCLUSIONS

The solution behaviors of hydrophilic POM macroions are dominated by the macroion-counterion interaction. The strength of this attractive force determines the degree of counterion association and consequently controls the nature of macroion-macroion interaction—when it becomes attractive, blackberry formation occurs with the blackberry size calibrates the strength of the attraction. Counterion exchange around macroions can be achieved as macroions accurately choose counterions based on their valance and hydrated size. Counterion distributions inside and around macroions can be associated with many features of the macroions, including the self-recognition feature of POM macroions during their self-assembly. As the simplest model, POM macroions can be applied as models to understand and mimic some biological phenomenon such as the chiral recognition, virus shell formation, and protein ion channels.

## ACKNOWLEDGMENTS

T.L. acknowledges support from NSF (CHE1607138), the Materials Science of Actinides Center, an Energy Frontier Research Center funded by the U.S. Department of Energy, Office of Science, Office of Basic Energy Sciences under Award Number DE-SC0001089 and the University of Akron.

## REFERENCE

1. Hill, C. L. *Chem. Rev.* **1998**, *98*(1), 1.
2. Long, D.-L.; Burkholder, E.; Cronin, L. *Chem. Soc. Rev.* **2007**, *36*(1), 105.
3. Jing, B.; Hutin, M.; Connor, E.; Cronin, L.; Zhu, Y. *Chem. Sci.* **2013**, *4*(10), 3818.
4. Li, H.; Jia, Y.; Wang, A.; Cui, W.; Ma, H.; Feng, X.; Li, J. *Chem. Eur. J.* **2014**, *20*(2), 499.
5. Fielden, J.; Sumliner, J. M.; Han, N.; Geletii, Y. V.; Xiang, X.; Musaev, D. G.; Lian, T.; Hill, C. L. *Chem. Sci.* **2015**, *6*(10), 5531.
6. Guo, W.; Luo, Z.; Lv, H.; Hill, C. L. *ACS Catal.* **2014**, *4*(4), 1154.
7. Liu, T. *Langmuir* **2009**, *26*(12), 9202.
8. Yin, P.; Li, D.; Liu, T. *Chem. Soc. Rev.* **2012**, *41*(22), 7368.
9. Müller, A.; Roy, S. *Coord. Chem. Rev.* **2003**, *245*(1), 153.
10. Müller, A.; Sarkar, S.; Shah, S. Q. N.; Bögge, H.; Schmidtman, M.; Sarkar, S.; Kögerler, P.; Hauptfleisch, B.; Trautwein, A. X.; Schünemann, V. *Angew. Chem. Int. Ed. Engl.* **1999**, *38*(21), 3238.
11. Todea, A. M.; Merca, A.; Bögge, H.; van Slageren, J.; Dressel, M.; Engelhardt, L.; Luban, M.; Glaser, T.; Henry, M.; Mueller, A. *Angew. Chem. Int. Ed. Engl.* **2007**, *119*(32), 6218.
12. Müller, A.; Das, S. K.; Fedin, V. P.; Krickemeyer, E.; Beugholt, C.; Bögge, H.; Schmidtman, M.; Hauptfleisch, B. *Z. Anorg. Allg. Chem.* **1999**, *625*(7), 1187.
13. Mal, S. S.; Kortz, U. *Angew. Chem. Int. Ed. Engl.* **2005**, *44*(24), 3777.
14. Howell, R. C.; Perez, F. G.; Jain, S.; Horrocks, D., Jr.; Rheingold, A. L.; Francesconi, L. C. *Angew. Chem. Int. Ed. Engl.* **2001**, *40*(21), 4031.
15. Müller, A.; Krickemeyer, E.; Bögge, H.; Schmidtman, M.; Peters, F. *Angew. Chem. Int. Ed. Engl.* **1998**, *37*(24), 3359.
16. Botar, B.; Kögerler, P.; Hill, C. L. *Chem. Commun.* **2005**, *25*, 3138.
17. Nyman, M.; Burns, P. C. *Chem. Soc. Rev.* **2012**, *41*(22), 7354.
18. Qiu, J.; Burns, P. C. *Chem. Rev.* **2012**, *113*(2), 1097.
19. Fang, X.; Kögerler, P.; Furukawa, Y.; Speldrich, M.; Luban, M. *Angew. Chem. Int. Ed. Engl.* **2011**, *50*(22), 5212.
20. Zhang, J.; Hao, J.; Wei, Y.; Xiao, F.; Yin, P.; Wang, L. *J. Am. Chem. Soc.* **2009**, *132*(1), 14.
21. Zhang, Z. M.; Li, Y. G.; Yao, S.; Wang, E. B.; Wang, Y. H.; Clérac, R. *Angew. Chem. Int. Ed. Engl.* **2009**, *121*(9), 1609.
22. Burns, P. C.; Kubatko, K. A.; Sigmon, G.; Fryer, B. J.; Gagnon, J. E.; Antonio, M. R.; Soderholm, L. *Angew. Chem. Int. Ed. Engl.* **2005**, *44*(14), 2135.
23. Sigmon, G. E.; Unruh, D. K.; Ling, J.; Weaver, B.; Ward, M.; Pressprich, L.; Simonetti, A.; Burns, P. C. *Angew. Chem. Int. Ed. Engl.* **2009**, *48*(15), 2737.
24. Müller, A.; Diemann, E.; Kuhlmann, C.; Eimer, W.; Serain, C.; Tak, T.; Knöchel, A.; Pranzas, P. K. *Chem. Commun.* **2001**, *19*, 1928.
25. Liu, T.; Diemann, E.; Li, H.; Dress, A. W.; Müller, A. *Nature* **2003**, *426*(6962), 59.
26. Verhoeff, A. A.; Kistler, M. L.; Bhatt, A.; Pigga, J.; Groenewold, J.; Klokkenburg, M.; Veen, S.; Roy, S.; Liu, T.; Kegel, W. K. *Phys. Rev. Lett.* **2007**, *99*(6), 066104.
27. Liu, T.; Imber, B.; Diemann, E.; Liu, G.; Cokleski, K.; Li, H.; Chen, Z.; Müller, A. *J. Am. Chem. Soc.* **2006**, *128*(49), 15914.

28. Kistler, M. L.; Bhatt, A.; Liu, G.; Casa, D.; Liu, T. *J. Am. Chem. Soc.* **2007**, *129*(20), 6453.
29. Sogami, I.; Ise, N. *J. Chem. Phys.* **1984**, *81*(12), 6320.
30. Chu, B.; Hsiao, B. S. *Chem. Mater. Rev.* **2001**, *101*(6), 1727.
31. Pigga, J. M.; Kistler, M. L.; Shew, C. Y.; Antonio, M. R.; Liu, T. *Angew. Chem. Int. Ed. Engl.* **2009**, *48*(35), 6538.
32. Kistler, M. L.; Liu, T.; Gouzerh, P.; Todea, A. M.; Müller, A. *Dalton Trans.* **2009**, *26*, 5094.
33. Pigga, J. M.; Teprovich, J. A., Jr.; Flowers, R. A.; Antonio, M. R.; Liu, T. *Langmuir* **2010**, *26*(12), 9449.
34. Haso, F.; Fang, X.; Yin, P.; Li, D.; Ross, J. L.; Liu, T. *Chem. Commun.* **2013**, *49*(6), 609.
35. Oleinikova, A.; Weingärtner, H.; Chaplin, M.; Diemann, E.; Bögge, H.; Müller, A. *ChemPhysChem* **2007**, *8*(5), 646.
36. Liu, G.; Kistler, M. L.; Li, T.; Bhatt, A.; Liu, T. *J. Cluster Sci.* **2006**, *17*(2), 427.
37. Liu, T. *J. Am. Chem. Soc.* **2003**, *125*(2), 312.
38. Liu, T. *J. Am. Chem. Soc.* **2002**, *124*(37), 10942.
39. Liu, G.; Cai, Y.; Liu, T. *J. Am. Chem. Soc.* **2004**, *126*(51), 16690.
40. Liu, G.; Liu, T. *Langmuir* **2005**, *21*(7), 2713.
41. Liu, G.; Liu, T.; Mal, S. S.; Kortz, U. *J. Am. Chem. Soc.* **2006**, *128*(31), 10103.
42. Zhang, J.; Li, D.; Liu, G.; Glover, K. J.; Liu, T. *J. Am. Chem. Soc.* **2009**, *131*(42), 15152.
43. Gil, A.; Karhánek, D.; Miró, P.; Antonio, M. R.; Nyman, M.; Bo, C. *Chem. Eur. J.* **2012**, *18*(27), 8340.
44. Nyman, M.; Alam, T. M. *J. Am. Chem. Soc.* **2012**, *134*(49), 20131.
45. Nyman, M.; Rodriguez, M. A.; Alam, T. M. *Eur. J. Inorg. Chem.* **2011**, *2011*(14), 2197.
46. Li, D.; Simotwo, S.; Nyman, M.; Liu, T. *Chem. Eur. J.* **2014**, *20*(6), 1683.
47. Zlotnick, A.; Johnson, J. M.; Wingfield, P. W.; Stahl, S. J.; Endres, D. *Biochemistry* **1999**, *38*(44), 14644.
48. Casini, G. L.; Graham, D.; Heine, D.; Garcea, R. L.; Wu, D. T. *Virology* **2004**, *325*(2), 320.
49. Zlotnick, A. *Virology* **2003**, *315*(2), 269.
50. Zlotnick, A.; Aldrich, R.; Johnson, J. M.; Ceres, P.; Young, M. J. *Virology* **2000**, *277*(2), 450.
51. Prevelige, P. E., Jr.; Thomas, D.; King, J. *Biophys. J.* **1993**, *64*(3), 824.
52. Marcus, Y.; Hefter, G. *Chem. Rev.* **2006**, *106*(11), 4585.
53. Antonio, M. R.; Nyman, M.; Anderson, T. M. *Angew. Chem. Int. Ed. Engl.* **2009**, *121*(33), 6252.
54. Fullmer, L. B.; Molina, P. I.; Antonio, M. R.; Nyman, M. *Dalton Trans.* **2014**, *43*(41), 15295.
55. Mishra, P. P.; Pigga, J.; Liu, T. *J. Am. Chem. Soc.* **2008**, *130*(5), 1548.
56. Zhou, Y.; Morais-Cabral, J. H.; Kaufman, A.; MacKinnon, R. *Nature* **2001**, *414*(6859), 43.
57. Pinto, L. H.; Dieckmann, G. R.; Gandhi, C. S.; Papworth, C. G.; Braman, J.; Shaughnessy, M. A.; Lear, J. D.; Lamb, R. A.; DeGrado, W. F. *Proc. Natl. Acad. Sci. U.S.A.* **1997**, *94*(21), 11301.
58. Kang, Y.; Zhang, Z.; Shi, H.; Zhang, J.; Liang, L.; Wang, Q.; Ågren, H.; Tu, Y. *Nanoscale* **2014**, *6*(18), 10666.
59. Galzi, J. -L.; Devillers-Thiery, A.; Hussy, N.; Bertrand, S.; Changeux, J. -P.; Bertrand, D. *Nature* **1992**, *359*(6395), 500.
60. Petina, O.; Rehder, D.; Haupt, E. T.; Grego, A.; Weinstock, I. A.; Merca, A.; Bögge, H.; Szakács, J.; Müller, A. *Angew. Chem. Int. Ed. Engl.* **2011**, *50*(2), 410.
61. Mahon, E.; Garai, S.; Müller, A.; Barboiu, M. *Adv. Mater.* **2015**, *27*(35), 5165.
62. Flynn, S. L.; Szymanski, J. E.; Gao, Y.; Liu, T.; Burns, P. C.; Fein, J. B. *Geochim. Cosmochim. Acta* **2015**, *156*, 94.

63. Soltis, J. A.; Wallace, C. M.; Penn, R. L.; Burns, P. C. *J. Am. Chem. Soc.* **2015**, *138*(1), 191.
64. Gao, Y.; Haso, F.; Szymanowski, J. E.; Zhou, J.; Hu, L.; Burns, P. C.; Liu, T. *Chem. Eur. J.* **2015**, *21*(51), 18785.
65. Gao, Y.; Szymanowski, J. E.; Sun, X.; Burns, P. C.; Liu, T. *Angew. Chem. Int. Ed. Engl.* **2016**, *55*(24), 6887.
66. Liu, T.; Langston, M. L.; Li, D.; Pigga, J. M.; Pichon, C.; Todea, A. M.; Müller, A. *Science* **2011**, *331*(6024), 1590.
67. Haso, F.; Li, D.; Garai, S.; Pigga, J. M.; Liu, T. *Chem. Eur. J.* **2015**, *21*(38), 13234.
68. Yin, P.; Zhang, J.; Li, T.; Zuo, X.; Hao, J.; Warner, A. M.; Chattopadhyay, S.; Shibata, T.; Wei, Y.; Liu, T. *J. Am. Chem. Soc.* **2013**, *135*(11), 4529.
69. Yin, P.; Zhang, Z.-M.; Lv, H.; Li, T.; Haso, F.; Hu, L.; Zhang, B.; Bacsá, J.; Wei, Y.; Gao, Y.; Hou, Y.; Li, Y.-G.; Hill, C. L.; Wang, E.-B.; Liu, T. *Nat. Commun.* **2015**, *6*, 1–8.
70. Chaumont, A.; Wipff, G. *Phys. Chem. Chem. Phys.* **2008**, *10*(46), 6940.
71. Chaumont, A.; Wipff, G. *C. R. Chim.* **2012**, *15*(2), 107.
72. Liu, Z.; Liu, T.; Tsige, M. *Sci. Rep.* **2016**, *6*, 1–9.

This page intentionally left blank





# Electron Transfer–Oxygen Transfer Reactions and Beyond With Polyoxometalates

R. Neumann<sup>1</sup>

Weizmann Institute of Science, Rehovot, Israel

<sup>1</sup>Corresponding author: e-mail address: Ronny.Neumann@weizmann.ac.il

## Contents

1. Mechanisms for the Aerobic Oxidation of Organic Compounds	68
2. The H <sub>5</sub> PV <sub>2</sub> Mo <sub>10</sub> O <sub>40</sub> Polyoxometalate and Electron Transfer Oxidations	70
3. The First Example of Electron Transfer–Oxygen Transfer Catalyzed by H <sub>5</sub> PV <sub>2</sub> Mo <sub>10</sub> O <sub>40</sub>	72
4. Oxidation of Sulfides	73
5. Oxidation of Primary and Vicinal Alcohols	76
6. Oxidation of via Activation of C–H Bonds Revisited	79
7. Insertion of Oxygen Into a Carbon–Metal Bond	84
8. The Structure of H <sub>5</sub> PV <sub>2</sub> Mo <sub>10</sub> O <sub>40</sub> During the Catalytic Reaction	85
9. Conclusions	87
Acknowledgments	89
References	89

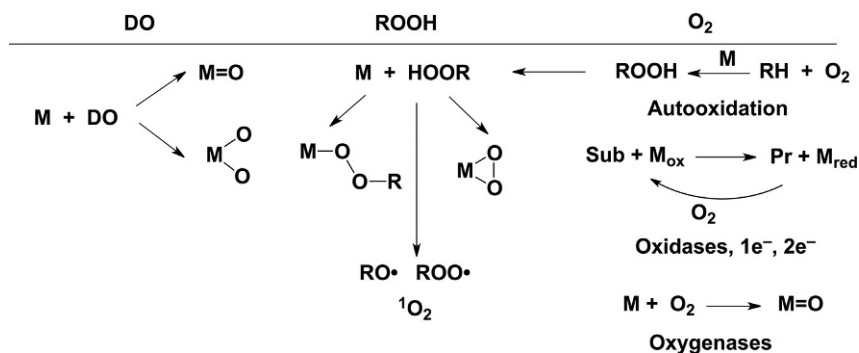
## Abstract

The unique ability of H<sub>5</sub>PV<sub>2</sub>Mo<sub>10</sub>O<sub>40</sub> to catalyze electron transfer–oxygen transfer oxidations via activation of sulfides, and carbon–hydrogen, carbon–carbon, and carbon metal bonds, is discussed in the context of sustainable transformations of arenes, the deconstruction of carbohydrates to synthesis gas as a liquid fuel precursor and the prospects for hydroxylation of alkanes. Emphasis is placed on the mechanistic aspects of these reactions including isolation and or observation of intermediates, and the importance of solvents on the oxidation potential of H<sub>5</sub>PV<sub>2</sub>Mo<sub>10</sub>O<sub>40</sub>. Descriptions possible structures of reactive intermediates as deduced from EPR spectroscopy and DFT calculations are also included.



## 1. MECHANISMS FOR THE AEROBIC OXIDATION OF ORGANIC COMPOUNDS

One can consider three basic types of oxygen donors for the metal-catalyzed oxygenation of organic compounds, [Scheme 1](#). (a) Oxygen donors, **DO**, that can broadly vary from hypochlorite, iodosobenzene, periodate, nitrous oxide, and various other inorganic or organic donors. These compounds can be activated by metal species to yield high-valent metal-oxo species, or metal-dioxo species. Such compounds have a very broad range activity ranging from hydroxylation of C–H bonds, addition to nucleophiles to carbon–carbon bond cleavage reactions. (b) Peroxides such as peroxy acids, hydrogen peroxide, and other organic and inorganic analogs such as *t*-butylhydroperoxide and peroxosulfate that can react in nonredox pathways to yield end-on and side-on metal-peroxo species that react as electrophiles to nucleophilic substrates such as alkenes and sulfides. Alternatively, metal complexes of higher oxidation potential lead to homolysis of the O–O bond and formation of radicals that can react via hydrogen atom transfer reactions. Under appropriate conditions even the “dark” formation for singlet oxygen is possible that has its signature reactivity. (c) Molecular oxygen has its own possible modes of reaction as will be amplified upon also below. It is, however, worthwhile to note that O<sub>2</sub>-based reaction pathways can be interconnected with those using peroxides and those forming metal-oxo species. For example, O<sub>2</sub> in autooxidation reactions leads to intermediate formation of hydroperoxides. Furthermore, monooxygenase enzymes and their mimics catalyze oxygenation via

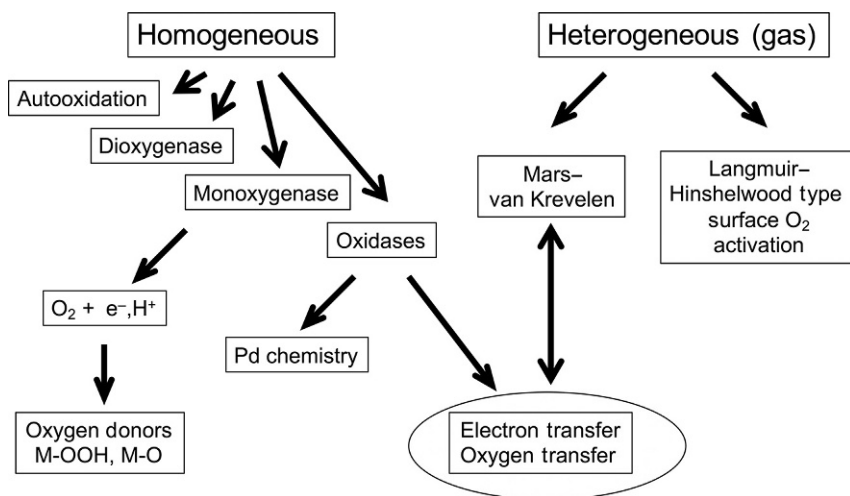


**Scheme 1** General overview of metal-catalyzed oxidation.

formation of reactive iron–oxo species (DO) from  $O_2$  and two electrons and two protons.

One can zoom in on the various known mechanistic pathways that utilize  $O_2$  in the context of both heterogeneous gas phase reactions and homogeneous liquid phase reactions as shown in [Scheme 2](#).

In the liquid phase, hydrocarbons most ubiquitously react via an autooxidation mechanism that is initiated by the formation of a carbon-centered radical, typically after a hydrogen atom transfer step. The carbon-centered radical usually reacts at a diffusion-controlled rate with  $O_2$  to yield a peroxy intermediate that propagates the radical chain auto-oxidation, until the chain is terminated. These reactions have a synthetically limited scope yet they are crucial in industrial important syntheses of the benzoic acid, terephthalic acid, phenol and adipic acid. In nature, mono-oxygenase enzymes are dominant for the activation of  $O_2$  and oxygenation. Although there are mechanistic variants, in general, the reactions proceed via the expenditure of electron donors or reducing agents and protons to yield intermediate and often very reactive higher valent-oxo and also peroxy species. Dioxygenase type reactions where the O–O of  $O_2$  is homolytically split to yield two metal-oxo species are rather rare, however, have been documented as being moderately effective for the epoxidation and dihydroxylation of alkenes. Dehydrogenation or oxidation without oxygen



**Scheme 2** Pathways for heterogeneous gas phase and homogeneous liquid phase oxidation and oxygenation reactions using molecular oxygen.

transfer is also rather common, for example, in the oxidation of alcohols to ketones or aldehydes. Particularly common is the use of palladium(II) catalysts that are also active in Wacker-type reactions that involve addition to C–C double or triple bonds coupled with dehydrogenation. Heterogeneous gas phase oxidations typically require elevated temperatures, 250°C and above, and can be divided into two major categories. First are those catalyzed by metals usually involve Langmuir–Hinshelwood or related Eley–Rideal type chemisorption of the hydrocarbon and/or O<sub>2</sub> to the metal followed by poorly understood oxygen transfer. The silver metal-catalyzed aerobic epoxidation of ethylene to ethylene oxide is an important example of such a reaction. Second are those catalyzed by metal oxides that proceed by the Mars–van Krevelen mechanism where the reaction is initiated by what is thought to be either a proton-coupled electron transfer (PCET) or a hydrogen atom transfer reaction from the substrate to the metal oxide. In certain cases, dehydrogenation only occurs, for example, butane to butadiene or methanol to formaldehyde. In other cases, substrate activation is followed by oxygen transfer from the reduced metal oxide to the hydrocarbon as observed, for example, in the synthesis of maleic anhydride and phthalic anhydride.

About 15 years ago, we asked ourselves can Mars–van Krevelen type reactions found until then only in the realm of high-temperature gas-phase reactions be adapted to low-temperature liquid-phase homogeneous reactions? Herein, we review the developments in this area with emphasis on the synthetic applications and mechanistic understanding made since about 2009.



## 2. THE H<sub>5</sub>PV<sub>2</sub>Mo<sub>10</sub>O<sub>40</sub> POLYOXOMETALATE AND ELECTRON TRANSFER OXIDATIONS

Catalytic dehydrogenation of organic substrates or catalytic oxidase reactions is a synthetically useful class of reactions where two hydrogen atoms are removed from a substrate, for example, synthesis of alkynes from alkenes or aldehydes/ketones from alcohols and many more for a variety of transformations. In the 1970s Matveev and Kozhevnikov and their research group showed that the H<sub>3+x</sub>PV<sub>x</sub>Mo<sub>12-x</sub>O<sub>40</sub> ( $x=1-6$ ) phosphovanadomolybdate Keggin type compounds could be used as oxidative dehydrogenation catalysts, although the number of catalytic turnovers was limited (1). Our group was intrigued by this research and from 1988 to

2000, we began to study the activity of  $\text{H}_5\text{PV}_2\text{Mo}_{10}\text{O}_{40}$ , that has an  $\alpha$ -Keggin structure, Fig. 1 (2). This compound has central tetrahedral phosphate moiety that is surrounded by 12 molybdenum and vanadium addenda that are arranged as 4  $\text{M}_3\text{O}_9$  triads. In its orange-colored oxidized form, all the addenda metals have empty  $d$  orbitals and have tetragonally distorted octahedral coordination. Upon reduction, the compounds turn green and then blue with an absorption maximum and 700–750 nm that varies according to the number of electrons on the reduced polyoxometalate. Most of the electron density is located on the vanadium atoms.

Our synthetically oriented research in this area that included dehydrogenation of dienes to arenes, alcohol and amine dehydrogenation, and well as phenol dimerization among other transformations has been previously reviewed. A mechanistic study in 1992 on the oxidative dehydrogenation of  $\alpha$ -terpinene to  $p$ -cymene showed that there was an equilibrium redox reaction that yielded an  $\alpha$ -terpinene radical– $[\text{PV}^{\text{IV}}\text{V}^{\text{V}}\text{Mo}_{10}\text{O}_{40}]^{6-}$  ion pair intermediate through a PCET reaction (3). The cation radical of  $\alpha$ -terpinene was isolated and studied by EPR spectroscopy. This led to the generalization that  $\text{H}_5\text{PV}^{\text{V}}_2\text{Mo}_{10}\text{O}_{40}$  was an electron transfer (ET) oxidant wherein the reduced  $\text{H}_7\text{PV}^{\text{IV}}_2\text{Mo}_{10}\text{O}_{40}$  formed in the reaction could be reoxidized by  $\text{O}_2$  to yield the dehydrogenated substrate and  $\text{H}_2\text{O}$  as products, Scheme 3.

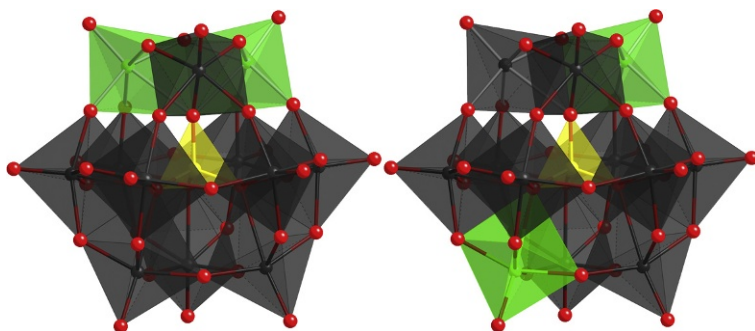
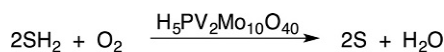


Fig. 1 Two of the five isomers of  $\text{H}_5\text{PV}_2\text{Mo}_{10}\text{O}_{40}$  showing a vicinal and distal isomer.



**Scheme 3** Aerobic oxidative dehydrogenation of substrates catalyzed by  $\text{H}_5\text{PV}_2\text{Mo}_{10}\text{O}_{40}$ .

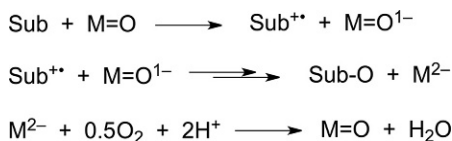


### 3. THE FIRST EXAMPLE OF ELECTRON TRANSFER–OXYGEN TRANSFER CATALYZED BY $\text{H}_5\text{PV}_2\text{Mo}_{10}\text{O}_{40}$

Up to the year 2000,  $\text{H}_5\text{PV}_2\text{Mo}_{10}\text{O}_{40}$  had only been used as an electron transfer oxidant and the question was: Could  $\text{H}_5\text{PV}_2\text{Mo}_{10}\text{O}_{40}$  react also as an electron transfer–oxygen transfer (ET–OT) catalyst? The implication was that such a catalytic oxygenation reaction would be a homogeneous analog of a heterogeneous gas phase Mars–van Krevelen reaction. In generalized form this kind of transformation can be summarized in a generic way as shown in Scheme 4. It should also be noted that formally this is also a monooxygenase reaction, where the substrate acts as electron and proton donor, since in the reaction scheme water is formed. The mechanism, however, is completely different than that observed for monooxygenase enzymes. Most notably, it is the *reduced* metal oxide species that is the oxygen transfer agent rather than a higher valent metal–oxo species commonly the active intermediate in monooxygenase enzymes and their mimics.

In a comprehensive study, we showed that  $\text{H}_5\text{PV}_2\text{Mo}_{10}\text{O}_{40}$  indeed was a catalyst for ET–OT reactions where the oxygenation of activated arenes with weak benzylic C–H bonds, such as xanthene and alike as well as arenes of low oxidation potential such as anthracene was possible (4). The crucial verification of the ET–OT mechanism was by observation of the oxygen transfer step from 18–O labeled  $\text{H}_5\text{PV}_2\text{Mo}_{10}\text{O}_{40}$  to both xanthene and anthracene. The research was supported by various kinetic measurements such as correlation of the rate as a function of the ionization potential of the substrate and deuterium isotope effects, substrate probes and isolation of intermediates, and their identification by EPR and NMR spectroscopy.

One key question that arose during this research was: How could one reconcile the observation that  $\text{H}_5\text{PV}_2\text{Mo}_{10}\text{O}_{40}$ , with an oxidation potential of 0.7 V vs NHE is able to oxidize substrates by electron transfer such as xanthene and anthracene that have an oxidation potential that is higher than 1.3 V? At this point, we realized that the difference between the oxidation



**Scheme 4** A generic ET–OT catalytic reaction.

potential of  $\text{H}_5\text{PV}_2\text{Mo}_{10}\text{O}_{40}$  and target substrates excludes the possibility of an inner sphere electron transfer. Correction of the free energy,  $\Delta G^\circ$ , under prevailing reaction conditions using Marcus theory can give the corrected free energy value,  $\Delta G^{\circ'}$ :

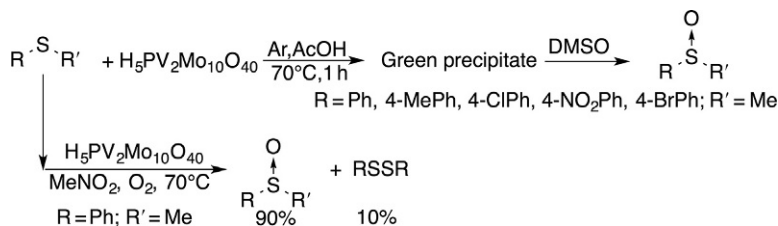
$$\Delta G^{\circ'} = \Delta G^\circ + \frac{331.2B}{r_{12}D}(Z_1 - Z_2 - 1) \quad \text{where } B = 10^{-21.9r_{12}} \sqrt{\mu/DT}$$

At a null ion strength,  $\mu = 0$ ,  $B = 1$  and therefore  $\Delta G^{\circ'}$  is a function of (i) the radius  $r_{12}$  is approximately  $7.3 \text{ \AA}$  assuming a  $r_1 = 5.6 \text{ \AA}$  for  $\text{H}_5\text{PV}_2\text{Mo}_{10}\text{O}_{40}$  and  $r_2 = 1.7 \text{ \AA}$  assuming a side on interaction between the polyoxometalate and the aromatic substrate. (ii)  $D$  is the dielectric constant, of the solvent. The most important factor, however, are the relative charges of the polyanion ( $Z_1 = -5$ ) and substrate ( $Z_2 = 0$ ). The calculations show the very strong positive influence of the negative charge of the polyoxometalate on  $\Delta G^{\circ'}$ . Therefore, the inherent anionic nature of the polyoxometalates is advantageous to their activity as electron transfer oxidants. Although this research provided a robust mechanistic setting for the possibility of ET–OT reactions, the specific oxygenation reactions studied, e.g., xanthene to xanthone and anthracene to anthraquinone were not of synthetic utility.

## 4. OXIDATION OF SULFIDES

Although the oxygenation of sulfides to sulfoxides with  $\text{H}_2\text{O}_2$  is a known reaction that can be catalyzed by many  $d^0$  metal-based catalysts and in some cases just in polar solvents such as methanol and perfluoroalcohols, similar catalytic oxygenation to sulfoxides or sulfones with  $\text{O}_2$  are rare and typically require rather extreme conditions. Despite this, we found that the ET–OT oxidation of sulfides with  $\text{H}_5\text{PV}_2\text{Mo}_{10}\text{O}_{40}$  is possible (5). Under anaerobic reaction conditions various arylmethyl sulfides,  $\text{ArSMe}$ , reacted with  $\text{H}_5\text{PV}_2\text{Mo}_{10}\text{O}_{40}$  in acetic acid at  $70^\circ\text{C}$  for 1 h gave a green precipitate that upon dissolution and analysis by GC showed the 100% selective formation of the corresponding sulfides,  $\text{ArS(O)Me}$ . By carrying out the reaction under various different conditions, a mechanistic scheme was proposed for this reaction, Scheme 5.

First, the reaction of  $\text{PhSMe}$  with  $\text{H}_5\text{PV}_2\text{Mo}_{10}\text{O}_{40}$  room temperature yielded a homogeneous green solution that is associated with a charge transfer complex via an ET reaction from the sulfide to the polyoxometalate. The



**Scheme 5** Oxygenation of ArSMe to the ArS(O)Me with  $\text{H}_5\text{PV}_2\text{Mo}_{10}\text{O}_{40}$  under anaerobic and aerobic conditions.

charge transfer complex had a UV–vis spectrum that showed two peaks, at  $\lambda_{\text{max}} = 650$  and 887 nm, which were assigned to strongly red shifted absorption of  $\text{PhSMe} + \bullet$  at 650 nm and a one-electron reduced polyoxometalate at 887 nm, Fig. 2.

Further support for the formation of a charge transfer complex between a sulfide and  $\text{H}_5\text{PV}_2\text{Mo}_{10}\text{O}_{40}$  was obtained by reacting thianthrene or diphenyl sulfide with  $\text{H}_5\text{PV}_2\text{Mo}_{10}\text{O}_{40}$ , which allowed the EPR observation of the cation radicals of thianthrene and diphenyl sulfide along with the one-electron reduced polyoxometalate, Fig. 3.

Finally, a Hammett plot obtained by reacting various sulfides, ArSMe with  $\text{H}_5\text{PV}_2\text{Mo}_{10}\text{O}_{40}$ , gave a slope,  $\rho = -3.6$ , supportive of the formation of a cation radical. Although in reactions using ArSMe substrates, the actual determination of the structure of the green precipitate was not possible, a similar reaction with  $\text{Et}_2\text{S}$  did allow the crystallization of this intermediate, which proved the complexation of the sulfide to a vanadium center that was “supported” on the polyoxometalate. An aerobic reaction was possible if the formation of the green precipitate could be avoided. This, for example, was possible by using nitromethane as a solvent, where a turnover frequency of  $\sim 3 \text{ h}^{-1}$  for PhSMe as substrate was observed at  $70^\circ\text{C}$  under 1 bar  $\text{O}_2$ . Interestingly, in this reaction, the major product (90% selectivity) was again the sulfoxide, but also a minor product, PhSSPh was observed (10% selectivity), that is known to be a fingerprint of a cation radical intermediate.

One notable observation in this research was that aromatic compounds with sulfur heteroatoms such as benzothiophene did not yield oxygenation products, even though a reaction between them and  $\text{H}_5\text{PV}_2\text{Mo}_{10}\text{O}_{40}$  clearly led to the reduction of the polyoxometalate and the formation of cation radicals. Interesting, also was the realization that the more extended the  $\pi$ -system the easier it should be to form a



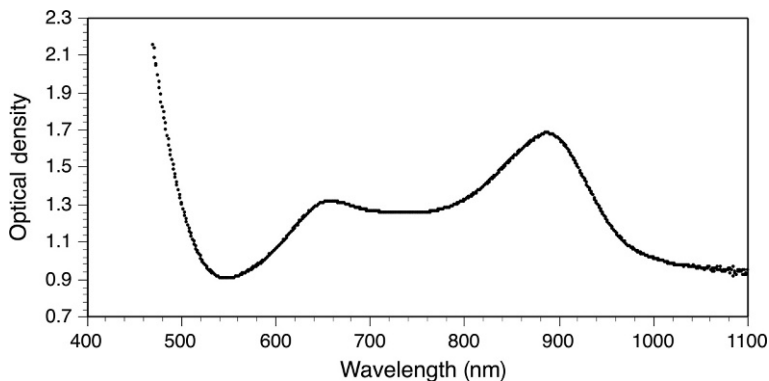


**Fig. 2** The visible spectrum of  $\text{H}_5\text{PV}^{\text{V}}\text{V}^{\text{V}}\text{Mo}_{10}\text{O}_{40}\text{-PhSMe}^{+\bullet}$ . Reprinted with permission from Khenkin, A.M.; Leitun, G.; Neumann, R. *J. Am. Chem. Soc.* **2010**, 132, 11446–11448. Copyright 2010 American Chemical Society.

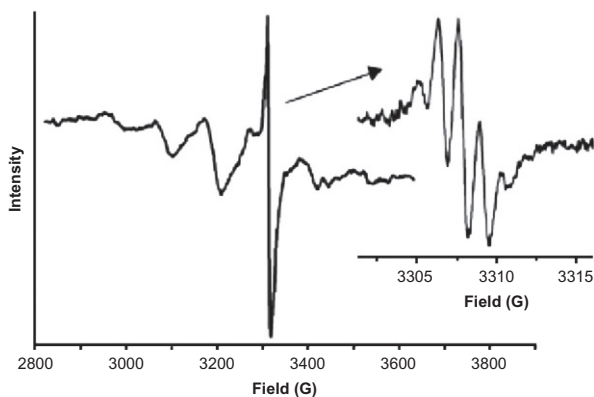
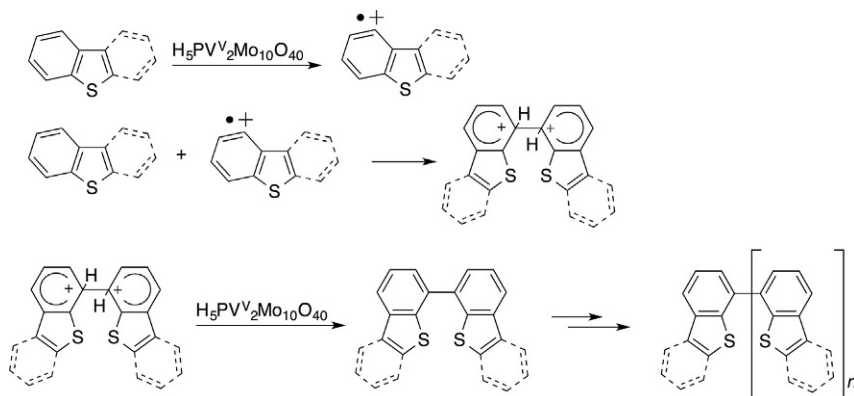


**Fig. 3** EPR spectrum resulting from a reaction of thianthrene and  $\text{H}_5\text{PV}_2\text{Mo}_{10}\text{O}_{40}$ . Reprinted with permission from Khenkin, A.M.; Leitun, G.; Neumann, R. *J. Am. Chem. Soc.* **2010**, 132, 11446–11448. Copyright 2010 American Chemical Society.

cation radical, that is, for example, the order of reactivity should be 2,7-dimethylbenzothiophene > dibenzothiophene > benzothiophene. Furthermore, heating up solutions containing sulfur-heteroaromatic compounds led to formation of benzothiophene-based polymers via the reaction of cation radicals with excess substrate, [Scheme 6 \(6\)](#). This type of polymerization proved to be useful in reducing the amount of such heteroaromatic compounds in fuels, which are refractory to common hydrodesulfurization (HDS) processes used in the oil refinery industry. Sub-ppm levels of sulfur-containing compounds were accessible.

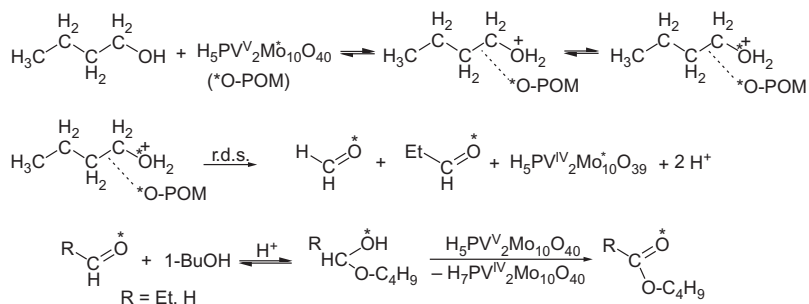


**Scheme 6** Polymerization of benzothiophene and dibenzothiophene catalyzed by  $\text{H}_5\text{PV}_2\text{Mo}_{10}\text{O}_{40}$ .

## 5. OXIDATION OF PRIMARY AND VICINAL ALCOHOLS

An important new application of  $\text{H}_5\text{PV}_2\text{Mo}_{10}\text{O}_{40}$  was in the unique oxidation of primary alcohols. Typically, such alcohols are aerobically oxidized via C–H bond activation to yield aldehydes as initial products that then are often further oxidized to carboxylic acids. Surprisingly, in the presence of  $\text{H}_5\text{PV}_2\text{Mo}_{10}\text{O}_{40}$ , this reaction was completely inhibited and instead oxidative carbon–carbon bond cleavage occurred via an ET–OT mechanism resulting in the initial formation of carbonyl compounds (7). For example, 1-butanol yielded formaldehyde and propionaldehyde as initial products while *i*-butanol yielded acetone and formaldehyde. Since the reaction conditions were acidic, and the alcohol substrate is in excess by definition, hemiacetals or acetals are immediately formed from the initial aldehyde intermediates. The later are then further oxidized to esters as the observable products, [Scheme 7](#).

This reactivity is not easily reconcilable to an ET–OT mechanism, since such alcohols have high oxidation potentials. Yet the observation of only C–C bond cleavage, and the absence of C–H bond activation in the rate determining step, as also verified by the absence of a deuterium isotope effect, seems to exclude an HAT type mechanism. Furthermore, an association complex prior to ET between the polyoxometalate and 1-butanol was observed by  $^{13}\text{C}$  NMR. Likely such an association complex changes the thermodynamics of the reaction. Noticeably, although the primary alcohol is apparently protonated, alkenes were not observed, nor were alkenes



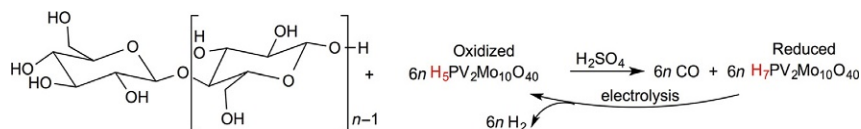
**Scheme 7** Pathway for the oxidation of 1-butanol by  $\text{H}_5\text{PV}_2\text{Mo}_{10}\text{O}_{40}$  via an ET–OT mechanism.

susceptible to C–C bond cleavage. Secondary alcohols did undergo dehydration and were not oxidized. In the oxidation reaction, the ET step was deduced from the reduction of  $\text{H}_5\text{PV}_2\text{Mo}_{10}\text{O}_{40}$  and the subsequent OT was proven by isotope incorporation into the products from 18-O labeled  $\text{H}_5\text{PV}_2\text{Mo}_{10}\text{O}_{40}$ . Kinetic experiments yielded a low negative  $\Delta S^\ddagger_{338} = -47.2 \text{ cal mol}^{-1} \text{ K}^{-1}$  indicative a highly ordered transition state in the rate determining step.

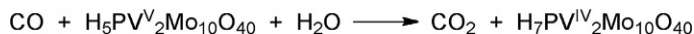
It is also notable that vicinal diols react in an identical manner although such C–C bond cleavage reactions are more common. Thus, C–C bond cleavage of 1,2-ethanediol leads to formation of formaldehyde, which then reacts with excess 1,2-ethanediol to yield 1,3-dioxolane and 2-hydroxyethylformate. Interestingly, it was possible here to clearly assess the importance of the formation of an association complex between  $\text{H}_5\text{PV}_2\text{Mo}_{10}\text{O}_{40}$  and the substrate. Thus, a comparison of the reactivity of *cis*-1,2-cyclohexanediol with *trans*-1,2-cyclohexanediol showed that the former was 15 times more reactive, even though the oxidation potentials of the substrates alone could be considered to be identical.

A further use of this unique C–C bond cleavage of primary and vicinal alcohols was in the oxidation of carbohydrates, in principle, of any type. Notably, Wasserschied and coworkers reported on such an oxidation of sugars such as glucose using  $\text{H}_5\text{PV}_2\text{Mo}_{10}\text{O}_{40}$  as catalyst in water at elevated temperatures and 30 bar  $\text{O}_2$  (8). Conversions tended to be high although selectivity to the formation of their desired product, formic acid, was only about 50% with coformation of  $\text{CO}_2$ . Unfortunately, cellulose was not reactive, because it is insoluble in water. We decided to further explore these oxidation reactions of carbohydrates (9). First, using glucose as a substrate, we found that under milder oxidation conditions, 1 bar  $\text{O}_2$ , in

methanol/water as solvent, glucose was quantitatively oxidized to formic acid and its methyl ester and formaldehyde and its mono- and dimethylated analogs. Further use of  $^{13}\text{C}$  labelled substrates revealed that the primary alcohol (C-6) was the source of formaldehyde and derivatives, while the carbon atoms (aldehyde C-1 and secondary alcohols C-2 to C-5) were oxidized to formic acid and methyl formate. A small amount of  $\text{CO}_2$  was also formed that was traced back to the C-5 carbon which is a hemiacetal in the pyranose conformation. In principle, such an ET–OT reaction converts all the carbon atoms to an oxidized product, e.g., formic acid, while the  $\text{H}_5\text{PV}_2\text{Mo}_{10}\text{O}_{40}$  is reduced and protonated by two electrons and protons as presented in generic [Scheme 4](#). Molecular oxygen is then used to form  $\text{H}_2\text{O}$ . While such a reaction is useful in the context of aerobic oxidation and formic acid and/or esters as a product, there is also a larger issue of the use of terrestrial biomass as renewable energy sources, which contains cellulose and hemicellulose as the major components. Thus, there is much interest in use of such biomass, typically agriculture waste such as wheat straw, rice hulls, and corn stover as well as various grasses. We hypothesized that (a) formic acid was a less desirable product in the context of renewable energy and (b) the electrons and protons “stored” on the polyoxometalate were being “wasted” in the formation water. We, therefore, redesigned the ET–OT reaction conditions. First, by carrying out the reaction in rather concentrated sulfuric acid as solvent quantitative conversion can easily be obtained and one can dehydrate formic acid to form carbon monoxide,  $\text{CO}$ . Second, instead of using  $\text{O}_2$  to reoxidize the polyoxometalate, the electrons and protons could be combined electrochemically to yield hydrogen. In this manner cellulose, essentially polyglucose can be completely deconstructed to yield  $\text{CO}$  and  $\text{H}_2$  or synthesis gas, where the two components are formed in separate chemical steps allowing their easy separation if so desired. The concept is summarized in [Scheme 8](#). Synthesis gas can be used in various energy-related process, for example, the formation of methanol as a fuel, or hydrocarbons via the Fischer–Tropsch reaction. Hydrogen can be used for ammonia synthesis via the Haber–Bosch process.



**Scheme 8** Formation of  $\text{CO}$  and  $\text{H}_2$  from cellulose in 80% sulfuric acid.



**Scheme 9** Water–gas shift of CO to CO<sub>2</sub> and H<sub>2</sub> (released electrochemically).

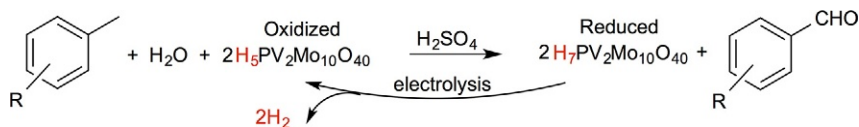
As it turned out, the CO formed could also be oxidized further to CO<sub>2</sub> resulting in the formation of an equivalent amount of reduced polyoxometalate. Such a reaction is in essence a variant of a water–gas shift reaction, [Scheme 9](#). In this way, the ration of H<sub>2</sub>/CO can be varied from 1:1 all the way to pure H<sub>2</sub>.

Finally, it should be noted that contrary to an initial question mark on the use of sulfuric acid as a solvent, it is in fact widely used in oil refineries and also for the formation of phosphoric acid from phosphate rock. In fact, used properly it is quite benign. Furthermore, in the context of this conversion of carbohydrate biomass promoted by H<sub>5</sub>PV<sub>2</sub>Mo<sub>10</sub>O<sub>40</sub> it also has significant additional advantages. First, H<sub>5</sub>PV<sub>2</sub>Mo<sub>10</sub>O<sub>40</sub> is synthesized in sulfuric acid so it is intrinsically stable and the reaction solution can be recycled many, many times without catalyst degradation. Second, since the substrates, cellulose, and hemicellulose are solid, but all the products are gases, the separation of the catalyst and solvent from the products is not needed.



## 6. OXIDATION OF VIA ACTIVATION OF C–H BONDS REVISITED

An interesting insight from the aforementioned oxidation of carbohydrates in sulfuric acid was also the observation that the reactions were significantly accelerated compared to what we had observed over many years when carrying out ET–OT reactions in organic solvents. Although the reason was not immediately clear, this observation did lead to the reexamination of the redox properties of H<sub>5</sub>PV<sub>2</sub>Mo<sub>10</sub>O<sub>40</sub> in aqueous sulfuric solutions and also a reinvestigation of the oxidation of alkylarenes, notably toluene and its derivatives that previously did not react in acetic acid, acetonitrile, or other organic solvents ([10](#)). Impetus for this study was also the knowledge that the transformation of toluene and its derivatives to the corresponding benzaldehyde compounds are not a trivial transformation from the sustainability point of view, despite the apparent simplicity of the transformation. In fact, methylarenes cannot be oxidized with O<sub>2</sub> since the autooxidation reactions prevalent under such conditions lead to the invariable formation of the overoxidized carboxylic acid products. Thus, benzaldehyde derivatives are formed from the corresponding methylarenes, for example, by using the chromates in acetic anhydride, halogenation followed



**Scheme 10** Oxidation of methylarenes to the corresponding benzaldehyde derivatives with  $\text{H}_5\text{PV}_2\text{Mo}_{10}\text{O}_{40}$  in sulfuric acid.

by hydrolysis, or from benzene derivatives via carbonylation by various methods. All these techniques produce copious amounts of waste. Based on the transformation observed with carbohydrates, a similar scheme for oxygenation of toluene derivatives was devised, [Scheme 10](#).

In general, the results showed the highly efficient formation of  $\text{ArCHO}$  in almost all cases with practically no formation of carboxylic acids; no sulfonated products were detected. For toluene and ring-halogenated toluene substrates as electron withdrawing moieties nearly quantitative yields of  $\text{ArCHO}$  were obtained. Alkylated toluene derivatives yielded the selective formation of the corresponding tolualdehydes, except for the case of 4-cymene where oxidation occurred at the primary Me carbon and the tertiary *i*-propyl moiety. Thus, the important observation that oxygenation of toluene with  $\text{H}_5\text{PV}_2\text{Mo}_{10}\text{O}_{40}$  is possible in aqueous 50% sulfuric acid but not in an organic solvent was verified. To explain this change in reactivity, it was surmised that the strong acidic medium leads to the increase in the redox potential of  $\text{H}_5\text{PV}_2\text{Mo}_{10}\text{O}_{40}$ . This can be observed from cyclic voltammetry measurements, [Fig. 4](#), where the redox potential obtained is plotted as a function of the sulfuric acid concentration. Clearly, the effect is dramatic with an increase in the oxidation potential of more than 0.7 V when going from  $\text{H}_2\text{O}$  to 80% aqueous sulfuric acid.

Density functional theory (DFT) calculations were used to explain the change in reactivity. The calculations showed that there was no electron transfer from toluene to  $\text{H}_5\text{PV}_2\text{Mo}_{10}\text{O}_{40}$ ; the reaction was endergonic. However, in even 50% sulfuric acid  $\text{H}_5\text{PV}_2\text{Mo}_{10}\text{O}_{40}$  is protonated to yield a cation  $[\text{H}_6\text{PV}_2\text{Mo}_{10}\text{O}_{40}]^+$  in a reaction that is slightly exergonic. Additionally, the proton affinity of the reduced polyoxometalate is even higher meaning that protonation favors the reduction of  $\text{H}_5\text{PV}_2\text{Mo}_{10}\text{O}_{40}$  both kinetically and thermodynamically. As a result, an ET reaction between  $\text{H}_5\text{PV}_2\text{Mo}_{10}\text{O}_{40}$  in sulfuric acid and toluene is exergonic by nearly 6 kcal/mol. From this, a reaction scheme for the ET–OT oxidation of toluene under these conditions can be proposed and compared to that of xanthene in an organic solvent, [Scheme 11](#). In the xanthene oxygenation, the

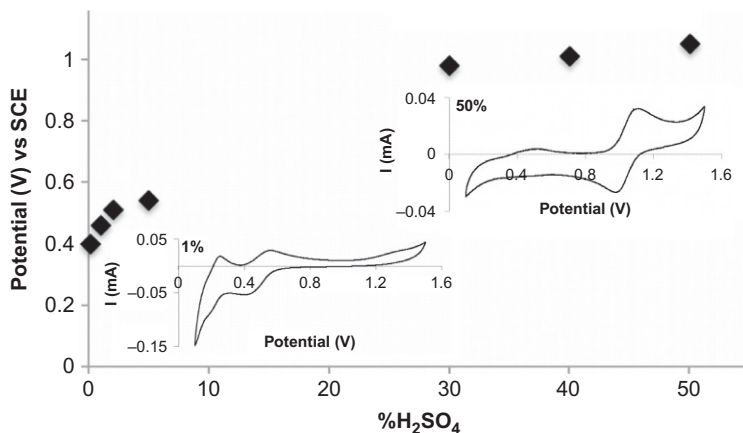
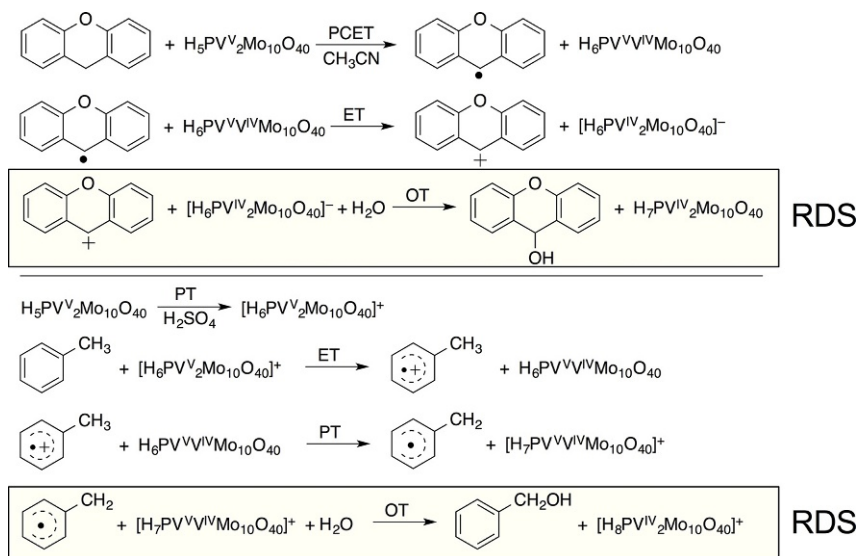


**Fig. 4** The redox potential of  $\text{H}_5\text{PV}_2\text{Mo}_{10}\text{O}_{40}$  as a function of the sulfuric acid concentration. Reprinted with permission from Sarma, B.B.; Efremenko, I.; Neumann, R. *J. Am. Chem. Soc.* **2015**, *137*, 5916–5922. Copyright 2013 American Chemical Society.



**Scheme 11** Pathways for the oxygenation of xanthene in organic solvent versus that of toluene in sulfuric acid, both with  $\text{H}_5\text{PV}_2\text{Mo}_{10}\text{O}_{40}$ .

reaction is initiated by a PCET as determined by kinetic isotope effect experiments. Further electron transfer yields a benzylic cation that in the case of xanthene is stabilized by the lone pair on the oxygen atom and can be isolated and observed at room temperature by  $^1\text{H}$  NMR. Oxygen transfer

then occurs to yield xanthenol as initial product. Note that in both cases, the initial verified products are the respective alcohols that then further react to yield the final products, xanthone and benzaldehyde, respectively. In the oxygenation of toluene, the reaction sequence is different. First, electron transfer from toluene to  $[\text{H}_6\text{PV}_2\text{Mo}_{10}\text{O}_{40}]^+$  yields the cation radical of toluene followed by proton transfer to yield the radical, that then is oxygenated by oxygen transfer from the polyoxometalate. This oxygen transfer step is rate-determining in both reactions.

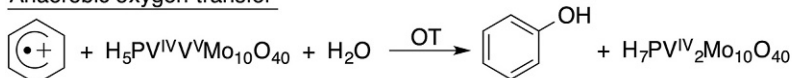
The ability of  $\text{H}_5\text{PV}_2\text{Mo}_{10}\text{O}_{40}$  dissolved in sulfuric acid to oxidize toluene led to the research question whether this mode of reactivity could also lead to the oxidation of benzene to phenol. This is a highly desirous transformation since the presently used process for phenol is one of very poor atom economy. Direct oxidation of benzene to phenol is often considered one of the “holy grails” of oxidation chemistry. The possible pathways from benzene to phenol with  $\text{H}_5\text{PV}_2\text{Mo}_{10}\text{O}_{40}$  are summarized in [Scheme 12 \(11\)](#).

The first step was to test if the formation of the benzene cation radical was indeed accessible as it was in all the other substrates discussed earlier. Upon the formation of the cation radical, there was also the question if oxygen transfer from the polyoxometalate was viable, that is was an ET–OT reaction realistic. If not, the possibility oxidation of the cation radical directly with  $\text{O}_2$  was also a possibility to take under consideration. The formation of the benzene cation radical was probed in two ways. First, UV–vis spectroscopy indicated the formation of a charge transfer complex implying an ET reaction, where both peaks assignable to the benzene cation radical and reduced polyoxometalate were observed, [Fig. 5](#).

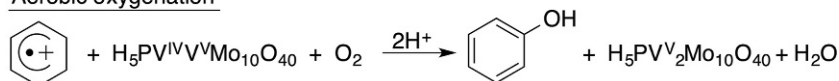
#### Electron transfer



#### Anaerobic oxygen transfer



#### Aerobic oxygenation



**Scheme 12** ET oxidation of benzene by  $\text{H}_5\text{PV}_2\text{Mo}_{10}\text{O}_{40}$  and subsequent pathways to phenol.



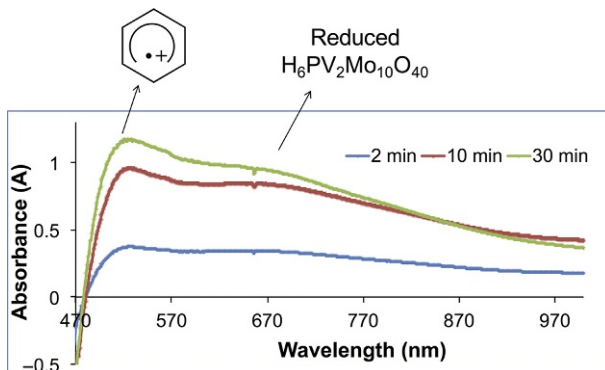


Fig. 5 Visible spectrum of benzene and  $\text{H}_5\text{PV}_2\text{Mo}_{10}\text{O}_{40}$  in 80%  $\text{H}_2\text{SO}_4$ .

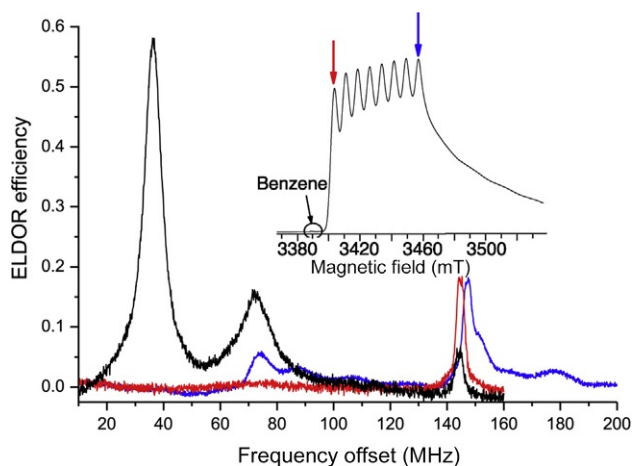


Fig 6 ELDOR detected NMR of  $^{13}\text{C}_6\text{H}_6/\text{H}_5\text{PV}_2\text{Mo}_{10}\text{O}_{40}$ . The color of the spectrum corresponds to the field positions according to the arrows. Reprinted with permission from Sarma, B.B.; Carmieli, R.; Collauto, A.; Efremenko, I.; Martin, J.M.L.; Neumann, R. *ACS Catal.* **2016**, *6*, 6403–6407. Copyright 2016 American Chemical Society.

More definitive evidence was possible via the use of both X-band and W-band EPR spectroscopy, notably the latter. In Fig. 6, one can see in the insert the W-band spectrum where the strong 8-line peak of V(IV) incorporated in the polyoxometalate can be observed. A small peak at  $g=2$  was also observed. The assignment of this peak to the benzene radical was possible by measuring the ELDOR detected NMR of a mixture of  $^{13}\text{C}$  benzene and  $\text{H}_5\text{PV}_2\text{Mo}_{10}\text{O}_{40}$ . When such a spectrum was measured at the  $g=2$  peak, a signal at 36 MHz associate to the Larmor frequency of  $^{13}\text{C}$  atoms was obtained, meaning that the radical is in close proximity to

the 13-C atoms. Signals associable to hydrogen atoms were also observed. It should be noted that the intensity of benzene radical is weak although clearly present. DFT calculations showed that this was actually expected since most of the charge transfer complex is present as an open-shell singlet. Additional EPR experiments, not shown, notably a 13-C Mims ENDOR spectrum measured at the field position of the benzene species verified the assignment.

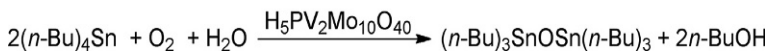
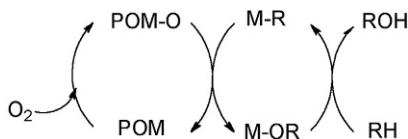
After spectroscopically showing that an ET reaction between benzene and  $\text{H}_5\text{PV}_2\text{Mo}_{10}\text{O}_{40}$  is possible, the possibility of an OT reaction was probed. It was observed such a reaction did not occur to yield phenol. A study for such an anaerobic reaction pathway by DFT showed that while overall the reaction was exergonic a low energy intermediate formed after charge transfer presented a high thermodynamic barrier to an oxygen transfer reaction. On the other hand, in the presence of  $\text{O}_2$  and despite its very low solubility in the reaction solvent, oxidation to yield phenol with high selectivity was viable at  $170^\circ\text{C}$  although the reaction was slow. The reactivity observed presents a new paradigm for benzene oxidation that will be further investigated.



## 7. INSERTION OF OXYGEN INTO A CARBON-METAL BOND

An important further challenge in the field of C–H bond activation is that of alkanes to form their hydroxylation products. This topic is of importance in the transformation of natural gas to liquid fuels under mild conditions. The approach taken above of discussed earlier of activation of alkanes by electron transfer seems improbable due to the very high oxidation potentials of alkenes. Dimerization and further oligomerization of alkanes from natural gas is also a potentially valuable liquefaction process. One option to realize such a hydroxylation reaction is by C–H activation with a electrophilic catalyst to yield an alkyl metal-based intermediate. The question that we asked in our research was—upon formation of such a metal–carbon (alkyl) intermediate, would oxygen insertion by an ET–OT mechanism be feasible to form the eventual hydroxylated product. The concept is summarized in [Scheme 13](#), where one can see all the proposed reaction parts, alkane activation, oxygen insertion and release of product, and regeneration of the oxygen donor with  $\text{O}_2$ .

In order to probe such a possibility we used tetrabutyl tin as a model substrate ([12](#)). Common to all the reactions presented earlier indeed  $(n\text{-Bu})_4\text{Sn}$  in the presence of  $\text{H}_5\text{PV}_2\text{Mo}_{10}\text{O}_{40}$  clearly showed an electron transfer

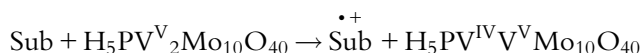


**Scheme 13** A hypothetical hydroxylation of alkanes using a polyoxometalate as oxygen donor and  $\text{O}_2$  as terminal oxidant.

interaction as probed by X-band EPR and  $^{13}\text{C}$  NMR. Furthermore, we were able to isolate and identify the ion pairs formed after electron transfer by use of electrospray ionization mass spectrometry. Interestingly, the oxygen transfer reaction is selective to the formation of 1-butanol only. Under catalytic conditions again only the primary alcohol was the observed hydroxylation product although some dehydrogenation occurred to yield a mixture of isomeric butenes.

## 8. THE STRUCTURE OF $\text{H}_5\text{PV}_2\text{Mo}_{10}\text{O}_{40}$ DURING THE CATALYTIC REACTION

In the earlier discussion, we have shown the various reactions recently reported on the activation of C–H, C–C, and C–M bonds via initial electron transfer for the substrate to  $\text{H}_5\text{PV}_2\text{Mo}_{10}\text{O}_{40}$ . The structure of  $\text{H}_5\text{PV}_2\text{Mo}_{10}\text{O}_{40}$  in its oxidized form has been intensively studied by us using X-ray diffraction and X-ray photoelectron spectroscopy in order to understand its stability and its reconstitution after decomposition at high temperature (13). However, the structure of  $\text{H}_5\text{PV}_2\text{Mo}_{10}\text{O}_{40}$  upon reduction and during a reaction where oxygen transfer occurs from the framework of the polyoxometalate to the organic substrate required in situ observation of possible intermediates that proved to be possible using various EPR techniques since a V(IV) species as is obvious from the following equation:



The issues that complicated such a study are:

1. Complexity due to five positional isomers that cannot be separated and are in dynamic equilibrium.
2. DFT calculations showed the one-electron reduced isomers of  $[\text{PV}^{\text{IV}}\text{V}^{\text{V}}\text{Mo}_{10}\text{O}_{40}]^{6-}$  are of equal energy.

3. Possible equilibrium dissociation of  $V^{IV}$  from reduced  $H_5PV_2Mo_{10}O_{40}$  as vanadyl dication,  $VO^{2+}$ .
4. Experimentally unknown position of protons as counter cations. DFT indicates preference for bridging oxygen atoms,  $V-O-V$ .

Upon addition of sodium ascorbate to an acetonitrile solution of  $H_5PV_2Mo_{10}O_{40}$ , the polyoxometalate is reduced according to the equation above (14). Interestingly and initially unexpectedly, the X-band continuous wave EPR spectrum of  $V(IV)$ , which was anisotropic, showed the formation of two species, I and II, that had different and discernible  $g$  values and hyperfine constants,  $A$ . By labelling  $H_5PV_2Mo_{10}O_{40}$  with  $^{17}O$  atoms, it was possible to show using a W-band HYSORE experiment that in species I the  $V(IV)$  atom was not in the close vicinity of the oxygen or molybdenum atoms of the polyoxometalate. This was not the case for species II that also showed an interaction between  $V(IV)$  and the central phosphorous atom as measured by W-band Mims ENDOR spectroscopy. The species were identified as follows. Species I had no magnetic nuclei of the polyoxometalate structure in its close vicinity and was assigned to hydrated  $VO^{2+}$  as an ion pair,  $[PV^VMo_{10}O_{39}]^{8-}[V^{IV}O^{2+}]$ , supported on a lacunary (defect) form of the polyoxometalate. This species originates from isomers with proximal vanadium atoms. Species II had the following attributes: (1)  $^{95}Mo$  nuclei with large coupling constants (7.5 MHz) are connected to  $V^{IV}$  through a single oxygen atom,  $^{95}Mo$  nuclei with smaller coupling constants (1.3 MHz) are connected through more than a single oxygen bridge. (2) The  $V(IV)$  atom interacted with terminal, axially bound  $^{17}O$  atoms with coupling constants of  $\sim 9.5$  MHz and to bridging equatorial  $^{17}O$  atoms and more distal  $^{17}O$  atoms with smaller coupling constants,  $\sim 2.7$  MHz. (3) Weak interactions were observed between the  $V(IV)$  center and  $^{31}P$  and  $^{51}V$  nuclei with large but observable coupling constants. It was therefore concluded that species II originates from isomers with distal vanadium atoms where the  $V^{IV}$  remains incorporated in the polyoxometalate retaining its complete (plenary) Keggin structure upon reduction. It should be noted here that upon reoxidation, species I returns to its plenary structure. It was also observed that species II was reoxidized more quickly than species I, magnifying the importance of the polyoxometalate framework for the completion of the catalytic cycle with  $O_2$ .

The identification of two species led to the further question if both were reactive in oxygen transfer to a substrate. This was probed using the simple oxidation of  $^{13}CO$  to  $^{13}CO_2$  where it would be possible to investigate  $V(IV)$ -CO interactions by EPR techniques (15). Indeed, the results were

definitive, only species I, generically described as  $[\text{PV}^{\text{V}}\text{Mo}_{10}\text{O}_{39}]^{8-}[\text{V}^{\text{IV}}\text{O}^{2+}]$  was active in oxygen transfer. It should be noted that these low temperature techniques,  $\sim 10$  K, do not exclude the observation that under reaction conditions there is electron transfer between the polyoxometalate species and also exchange between different structures.

In order to further understand these experimental studies that highlighted the importance of defect structures, such as  $[\text{PV}^{\text{V}}\text{Mo}_{10}\text{O}_{39}]^{8-}[\text{V}^{\text{IV}}\text{O}^{2+}]$  appropriate, DFT calculations were carried out in order to suggest possible more exact structures of species I and to provide additional understanding of the dynamics of the oxygen transfer step, which is the unique property of  $\text{H}_5\text{PV}_2\text{Mo}_{10}\text{O}_{40}$ . In fact, other vanadium-containing polyoxometalates can be efficient in electron transfer compounds, but do not elicit oxygen transfer subsequent to electron transfer (16).

ET–OT reactions of  $\text{H}_5\text{PV}_2\text{Mo}_{10}\text{O}_{40}$  require the involvement of protons and often water and thus the proton counter cations and water molecules on the polyoxoanion surface were explicitly considered. We found that the most stable key intermediate features a displacement of the metal atom from the Keggin structure, that is a defect, and coordinatively unsaturated sites are formed on the  $\text{H}_5\text{PV}_2\text{Mo}_{10}\text{O}_{40}$  surface (17). Such *metal defects* are favored at vanadium sites. After initial electron transfer from the substrate, for example, anthracene or xanthene, subsequent coordination allows for formation of reactive ensembles on the catalyst surface for which the selective oxygen transfer step becomes feasible. Calculated geometries and energies of metal defect structures support the experimentally observed intermediates where  $\text{VO}^{2+}$  species that are involved in the oxygen transfer step are somewhat detached from the polyoxometalate, Fig. 7.

Thus, both the EPR experiments and DFT calculations point to a situation where in order for oxygen transfer to occur a defect structure is involved that requires at least a partial detachment of the reactive  $\text{VO}^{2+}$  moiety from the polyoxometalate plenary structure.



## 9. CONCLUSIONS

Originally, the principle that guided the use of the most studied phosphovanadomolybdate,  $\text{H}_5\text{PV}_2\text{Mo}_{10}\text{O}_{40}$ , as an oxidation catalyst was that the two-electron reduced forms,  $\text{H}_7\text{PV}^{\text{IV}}_2\text{Mo}_{10}\text{O}_{40}$  or  $\text{H}_5\text{PV}^{\text{IV}}_2\text{Mo}_{10}\text{O}_{39}$ , can be reoxidized by  $\text{O}_2$  with coformation of water. In early years, this type of reactivity led to oxidative dehydrogenation

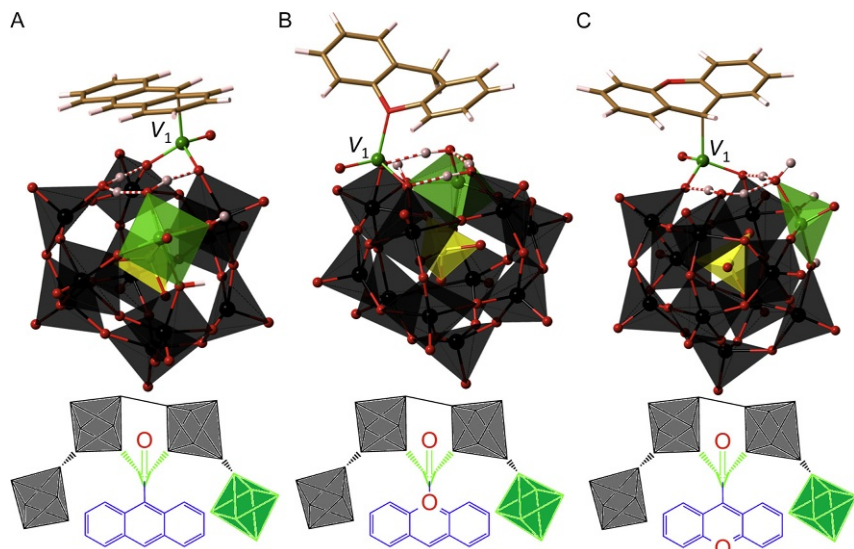


**Fig. 7** Nondissociative complexes of anthracene (A) and xanthene (B) with defect structures of the polyoxometalate and a dissociative complex of xanthene of similar free energy (C). Reprinted with permission from Efremenko, I.; Neumann, R. *J. Am. Chem. Soc.* **2012**, 134, 20669–20680. Copyright 2013 American Chemical Society.

reactions that proceeded by electron transfer from the substrate to the catalyst. In 2000, it was shown for the first time using anthracene and xanthene as model substrates that oxygenation of the substrate could follow the initial electron step. The oxygen atom was transferred from the reduced polyoxometalate to substrate. This kind of reactivity was coined by us as being ET–OT, reactivity based on the mechanistic studies performed. Generally speaking, this reactivity at low temperature in solution is reminiscent if not identical to previously known Mars–van Krevelen reaction observed in high temperature, heterogeneous, gas phase reactions discovered many years ago. In the following years (2008–2010), new types of transformations were namely the oxidation of primary and also vicinal alcohols by C–C bond cleavage rather than the typical oxidation via C–H bond activation, as well as the aerobic oxidation or polymerization of sulfides. The possibility of inserting an oxygen atom from the polyoxometalate into a tin–carbon bond to form the primary alcohol is enticing toward the possibility of eventual hydroxylation of alkanes. Latter on use of aqueous sulfuric was shown to be advantageous for the quantitative deconstruction of carbohydrates such as cellulose and hemicellulose to synthesis gas. The observation that reactions were accelerated in aqueous sulfuric acid lead to the observation that

methylarenes (toluene and its derivatives) could be cleanly oxidized to the corresponding benzaldehyde derivatives, generally in very high yields. This effect of acidity was connected to an increase in the oxidation potential of the polyoxometalate that then could be translated to electron transfer initiated oxidation of benzene to phenol with O<sub>2</sub>. In parallel, it was observed by EPR spectroscopy that different isomers of one-electron reduced H<sub>5</sub>PV<sub>2</sub>Mo<sub>10</sub>O<sub>40</sub> yielded different structure types; one where the compound retains its complete structure and another where a VO<sup>2+</sup> species is defect in the structure or supported on the polyoxometalate. It was shown that this latter species is the active one in oxygen transfer reactions. The structure of this defect species was also confirmed by DFT calculations that gave more insight into the importance of defects and the complicated manner in which oxygen transfer may occur.

## ACKNOWLEDGMENTS

This research has been supported over the years by the Israel Science Foundation, the German-Israeli Project Cooperation, the Minerva Foundation, the European Community, the Roger and Bernice Center for Catalysis, and the Helen and Martin Kimmel Center for Molecular Design. The research described has been carried out by many. Recent research was done by Alexander M. Khenkin, Bidyut-Bikash Sarma, Hila Goldberg, Ilia Kaminker, Irena Efremenko, Delina Barats, Linda J. W. Shimon, Lev Weiner, Gregory Leituss, Leonid Konstantinovski, and Daniella Goldfarb. R.N. is the Rebecca and Israel Sieff Professor of Organic Chemistry.

## REFERENCES

1. Kozhevnikov, I. V.; Matveev, K. I. *Appl. Catal.* **1983**, *5*, 135–150.
2. (a) Neumann, R.; Khenkin, A. M. *Chem. Commun.* **2006**, 2529–2538; (b) Neumann, R. *Inorg. Chem.* **2010**, *49*, 3594–3601.
3. Neumann, R.; Levin, M. *J. Am. Chem. Soc.* **1992**, *114*, 7278–7286.
4. (a) Khenkin, A. M.; Neumann, R. *Angew. Chem. Int. Ed.* **2000**, *39*, 4088–4090; (b) Khenkin, A. M.; Weiner, L.; Wang, Y.; Neumann, R. *J. Am. Chem. Soc.* **2001**, *123*, 8531–8542.
5. Khenkin, A. M.; Leituss, G.; Neumann, R. *J. Am. Chem. Soc.* **2010**, *132*, 11446–11448.
6. Khenkin, A. M.; Neumann, R. *ChemSusChem* **2011**, *4*, 346–348.
7. Khenkin, A. M.; Neumann, R. *J. Am. Chem. Soc.* **2008**, *130*, 14474–14476.
8. Wölfel, R.; Taccardi, N.; Bösmann, N.; Wasserscheid, P. *Green Chem.* **2011**, *11*, 2759–2763.
9. Sarma, B. B.; Neumann, R. *Nat. Commun.* **2014**, *5*, 4621.
10. Sarma, B. B.; Efremenko, I.; Neumann, R. *J. Am. Chem. Soc.* **2015**, *137*, 5916–5922.
11. Sarma, B. B.; Carmieli, R.; Collauto, A.; Efremenko, I.; Martin, J. M. L.; Neumann, R. *ACS Catal.* **2016**, *6*, 6403–6407.
12. Khenkin, A. M.; Efremenko, I.; Martin, J. M. L.; Neumann, R. *J. Am. Chem. Soc.* **2013**, *135*, 19304–19310.
13. Barats–Damatov, D.; Shimon, L. J. W.; Feldman, Y.; Bendikov, T.; Neumann, R. *Inorg. Chem.* **2015**, *54*, 628–634.

14. Kaminker, I.; Goldberg, H.; Neumann, R.; Goldfarb, D. *Chem. A Eur. J.* **2010**, *16*, 10014–10020.
15. Goldberg, H.; Kaminker, I.; Goldfarb, D.; Neumann, R. *Inorg. Chem.* **2009**, *48*, 7947–7952.
16. Khenkin, A. M.; Neumann, R. *J. Organometal. Chem.* **2015**, *793*, 134–138.
17. Efremenko, I.; Neumann, R. *J. Am. Chem. Soc.* **2012**, *134*, 20669–20680.





# Oxygen–Isotope Exchange and Metastable Dissociation in Oxides

W.H. Casey<sup>1</sup>

University of California, Davis, CA, United States

<sup>1</sup>Corresponding author: e-mail address: whcasey@ucdavis.edu

## Contents

1. Introduction	92
2. Broad Reactivity Trends for Dissolving Materials and Glasses	94
3. Acid–Base Chemistry and Reactivity in Niobates	98
4. The Transition to a Partly Detached Structure in $\text{MAI}_{12}$ Cations	102
5. Metastable Intermediates	105
6. Conclusions	112
Acknowledgments	113
References	113

## Abstract

To understand the corrosion of bulk oxide materials at the molecular scale, oxygen–isotope exchanges were examined in two classes of nanometer-sized ions, one cation and one anion, and subsets that differ by targeted single-atom substitutions. In niobate anions, the different oxygen sites within each molecule differ by  $\sim 10^3$ – $10^4$  in overall rates of isotopic exchange, yet all structural oxygens exhibit similar pH dependencies that relate to the dissociation pathways. In aluminate cations of the  $\epsilon$ -Keggin structure, single-atom substitutions cause a  $10^7$ – $10^{10}$  variation of rates of oxygen–isotopic exchange into two sets of  $\mu_2$ -OH. Molecular-dynamic simulations indicate that metastable forms of these structures exist as loose, long-lived intermediates. A series of common steps is observed to access the intermediate structures, and these are best resolved in the symmetric  $\epsilon$ -Keggin aluminate ions. In the first step, solvation forces, or a nucleophile, cause a near-surface metal to partly detach from a deeper over-bonded oxygen via concerted motions of many atoms. Isotopically distinct oxygens then add to the newly undercoordinated metal in the partly detached metastable state. Protons transfer to more basic oxygens and oxygens shuffle. Finally, the metastable structure collapses and dehydrates. The number of such metastable states depends on the symmetry and composition of the starting structure and access to the metastable state controls the overall rates. Surprisingly, polyoxometalate ions with only 40–100 atoms already seem to capture much of the macroscopic chemistry observed for dissolving minerals and glasses.

## ABBREVIATIONS

- ox** oxalate  
**ssal** sulfosalicylate  
**sal** salicylate  
**mMal** methylmalonate



## 1. INTRODUCTION

My research group undertook close study of polyoxometalate ions in order to understand how bulk oxide materials and minerals react in water at the molecular scale. The features that control the surface chemistry of minerals and glasses in water are nanometers in scale. These are conspicuous features in atomic-force microscopy images. They include the kink sites and unit-cell-high steps, where mass is added or removed from the interfaces as the material grows or dissolves in solution. Spanning beyond this microscopic scale to understand molecular controls on the reactions, however, is difficult. It is impossible to intuit the rate-controlling steps in such complicated reactions without knowledge of the elementary steps (1), and there must be hundreds or thousands of such steps in the reaction networks. To span the enormous range in scales, the field came to rely heavily on simulations and electronic-structure calculations to infer the molecular steps that they could not observe.

Any molecular-scale interpretations were often based upon an imagined fragment of the mineral (or glass) structure and electronic-structure calculations. Thus, for example, two decades were spent running experiments on bulk materials in water, like silica ( $\text{SiO}_2$ ), and then interpreting the results using electronic-structure calculations on a few atoms (2). In such models, the local acid-base chemistry of the dissociating oxygen is often considered paramount and uninfluenced by the rest of the structure. The flaw of these simulations is the mismatch in scales—it was never demonstrated that these imagined molecular fragments capture the essential chemistry of the nanometer-sized structure. Acceptance was largely a matter of faith.

Polyoxometalate ions, however, provide the experimental models that could answer exactly this question and advance an understanding of aqueous reactions at the molecular scale. Unlike minerals or glasses, the structure of these ions in solution, which are also nanometer in size, can be known unequivocally. Furthermore, the mechanisms of reactions at these ions are approachable by both experiment and simulation. While there are

certainly features of extended oxides that cannot be reproduced in an oxide polyoxometalate ion, a theory for molecular-scale reactions at interfaces could be tested fairly. The simulations and the experiments are both at the same scale, and these polyoxometalate ions even exist in nature (3), so it is hard to dismiss the conclusions as environmentally irrelevant.

In this paper I discuss pathways for oxygen–isotope exchanges and dissociations of two large ions—both an anion and a cation (Fig. 1), that have a few dozen to a 100 atoms. Of course a wealth of information exists from  $^{17}\text{O}$  NMR about oxygen–isotope exchange in polyoxometalate ions (4), but unlike in those previous studies, I review results for sets of isostructural molecules that differ only by targeted single-atom substitutions. As I show, these substitutions have profound, systematic, and understandable effects on the

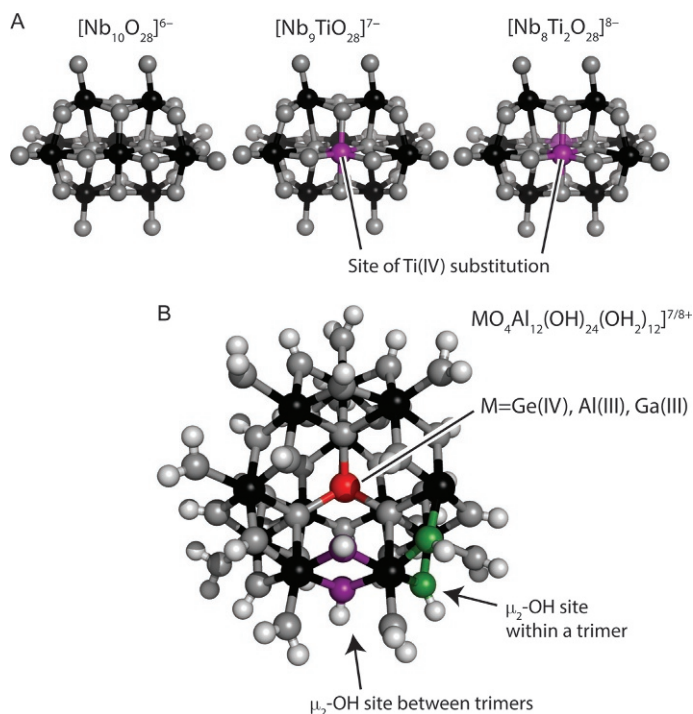


**Fig. 1** The two experimental molecules. (A) The polyoxometalate anions:  $[\text{Nb}_{10}\text{O}_{28}]^{6-}$ ,  $[\text{Nb}_9\text{TiO}_{28}]^{7-}$ , and  $[\text{Nb}_8\text{Ti}_2\text{O}_{28}]^{8-}$  with the site of Ti(IV) substitution colored *purple*. Other metals are *black* and oxygens are *dark gray*. (B) The  $[\text{MAIO}_4\text{Al}_{12}(\text{OH})_{24}(\text{OH}_2)_{12}]^{7/8+}$  cation, where  $M = \text{Al(III), Ga(III), or Ge(IV)}$ . The site of metal substitution in the inert center of the molecule is shown in *red*, and the two sets of hydroxyl bridges for which oxygen–isotope-exchange rates were measured are identified with *green* and *purple* colors. Oxygens are *dark gray*, protons are *white*, and nonhighlighted Al(III) metals are *black*.

rates of isotopic exchange. They are sufficiently simple that pathways can be postulated, and, in some cases, the rate-controlling steps can be identified.



## 2. BROAD REACTIVITY TRENDS FOR DISSOLVING MATERIALS AND GLASSES

Some trends are apparent if one looks at the dissolution kinetics of minerals on the bulk scale. First, for minerals without a polymeric fabric, such as the simple rocksalt-oxide structures with the stoichiometry: MO, or an orthosilicate mineral with the stoichiometry  $M_2SiO_4$  (orthosilicates have  $[SiO_4]^{4-}$  tetrahedra isolated from one another), the rates recapture the familiar trends found for ligand exchange around octahedral aqua ions (Fig. 2).

These trends are observed because the overall coordination number of the metal is retained in both cases. The Ni(II) is hexacoordinated to oxygens in the mineral bunsenite, NiO(s), and in the  $[Ni(OH_2)_6]^{2+}$  ion that is released by dissolving bunsenite. The time scales for these two processes, water exchange around an ion and dissolution of a mineral, are vastly different. Rates of water exchange around  $[Ni(OH_2)_6]^{2+}$  are milliseconds or less, whereas the rates of elimination of a monolayer on NiO(s) take many, many hours or days. In both cases, however, Ni(II) undergoes a set of ligand-exchange reactions that preserve the octahedral coordination of the metal to oxygens. Similarly, at the surface of a step on a mineral interface, stepwise ligand-exchange reactions replace bridging oxygens with solvation waters.

The reactivity trends are both familiar and odd. For example, the trend for minerals of pure composition is shown in Fig. 2A. Minerals with only octahedrally coordinated  $d^8$  Ni(II) (e.g., NiO(s)) dissolve slower than, say, an identical mineral made up of  $d^5$  Mn(II) (MnO(s)) because of ligand-field stabilization of the octahedral geometry. Similarly, reactivity to ligand exchange among alkaline-earth metals reflects ion size: Be(II) < Mg(II) < Ca(II) as does the dissolution rates of the corresponding simple minerals. The orthosilicate minerals trend is:  $Be_2SiO_4 < Mg_2SiO_4 < Ca_2SiO_4$ . Of course, this reactivity trend says nothing about the rate-controlling elementary steps.

There are also key differences. The mineral larnite,  $Ca_2(SiO_4)$ , dissolves much faster than the mineral forsterite,  $Mg_2(SiO_4)$ , as one expects, even though the two phases are isostructural. However, if an isostructural mineral is made with by combining the two metals in equal proportions,

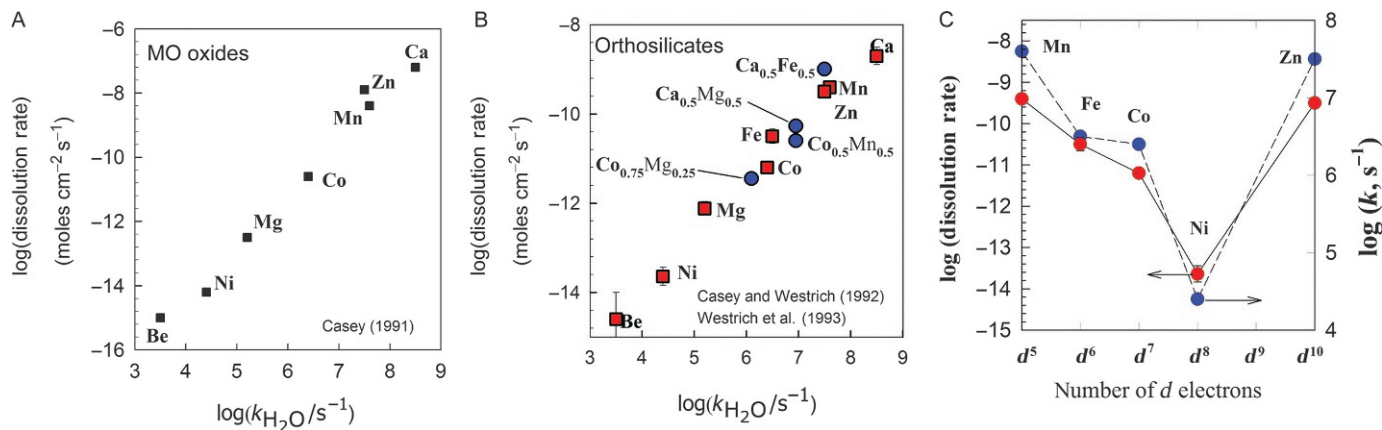


**Fig. 2** Dissolution rates at pH 2 of simple oxide (A) and orthosilicate (B and C) minerals containing divalent metals. In A and B the abscissa is the rate of exchange of water from the corresponding metal ion (e.g.,  $\text{Mg}^{2+}(\text{aq})$ ), and the ordinate is the dissolution rate of the mineral (e.g.,  $\text{Mg}_2\text{SiO}_4$ , forsterite) normalized to area. The oxide minerals have the rocksalt structure. The orthosilicate minerals (5) have the stoichiometry:  $\text{M}_2\text{SiO}_4(\text{s})$  and isolated  $\text{SiO}_4^{4-}$  tetrahedra. The end-member compositions of orthosilicates are shown in *red squares* in (B), whereas the mixed-metal compositions are shown as *blue dots*. For the mixed-metal compositions, dissolution rates are plotted against the weighted sum of the logarithm of rates of water exchange for the component ions. Note that the dissolution rates for mixed-metal compositions (*blue dots* in (B)) fall intermediate between the end-member compositions. The rates of ligand exchange of the aquated ions (●) and the dissolution rates of the orthosilicate minerals (●) at pH 2 are plotted as a function of the number of *d* electrons in (C), illustrating the role of ligand-field stabilization in the rates. Panels (B) and (C) are adapted from Ref. Casey, W.H.; Swaddle, T.W. *Reviews of Geophysics* **2003**, 41 (2), 4/1–4/20.

as in the mineral monticellite,  $\text{MgCa}(\text{SiO}_4)$ , a dissolution rate that is an *average* of the two end-member rates is observed (Fig. 2). These ionic minerals react as though both heterometals contribute to the reactivity. This is interesting.

Materials with a polymeric structure, such as a silicate fabric, dissolve in complicated fashions because the polymer resists hydrolysis more than other components. Thus, not surprisingly, polymerizing the isolated silicate tetrahedra into covalent chains, sheets, or frameworks has a profound effect on dissolution reactivities and stoichiometries. In Fig. 3, the flux of materials is shown from two minerals that differ only in the organization of the silicate tetrahedra. In one case, the silicate groups are organized into isolated three-membered rings. These are highly energetic, and the material dissolves very quickly with equal fluxes of calcium and silicon. If the silicate groups are organized into polymeric chains, however, the rates of dissolution are much slower and the fluxes of calcium and silicon diverge because silica builds up on the dissolving surface. The key point is that small changes in the polymer structure have large effects on the dissolution rates of the solid and the fluxes of elements. In minerals, the changes in polymer structures are discrete. The polymer, for example, is either a ring or a chain or a double chain or a framework, but the changes in polymeric structure in glasses can be continuous. Unlike minerals, glass polymers require statistical descriptions of the polymer network.

Dissolution rates of oxide minerals also exhibit a broad amphoteric variation with pH that resembles other oxide reactions in water, such as ester hydrolysis, oxygen–isotope exchange in sugars (7), and pesticide hydrolysis (8). An example is shown in Fig. 4 where the dissolution rates of the tectoaluminosilicate mineral, orthoclase ( $\text{KAlSi}_3\text{O}_8$ ; from Ref. (9)) are compared with rates of oxygen–isotope exchanges into anomeric oxygens in three sugars. In this broad amphoteric chemistry, the minimum in rates can be moved to more acidic or basic conditions with the overall proton affinity of the molecule (or the surface). For interfaces, the Brønsted acid–base chemistry of surface oxygens manifests as measurable positive or negative net surface charge (10). Dissolution rates correlate with these charge concentrations and can be proton-promoted, hydroxyl-promoted, or unpromoted. Practically, these terms mean that rates go up as pH drops (proton-promoted), as pH increases (hydroxyl-promoted) and the unpromoted region is where rates are independent of pH; here, water molecules are the most effective nucleophile. All three such regions can be seen in Fig. 4.

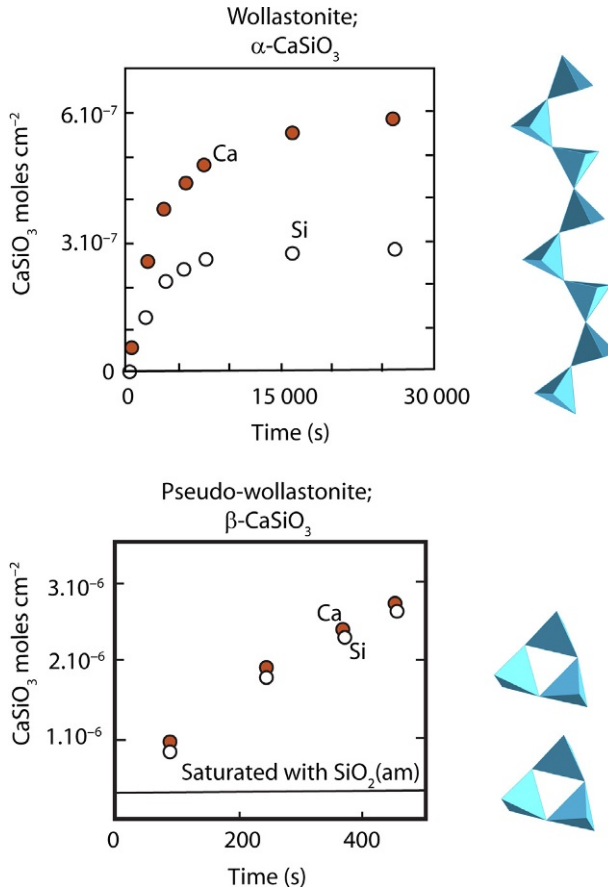


**Fig. 3** The dissolution of two forms of CaSiO<sub>3</sub> in acidic (initially pH 2) solutions reflects the linkages of the silicate polymer. In the curves, moles of dissolved silicon (○) and calcium (●) are divided by the area of the solid so that the slope of the curves gives the dissolution fluxes directly. (*top, incongruent* dissolution) Wollastonite ( $\alpha$ -CaSiO<sub>3</sub>) has silicate groups linked in chains and the flux of silicon and calcium differs remarkably from the stoichiometry as saturation with amorphous silica, a solid reaction product, is approached. (*bottom*) Pseudowollastonite ( $\beta$ -CaSiO<sub>3</sub>) has silicate groups in highly energetic three-membered rings. Fluxes of dissolved calcium and silicon are virtually identical and dissolution is more rapid, so much so that the solution composition far exceeds the saturation point with amorphous silica. The *horizontal line* identifies the point at which the solution was supersaturated with amorphous silica (6).

Exceptions are easily found. In strongly acidic solutions, more polymerized minerals sometimes dissolve incongruently, meaning that one metal is released by acid hydrolysis to leave a porous structure behind. The most familiar such case is the dealumination of zeolite minerals in acids. These

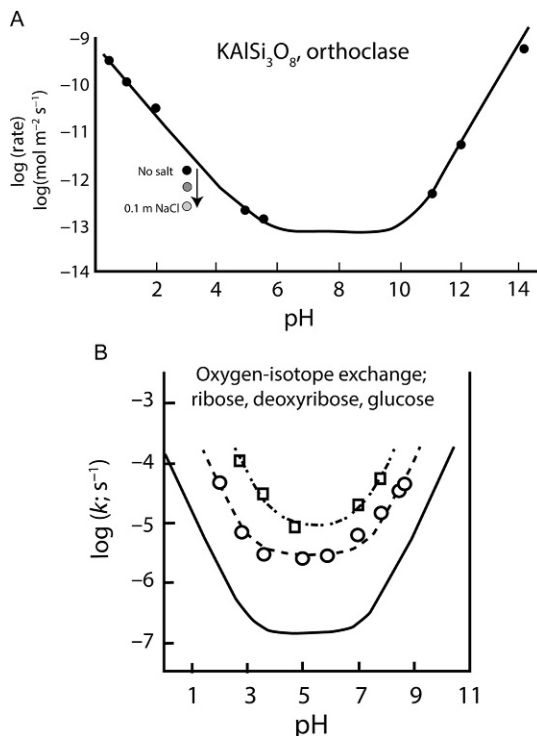


**Fig. 4** Amphoteric variation in rates. (A) Rates of dissolution of the common mineral orthoclase ( $\text{KAlSi}_3\text{O}_8$ ) as a function of pH at 25°C (9) and (B) rates of isotopic exchange of oxygen into three sugars at 25°C (7b) as a function of pH; (D-ribose, square symbol; D-2-deoxyribose, open circle; and glucose, line).

materials are tectoaluminosilicate minerals, meaning that the polymeric metals have bridging bonds only. Acid or hydrothermal treatment replaces Al(III) with protons within the framework structure, leaving behind catalytic Brønsted acid sites.



### 3. ACID-BASE CHEMISTRY AND REACTIVITY IN NIOBATES

The role of acid-base chemistry in the kinetics of isotope exchange and dissociation of polyoxometalates has been studied before (4a,b,g,11), but much more detailed information is available if one studies versions of polyoxometalate anions that differ by single-atom substitutions. Substitutions of Ti(IV) in the decaniobate structure, for example, change the net molecular charge without changing the structure. The first set of such



substituted molecules are:  $[\text{H}_x\text{Nb}_{10}\text{O}_{28}]^{(6-x)-}$ ,  $[\text{H}_x\text{Nb}_9\text{TiO}_{28}]^{(7-x)-}$ , and  $[\text{H}_x\text{Nb}_8\text{Ti}_2\text{O}_{28}]^{(8-x)-}$  ions. These decametalate ions are synthesized in solvent that was enriched to  $\sim 40\%$  in  $^{17}\text{O}$  (12). The salts are crystallized, separated, and, to begin an experiment, dissolved back into isotopically normal solutions.

The  $^{17}\text{O}$ -NMR signals for the various oxygen sites, which are given alphabetic labels, are spectrally well resolved (Fig. 5). The molecules are very stable in aqueous solution. For the  $[\text{H}_x\text{Nb}_{10}\text{O}_{28}]^{(6-x)-}$  molecule, for example, there are three metal positions, all containing Nb(V), and seven oxygen sites, all of which are evident in an NMR spectrum. There are two sets of  $\eta = \text{oxo}$  (Sites F, G), three  $\mu_2\text{-oxo}$  (Sites C, D, and E), one set of four  $\mu_3\text{-oxo}$  (Site B), and two central  $\mu_6\text{-oxo}$  (Site A). The two central  $\mu_6\text{-oxo}$  are inert to isotopic exchange unless the molecule completely dissociates and then reforms from isotopically normal bulk solution. Thus, the constant  $^{17}\text{O}$  signal for the  $\mu_6\text{-oxo}$ , labeled “A” in Fig. 5, means that the  $[\text{H}_x\text{Nb}_{10}\text{O}_{28}]^{(6-x)-}$  molecule remains intact even as the  $^{17}\text{O}$ -NMR signals for some oxo sites

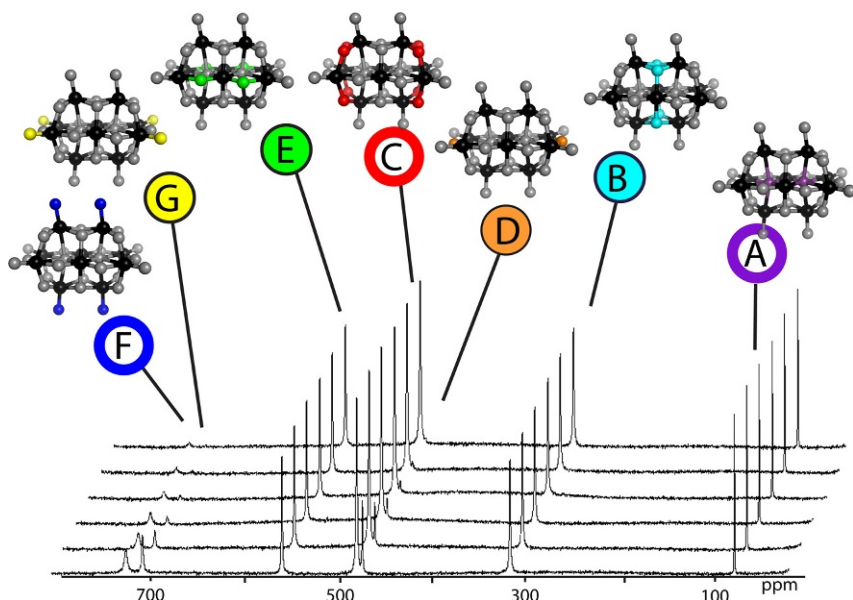


**Fig. 5** An  $^{17}\text{O}$ -NMR spectrum of the  $[\text{H}_x\text{Nb}_{10}\text{O}_{28}]^{(6-x)-}$  molecule with the various oxygen sites labeled. In this case, the molecule was isotopically enriched to  $\sim 40\%$  in  $^{17}\text{O}$ , crystallized as a tetramethylammonium salt and redissolved into an isotopically normal background electrolyte (4e, 12a, 13). The oxygens are identified by letter and color coded to match later figures in this paper. Note that some of the signals disappear with time due to steady isotopic exchange with the solution.

diminish as they undergo steady isotopic exchange with the solution. The rates of isotopic equilibration are fit to a simple exponential rate law:  $I(t) = I_0 e^{-kt}$ , where  $I$  = intensity;  $k = 1/\tau$  and has units of  $s^{-1}$ ;  $\tau$  is a characteristic time for disappearance of the signal and has units of  $s$ .

Two features become apparent when one compiles the thus-calculated oxygen–isotope–exchange rates for the various oxygens in all three molecules. First, within a given molecule, such as the  $[H_xNb_{10}O_{28}]^{(6-x)-}$  ion (Fig. 6), all of the exchangeable oxygens exhibit nearly the same pH dependence for their rates of isotopic exchange. The total range for all oxygens in that molecule differ by a range of  $\sim 10^3 \sim 10^4$ , as shown in Fig. 6 for the  $[H_xNb_{10}O_{28}]^{(6-x)-}$  ion and Fig. 7 for the  $[H_xNb_8Ti_2O_{28}]^{(8-x)-}$  ion. In the case of the  $[H_xNb_8Ti_2O_{28}]^{(8-x)-}$ , for example, all rates increase as pH decreases.

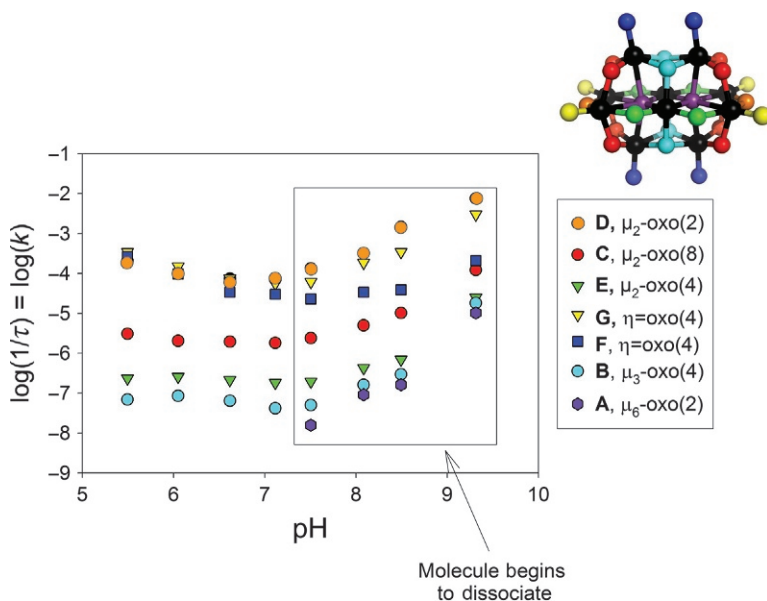


**Fig. 6** Rates of oxygen–isotope exchange for seven sites in the  $[H_xNb_{10}O_{28}]^{(6-x)-}$  molecule as a function of solution pH. The letter designation and coordination chemistry of the various oxygens are shown in the legend. The ion structure is color coded to correspond to the rate data so that individual oxygens can be identified and the number in parenthesis indicates how many of those particular oxygens exist in a molecule. The rate of loss of signal from the A site, the central  $\mu_6$ -oxo, indicates dissociation of the molecule. Note that all oxygen sites have roughly the same pH dependence to dissociation and that this variation is also observed for dissociation of the molecule. The units are  $s^{-1}$  and are determined by fitting an exponential rate law to the loss of  $^{17}O$ -NMR signal as a function of time (12,14a) (see also Ref. (4e,13)).

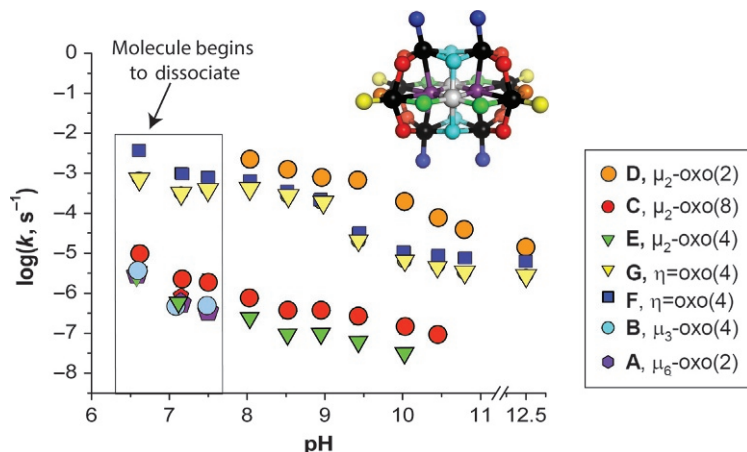


**Fig. 7** Rates of oxygen–isotope exchange for seven sites in the  $[\text{H}_x\text{Nb}_8\text{Ti}_2\text{O}_{28}]^{(8-x)-}$  molecule as a function of solution pH. The letter designation and coordination chemistry of the various oxygens are shown in the legend, as in Fig. 6, and the ion structure is color coded to correspond to the rate data. The number in parenthesis indicates how many of those particular oxygens exist in a molecule. The rate of loss of signal from the A site, the central  $\mu_6$ -oxo, indicates dissociation of the molecule. Note that all oxygen sites have roughly the same pH dependence to dissociation and isotopic exchange (12,14a).

Second, dissociation of the molecule, as indicated by diminution of the  $^{17}\text{O}$ -NMR signals from the central  $\mu_6$ -oxo, has the same pH dependence as the rates of isotope exchange (Figs. 6 and 7). Thus, whatever molecular motions activate the structure to dissociate also seem to be involved in the pathways for isotopic exchange. For the  $[\text{H}_x\text{Nb}_{10}\text{O}_{28}]^{(6-x)-}$  ion, dissociation is apparent when pH is raised and is slower than the isotope exchanges at other sites. For the  $[\text{H}_x\text{Nb}_8\text{Ti}_2\text{O}_{28}]^{(8-x)-}$ , dissociation is evident in acidic solutions, where the loss of signal for Site A is at about the same rate as isotopic exchange of other relatively unreactive bridging oxygens.

The fact that all oxygens exhibit the same pH dependence to isotopic exchange and dissociation suggests that these reactions involve concerted motions of all atoms. The reactivity of any particular oxygen to isotopic exchange can be modified somewhat by choice of a different background electrolyte (12b). The effect is regiospecific in the decaniobate ion, with some oxygens remaining unaffected by choice of the background electrolyte while others varying by  $\sim 10^2$ . The observation indicates that charge separations are important to the isotopic-exchange pathways, which can be facilitated by counterions. Such a conclusion is consistent with many studies indicating that polyoxometalate ions are coordinated, and perhaps are stabilized by, electrostatic interactions with counterions (15).

The pH dependencies reflect the total unprotonated charge of the molecules,  $-6$  for  $[\text{Nb}_{10}\text{O}_{28}]^{6-}$ ,  $-7$  for  $[\text{Nb}_9\text{TiO}_{28}]^{7-}$ , and  $-8$  for  $[\text{Nb}_8\text{Ti}_2\text{O}_{28}]^{8-}$ , which is a measure of their relative affinity for protons and overall basicity. Correspondingly, the  $[\text{Nb}_8\text{Ti}_2\text{O}_{28}]^{8-}$  ion is the strongest base in the series, and it exhibits proton-enhanced rates of isotopic exchange of all structural oxygens, over a  $\sim 10^3$  range (Fig. 7). In contrast, the  $[\text{Nb}_{10}\text{O}_{28}]^{6-}$  ion is the weakest base and the pH dependence of oxygen–isotopic-exchange rates is enhanced by  $[\text{OH}^-]$ , although there is some evidence for proton-enhanced pathways at low pH (Fig. 6). Data for the  $[\text{H}_x\text{Nb}_9\text{TiO}_{28}]^{(7-x)-}$  molecule are not shown, but the oxygen sites in this molecule exhibit an amphoteric variation in rates that falls intermediate between the  $[\text{H}_x\text{Nb}_{10}\text{O}_{28}]^{(6-x)-}$  and  $[\text{H}_x\text{Nb}_8\text{Ti}_2\text{O}_{28}]^{(8-x)-}$  ions. In this molecule, rates increase with  $[\text{OH}^-]$  concentration at high pH, with  $[\text{H}_3\text{O}^+]$  at lower pH and exhibit a conspicuous minimum in rates at near-neutral pH conditions. This minimum is shifted to higher pH values than the one observed for the  $[\text{H}_x\text{Nb}_{10}\text{O}_{28}]^{(6-x)-}$  ion, as one expects since the  $[\text{H}_x\text{Nb}_9\text{TiO}_{28}]^{(7-x)-}$  molecule is a stronger base. All of these observations are consistent with an amphoteric chemistry dominated by the *average* proton affinities of each molecule, and not the affinity of a particular exchanging oxygen bridge. Stated differently, the proton affinities of the oxygens involved in the isotope-exchange reaction are similar to one another.



#### 4. THE TRANSITION TO A PARTLY DETACHED STRUCTURE IN $\text{MAI}_{12}$ CATIONS

The idea that reactions at the nanometer size are controlled by metastable equilibria is best illustrated by detailed studies of Group 13 cations that all have the structure of the  $\epsilon$ -isomer of the Baker–Figgis–Keggin structure. These have the stoichiometry:  $[\text{MO}_4\text{Al}_{12}(\text{OH})_{24}(\text{OH}_2)_{12}]^{7/8+}$ . The “M” site can be Al(III), Ga(III), or Ge(IV), and in this chapter, the abbreviations:  $[\text{AlO}_4\text{Al}_{12}(\text{OH})_{24}(\text{OH}_2)_{12}]^{7+} = \text{AlAl}_{12}$ ,  $[\text{GaO}_4\text{Al}_{12}(\text{OH})_{24}(\text{OH}_2)_{12}]^{7+} = \text{GaAl}_{12}$ , and  $[\text{GeO}_4\text{Al}_{12}(\text{OH})_{24}(\text{OH}_2)_{12}]^{8+} = \text{GeAl}_{12}$  are used.

There are two sets of 12  $\mu_2$ -OH in each structure that differ slightly from one another—one set of 12  $\mu_2$ -OH lies *within* one of the four trimeric groups that comprise the  $\epsilon$ -Keggin structure, shown in green in Fig. 1. Another set of 12  $\mu_2$ -OH links each trimeric fragment (Fig. 1 bottom), which is shown in purple. Beyond this difference, the oxygens have identical coordination

environments; the  $\langle \text{Al–O} \rangle$  bond lengths, for example, are virtually identical. The single central “M” metal is tetrahedrally coordinated to four  $\mu_4$ -oxo, and these oxygens are inert to steady isotopic exchange. The rates of isotopic exchange for all other oxygen sites in these molecules have been measured via  $^{17}\text{O}$ -NMR (*4i, k–m, 16*). The rates of isotopic exchange of the 12 bound waters with bulk solution all lie in the millisecond time range, which is the range that is expected for Al(III) complexes of similar charge densities (*17*) (*Table 1*). Rates of water exchanges with bulk solution for the 12 sites on each of the  $\text{AlAl}_{12}$ ,  $\text{GaAl}_{12}$ , and  $\text{GeAl}_{12}$  all lie within a factor of  $\sim 5$  of one another, which contrasts sharply with the wide range observed for isotope exchanges into the hydroxide bridges.

The central metal in the  $\text{MAl}_{12}$  molecule exerts an enormous effect on the rates of exchange of both sets of  $\mu_2$ -OH. The rates of exchange of  $\mu_2$ -OH across the entire set of molecules differ by factors of at least  $\sim 10^7$  (*Fig. 8*) depending

**Table 1** A Compilation of Rate Coefficients and Activation Parameters for Exchange of Water Molecules From the Inner-Coordination Sphere of Al(III) Complexes to the Bulk Solution, as Determined From  $^{17}\text{O}$ -NMR

Species	$k_{\text{ex}}^{298}$ ( $\text{s}^{-1}$ ) ( $\pm 1\sigma$ )	$\Delta H^\ddagger$ ( $\text{kJ mol}^{-1}$ )	$\Delta S^\ddagger$ ( $\text{J K}^{-1} \text{mol}^{-1}$ )	Source
<b>Monomeric complexes</b>				
$\text{Al}(\text{H}_2\text{O})_6^{+3}$	1.29( $\pm 0.03$ )	85 ( $\pm 3$ )	42 ( $\pm 9$ )	(18)
$\text{Al}(\text{H}_2\text{O})_5\text{OH}^{2+}$	31,000( $\pm 7750$ )	36 ( $\pm 5$ )	−36 ( $\pm 15$ )	(19)
$\text{AlF}(\text{H}_2\text{O})_5^{2+}$	240( $\pm 34$ )	79 ( $\pm 3$ )	17 ( $\pm 10$ )	(20)
$\text{AlF}_2(\text{H}_2\text{O})_4^+$	16,500( $\pm 980$ )	65 ( $\pm 2$ )	53 ( $\pm 6$ )	(20)
$\text{Al}(\text{ssal})^+$	3000( $\pm 240$ )	37 ( $\pm 3$ )	−54 ( $\pm 9$ )	(21)
$\text{Al}(\text{sal})^+$	4900( $\pm 340$ )	35 ( $\pm 3$ )	−57 ( $\pm 11$ )	(21)
$\text{Al}(\text{mMal})^+$	660( $\pm 120$ )	66 ( $\pm 1$ )	31 ( $\pm 2$ )	(22)
$\text{Al}(\text{mMal})_2^-$	6900( $\pm 140$ )	55 ( $\pm 3$ )	13 ( $\pm 11$ )	(22)
$\text{Al}(\text{ox})^+$	109( $\pm 14$ )	69 ( $\pm 2$ )	25 ( $\pm 7$ )	(23)
<b>Multimeric complexes</b>				
$\text{AlAl}_{12}$	1100( $\pm 100$ )	53 ( $\pm 12$ )	−7 ( $\pm 25$ )	(4k, 16a)
$\text{GaAl}_{12}$	227( $\pm 43$ )	63 ( $\pm 7$ )	29 ( $\pm 21$ )	(4l)
$\text{GeAl}_{12}$	190( $\pm 43$ )	56 ( $\pm 7$ )	20 ( $\pm 21$ )	(4m)

From Lee, A.P.; Phillips, B.L.; Casey, W.H. *Geochim. Cosmochim. Acta* **2002**, 66 (4), 577–587.

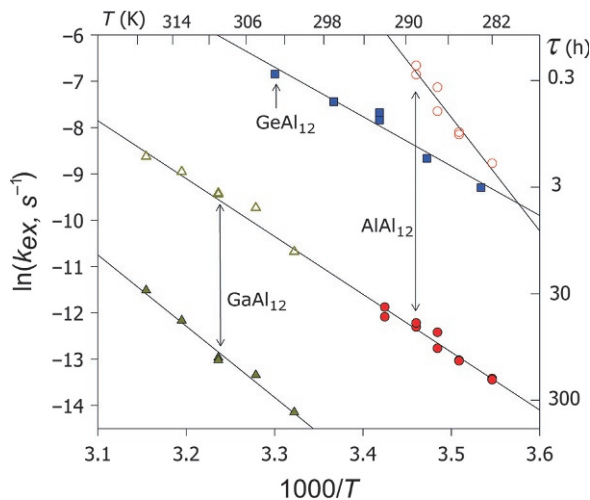


**Fig. 8** The oxygen–exchange rates ( $k$ ,  $s^{-1}$ ; left-hand-side) and average lifetimes ( $\tau_i$ ;  $i = 1, 2$ ; right-hand-side) for the two  $\mu_2$ -OH sites in each of the  $AlAl_{12}$ ,  $GaAl_{12}$ , and  $GeAl_{12}$  molecules, as measured in  $^{17}O$ -NMR experiments ( $4k-m$ ). The *open and closed symbols* correspond to fast- and slow-reacting  $\mu_2$ -OH sites in the same molecule and are color coded:  $AlAl_{12} = (\bullet, \circ)$ ,  $GaAl_{12} = (\blacktriangle, \triangle)$ , and  $GeAl_{12} = (\blacksquare)$ . Arrows link the values of  $\tau_1$  and  $\tau_2$  within to each molecule. There is no value of  $\tau_2$  for the  $GeAl_{12}$  since the rates are too fast to measure. Note that the rates span at least a factor of  $10^7$  in rates depending upon the metal in the inert “M” site of the  $[MO_4Al_{12}(OH)_{24}(OH_2)_{12}]^{7/8+}$  molecules and could be as high as  $10^{10}$  if the typical  $\sim 10^3$  difference in  $\tau_1$  and  $\tau_2$  values is also observed for the  $GeAl_{12}$  molecule.

upon the metal in the inert “M” site of the  $[MO_4Al_{12}(OH)_{24}(OH_2)_{12}]^{7/8+}$  molecules. The two sets of  $\mu_2$ -OH colored green and purple in Fig. 1 yield time constants for exchange ( $\tau_1$ ,  $\tau_2$ ) (Fig. 8) and these differ by  $\sim 10^3$  within a single molecule. The range could be as high as  $\sim 10^{10}$  if the typical  $\sim 10^3$  difference in  $\tau_1$  and  $\tau_2$  values is found for the  $AlAl_{12}$  and  $GaAl_{12}$  molecules is also observed for the  $GeAl_{12}$  molecule. The rates are compiled in Fig. 8 for both sets of  $\mu_2$ -OH bridges in all three molecules:  $AlAl_{12}$ ,  $GaAl_{12}$ , and  $GeAl_{12}$ .

No pH variation was detected in exchange rates of oxygens into  $\mu_2$ -OH bridges for the  $GaAl_{12}$  and  $AlAl_{12}$  molecules ( $4k-m$ ), although experiments could only be conducted over a narrow range ( $4.2 < \text{pH} < 6.5$ ). The isotope–exchange rates for the less-labile  $\mu_2$ -OH bridge in the  $GeAl_{12}$  cluster exhibited a near-first-order dependence on proton concentration ( $4m$ ), and, of course, the more labile  $\mu_2$ -OH bridge reacted too quickly for NMR measurement by injection.



## 5. METASTABLE INTERMEDIATES

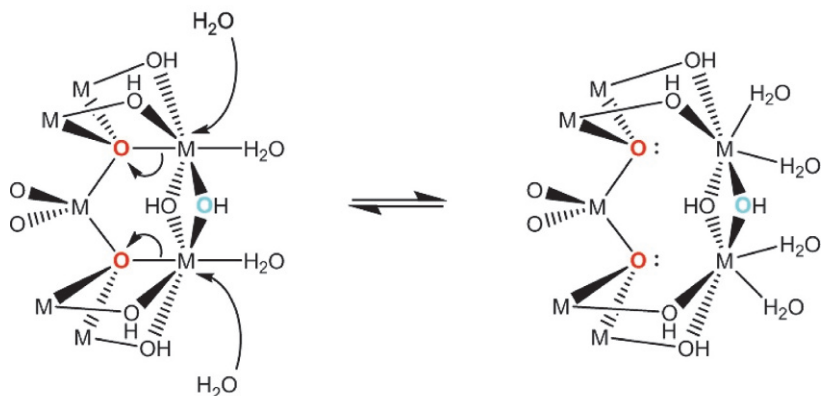
The ions described earlier were chosen because they were at an appropriate scale for dynamic simulation. Correspondingly, Rustad *et al.* (14b) built a force field for Al(III) hydrolysis in water and from his simulations postulated a mechanism that explains the enormous sensitivity of the rates of exchange of hydroxyl bridges in the  $MAI_{12}$  cations. He later extended the model to treat the niobate ions in water (14), which will be discussed later. Although the two experimental sets of molecules differ considerably in charge and structure, a similar set of reaction steps to produce a metastable form of the structure could be identified. The central idea is that loose metastable structures form that are essential to the rates of isotopic exchange of bridging oxygens. Forming the metastable structure involves concerted motions of all atoms. They cannot be intuited by examining the static, stable form of the molecule nor can a separated fragment of the structure be assumed to capture the entire chemistry.

The  $MAI_{12}$  set of molecules were particularly well suited for unraveling the mechanism because they had such high symmetry that the number of potential metastable intermediates was limited. The reaction pathway identified in the molecular–dynamic simulations is illustrated in Fig. 9 for the  $MAI_{12}$  series of molecules.

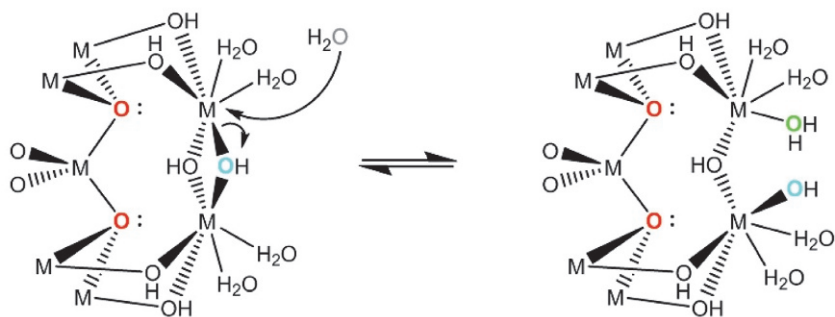
The metastable forms are established via a predictable series of steps:

- Step 1.** A loose, metastable form of the structure forms by partial detachment of a surface metal from the deeper and often overbonded oxygens. Solvation forces, and nucleophiles such as  $OH^-$  and  $H_2O$ , induce the detachment. The overbonded oxygen is the central  $\mu_4-O$  for the  $MAI_{12}$  series of molecules and the central  $\mu_6-O$  for the series of niobate ions. The energy required to establish this partly detached structure depends upon concerted motions of all atoms in the molecule and, of course, several sets can exist that are accessible via different transformations. Because charge separations are involved in forming the metastable structure, counterions can influence the rates, as discussed earlier.
- Step 2.** Oxygens add to the newly undercoordinated metals in the loose, metastable structure. In the case of the  $AlAl_{12}$  molecule (Fig. 9) the result is a dimer-like intermediate at the top of the  $\epsilon$ -Keggin structure. This loose structure forms by the lifting

### Step 1: Stepwise partial detachment



### Step 2: Addition of water; hydrolysis



### Step 3: $\mu_2$ -O<sub>2</sub>H<sub>3</sub> bridge formation

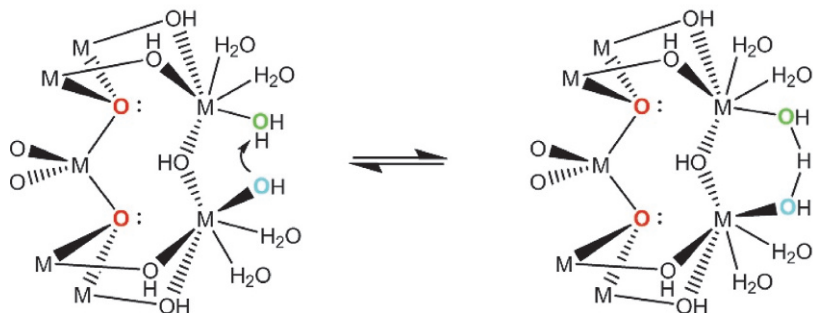


**Fig. 9** A series of reaction steps postulated by Rustad *et al.* (24) that account for the  $^{17}\text{O}$ -NMR data for the  $\text{MAI}_{12}$  series of the reactions. First is stepwise detachment of surface metals from deeper overbonded oxygens, here the  $\mu_2$ -oxo that bond to the “M” site. Detachment is induced by solvation forces in this case. In the second step, isotopically normal oxygens add to the now-undercoordinated metals; in this example, it is as a water molecule. The third and fourth steps are bond rupture and proton transfers, which in the  $\text{MAI}_{12}$  molecules forms a  $\mu_2$ -O<sub>2</sub>H<sub>3</sub><sup>+</sup> bridge. The bridge dehydrates and reestablishes to release the isotopic tag and in the last step, the metastable structure collapses. In the  $\text{MAI}_{12}$  series of molecules, the energy to form the loose metastable structure in Step 1 depends very sensitively on the strength of M- $\mu_2$ -oxo bonding (see Fig. 10).



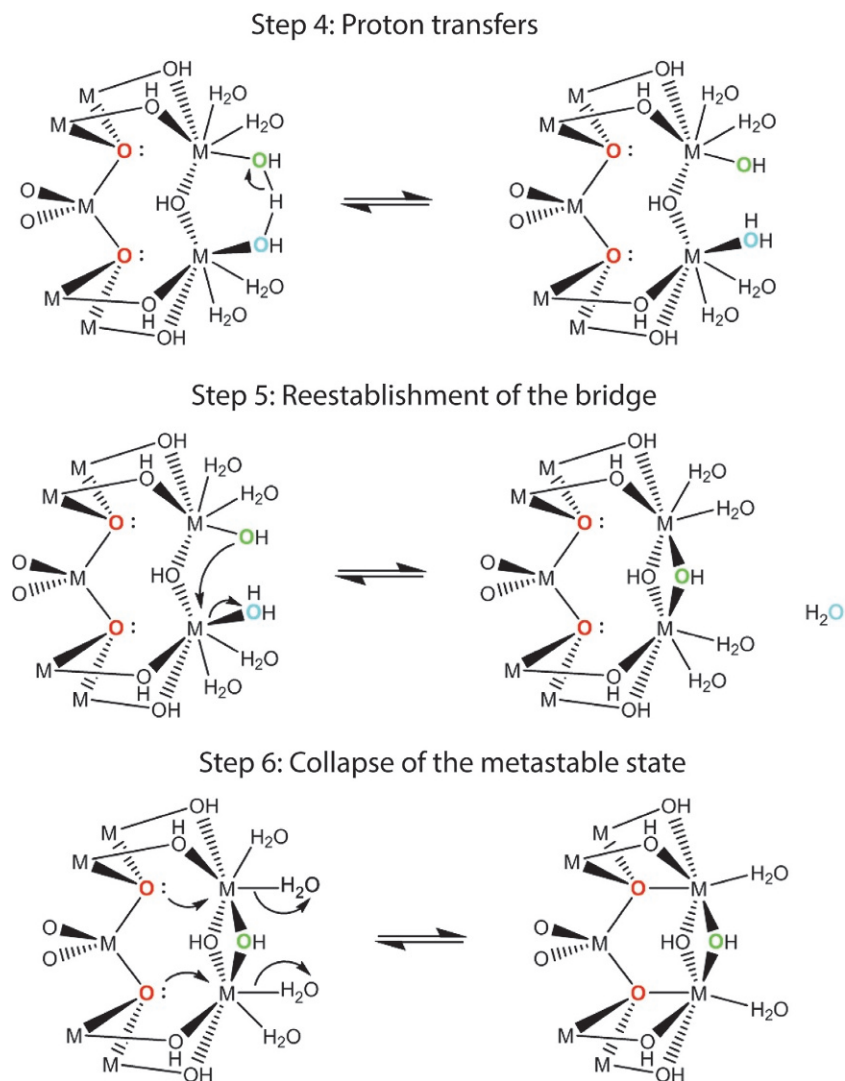


Fig. 9—Cont'd

of two hexacoordinated Al(III) away from the  $\mu_4$ -O. This lifting is of course undoubtedly actually stepwise but is illustrated as a simultaneous reaction in Fig. 9 to save space. In the case of the niobates, which have lower symmetry than the  $\text{MAI}_{12}$  molecules, many sets of intermediates could form (14b), but all require partial detachment of a metal from the overbonded  $\mu_6$ -O (see later).

- Step 3.** Protons transfer among oxygens in the metastable structure. For the  $\epsilon$ -Keggin structures, one of the  $\mu_2$ -OH bridges in the dimer-like intermediate protonates to form a  $\mu_2$ -O<sub>2</sub>H<sub>3</sub><sup>+</sup>. In the niobates, the protons transfer to structural oxo bridges and to solvent.
- Step 4.** Bridging and nonbridging oxygens swap. In the case of the  $\epsilon$ -Keggin structure, the swapping is via a water molecule in the  $\mu_2$ -O<sub>2</sub>H<sub>3</sub><sup>+</sup> bridge, which returns to form a  $\mu_2$ -OH and release an <sup>17</sup>O-enriched water to solution.
- Step 5.** The metastable structure collapses (Fig. 9) and dehydrates to release the isotopic tag to solution.

For the MAI<sub>12</sub> molecules, “M” metals influence the reaction by constraining access to the metastable state that is essential to isotopic exchange. The two types of  $\mu_2$ -OH in the  $\epsilon$ -Al<sub>13</sub> structures differ subtly in the structure, lying either *cis* or *trans* to the  $\mu_4$ -O, but do not differ much in the structure of the intermediates formed. One set of  $\mu_2$ -OH has more energetic latitude to form the intermediate structure and the energies of forming the intermediate scale GaAl<sub>12</sub> > AlAl<sub>12</sub> > GeAl<sub>12</sub>, just as is expected from the experimental observations (24) (Fig. 10). Key to the reaction is the strength of the bond between the M site and the  $\mu_4$ -O, which affects the facility with which the metastable structure can be accessed. The energies of forming this dimer-like cap for the GaAl<sub>12</sub>, AlAl<sub>12</sub>, and GeAl<sub>12</sub> molecules, are shown along with Rustad’s force-field result, as Fig. 10.

A similar set of low-energy transitions to metastable structures can be identified for the niobate series of molecules, but the unique tie to experimental data is unclear because of the lack of symmetry in the molecules. But what was found in the isostructural niobate series of [H<sub>x</sub>Nb<sub>10</sub>O<sub>28</sub>]<sup>(6-x)-</sup>, [H<sub>x</sub>Nb<sub>9</sub>TiO<sub>28</sub>]<sup>(7-x)-</sup>, and [H<sub>x</sub>Nb<sub>8</sub>Ti<sub>2</sub>O<sub>28</sub>]<sup>(8-x)-</sup>, is that a single-atom substitution, well away from the sites of isotopic exchange, has an enormous effect on the kinetics of oxygen–isotope exchange and dissociation.

Rustad *et al.* also built a force field for molecular-dynamic simulations of these niobate anions in a dissociating water solvent (14b). As with the MAI<sub>12</sub> Keggin ions, he found that the molecules were constantly sampling their energy landscape and forming metastable forms of their structures via a similar set of steps as those outlined earlier. The steps were similar, although the number and character of the metastable structures were very sensitive to the symmetry and composition of the starting structures.

As with the aluminate ions, the first step is detachment of one of the three metals from the deep overbonded  $\mu_6$ -oxo via solvation forces. This detachment forms an intermediate structure (Fig. 11) with loosely bonded set of

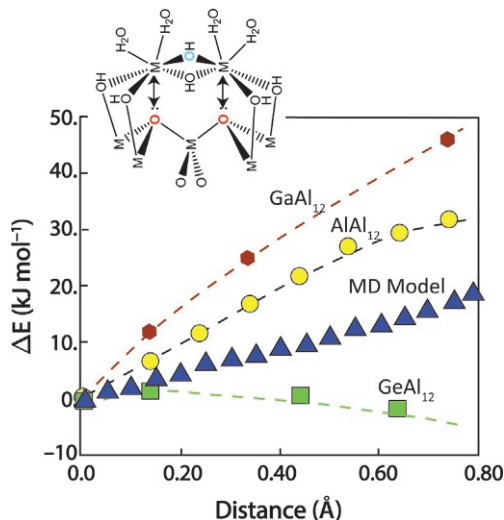


**Fig. 10** Calculated energies at the DFT/ccpVDZ/B3LYP level of theory to form the dimer-like intermediate structure at the cap of the  $\text{MAl}_{12}$  ion as a function of the various metals (Ge(IV), Al(III), or Ga(III)) in the central “ $\text{M}(\text{O})_4$ ” position (24). The energy to form the dimer-like intermediate structure depends sensitively upon the strength of the bond between the central metal and the inert  $\mu_4$ -oxo. A highly charged metal like Ge(IV) polarizes that bond and makes the adjacent bond to an  $\text{Al}(\text{O})_6$  correspondingly weaker so that the intermediate forms easily. The reverse is true as well—placement of a large metal with relatively low charge in the central position, like Ga(III), weakens bonds to the  $\mu_4$ -oxo and, correspondingly, the bond to the adjacent  $\text{Al}(\text{O})_6$  site is stronger and forming the intermediate is less favored. The rates of exchange of the outer  $\mu_2$ -OH trend:  $\text{GeAl}_{12} > \text{AlAl}_{12} > \text{GaAl}_{12}$ . Also shown is the potential-energy trend for the molecular-dynamics model that was used to identify the reaction coordinate (24).

metals. The second step is addition of an isotopically normal oxygen, which can be either a  $\text{H}_2\text{O}$ ,  $\text{OH}^-$ , or  $\text{H}_3\text{O}^+$ . The added oxygen can be in any form because the protons reshuffle immediately to more basic oxygens in the niobate structures or to the solvent. Thus, he termed the reactions “*oxygen-stuffing reactions*” because of the similar character regardless of the incoming nucleophile and because of the proton ambiguity. Access to this metastable state involves concerted motions by all oxygens in the nanometer-sized structure, which is a second reason why single-atom substitutions affect the kinetics of the reaction, as is observed. Protons do not activate individual bridging oxygens to isotopic exchange, they activate the entire molecule.

Several points are important in this model: (i) all atoms are involved in forming the intermediate; thus changes in composition have an averaging

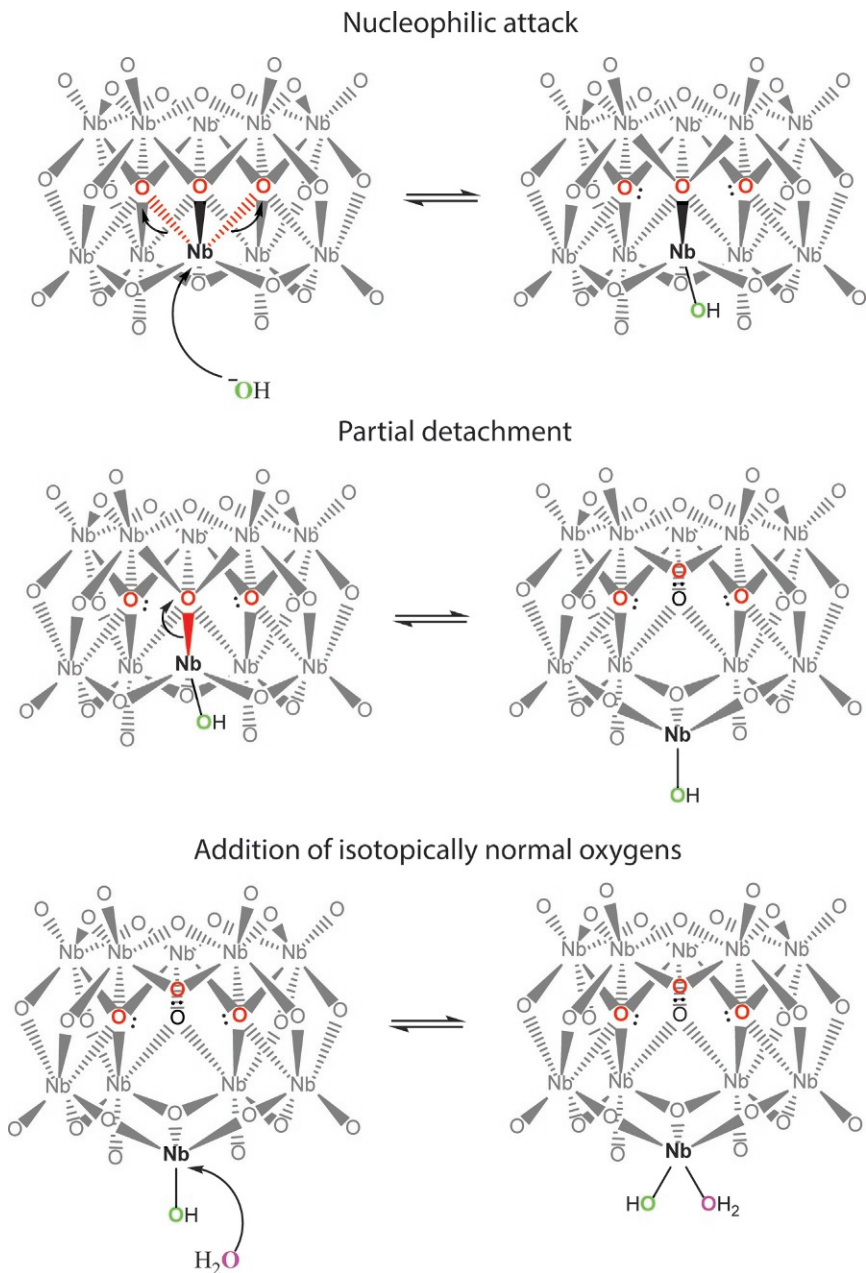


**Fig. 11** A reaction that yields one possible metastable form of the  $[\text{H}_x\text{Nb}_{10}\text{O}_{28}]^{(6-x)-}$  molecule. The steps are broadly similar to those illustrated in Fig. 9 for the MAI<sub>12</sub> series of molecules, although these are structurally very dissimilar. The first step is partial detachment of a surface metal from a deeper overbonded oxygen, which in this molecule is the central  $\mu_6$ -oxo (Site A). An oxygen adds to the now-undercoordinated metal, which can be as a hydroxide ion, a hydronium, or a water molecule. Protons transfer to more basic oxygens and the metastable form exists for an appreciable lifetime. At some point the oxygens shuffle to a bridging position and the metastable structure collapses.

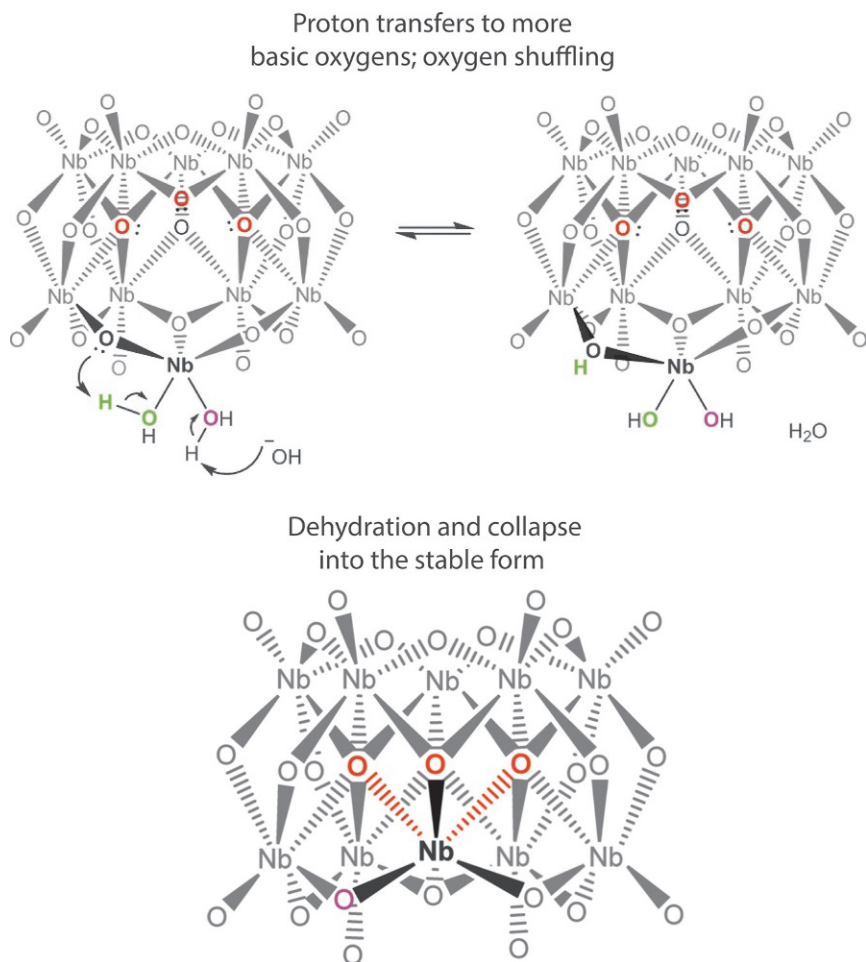


Fig. 11—Cont'd

effect on reactivity. (ii) The number of accessible metastable forms reflects the energy landscape, which in turn reflects the molecule's symmetry and composition. The  $\text{MA}_{12}$  molecules have  $T_d$  symmetry, but the  $[\text{Nb}_{10}\text{O}_{28}]^{6-}$  ion has  $D_{2d}$  symmetry and thus a more complicated energy landscape to explore. This landscape is further complicated by the Ti(IV) substitutions. (iii) The energy barrier to forming the intermediate structures can be dramatically affected by single-atom substitutions. (iv) These intermediate structures seem to be implied in both dissociation pathways and in oxygen–isotope–exchange rates, and it is not difficult to see that a

molecule with little energy could experience exchange of some oxygens at varying rates but that a molecule with much energy dissociates via the same metastable intermediate.

Thus, for example, the  $\mu_3$ -oxo in the center of the  $[\text{H}_x\text{Nb}_{10}\text{O}_{28}]^{(6-x)-}$  anion only begin to exchange oxygen isotopes when there is also evidence for isotopic exchange of the normally inert  $\mu_6$ -oxo, which indicates that the molecule is dissociating. The  $\mu_3$ -oxo exchange at rates that are 2–3 times faster than the rates of dissociation, as indicated by isotopic equilibration of the  $\mu_6$ -oxo (Fig. 6).



## 6. CONCLUSIONS

What results on two limited polyoxometalate systems means for scientists studying interfacial reactions is actually profound. For both of these cluster ions, the pathways for isotopic exchange and dissociation would *never* have been identified without considering the entire structure and how it interacted dynamically with solution. A truncated model, for example, attempting to treat  $\text{SiO}_2$  dissolution via a silicate dimer ( $2k-n$ ) is worse than useless because it is misleading. To emphasize this point even further, niobate molecules have been synthesized with siloxane and silanol groups ( $4j$ ). In these Si-substituted niobates, the siloxane (Si–O–Si) and silanol ( $>\text{Si-OH}$ ) groups exhibit the same pH dependencies, and overall reactivities, to oxygen–isotopic substitution as all other oxygens in the molecule.

Thus, the setting is everything—even such simple reactions as isotope exchanges are controlled by access to metastable structures that are unique to the entire structure have their own acid–base chemistry and exist for long lifetimes. Access to the metastable states reflects the entire nanometer-sized structure and its interactions with solution.

A second point concerns that the daunting amount of structural information needed to constrain a reaction pathway at these nanometer-sized features in aqueous solutions at molecular scales. The amount of information needed to detail the reaction pathway in the  $\text{MAI}_{12}$  ions, for example, was considerable. The reaction pathways would also never have been identified without close coupling of experiment to simulation, and without accurate information about the structures in solution. There is no equivalent structural detail available for any interfacial reaction on any mineral, which is why the community relied so much on simulation of

inferred key fragments to understand the molecular transformations and transition states. Stated succinctly, any model for molecular-scale reactions on the nanometer-sized features on a mineral or glass surface must be structurally faithful to the actual site of reaction or it will miss the essential chemistry.

## ACKNOWLEDGMENTS

This work is not my own. I review research here from my long-time collaborator Jim Rustad, several graduate students, post-doctoral researchers, and undergraduate students, including Drs. Andy Ohlin, Eric Villa, Edina Balogh, Rene Johnson, Alasdair Lee. The author particularly thanks Prof. James Rustad, formerly of UCD and now of the Office of Basic Energy Science at the U.S. Department of Energy, who developed the models for metastable isotopic exchange and dissociation from working with me for over two decades. Prof. Brian Phillips of SUNY-Stony Brook was essential to experiments on the MAL<sub>12</sub> molecules. Also, the author thanks Dr. Anna Oliveri, who is an accomplished artist as well as a scientist, for help with the illustrations, along with Mr. Chris Colla. This paper summarizes research supported by the U.S. Department of Energy, recently via Grant DE-FG02-05ER15693.

## REFERENCES

1. (a) Boudart, M.; Djega-Mariadasson, G. *Kinetics of Heterogeneous Catalytic Reactions*; 1984; p222; (b) Lichtner, P. C. *Am. J. Sci.* **2016**, *316*(5), 437–469.
2. (a) Lasaga, A. C.; Gibbs, G. V. *Phys. Chem. Miner.* **1988**, *16*(1), 29–41; (b) Casey, W. H.; Lasaga, A. C.; Gibbs, G. V. *Geochim. Cosmochim. Acta* **1990**, *54*(12), 3369–3378; (c) –Kubicki, J. D.; Xiao, Y.; Lasaga, A. C. *Geochim. Cosmochim. Acta* **1993**, *57*(16), 3847–3853; (d) Kubicki, J. D.; Blake, G. A.; Apitz, S. E. *Am. Mineral.* **1996**, *81*(7–8), 789–799; (e) Xiao, Y.; Lasaga, A. C. *Geochim. Cosmochim. Acta* **1994**, *58*(24), 5379–5400; (f) Pel'menschikov, A.; Strandh, H.; Pettersson, L. G. M.; Leszczynski, J. *J. Phys. Chem. B* **2000**, *104*(24), 5779–5783; (g) Pel'menschikov, A.; Leszczynski, J.; Pettersson, L. G. M. *J. Phys. Chem. A* **2001**, *105*(41), 9528–9532; (h) Del Bene, J. E.; Runge, K.; Bartlett, R. J. *Comput. Mater. Sci.* **2003**, *27*(1–2), 102–108; (i) Xiao, Y.; Lasaga, A. C. *Geochim. Cosmochim. Acta* **1996**, *60*(13), 2283–2295; (j) Felipe, M. A.; Xiao, Y.; Kubicki, J. D. In: *Reviews in Mineralogy & Geochemistry*; Cygan, Randall T., Kubicki, James D., Eds.; Molecular Modeling Theory, 42, 2001; pp 485–531; (k) Criscenti, L. J.; Brantley, S. L.; Mueller, K. T.; Tsomaia, N.; Kubicki, J. D. *Geochim. Cosmochim. Acta* **2005**, *69*(9), 2205–2220; (l) Criscenti, L. J.; Kubicki, J. D.; Brantley, S. L. *J. Phys. Chem. A* **2006**, *110*(1), 198–206; (m) Wallace, A. F.; Gibbs, G. V.; Dove, P. M. *J. Phys. Chem. A* **2010**, *114*(7), 2534–2542; (n) Nangia, S.; Garrison, B. J. *J. Phys. Chem.* **2008**, *112*(10), 2027–2033; (o) Morrow, C. P.; Nangia, S.; Garrison, B. J. *J. Phys. Chem.* **2009**, *113*(7), 1343–1352; (p) Morrow, C. P.; Olsen, A. A.; Kubicki, J. D. *Am. Mineral.* **2014**, *99*(11–12), 2303–2312.
3. (a) Burns, P. C.; Kubatko, K.-A.; Sigmon, G.; Fryer, B. J.; Gagnon, J. E.; Antonio, M. R.; Soderholm, L. *Angew. Chem. Int. Ed.* **2005**, *44*(14), 2135–2139; (b) Swallow, A. G.; Ahmed, F. R.; Barnes, W. H. *Acta Crystallogr.* **1966**, *21*(3), 397–405; (c) Furrer, G.; Phillips, B. L.; Ulrich, K. U.; Pothig, R.; Casey, W. H. *Science* **2002**, *297*(5590), 2245–2247.

4. (a) Harrison, A. T.; Howarth, O. W. *J. Chem. Soc., Dalton Trans.* **1972–1999**, 1985(9), 1953–1957; (b) Howarth, O. W.; Kelly, P. *J. Chem. Soc., Chem. Commun.* **1988**, 18, 1236–1238; (c) Andersson, I.; Pettersson, L.; Hastings, J. J.; Howarth, O. W. *J. Chem. Soc., Dalton Trans.* **1996**, 16, 3357–3361; (d) Howarth, O. W. *Dalton Trans.* **2004**, 3, 476–481; (e) Klemperer, W. G.; Marek, K. A. *Eur. J. Inorg. Chem.* **2013**, 2013(10–11), 1762–1771; (f) Taube, F.; Andersson, I.; Toth, I.; Bodor, A.; Howarth, O.; Pettersson, L. *J. Chem. Soc. Dalton Trans.* **2002**, 23, 4451–4456; (g) Pettersson, L.; Andersson, I.; Taube, F.; Toth, I.; Hashimoto, M.; Howarth, O. W. *Dalton Trans.* **2003**, 1, 146–152; (h) Hampson, M. R.; Hodgkinson, P.; Evans, J. S. O.; Harris, R. K.; King, I. J.; Allen, S.; Fayon, F. *Chem. Commun.* **2004**, 4, 392–393; (i) Loring, J.; Yu, P.; Phillips, B. L.; Casey, W. H. *Geochim. Cosmochim. Acta* **2004**, 68(13), 2791–2798; (j) Johnson, R. L.; Villa, E. M.; Ohlin, C. A.; Rustad, J. R.; Casey, W. H. *Chem. A Eur. J.* **2011**, 17, 9359–9367; (k) Casey, W. H.; Phillips, B. L.; Karlsson, M.; Nordin, S.; Nordin, J. P.; Sullivan, D. J.; Neugebauer–Crawford, S. *Geochim. Cosmochim. Acta* **2000**, 64(17), 2951–2964; (l) Casey, W. H.; Phillips, B. L. *Geochim. Cosmochim. Acta* **2001**, 65(5), 705–714; (m) Lee, A. P.; Phillips, B. L.; Casey, W. H. *Geochim. Cosmochim. Acta* **2002**, 66(4), 577–587; (n) Black, J. R.; Nyman, M.; Casey, W. H. *J. Am. Chem. Soc.* **2006**, 128(45), 14712–14720; (o) Klemperer, W. G.; Shum, W. J. *Am. Chem. Soc.* **1976**, 98(25), 8291–8293.
5. (a) Westrich, H. R.; Cygan, R. T.; Casey, W. H.; Zemitis, C.; Arnold, G. W. *Am. J. Sci.* **1993**, 293(9), 869–893; (b) Casey, W. H.; Westrich, H. R. *Nature* **1992**, 355(6356), 157–159; (c) Casey, W. H. *J. Colloid Interface Sci.* **1991**, 146(2), 586–589.
6. (a) Ohlin, C. *Nat. Mater.* **2010**, 9, 11–19; (b) Casey, W. H.; Westrich, H. R.; Banfield, J. F.; Ferruzzi, G.; Arnold, G. W. *Nature* **1993**, 366(6452), 253–256; (c) Casey, W. H. *Environ. Chem.* **2015**, 12(1), 1–19.
7. (a) Mega, T. L.; Cortes, S.; Van Etten, R. L. *J. Org. Chem.* **1990**, 55(2), 522–528; (b) Cortes, S. J.; Mega, T. L.; Van Etten, R. L. *J. Org. Chem.* **1991**, 56(3), 943–947.
8. (a) Schwarzenbach, R. P.; Gschwend, P. M.; Imboden, D. M. *Environmental Organic Chemistry*, Wiley–Interscience: Hoboken, NJ, 1993, 681; (b) Larson, R. A.; Weber, E. J. *Reaction Mechanisms in Environmental Organic Chemistry*; Lewis: Boca Raton, FL, 1994.
9. Skorina, T.; Allanore, A. *Green Chem.* **2015**, 17(4), 2123–2136.
10. Sposito, G. *The Surface Chemistry of Natural Particles*. Oxford University Press: Oxford, 2004.
11. Heath, E.; Howarth, O. W. *J. Chem. Soc., Dalton Trans.* **1981**, 5, 1105–1110.
12. (a) Villa, E. M.; Ohlin, C. A.; Balogh, E.; Anderson, T. M.; Nyman, M. D.; Casey, W. H. *Angew. Chem. Int. Ed.* **2008**, 47, 4844–4846; (b) Villa, E. M.; Ohlin, C. A.; Casey, W. H. *Chem. A Eur. J.* **2010**, 16, 8631–8634; (c) Villa, E. M.; Ohlin, C. A.; Casey, W. H. *J. Am. Chem. Soc.* **2010**, 132(14), 5264–5272.
13. Marek, K. A. *Polyoxoniobates: How Solution Chemistry Helps to Understand the Solid State*; University of Illinois: Champaign–Urbana, 2001.
14. (a) Villa, E. M.; Ohlin, C. A.; Rustad, J. R.; Casey, W. H. *J. Am. Chem. Soc.* **2010**, 132, 5264–5274; (b) Rustad, J. R.; Casey, W. H. *Nat. Mater.* **2012**, 11, 223–226.
15. (a) Antonio, M. R.; Nyman, M.; Anderson, T. M. *Angew. Chem., Int. Ed.* **2009**, 48(33), 6136–6140; (b) Oliveri, A. F.; Pilgrim, C. D.; Qiu, J.; Colla, C. A.; Burns, P. C.; Casey, W. H. *Eur. J. Inorg. Chem.* **2016**, 2016(6), 797–801; (c) Qiu, J.; Vlasisavljevich, B.; Jouffret, L.; Nguyen, K.; Szymanowski, J. E. S.; Gagliardi, L.; Burns, P. C. *Inorg. Chem.* **2015**, 54(9), 4445–4455.
16. (a) Phillips, B. L.; Casey, W. H.; Karlsson, M. *Nature* **2000**, 404(6776), 379–382; (b) Lee, A. P.; Phillips, B. L.; Olmstead, M. M.; Casey, W. H. *Inorg. Chem.* **2001**, 40(17), 4485–4487; (c) Phillips, B. L.; Lee, A.; Casey, W. H. *Geochim. Cosmochim. Acta* **2003**, 67(15), 2725–2733.



17. (a) Helm, L.; Merbach, A. E. *Chem. Rev.* **2005**, *105*(6), 1923–1959; (b) Casey, W. H. *Chem. Rev.* **2006**, *106*(1), 1–16.
18. Hugli-Cleary, D.; Helm, L.; Merbach, A. E. *Helv. Chim. Acta* **1985**, *68*(3), 545–554.
19. (a) Nordin, J. P.; Sullivan, D. J.; Phillips, B. L.; Casey, W. H. *Inorg. Chem.* **1998**, *37*(19), 4760–4763; (b) Swaddle, T. W.; Rosenqvist, J.; Yu, P.; Bylaska, E.; Phillips, B. L.; Casey, W. H. *Science* **2005**, *308*, 1450–1453.
20. Yu, P.; Phillips, B. L.; Casey, W. H. *Inorg. Chem.* **2001**, *40*(18), 4750–4754.
21. Sullivan, D. J.; Nordin, J. P.; Phillips, B. L.; Casey, W. H. *Geochim. Cosmochim. Acta* **1999**, *63*(10), 1471–1480.
22. Casey, W. H.; Phillips, B. L.; Nordin, J. P.; Sullivan, D. J. *Geochim. Cosmochim. Acta* **1998**, *62*(16), 2789–2797.
23. Phillips, B. L.; Crawford, S. N.; Casey, W. H. *Geochim. Cosmochim. Acta* **1997**, *61*(23), 4965–4973.
24. Rustad, J. R.; Loring, J. S.; Casey, W. H. *Geochim. Cosmochim. Acta* **2004**, *68*(14), 3011–3017.

This page intentionally left blank



# Polyoxometalate Multielectron Catalysts in Solar Fuel Production

S.M. Lauinger, Q. Yin, Y.V. Geletii, C.L. Hill<sup>1</sup>

Emory University, Atlanta, GA, United States

<sup>1</sup>Corresponding author: e-mail address: chill@emory.edu

## Contents

1. Introduction	118
2. Definitions	119
2.1 Reaction Thermodynamics of Water Splitting	119
2.2 Photochemical Generation of Oxidant/Reductant	121
3. Water Splitting Overview	123
3.1 Experimental Approaches to Evaluate WOCs and Water Reduction Catalysts	123
3.2 Comparison of Catalytic Activity of Different Systems	123
4. Water Oxidation Catalysts	124
4.1 Ru-Substituted	124
4.2 Co-Substituted	129
4.3 Ni-Substituted	132
4.4 Others	133
5. Water Reduction Catalysts	134
6. Immobilization of Polyoxometalate WOCs	137
6.1 Methods of Immobilization	138
6.2 Characterizing the Immobilized System	140
7. Assessment of Catalytic Activity	143
7.1 Stability of the Light-Driven Systems	143
7.2 Acid/Base Properties of Polyoxometalates, Speciation, Redox Potentials	144
7.3 The "Purity" of Polyoxometalate WOCs	145
8. Stability in POM Catalytic Systems	145
9. Conclusions	148
Acknowledgments	149
References	149

## Abstract

Catalysts in solar fuel research have greatly increased in the last few years. Significantly, the development of molecular, selective, and faster catalysts for both water oxidation or water reduction based on polyoxometalates has led to advances in the understanding of water splitting systems. Recent studies have combined molecular catalysts with substrates or electrode surfaces in order to evaluate these catalysts when immobilized.

Quantitative and qualitative investigations of molecular speciation and the catalytic mechanism during water oxidation with polyoxometalates are not simple, but recent reports have provided multiple complementary physicochemical, spectroscopic, and other techniques for the comprehension of catalyst stability. This review provides an up-to-date assessment of polyoxometalate-based water oxidation/reduction catalysts as well as immobilized species for the production of solar fuel.



## 1. INTRODUCTION

Transition metal–oxygen cluster polyanions, more simply termed polyoxometalates or “POMs,” have been increasingly popular targets of both fundamental and applied research the last 2 decades (1). This derives in part from the extraordinary diversity, synthetic accessibility, and intrinsic robustness of POMs to oxidative, thermal, and hydrolytic decomposition (2). The pH ranges of hydrolytic stability depend on the principal transition metal in the POM framework (W, Mo, V, Nb, and Ta, in order of prevalence) but range from pH 0 and below to pH 14 and above. Furthermore, both the parent  $d^0$  POMs and their myriad  $d$ -electron–metal and/or  $f$ -electron–metal–substituted derivatives have a rich and tunable redox chemistry. These general features, combined with alterable acid–base properties, have made POMs useful catalysts (3) for many commercial processes and targets for fundamental studies in magnetism, biological activity (antiviral and antitumoral chemotherapy), active materials, and other areas (4).

The projected shortfall in available energy to power our civilization and the increasingly evident, severe impacts of fossil fuel consumption on earth’s environment are becoming ever more evident to the scientific community (5). The global population is expected to double in the lifetimes of a substantial majority of the people alive today. This coupled with the simultaneous, substantial, and ongoing increases in the standard of living worldwide in the coming few decades make these linked energy availability and environmental destruction issues of major concern, and not just to the research community.

One of the most rapidly growing research topics in POM research has been in solar fuel production, also referred to as artificial photosynthesis. The recent onslaught in activity has paralleled the growing energy and environmental concerns above and also the amount of funding available for basic and applied research in solar fuels. Thanks to a great deal of recent research into solar electricity production (solar panels, DSSCs, etc.), simultaneous

with the production of ever cheaper Si-based solar panels in a booming international market for these items, solar electricity has come down several-fold in cost since 2006. It now rivals the cost of conventional electricity, generated from a mix of fossil fuel, nuclear, and hydroelectric sources. But while the future looks bright for cost-effective solar electricity, this is currently not the case for solar fuel. The requirements for financially viable solar fuels are daunting: materials for intense and broad absorption of visible and near-IR sunlight with charge separation must be efficiently coupled with a water oxidation catalyst (WOC) and a water or CO<sub>2</sub> reduction catalyst(s). Furthermore, these three units must function together in a device that exhibits high quantum and chemical efficiency for fuel and O<sub>2</sub> production for extended periods without losses in these parameters.

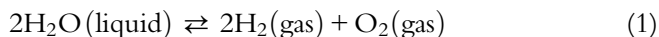
The stability of POMs combined with their extensive synthetic tunability, have made them attractive for studies of light absorption with charge separation, water reduction catalysis, and most expansively, water oxidation catalysis. This chapter summarizes the activity in these areas in approximately the last 10 years. Earlier but still quite recent reviews on POM WOC chemistry (6) are out of date, and recent *Chemical Review* articles on WOCs, in general (7), do not probe the details of the POM systems in full, current detail.



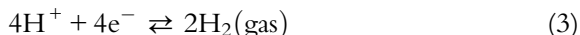
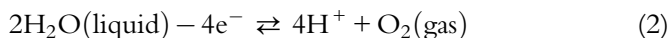
## 2. DEFINITIONS

### 2.1 Reaction Thermodynamics of Water Splitting

In this chapter, the splitting of water into O<sub>2</sub> and H<sub>2</sub> is defined as the reaction in Eq. (1):



This reaction can be considered as a sum of two half-reactions: water oxidation and water reduction, Eqs. (2) and (3):



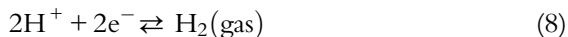
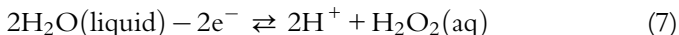
In this case, water reduction is presented as a proton reduction. The reaction in Eq. (3) is the basis for the standard reference hydrogen electrode (SHE), wherein the potential of the SHE is described as the potential of a platinum electrode in a theoretically ideal 1 N acid solution in which the activity coefficient of H<sup>+</sup> is assigned to be 1.00. Similarly, the potential of

the normal hydrogen electrode (NHE) reference is the potential of a platinum electrode in a 1 N acid solution. By convention, these potentials are declared to be zero at all temperatures. Since the activity coefficients of hydrogen ions in diluted solutions are close to 1.00, the difference between NHE and SHE is very small and for practical purposes, the difference can be ignored. In this chapter, we will use NHE as the reference potential where standard conditions are defined as 25°C with a partial pressure of 1 bar of each gas involved in the reaction. The thermodynamics (Gibb's energy) of the overall reaction in Eq. (1) is pH independent, and undoubtedly depends on temperature and ionic strength under standard conditions  $\Delta G = 4.92$  V or 474 kJ/mol (8). In contrast, the thermodynamics of the two half-reactions in Eqs. (2) and (3) are pH dependent and according to the Nernst law under standard conditions (25°C, zero ionic strength, a partial pressure of 1 bar of O<sub>2</sub> or H<sub>2</sub>), the  $\Delta G$  (in V vs NHE) of water oxidation and reduction calculated per one electron is shown in Eqs. (4) and (5):

$$\Delta G(\text{Eq. 1}) = 1.299 - 0.0591 \times \text{pH} \quad (4)$$

$$\Delta G(\text{Eq. 2}) = 0.0591 \times \text{pH} \quad (5)$$

In contrast, the splitting of water to H<sub>2</sub>O<sub>2</sub> and H<sub>2</sub> is defined as the reaction in Eq. (6) with two half-reactions in Eqs. (7) and (8) with  $\Delta G$  in Eqs. (9) and (10):



$$\Delta G(\text{Eq. 7}) = 0.0591 \times \text{pH} \quad (9)$$

$$\Delta G(\text{Eq. 7}) = 1.763 - 0.0591 \times \text{pH} \quad (10)$$

The reactions in Eqs. (2) and (7) are commonly referred to as four- and two-electron water oxidation, respectively. Importantly, water oxidation can be referred to as a two-electron process only if H<sub>2</sub>O<sub>2</sub> is formed as a discrete molecule.

Recently, it has been proposed to decouple hydrogen and oxygen evolution in water electrolysis using an electron-coupled proton buffer (ECPB) (4g, 9). In conventional water electrolysis, simultaneous formation of H<sub>2</sub> and O<sub>2</sub> requires spatially separated production. The ECPB uses a solution of electrochemically active electrolytes, e.g., POMs, as a sacrificial donor or acceptor of electrons to perform a half-reaction of water splitting and to

move the reduced/oxidized electrolyte species to a separate location where the second half-reaction occurs. It would be particularly interesting if ECPB produced high OER (or HER) catalytic activity due to the fact that it would not be necessary to use expensive catalytically active electrodes for water electrolysis.

This ECPB idea is conceptually similar to using electrochemically active electrolytes, including POMs, to store electrical energy in redox or redox flow batteries (10), or in converting chemical energy of biomass into energy stored in solutions of the redox-active electrolytes (11).

## 2.2 Photochemical Generation of Oxidant/Reductant

The mechanism of photochemical generation of  $[\text{Ru}(\text{bpy})_3]^{3+}$  in the presence of persulfate as a sacrificial electron acceptor is described in numerous publications (12). The excited state  $[\text{Ru}(\text{bpy})_3]^{2+*}$  formed after a photon absorption by  $[\text{Ru}(\text{bpy})_3]^{2+}$  is oxidatively quenched by  $\text{S}_2\text{O}_8^{2-}$  to form  $[\text{Ru}(\text{bpy})_3]^{3+}$  and  $\text{SO}_4^{\cdot-}$  radical. The latter oxidizes the second  $[\text{Ru}(\text{bpy})_3]^{2+}$  to  $[\text{Ru}(\text{bpy})_3]^{3+}$ . The overall reaction stoichiometry is in Eq. (11) (Fig. 1).



The quantum yield,  $\phi$ , is defined by  $\phi = (2 \times [\text{Ru}(\text{bpy})_3]^{3+})/N_{hv}$ , where  $N_{hv}$  is the total number of photons absorbed by  $[\text{Ru}(\text{bpy})_3]^{2+}$  and strongly

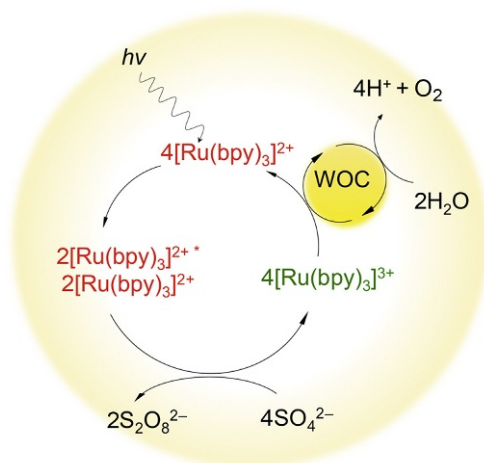


**Fig. 1** Schematic of the homogeneous photocatalytic water oxidation cycle with  $[\text{Ru}(\text{bpy})_3]^{2+}/\text{S}_2\text{O}_8^{2-}$  system.

depends on concentrations and ionic strength in the system. The quantum yield decreases with  $S_2O_8^{2-}$  consumption in the reaction. Side reactions including the self-decomposition of  $[Ru(bpy)_3]^{3+}$  and catalytic oxidation of bpy-ligand decreases the overall reaction selectivity,  $S(t) = 0.25 \times d(O_2)/d([Ru(bpy)_3]^{3+})$ . Moreover, the selectivity changes during the course of the reaction. Since  $[Ru(bpy)_3]^{3+}$  is unstable under close to neutral pH, its reaction with a catalyst must be faster than the self-decomposition. In this case, the generation of  $[Ru(bpy)_3]^{3+}$  becomes a rate determining step in water oxidation. Under steady-state conditions, the rate of  $[Ru(bpy)_3]^{3+}$  formation is equal to the rate of its consumption. In most reactions, it can be consumed via three pathways: self-decomposition, water oxidation, or catalytic oxidation of the organic components (bpy-ligand) present in the system. With an increase of catalyst concentration, the self-decomposition becomes negligibly slow.

Oxidation of bpy-ligand is a complex multielectron process, which could proceed up to  $CO_2$  formation. On the whole, the rate of  $O_2$  formation can be expressed in Eq. (12):

$$d(O_2)/dt = F \times \phi \times S \quad (12)$$

where  $F$  is photon flux and  $S$  is selectivity. All three values,  $F$ ,  $\phi$ , and  $S$ , change with the reaction progress. The average reaction selectivity can be estimated by the final  $O_2$  yield per oxidant,  $Y = 0.5(O_2)/(S_2O_8^{2-})$ . Then the initial rate,  $R_o$ , of  $O_2$  formation is in Eq. (13):

$$R_o = d(O_2)/dt \approx Y \times F_o \times \phi_o \quad (13)$$

In the correctly designed experiment, the light emission spectrum should overlap with the absorption spectrum of  $[Ru(bpy)_3]^{2+}$  (a rather narrow peak with a maximum at 450 nm) and a photon flux should not be too high allowing all photons to be absorbed by the photosensitizer. In this case, the value of  $F_o$  can be determined experimentally by measuring the incident light power and the initial quantum yield can be estimated using Eq. (14):

$$\phi_o \approx R_o/Y \times F_o \quad (14)$$

$$TOF_{app} = R_o/(cat) \quad (15)$$

At the same time, the value of  $TOF_{app}$  calculated from Eq. (15) does not make much sense and cannot be used to compare the activities in different systems.

The reduction potential of the  $[Ru(bpy)_3]^{3+}/[Ru(bpy)_3]^{2+*}$  couple is very negative,  $-0.87$  V. This allows the generation of a strong



reductant by quenching  $[\text{Ru}(\text{bpy})_3]^{2+*}$ . For a long time methyl viologen ( $\text{MV}^{2+}$ ,  $N,N'$ -dimethyl-4,4'-bipyridinium,  $E^\circ$  of  $\text{MV}^{2+}/\text{MV}^{+\bullet}$  couple is  $-0.45$  V) was used as such quencher to form  $\text{MV}^{+\bullet}$  and  $[\text{Ru}(\text{bpy})_3]^{3+}$ . The latter one can be removed from the system by adding a sacrificial electron donor, such as triethanolamine. The reaction product  $\text{MV}^{+\bullet}$  is rather stable and can be used for water reduction. Recently, another strategy based on quenching  $[\text{Ru}(\text{bpy})_3]^{2+*}$  directly by the catalyst has been developed (13). In addition, the photosensitizer  $[\text{Ir}(\text{ppy})_2(\text{dtbbpy})][\text{PF}_6]$ , ((4,4'-di-*tert*-butyl-2,2'-bipyridine)bis[(2-pyridinyl)phenyl]iridium(III) hexafluorophosphate) showed better results than  $[\text{Ru}(\text{bpy})_3]^{2+}$  (14). Since the quantum yield in these systems  $\phi = (\text{reduced catalyst})/N_{h\nu}$  is low, the rate of  $\text{H}_2$  formation is slow. It takes 7 days to reach TON of approximately 6500 (14b).



### 3. WATER SPLITTING OVERVIEW

#### 3.1 Experimental Approaches to Evaluate WOCs and Water Reduction Catalysts

More often than not, water oxidation/reduction reactions are studied by means of a strong oxidant in acidic media with  $\text{Ce}^{\text{IV}}$  or at close to neutral pH using  $[\text{Ru}(\text{bpy})_3]^{3+}$ , combined with either a strong reducing agent, photochemical in situ generation of  $[\text{Ru}(\text{bpy})_3]^{3+}$ , or by applying an appropriate electrochemical potential on an electrode. Side reactions and frequently bpy-ligand oxidation, may significantly decrease reaction selectivity, defined as the ratio of the  $\text{O}_2/\text{H}_2$  yield per consumed oxidant/reductant, respectively. Therefore, verification of the selectivity is obligatory. The photochemically induced generation of oxidant/reductant is a complex process, which requires a separate and thorough interpretation.

#### 3.2 Comparison of Catalytic Activity of Different Systems

The rate of a catalytic reaction normalized per amount of a catalyst seems to be an all-encompassing value, which could be used to quantify the intrinsic catalytic activity of a given catalyst. But this is only a defensible approach in the case of uniform experimental conditions for all water oxidation/reduction catalytic species. Unfortunately, not all systems can perform under one set of conditions. There have not been any established agreements on how to compare catalyst's activity of different systems in the literature. To date, a single value that quantifies a catalyst's activity does not exist. In our previous review (6b), we discussed this problem and defined turnover number (TON) and turnover frequency (TOF) in terms of water

oxidation. The TON has been interpreted as the experimental number calculated as the ratio of product  $O_2$  molecules formed per catalyst molecule. TOF is defined as  $d(\text{TON})/dt$  but is in actuality an experimental number dependent on the particular experimental conditions used. For that reason, the TOF number is unsuitable for quantification of the intrinsic properties of the catalyst and should be called the *apparent* TOF,  $\text{TOF}_{\text{app}}$ . As a result, the  $\text{TOF}_{\text{app}}$  may significantly depend on redox potentials of oxidant or reductant during water oxidation. The highest achievable TON,  $\text{TOF}_{\text{max}}$ , is independent of reagent concentrations and could potentially characterize the intrinsic activity of the reactive site in a quantitative manner; however, the measurement of  $\text{TOF}_{\text{max}}$  presents a challenge and requires some knowledge of the reaction rate law and the reaction mechanism.



## 4. WATER OXIDATION CATALYSTS

Critical challenges in the development of viable POM multielectron catalysts for solar fuel production are optimization of activity, selectivity, and stability under water splitting conditions. Water oxidation and reduction catalysts composed of all inorganic POMs have advanced the field of water splitting over the past decade. The following discussion of current published POM WOCs is organized in terms of the transition metal serving as the active sites in the catalyst. Fig. 2 shows X-ray crystal structures of generic POM WOCs with varying numbers of transition metals. Each structure is associated to respective published works in Table 1. Table 1 is organized in a chronological format.

### 4.1 Ru-Substituted

In 2004, the di-Ru<sup>III</sup>-substituted POM,  $\text{Na}_{14}[\text{Ru}_2\text{Zn}_2(\text{H}_2\text{O})_2(\text{ZnW}_9\text{O}_{34})_2]$ , (**Ru<sub>2</sub>Zn<sub>2</sub>**), was investigated for electrochemical  $O_2$  generation measured using a Clark sensor (15). In contrast, these authors reported that a monosubstituted-Ru POM (43),  $[\text{PW}_{11}\text{O}_{39}\text{Ru}^{\text{III}}(\text{H}_2\text{O})]^{4-}$ , (**RuP**) produced no  $O_2$ . Thus

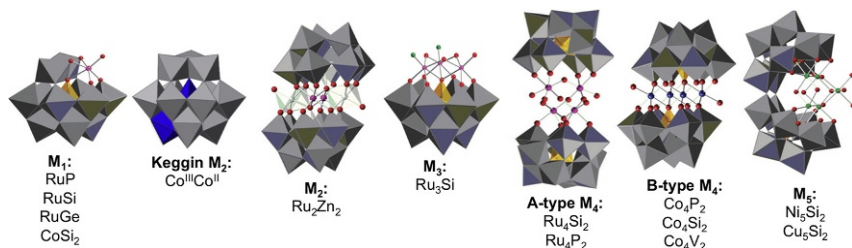


**Fig. 2** X-ray crystal structures of polyoxometalate (POM) water oxidation catalysts (WOCs) from monosubstituted (M<sub>1</sub>) to pentasubstituted (M<sub>5</sub>).

**Table 1** POM Water Oxidation Catalysts

POM	Conditions for O <sub>2</sub> Measurement	pH	TON	TOF <sub>apparent</sub>	Stability Assessment	References
Na <sub>14</sub> [Ru <sup>III</sup> Zn <sub>2</sub> (H <sub>2</sub> O) <sub>2</sub> (ZnW <sub>9</sub> O <sub>34</sub> ) <sub>2</sub> ]	Pulsed voltammetry	8	—	—	—	(15)
[Ru <sup>III</sup> (OH) <sub>2</sub> (γ-SiW <sub>10</sub> O <sub>36</sub> )] <sup>4-</sup>	—	—	—	—	—	(16)
Rb <sub>8</sub> K <sub>2</sub> [{Ru <sub>4</sub> O <sub>4</sub> (OH) <sub>2</sub> (H <sub>2</sub> O) <sub>4</sub> }- (γ-SiW <sub>10</sub> O <sub>36</sub> ) <sub>2</sub> ]	[Ru(bpy) <sub>3</sub> ] <sup>3+</sup>	1, 7	—	0.45–0.60 s <sup>-1</sup>	—	(17)
	[Ru(bpy) <sub>3</sub> ] <sup>2+</sup> and S <sub>2</sub> O <sub>8</sub> <sup>2-</sup>	7.2	180	0.08 s <sup>-1</sup>	—	(18)
		3–4	—	—	UV-vis, CV, catalyst aging, DLS, SAXS, bpy poisoning	(19a,b)
Cs <sub>10</sub> [{Ru <sub>4</sub> O <sub>4</sub> (μ-O) <sub>2</sub> (μ-H <sub>2</sub> O) <sub>4</sub> }- (γ-SiW <sub>10</sub> O <sub>36</sub> ) <sub>2</sub> ]	Ce(IV) system	0.6	—	—	—	(20)
	[Ru(bpy) <sub>3</sub> ] <sup>2+</sup> and S <sub>2</sub> O <sub>8</sub> <sup>2-</sup>	7	—	—	—	(19c)
	[Ru{(m-dpp)Ru(bpy) <sub>2</sub> }] <sub>3</sub> (PF <sub>6</sub> ) <sub>8</sub> and S <sub>2</sub> O <sub>8</sub> <sup>2-</sup>	5.8, 7.2	—	0.008 s <sup>-1</sup>	UV-vis	(21)
	H <sub>2</sub> O <sub>2</sub>	—	—	>1.27 s <sup>-1</sup>	—	(22)
	[Ru(bpy) <sub>3</sub> ] <sup>2+</sup> and S <sub>2</sub> O <sub>8</sub> <sup>2-</sup>	—	—	280 s <sup>-1</sup>	—	(19d)
K <sub>14</sub> [(IrCl <sub>4</sub> )KP <sub>2</sub> W <sub>20</sub> O <sub>72</sub> ]	[Ru(bpy) <sub>3</sub> ] <sup>2+</sup> and S <sub>2</sub> O <sub>8</sub> <sup>2-</sup>	7.2	—	—	DLS, catalyst aging	(23)
Cs <sub>9</sub> [(γ-PW <sub>10</sub> O <sub>36</sub> ) <sub>2</sub> Ru <sub>4</sub> <sup>IV</sup> O <sub>5</sub> (OH)(OH <sub>2</sub> ) <sub>4</sub> ]	[Ru(bpy) <sub>3</sub> ] <sup>2+</sup> and S <sub>2</sub> O <sub>8</sub> <sup>2-</sup>	5.8, 7	120	0.13 s <sup>-1</sup> (initial)	—	(24)
[Ru <sup>III</sup> (H <sub>2</sub> O)SiW <sub>11</sub> O <sub>39</sub> ] <sup>5-</sup> , [Ru <sup>III</sup> (H <sub>2</sub> O)GeW <sub>11</sub> O <sub>39</sub> ] <sup>5-</sup>	Ce(IV) system	0.6	20, 50	—	—	(25)

*Continued*

**Table 1** POM Water Oxidation Catalysts—cont'd

POM	Conditions for O <sub>2</sub> Measurement	pH	TON	TOF <sub>apparent</sub>	Stability Assessment	References
Na <sub>10</sub> [Co <sub>4</sub> (H <sub>2</sub> O) <sub>2</sub> (α-PW <sub>9</sub> O <sub>34</sub> ) <sub>2</sub> ]	[Ru(bpy) <sub>3</sub> ] <sup>3+</sup>	8	1000	>5 s <sup>-1</sup>	UV, vis, <sup>31</sup> P NMR, CV, catalyst aging, bpy poisoning test, reuse of catalyst	(26)
	[Ru(bpy) <sub>3</sub> ] <sup>2+</sup> and S <sub>2</sub> O <sub>8</sub> <sup>2-</sup>	8	224	>5 s <sup>-1</sup>	—	(27a)
α-K <sub>6</sub> Na[ <sub>3</sub> {Ru <sub>3</sub> O <sub>3</sub> (H <sub>2</sub> O)Cl <sub>2</sub> }(SiW <sub>9</sub> O <sub>34</sub> ) <sub>2</sub> ]	[Ru(bpy) <sub>3</sub> ] <sup>2+</sup> and S <sub>2</sub> O <sub>8</sub> <sup>2-</sup>	5.8	23	0.7 s <sup>-1</sup> (initial)	FTIR, UV-vis, DLS, TEM, catalyst reuse	(28)
K <sub>11</sub> Na <sub>1</sub> [Co <sub>4</sub> (H <sub>2</sub> O) <sub>2</sub> (SiW <sub>9</sub> O <sub>34</sub> ) <sub>2</sub> ].26H <sub>2</sub> O	[Ru(bpy) <sub>3</sub> ] <sup>2+</sup> and S <sub>2</sub> O <sub>8</sub> <sup>2-</sup>	5.8	23	0.4 s <sup>-1</sup> (initial)	FTIR, UV-vis, DLS, TEM, catalyst reuse	(28)
K <sub>11</sub> Na <sub>1</sub> [Ni <sub>4</sub> (H <sub>2</sub> O) <sub>2</sub> (SiW <sub>9</sub> O <sub>34</sub> ) <sub>2</sub> ].27H <sub>2</sub> O						
(NH <sub>4</sub> ) <sub>3</sub> [CoMo <sub>6</sub> O <sub>24</sub> H <sub>6</sub> ].7H <sub>2</sub> O	[Ru(bpy) <sub>3</sub> ] <sup>2+</sup> and S <sub>2</sub> O <sub>8</sub> <sup>2-</sup>	8	—	0.11 s <sup>-1</sup> (initial)	DLS, EDX	(29)
(NH <sub>4</sub> ) <sub>6</sub> [Co <sub>2</sub> Mo <sub>10</sub> O <sub>38</sub> H <sub>4</sub> ].7H <sub>2</sub> O	[Ru(bpy) <sub>3</sub> ] <sup>2+</sup> and S <sub>2</sub> O <sub>8</sub> <sup>2-</sup>	8	—	0.16 s <sup>-1</sup> (initial)	—	(29)
[ <sub>3</sub> {Co <sub>4</sub> (μ-OH)(H <sub>2</sub> O) <sub>3</sub> }(Si <sub>2</sub> W <sub>19</sub> O <sub>70</sub> ) <sub>2</sub> ] <sup>11-</sup>	[Ru(bpy) <sub>3</sub> ] <sup>2+</sup> and S <sub>2</sub> O <sub>8</sub> <sup>2-</sup>	5–9	80	0.1 s <sup>-1</sup>	UV-vis, X-ray crystallography, bpy poisoning test	(30)
{Co <sub>9</sub> (H <sub>2</sub> O) <sub>6</sub> (OH) <sub>3</sub> (HPO <sub>4</sub> ) <sub>2</sub> (PW <sub>9</sub> O <sub>34</sub> ) <sub>3</sub> } <sup>16-</sup>	NaClO	7–9	20	0.01 s <sup>-1</sup> (initial)	Catalyst reuse	(31)
K <sub>10</sub> H <sub>2</sub> [Ni <sub>5</sub> (OH) <sub>6</sub> (OH <sub>2</sub> ) <sub>3</sub> (Si <sub>2</sub> W <sub>18</sub> O <sub>66</sub> )].34H <sub>2</sub> O	[Ru(bpy) <sub>3</sub> ] <sup>2+</sup> and S <sub>2</sub> O <sub>8</sub> <sup>2-</sup>	8	—	—	UV-vis, FTIR, DLS	(32)

$([\text{Ru}(\text{C}_{12}\text{N}_2\text{H}_8)_3\text{CH}_3\text{OH}][\text{Mo}_6\text{O}_{19}])$	$\text{S}_2\text{O}_8^{2-}$	—	—	—	Catalyst reuse	(33)
$[\text{Ru}(\text{C}_{12}\text{N}_2\text{H}_8)_3][(\text{C}_2\text{H}_8\text{N}_2)_2(\text{C}_3\text{H}_7\text{NO})]$ $[\text{Mo}_5\text{S}_2\text{O}_{23}]$						
$[\text{Ru}(\text{C}_{12}\text{N}_2\text{H}_8)_3\text{CH}_3\text{CN}]_2[\text{Mo}_8\text{O}_{26}]$						
$\text{K}_7[\text{Co}^{\text{III}}\text{Co}^{\text{II}}(\text{H}_2\text{O})\text{W}_{11}\text{O}_{39}]$	$[\text{Ru}(\text{bpy})_3]^{2+}$ and $\text{S}_2\text{O}_8^{2-}$ and thermal method	9	360	$0.5 \text{ s}^{-1}$ (initial)	Laser flash photolysis, DLS, CV, FTIR, EDX, catalyst recycling, isotope labeling	(34)
$\text{K}_{10}[\text{Co}(\text{H}_2\text{O})_2(\gamma\text{-SiW}_{10}\text{O}_{35})_2]\cdot 23\text{H}_2\text{O}$	$[\text{Ru}(\text{bpy})_3]^{2+}$ and $\text{S}_2\text{O}_8^{2-}$	9	313	$3.2 \text{ s}^{-1}$	UV/vis, LSV, cathodic adsorption stripping analysis	(35)
$\text{Na}_{10}[\text{Co}_4(\text{H}_2\text{O})_2(\text{VW}_9\text{O}_{34})_2]\cdot 35\text{H}_2\text{O}$	$[\text{Ru}(\text{bpy})_3]^{2+}$ and $\text{S}_2\text{O}_8^{2-}$	9	35	$1000 \text{ s}^{-1}$	UV-vis, FTIR, DLS, THpANO <sub>3</sub> toluene extraction, effect of pH, buffer, and buffer concentration	(36)
$\left[ \left\{ \text{Co}_4(\text{OH})_3(\text{PO}_4) \right\}_4 (\text{GeW}_9\text{O}_{34})_4 \right]_3^{2-}$	$[\text{Ru}(\text{bpy})_3]^{2+}$ and $\text{S}_2\text{O}_8^{2-}$	9	70	$0.1 \text{ s}^{-1}$	—	(37)
$[\text{Mn}_4\text{O}_3(\text{CH}_3\text{COO})_3(\text{A-}\alpha\text{-SiW}_9\text{O}_{34})]^{6-}$	$[\text{Ru}(\text{bpy})_3]^{2+}$ and $\text{S}_2\text{O}_8^{2-}$	9	5.2	$0.0007 \text{ s}^{-1}$	—	(38)
$\text{Na}_{24}[\text{Ni}_{12}(\text{OH})_9(\text{CO}_3)_3(\text{PO}_4)(\text{SiW}_9\text{O}_{34})_3]\cdot 56\text{H}_2\text{O}$	$[\text{Ru}(\text{bpy})_3]^{2+}$ and $\text{S}_2\text{O}_8^{2-}$	9	128.2	$0.20 \text{ s}^{-1}$ (initial)	DLS, UV-vis, catalyst aging, THpANO <sub>3</sub> toluene extraction,	(39)
$\text{Na}_{25}[\text{Ni}_{13}(\text{H}_2\text{O})_3(\text{OH})_9(\text{PO}_4)(\text{SiW}_9\text{O}_{34})_3]\cdot 50\text{H}_2\text{O}$		9	147.6	$0.25 \text{ s}^{-1}$ (initial)	capillary electrophoresis	
$\text{Na}_{50}[\text{Ni}_{25}(\text{H}_2\text{O})_2(\text{OH})_{18}(\text{CO}_3)_2(\text{PO}_4)_6(\text{SiW}_9\text{O}_{34})_6]\cdot 85\text{H}_2\text{O}$		9	204.5	$0.34 \text{ s}^{-1}$ (initial)		

Continued

**Table 1** POM Water Oxidation Catalysts—cont'd

POM	Conditions for O <sub>2</sub> Measurement	pH	TON	TOF <sub>apparent</sub>	Stability Assessment	References
$[\text{Fe}_{11}(\text{H}_2\text{O})_{14}(\text{OH})_2(\text{W}_3\text{O}_{10})_2(\alpha\text{-SbW}_9\text{O}_{33})_6]^{27-}$	$[\text{Ru}(\text{bpy})_3]^{2+}$ and $\text{S}_2\text{O}_8^{2-}$	10	1815	$6.3 \text{ s}^{-1}$	UV-vis, FTIR, XPS, DLS, TEM, catalyst reuse, capillary electrophoresis	(40)
$[\text{Cu}_5(\text{OH})_4(\text{H}_2\text{O})_2(\text{A-}\alpha\text{-SiW}_9\text{O}_{33})_2]^{10-}$	$[\text{Ru}(\text{bpy})_3]^{2+}$ and $\text{S}_2\text{O}_8^{2-}$	9	91	—	UV-vis, FTIR, XPS, DLS, TEM, catalyst reuse, THpANO <sub>3</sub> toluene extraction, capillary electrophoresis, laser flash photolysis	(41)
$[(\text{A-}\alpha\text{-SiW}_9\text{O}_{34})_2\text{Co}_8(\text{OH})_6(\text{H}_2\text{O})_2(\text{CO}_3)_3]^{16-}$	$[\text{Ru}(\text{bpy})_3]^{2+}$ and $\text{S}_2\text{O}_8^{2-}$	5,8, 9	1436	$10 \text{ s}^{-1}$	UV-vis, FTIR, XPS, DLS, catalyst aging, mass spectrometry	(42)

they suggested that the presence of two ruthenium atoms was a key factor for electrocatalytic water oxidation activity. Computational investigations of a similar di-Ru<sup>III</sup>-substituted POM ( $[\text{Ru}_2^{\text{III}}(\text{OH})_2(\gamma\text{-SiW}_{10}\text{O}_{36})]^{4-}$ ) showed high catalytic water oxidation activity but was hydrolytically unstable (16).

In 2008, the Bonchio group and Hill group simultaneously reported that  $[\{\text{Ru}_4\text{O}_4(\text{OH})_2(\text{H}_2\text{O})_4\} - (\gamma - \text{SiW}_{10}\text{O}_{36})^{10-}]$ , (**Ru<sub>4</sub>Si<sub>2</sub>**), is a highly active WOC using strong oxidant  $\text{Ce}^{\text{IV}}$  at pH 0.6 (20) and  $[\text{Ru}(\text{bpy})_3]^{3+}$  as the oxidant at neutral pH, respectively (17). Since then, **Ru<sub>4</sub>Si<sub>2</sub>** has been extensively studied by many groups in combination under homogeneous conditions using the visible-light photosensitizer ( $[\text{Ru}(\text{bpy})_3]^{2+}$ ) and the sacrificial electron acceptor ( $\text{S}_2\text{O}_8^{2-}$ ) over a variety of conditions (differing buffers, differing pH values, etc.) (19). Later, the analogous **Ru<sub>4</sub>P<sub>2</sub>** POM was synthesized and shown to be a WOC but a somewhat less efficient one (lower O<sub>2</sub> yields under similar photochemical conditions) (24). In 2009, Geletii *et al.* established the increased reaction rate of the  $[\text{Ru}(\text{bpy})_3]^{3+}$  reduction in the presence of **Ru<sub>4</sub>Si<sub>2</sub>** during O<sub>2</sub> generation reactions (19a). Furthermore, by adding  $[\text{Ru}(\text{bpy})_3]^{2+}$  to the catalytic system, the overall reaction is completed in a shorter time, but the fast initial step is inhibited. In another method, Orlandi *et al.* reported the nanosecond flash photolysis kinetics of hole transfer from a photogenerated Ru<sup>III</sup>-pyridine complex to **Ru<sub>4</sub>Si<sub>2</sub>** (19c).

In 2011, Murakami *et al.* synthesized and characterized two mononuclear Ru-complexes,  $[\text{Ru}^{\text{III}}(\text{H}_2\text{O})\text{SiW}_{11}\text{O}_{39}]^{5-}$  (**RuSi**) and  $[\text{Ru}^{\text{III}}(\text{H}_2\text{O})\text{GeW}_{11}\text{O}_{39}]^{5-}$  (**RuGe**) for water oxidation with strong oxidant,  $\text{Ce}^{\text{IV}}$  (25). Maximum TONs were reported up to 20 and 50, respectively. The increased water oxidation activity presumably derived in part from a change in the central heteroatom in the Keggin polytungstate from Si to Ge. Previously mentioned mononuclear  $[\text{PW}_{11}\text{O}_{39}\text{Ru}^{\text{III}}(\text{H}_2\text{O})]^{4-}$  showed no electrochemical water oxidation, whereas these mononuclear Ru-complexes studied under  $\text{Ce}^{\text{IV}}$  oxidant were reported to be active. This illustrates the significance of the specific oxidative and other experimental conditions used to study each catalytic species.

## 4.2 Co-Substituted

In 2010, the earth-abundant POM,  $\text{Na}_{10}[\text{Co}_4(\text{H}_2\text{O})_2(\alpha\text{-PW}_9\text{O}_{34})_2]$ , (**Co<sub>4</sub>P<sub>2</sub>**) catalyst was recognized as a fast WOC with TONs reaching 1000 in under 3 min in the presence of  $[\text{Ru}(\text{bpy})_3]^{3+}$  at pH 8 (26). In later studies, **Co<sub>4</sub>P<sub>2</sub>** activity was noted and studied in the  $[\text{Ru}(\text{bpy})_3]^{2+}/\text{S}_2\text{O}_8^{2-}$  photochemical systems (27). Under electrochemical water oxidation

conditions in pH 8.0 sodium phosphate buffer, and a high concentration (500  $\mu\text{M}$ ) of the  $\text{Co}_4\text{P}_2$  molecular catalyst were shown to form  $\text{CoO}_x$  on the glassy carbon working electrode surface (44). Under similar electrochemical conditions but with low  $\text{Co}_4\text{P}_2$  concentrations (2.5  $\mu\text{M}$ ), deposited  $\text{CoO}_x$  did not form, emphasizing the importance of several solution and electrochemical parameters for conducting stability and mechanistic studies on these POM WOCs (45). Thorough studies of the  $\text{Co}_4\text{P}_2$  conducted over the past 5 years have established its stability under oxidant-driven homogeneous catalytic water oxidation conditions and the not-so-innocent role of pH and buffer (46). More discussion on POM WOC stability studies is presented in a subsequent section.

In the case of the P- and Si-heteroatom,  $\text{Ru}_4\text{Si}_2$  displays higher water oxidation activity under photochemical light-driven systems. For that reason, Zhu and coworkers inferred that the Si-centered analogue of  $\text{Co}_4\text{P}_2$  may be a more active WOC and synthesized a similar complex,  $[\{\text{Co}_4(\mu\text{-OH})(\text{H}_2\text{O})_3\}(\text{Si}_2\text{W}_{19}\text{O}_{70})]^{11-}$  ( $\text{Co}_4\text{Si}_2$ ) that resulted in two isomers present in a 1:1 ratio (30). The maximum number of turnovers reaches 80 at pH 9; however, under the conditions used in the  $\text{Co}_4\text{P}_2$  studies (photosensitizer/sacrificial electron acceptor systems at pH 8) (27a), a  $\text{TON}_{\text{max}}$  of 220 greatly surpasses the  $\text{Co}_4\text{Si}_2$   $\text{TON}_{\text{max}}$  of  $\sim 58$ . Although the  $\text{Co}_4\text{Si}_2$  isomers are not analogous to  $\text{Co}_4\text{P}_2$ , these early studies suggested that designing POM WOCs is more complex than can be predicted.

In 2012, a nonnuclear cobalt-containing POM,  $\{\text{Co}_9(\text{H}_2\text{O})_6(\text{OH})_3(\text{HPO}_4)_2(\text{PW}_9\text{O}_{34})_3\}^{16-}$ , ( $\text{Co}_9$ ) was reported to be an effective WOC using hypochlorite,  $\text{ClO}^-$ , as the oxidant. No heterogeneous  $\text{CoO}_x$  catalyst from breakdown of this POM under turnover conditions was observed (31). Remarkably,  $\text{Co}_9$  was found to perform continuously upon addition of oxidant over the course of a week without any significant sign of decomposition.

A cobalt-containing Keggin POM,  $\text{K}_7[\text{Co}^{\text{III}}\text{Co}^{\text{II}}(\text{H}_2\text{O})\text{W}_{11}\text{O}_{39}]$ , ( $\text{Co}^{\text{III}}\text{Co}^{\text{II}}$ ), was found to be a catalyst for  $\text{O}_2$  production under both photochemical conditions using a photosensitizer/sacrificial electron acceptor systems at pH 9, as well as a thermal conditions (47). The catalytic activity of this mixed-valent Keggin WOC was higher than a series of other Co-based Keggin POMs. The authors proposed that the  $\text{Co}^{\text{III}}$  center presumably maintains the stability of the structure, while the  $\text{Co}^{\text{II}}$  atom functions as the active site for water oxidation. During pH effect studies, increasing the borate buffer from pH 9 to 10 resulted in lower  $\text{O}_2$  production due to the escalation of photosensitizer degradation. In changing the



borate buffer again from pH 9 to 8, lower O<sub>2</sub> production was correlated with a lower buffering capacity. In pH 8 reactions, the pH after the catalysis dropped to 2.7, supporting the lack of buffering capacity in these cases. This Keggin POM was also discovered to efficiently catalyze hydrogen evolution (48), a point to be discussed in a following section.

A mononuclear-cobalt(II)-substituted POM, K<sub>10</sub>[Co(H<sub>2</sub>O)<sub>2</sub>(γ-SiW<sub>10</sub>O<sub>35</sub>)<sub>2</sub>]<sub>23</sub>·23 H<sub>2</sub>O (**Co<sup>II</sup>Si<sub>2</sub>**) was investigated for water oxidation under photosensitizer/sacrificial electron acceptor conditions at pH 9, acquiring a TOF of 3.2 s<sup>-1</sup> (35). Structural analogues with Ni and Mn resulted in little water oxidation activity, suggesting that the cobalt centers are essential for catalyst activity. The structural simplicity of this mononuclear single-site metal complex relative to **Co<sub>4</sub>P<sub>2</sub>** where there are two peripheral (solvent accessible) cobalt sites with two inner (solvent inaccessible) cobalt atoms connected by bridging oxo groups made mechanistic studies of **Co<sup>II</sup>Si<sub>2</sub>** simpler than **Co<sub>4</sub>P<sub>2</sub>**. This study also supports the findings of the **Co<sup>III</sup>Co<sup>II</sup>** mixed-valent Keggin POM discussed previously. The stability of this mononuclear-cobalt POM was assessed via catalyst aging in buffer followed by voltammetry measurements. Furthermore, cathodic adsorptive stripping analysis measured small amounts of Co<sup>2+</sup> anions after 1.5 h of aging, but the Co<sup>2+</sup> concentration remained unchanged before and after aging, suggesting that no Co<sup>2+</sup> was released under the conditions of this buffer aging experiment.

In 2014, Lv *et al.* described the exceptionally fast Na<sub>10</sub>[Co<sub>4</sub>(H<sub>2</sub>O)<sub>2</sub>(VW<sub>9</sub>O<sub>34</sub>)<sub>2</sub>]<sub>35</sub>·35H<sub>2</sub>O (**Co<sub>4</sub>V<sub>2</sub>**) with TOF over 1000 s<sup>-1</sup> under light-driven photochemical conditions (36). The difference between the geometrically similar structures of **Co<sub>4</sub>P<sub>2</sub>** was ascribed to differing electronic structures probed by UV-visible spectra, temperature-dependent magnetism measurements, and DFT calculations. Importantly, the water oxidation activity of **Co<sub>4</sub>V<sub>2</sub>** was compared directly to equivalent amounts of Co(NO<sub>3</sub>)<sub>2</sub>. The reactions exhibited contrasting kinetic profiles and initial rates, indicating that Co<sup>2+</sup> was not leaching from the Co-containing POM under turnover conditions.

Han *et al.* reported a series of isostructural cobalt-phosphate (Co-Pi)-based molecular POMs [**Co<sub>4</sub>Si<sub>4</sub>**], [**Co<sub>4</sub>Ge<sub>4</sub>**], [**Co<sub>4</sub>P<sub>4</sub>**], and [**Co<sub>4</sub>As<sub>4</sub>**] (37). Notably, all four compounds generated O<sub>2</sub> using the photochemical [Ru(bpy)<sub>3</sub>]<sup>2+</sup>/S<sub>2</sub>O<sub>8</sub><sup>2-</sup> system. The trend in O<sub>2</sub> yield was **Co<sub>4</sub>P<sub>4</sub>** ≤ **Co<sub>4</sub>Si<sub>4</sub>** < **Co<sub>4</sub>As<sub>4</sub>** < **Co<sub>4</sub>Ge<sub>4</sub>** with the highest TON of 38.7. Under electrochemical conditions, the formation of a precipitate was observed at higher

catalyst concentrations. Analysis of the formed nanoparticles revealed W, Ru, and Co together, suggesting that cobalt oxide was not being formed. It should be noted that the formation of nanoparticles from the POMs was tested for and not detected in the homogeneous photochemical system. The same experiment was conducted using  $\text{Co}(\text{NO}_3)_2$  and after 15 min of illumination, nanoparticles were detected. These experiments support the conclusion that metal oxide nanoparticles are not a result of hydrolytic decomposition of these POM WOCs.

Mimicking the oxygen-evolving center (OEC) of photosystem II, a double  $\text{Co}^{\text{II}}_4\text{O}_3^-$  core POM  $[(\text{A}-\alpha\text{-SiW}_9\text{O}_{34})_2\text{Co}_8(\text{OH})_6(\text{H}_2\text{O})_2(\text{CO}_3)_3]^{16-}$  (**Co<sub>8</sub>Si<sub>2</sub>**) was recently synthesized and studied using the photochemical water oxidation system (42). The bioinspired catalyst showed high activity reaching a TON of 1436 at pH 9.

### 4.3 Ni-Substituted

The first Ni-containing POM WOC,  $\text{K}_{10}\text{H}_2[\text{Ni}_5(\text{OH})_6(\text{OH}_2)_3(\text{Si}_2\text{W}_{18}\text{O}_{66})] \cdot 34\text{H}_2\text{O}$  (**Ni<sub>5</sub>Si<sub>2</sub>**), was reported by Zhu *et al.* (32). It should be noted that other Ni-containing POMs have been synthesized but were unable to generate  $\text{O}_2$  (28). Water oxidation experiments in both the dark reaction with  $[\text{Ru}(\text{bpy})_3]^{3+}$  as the oxidant, and light-driven reactions with  $[\text{Ru}(\text{bpy})_3]^{2+}/\text{S}_2\text{O}_8^{2-}$  revealed that **Ni<sub>5</sub>Si<sub>2</sub>** forms an insoluble complex with  $[\text{Ru}(\text{bpy})_3]^{n+}$ ; furthermore, the solution containing **Ni<sub>5</sub>Si<sub>2</sub>** and the photosensitizer was filtered prior to light illumination which resulted in no  $\text{O}_2$  generation. This suggests that the **Ni<sub>5</sub>Si<sub>2</sub>**- $[\text{Ru}(\text{bpy})_3]^{n+}$  complex may be more active for water oxidation than freely diffusing **Ni<sub>2</sub>Si<sub>2</sub>**. Replacing **Ni<sub>5</sub>Si<sub>2</sub>** with  $\text{Ni}(\text{NO}_3)_2$  and filtering the reaction system prior to illumination proceeded to evolve oxygen, demonstrating that no  $\text{Ni}^{2+}$  species are leached from the POM-photosensitizer complex.

Three new polynuclear Ni-based POMs were recently reported,  $\text{Na}_{24}[\text{Ni}_{12}(\text{OH})_9(\text{CO}_3)_3(\text{PO}_4)(\text{SiW}_9\text{O}_{34})_3] \cdot 56\text{H}_2\text{O}$  (**Ni<sub>12</sub>Si<sub>3</sub>**),  $\text{Na}_{25}[\text{Ni}_{13}(\text{H}_2\text{O})_3(\text{OH})_9(\text{PO}_4)(\text{SiW}_9\text{O}_{34})_3] \cdot 50\text{H}_2\text{O}$  (**Ni<sub>13</sub>Si<sub>3</sub>**), and  $\text{Na}_{50}[\text{Ni}_{25}(\text{H}_2\text{O})_2(\text{OH})_{18}(\text{CO}_3)_2(\text{PO}_4)_6(\text{SiW}_9\text{O}_{34})_6] \cdot 85\text{H}_2\text{O}$  (**Ni<sub>25</sub>Si<sub>6</sub>**) (39). The water oxidation activity of these Ni-POMs was investigated with the  $[\text{Ru}(\text{bpy})_3]^{2+}/\text{S}_2\text{O}_8^{2-}$  light-driven protocol. The photocatalytic efficiency trend was **Ni<sub>12</sub>Si<sub>3</sub>** < **Ni<sub>13</sub>Si<sub>3</sub>** < **Ni<sub>25</sub>Si<sub>6</sub>** ( $\text{TON}_{\text{max}} = 124$ ), potentially related to the number of Ni active sites. Interestingly, sandwich-type Ni-POMs (**Ni<sub>4</sub>P<sub>2</sub>** and **Ni<sub>4</sub>Si<sub>2</sub>**) were

synthesized and showed no catalytic water oxidation activity. Similar to the previously discussed **Ni<sub>5</sub>Si<sub>2</sub>**, but at higher concentrations of catalyst, an insoluble POM-[Ru(bpy)<sub>3</sub>]<sup>n+</sup> complex forms.

#### 4.4 Others

In 2009, Cao *et al.* described the first Ir-substituted POM WOC, [(IrCl<sub>4</sub>)KP<sub>2</sub>W<sub>20</sub>O<sub>72</sub>]<sup>14-</sup> (**23**). The water oxidation ability was measured using [Ru(bpy)<sub>3</sub>]<sup>3+</sup> at pH 7.2 via electrochemical measurements. Furthermore, O<sub>2</sub> evolution was quantified by gas chromatography. Stability studies of the Ir-POM in water imply a dissociation of the POM to [IrCl<sub>4</sub>(H<sub>2</sub>O)<sub>2</sub>]<sup>-</sup> and [KP<sub>2</sub>W<sub>20</sub>O<sub>72</sub>]<sup>13-</sup>. Further water oxidation investigations of the dissociation products indicate that both [IrCl<sub>4</sub>(H<sub>2</sub>O)<sub>2</sub>]<sup>-</sup> and IrCl<sub>3</sub> show similar activities while the [KP<sub>2</sub>W<sub>20</sub>O<sub>72</sub>]<sup>13-</sup> portion is inactive for water oxidation. This study was inconclusive regarding the formation of IrO<sub>2</sub> nanoparticles.

With ongoing studies of multimetal POM “sandwich-type” WOCs, Car and coworkers probed a new design with an open, trivacant triruthenium-substituted POM, α-K<sub>6</sub>Na[ {Ru<sub>3</sub>O<sub>3</sub>(H<sub>2</sub>O)Cl<sub>2</sub> } (SiW<sub>9</sub>O<sub>34</sub>) ], (**Ru<sub>3</sub>Si**) that features accessible active metal centers for oxidation catalysis (**28**). **Ru<sub>3</sub>Si** was compared to sandwich-type POMs K<sub>11</sub>Na<sub>1</sub>[Co<sub>4</sub>(H<sub>2</sub>O)<sub>2</sub>(SiW<sub>9</sub>O<sub>34</sub>)<sub>2</sub>] (**Co<sub>4</sub>Si<sub>2</sub>**) and K<sub>11</sub>Na<sub>1</sub>[Ni<sub>4</sub>(H<sub>2</sub>O)<sub>2</sub>(SiW<sub>9</sub>O<sub>34</sub>)<sub>2</sub>] (**Ni<sub>4</sub>Si<sub>2</sub>**) for catalytic activity under photocatalytic conditions, [Ru(bpy)<sub>3</sub>]<sup>2+</sup>/S<sub>2</sub>O<sub>8</sub><sup>2-</sup> at pH 5.8. The maximum TON (**23**) was reached for **Ru<sub>3</sub>Si** after 120 min (lower TON value was noted for **Co<sub>4</sub>Si<sub>2</sub>** and **Ni<sub>4</sub>Si<sub>2</sub>**), were higher. During catalysis, **Ru<sub>3</sub>Si** binds to the [Ru(bpy)<sub>3</sub>]<sup>3+</sup> photosensitizer to form a **Ru<sub>3</sub>Si**-[Ru(bpy)<sub>3</sub>]<sup>n+</sup> complex and a brown precipitate. Interestingly, the complex was found to be active for O<sub>2</sub> generation and subsequent collection of the complex by centrifugation provided reusability of the catalyst three times with comparable O<sub>2</sub> yield to the original, as-prepared, molecular **Ru<sub>3</sub>Si**.

In 2015, the first iron-containing POM WOC, [Fe<sub>11</sub>(H<sub>2</sub>O)<sub>14</sub>(OH)<sub>2</sub>-(W<sub>3</sub>O<sub>10</sub>)<sub>2</sub>(α-SbW<sub>9</sub>O<sub>33</sub>)<sub>6</sub>]<sup>27-</sup> (**Fe<sub>11</sub>Sb<sub>6</sub>**), was developed (**40**). Under photochemical water oxidation, the TON<sub>max</sub> reached 1815 with an initial TOF of 6.3 s<sup>-1</sup>. Recently, the first copper-containing POM WOC, [Cu<sub>5</sub>(OH)<sub>4</sub>(H<sub>2</sub>O)<sub>2</sub>(A-α-SiW<sub>9</sub>O<sub>33</sub>)<sub>2</sub>]<sup>10-</sup> (**Cu<sub>5</sub>Si<sub>2</sub>**), was tested for photochemical water oxidation, resulting in a TON<sub>max</sub> of 61. A series of Cu-based POMs were described (**Cu<sub>2</sub>Si<sub>2</sub>**, **Cu<sub>4</sub>Si<sub>2</sub>**, **Cu<sub>6</sub>Sb<sub>2</sub>**, and **Cu<sub>20</sub>P<sub>8</sub>**) but only **Cu<sub>5</sub>Si<sub>2</sub>** generated O<sub>2</sub> (**41**).

Ruthenium photosensitizer–POM hybrids,  $[\text{Ru}(\text{C}_{12}\text{N}_2\text{H}_8)_3][(\text{C}_2\text{H}_8\text{N}_2)_2(\text{C}_3\text{H}_7\text{NO})][\text{Mo}_5\text{S}_2\text{O}_{23}]$ ,  $([\text{Ru}(\text{C}_{12}\text{N}_2\text{H}_8)_3\text{CH}_3\text{OH}][\text{Mo}_6\text{O}_{19}])$ , and  $[\text{Ru}(\text{C}_{12}\text{N}_2\text{H}_8)_3\text{CH}_3\text{CN}]_2[\text{Mo}_8\text{O}_{26}]$  were synthesized in a new category of POM WOCs (33). The three complexes were shown to oxidize water in the presence of  $\text{S}_3\text{O}_8^{2-}$ . The trend in catalytic efficiency was determined to increase with increasing Mo active sites. Critical control experiments revealed that there was no  $\text{O}_2$  generated for the POM and the ruthenium photosensitizer individually. The  $[\text{Mo}_8]$ –PS complex was subjected to three consecutive photo-driven water oxidation runs with no additional catalyst or sacrificial electron acceptor introduced and there was little decrease in the quantity of  $\text{O}_2$  evolved.



## 5. WATER REDUCTION CATALYSTS

Catalytic dehydrogenation of alcohols and organic substrates using POMs has been extensively studied (49). The first  $\text{H}_2$  evolution study involving POMs was reported in 1982 (50). Table 2 lists POM water reduction catalysts (WRCs) and is organized in a chronological format. The system consisted of  $[\text{NH}_3\text{Pr}^f]_5[\text{W}_6\text{O}_{20}(\text{OH})]$  and colloidal Pt at neutral pH. Under UV light illumination, hydrogen formation occurred and was confirmed by mass spectroscopy. No  $\text{H}_2$  evolution was observed in the absence of Pt.

In 1987, Kiwi and Grätzel disclosed a system of  $(\text{SiW}_{12}\text{O}_{40})$ -loaded titania for the evolution of hydrogen from water (51). In this system, n-type  $\text{TiO}_2$  electrodes replaced the need for a Pt cocatalyst. During photolysis, hydrogen generation was monitored by GC. Upon UV illumination, the POM removes electrons from the conduction band of the  $\text{TiO}_2$ . The resulting reduced POM is capable of reducing water to generate  $\text{H}_2$ . The stability of this hybrid system was not characterized for POM leaching or decomposition.

It was not until 2011 when the next POM WRC was reported. Zhang *et al.* described a sandwich-type POM,  $\text{K}_{11}\text{H}[\text{Sn}_4(\text{SiW}_9\text{O}_{34})_2] \cdot 25\text{H}_2\text{O}$  (**Sn<sub>4</sub>Si<sub>2</sub>**) that was capable of visible-light photocatalytic  $\text{H}_2$  evolution with Pt cocatalyst and methanol sacrificial agent (52). Hydrogen evolution was observed over five consecutive runs. No other stability assessments were conducted.

A heteropolyoxoniobate,  $\text{K}_{10}[\text{Nb}_2\text{O}_2(\text{H}_2\text{O})_2][\text{SiNb}_{12}\text{O}_{40}] \cdot 12\text{H}_2\text{O}$  (**Nb<sub>2</sub>Si**), was reported for photocatalytic water splitting activity with **Nb<sub>2</sub>Si** loaded onto Pt cocatalyst in a 20% methanol solution (53). A  $\text{TON}_{\text{max}}$  of 44 was reported after 7.4 h. In a separate experiment in pure water with

**Table 2** POM Water Reduction Catalysts

POM	Conditions for H <sub>2</sub> Measurement	pH	TON	Stability Assessment	References
[NH <sub>3</sub> Pr <sup>I</sup> ] <sub>5</sub> [W <sub>6</sub> O <sub>20</sub> (OH)]	Colloidal Pt	7	—	—	(50)
(SiW <sub>12</sub> O <sub>40</sub> ) <sub>4</sub> -loaded titania	—	1–12	—	—	(51)
K <sub>11</sub> H[Sn <sub>4</sub> (SiW <sub>9</sub> O <sub>34</sub> ) <sub>2</sub> ] <sub>2</sub> ·25H <sub>2</sub> O	Pt NPs and 20% MeOH	—	—	—	(52)
K <sub>10</sub> [Nb <sub>2</sub> O <sub>2</sub> (H <sub>2</sub> O) <sub>2</sub> ][SiNb <sub>12</sub> O <sub>40</sub> ] <sub>2</sub> ·12H <sub>2</sub> O	Pt and 20% MeOH	—	44	Powder XRD	(53)
KNa <sub>2</sub> [Nb <sub>24</sub> O <sub>72</sub> H <sub>21</sub> ] <sub>2</sub> ·38H <sub>2</sub> O, K <sub>2</sub> Na <sub>2</sub> [Nb <sub>32</sub> O <sub>96</sub> H <sub>28</sub> ] <sub>2</sub> ·80H <sub>2</sub> O, K <sub>12</sub> [Nb <sub>12</sub> O <sub>72</sub> H <sub>21</sub> ] <sub>4</sub> ·107H <sub>2</sub> O	<sup>-</sup> Co <sup>III</sup> (dmgH) <sub>2</sub> pyCl and TEA	—	—	—	(54)
a-K <sub>5</sub> [AlSiW <sub>11</sub> (H <sub>2</sub> O) <sub>39</sub> ] <sub>2</sub> ·13H <sub>2</sub> O	Pt, eosin Y, and TEOA	—	473	UV-vis	(55)
[P <sub>2</sub> W <sub>17</sub> O <sub>61</sub> {O(SiC <sub>36</sub> H <sub>23</sub> N <sub>3</sub> O <sub>2</sub> Ir) <sub>2</sub> }] <sub>6</sub> <sup>-</sup>	—	—	—	—	(57)
Na <sub>10</sub> [Mn <sub>4</sub> (H <sub>2</sub> O) <sub>2</sub> (VW <sub>9</sub> O <sub>34</sub> ) <sub>2</sub> ]	[Ru(bpy) <sub>3</sub> ] <sup>2+</sup> and TEOA	9.5	42	UV-vis, FTIR, <sup>51</sup> V NMR, EA	(13)
Na <sub>6</sub> K <sub>4</sub> [Ni <sub>4</sub> (H <sub>2</sub> O) <sub>2</sub> (PW <sub>9</sub> O <sub>34</sub> ) <sub>2</sub> ] <sub>2</sub> ·32H <sub>2</sub> O	([Ir(ppy) <sub>2</sub> (dtbbpy)] <sub>2</sub> )[PF <sub>6</sub> ] <sub>2</sub> and TEOA	—	6500	UV-vis, FTIR, DLS, TEM, mercury poisoning	(14b)
Na <sub>7</sub> H <sub>10</sub> [Co <sub>6</sub> (H <sub>2</sub> O) <sub>2</sub> (PW <sub>9</sub> O <sub>34</sub> ) <sub>2</sub> (PW <sub>6</sub> O <sub>26</sub> )] <sub>2</sub> ·30H <sub>2</sub> O	Eosin Y and TEOA	—	—	—	(56)
K <sub>7</sub> [Co <sup>III</sup> Co <sup>II</sup> (H <sub>2</sub> O)W <sub>11</sub> O <sub>39</sub> ]	Pt, Easin Y, and TEOA	—	100	UV-vis, DLS, FTIR, catalyst reuse	(48)
Na <sub>28</sub> [{Ni <sub>4</sub> (OH) <sub>3</sub> AsO <sub>4</sub> } <sub>4</sub> (B-α-PW <sub>9</sub> O <sub>34</sub> ) <sub>4</sub> ] <sub>2</sub> ·120H <sub>2</sub> O	([Ir(ppy) <sub>2</sub> (dtbbpy)] <sub>2</sub> )[PF <sub>6</sub> ] <sub>2</sub> and TEOA or TEA	—	580	UV-vis, FTIR, DLS, mercury poisoning test	(14a)
Na <sub>3</sub> K <sub>7</sub> [Cu <sub>4</sub> (H <sub>2</sub> O) <sub>2</sub> (B-α-PW <sub>9</sub> O <sub>34</sub> ) <sub>2</sub> ] <sub>2</sub> ·30H <sub>2</sub> O	([Ir(ppy) <sub>2</sub> (dtbbpy)] <sub>2</sub> )[PF <sub>6</sub> ] <sub>2</sub> and TEOA	—	1270	UV-vis, FTIR, DLS, TEM, SEM, EDX	(58)

a NiO cocatalyst, overall water splitting as well as an increase in H<sub>2</sub> evolution under UV irradiation was observed.

Several new polyoxoniobates, KNa<sub>2</sub>[Nb<sub>24</sub>O<sub>72</sub>H<sub>21</sub>] $\cdot$ 38H<sub>2</sub>O (**Nb<sub>24</sub>**), K<sub>2</sub>Na<sub>2</sub>[Nb<sub>32</sub>O<sub>96</sub>H<sub>28</sub>] $\cdot$ 80H<sub>2</sub>O (**Nb<sub>32</sub>**), and K<sub>12</sub>[Nb<sub>24</sub>O<sub>72</sub>H<sub>21</sub>]<sub>4</sub> $\cdot$ 107H<sub>2</sub>O (**Nb<sub>96</sub>**), were developed with varying cluster sizes and geometries for UV-photocatalytic H<sub>2</sub> evolution without the use of Pt cocatalyst (54). In this photocatalytic system, the **Nb<sub>n</sub>** WRC, Co<sup>III</sup>(dmgH)<sub>2</sub>pyCl cocatalyst (dmgH = dimethylglyoxime and py = pyridine) and 10% triethylamine (TEAO) sacrificial electron donor were mixed under UV illumination for H<sub>2</sub> evolution. After 12 h, a total of 5657  $\mu\text{mol h}^{-1} \text{g}^{-1}$  of H<sub>2</sub> was observed for **Nb<sub>96</sub>** as compared to 4704  $\mu\text{mol h}^{-1} \text{g}^{-1}$  when using Pt as cocatalyst. Without any cocatalyst, the H<sub>2</sub> evolution rate for **Nb<sub>96</sub>** only reached 1654  $\mu\text{mol h}^{-1} \text{g}^{-1}$ .

Liu *et al.* described a visible-light photocatalytic hydrogen evolution catalyst complex. Eosin Y (EY) photosensitizer was combined with POM,  $\alpha$ -K<sub>5</sub>[AlSiW<sub>11</sub>(H<sub>2</sub>O)O<sub>39</sub>] $\cdot$ 13H<sub>2</sub>O (**AlSiW<sub>11</sub>**) to create the EY-(**AlSiW<sub>11</sub>**) complex (55). Hydrogen evolution was observed by this complex in the presence of Pt cocatalyst and triethanolamine (TEOA) electron donor. In this dye-sensitization system, the interaction between **AlSiW<sub>11</sub>** was found to help stabilize the EY-dye by reducing its reactivity. At pH 10, the TON reached 473 after four reaction cycles. The activity decreased after 5 h of visible-light irradiation, indicating instability at longer times.

Similarly, Wu *et al.* developed the POM WRC Na<sub>7</sub>H<sub>10</sub>[Co<sub>6</sub>(H<sub>2</sub>O)<sub>2</sub>(PW<sub>9</sub>O<sub>34</sub>)<sub>2</sub>(PW<sub>6</sub>O<sub>26</sub>)] $\cdot$ 30H<sub>2</sub>O (**Co<sub>6</sub>P<sub>3</sub>**) sensitized with EY-dye (56). In the presence of TEOA and visible-light irradiation, H<sub>2</sub> generation occurs with an initial TOF of 10 h<sup>-1</sup>. The impact of dye-sensitizer concentration was investigated in order to find the critical concentration of EY needed to enhance H<sub>2</sub> evolution. The EY-anions proved to be essential for H<sub>2</sub> evolution. A comparison of the **AlSiW<sub>11</sub>** and **Co<sub>6</sub>P<sub>3</sub>** WRCs in a different reduction system would provide insight into the POMs as a catalyst species.

Artero and coworkers developed a Pt-free WRC composed of covalently linked Ir<sup>III</sup>-photosensitized POM complex, [P<sub>2</sub>W<sub>17</sub>O<sub>61</sub>{O(SiC<sub>36</sub>H<sub>23</sub>N<sub>3</sub>O<sub>2</sub>Ir)<sub>2</sub>}]<sup>6-</sup> (**Ir-P<sub>2</sub>W<sub>17</sub>**) (57). Under visible-light irradiation, this complex was able to generate H<sub>2</sub> with a TON of 41 after 7 days.

Lv *et al.* synthesized a sandwich-type POM, Na<sub>10</sub>[Mn<sub>4</sub>(H<sub>2</sub>O)<sub>2</sub>(VW<sub>9</sub>O<sub>34</sub>)<sub>2</sub>] (**Mn<sub>4</sub>V<sub>2</sub>**), isostructural to many efficient WOCs, in an effort to create a hydrolytically stable molecular WRC (13). **Mn<sub>4</sub>V<sub>2</sub>** showed no

activity for water oxidation, yet in the presence of  $[\text{Ru}(\text{bpy})_3]^{2+}$  photosensitizer and TEOA sacrificial electron donor,  $\text{Mn}_4\text{V}_2$  catalyzed hydrogen evolution, reaching a TON of 42 after 5.5 h of irradiation at pH 9.5. Isotope labeling confirmed the origin of  $\text{H}_2$  ( $\text{D}_2$ ) from  $\text{H}_2\text{O}$  or  $\text{D}_2\text{O}$ . A proposed mechanism for light-driven hydrogen evolution is consistent with quenching of the excited state  $[\text{Ru}(\text{bpy})_3]^{2+*}$  by  $\text{Mn}_4\text{V}_2$  through oxidative electron transfer, wherein reduced  $\text{Mn}_4\text{V}_2$  can reduce water to produce  $\text{H}_2$ . The resulting  $[\text{Ru}(\text{bpy})_3]^{3+}$  is reduced by TEOA to regenerate  $[\text{Ru}(\text{bpy})_3]^{2+}$ .

Following the development of  $\text{Mn}_4\text{V}_2$  WRC, Lv *et al.* synthesized several other sandwich-type POM WRC including,  $\text{Na}_6\text{K}_4[\text{Ni}_4(\text{H}_2\text{O})_2(\text{PW}_9\text{O}_{34})_2] \cdot 32\text{H}_2\text{O}$  ( $\text{Ni}_4\text{P}_2$ ) (14b). Using the light absorber  $[\text{Ir}(\text{ppy})_2(\text{dtbbpy})]^+$  and TEOA sacrificial electron donor,  $\text{Ni}_4\text{P}_2$  reached a TON for  $\text{H}_2$  evolution of nearly 6500 under visible-light irradiation over 1 week. Lv *et al.* also prepared WRC  $\text{Na}_3\text{K}_7[\text{Cu}_4(\text{H}_2\text{O})_2(\text{B}-\alpha\text{-PW}_9\text{O}_{34})_2] \cdot 30\text{H}_2\text{O}$  ( $\text{Cu}_4\text{P}_2$ ) and studied  $\text{H}_2$  production under visible-light irradiation in the  $[\text{Ir}(\text{ppy})_2(\text{dtbbpy})]^+$  and TEOA system (58). Under optimized conditions, a turnover of  $\sim 1270$  was measured after 5 h of irradiation. Without all WRC, photosensitizer, or electron donor components, negligible  $\text{H}_2$  was generated.

Another Ni-containing POM WRC,  $\text{Na}_{28}[\{\text{Ni}_4(\text{OH})_3\text{AsO}_4\}_4(\text{B}-\alpha\text{-PW}_9\text{O}_{34})_4] \cdot 120\text{H}_2\text{O}$  ( $\text{Ni}_{16}\text{As}_4\text{P}_4$ ) was reported as the POM with the largest number of Ni ions incorporated into a single carbon-free POM cluster (14a). The  $\text{Ni}_{16}\text{As}_4\text{P}_4$  POM was shown to reduce water to generate  $\text{H}_2$ , but only with a  $\text{TON}_{\text{max}}$  of 580 using TEOA electron donor and  $[\text{Ir}(\text{ppy})_2(\text{dtbbpy})]^+$  photosensitizer. More Ni(II) centers did not result in a higher catalytic efficiency relative to  $\text{Ni}_4\text{P}_2$ .



## 6. IMMOBILIZATION OF POLYOXOMETALATE WOCs

Investigating the geometrical and electronic structure as well as reactivity of catalysts immobilized on photoelectrode and other surfaces is a core component in the ultimate development or integrated, effective solar water splitting devices. This section focuses on the immobilization techniques for POM WOC species. Research on other surface bound molecular catalysts has been described in review and journal articles elsewhere (47,59). Recent studies of polyoxometalates incorporated onto the surfaces of photoanodes for water oxidation have monitored the activity and stability of these immobilized catalyst species (60). Table 3 gives a comprehensive list of POMs immobilized for water oxidation.

Carbon-based materials have been used for supports in electrochemical studies, because there is substantial adhesion of anionic POM WOCs to the extended  $\pi$  clouds of the graphene-like structures. These materials comprise single-walled or multiwalled carbon nanotubes (SWCNTs or MWCNTs), graphene, mesoporous carbon nitride (MCN), carbon paste, and carbon-based polymers (pendant polyamidoamine (PAMAM), protonated polyaniline (PANI), and poly(diallyldimethylammonium chloride) (PDDA)).

Photoelectrochemical reactions for water splitting have been streamlined using light-absorbing metal oxide supports bearing surface bound WOCs. No sacrificial agent is necessary in such photoelectrocatalytic system.

## 6.1 Methods of Immobilization

POM WOC immobilization has been predominantly electrostatic in nature, including anion- $\pi$  interactions (these also involve dispersion and electron donor-acceptor interactions), pH or point of zero charge (pzc), entrapment through layer-by-layer (LBL) assembly, and vacuum-assisted impregnation. Supports that have been covalently modified to have cationic surfaces rely on electrostatic immobilization of the catalyst species.

Carbon nanotubes (CNTs) with extended three-dimensional electronically conducting large surface areas have been exhaustively studied (73,74) and chemical functionalization of CNT-based electrodes provides additional features that make immobilization of catalytic species attractive. Toma *et al.* modified MWCNTs with surface bound PAMAM units bearing tertiary and primary amino groups that electrostatically bind  $\text{Ru}_4\text{Si}_2$ , at pH values where the amines are protonated (61). Compared to amorphous carbon functionalized with  $\text{Ru}_4\text{Si}_2$ , the electrocatalytic activity of  $\text{Ru}_4\text{Si}_2$  on the derivatized MWCNTs was significantly higher, presumably due to enhanced electron transfer events in the CNTs. In a similar approach, MWCNTs and SWCNTs were functionalized with 2-aminoethyltrimethylammonium chloride to which high loadings of electrostatically bound  $\text{Ru}_4\text{Si}_2$  for water splitting applications could be achieved (62).

Graphene is believed to be an ideal electrocatalytic surface because of its high stability, conductivity, and extensive  $\pi$  electronic structure suitable for electrostatic and other interactions with various types of molecular catalysts. Graphene is an exceptional charge carrier transport; the electrical communication between the immobilized species and the support is advantageous in electrochemistry. POMs readily adsorb onto graphene



and graphene oxide without modification of the surface. Electrochemical water oxidation studies of **Ru<sub>4</sub>Si<sub>2</sub>** on graphene grown on ITO electrodes show excellent catalytic activity and stability (65). The POM-graphene system displayed higher catalytic activity compared to RuO<sub>2</sub> on graphene, where the amount of RuO<sub>2</sub> would be about 200 times more than the amount possible from a complete decomposition of **Ru<sub>4</sub>Si<sub>2</sub>**. A new non-noble metal-containing POM, mixed-valent **Mn<sub>16</sub>** polyanion supported on graphene showed comparable electrochemical water oxidation to **Ru<sub>4</sub>Si<sub>2</sub>**-graphene system (68).

Some forms of functionalized graphene have been shown to enhance the binding of anionic POMs; however, chemical reduction methods that enrich the sp<sup>2</sup> connectivity of graphene can result in surface defects. Quintana *et al.* have functionalized graphene with polyaminoamide (PAMAM) dendron, whereby protonated tertiary and primary amino groups act as electrostatic anchors for **Ru<sub>4</sub>Si<sub>2</sub>** (75). The resulting hybrid material show high electron transfer rates, enhancing the electrocatalytic performance relative to CNTs and unmodified graphene.

Wu *et al.* used a mesoporous carbon nitride (MCN) support with -NH<sub>2</sub> and -NH functional group sites for electrostatic binding of the anionic **Co<sub>4</sub>P<sub>2</sub>** (64). Furthermore, this surface provided sufficient electron transfer to the ITO electrode for effective water oxidation from the POM/electrolyte interface. To assemble the system, Wu *et al.* used a vacuum-assisted entrapment two-step process. In the first step, the synthesized MCN was vacuum-treated to remove impurities and air trapped in the mesopores followed by soaking in an aqueous **Co<sub>4</sub>P<sub>2</sub>** solution for 24 h, allowing the **Co<sub>4</sub>P<sub>2</sub>** to fill the pores of the MCN by capillary forces. During the process, the -NH<sub>2</sub> functional groups were protonated, promoting electrostatic binding within the mesopores of the MCN.

Another entrapment technique to fabricate catalytic electrodes for POM-based WOC-incorporated anionic POMs with organic and inorganic cationic units combined with LBL assembly driven by electrostatic forces (76) for electrochemical water oxidation (67). Anwar *et al.* prepared films by imbedded **Ru<sub>4</sub>Si<sub>2</sub>** and conducting polypyrrole with a Ru(II)-metalodendrimer photosensitizer onto GCE and ITO electrodes using LBL assembly.

Semiconductor metal oxides are known for their robust properties and charge transfer capacity. Metal oxides with applications as photoelectrodes provide economical and recyclable methods for energy production, but lack the fast and selective qualities of molecular catalysts. Common

light-absorbing (UV and visible range) oxides, such as  $\text{TiO}_2$ ,  $\text{ZnO}_2$ ,  $\text{ZrO}_2$ ,  $\text{Fe}_2\text{O}_3$ , and  $\text{SnO}_2$  have been studied as supports for POM WOCs. Xiang *et al.* first constructed a triadic photoanode composed of nanoporous  $\text{TiO}_2$ ,  $\text{ZrO}_2$ , and  $\text{SnO}_2$  films sensitized with  $[\text{Ru}(\text{bpy})_2(\text{dpbpy})]^{2+}$  (P2) (70). The surface bound cation was used to electrostatically interact with homogeneous  $\text{Ru}_4\text{Si}_2$ ; however, the catalyst loading remained dependent on the pzc for each metal oxide surface. Transient absorption analysis investigated the charge separation dynamics of the system. In the presence of  $\text{Ru}_4\text{Si}_2$ , the electron transfer from P2 to  $\text{TiO}_2$  was found to be the main pathway with ultrafast electron transfer from  $\text{Ru}_4\text{Si}_2$  to the oxidized P2. Photoelectrochemical measurements of the triad system resulted in a photocurrent enhancement although no oxygen measurements were conducted.

In a following triad study, a novel dye,  $[\text{Ru}(5\text{-crownphen})_2(\text{H}_2\text{dpbpy})]$  ( $\text{H}_2$ ) was prepared and bound to  $\text{TiO}_2$ . This triad afforded a higher  $\text{O}_2$  quantum yield compared to the previously reported P2 sensitizer (71). Furthermore, no catalyst desorption was observed with the  $\text{H}_2$  dye when the photoelectrocatalytic experiments were conducted below the pzc of  $\text{TiO}_2$ . The increased binding affinity of  $\text{Ru}_4\text{Si}_2$  to the  $\text{H}_2$  dye significantly enhanced the performance of the triad system for water splitting. This research also investigated the difference in optimal pH ranges of homogeneous and  $\text{TiO}_2$ -bound catalyst.

In a different approach, nanoporous  $\text{TiO}_2$  films have been modified with silylating agent, 3-aminopropyltrimethoxysilane (APS), resulting in a quaternary ammonium surface that exhibits an enhanced capability of strongly binding  $\text{Ru}_4\text{Si}_2$  and  $\text{Ru}_4\text{P}_2$  WOC (72). Under UV illumination, photoelectrochemical measurements indicated an enhanced photocurrent compared to bare  $\text{TiO}_2$  electrodes (Fig. 3).

## 6.2 Characterizing the Immobilized System

In order to recover and recycle molecular catalysts, immobilization is necessary; however, supported catalyst systems are not predictable and hence need to be characterized and evaluated for activity. In many cases, POM WOCs adsorb to surfaces in low concentrations, which result in difficult characterization of the active catalyst species under turnover conditions. Extensive investigations of the systems before and after catalysis are necessary to establish the integrity of the heterogenized catalyst species. In more recent immobilized POM studies, exhaustive characterization after turnover conditions has become the convention.

In 2012, Wu *et al.* characterized  $\text{Co}_4\text{P}_2$  on MCN by a combination of TEM, TGA, small angle PXRD, wide-angle PXRD, and FTIR to confirm

**Table 3** Immobilized POM WOCs

POM	System (Substrate)	TOF	System Characterization (Before Catalysis)	Stability Assessment (After Catalysis)	References
$M_{10}[\{\text{Ru}_4\text{O}_4(\text{OH})_2(\text{H}_2\text{O})_4\}-\text{(\gamma-SiW}_{10}\text{O}_{36})_2\}]$ , M = Cs, Li	<b>Ru<sub>4</sub>Si<sub>2</sub></b> on MWCNTs/ITO	—	Raman, AFM, TGA, SACS, STEM, HRTEM, EDX	—	(61)
$M_{10}[\{\text{Ru}_4\text{O}_4(\text{OH})_2(\text{H}_2\text{O})_4\}-\text{(\gamma-SiW}_{10}\text{O}_{36})_2\}]$	<b>Ru<sub>4</sub>Si<sub>2</sub></b> on functionalized SWCNTs and MWCNTs/ITO	$0.085 \text{ s}^{-1}$	Raman, TEM, SEM, TGA	—	(62)
$M_{10}[\{\text{Ru}_4\text{O}_4(\text{OH})_2(\text{H}_2\text{O})_4\}-\text{(\gamma-SiW}_{10}\text{O}_{36})_2\}]$	<b>Ru<sub>4</sub>Si<sub>2</sub></b> on Dendron functionalized graphene/ITO	—	Raman, XPS, HRTEM, AC-TEM, HAADF-STEM, EDX, XPS	O <sub>2</sub> evolution current recorded at 1.1 V vs Ag/AgCl	(63)
$\text{Na}_{10}[\text{Co}_4(\text{H}_2\text{O})_2(\alpha\text{-PW}_9\text{O}_{34})_2]$	<b>Co<sub>4</sub>P<sub>2</sub></b> on mesoporous carbon nitride/ITO	$0.3 \text{ s}^{-1}$	TEM, TGA, FTIR, AFM, XANES, powder XRD	UV-vis, XRD	(64)
$\text{Rb}_8\text{K}_2[\{\text{Ru}_4\text{O}_4(\text{OH})_2(\text{H}_2\text{O})_4\}-\text{(\gamma-SiW}_{10}\text{O}_{36})_2\}]$	<b>Ru<sub>4</sub>Si<sub>2</sub></b> on graphene/GCE, ITO	$0.01 \text{ s}^{-1}$	CV, SEM, EDX	SEM, EDX	(65)
Cs <sub>15</sub> K [Co <sub>9</sub> (H <sub>2</sub> O) <sub>6</sub> (OH) <sub>3</sub> (HPO <sub>4</sub> ) <sub>2</sub> (PW <sub>9</sub> O <sub>34</sub> ) <sub>3</sub> ·41H <sub>2</sub> O	<b>Co<sub>9</sub></b> in amorphous carbon paste	—	FTIR, TGA, EDX, powder XRD	FTIR, EDX, powder XRD	(66)
$\text{Na}_{10}[\{\text{Ru}_4\text{O}_4(\text{OH})_2(\text{H}_2\text{O})_4\}-\text{(\gamma-SiW}_{10}\text{O}_{36})_2\}]$	<b>Ru<sub>4</sub>Si<sub>2</sub></b> LBL assembly with Ru <sup>II</sup> -metlloendrimer/GCE, ITO	—	Raman, CV, XPS, AFM, SEM, EDX	CV	(67)

Continued

**Table 3** Immobilized POM WOCs—cont'd

POM	System (Substrate)	TOF	System Characterization (Before Catalysis)	Stability Assessment (After Catalysis)	References
$[\text{Mn}^{\text{III}}_{10}\text{Mn}^{\text{II}}_6(\text{OH})_6(\text{PO}_4)_4(\text{A-SiW}_9\text{O}_{34})_4]^{29-}$	<b>Mn<sub>16</sub></b> on graphene/ITO	$1.1 \text{ s}^{-1}$	SEM, EDX, XPS, CV, RRDE, Tafel plot	—	(68)
$\text{Na}_{10}[\text{Co}_4(\text{H}_2\text{O})_2(\alpha\text{-PW}_9\text{O}_{34})_2]$	<b>Co<sub>4</sub>P<sub>2</sub></b> on MIL-101/GCE	$0.007 \text{ s}^{-1}$	XRD, FTIR, XPS, XANES, TEM, EDX	XRD, FTIR, XPS, XANES, DLS, catalyst reuse, THpANO <sub>3</sub> toluene extraction	(69)
$\text{Rb}_8\text{K}_2[\{\text{Ru}_4\text{O}_4(\text{OH})_2(\text{H}_2\text{O})_4\}(\gamma\text{-SiW}_{10}\text{O}_{36})_2]$	<b>Ru<sub>4</sub>Si<sub>2</sub></b> on [Ru(bpy) <sub>2</sub> (dpbpy)] <sup>2+</sup> -sensitized TiO <sub>2</sub> , ZrO <sub>2</sub> , and SnO <sub>2</sub> /FTO	$0.025 \text{ s}^{-1}$	UV-vis, FTIR, ICP-OES, transient absorption	UV-vis	(70)
	<b>Ru<sub>4</sub>Si<sub>2</sub></b> on [Ru(bpy) <sub>2</sub> (H <sub>4</sub> dpbpy)] <sup>2+</sup> and [Ru(5-crownphen) <sub>2</sub> (H <sub>2</sub> dpbpy)]-sensitized TiO <sub>2</sub> /FTO	—	UV-vis, transient absorption	UV-vis	(71)
	<b>Ru<sub>4</sub>Si<sub>2</sub></b> and <b>Ru<sub>4</sub>P<sub>2</sub></b> on modified TiO <sub>2</sub> /FTO		FTIR, confocal Raman, SEM, TEM, STEM, EDX, UV-vis	FTIR, confocal Raman, SEM, EDX, UV-vis, LSV	(72)

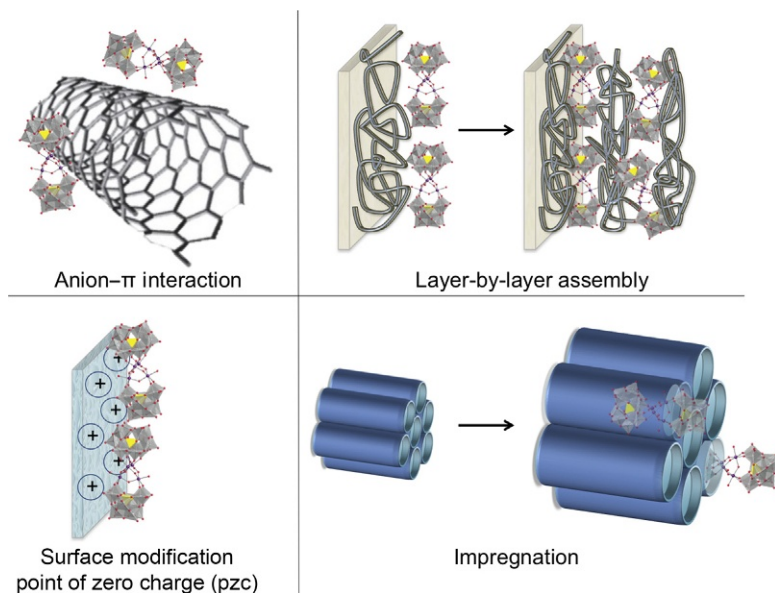


**Fig. 3** Schematic of immobilization methods of POM WOCs on substrates illustration anion- $\pi$  interaction, layer-by-layer assembly, surface modification, and impregnation.

the encapsulation of  $\mathbf{Co}_4\mathbf{P}_2$  in MCN (64). Along with long-term electrolysis measurements, with a TOF  $\sim 0.3 \text{ s}^{-1}$ , Wu *et al.* monitored changes in the system through UV-vis spectra and XRD patterns of  $\mathbf{Co}_4\mathbf{P}_2$  MCN on ITO before and after electrolysis.

In 2015, Lauinger *et al.* characterized  $\mathbf{Ru}_4\mathbf{Si}_2$  and  $\mathbf{Ru}_4\mathbf{P}_2$  on  $\text{TiO}_2$  nanoparticles and nanoporous films through a variety of methods including FTIR, confocal Raman, SEM, EDX, and long-term bulk electrolysis measurements (72). After 24 h stability tests, the integrity of the POM was investigated by comparing the FTIR, Raman, EDX, and UV-vis spectra before and after photoelectrocatalytic water oxidation.

Similarly, Soriano-López *et al.* investigated the stability of  $\mathbf{Co}_9$  in carbon paste after  $>8$  h of electrochemistry using FTIR, EDX, and powder XRD before and after this long-term turnover conditions (66).

## 7. ASSESSMENT OF CATALYTIC ACTIVITY

### 7.1 Stability of the Light-Driven Systems

Water oxidation reaction stops when a sacrificial electron acceptor is consumed. Ideally, in the photochemical  $[\text{Ru}(\text{bpy})_3]^{2+}/\text{S}_2\text{O}_8^{2-}$  system, after addition of a new portion of  $\text{S}_2\text{O}_8^{2-}$ , the kinetics of  $\text{O}_2$  formation

should be the same as in the first run if the catalyst is stable. Thus, the stability of the catalyst can be assessed by reuse and repeatable quantum yield. Practically, due to an inevitable consumption of  $[\text{Ru}(\text{bpy})_3]^{2+}$  in the first run, the rate and the yield of  $\text{O}_2$  formation is lower in subsequent consecutive runs, which does not exclusively indicate the catalyst deactivation. If the catalyst is isolated after the first run and then reused, this could be considered evidence for the catalysts stability. However, this approach should be used with caution. The procedure of the catalyst isolation should guarantee the pureness of the isolated complex. The stability of the light-driven water reduction steps can also be limited by the stability of photosensitizer (14b).

## 7.2 Acid/Base Properties of Polyoxometalates, Speciation, Redox Potentials

In natural photosynthesis, water oxidation occurs in the oxygen evolving center (OEC). The OEC consists of an approximate cube of one calcium atom and three manganese atoms with a fourth manganese atom attached to the cube by bridging oxygens. The absorption of one photon triggers the removal of one electron from the OEC catalytic site. In total, four photons accumulate four holes in the OEC to oxidize water. This process is described by the Kok cycle. In order to avoid a charge accumulation, one proton is released in each one-electron transfer reaction. This process is called a proton-coupled electron transfer (PCET). If water is oxidized through the mechanism similar to the Kok cycle, then WOCs in the resting state must have four protons. The distribution of protonated states of WOCs in different oxidation states is described by four  $pK_a$  values in the resting state: three  $pK_a$ 's in 1-electron oxidized states, two in the 2-electron oxidized state, etc. The combination of five speciation diagrams for five oxidation states of WOC is described by the Pourbaix diagram of the catalytic system. This diagram describes the dominant species present in solution at a given pH and potential. Any claim that 1-electron oxidation proceeds via PCET mechanism must be confirmed by a Pourbaix diagram. At the same time, the construction of a Pourbaix diagram is an extremely complex task. So far, no POM-based WOCs are characterized by a Pourbaix diagram. Therefore, any claim that 1-electron oxidation of WOCs proceeding via PCET mechanism requires extraordinary evidence. Keeping in mind that POMs are highly negatively charged anions (typically in the range from  $-9$  to  $-12$ ), the removal of four electrons does not result in a dramatic change of the total charge. Accordingly, the necessity of PCET pathways for all four 1-electron processes for POM WOCs is not questionable. Certainly, one or two of these 1-electron processes can proceed via PCET and it

was recently demonstrated that water oxidation can be significantly accelerated by buffer (such as in phosphate buffer) anions via the mechanism of base-assisted electron transfer (77). It was shown that the activity of  $\text{Co}_4\text{P}_2$  and  $\text{Co}_4\text{V}_2$  is dependent whether the reaction proceeds in phosphate or borate buffers. At pH 8 the reaction proceeds more efficiently in borate buffer (26,27,36). The interpretation of buffer effect is complex, but the repulsion between highly negatively charged POMs and buffer anions makes the base-assisted electron transfer doubtful.

### 7.3 The “Purity” of Polyoxometalate WOCs

Under turnover conditions, a catalyst is present in solutions in different oxidation and protonation states. The distribution of species can be controlled thermodynamically or kinetically. Catalyst “purity” in an equilibrating catalyst system does not make much sense. In fact, the fundamental question is the nature of the  $\text{O}_2$ -releasing species. This phenomenon also addresses the nature of the true catalyst.

The general definition of the catalyst stability is not trivial. From a practical point of view it would be more utilitarian to define the stability of a catalytic system. Typically, the stability of the catalytic system is defined by the maximum TON that can be achieved in the system. Earlier we established that the stability of the light-driven water oxidation system is limited by the stability of the photosensitizer. The stability of WOC can also be defined by the maximum TON that can be achieved providing that all other constituents are stable and sacrificial reagents are not consumed (including the buffer capacity). This definition does not specify the nature of  $\text{O}_2$ -releasing intermediate(s). The true catalyst might be a decomposition product of the initially introduced catalyst but the whole system might be stable. Therefore, the stability of a catalytic system does not prove that the true catalyst is the complex initially introduced into the system.



## 8. STABILITY IN POM CATALYTIC SYSTEMS

The stability of WOCs has long been a critical issue for the development of both practical and model water splitting systems (6b,26,78). For traditional heterogeneous WOCs, these issues often present as stability against corrosion under certain water oxidation conditions (79). Under different conditions of pH, applied potential, and chemical environments, the solid-state catalysts may well dissolve into solution. As of the time of writing this chapter, one of the holy grails for water oxidation catalysis is the discovery of an acid-compatible earth-abundant element WOC (78f,g,79a).

Similar concerns about stability also apply for molecular WOCs (6b, 26, 78c–e, 80). For such catalysts, however, one is much more concerned with the stability of the organic ligands that support the transition metal active sites. Organic and organometallic ligands as well as organic substituents are susceptible to both hydrolytic and oxidative degradation (6b, 26, 78d). Unfortunately, the lack of organic ligand stability not only limits the TON but also less appreciated is that oxidative removal of organic ligands can facilitate formation of the metal oxide (e.g.,  $\text{RuO}_2$  and  $\text{CoO}_x$  for WOCs based on those metals) and these metal oxides are also known WOCs.

The development of POMs as WOC candidates potentially overcomes these traditional shortcomings of coordination compound or organometallic WOCs. POM WOCs such as  $\text{Co}_4\text{P}_2$  comprise fully oxidized ( $d^0$ ) metal oxide polyanions functioning as multidentate ligands for one or more d-electron transition metals involved in the multielectron redox processes (e.g., oxidation of  $\text{H}_2\text{O}$  to  $\text{O}_2$ ). Thus such POMs are stable to oxidative degradation. POMs also represent thermodynamic minima hydrolytically in certain pH ranges depending on the framework transition metal (POMs of W, Mo, and V tend to be stable in acid, while those of Nb and Ta are stable in base). As many investigators have noted, POMs in several ways, represent soluble and thus experimentally tractable analogues of metal oxides. At the same time, these discrete cluster anions are distinct from transition metal oxides as they bear high charges that are electrostatically compensated by commensurately high numbers of counter-cations.

The extensive use of crystallization to obtain pure single crystalline structures of POMs may further exacerbate the misconception that POMs are simply “soluble transition metal oxides”—in aqueous solution, equilibria of numerous polyanionic metal oxide, and/or metal hydroxides are frequently operable (81). The synthetic steps taken to produce different POMs usually involve shifting the chemical equilibrium via adjustments in pH, temperature, chemical potential, and counter-cations. Historically, many POM systems are famously challenging to characterize due to their complexity. As many as 40 different species may be present in a single equilibrium model (81). Thus, it is not surprising that certain crystalline POM species may revert back to equilibrium species upon dissolution, especially since some POM equilibrations may be slower than POM catalyst syntheses in aqueous solution themselves.

Most of the POM WOCs listed in Table 1 have not been adequately characterized with respect to the easily overlooked factors noted earlier:



pH, solution potential, and other ionic species present. The likely existence of different  $pK_a$  values for some of these POMs alone should give us pause in identifying the “active species” in a POM WOC system. While we have developed a preliminary Pourbaix diagram for the  $\text{Ru}_4\text{Si}_2$  system, this type of information is rarely found in the POM literature (82). There have been recent efforts to construct such diagrams even for well-known electrocatalysts such as  $\text{CoO}_x$  (83). Given the lack of detailed study on the speciation of POM WOCs, questions must be raised about what one means when stating that certain POMs are WOCs. It is not unreasonable to think that different solution phase species including different protonation states, oxidation states, and possible dimer variants of these POMs may be the principal “active species” instead of the crystalline starting material.

More precisely, we take “thermodynamic stability” of these POMs to mean that solubilizing these POMs does not lead to significant decomposition of the overall polyanionic structure within the timeframe of the water oxidation reactions under study. At the very least, Table 1 gives a list of metastable species that have been shown to be active in water oxidation reactions under turnover conditions. It is now appropriate to reflect back upon the last few decades of POM chemistry and realize that while our understanding of POM self-assembly and equilibration has come a long way since the seminal studies on the H-Mo-V-P systems (81,84), there is still much that we do not know about the speciation of POMs in solution.

The oxidative stability of POM WOCs relates to their stability under catalytic turnover conditions. Owing to the oxidatively robust nature of the POM framework itself, the most likely decomposition pathway available to most homogeneous POM WOC systems is the leaching of the redox-active transition metal ions directly into the solution, forming metal aqua, metal hydroxide, and/or metal oxide species. However, under various conditions, all four forms of metal-oxo species can be converted into each other and may, at times, exist in equilibrium (85). This makes stability analyses of POM WOC systems particularly daunting and identification of the principal “active species” ambiguous.

A prime example of such a case lies in the scrutiny of the  $\text{Co}_4\text{P}_2$  system. Stracke *et al.* demonstrated that  $\text{Co}_4\text{P}_2$  does indeed decompose to form cobalt oxide films on the working electrode under electrocatalytic conditions, experimental conditions that were not used in the original paper (44). Given the extensive number of cobalt complexes that may serve as precursors for the electrodeposition of cobalt oxide under potentiostatic or voltage cycling conditions (86), it is reasonable to believe that a similar

process may indeed take place when applied to  $\text{Co}_4\text{P}_2$ . While the exact mechanism that leads to the oxidative instability of the  $\text{Co}_4\text{P}_2$  under electrocatalytic conditions is unknown, we may nevertheless speculate that under oxidative conditions,  $\text{Co}^{\text{III}}$  may rapidly exchange ligands. In the presence of an electrophilic electrode surface,  $\text{Co}^{\text{III}}$  could form  $\text{Co}-\text{O}-\text{X}$  bonds that eventually lead to the leaching of the cobalt ions and formation of a cobalt oxide film on the electrode surface. Alternatively, given the high potential of these electrochemical systems, an alternative potential decomposition pathway that involves the oxidative breakdown of the tungstate framework via the formation of a peroxotungstate species leading to a complete degradation of  $\text{Co}_4\text{P}_2$  with accompanying full release of hydrated freely diffusing cobalt ions is possible.

Ultimately, Vickers *et al.* demonstrated that the  $\text{Co}_4\text{P}_2$  model system is indeed the main WOC under homogeneous reaction conditions, showing that it is oxidatively stable when paired with a homogeneous oxidant and that the electrolytic decomposition of  $\text{Co}_4\text{P}_2$  at an electrode surface does not apply to the homogeneous reaction conditions reported initially (27b). This paper explains many criteria that can be used to distinguish between homogeneous and heterogeneous water oxidation catalysis and molecular WOCs in general (and POM WOCs in particular). A new protocol for the extraction of highly negatively charged POM WOCs using tetra-*n*-heptylammonium nitrate dissolved in toluene to identify the active species for water oxidation was also established that should now be used to examine the oxidative stability of all new and old POM WOCs in homogeneous systems.

The careful examination of  $\text{Co}_4\text{P}_2$  stability and inquiries into the question, “what is the main active species?” by multiple research groups culminated in a number of established techniques and procedures that are useful for the study of POM WOCs and molecular catalysts in general. Summaries of most of these methodologies can also be found in a separate review (78d). In addition, recent advances in heterogenizing molecular WOCs on electrode surfaces provide protocols and criteria to assess the stability, rates, and molecular nature of immobilized WOCs (87).



## 9. CONCLUSIONS

POM catalyst development is an integral part of the broader efforts on renewable energy research. The molecular nature of these metal oxide polyanions (polyoxometalates, “POMs”) continue to present unique

opportunities in the investigation of water splitting systems. Moving forward, there is substantial interest for further advancements in POM WOC design for different catalytic conditions as well as their immobilization. At the same time, investigations have shown that we must pay significant attention to the stability of the catalysts, especially when heterogenized on electrode surfaces. Studying the speciation and the mechanism of catalysis with POMs is not straightforward, but is essential for garnering fundamentally useful insights into catalysis by POM-based systems and, by extension, many heterogeneous metal oxide systems. The explosion in POM WOC studies in the last 6 years is a testament to the intrinsic intellectual and potential practical value of this research.

## ACKNOWLEDGMENTS

We thank the Department of Energy, Office of Basic Sciences, Solar Photochemistry program (grant number: DE-FG02-07ER15906) for support of this work. Earlier, completed work on the water reduction catalysts was funded by the National Science Foundation (grant number CHE-0911610) to C.L.H.

## REFERENCES

1. (a) Pope, M. T.; Müller, A. *Angew. Chem.* **1991**, *103*(1), 56–70; (b) Hill, C. L. *Special Thematic Issue on Polyoxometalates* **1998**, *98*(1), 1–390; (c) Borrás-Almenar, J. J.; Clemente-Juan, J. M.; Clemente-Leon, M.; Coronado, E.; Galán-Mascarós, J. R.; Gómez-García, C. J. In *Polyoxometalate Chemistry: From Topology via Self-Assembly to Applications*; Pope, M. T., Müller, A., Eds.; Kluwer: Dordrecht: The Netherlands, 2001; p 231; (d) Borrás-Almenar, J. J.; Coronado, E.; Müller, A.; Pope, M. T. In Vol. 98; *Proceedings of the NATO Advanced Study Institute, Tenerife, Spain from 25 August to 4 September 2001*; Kluwer Academic Publishers: Dordrecht, 2003; p 484; (e) Long, D.-L.; Tsunashima, R.; Cronin, L. *Angew. Chem. Int. Ed.* **2010**, *49*, 1736–1758; (f) Miras, H. N.; Yan, J.; Long, D.-L.; Cronin, L. *Chem. Soc. Rev.* **2012**, *41*, 7403–7430; (g) Neumann, R. *Inorg. Chem.* **2010**, *49*, 3594–3601.
2. Hill, C. L. In *Comprehensive Coordination Chemistry-II: From Biology to Nanotechnology*; Wedd, A. G. Ed.; Vol. 4; Elsevier Ltd.: Oxford, UK, 2004; pp 679–759.
3. (a) Hill, C. L.; Prosser-McCartha, C. M. *Coord. Chem. Rev.* **1995**, *143*, 407–455; (b) Neumann, R. *Prog. Inorg. Chem.* **1998**, *47*, 317–370; (c) Okuhara, T.; Mizuno, N.; Misono, M. *Adv. Catal.* **1996**, *41*, 113–252; (d) Kozhevnikov, I. V. *Chem. Rev.* **1998**, *98*(1), 171–198; (e) Moffat, J. B. *Metal–Oxygen Clusters: The Surface and Catalytic Properties of Heteropoly Oxometalates*, Vol. 9; Kluwer Academic/Plenum Publishers: New York, 2001; p. 308.
4. (a) Clemente-Juan, J. M.; Coronado, E.; Gaita-Arino, A. *Chem. Soc. Rev.* **2012**, *41*(22), 7464–7478; (b) Hasenknopf, B.; Micoine, K.; Lacôte, E.; Thorimbert, S.; Malacria, M.; Thouvenot, R. *Eur. J. Inorg. Chem.* **2008**, 5001–5013; (c) Proust, A.; Matt, B.; Villanneau, R.; Guillemot, G.; Gouzerh, P.; Izzet, G. *Chem. Soc. Rev.* **2012**, *41*, 7605–7622; (d) Rhule, J. T.; Hill, C. L.; Judd, D. A.; Schinazi, R. F. *Chem. Rev.* **1998**, *98*(1), 327–357; (e) Zhang, T.; Liu, S.; Kurth, D. G.; Faul, C. F. J. *Adv. Funct. Mater.* **2009**, *19*, 642–652; (f) Nohra, B.; El Moll, H.; Rodriguez-Albelo, L. M.; Mialane, P.; Marrot, J. é.; Mellot-Draznieks, C.; O’Keeffe, M.; Ngo Biboum, R.;

- Lemaire, J.; Keita, B.; Nadjo, L.; Dolbecq, A. *J. Am. Chem. Soc.* **2011**, *133*, 13363–13374; (g) Rausch, B.; Symes, M. D.; Chisholm, G.; Cronin, L. *Science* **2014**, *345*(6202), 1326–1330.
- (a) daSilva, C. G. A. *Energy* **2010**, *35*, 1312–1316; (b) Lewis, N. S.; Nocera, D. G. *Proc. Natl. Acad. Sci.* **2006**, *103*(43), 15729–15735.
  - (a) Geletii, Y. V.; Yin, Q.; Hou, Y.; Huang, Z.; Ma, H.; Song, J.; Besson, C.; Luo, Z.; Cao, R.; O'Halloran, K. P.; Zhu, G.; Zhao, C.; Vickers, J. W.; Ding, Y.; Mohebbi, S.; Kuznetsov, A. E.; Musaev, D. G.; Lian, T.; Hill, C. L. *Isr. J. Chem.* **2011**, *51*, 238–246; (b) Lv, H.; Geletii, Y. V.; Zhao, C.; Vickers, J. W.; Zhu, G.; Luo, Z.; Song, J.; Lian, T.; Musaev, D. G.; Hill, C. L. *Chem. Soc. Rev.* **2012**, *41*, 7572–7589; (c) Song, Y.-F.; Tsunashima, R. *Chem. Soc. Rev.* **2012**, *41*(22), 7384–7402; (d) Izarova, N. V.; Pope, M. T.; Kortz, U. *Angew. Chem. Int. Ed.* **2012**, *51*(38), 9492–9510; (e) Wang, S.-S.; Yang, G.-Y. *Chem. Rev.* **2015**, *115*(11), 4893–4962; (f) Streb, C. *Dalton Trans.* **2012**, *41*, 1651–1659.
  - (a) Kärkäs, M. D.; Verho, O.; Johnston, E. V.; Åkermark, B. *Chem. Rev.* **2014**, *114*, 11863–12001; (b) Young, K. J.; Martini, L. A.; Milot, R. L.; III, R. C. S.; Batista, V. S.; Schmuttenmaer, C. A.; Crabtree, R. H.; Brudvig, G. W. *Coord. Chem. Rev.* **2012**, *256*(21–22), 2503–2520; (c) Lopez, X.; Carbo, J. J.; Bo, C.; Poblet, J. M. *Chem. Soc. Rev.* **2012**, *41*(22), 7537–7571; (d) Blakemore, J. D.; Crabtree, R. H.; Brudvig, G. W. *Chem. Rev.* **2015**, *115*(23), 12974–13005.
  - Green, M. J.; Hill, H. *Methods Enzymol.* **1984**, 3–22.
  - (a) Symes, M. D.; Cronin, L. *Nat. Chem.* **2013**, *5*(5), 403–409; (b) Weinstock, I. A.; Barbuzzi, E. M. G.; Wemple, M. W.; Cowan, J. J.; Reiner, R. S.; Sonnen, D. M.; Heintz, R. A.; Bond, J. S.; Hill, C. L. *Nature* **2001**, *414*(6860), 191–195.
  - (a) Pratt, H. D., III; Hudak, N. S.; Fang, X.; Anderson, T. M. *J. Power Sources* **2013**, *236*, 259–264; (b) Soloveichik, G. L. *Chem. Rev.* **2015**, *115*(20), 11533–11558.
  - (a) Liu, W.; Mu, W.; Liu, M.; Zhang, X.; Cai, H.; Deng, Y. *Nat. Commun.* **2014**, *5*, 3208; (b) Mal, S. S.; Nsouli, N. H.; Dickman, M. H.; Kortz, U. *Dalton Trans.* **2007**, 2627–2630.
  - (a) Huang, Z.; Geletii, Y. V.; Musaev, D. G.; Hill, C. L.; Lian, T. *Ind. Eng. Chem. Res.* **2012**, *51*(37), 11850–11859; (b) White, H. S.; Becker, W. G.; Bard, A. J. *J. Phys. Chem.* **1984**, *88*(9), 1840–1846; (c) Kaledin, A. L.; Huang, Z.; Geletii, Y. V.; Lian, T.; Hill, C. L.; Musaev, D. G. *J. Phys. Chem. A* **2010**, *114*, 73–80; (d) Kaledin, A. L.; Huang, Z.; Yin, Q.; Dunphy, E. L.; Constable, E. C.; Housecroft, C. E.; Geletii, Y. V.; Lian, T.; Hill, C. L.; Musaev, D. G. *J. Phys. Chem. A* **2010**, *114*, 6284–6297; (e) Huang, Z.; Geletii, Y. V.; Wu, D.; Anfuso, C. L.; Musaev, D. G.; Hill, C. L.; Lian, T. In *Interfacial Charge Transfer Dynamics in TiO<sub>2</sub>-Sensitizer-Ru<sub>4</sub>POM Photocatalytic Systems for Water Oxidation*; SPIE Proceedings, 2011, 8109 (Solar Hydrogen and Nanotechnology VI), San Diego, CA, San Diego, CA; 2011 pp 810903–810910; (f) Fukuzumi, S.; Jung, J.; Yamada, Y.; Kojima, T.; Nam, W. *Chem. Asian J.* **2016**, *11*(8), 1138–1150.
  - Lv, H.; Song, J.; Zhu, H.; Geletii, Y. V.; Bacsa, J.; Zhao, C.; Lian, T.; Musaev, D. G.; Hill, C. L. *J. Catal.* **2013**, *307*, 48–54.
  - (a) Lv, H.; Chi, Y.; Leusen, J. V.; Kögerler, P.; Chen, Z.; Bacsa, J.; Guo, W.; Lian, T.; Hill, C. L. *J. Chem. Eur.* **2015**, *21*(48), 17363–17370; (b) Lv, H.; Guo, W.; Wu, K.; Chen, Z.; Bacsa, J.; Musaev, D. G.; Geletii, Y. V.; Lauinger, S. M.; Lian, T.; Hill, C. L. *J. Am. Chem. Soc.* **2014**, *136*(40), 14015–14018.
  - Howells, A. R.; Sankarraj, A.; Shannon, C. J. *Am. Chem. Soc.* **2004**, *126*, 12258–12259.
  - Quiñero, D.; Wang, Y.; Morokuma, K.; Khavrutskii, L. A.; Botar, B.; Geletii, Y. V.; Hill, C. L.; Musaev, D. G. *J. Phys. Chem.* **2006**, *110*, 170–173.
  - Geletii, Y. V.; Botar, B.; Kögerler, P.; Hillesheim, D. A.; Musaev, D. G.; Hill, C. L. *Angew. Chem. Int. Ed.* **2008**, *47*, 3896–3899.

18. Geletii, Y. V.; Huang, Z.; Hou, Y.; Musaev, D. G.; Lian, T.; Hill, C. L. *J. Am. Chem. Soc.* **2009**, *131*, 7522–7523.
19. (a) Geletii, Y. V.; Besson, C.; Hou, Y.; Yin, Q.; Musaev, D. G.; Quinonero, D.; Cao, R.; Hardcastle, K. I.; Proust, A.; Kögerler, P.; Hill, C. L. *J. Am. Chem. Soc.* **2009**, *131*(47), 17360–17370; (b) Kuznetsov, A. E.; Geletii, Y. V.; Hill, C. L.; Morokuma, K.; Musaev, D. G. *J. Am. Chem. Soc.* **2009**, *131*, 6844–6854; (c) Orlandi, M.; Argazzi, R.; Sartorel, A.; Carraro, M.; Scorrano, G.; Bonchio, M.; Scandola, F. *Chem. Commun.* **2010**, *46*, 3152–3154; (d) Natali, M.; Orlandi, M.; Berardi, S.; Campagna, S.; Bonchio, M.; Sartorel, A.; Scandola, F. *Inorg. Chem.* **2012**, *51*, 7324–7331; (e) Sartorel, A.; Bonchio, M.; Campagna, S.; Scandola, F. *Chem. Soc. Rev.* **2013**, *42*, 2262–2280; (f) Dau, H.; Limberg, C.; Reier, T.; Risch, M.; Roggan, S.; Strasser, P. *Chem. Cat. Chem.* **2010**, *2*, 724–761; (g) Sartorel, A.; Miro, P.; Salvadori, E.; Romain, S.; Carraro, M.; Scorrano, G.; Valentin, M. D.; Llobet, A.; Bo, C.; Bonchio, M. *J. Am. Chem. Soc.* **2009**, *131*, 16051–16053.
20. Sartorel, A.; Carraro, M.; Scorrano, G.; Zorzi, R. D.; Geremia, S.; McDaniel, N. D.; Bernhard, S.; Bonchio, M. *J. Am. Chem. Soc.* **2008**, *130*(15), 5006–5007.
21. Puntoriero, F.; Ganga, G. L.; Sartorel, A.; Carraro, M.; Scorrano, G.; Bonchio, M.; Campagna, S. *Chem. Commun.* **2010**, *46*, 4725–4727.
22. Sartorel, A.; Truccolo, M.; Berardi, S.; Gardan, M.; Carraro, M.; Toma, F. M.; Scorrano, G.; Prato, M.; Bonchio, M. *Chem. Commun.* **2011**, *47*, 1716–1718.
23. Cao, R.; Ma, H.; Geletii, Y. V.; Hardcastle, K. I.; Hill, C. L. *Inorg. Chem.* **2009**, *48*, 5596–5598.
24. Besson, C.; Huang, Z.; Geletii, Y. V.; Lense, S.; Hardcastle, K. I.; Musaev, D. G.; Lian, T.; Proust, A.; Hill, C. L. *Chem. Commun.* **2010**, 2784–2786.
25. Murakami, M.; Hong, D.; Suenobu, T.; Yamaguchi, S.; Ogura, T.; Fukuzumi, S. *J. Am. Chem. Soc.* **2011**, *133*, 11605–11613.
26. Yin, Q.; Tan, J. M.; Besson, C.; Geletii, Y. V.; Musaev, D. G.; Kuznetsov, A. E.; Luo, Z.; Hardcastle, K. I.; Hill, C. L. *Science* **2010**, *328*, 342–345.
27. (a) Huang, Z.; Luo, Z.; Geletii, Y. V.; Vickers, J.; Yin, Q.; Wu, D.; Hou, Y.; Ding, Y.; Song, J.; Musaev, D. G.; Hill, C. L.; Lian, T. *J. Am. Chem. Soc.* **2011**, *133*, 2068–2071; (b) Vickers, J. W.; Lv, H.; Sumliner, J. M.; Zhu, G.; Luo, Z.; Musaev, D. G.; Geletii, Y. V.; Hill, C. L. *J. Am. Chem. Soc.* **2013**, *135*(38), 14110–14118; (c) Lv, H.; Rudd, J. A.; Zhuk, P. F.; Lee, J. Y.; Constable, E. C.; Housecroft, C. E.; Hill, C. L.; Musaev, D. G.; Geletii, Y. V. *RSC Adv.* **2013**, *3*, 20647–20654.
28. Car, P.-E.; Guttentag, M.; Baldrige, K. K.; Albertoa, R.; Patzke, G. R. *Green Chem.* **2012**, *14*, 1680–1688.
29. Tanaka, S.; Annaka, M.; Sakai, K. *Chem. Commun.* **2012**, *48*, 1653–1655.
30. Zhu, G.; Geletii, Y. V.; Kögerler, P.; Schilder, H.; Song, J.; Lense, S.; Zhao, C.; Hardcastle, K. I.; Musaev, D. G.; Hill, C. L. *Dalton Trans.* **2012**, *41*(7), 2084–2090.
31. Goberna-Ferrón, S.; Vigarà, L.; Soriano-López, J.; Galán-Mascarós, J. R. *Inorg. Chem.* **2012**, *51*(21), 11707–11715.
32. Zhu, G.; Glass, E. N.; Zhao, C.; Lv, H.; Vickers, J. W.; Geletii, Y. V.; Musaev, D. G.; Song, J.; Hill, C. L. *Dalton Trans.* **2012**, *41*(42), 13043–13049.
33. Gao, J.; Cao, S.; Tay, Q.; Liu, Y.; Yu, L.; Ye, K.; Mun, P. C. S.; Li, Y.; Rakesh, G.; Loo, S. C. J.; Chen, Z.; Zhao, Y.; Xue, C.; Zhang, Q. *Sci. Rep.* **2013**, *2013*(3), 1–5.
34. Song, F.; Ding, Y.; Ma, B.; Wang, C.; Wang, Q.; Du, X.; Fu, S.; Song, J. *Energy Environ. Sci.* **2013**, *6*(4), 1170–1184.
35. Xiang, R.; Ding, Y.; Zhao, J. *Chem. Asian J.* **2014**, *9*(11), 3228–3237.
36. Lv, H.; Song, J.; Geletii, Y. V.; Vickers, J. W.; Sumliner, J. M.; Musaev, D. G.; Kögerler, P.; Zhuk, P. F.; Bacsá, J.; Zhu, G.; Hill, C. L. *J. Am. Chem. Soc.* **2014**, *136*(26), 9268–9271.

37. Han, X.-B.; Zhang, Z.-M.; Zhang, T.; Li, Y.-G.; Lin, W.; You, W.; Su, Z.-M.; Wang, E.-B. *J. Am. Chem. Soc.* **2014**, *136*, 5359–5366.
38. Al-Oweini, R.; Sartorel, A.; Bassil, B. S.; Natali, M.; Berardi, S.; Scandola, F.; Kortz, U.; Bonchio, M. *Angew. Chem. Int. Ed.* **2014**, *126*(42), 11364–11367.
39. Han, X.-B.; Li, Y.-G.; Zhang, Z.-M.; Tan, H.-Q.; Lu, Y.; Wang, E.-B. *J. Am. Chem. Soc.* **2015**, *137*, 5486–5493.
40. Du, X.; Ding, Y.; Song, F.; Ma, B.; Zhao, J.; Song, J. *Chem. Commun.* **2015**, *51*, 13925–13928.
41. Yu, L.; Du, X.; Ding, Y.; Chen, H.; Zhou, P. *Chem. Commun.* **2015**, *51*, 17443–17446.
42. Wei, J.; Feng, Y.; Zhou, P.; Yan, L.; Xu, J.; Xiang, R.; Ding, Y.; Zhao, C.; Fan, L.; Hu, C. *ChemSusChem* **2015**, *8*(16), 2630–2634.
43. Rong, C.; Pope, M. T. *J. Am. Chem. Soc.* **1992**, *114*, 2932–2938.
44. Stracke, J. J.; Finke, R. G. *J. Am. Chem. Soc.* **2011**, *133*, 14872–14875.
45. Stracke, J. J.; Finke, R. G. *ACS Catal.* **2013**, *3*(6), 1209–1219.
46. (a) Schiwon, R.; Klingan, K.; Dau, H.; Limberg, C. *Chem. Commun.* **2014**, *50*, 100–102; (b) Natali, M.; Berardi, S.; Sartorel, A.; Bonchio, M.; Campagna, S.; Scandola, F. *Chem. Commun.* **2012**, *48*(70), 8808–8810; (c) Ohlin, C. A.; Harley, S. J.; McAlpin, J. G.; Hocking, R. K.; Mercado, B. Q.; Johnson, R. L.; Villa, E. M.; Fidler, M. K.; Olmstead, M. M.; Spiccia, L.; Britt, R. D.; Casey, W. H. *Chem. Eur. J.* **2011**, *17*, 4408–4417; (d) Lieb, D.; Zahl, A.; Wilson, E. F.; Streb, C.; Nye, L. C.; Meyer, K.; Ivanović-Burmazović, I. *Inorg. Chem.* **2011**, *50*(18), 9053–9058.
47. Alibabaei, L.; Brennaman, M. K.; Norris, M. R.; Kalanyan, B.; Song, W.; Logo, M. D.; Concepcion, J. J.; Binstead, R. A.; Parsons, G. N.; Meyer, T. J. *Proc. Natl. Acad. Sci.* **2013**, *110*(50), 20008–20013.
48. Zhao, J.; Ding, Y.; Wei, J.; Du, X.; Yu, Y.; Han, R. *Int. J. Hydrogen Energy* **2014**, *39*(33), 18908–18918.
49. (a) Yamase, T.; Watanabe, R. *J. Chem. Soc. Dalton Trans.* **1986**, (8), 1669–1675; (b) Akid, R.; Darwent, J. R. *J. Chem. Soc. Dalton Trans.* **1985**, (2), 395–399; (c) Darwent, J. R. *J. Chem. Soc. Chem. Commun.* **1982**, *14*, 798–799; (d) Hill, C. L.; Bouchard, D. A. *J. Am. Chem. Soc.* **1985**, *107*(18), 5148–5157; (e) Ioannidis, A.; Papaconstantinou, E. *Inorg. Chem.* **1985**, *24*(3), 439–441; (f) Dang, L. Q.; You, W. S.; Zhang, X.; Huang, C. Y.; Lei, Z. B.; Sun, Z. G.; Li, C. *Chin. Chem. Lett.* **2006**, *17*(7), 973–976; (g) Yamase, T. *Inorg. Chim. Acta* **1983**, *76*(1), L25–L27; (h) Yamase, T.; Takabayashi, N.; Kaji, M. *J. Chem. Soc. Dalton Trans.* **1984**, (5), 793–799; (i) Yamase, T.; Cao, X.; Yazaki, S. *J. Mol. Catal. A: Chem.* **2007**, *262*, 119–127.
50. Yamase, T. *Inorg. Chim. Acta* **1982**, *64*(3), L155–L156.
51. Kiwi, J.; Grätzel, M. *J. Phys. Chem.* **1987**, *91*(27), 6673–6677.
52. Zhang, Z.; Lin, Q.; Zheng, S.-T.; Bu, X.; Feng, P. *Chem. Commun.* **2011**, *47*, 3918–3920.
53. Zhang, Z.; Lin, Q.; Kurunthu, D.; Wu, T.; Zuo, F.; Zheng, S.-T.; Bardeen, C. J.; Bu, X.; Feng, P. *J. Am. Chem. Soc.* **2011**, *133*, 6934–6937.
54. Huang, P.; Qin, C.; Su, Z.-M.; Xing, Y.; Wang, X.-L.; Shao, K.-Z.; Lan, Y.-Q.; Wang, E.-B. *J. Am. Chem. Soc.* **2012**, *134*(34), 14004–14010.
55. Liu, X.; Li, Y.; Peng, S.; Lu, G.; Li, S. *Int. J. Hydrogen Energy* **2012**, *37*(17), 12150–12157.
56. Wu, W.; Teng, T.; Wu, X.-Y.; Dui, X.; Zhang, L.; Xiong, J.; Wu, L.; Lua, C.-Z. *Catal. Commun.* **2015**, *64*, 44–47.
57. Matt, B.; Fize, J.; Moussa, J.; Amouri, H.; Pereira, A.; Artero, V.; Izzet, G.; Proust, A. *Energy Environ. Sci.* **2013**, *6*, 1504–1508.
58. Lv, H.; Gao, Y.; Guo, W.; Lauinger, S. M.; Chi, Y.; Bacsá, J.; Sullivan, K. P.; Wieliczko, M.; Musaev, D. G.; Hill, C. L. *Inorg. Chem.* **2016**, *55*, 6750–6758.

59. (a) Li, F.; Li, L.; Tong, L.; Daniel, Q.; Göthelid, M.; Sun, L. *Chem. Commun.* **2014**, *50*, 13948–13951; (b) Blakemore, J. D.; Crabtree, R. H.; Brudvig, G. W. *Chem. Rev.* **2015**, *115*, 12974–13005; (c) Xue, L.-X.; Meng, T.-T.; Yang, W.; Wang, K.-Z. *J. Photochem. Photobiol. B Biol.* **2015**, *152*(Part A (Special Issue on Artificial Photosynthesis)), 95–105; (d) Stevens, M. B.; Enman, L. J.; Batchellor, A. S.; Cosby, M. R.; Vise, A. E.; Trang, C. D. M.; Boettcher, S. W. *Chem. Mater.* **2016**, .
60. Li, W.; He, D.; Sheehan, S. W.; He, Y.; Thorne, J. E.; Yao, X.; Brudvig, G. W.; Wang, D. *Energy Environ. Sci.* **2016**, *9*, 1794–1802.
61. Toma, F. M.; Sartorel, A.; Iurlo, M.; Carraro, M.; Parisse, P.; Maccato, C.; Rapino, S.; Gonzalez, B. R.; Amenitsch, H.; Ros, T. D.; Casalis, L.; Goldoni, A.; Marcaccio, M.; Scorrano, G.; Scoles, G.; Paolucci, F.; Prato, M.; Bonchio, M. *Nat. Chem.* **2010**, *2*, 826–831.
62. Toma, F. M.; Sartorel, A.; Iurlo, M.; Carraro, M.; Rapino, S.; Hooper-Burkhardt, L.; Ros, T. D.; Marcaccio, M.; Scorrano, G.; Paolucci, F.; Bonchio, M.; Prato, M. *ChemSusChem* **2011**, *4*, 1447–1451.
63. Quintana, M.; Lopez, A. M.; Rapino, S.; Toma, F. M.; Iurlo, M.; Carraro, M.; Sartorel, A.; Maccato, C.; Ke, X.; Bittencourt, C.; Ros, T. D.; Tendeloo, G. V.; Marcaccio, M.; Paolucci, F.; Prato, M.; Bonchio, M. *ACS Nano* **2012**, *7*, 811–817.
64. Wu, J.; Liao, L.; Yan, W.; Xue, Y.; Sun, Y.; Yan, X.; Chen, Y.; Xie, Y. *ChemSusChem* **2012**, *5*(7), 1207–1212.
65. Guo, S.-X.; Liu, Y.; Lee, C.-Y.; Bond, A. M.; Zhang, J.; Geletii, Y. V.; Hill, C. L. *Energy Environ. Sci.* **2013**, *6*(9), 2654–2663.
66. Soriano-López, J.; Goberna-Ferrón, S.; Vígara, L.; Carbó, J. J.; Poblet, J. M.; Galán-Mascarós, J. R. *Inorg. Chem.* **2013**, *52*(9), 4753–4755.
67. Anwar, N.; Sartorel, A.; Yaqub, M.; Wearen, K.; Laffir, F.; Armstrong, G.; Dickinson, C.; Bonchio, M.; McCormac, T. *ACS Appl. Mater. Interfaces* **2014**, *6*, 8022–8031.
68. Xing, X.; Wang, M.; Lie, R.; Zhang, S.; Zhang, K.; Li, B.; Zhang, G. *Green Energy Environ.* **2016**, *1*(2), 138–143.
69. Hana, J.; Wang, D.; Du, Y.; Xi, S.; Chen, Z.; Yin, S.; Zhou, T.; Xu, R. *Appl. Catal. A Gen.* **2016**, *521*, 83–89.
70. Xiang, X.; Fielden, J.; Rodriguez-Cordoba, W.; Huang, Z.; Zhang, N.; Luo, Z.; Musaev, D. G.; Lian, T.; Hill, C. L. *J. Phys. Chem. C* **2013**, *117*, 918–926. Copyright (C) 2013 American Chemical Society (ACS). All Rights Reserved.
71. Fielden, J.; Sumliner, J. M.; Han, N.; Geletii, Y. V.; Xiang, X.; Musaev, D. G.; Lian, T.; Hill, C. L. *Chem. Sci.* **2015**, *6*, 5531–5543.
72. Lauinger, S. M.; Sumliner, J. M.; Yin, Q.; Xu, Z.; Liang, G.; Glass, E. N.; Lian, T.; Hill, C. L. *Chem. Mater.* **2015**, *27*(17), 5886–5891.
73. Volder, M. F. L. D.; Tawfick, S. H.; Baughman, R. H.; Hart, A. J. *Science* **2013**, *339*(6119), 535–539.
74. Srivastava, S. *Adv. Mater. Lett.* **2013**, *4*(1), 2–8.
75. (a) Quintana, M.; López, A. M.; Rapino, S.; Toma, F. M.; Iurlo, M.; Carraro, M.; Sartorel, A.; Maccato, C.; Ke, X.; Bittencourt, C.; Da Ros, T.; Van Tendeloo, G.; Marcaccio, M.; Paolucci, F.; Prato, M.; Bonchio, M. *ACS Nano* **2013**, *7*(1), 811–817; (b) Ke, X.; Turner, S.; Quintana, M.; Hadad, C.; Montellano-López, A.; Carraro, M.; Sartorel, A.; Bonchio, M.; Prato, M.; Bittencourt, C.; Tendeloo, G. V. *Small* **2013**, *9*(23), 3922–3927; (c) Ma, C.; Piccinin, S.; Fabris, S. *Phys. Chem. Chem. Phys.* **2014**, *16*, 5333–5341.
76. Ma, H.; Shi, S.; Zhang, Z.; Pang, H.; Zhang, Y. J. *Electroanal. Chem.* **2010**, *648*(2), 128–133.
77. Song, N.; Concepcion, J. J.; Binstead, R. A.; Rudd, J. A.; Vannucci, A. K.; Dares, C.; Coggins, M. K.; Meyer, T. J. *Proc. Natl. Acad. Sci.* **2015**, *112*(16), 4935–4940.

78. (a) Artero, V.; Fontecave, M. *Chem. Soc. Rev.* **2013**, 42(6), 2338–2356; (b) Crabtree, R. H. *Chem. Rev.* **2012**, 112, 1536–1554; (c) Fukuzumi, S.; Hong, D. *Eur. J. Inorg. Chem.* **2014**, 2014(4), 645–659; (d) Stracke, J. J.; Finke, R. G. *ACS Catal.* **2014**, 4(3), 909–933; (e) Sumliner, J. M.; Lv, H.; Fielden, J.; Geletii, Y. V.; Hill, C. L. *Eur. J. Inorg. Chem.* **2014**, 4, 635–644; (f) Walter, M. G.; Warren, E. L.; McKone, J. R.; Boettcher, S. W.; Mi, Q.; Santori, E. A.; Lewis, N. S. *Chem. Rev.* **2010**, 110(11), 6446–6473; (g) Kudo, A.; Miseki, Y. *Chem. Soc. Rev.* **2009**, 38(1), 253–278.
79. (a) Guerrini, E.; Trasatti, S. In *Catalysis for Sustainable Energy Production*; Wiley-VCH Verlag GmbH & Co. KGaA: Weinheim, 2009; pp 235–269; (b) Kanan, M. W.; Nocera, D. G. *Science* **2008**, 321, 1072–1075; (c) Trasatti, S. *Electrochim. Acta* **1991**, 36(2), 16.
80. Artero, V.; Fontecave, M. *Chem. Soc. Rev.* **2012**, 42, 2338–2356.
81. Pettersson, L. In *Topics in Molecular Organization and Engineering—Polyoxometalates: From Platonic Solids to Anti-Retroviral Activity*; Pope, M. T., Müller, A., Eds.; Kluwer Academic Publishers: Netherlands, 1993; pp 27–40.
82. Ogo, S.; Miyamoto, M.; Ide, Y.; Sano, T.; Sadakane, M. *Dalton Trans.* **2012**, 41(33), 9901–9907.
83. Gerken, J. B.; McAlpin, J. G.; Chen, J. Y. C.; Rigsby, M. L.; Casey, W. H.; Britt, R. D.; Stahl, S. S. *J. Am. Chem. Soc.* **2011**, 133, 14431–14442.
84. (a) Pope, M. T.; Müller, A. *Topics in Molecular Organization and Engineering*. Vol. 10. ER Academic Publishers: Boston, 1994; (b) Kim, K. C.; Pope, M. T. *J. Am. Chem. Soc.* **1999**, 121(37), 8512–8517; (c) Thiel, J.; Molina, P. I.; Symes, M. D.; Cronin, L. *Cryst. Growth Des.* **2012**, 12(2), 902–908.
85. Hill, C. L.; Vickers, J. W.; Sumliner, J. M.; Lv, H.; Geletii, Y. V. In *Importance of Buffer in the Design and Study of Solar Fuel Production*; 247th ACS National Meeting & Exposition, Dallas, TX, United States, March 16–20, ENFL-146; 2014.
86. Roger, I.; Symes, M. D. *J. Mater. Chem. A* **2016**, 4(18), 6724–6741.
87. Sheehan, S. W.; Thomsen, J. M.; Hintermair, U.; Crabtree, R. H.; Brudvig, G. W.; Schmuttenmaer, C. A. *Nat. Commun.* **2015**, 6, 6469.





# $[\text{Co}_9(\text{H}_2\text{O})_6(\text{OH})_3(\text{HPO}_4)_2(\text{PW}_9\text{O}_{34})_3]^{16-}$ : A Highly Efficient Catalyst for Water Oxidation

J. Soriano-López<sup>\*,†</sup>, S. Goberna-Ferrón<sup>\*</sup>, J.J. Carbó<sup>†</sup>, J.M. Poblet<sup>†</sup>,  
J.R. Galán-Mascarós<sup>\*,‡,1</sup>

<sup>\*</sup>Institute of Chemical Research of Catalonia (ICIQ), Tarragona, Spain

<sup>†</sup>Universitat Rovira i Virgili, Tarragona, Spain

<sup>‡</sup>ICREA, Passeig Lluís Companys, Barcelona, Spain

<sup>1</sup>Corresponding author: e-mail address: jrgalan@iciq.es

## Contents

1. Introduction	156
2. Homogeneous Electrocatalytic Water Oxidation Activity of $\text{Co}_9$	158
3. Characterization of the Catalytic Activity of $\text{Co}_9$ With NaClO	161
3.1 Long-Term Stability of $\text{Co}_9$ in Turnover Conditions	164
4. Stability and Solution Speciation Under Catalytic Water Oxidation Conditions	166
4.1 Speciation in Water and Phosphate Buffer	166
4.2 Dependency of the Speciation on pH	168
4.3 Speciation Under Catalytic Oxygen Evolution Conditions	169
5. Heterogeneous WOC With Modified $\text{Co}_9$ /Carbon Paste Electrodes	171
5.1 Comparison With Cobalt Oxide	174
5.2 Effect of the pH on the Catalytic Performance	176
6. Conclusions	177
References	178

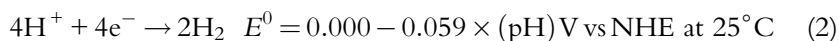
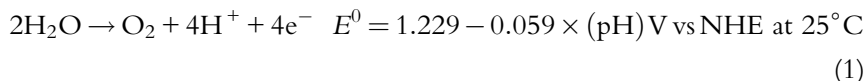
## Abstract

Water oxidation catalysis is generally considered one of the major hurdles in the development of an efficient water splitting process. Most available catalysts are either too expensive, too unstable, or too slow for real technological applications. In this chapter we illustrate the major features of an interesting candidate, the nonanuclear polyoxometalate  $[\text{Co}_9(\text{H}_2\text{O})_6(\text{OH})_3(\text{HPO}_4)_2(\text{PW}_9\text{O}_{34})_3]^{16-}$  ( $\text{Co}_9$ ). This POM, as others of its kind, has demonstrated to be a robust and fast catalyst promoting oxygen evolution in homogeneous and heterogeneous conditions. In addition to its excellent performance, and prospects, we are including many experimental data that confirm its genuine catalytic activity. This is a key issue since the harsh conditions of oxygen evolution are prone to provoke a major evolution in the catalyst or precatalyst. Being all inorganic and obtained from earth-abundant metals,  $\text{Co}_9$  matches most of the requirements to be successfully implemented in an overall water splitting process.



## 1. INTRODUCTION

Natural photosynthesis produced in higher green plants, cyanobacteria, and algae uses the sunlight for converting water and carbon dioxide into oxygen and sugars, respectively, through a sequence of complex reactions (1). The aim of artificial photosynthesis is to reproduce at large scale the processes of the oxygen-evolving photosynthesis, where the sunlight is converted into spatially separated electron/hole pairs employing a photovoltaic cell, and charges are captured with catalysts that mediate water splitting. Water oxidation catalysis (WOC) takes place at the anode when the catalyst captures four holes, evolving oxygen, while hydrogen is produced in a separate catalyst at the cathode when it captures four electrons (2). So thus, solar energy is stored in chemical bonds in the form of  $H_2$  and  $O_2$ . On this regard, efficient electrocatalysts for water splitting must operate close to the Nernstian potentials ( $E$ ) for both water oxidation and proton reduction semi-reactions involved in water splitting:



Of these two reactions, the water oxidation is considered the bottleneck reaction in water splitting, since it requires a four-electron oxidation of two water molecules coupled to the removal of four protons to form a relatively weak oxygen–oxygen bond. Moreover, in addition to the thermodynamic demands of water splitting, additional potential is needed to overcome activation barriers, concentration effects, and voltage drops, due to resistance, to attain a given catalytic activity. This is known as overpotential,  $\eta$ . Furthermore, water oxidation catalysts must be stable under strong oxidizing environments, since, even at the thermodynamic limit, most chemical functional groups degrade due to the oxidizing power required by the oxidation of water (2).

Nowadays, commercially available water electrolyzers are not financially attractive compared to the fossil fuels. The reason for their low commercial impact is the lack of a stable and inexpensive water oxidation catalyst, since most of existing water oxidation catalysts are based on noble metal, or require the use of highly alkaline conditions working at low efficiencies.

Therefore, the main challenge is the search for a robust, efficient, and inexpensive water oxidation catalyst (3).

The state of the art in terms of feasible industrial applications is led by heterogeneous transition-metal oxides. Probably, the most remarkable result is the incorporation of an electrodeposited phosphate oxide cobalt layer ( $\text{Co-P}_i$ ) onto the anode of a silicon-based solar cell (4). An “artificial leaf” concept, able to split water by direct irradiation with sunlight working at neutral pH, was developed with this catalyst (5). Unfortunately, it shows a pH-dependent degradation with time (6), making the artificial leaf, at the moment, too costly to compete with other hydrogen production procedures.

Homogeneous WOCs have shown superior performance in terms of rates and efficiency (7). In addition, they are easy to optimize and process, and allow for a better understanding of the reaction mechanisms. The most studied are ruthenium-based complexes (8), since the discovery of Meyer’s “blue dimer,” a  $\mu$ -oxo-bridged ruthenium dimer coordinated by polypyridyl ligands (9). However, most of these catalysts are transition-metal complexes with organic ligands, which are unstable toward oxidative deactivation due to the strong oxidizing conditions during the water splitting process. For this reason POMs are very attractive materials, since they are transition-metal oxides stabilized with all-inorganic multidentate ligands with a very high stability toward oxidative degradation, and their oxo-bridged structure also allows for reversible proton exchange with the solvent, a feature usually combined with the subsequent oxidation steps in the reaction mechanism of WOCs.

The first purely inorganic species showing WOC activity was a tetranuclear ruthenium-based POM (10). Since then, other POMs have demonstrate to be active as WOCs (11). Probably, the most remarkable breakthrough was a cobalt-containing POM,  $[\text{Co}_4(\text{H}_2\text{O})_2(\text{PW}_9\text{O}_{34})_2]^{10-}$  ( $\text{Co}_4$ ), which represented the first carbon-free WOC obtained from Earth-abundant materials (12). Nonetheless, the molecular nature of cobalt-containing POMs acting as catalysts for the water oxidation has been put into question, since the formation of active  $\text{CoO}_x$  films competes with the genuine POM activity in certain conditions (13). This is a common problem for all homogeneous catalysts, because the oxidative degradation of the organic ligands leads to the formation of the corresponding metal oxide (14). Still, the origin of  $\text{CoO}_x$  formation in cobalt-containing POMs is far different. It arises from a solution equilibrium that liberate traces of  $\text{Co}^{2+}$  ions can act as precursors of the oxide. In fact, oxide formation from aqueous cobalt ions can be avoided by the use of chelating agents able to trap these ions in solution (12,15).

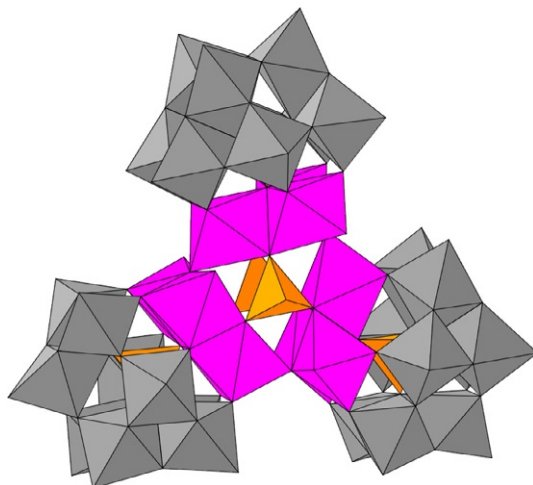


**Fig. 1** Molecular representation of the polyanion  $[\text{Co}_9(\text{H}_2\text{O})_6(\text{OH})_3(\text{HPO}_4)_2(\text{PW}_9\text{O}_{34})_3]^{16-}$  ( $\text{Co}_9$ ).  $\text{WO}_6 = \text{gray}$  octahedra;  $\text{CoO}_6 = \text{pink}$  octahedra;  $\text{PO}_4 = \text{orange}$  tetrahedra.

In this chapter is presented the WOC activity of a high nuclearity non-acobalt POM,  $[\text{Co}_9(\text{H}_2\text{O})_6(\text{OH})_3(\text{HPO}_4)_2(\text{PW}_9\text{O}_{34})_3]^{16-}$  ( $\text{Co}_9$ ). The synthesis and structure of this POM was already described by Weakley *et al.* in 1984 (16). This polyanion is composed by three trilacunary B- $\alpha$ -Keggin units, where three  $\text{Co}^{2+}$  ions occupy the octahedral vacant positions in each Keggin fragment, yielding triangular edge-sharing  $\text{Co}_3\text{O}_{12}$  moieties, as seen in Fig. 1. The three Keggin fragments are then connected by three hydroxyl bridges and two  $\text{HPO}_4^{2-}$  anions forming a triangle of triangles. Six of the nine Co ions complete their coordination sphere with terminal water molecules prone to be oxidized. This POM has shown good catalytic activity in bulk water electrolysis in both homogeneous (17) and heterogeneous conditions (18). In the same way, aqueous solutions of  $\text{Co}_9$  rapidly evolve oxygen by the addition of a chemical oxidant, such as  $\text{NaClO}$ . In addition, small-angle X-ray scattering (SAXS) experiments are carried out to investigate in detail the speciation under catalytic working conditions, confirming the remarkable stability of  $\text{Co}_9$  in water oxidation conditions (19).

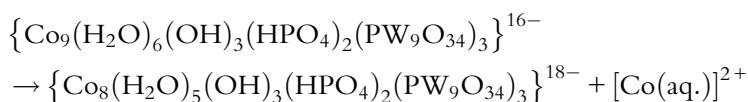


## 2. HOMOGENEOUS ELECTROCATALYTIC WATER OXIDATION ACTIVITY OF $\text{Co}_9$

When bulk water electrolysis is carried out at an anodic overpotential of 600 mV (1.41 V vs NHE, herein all the potentials are shown vs the NHE

electrode, unless otherwise stated) in a sodium phosphate-buffered neutral solution, negligible oxygen evolution currents are observed. Addition of **Co<sub>9</sub>** POM to the solution dramatically increases the oxygen evolution, with the corresponding current reaching over 3 mA. This is the typical behavior of a homogeneous water oxidation catalyst (WOC). A deposited film was identified as cobalt oxide, analogous to the Co-P<sub>1</sub> catalyst. Indeed, this is quite often the case for homogeneous WOCs, although many times it remains unnoticed (8, 13a, 14d). Further experiments demonstrated that the deposited CoO<sub>x</sub> film was enough, quantitatively, to account for the recorded activity.

This is a very important issue in homogeneous WOCs, and a possibility that needs to be explored beyond any reasonable doubt. In WOCs containing organic fragments, the origin for the in situ generation of an active metal oxide is due to the redox instability of the compound. However, this was surprising in a POM, since its composition (high valence metal centers and oxo groups) was always considered redox stable. We rationalized that the origin of the CoO<sub>x</sub> deposition should be different than in previous WOCs. POMs are indeed redox stable, but in solution they participate in complex equilibria, that includes leaching of the metal dication into solution:



The appearance of aqueous Co<sup>2+</sup> species should be the major source for the formation of CoO<sub>x</sub>, since in such highly oxidizing conditions Co<sup>2+</sup> cations are unstable, outside the protection of the POM. Probing this hypothesis, we were able to avoid the formation of an oxide film on the anode by addition of a chelating agent. Addition of 2,2'-bipyridyl (bpy) rapidly traps the free cations to form [Co(bpy)<sub>3</sub>]<sup>2+</sup>, which under oxidation conditions yields the highly inert [Co(bpy)<sub>3</sub>]<sup>3+</sup> species. Bulk water electrolysis in the presence of the **Co<sub>9</sub>** POM and an excess of bpy also shows the appearance of a catalytic current that can be assigned entirely to the homogeneous POM species. After water electrolysis is carried out in these conditions for hours no film deposition occurs, as confirmed by surface-sensitive techniques.

Cyclic voltammetry data employing a glassy carbon electrode as anode (Fig. 2) are also very distinct depending on the presence of bpy. In the absence of this chelating ligand, an oxidation wave appears just above 0.75 V, whereas in the presence of bpy there is no oxidation process up

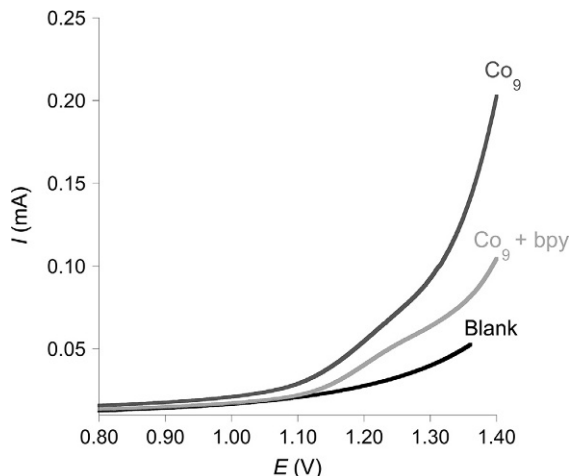


**Fig. 2** Cyclic voltammogram of a 1.0 mM solution of **Co<sub>9</sub>** (dark gray line), with the presence of 1.4 mM of bpy (bright gray line), and in the absence of catalyst (black line).

to 1.10 V, corresponding to the catalytic water oxidation wave. This difference should be attributed to the formation of a cobalt oxide film on the electrode surface in the former experiment, since this potential is not enough to oxidize water, as already stated by Nocera and coworkers (20). The differences observed in these two experiments corroborate again the presence of a cobalt oxide catalyst in the absence of bpy and, in addition, they also support the negligible participation of  $\text{CoO}_x$  when a chelating agent is present in solution. All these experiments confirmed the genuine WOC activity of **Co<sub>9</sub>**.

The efficiency for oxygen evolution in the **Co<sub>9</sub>**/bpy solutions reaches only 90%. The rest of the anodic current should be related to the electrochemical  $[\text{Co}(\text{bpy})_3]^{2+}/[\text{Co}(\text{bpy})_3]^{3+}$  oxidation. During long-term electrolysis the catalytic current starts to decrease, as a fine pink precipitate is formed. This salt was identified as  $\{[\text{Co}(\text{bpy})_3]^{3+}\}_4\text{A}_4\{\text{Co}_9\}$  stoichiometry ( $\text{A} = \text{Na}^+$  or  $\text{K}^+$ ). Thus, removal of the active species from solution is the major parameter decreasing the catalytic current, and not intrinsic deactivation or fatigue.

The kinetics of the **Co<sub>9</sub>**-catalyzed water oxidation can be studied by steady-state current density. These data allow constructing the Tafel plots represented in Fig. 3, which show the typical linear trend expected for a catalytic process (at low overpotentials). Measurable current density is observed above 1.15 V for a 1 mM **Co<sub>9</sub>** concentration, which corresponds to an overpotential  $\eta = 353$  mV, whereas the overpotential needed to reach  $1 \text{ mA cm}^{-2}$  is  $\eta = 776$  mV. The calculated Tafel slope is consistent in the

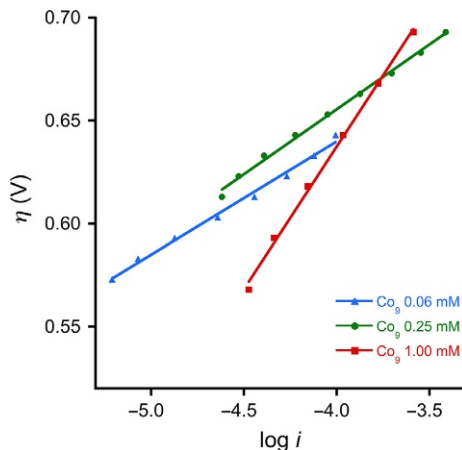


**Fig. 3** Steady-state Tafel data acquired at different **Co<sub>9</sub>**/bpy concentrations: 0.06/0.16 mM, Tafel slope = 55 mV decade<sup>-1</sup> (triangles); 0.25/0.68 mM, Tafel slope = 63 mV decade<sup>-1</sup> (circles); 1.00/2.80 mM, Tafel slope = 138 mV decade<sup>-1</sup> (squares).

130–140 mV decade<sup>-1</sup> range. This slope indicates that the rate-determining step is electrochemical (21), arising from electron-transfer processes.

Surprisingly, the Tafel slopes clearly depend on the **Co<sub>9</sub>** concentration, even if it should be concentration independent. For instance, the Tafel slope decreases to the 55–65 mV decade<sup>-1</sup> range below 0.25 mM. In this case the rate-determining step arises from a chemical step (4,20). This change could suggest a different rate-limiting step depending on the concentration of the active species. However, due to the bulky and highly charge nature of the POM, we think that the most plausible explanation is the participation of additional species, as the bpy ligand, for example. Indeed, a bpy layer is formed at high concentration on the FTO electrode, which could easily prevent a fast electron transfer. This is avoided at very low concentrations. This would be at the origin of the lower Tafel slopes, and faster kinetics in very diluted conditions.



### 3. CHARACTERIZATION OF THE CATALYTIC ACTIVITY OF **Co<sub>9</sub>** WITH NaClO

We also examined the oxygen evolution catalysis by mixing a strong chemical oxidant and **Co<sub>9</sub>** in homogeneous conditions. Around neutral pH ( $6 \leq \text{pH} \leq 8$ ), no oxygen evolution was observed for periodate (22), oxone

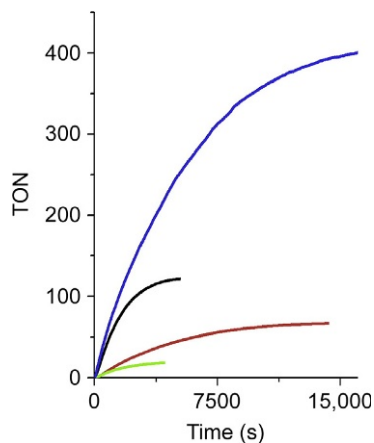


**Fig. 4** Oxygen evolution profile for a 1.0 mM  $\text{Co}_9$  solution in a pH 8  $\text{NaPi}$  buffer after the addition of different equivalents of  $\text{NaClO}$  as the oxidant: 100 equiv., green; 1000 equiv., red; 3300 equiv., black; 33,000 equiv., blue.

(23), persulfate, or even chlorine.  $\text{Co}_9$  was able to promote oxygen evolution only when added to a sodium hypochlorite solution.  $\text{NaClO}$  has been used for the characterization of homogeneous WOCs at neutral pH in the past, although as an O-containing oxidant, it has some drawbacks related with the nature of the  $\text{O}_2$  evolved during water oxidation experiment. This will be discussed in detail later. Still, as a model system, it allows studying the performance of the  $\text{Co}_9$  catalyst during oxygen evolution.

As depicted in Fig. 4, the catalytic process reaches a turnover number (TON) of 20 for an initial 100:1 oxidant/ $\text{Co}_9$  ratio, with an initial TOF over  $40 \text{ h}^{-1}$ .  $\text{NaClO}$  is a two-electron oxidant; so thus, this TON reflects 40% efficiency. This efficiency, far from being quantitative, indicates that there are competing reactions, probably disproportionation of hypochlorite to yield chloride and chlorite (vide infra). TON and TOF increase following an increase in the oxidant/ $\text{Co}_9$  ratio, reaching a sensational increase of TON of over 400 and an initial TOF of  $350 \text{ h}^{-1}$ . Accordingly, efficiency decreases reaching only a 2.5% for 33,000:1 ratio.

We also studied the effect of other parameters, such as temperature. Higher temperatures improve both dynamics and efficiency of the catalytic process. Fig. 5 shows that the total yield doubles when increasing from  $15^\circ\text{C}$  to  $25^\circ\text{C}$ , and optimum performance with 50% efficiency is achieved at  $35^\circ\text{C}$ . Although faster WOCs have been reported, it is important to note



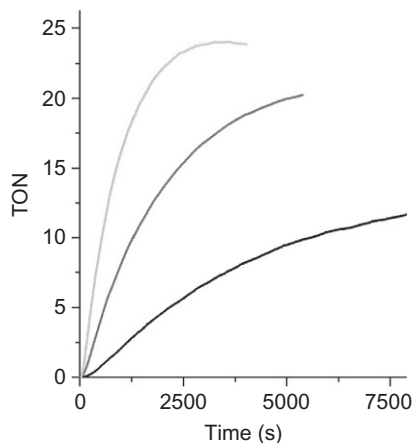


**Fig. 5** Oxygen evolution profile for a 1.0 mM **Co<sub>9</sub>** solution in a pH 8 NaPi buffer after the addition of 100 equiv. of NaClO as a function of the temperature: 15°C, *black*; 25°C, *dark gray*; 35°C, *bright gray*.

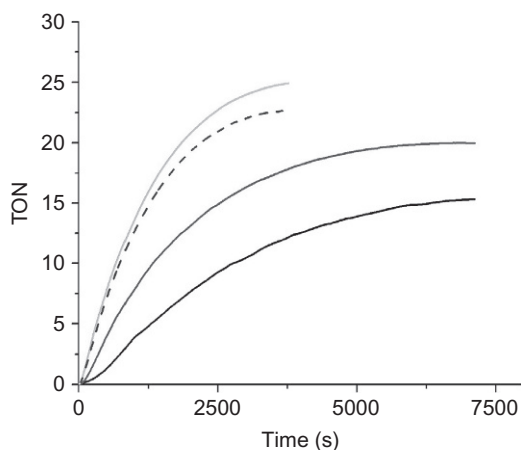


**Fig. 6** Oxygen evolution profile for a 1.0 mM **Co<sub>9</sub>** solution after the addition of 100 equiv. of NaClO at 25°C as a function of the pH 7.0, *black line*; 8.0, *dark gray line*; 9.0 *bright gray line*; 9.0 in the presence of a 10-fold excess of bpy, *dashed black line*.

that TOF depends not only on the catalyst but also on the oxidant. Hypochlorite is particularly slow. The fastest WOC reported from hypochlorite water oxidation showed a much slower TOF of 12 h<sup>-1</sup> (24). Regarding pH, we observed comparable TON numbers in the 7–9 range (Fig. 6), with

some differences in the initial kinetics. At lower pH the reaction is slower with an initial TOF of  $19 \text{ h}^{-1}$  (pH 7) and the catalytic cycle is twice as fast at higher pH reaching an initial TOF of  $73 \text{ h}^{-1}$  (pH 9).

Characterization data of the **Co<sub>9</sub>** solutions after the oxygen evolution reaction rule out the possible decomposition of the POM, yielding  $\text{CoO}_x$ . UV–vis spectroscopy shows the signature absorption bands of **Co<sub>9</sub>**, without the appearance of any additional band from any other species. Dynamic light scattering (DLS) analysis shows identical results, confirming the absence of nanoparticles in suspension. Even **Co<sub>9</sub>** can be recovered from solution by recrystallization with additional alkali cations or by slow evaporation of the reaction media. The recovered salt is identical to the starting sample, as proven by IR spectroscopy and X-ray diffraction. The experiments were repeated with the addition of a 10-fold excess of bpy per Co atom, showing consistent results, contrary to what is observed in electrochemical conditions. All of these experimental evidences confirm that, under the described experimental conditions, **Co<sub>9</sub>** is the main active species throughout oxidation.

### 3.1 Long-Term Stability of **Co<sub>9</sub>** in Turnover Conditions

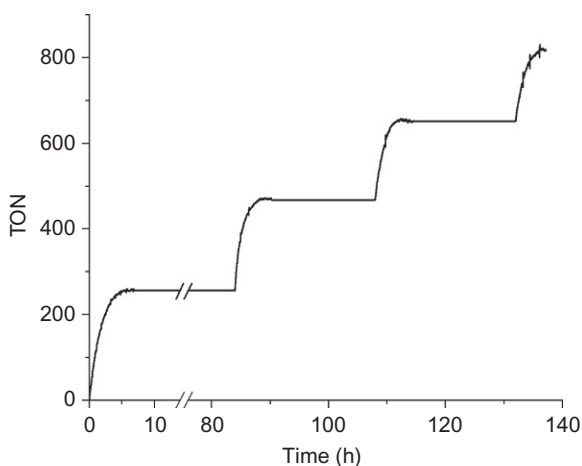
**Co<sub>9</sub>** shows remarkable stability and continuous catalytic performance. Once oxygen evolution stops, the limiting reagent is determined by the addition of equivalents of oxidant or catalyst. No effect is observed upon addition of catalyst. On the contrary, by successive additions of oxidant,  $\text{O}_2$  evolution is restarted performing identical TON and TOF through multiple additions (Table 1). These experiments demonstrate that **Co<sub>9</sub>** remains quantitatively intact in solution in the long term since decomposition to other species would result in significant changes in the catalytic activity (13a). The addition of 1000 equiv. of oxidant to a **Co<sub>9</sub>** (1 mM)  $\text{NaP}_i$  pH 8 buffer [0.9 M] solution every 2 h yields a final cumulative TON of 180, and a constant initial TOF of  $69 \pm 2 \text{ h}^{-1}$  (after three cycles). The addition of 3300 equiv. of oxidant every  $\approx 2 \text{ h}$  yields a total cumulative TON  $> 880$  and a constant initial TOF  $\approx 370 \pm 20 \text{ h}^{-1}$  (after five cycles). The mean TOF over the reaction time holds over  $100 \text{ h}^{-1}$ .

In addition, **Co<sub>9</sub>** remains active for weeks in solution, with no signs of fatigue or decomposition. As can be seen in Fig. 7, oxygen evolution is restarted upon successive additions of equivalents of oxidant and in the presence of a 10-fold excess of bpy after very long periods of time ( $> 120 \text{ h}$ ).

**Table 1** Manometry Data for Co<sub>9</sub>-Catalyzed Oxygen Evolution in a pH 8 NaP<sub>i</sub> Buffer Solution After Successive Additions of NaClO as the Oxidant at 25°C

[Co <sub>9</sub> ] (mM)	Oxidant Equivalents	Time of Addition (h)	TON	TOF <sub>i</sub> (h <sup>-1</sup> )	TON <sub>c</sub>
10 <sup>-1</sup>	10 <sup>3</sup>	0	75	70	75
10 <sup>-1</sup>	10 <sup>3</sup>	2.5	55	69	130
10 <sup>-1</sup>	10 <sup>3</sup>	5.0	50	67	180
10 <sup>-2</sup>	3.3 × 10 <sup>4</sup>	0	148	391	148
10 <sup>-2</sup>	3.3 × 10 <sup>4</sup>	1.6	158	379	306
10 <sup>-2</sup>	3.3 × 10 <sup>4</sup>	3.0	217	367	523
10 <sup>-2</sup>	3.3 × 10 <sup>4</sup>	4.5	200	355	723
10 <sup>-2</sup>	3.3 × 10 <sup>4</sup>	6.0	165	343	888
10 <sup>-2</sup>	3.3 × 10 <sup>4</sup>	0	255	391	255
8 × 10 <sup>-3</sup>	3.3 × 10 <sup>4</sup>	84.0	215	468	470
6 × 10 <sup>-3</sup>	3.3 × 10 <sup>4</sup>	108.0	180	586	650
5 × 10 <sup>-3</sup>	3.3 × 10 <sup>4</sup>	131.0	173	689	823

TON = total turnover number at the next addition or final time; TOF<sub>i</sub> = slope of the oxygen evolution curve at the oxidant addition time; TON<sub>c</sub> = cumulative TON.

**Fig. 7** Oxygen evolution profile in 1 M pH 8 NaP<sub>i</sub> buffer solutions after successive additions of NaClO as the oxidant at 25°C.



## 4. STABILITY AND SOLUTION SPECIATION UNDER CATALYTIC WATER OXIDATION CONDITIONS

The homogeneous character of  $\text{Co}_9$  during the oxygen evolution reaction has been well established from postreaction characterization. In order to further assess its genuine activity we carried out SAXS analyses (25). SAXS is a powerful method used to identify and characterize the size, shape, and electron density contrast of particles in solution with much more precision than DLS (26), allowing identifying even traces of nanoparticles, such as  $\text{CoO}_x$  for instance.

### 4.1 Speciation in Water and Phosphate Buffer

SAXS analysis was performed in the phosphate buffer solutions used in electrochemical and chemical catalytic conditions, and also in neat water with the aim of benchmarking the  $\text{Co}_9$  speciation. Fig. 8 compares the experimental results with the theoretical data obtained from a simulated scattering curve of the crystal structure, certainly allowing for the identification of  $\text{Co}_9$  in solution. The characteristic shape of  $\text{Co}_9$  produces unique X-ray scattering curves, thus making this POM easily distinguishable from other clusters or nanoparticle derivatives.

The calculated form factor parameters of  $\text{Co}_9$  are summarized in Table 2. In these experiments the  $R_g$  of  $\text{Co}_9$  is consistent along all studied

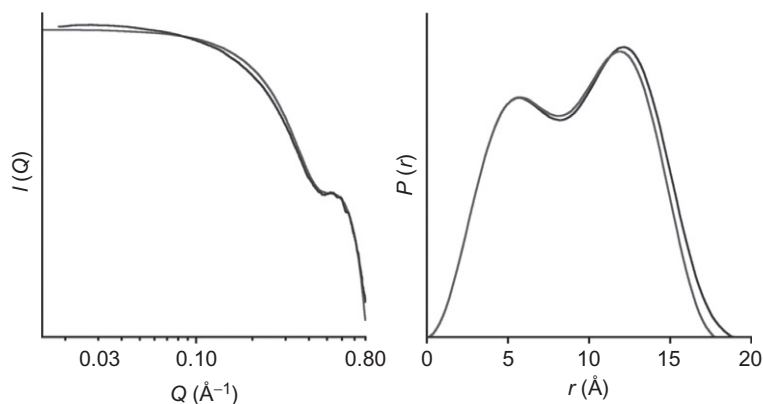


**Fig. 8** SAXS intensity (*left*) and Pair Distance Distribution Function (PDDF) (*right*) for 10 mM  $\text{Co}_9$  in a pH 8  $\text{NaPi}$  buffer solution (*black*) and for the simulated data from the crystal structure of  $\text{Co}_9$  (*gray*).

**Table 2** Calculated Form Factor Parameters for **Co<sub>9</sub>**

Concentration [mM]	$R_g$ (Guinier) [Å]	$R_g$ (PDDF) [Å]	$D_{\max}^a$ (PDDF) [Å]
<b>Simulated from Co<sub>9</sub> crystal structure</b>			
	7.1	7.0	18.8
<b>Co<sub>9</sub> in water</b>			
1	7.0	7.1	18.9
5	7.4	7.2	19.2
10	7.6	7.1	18.9
25	7.2	7.2	19.0
Av.	7.3	7.2	19.0
<b>Co<sub>9</sub> in a pH 7 NaP<sub>i</sub> buffer (50 mM) with NaNO<sub>3</sub> (1 M)</b>			
1	7.5	7.4	19.3
5	7.8	7.4	19.5
10	7.7	7.4	19.4
15	7.9	7.5	19.6
Av.	7.7	7.4	19.5
<b>Co<sub>9</sub> in a pH 8 NaP<sub>i</sub> buffer (0.9 M)</b>			
1	7.4	7.2	18.4
2	7.2	7.2	18.9
5	7.4	7.2	18.5
10	7.4	7.2	18.8
Av.	7.4	7.2	18.7

<sup>a</sup>Distance at which probability of X-ray scattering goes to 0, defined as diameter across the longest dimension of the cluster.

concentrations, indicating monodisperse solutions with no sign of aggregation or decomposition. The only differences between water and buffer solutions were found in the scattering curves (Fig. 9) representing the scattering intensity ( $I(Q)$ ) vs the magnitude of the scattering vector ( $Q$ ). The curve for neat water **Co<sub>9</sub>** shows a decrease in intensity at small  $Q$  values, or an interference peak at  $0.1 \text{ \AA}^{-1}$  indicating interparticle repulsion. This is

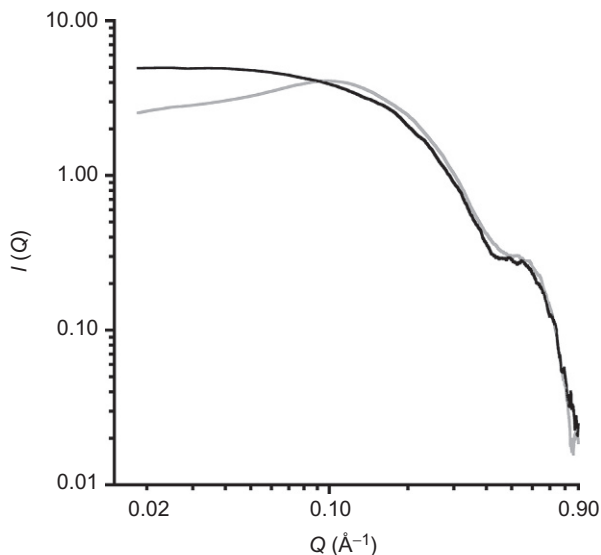


**Fig. 9** SAXS intensity for a 5 mM  $\text{Co}_9$  in water (gray) and in a  $\text{NaPi}$ -buffered solution (black).

not observed in the buffered  $\text{Co}_9$  solutions, since the interparticle repulsion disappears in the presence of buffer due to a reduction of the electrostatic forces between the cluster (27). Beyond this, both solutions are stable in the long term, showing no evolution with time of the particle speciation.

#### 4.2 Dependency of the Speciation on pH

SAXS data were collected for a  $\text{Co}_9$  aqueous solution at pH values ranging from 1.5 to 11. Above pH 11, cobalt hydroxide precipitates from solution. In neat water the self-buffering pH of  $\text{Co}_9$  is 8. Increasing the pH to 11 produces no changes in the SAXS signal as can be seen in Fig. 10 and Table 3, confirming the stability of  $\text{Co}_9$  in this  $8 < \text{pH} < 11$  range. The addition of HCl to decrease the pH to 6.5 and 5.5 again produces no changes. However, further decrease to pH 4.4–4.0 produces a change in the speciation. The SAXS curves at this pH range indicate a mixture of Keggin-sized species with the  $\text{Co}_9$  signal, which partially overlap. As the pH is lowered the Keggin-size signal becomes dominant, while the  $\text{Co}_9$  signal decreases until disappearing below pH 1.5. This suggests that  $\text{Co}_9$  dissociates in acidic conditions releasing  $[\text{Co}(\text{H}_2\text{O})_6]^{2+}$ , as it was reported for other Co-POMs (28). Therefore, we can assess that  $\text{Co}_9$  remains stable in the  $5.5 < \text{pH} < 11$  range.

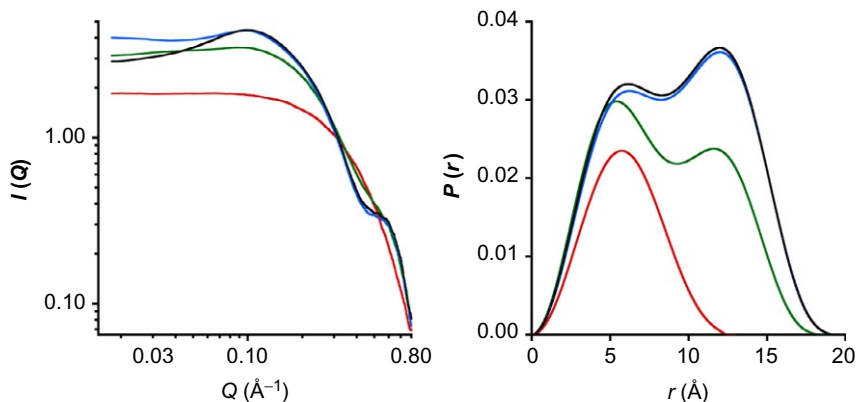


**Fig. 10** SAXS intensity (*left*) and PDDF (*right*) for a 5 mM aqueous **Co<sub>9</sub>** at pH 1.5 (*red*), 4.0 (*green*), 8.0 (*black*), and 11.0 (*blue*).

**Table 3** Calculated Form Factor Parameters for a 5 mM **Co<sub>9</sub>** Aqueous Solution With Variable pH

pH	$R_g$ (Guinier) [Å]	$R_g$ (PDDF) [Å]	$D_{max}$ (PDDF) [Å]
1.5	4.8	4.5	13.3
4	6.6	6.5	18.0
4.4	7.2	7.0	18.5
5.5	7.4	7.2	19.1
6.5	7.5	7.2	19.1
8	7.5	7.1	19.1
11	7.4	7.2	19.2

### 4.3 Speciation Under Catalytic Oxygen Evolution Conditions

For the study of the solution speciation under reaction conditions, SAXS data were collected after from the oxygen evolution reaction promoted by addition of **Co<sub>9</sub>** to a NaClO solution at pH 8 (Table 4). After 3 h of reaction, SAXS data confirm no nanoparticle formation. However, multiple additions of oxidant equivalents (Fig. 11) had a clear effect in the **Co<sub>9</sub>** signal, suggesting either a decrease of **Co<sub>9</sub>** concentration in solution or the presence of smaller species. This was in contradiction with the stability in phosphate buffer. However, when the same experiment of successive oxidant additions

**Table 4** Calculated Form Factor Parameters for  $\text{Co}_9$  After Successive Additions of NaClO (100:1, NaClO/ $\text{Co}_9$  Ratio)

Concentration <sup>a</sup> [mM]	NaClO (Added, 1 M) [mL]	T (Since 1st Addition) [h]	$R_g$ (Guinier) [Å]	$R_g$ (PDDF) [Å]	$D_{\text{max}}$ (PDDF) [Å]	Solution <sup>b</sup> pH <sub>i</sub> /pH <sub>f</sub>
<b><math>\text{Co}_9</math> in a pH 8 <math>\text{NaP}_i</math> buffer (0.9 M) water solution</b>						
1	0.2	3	6.8	6.9	18.6	7.9:7.6
0.92	0.18	5.5	6.9	6.9	18.4	8.0:7.6
0.84	0.16	8	7.0	7.1	18.3	8.1:7.7
0.77	0.14	10.5	7.0	7.0	19.0	8.1:7.7
<b><math>\text{Co}_9</math> in a pH 6 <math>\text{NaP}_i</math> buffer (0.05 M) water solution</b>						
1	0.2	2.5	7.0	7.1	18.7	8.3:6.4
0.92	0.18	5	7.4	7.1	18.7	8.2:6.8
0.84	0.16	7.5	7.05	7.2	18.4	8.7:7.0
0.77	0.14	10	6.8	7.2	18.5	9.6:8.2
<b><math>\text{Co}_9</math> in water</b>						
1	0.2	3	7.4	7.1	18.8	10.9:8.4
0.84	0.16	8	7.6	7.2	18.9	9.5:6.9
0.77	0.14	10.5	7.2	7.3	18.7	9.1:6.6

<sup>a</sup>Concentration was calculated taking into account the volume of NaClO added and the volume extracted for SAXS measurements.

<sup>b</sup>pH<sub>i</sub> refers to the pH measured just after adding NaClO; pH<sub>f</sub> refers to the pH measured before the next addition.

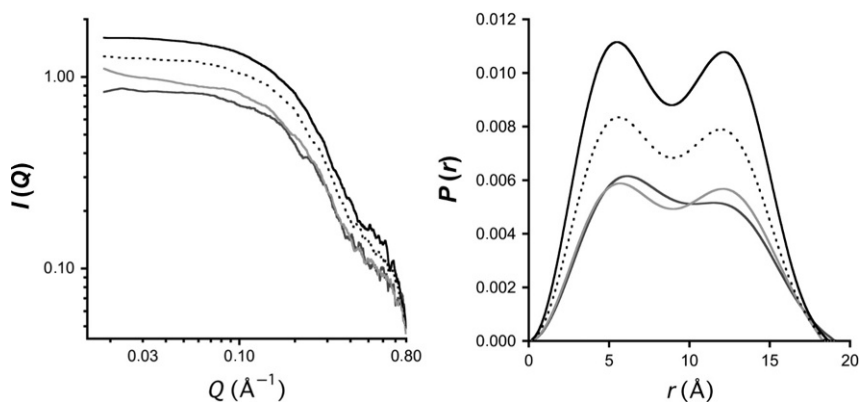


**Fig. 11** SAXS intensity (*left*) and PDDF (*right*) after successive additions of NaClO as the oxidant every ca. 2.5 h (100:1, oxidant/ $\text{Co}_9$  ratio) to a 1 mM  $\text{Co}_9$  solution in pH 8  $\text{NaP}_i$  solution. Data after first, second, third, and fourth additions of NaClO are shown in *black*, *dotted black line*, *bright gray*, and *dark gray*, respectively.



was carried out without the NaP<sub>i</sub> buffer, maintaining constant pH by small additions of acid, the speciation of the Co<sub>9</sub> solution is robust. To summarize, the Co<sub>9</sub> stability in solution is only affected by highly concentrated phosphate buffer associated with the oxygen evolution reaction, but not from the latter.



## 5. HETEROGENEOUS WOC WITH MODIFIED CO<sub>9</sub>/CARBON PASTE ELECTRODES

Although homogeneous catalysts present some advantages, such as faster kinetics or realistic mechanistic studies, in the search for industrial applications heterogeneous catalysts are preferred. Homogeneous conditions are only viable for high added value processes, but not for mass production of low-cost commodities. In the energy field, cost is a key parameter to compete with current technologies. Therefore, viable technological applications will require recycling and long-term unattended function (years), just to name a few. On this regard, polyoxometalates present a formidable opportunity since they may combine the best of both worlds. On one end they are excellent homogeneous catalysts offering good processability, optimization, fast kinetic rates, working in a large range of pH. On the other end, POMs can be immobilized into insoluble solid-state salts with a variety of counteranions (alkaline, alkaline earth, tetraalkyl ammonium, etc.), maintaining their intrinsic catalytic features. The only problem is their insulating character. Therefore, in order to build an electrocatalytic anode for water oxidation we will need a conducting support.

We used carbon black as conducting media to fabricate carbon paste-modified electrodes incorporating the Cs<sup>+</sup> salt of Co<sub>9</sub> (CsCo<sub>9</sub>) in increasing ratios (1%–60% in weight). The presence of the POM, even at very low contents, already gives rise to the appearance of a catalytic water oxidation wave in the CV data.

Steady-state water oxidation current density (*i*) follows a linear Tafel law in the 0.2 <  $\eta$  < 0.6 V, as can be seen in Fig. 12. The Tafel slope decreases very rapidly for a very small catalyst content, indicating faster kinetics and the appearance of a catalytic process. Above 3% catalyst content, the slope remains essentially constant in the 90–110 mV decade<sup>-1</sup> range. These values are between the expected values for an electron-transfer rate-limited process (120 mV decade<sup>-1</sup>) and a chemical rate-limited process (60 mV decade<sup>-1</sup>),

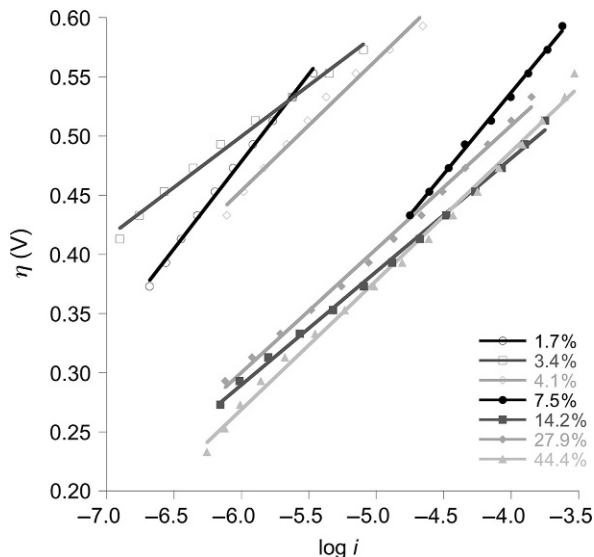


**Fig. 12** Steady-state Tafel data acquired in a pH 7  $\text{NaPi}$  buffer solution with POM-C anodes at different  $\text{CsCo}_9$ /carbon paste weight ratios.

suggesting there is a competition in the kinetics between catalytic water oxidation and electron transfer in the blend.

POM-C-modified electrodes exhibit exceptional stability during bulk water electrolysis. Fig. 13 shows how after an induction period of  $\approx 30$  min, where intensity decreases probably due to capacitance, the current remains constant for the rest of the experiment for over 8 h. This demonstrates the long-term stability of  $\text{CsCo}_9$  in heterogeneous conditions. Moreover, oxygen evolution reaches over 90% efficiency compared with the theoretical amount of oxygen expected (Fig. 14).

In order to determine if there is any chemical evolution of the catalysts during this reaction (in situ formation of  $\text{CoO}_x$  species) we used multiple characterization techniques to identify the structural and chemical nature of the modified electrodes after electrolysis. Spectroscopy, X-ray diffraction, and elemental analysis remain consistent with the initial data. Still, undetectable traces of  $\text{CoO}_x$  could be present. Although the participation of such impurities cannot quantitatively account for the observed catalytic performance, we decided to make a comparative analysis with  $\text{Co}_3\text{O}_4$  analogous electrodes. This comparison could confirm, once again, the genuine catalytic activity of the  $\text{Co}_9$  POM.

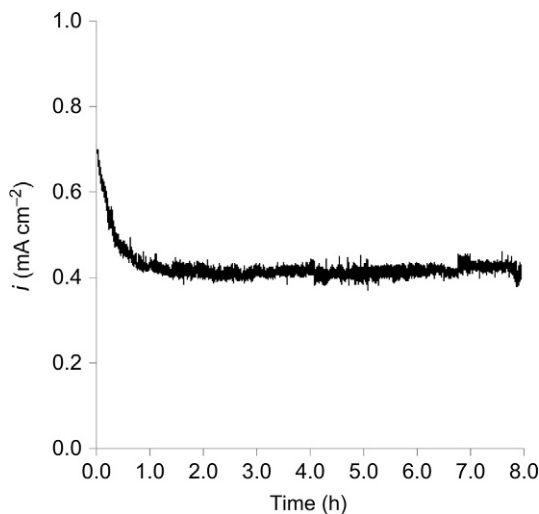


**Fig. 13** Current density at +1.3 V (vs NHE) with a 44% POM-C-modified electrode.

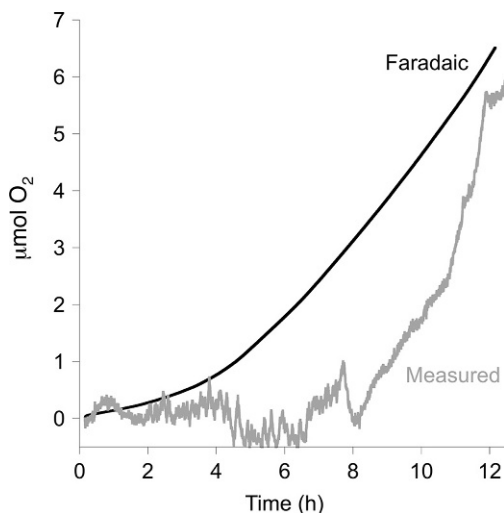


**Fig. 14** O<sub>2</sub> production measured with a fluorescence sensor (*gray line*) and theoretical production calculated for a quantitative Faradaic efficiency (*black line*) for water electrolysis with a 22% POM-C anode electrode with a pH 7 NaP<sub>i</sub> buffer applying a potential of 1.5 V vs NHE. The very long lag time arises from the complex experimental setup. The position of the electrode, perpendicular to the surface, traps the oxygen bubbles even at high stirring speed. Thus, the oxygen content increases following a very irregular pattern, as gas bubbles escape randomly from the electrode.

## 5.1 Comparison With Cobalt Oxide

Steady-state data for  $\text{Co}_3\text{O}_4$ -CP electrodes (Fig. 15 and Table 5) exhibit completely different kinetics than POM-C electrodes. Tafel slope increases when increasing the  $\text{Co}_3\text{O}_4$  content in the blend, just opposite to what is observed for  $\text{CsCo}_9$ . A 7.1% blend already shows  $87 \text{ mV decade}^{-1}$ , whereas increasing the oxide content to 40.7% also increases the slope to  $346 \text{ mV decade}^{-1}$ , which is too high for a catalytic process.

Regarding total current densities, comparison of the activity of both catalysts, taking into account the number of moles of Co atoms, highlights the superior performance of  $\text{CsCo}_9$  toward water oxidation. POM-C electrodes yield two orders of magnitude larger current densities than the corresponding  $\text{Co}_3\text{O}_4$  blends for equimolar amounts of cobalt content (Fig. 16). Actually, a huge excess of cobalt oxide is needed to reach similar activity. For example,  $2 \mu\text{mol}$  of total cobalt as  $\text{CsCo}_9$  (20 mg,  $0.22 \mu\text{mol}$ ) yields a much larger current density than  $125 \mu\text{mol}$  of total cobalt as  $\text{Co}_3\text{O}_4$  (20 mg,  $41.7 \mu\text{mol}$ ). These experiments indicate that most of the POM had to be converted into an oxide to reach such a high catalytic activity. Therefore, even if very small undetected amounts of  $\text{CsCo}_9$  decompose, leading to small traces of cobalt oxide during water oxidation, they cannot justify the high activity exhibited by the POM-C blends.

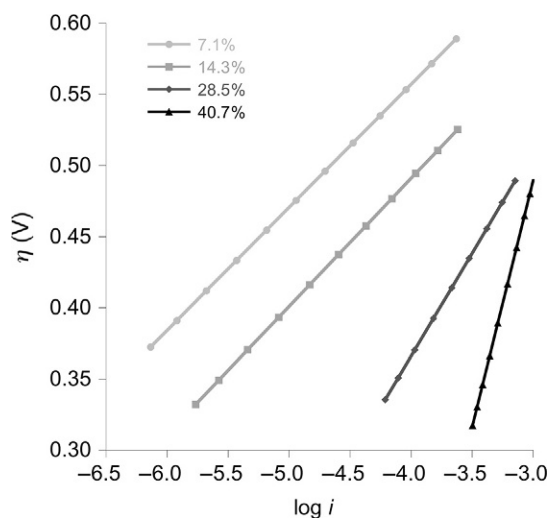
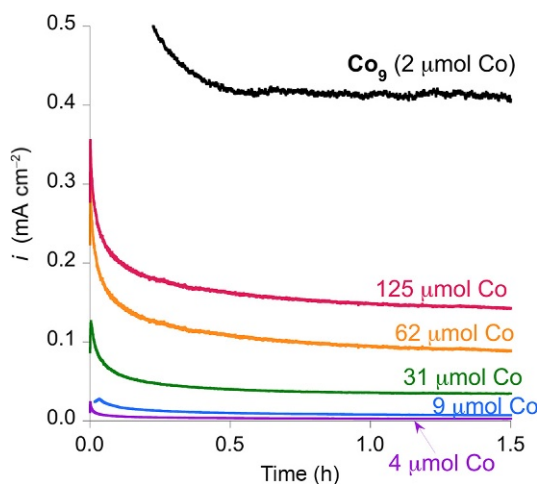


Fig. 15 Steady-state Tafel data acquired in a pH 7  $\text{NaP}_i$  buffer solution with POM-C anodes at different  $\text{Co}_3\text{O}_4$ /carbon paste weight ratios.

**Table 5** Tafel Slope and Overpotential Needed to Reach 1 mA cm<sup>-2</sup> for Catalytic Water Electrolysis With POM-C and Co<sub>3</sub>O<sub>4</sub>-CP Working Electrodes as a Function of the Catalyst Content

	Catalyst (wt.%)	$\eta$ (mV) ( $i = 1 \text{ mA cm}^{-2}$ )	Tafel Slope (mV decade <sup>-1</sup> )
CsCo <sub>9</sub>	1.7	841	178
	3.4	712	86
	4.1	725	110
	7.5	600	138
	14.2	525	96
	27.9	557	104
	44.4	537	109
Co <sub>3</sub> O <sub>4</sub>	7.1	643	87
	14.3	580	90
	28.5	510	145
	40.7	489	346

Data obtained from the steady-state Tafel experiments.



**Fig. 16** Current density at +1.3 (vs NHE) with a 44% POM-C electrode and with Co<sub>3</sub>O<sub>4</sub>-C working electrodes at different Co<sub>3</sub>O<sub>4</sub> contents. Labels indicate the total amount of Co in the blends.

## 5.2 Effect of the pH on the Catalytic Performance

POM-C electrodes display a robust performance in a large pH range during catalytic water electrolysis, being slightly lower in acid media (Fig. 17). This pH dependence is also distinct from Co-P<sub>i</sub> or CoO<sub>x</sub> (21a). Both are unstable at low pH due to corrosion, and the water oxidation wave monotonically increases from acid media to pH > 8 (6). At pH 8 and above, two different redox processes are clearly shown. Only one redox couple appears for 3 < pH < 8, at lower potentials than the catalytic wave. Below pH 3, no precatalytic redox processes are observed. On the contrary, the CsCo<sub>9</sub> CV data show no significant changes in intensity or position.

The comparative acid media behavior is an additional proof of the genuine catalytic activity of this POM (Fig. 18). Bulk water electrolysis at pH 1 shows no effect upon addition of CoO<sub>x</sub>, yielding identical values to those of the pure carbon paste electrodes. Aqueous Co<sup>2+</sup> is active in these conditions, but reaches a maximum current density for a  $\approx 18 \mu\text{mol}$  total content, that is, roughly twice the activity exhibited by the pure carbon paste electrode. The POM-C electrodes, remarkably, exhibit 100 times higher current densities even for a much lower cobalt content (2  $\mu\text{mol}$ ). This acid media activity is a unique feature for a metal oxide-based catalyst.

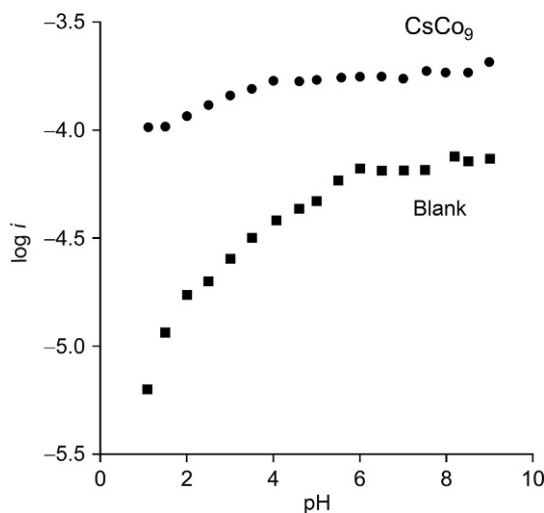
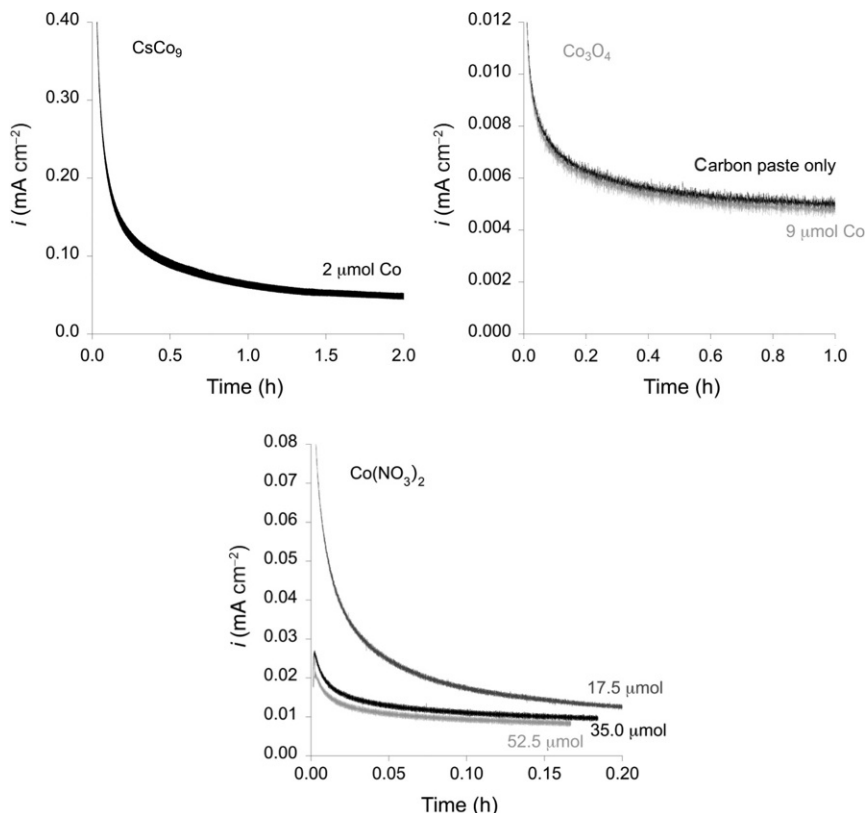


Fig. 17 Dependence on pH at +1.5 V (vs NHE) for a carbon paste (squares) and a 14% POM-C electrode (circles).



**Fig. 18** Bulk water electrolysis at pH 1 applying a potential of +1.5 V (vs NHE) with different working electrodes: POM-C blend (0.22  $\mu\text{mol}$  **CsCo<sub>9</sub>**); Co<sub>3</sub>O<sub>4</sub>-C blend (3  $\mu\text{mol}$  Co<sub>3</sub>O<sub>4</sub>); and with a carbon paste electrode, adding to the solution Co(NO<sub>3</sub>)<sub>2</sub> (17.5, 35.0, and 52.5  $\mu\text{mol}$ ). The numbers quoted in the plots indicate the total amount of cobalt content.



## 6. CONCLUSIONS

In summary, the catalytic activity toward oxygen evolution of the high nuclearity nonacobalt polyoxometalate [Co<sub>9</sub>(H<sub>2</sub>O)(OH)<sub>3</sub>(HPO<sub>4</sub>)<sub>2</sub>(PW<sub>9</sub>O<sub>34</sub>)<sub>3</sub>]<sup>16-</sup> (**Co<sub>9</sub>**) has been presented. This POM is a true and versatile WOC catalyst. It works in homogeneous and heterogeneous conditions and in a wide pH range. It promotes chemical and electrochemical water oxidation with a robust and kinetically fast performance. As a polyanion model, it highlights the advantages of POMs in the field of water oxidation, where they combine some of the advantages

of homogeneous and heterogeneous materials. On the latter, they are metal oxides, with the expected redox stability and rugged activity. On the former, **Co<sub>9</sub>** is a monodispersed, easy-processable material. Maybe the most remarkable prospect is its acid media features. Currently, only noble metal catalysts are viable components of an acid water splitting scheme, when these conditions and industrially preferred due to the excellent development of polymer-electrolyte membrane (PEM) technologies for water electrolysis and hydrogen production. A low-cost alternative could have an immediate impact on PEM electrolyzer costs, allowing much larger market penetration and better competitive analyses vs fossil fuels hydrogen production.

## REFERENCES

1. McEvoy, J. P.; Brudvig, G. W. *Chem. Rev.* **2006**, *106*, 4445–4483.
2. Kanan, M. W.; Nocera, D. G. *Science* **2008**, *321*, 1072–1075.
3. Galán-Mascarós, J. R. *ChemElectroChem* **2015**, *2*, 37–50.
4. Pijpers, J. J.; Winkler, M. T.; Surendranath, Y.; Buonassisi, T.; Nocera, D. G. *Proc. Natl. Acad. Sci. U.S.A.* **2011**, *108*, 10056–10061.
5. Nocera, D. G. *Acc. Chem. Res.* **2012**, *45*, 767–776.
6. Minguzzi, A.; Fan, F.-R. F.; Vertova, A.; Rondinini, S.; Bard, A. J. *Chem. Sci.* **2012**, *3*, 217–229.
7. (a) Liu, X.; Wang, F. *Coord. Chem. Rev.* **2012**, *256*, 1115–1136; (b) Duan, L.; Bozoglian, F.; Mandal, S.; Stewart, B.; Privalov, T.; Llobet, A.; Sun, L. *Nat. Chem.* **2012**, *4*, 418–423; (c) Barnett, S. M.; Goldberg, K. I.; Mayer, J. M. *Nat. Chem.* **2012**, *4*, 498–502; (d) Ellis, W. C.; McDaniel, N. D.; Bernhard, S.; Collins, T. J. *J. Am. Chem. Soc.* **2010**, *132*, 10990–10991.
8. Concepcion, J. J.; Jurs, J. W.; Brennaman, M. K.; Hoertz, P. G.; Patrocínio, A. O. T.; Murakami Iha, N. Y.; Templeton, J. L.; Meyer, T. J. *Acc. Chem. Res.* **2009**, *42*, 1954–1965.
9. Gersten, S. W.; Samuels, G. J.; Meyer, T. J. *J. Am. Chem. Soc.* **1982**, *104*, 4029–4030.
10. (a) Sartorel, A.; Carraro, M.; Scorrano, G.; De Zorzi, R.; Geremia, S.; McDaniel, N. D.; Bernhard, S.; Bonchio, M. *J. Am. Chem. Soc.* **2008**, *130*, 5006–5007; (b) Geletii, Y. V.; Botar, B.; Kögerler, P.; Hillesheim, D. A.; Musaev, D. G.; Hill, C. L. *Angew. Chem. Int. Ed. Engl.* **2008**, *47*, 3896–3899.
11. Lv, H.; Geletii, Y. V.; Zhao, C.; Vickers, J. W.; Zhu, G.; Luo, Z.; Song, J.; Lian, T.; Musaev, D. G.; Hill, C. L. *Chem. Soc. Rev.* **2012**, *41*, 7572–7589.
12. Yin, Q.; Tan, J. M.; Besson, C.; Geletii, Y. V.; Musaev, D. G.; Kuznetsov, A. E.; Luo, Z.; Hardcastle, K. I.; Hill, C. L. *Science* **2010**, *328*, 342–345.
13. (a) Stracke, J. J.; Finke, R. G. *J. Am. Chem. Soc.* **2011**, *133*, 14872–14875; (b) Natali, M.; Berardi, S.; Sartorel, A.; Bonchio, M.; Campagna, S.; Scandola, F. *Chem. Commun.* **2012**, *48*, 8808–8810.
14. (a) Hintermair, U.; Hashmi, S. M.; Elimelech, M.; Crabtree, R. H. *J. Am. Chem. Soc.* **2012**, *134*, 9785–9795; (b) Hong, D.; Murakami, M.; Yamada, Y.; Fukuzumi, S. *Energy Environ. Sci.* **2012**, *5*, 5708–5716; (c) Hong, D.; Jung, J.; Park, J.; Yamada, Y.; Suenobu, T.; Lee, Y.-M.; Nam, W.; Fukuzumi, S. *Energy Environ. Sci.* **2012**, *5*, 7606–7616; (d) Schley, N. D.; Blakemore, J. D.; Subbaiyan, N. K.; Incarvito, C. D.; D'Souza, F.; Crabtree, R. H.; Brudvig, G. W. *J. Am. Chem. Soc.* **2011**, *133*, 10473–10481.



15. Car, P.-E.; Guttentag, M.; Baldrige, K. K.; Alberto, R.; Patzke, G. R. *Green Chem.* **2012**, *14*, 1680–1688.
16. Weakley, T. J. R. *J. Chem. Soc. Chem. Commun.* **1984**, 1406–1407.
17. Goberna-Ferrón, S.; Vígara, L.; Soriano-López, J.; Galán-Mascarós, J. R. *Inorg. Chem.* **2012**, *51*, 11707–11715.
18. Soriano-López, J.; Goberna-Ferrón, S.; Vígara, L.; Carbó, J. J.; Poblet, J. M.; Galán-Mascarós, J. R. *Inorg. Chem.* **2013**, *52*, 4753–4755.
19. Goberna-Ferrón, S.; Soriano-López, J.; Galán-Mascarós, J. R.; Nyman, M. *Eur. J. Inorg. Chem.* **2015**, *2015*, 2833–2840.
20. Surendranath, Y.; Kanan, M. W.; Nocera, D. G. *J. Am. Chem. Soc.* **2010**, *132*, 16501–16509.
21. (a) Gerken, J. B.; McAlpin, J. G.; Chen, J. Y. C.; Rigsby, M. L.; Casey, W. H.; Britt, R. D.; Stahl, S. S. *J. Am. Chem. Soc.* **2011**, *133*, 14431–14442; (b) Dau, H.; Limberg, C.; Reier, T.; Risch, M.; Roggan, S.; Strasser, P. *ChemCatChem* **2010**, *2*, 724–761.
22. Parent, A. R.; Brewster, T. P.; DeWolf, W.; Crabtree, R. H.; Brudvig, G. W. *Inorg. Chem.* **2012**, *51*, 6147–6152.
23. Limburg, J.; Vrettos, J. S.; Chen, H.; de Paula, J. C.; Crabtree, R. H.; Brudvig, G. W. *J. Am. Chem. Soc.* **2001**, *123*, 423–430.
24. Limburg, J.; Vrettos, J. S.; Liable-Sands, L. M.; Rheingold, A. L.; Crabtree, R. H.; Brudvig, G. W. *Science* **1999**, *283*, 1524–1527.
25. Blanchet, C. E.; Svergun, D. I. *Annu. Rev. Phys. Chem.* **2013**, *64*, 37–54.
26. Stracke, J. J.; Finke, R. G. *ACS Catal.* **2014**, *4*, 909–933.
27. Putnam, C. D.; Hammel, M.; Hura, G. L.; Tainer, J. A. *Q. Rev. Biophys.* **2007**, *40*, 191–285.
28. Ohlin, C. A.; Harley, S. J.; McAlpin, J. G.; Hocking, R. K.; Mercado, B. Q.; Johnson, R. L.; Villa, E. M.; Fidler, M. K.; Olmstead, M. M.; Spiccia, L.; Britt, R. D.; Casey, W. H. *Chem. Eur. J.* **2011**, *17*, 4408–4417.

This page intentionally left blank



# Polyoxometalate-Functionalized Nanocarbon Materials for Energy Conversion, Energy Storage, and Sensor Systems

C.-G. Lin, J. Hu, Y.-F. Song<sup>1</sup>

State Key Laboratory of Chemical Resource Engineering, Beijing University of Chemical Technology, Beijing, PR China

<sup>1</sup>Corresponding author: e-mail addresses: songyufei@hotmail.com; songyf@mail.buct.edu.cn

## Contents

1. Introduction	182
2. Synthesis of the POM/Nanocarbon Composites	183
2.1 Covalent Functionalization Methods	184
2.2 Noncovalent Functionalization Methods	184
3. Applications of the POM/Nanocarbon Composites	185
3.1 Electrocatalysis	185
3.2 Energy Storage	196
3.3 Sensors and Environmental Pollutants	204
4. Conclusions	208
References	209

## Abstract

The development of advanced composite materials based on polyoxometalates (POMs) and nanostructured carbons has attracted significant attention as they combine the unique chemical reactivity of POMs and the unparalleled electronic properties of nanocarbons. The exceptional properties of the resultant composites have been widely employed in catalysis, energy conversion and storage, molecular sensors and electronics. In this chapter, we report the latest progress on POM/CNT (CNT=carbon nanotubes) and POM/graphene nanocomposites with a focus on energy materials for water splitting and fuel cells, electrode materials for batteries and supercapacitors, as well as functional materials for environmental pollutant sensing. Current applications are critically assessed and promising future target systems are discussed.

<sup>☆</sup>Part of this paper is adapted and reproduced from our previous work (<http://pubs.rsc.org/en/content/articlelanding/2015/ee/c4ee03749a>).

## ABBREVIATIONS

- [C<sub>8</sub>Py][PF<sub>6</sub>]** *n*-Octylpyridinium hexafluorophosphate  
**AA** ascorbic acid  
**Al<sub>13</sub>** [AlO<sub>4</sub>Al<sub>12</sub>(OH)<sub>24</sub>(H<sub>2</sub>O)<sub>12</sub>]<sup>7+</sup>  
**CNT** carbon nanotube  
**CNTP** carbon nanotube paste  
**CS** chitosan  
**Cs-PMo<sub>12</sub>** Cs<sub>3</sub>PMo<sub>12</sub>O<sub>40</sub>  
**DMFC** direct methanol fuel cell  
**GC/GCE** glassy carbon/glassy carbon electrode  
**GNs** graphene nanosheets  
**GO** graphene oxide  
**HR-TEM** high resolution transmission electron microscopy  
**LbL** layer-by-layer  
**MCBs** molecular cluster batteries  
**MWNTs** multiwalled carbon nanotubes  
**NN** nanonet  
**NPs** nanoparticles  
**OEAs** oxygen-evolving anodes  
**ORR** oxygen reduction reaction  
**P<sub>5</sub>W<sub>30</sub>** [NaP<sub>5</sub>W<sub>30</sub>O<sub>110</sub>]<sup>14-</sup>  
**PDDA** poly(diallyldimethylammonium chloride)  
**PMo<sub>12</sub>** [PMo<sub>12</sub>O<sub>40</sub>]<sup>3-</sup>  
**POMs** polyoxometalates  
**PV<sub>2</sub>Mo<sub>10</sub>** [PV<sub>2</sub>Mo<sub>10</sub>O<sub>40</sub>]<sup>5-</sup>  
**PW<sub>12</sub>** [PW<sub>12</sub>O<sub>40</sub>]<sup>3-</sup>  
**Py** pyrene  
**rGo** reduced graphene oxide  
**SEI** solid electrolyte interphase  
**SiMo<sub>12</sub>** [SiMo<sub>12</sub>O<sub>40</sub>]<sup>4-</sup>  
**SiW<sub>12</sub>** [SiW<sub>12</sub>O<sub>40</sub>]<sup>4-</sup>  
**SWNTs** single-walled carbon nanotubes  
**TEM** transmission electron microscopy  
**TOF** turnover frequency  
**UV** ultraviolet  
**WOC** water oxidation catalyst



## 1. INTRODUCTION

Over the last decade, it has been world widely acknowledged that the global energy consumption of fossil fuels vastly exceeds the production. Solutions for the sustainable energy conversion and energy storage are urgently demanded. As such, the development of advanced functional materials that

allow efficient conversion of solar or electrical energy into storable energy, e.g., in the form of chemical bonds (e.g.,  $H_2$ ) is causing great attention from scientific and industrial communities (1–5). Recent studies have demonstrated that the advanced composite materials based on polyoxometalates (POMs) and nanocarbons including carbon nanotubes (CNTs) and graphene have shown great potential to meet the challenges in electrocatalysis, energy storage, sensor devices, and other cutting-edge technologies (6–8).

POMs are a class of discrete anionic molecular metal oxides of early transition metals (e.g., V, Mo, W), usually constructed via the condensation of metal oxide polyhedrons in a corner-, edge-, and even face- sharing manner (9). POM anions exhibit intriguing chemical and physical features, allowing them to be employed in various research fields such as catalysis, energy conversion, and molecular electronics (10,11). Nanocarbon materials, including CNTs and graphene, have been extensively used in energy conversion, electrochemistry, and electronics due to their unique nanosized structures with exceptional electrical and spectroscopic features (12–17). However, POMs are typically salts with negligible conductivity (18) making them unsuitable for direct use in electrical energy conversion/storage or amperometric sensing. In addition, it was shown that the POMs dispersion on nanocarbon materials such as graphene significantly modifies the electronic structure of the POMs. As a result, it is highly important to investigate on the molecular level these profound changes essentially in order to have a better understanding the device performance (19). In recent years, researchers have started to harness the synergistic effects between POMs and nanocarbon materials by developing a range of composite materials to address the pressing global energy challenges (20,21).

Based on recent advances in the chemical modification of nanocarbons, advanced functional materials are now available that combine high surface area and electrical conductivity with the ability to intimately link reactive species such as POMs to the nanocarbon surface through a range of intermolecular or covalent interactions. This in turn allows a molecular dispersion of POMs on the nanocarbon, so that each individual cluster anion can be electronically addressed and can be involved energy and electron transfer processes (22,23).



## 2. SYNTHESIS OF THE POM/NANOCARBON COMPOSITES

Two main pathways for the preparation of the POM/nanocarbon composites can be identified; their main advantages and disadvantages together with potential future directions are described later.

## 2.1 Covalent Functionalization Methods

Covalent attachment of POMs to nanocarbons requires access to stable organo-functionalized POMs. This by itself is often synthetically challenging and typical functionalization groups are restricted to organo-functionalized alkoxides, silanes, phosphonates, and imides (24,25). Often, one organic functionalization group can only be linked to one specific cluster type, so that currently no unified functionalization strategy exists. In addition, the functionalization step can be carried out during the actual cluster assembly (*direct functionalization*) or after the cluster has been synthesized (*postfunctionalization*), making it more difficult for the nonexpert to choose the ideal synthetic approach (24,25). Further, the bonding between POM and functional organic group is often relatively weak so that the application range is seriously hampered. Thus, the development of general functionalization routes leading to stable, long-lived organic-inorganic hybrid materials is one major challenge of modern POM research.

To date, the typical approaches used to functionalize nanocarbons with POMs employ POM clusters, where a pendant amine has been introduced via the functional group. This moiety can then be linked to oxidized nanocarbons through the formation of amides (26,27).

## 2.2 Noncovalent Functionalization Methods

Noncovalent bonding can be achieved using a range of intermolecular interactions between POMs and nanocarbons.

*Electrostatic Interactions:* The current state-of-the-art is the use of electrostatic interactions to attach anionic POMs to positively charged nanocarbons. Cationic functionalization of nanocarbons can be achieved by (a) covalent attachment of cations, typically to oxidized CNTs or graphene where  $-OH$  and  $-COOH$  groups are available for further functionalization (8) and (b) through intermolecular interactions, e.g., van der Waals interactions (28) or  $\pi-\pi$  interactions which are used to attach cationic species to the nanocarbon surface (29).

*$\pi-\pi$  Interactions:* When an extended aromatic system (e.g., pyrene (Py)) is covalently attached to a POM, this hybrid molecule can be linked to nanocarbons through  $\pi-\pi$  stacking interactions (30,31). As described earlier, this approach, however, requires access to organo-functionalized POMs which in itself is still challenging (see Section 2.1).

*Layer-by-Layer (LbL) Assembly:* LbL assembly can be achieved by repeatedly stacking POMs and nanocarbons using wet-chemical deposition methods. By cationic modification of the nanocarbon, strong electrostatic interactions can be used to stack the alternating POM and nanocarbon layers (32). It should be noted that the LbL structures where the electronic interaction and dispersion of POM and nanocarbon might not be ideal. However, the simplicity and variability of this preparation method have made it one of the most commonly used techniques for the fabrication of energy conversion devices (33).

In addition to these well-known assembly methods for POM/nanocarbon composites, electro-assisted or photo-assisted assembly has also been used to fabricate POM/nanocarbon composite materials (34–36). For example, Wu *et al.* (35) have successfully fabricated  $\text{H}_4\text{SiW}_{12}\text{O}_{40}$  ( $\text{SiW}_{12}$ )/reduced graphene oxide (rGO) nanocomposites through a  $\text{SiW}_{12}$ -catalyzed electrochemical reduction. During the reduction process,  $\text{SiW}_{12}$  transfers the electrons from the electrode to graphene oxide (GO), leading to a deep reduction of GO. The strong adsorption effect between the  $\text{SiW}_{12}$  clusters and rGO nanosheets induces the spontaneous assembly of  $\text{SiW}_{12}$  on rGO in a uniformly dispersed state, forming a porous and powder-type nanocomposite. The high porosity makes the material interesting as a cathode material for lithium ion batteries and high specific capacity ( $275 \text{ mA h g}^{-1}$ , 1.7 times the capacity of pure  $\text{SiW}_{12}$ ) was found.



### 3. APPLICATIONS OF THE POM/NANOCARBON COMPOSITES

Based on their general redox activity, POMs linked to nanocarbons can be employed for a wide range of electron transfer and storage processes. Currently, studies on POM/nanocarbon composites have been focused on electrocatalysts, electrochemical energy storage, and environmental pollutant sensing. The following sections will review these fields and provide an outlook at the challenges and future perspectives of the area.

#### 3.1 Electrocatalysis

The high redox activity of POMs makes them ideal for the catalytic transfer of electrons to or from a substrate (i.e., reductive or oxidative electrocatalysis). This is particularly appealing for the development of

multielectron transfer reactions which are typically hampered by high overpotential leading to low overall conversion efficiencies. POMs are ideal candidates to address this challenge as they can be chemically modified with highly redox-active metals (e.g., Co, Mn, Ru) (37,38). Thus, technologically relevant electrocatalysts for the splitting of water into oxygen and hydrogen as well as for oxidation and reduction reactions in fuel cells become accessible (39).

### 3.1.1 Water Oxidation

Water oxidation is generally considered the more challenging half-reaction of the water-splitting process. Often, high overpotentials are observed, even when noble metals such as platinum (overpotential: ca. 0.8 V) are employed as electrodes (40). To overcome this obstacle, highly functionalized POM-based water oxidation catalysts (WOCs) functionalized with redox-active metals such as Co and Ru have been developed (41,42). In 2010, Bonchio *et al.* (20) electrostatically assembled a prototype POM-WOC,  $(M_{10}[Ru_4(H_2O)_4(\mu-O)_4(\mu-OH)_2(\gamma-SiW_{10}O_{36})_2]) (=M_{10}Ru_4(SiW_{10})_2, M = Cs^+, Li^+)$  on multiwalled carbon nanotubes (MWNTs) as the conductive substrate to form an active water oxidation electrocatalyst (Fig. 1). The nanostructured composites were used as anodes in a water-splitting device and water oxidation with overpotentials as low as 0.35 V and turnover frequencies (TOFs) approaching those of the cluster in homogeneous solution (up to  $300\text{ h}^{-1}$ ) (43). The example illustrates that the high reactivity of the molecular WOC can be retained, while immobilizing the cluster on the electrically conducting MWNTs enables integration into a technological device.

Following this initial breakthrough, Bonchio *et al.* (29) noted that the binding of POMs onto CNTs was still not optimal and therefore devised new covalent and noncovalent approaches to functionalize the CNTs with cations (Fig. 2). In one example, Py-based cationic species were linked to CNTs by  $\pi$ - $\pi$  interactions using an innovative, solvent-free microwave procedure, thereby eliminating hazardous volatile organic solvents and also accelerating reaction time and maximizing product yields. The cationic CNTs obtained showed high binding affinity for the anionic POM-WOCs and the formation of nanostructured composite surfaces was observed upon drop casting the composite on electrode surfaces, giving access to high surface area electrocatalysts.

Compared with carbon nanotubes, graphene is highly stable, conductive and has a large surface area to volume ratio, making it ideal for



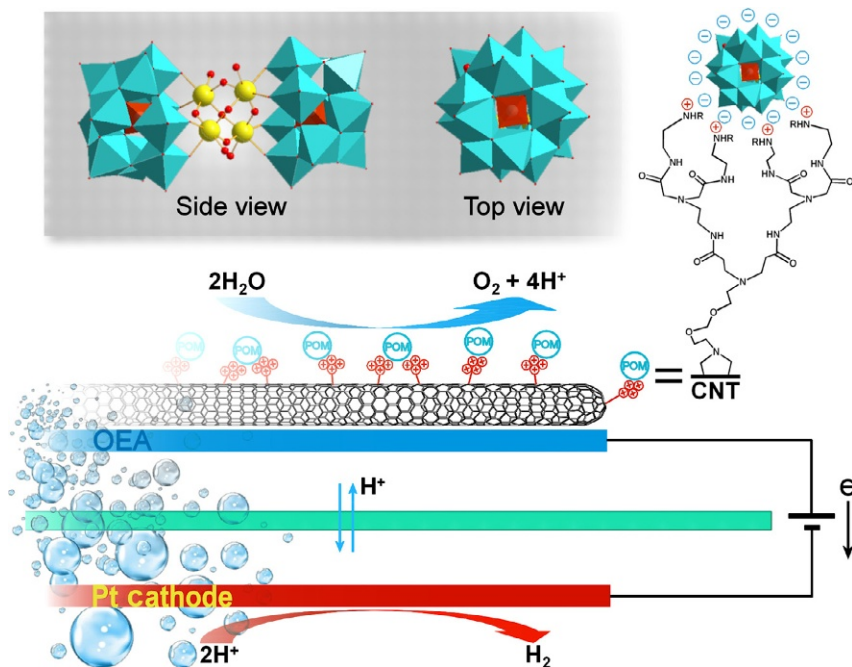


**Fig. 1** General scheme for a water-splitting electrocatalytic cell with the integrated nanostructured oxygen-evolving anodes (OEAs) based on with polyanionic ruthenium-containing POMs. (20) The POM used is  $[\text{Ru}_4(\text{H}_2\text{O})_4(\mu\text{-O})_4(\mu\text{-OH})_2(\gamma\text{-SiW}_{10}\text{O}_{36})_2]$ . Color scheme: blue, W; brown,  $\text{SiO}_4^{4-}$ ; yellow, Ru; red, O.

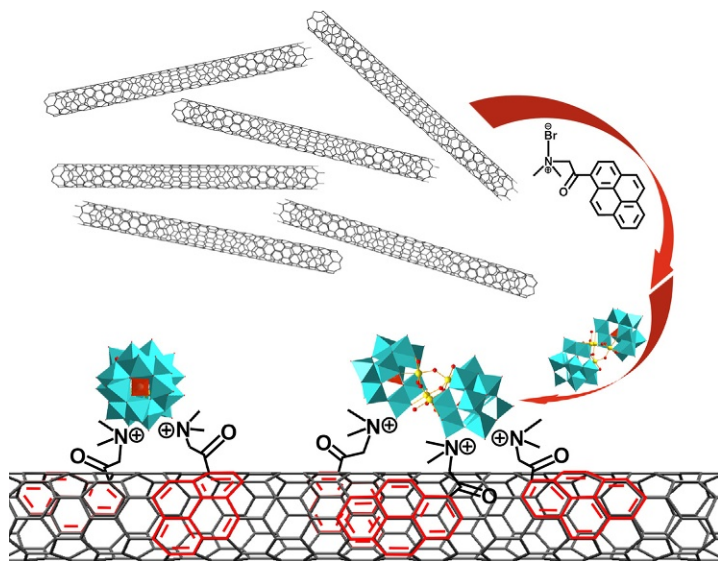


**Fig. 2** Schematic illustration of the CNT-bound POM catalyst: the CNTs are functionalized with an amphiphilic cationic pyrene derivative by  $\pi\text{-}\pi$  stacking; the anionic  $\text{Ru}_4(\text{SiW}_{10})_2$  is subsequently immobilized by electrostatic interactions (29).

electrochemical applications involving immobilized catalysts. Significant increases in electrocatalytic performance have been observed when graphene is used as the catalyst support (44). In 2013, Bonchio *et al.* (8) developed the a highly robust water oxidation electrocatalyst by combining their Ruthenium-based POM-WOC  $\text{Ru}_4(\text{SiW}_{10})_2$  with functionalized graphene. The graphene was covalently functionalized with organic hydrogen-bonding cations, allowing the anchoring of  $\text{Ru}_4(\text{SiW}_{10})_2$  by combination of electrostatic and hydrogen-bonding interactions (Fig. 3). The resulting hybrid material displays oxygen evolution at overpotentials as low as 300 mV at neutral pH with negligible loss of performance after 4 h testing. The authors suggested that the key aspect for the high catalytic activity and stability is the noninvasive and highly dispersed surface modification of the graphene platforms, which enables electron transport and accumulation across the extended  $\pi$ -bond network. In 2013, Hill *et al.* (45) studied a similar Ru-containing POMs/rGO composite using electrochemical analyses, in which graphene was electrochemically deposited on a glassy carbon or indium tin oxide (ITO) electrode from a GO solution/suspension. Subsequently, the POM anion was immobilized electrostatically onto graphene. The composite material showed excellent catalytic activity and high stability for the water oxidation reaction under neutral pH conditions, particularly in the presence of 1.0 M  $\text{Ca}(\text{NO}_3)_2$ , with a moderate overpotential of 0.35 V. These initial results show the great potential of the synergism between the Ru-containing POMs as catalysts and graphene as conductive support.

In summary, the conceptual viability of POM/CNT and POM/graphene composites for efficient water oxidation catalysis has been established. The next steps require the development of systems where the costly noble metal catalysts can be replaced by earth-abundant materials, while retaining high catalytic activity. One promising POM compound toward this end is a cobalt-based POM-WOC,  $[\text{Co}_4(\text{H}_2\text{O})_2(\text{PW}_9\text{O}_{34})_2]^{10-}$  (46). This highly active WOC ( $\text{TOF} > 5 \text{ s}^{-1}$ ) is based on earth-abundant metals only and when combined with nanocarbons could be a highly competitive heterogeneous electrocatalytic WOC.

### 3.1.2 Methanol Oxidation

The electrocatalytic oxidation of methanol using precious metal catalysts has attracted great interest as methanol is used as energy carrier

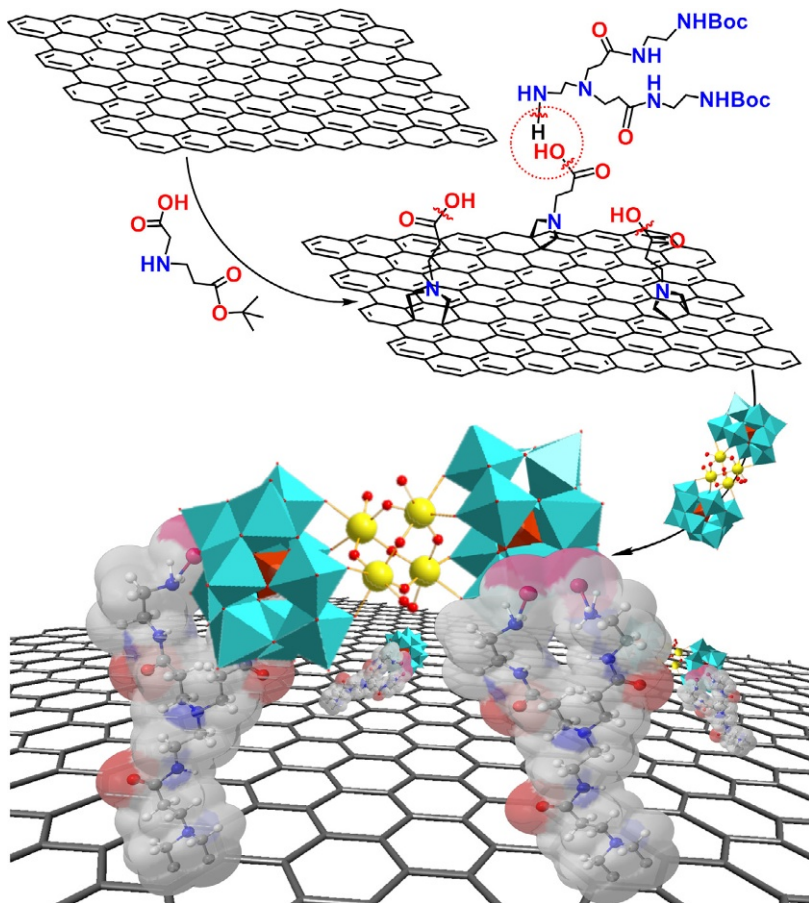


**Fig. 3** Synthesis of cationic graphene nanoplateforms supporting  $\text{Ru}_4(\text{SiW}_{10})_2$ . Graphene is covalently functionalized with organic cations, which then bind  $\text{Ru}_4(\text{SiW}_{10})_2$  through electrostatic interactions (8).

and electron donor in direct methanol fuel cells (DMFCs) (47). Current systems typically employ noble metals, often platinum, as the anode material for the electrocatalytic methanol oxidation in DMFCs. The electrooxidation of methanol on Pt is complicated by the formation of chemisorbed reaction intermediates such as CO, COH, and HCO which lead to catalyst poisoning (48). The incorporation of POMs into the electrode materials is one approach to address this: the clusters can be used as electrooxidation catalysts as well as electron and proton relays with remarkably chemical and thermal stability, allowing the long-term

use of POM-modified electrodes at temperatures  $>100^{\circ}\text{C}$ , thereby lowering the accumulation of catalyst poisons on the metal surface. However, it should be noted that most current systems still employ noble metal particles as active oxidation catalysts. Here, we will discuss the current catalytic systems for methanol oxidation electrodes and identify the most critical challenges which need to be addressed to advance the field.

In 2006, Chen *et al.* (49) firstly developed a new catalyst support based on CNTs modified with Keggin-type POMs  $\text{H}_3\text{PMo}_{12}\text{O}_{40}$  ( $\text{H}_3\text{PMo}_{12}$ ), and spontaneous and strong chemisorption of the POMs on the CNTs was observed. The composite was used as a redox-active support for highly dispersed Pt and Pt-Ru electrocatalysts which were deposited using electro-deposition methods. Catalytic tests showed that the combination of the unique electrical properties of the CNTs and the excellent redox properties and the high protonic conductivity of the POMs resulted in increased current densities, high specific activity, and improved cycle stability compared with the non-POM-modified systems. These results provided the first experimental evidence that POM-modified CNTs are viable catalyst supports for DMFCs (Fig. 4).

In 2008, Kim *et al.* (50) proposed a Pt@POMs/CNTs tricomponent composite for methanol oxidation which allows the reduction of the amount of noble metals used. Specifically, the POM anion of  $\text{PMo}_{12}\text{O}_{40}^{3-}$  was chemically impregnated into Pt-supported carbon nanotubes (Pt/CNT) catalysts via a colloidal method. This composite exhibited superior Pt-based mass activities with improved stability in the methanol oxidation, as compared with Pt/CNTs, Pt/C, and Pt-Ru/C. These findings demonstrate that similar tricomponent systems might be developed further and can give access to materials, where higher activity per gram of noble metal is observed, making the materials attractive for commercial developments. However, insight into the long-term performance of these systems is required compared with standard reference systems.

A different approach to optimize methanol oxidation performance is to increase the active surface area of the metal catalysts. This allows a reduction of the overall amount of noble metals employed. Guo *et al.* (51) developed the mixed metal composite Pt-Sn@ $\text{PMo}_{12}$ /CNTs using a microwave-heated polyol process. The authors reported that the presence of  $\text{PMo}_{12}$  resulted in homogeneously deposition of the Pt and Sn particles on the CNTs. The electrochemical surface area of the Pt-Sn@ $\text{PMo}_{12}$ /CNTs

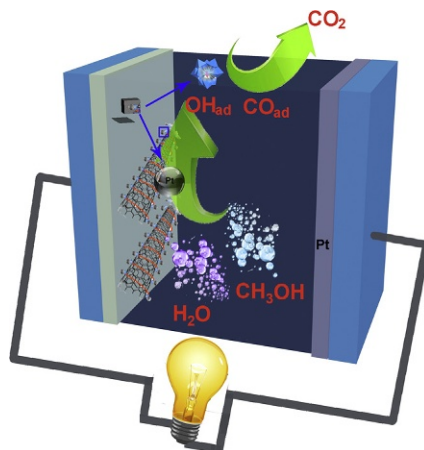


**Fig. 4** Electrochemical reactions in a direct methanol fuel cell functionalized with  $\text{PMo}_{12}$ -modified CNTs. The  $\text{PMo}_{12}$ /CNTs were used to support highly dispersed Pt and Pt-Ru electrocatalysts formed by electrodeposition. The presence of POMs was shown to effectively reduce catalyst poisoning and increased the catalytic performance (49).

catalyst ( $126.3 \text{ m}^2/\text{g}$ ) was 15.6% higher than that of Pt–Sn/CNTs catalyst, and it was more than three times higher than that of Pt/CNTs catalyst. This can be attributed to the smaller size and much improved uniform distribution of Pt particles, as well as the presence of  $\text{PMo}_{12}$  which might stabilize small Pt particles during their formation. In addition, it is suggested that  $\text{PMo}_{12}$  acts as cocatalyst for the methanol oxidation. The authors also showed that their system addresses the issue of catalyst poisoning since  $\text{PMo}_{12}$  and Sn promote the oxidation of carbon-based intermediates during the methanol electrooxidation and thereby enhance the electrocatalytic activity.

An innovative approach to deposit small Pt nanoparticles (NPs) on CNTs for methanol oxidation was reported (21), in which the in situ photochemically reduced Keggin cluster  $\text{H}_3\text{PW}_{12}\text{O}_{40}$  ( $=\text{H}_3\text{PW}_{12}$ ) as a redox mediator was applied to reduce the  $\text{Pt}^{\text{II}}$  precursor and to stabilize the NPs on the CNT surface (Fig. 5). The composite showed significantly increased electrocatalytic activity toward methanol oxidation compared with the traditional Pt/C catalyst and other reported Pt/CNT systems. In addition, the onset and peak potential for methanol oxidation by Pt@POM/CNT showed a shift to lower values relative to the Pt/C reference catalyst, indicating the enhanced oxidation performance of the composite. A similar photochemical assembly route was used by

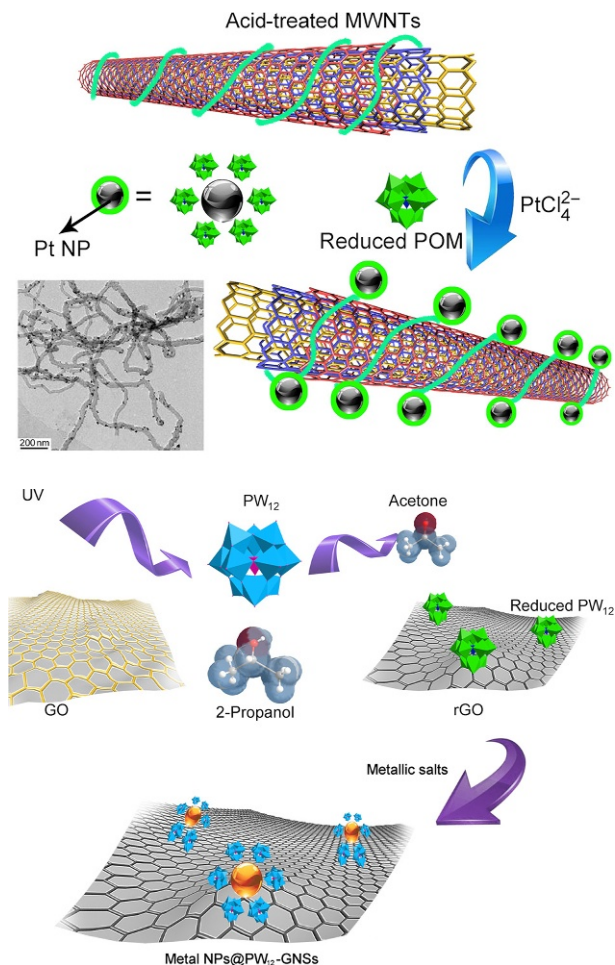


**Fig. 5** Top: Formation of Pt@POM/CNT composite electrocatalysts. The POM ( $\text{PW}_{12}$ ) is photochemically reduced using UV irradiation (electron donor: 2-propanol); the reduced  $\text{PW}_{12}$  is combined with MWNTs and  $\text{H}_2\text{PtCl}_4$ , giving the Pt@POM/CNT composite. Inset: TEM image of Pt@POM/CNT composite (21). Bottom: Preparation of the tricomponent metal NPs@POM/GNs composites. (1) Photoreduction of  $\text{PW}_{12}$  by 2-propanol under UV irradiation; (2) GO reduction by reduced  $\text{PW}_{12}$ , giving  $\text{PW}_{12}/\text{rGO}$  composites; (3) photoreduction of the  $\text{PW}_{12}/\text{rGO}$  composites by 2-propanol, giving reduced  $\text{PW}_{12}/\text{rGO}$ ; (4) reduction of noble metal salts by the reduced  $\text{PW}_{12}/\text{rGO}$ , giving noble metal NPs@ $\text{PW}_{12}/\text{GNS}$  (22). Top figure is reproduced from Li, S.; Yu, X.; Zhang, G.; Ma, Y.; Yao, J.; de Oliveira, P. Carbon **2011**, 49, 1906–1911 with permission of Elsevier Publishers.

Zhang *et al.* (22) to deposit Pt or Pd NPs on GO (Fig. 5) using  $PW_{12}$  to photochemically reduce the  $Pt^{II}$  or  $Pd^{II}$  precursors as well as the GO and simultaneously encapsulate and bind the NPs to the rGO surface. The composites showed significantly increased electrocatalytic methanol and formic acid oxidation activity compared with traditional carbon black-based catalysts. The studies highlight the multifunctionality offered by the POM as reductant, encapsulating agent and cocatalyst which is associated with its intrinsic redox activity.

Jiang *et al.* (52) focused on new approaches to electrostatically stabilize POM anions on cationic CNTs using self-assembly. To this end, CNTs functionalized with cationic, protonated chitosan (CS) were used to strongly bind the Keggin anions  $PMo_{12}$  and  $PW_{12}$  (Fig. 6). The procedure introduces homogenous surface functional groups with no detrimental effect on the CNT structure and can be carried out at room temperature without use of corrosive acids. Deposition of Pt-Ru NPs on these composites using an impregnation route gave particles with uniform spatial distribution and

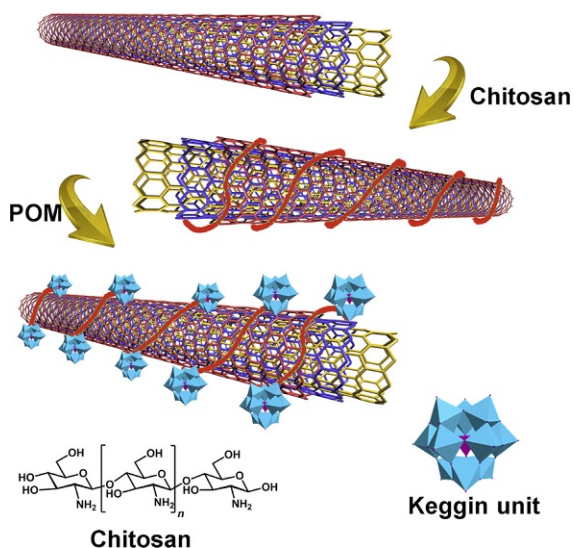


**Fig. 6** Schematic diagram of the functionalization of CNTs with chitosan and Keggin-type POMs ( $PMo_{12}$  and  $PW_{12}$ ). The combination of the cationic chitosan (schematically shown as a red line) and the anionic Keggin units are achieved through electrostatic interactions (52).

smaller particle size compared with materials prepared using conventional procedures. Electrochemical methanol oxidation tests showed a shift of the oxidation waves to more negative potential, and higher current densities for both Pt-Ru@PMO<sub>12</sub>/CS/CNTs and Pt-Ru@PW<sub>12</sub>/CS/CNTs compared with standard reference systems. Yuan *et al.* (53) investigated the Pt-Ru@PMO<sub>12</sub>/MWNT and Pt@PMO<sub>12</sub>/MWNT nanocomposites as methanol oxidation electrocatalysts, and the results indicated that the presence of the POM induces smaller size and higher dispersion of the Pt-Ru NPs. In addition, the composites showed high CO tolerance, making the materials interesting for technological deployment under industrial conditions.

In summary, current studies demonstrate that POM-modified nanocarbon electrodes can provide multiple benefits to modern methanol oxidation electrodes, particularly in the fields of metal NP deposition and stabilization, and reduced usage of noble metals. However, one major challenge in the fields is still the development of low overpotential electrodes for methanol oxidation which do not use noble metal catalysts. Therefore, access to highly active POM-based methanol oxidation catalysts which could act on a molecularly dispersed level might provide a facile and promising route to earth-abundant, technologically relevant materials. As such, many of the concepts described earlier in the field of POM/nanocarbon water oxidation catalysis might indeed be transferred to this related application.

### 3.1.3 Oxygen Reduction

Besides methanol oxidation, fuel cells also require efficient oxygen reduction catalysts to overcome the issues related with excessive overpotentials (54,55). Typically, noble metals such as Pt and Pd are the catalyst of choice despite their high cost (56,57). Thus, considerable efforts are underway to replace today's catalysts with earth-abundant materials. In this section, a series of POM/noble metal/nanocarbon composites as oxygen reduction catalysts will be critically discussed.

In 2010, Jiang *et al.* (58) introduced a novel Pd@POMs/PDDA/MWNT electrocatalyst (Fig. 7), with high potential as an effective non-Pt catalyst for the oxygen reduction reaction (ORR) in fuel cells. To this end, MWNTs were functionalized with poly(diallyldimethylammonium chloride) (PDDA), forming positively charged PDDA-MWNTs. POMs (PW<sub>12</sub>) were electrostatically attached to the MWNTs followed by reductive Pd deposition. The composite material possesses a much higher amount of metallic Pd compared with Pd/acid-treated MWNTs, and it would



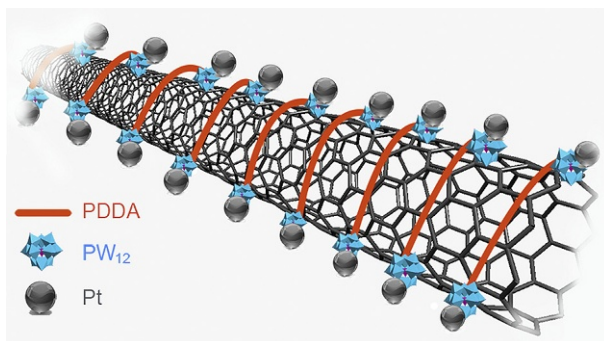


**Fig. 7** Self-assembly of Keggin-type POMs ( $PW_{12}$ ) on PDDA-functionalized MWNTs via electrostatic interactions and subsequent deposition of Pd NPs on POMs assembled PDDA–MWNTs by reductive chemical deposition (58).

facilitate the desorption of  $O_{ads}$ ; this is a critical parameter to maximize electrode performance, as limited oxygen desorption and bubble formation on the electrode can significantly increase the overpotential (59).

Initial steps were taken to replace the traditional noble metal particles for the ORR by cheaper metals. Zhang *et al.* (60) reported a facile, one-pot synthesis of Ag-NP-decorated CNTs by reaction of the acidized MWNTs with  $AgNO_3$  using in situ photo-reduced Keggin anions as reducing agent and bridging molecules, showing that cheaper silver NPs can be used as active reduction sites in the ORR. The composites showed a high electrocatalytic ORR activity due to the synergistic effect of Ag NPs and CNTs. For the POM-functionalized system, significantly increased ORR current densities were observed compared with nonfunctionalized CNTs.

The ORR activity of Ag NPs was substantiated in 2013 when a 2D-Ag nanonets (NNs) functionalized graphene was reported as a substitution for Pt catalysts for the ORR. The group used  $H_7[\beta-PMo(V)_4Mo(VI)_8O_{40}]$  as the reducing agent (Fig. 8) to deposit an Ag nanostructure on graphene (61). The as-prepared composites showed high electrocatalytic ORR activity associated with the high catalytic activity of the Ag NNs, and the excellent electron transfer properties of graphene nanosheets (GNs) reinforced by the presence of residual POM units and fragments arising from their decomposition. Compared with Pt/C catalyst, these composites are cheaper and more stable and significantly lower activity loss over time was reported. The results showed that oxygen reduction electrodes can be developed based on economically viable and technologically relevant metals when combined with POMs.

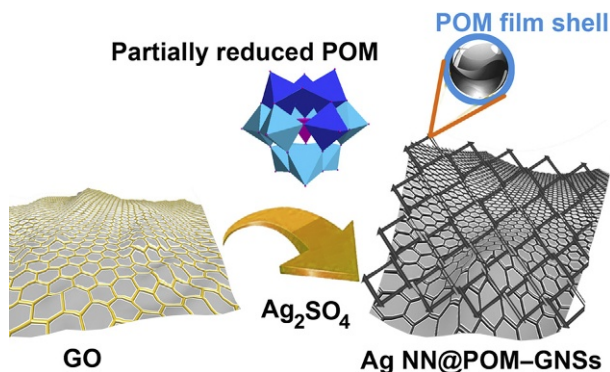


**Fig. 8** Polyoxometalate-mediated large-scale synthesis of 2D Ag NN@POM/GNs composites using the mixed-valent Keggin-type POM of  $H_7[\beta\text{-PMo(V)}_4\text{Mo(VI)}_8\text{O}_{40}]$  (61).

The Pt@POM/PDDA/MWNTs system discussed earlier is not limited to the ORR but can also be used for formic acid oxidation in fuel cells (62), in which the Pd NPs supported on POM/PDDA/MWNT show homogeneous dispersion and narrow particle size distribution. It is suggested that the presence of the POMs inhibits the agglomeration of Pd NPs. In comparison, the acid-treated MWNTs feature randomly located defects, resulting in a relatively poor dispersion and aggregation of Pd NPs.

Shanmugam *et al.* (63) showed that a  $[\text{PMo}_{12}\text{O}_{40}]^{3-}/\text{rGO}$  is a superior catalyst for nitrite electrooxidation compared with the two components alone. A 20-fold increase in activity compared with pure rGOs was observed. It is suggested that  $\text{PMo}_{12}$  assists the oxidation reaction of the graphene through the high electronegativity of metal-oxygen, resulting in the formation of the defect sites on the GNs (Fig. 9). The UV-vis and Raman spectroscopy revealed strong electron transfer interactions between the graphene sheets and POMs induced at the graphene defect sites. This led to a modification of the band gap energy and resulted in a more robust catalyst material.

These initial examples demonstrate that POM-modified nanocarbons are highly robust and versatile systems which can be employed in a wide range of technologically relevant electrocatalytic reactions. Future applications in various fields can be targeted by specific chemical modification of the POM reactivity.

### 3.2 Energy Storage

Electrochemical energy storage is currently one of the fastest growing fields (64,65). Most promising systems for electrochemical energy storage are

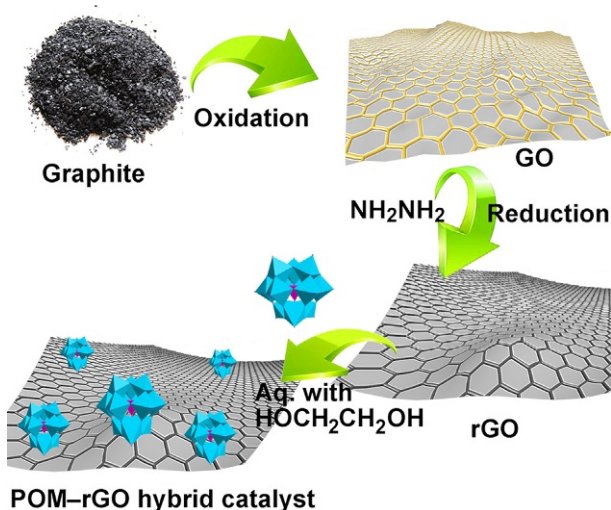


**Fig. 9** Schematic representation of the fabrication of POM-rGO composites (63). (1) Oxidation of graphite using a modified Hummer method; (2) reduction of GO by hydrazine hydrate, giving rise to rGO; (3) functionalization of the rGO with Keggin-type POMs under mild conditions giving the POM-rGO composite.

(1) batteries, where energy storage and release are based on chemical redox reactions and (2) supercapacitors where energy storage is based on a combination of electrostatic charge separation (double-layer capacitance) and electrochemical charge separation (pseudocapacitance) (66,67).

Owing to their high intrinsic electron storage capacity, their chemical tunability and high stability, POMs are ideal candidates for electrochemical energy storage (68–70). However, as POMs are molecular units, electronic conductivity between clusters is negligible, ideally each molecular cluster needs to be electrically linked to a conductive substrate in order to achieve high electronic conductivity (71). Thus, combining redox-active POMs as electron storage sites with nanostructured carbon materials as electrical conductors with high surface area is a promising approach for the design of high-capacity energy storage systems. This section summarizes recent progress in the design of POMs/CNTs or POMs/graphene composites as electrode materials for lithium ion batteries and supercapacitors and emphasizes key development areas, where POM-based research is urgently required.

### 3.2.1 Lithium Ion Batteries

Lithium ion batteries are at the forefront of battery research due to their high specific energy density. Recently, the first step has been taken to incorporate POMs in these systems, in which the POMs are employed as electron

storage sites, as well as electron transfer mediators. Thus far, studies have been focused mainly on Keggin and/or Dawson-type clusters hybridized with CNTs or graphene.

Awaga *et al.* (28,69,70) have introduced the concept of molecular cluster batteries (MCBs) for electrochemical energy storage. Their initial studies used a nanocomposite of  $(n\text{-Bu}_4\text{N})_3[\text{PMo}_{12}\text{O}_{40}]/\text{SWNTs}$ . Attachment of the cluster to the single-walled carbon nanotubes (SWNTs) was achieved by electrostatic interactions. Molecular dispersion of the POM clusters was achieved, resulting in smooth electron transfer and fast lithium ion diffusion (Fig. 10). The material was used to assemble a cathode and a specific capacity of up to  $320 \text{ mA h g}^{-1}$  was achieved. This compares favorably with a reference system of the pure identical cluster, where a specific capacity of  $260 \text{ mA h g}^{-1}$  was observed, showing the effectiveness of the electrical “wiring” of the POM toward the SWNTs.

Recently, Song *et al.* (30) developed a novel method to modify SWNTs with organo-functionalized  $[\text{SiW}_{11}\text{O}_{39}]^{7-}$  ( $\text{SiW}_{11}$ ) clusters. To this end, Py moieties were covalently attached to the cluster by silanol linkages. The functionalized clusters showed high affinity to bind to SWNT through  $\pi\text{-}\pi$  stacking, allowing the assembly of SWNT/Py- $\text{SiW}_{11}$  nanocomposite

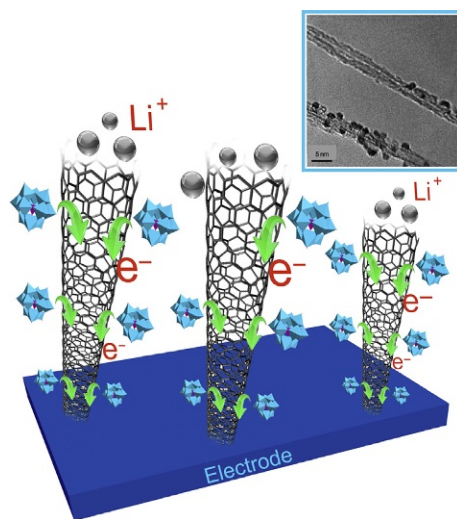


**Fig. 10** Schematic illustration of a molecular cluster battery (MCB) based on POM/SWNTs composites. Well-dispersed POM clusters are attached to CNTs via electrostatic interactions to improve electronic conductivity and ion diffusion. *Inset:* TEM image of POM/SWNT hybrid materials (28). *Reproduced from* Kawasaki, N.; Wang, H.; Nakanishi, R.; Hamanaka, S.; Kitaura, R.; Shinohara, H.; Yokoyama, T.; Yoshikawa, H.; Awaga, K. *Angew. Chem. Int. Ed.* **2011**, *50*, 3471–3474 with permission of John Wiley and Sons Publishers.

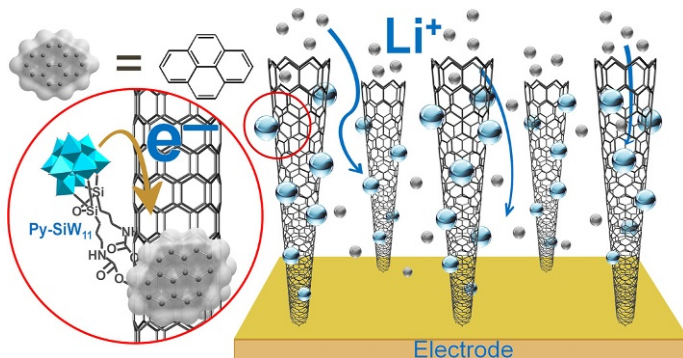


**Fig. 11** Schematic illustration of the Py-PW<sub>11</sub>/SWNTs nanocomposite as anode material covalently functionalized POM clusters were attached to the SWNTs through  $\pi$ - $\pi$  stacking interactions (30).

materials (Fig. 11). When utilized as the anode material, the composite exhibited excellent performance with an initial discharge capacity of  $1570 \text{ mA h g}^{-1}$ . Over longer periods (up to 100 cycles), high discharge capacities of  $580 \text{ mA h g}^{-1}$  were maintained, significantly enhancing the capacity of nonfunctionalized CNTs which are in the region of 400 and  $460 \text{ mA h g}^{-1}$ . To further expand this research, Py-functionalized Anderson-type cluster  $[\text{MnMo}_6\text{O}_{24}]^{3-}$  ( $\text{MnMo}_6$ ) was used to modify CNTs, giving rise to a Py-MnMo<sub>6</sub>/CNTs nanocomposite through  $\pi$ - $\pi$  interactions (31). The nanocomposite, as anode material, exhibited an initial discharge capacity of  $1898.5 \text{ mA h g}^{-1}$  and a high discharge capacity of  $665.3 \text{ mA h g}^{-1}$  for up to 100 cycles. AC electrochemical impedance spectroscopy studies revealed that a relatively lower solid electrolyte interphase (SEI) film resistance and charge transfer resistance were responsible for the electrochemical enhancement of the nanocomposite when compared with the pure components and their physical mixture (31).

Despite various noncovalent linkage modes for preparing POM/nanocarbon composites, one intractable problem is desorption of POMs during electrochemical measurement. Also, the bulky organic linkages between POMs and nanocarbons usually hamper the electron transfer, thus causing inefficient electronic connections. Song *et al.* (26) proposed a new method to overcome this obstacle by using direct covalent bonding. The amino-functionalized Keggin-type cluster  $[\text{SiW}_{11}\text{O}_{40}-(\text{SiCH}_2\text{CH}_2\text{CH}_2\text{NH}_2)_2]^{4-}$  ( $\text{SiW}_{11}\text{-NH}_2$ ) was covalently grafting onto sidewall of oxidized CNTs through the formation of strong amide bonds. By introducing more sidewall defects on CNTs via covalent modification,

the resulting CNTs/SiW<sub>11</sub>-NH<sub>2</sub> composites provided more pathways for Li<sup>+</sup> transfer and showed excellent electrochemical performance with high discharge capacity of 650 mA h g<sup>-1</sup> as anode material. The electrode performance was further improved when Anderson cluster [MnMo<sub>6</sub>O<sub>24</sub>-{(CH<sub>2</sub>)<sub>3</sub>CNH<sub>2</sub>}<sub>2</sub>]<sup>3-</sup> was used instead (27). The discharge capacity of the corresponding nanocomposites reached to 932 mA h g<sup>-1</sup> with high stability up to 100 cycles. The better performance of Anderson-type cluster could be attributed to its fast Li<sup>+</sup> insertion/extraction during charge/discharge process and its structural stability (27). However, as only a few POM anions thus far can be organically functionalized with a pendant amine group, the application of covalent attachment of POMs onto CNTs is limited.

Focusing on electrical “wiring” redox-active POMs onto conductive CNTs to achieve high electric performance of POM/CNTs nanocomposite, Song *et al.* (72) recently developed an innovative approach to periodically functionalize CNTs with POM nanocrystals. By using ultrasonication during the fabrication procedure, crystals of POMs with tunable size and shape can be regularly deposited onto CNTs giving rise to a highly stable anode material with superior electrochemical performance (Fig. 12). The nanostructure and chemical features of the POM/CNTs composite can be finely controlled over the ultrasonication intensity as well as the chemical ingredients of POMs. This novel approach is considered to be able to open new avenues for the bottom-up construction of nanopatterned POM/CNTs composite.

A different approach to maximize the electronic interactions between POM and nanocarbons was introduced by Paek *et al.* (73). The group used the ability of POMs to pillar sheets of GO to fabricate a highly ordered nanostructure composed of layered GO and Keggin-type aluminum POMs (Al<sub>13</sub>). Battery tests show that Al<sub>13</sub>-intercalated GO exhibits a significantly increased reversible capacity, compared with that of the pristine GO, highlighting that cluster-intercalated GOs stacks are promising materials for high-capacity electrodes. Future work using tungstate or molybdate POMs as highly redox-active pillaring agent might result in further improvement of the electrode capacity.

In 2010, Bubeck *et al.* (34) developed a green method to reduce GOs via a ultraviolet (UV)-irradiated photoreduction process. H<sub>3</sub>PW<sub>12</sub> was used as photocatalyst (Fig. 13) and also acted as an anionic surface active molecule, which increased the rGOs dispersibility in water by attaching to the surface of rGO. The group found that the conductivity of the POM-modified rGO can reach as high as 400 S m<sup>-1</sup>, compared with that of hydrazine-reduced

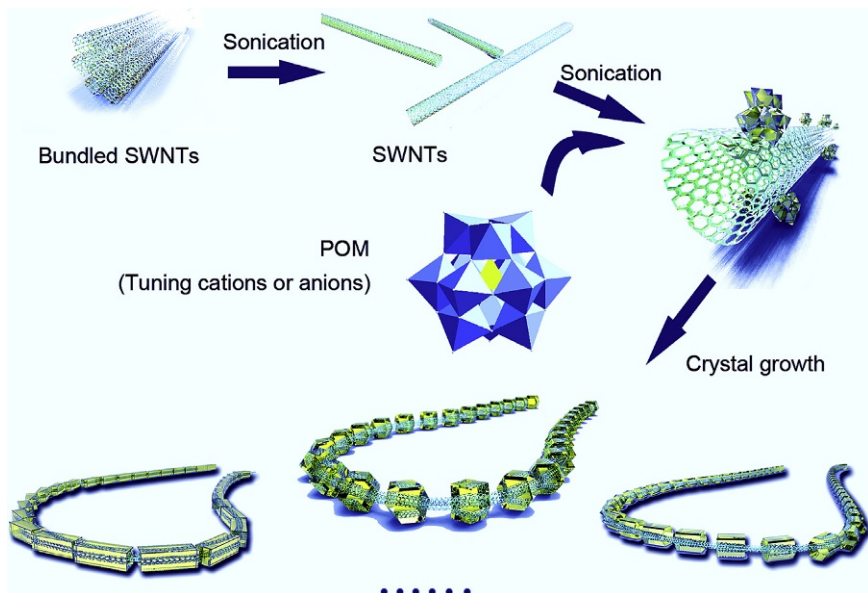


**Fig. 12** Schematic illustration of the ultrasonication-driven periodic patterning of POM nanocrystals on CNTs for lithium ion batteries (72). Reproduced from Hu, J.; Ji, Y.; Chen, W.; Streb, C.; Song, Y.-F. *Energy Environ. Sci.* **2016**, 9, 1095–1101 with permission of Royal Society of Chemistry Publishers.

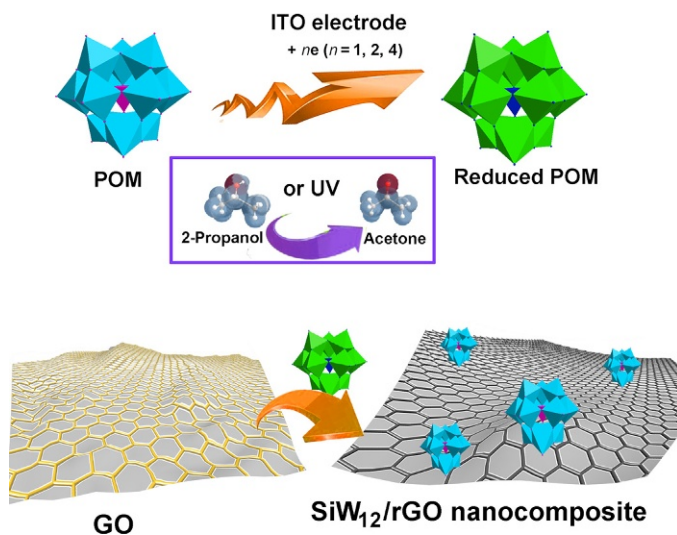


**Fig. 13** Electrochemical or photochemical reduction-assisted assembly of  $\text{SiW}_{12}/\text{rGO}$  nanocomposites (34,35). Electrochemical or photochemical reduction gives the reduced  $\text{SiW}_{12}$  cluster. Reaction with GO leads to the  $\text{SiW}_{12}/\text{rGO}$  nanocomposite, where GO is reduced in situ by the cluster.

GOs which is in the region of  $3 \times 10^{-6} \text{ S m}^{-1}$  only. The results demonstrate that the POM-assisted photoreduction method significantly increases electronic conjugation between GO sheets, resulting in dramatically higher electronic conductivity.

The initial results on POM-based battery electrodes highlight the need for highly redox-active molecular materials with chemical redox-tunability and high cycling stability. Future work requires the interdisciplinary collaboration between POM chemists, materials chemists, and battery researchers to optimize the components employed, to enable efficient electron transfer between components by enhancing their electronic linkage, and to develop strategies for device integration.

### 3.2.2 Supercapacitors

Carbon-based materials have been widely studied as electrode materials for supercapacitors, giving rise to devices with relatively low energy density (74,75). For automotive applications, the specific energy density needs to be increased. One approach is the embedding of materials capable of undergoing reversible multielectron transfer redox processes. The current gold-standard for supercapacitors is  $\text{RuO}_2$  as pseudocapacitive material, because of its fast and reversible multielectron transfer reactions with overlapping peak potentials (76). Recently, POMs have been suggested as chemically and economically viable replacements for the noble metal oxide due their unique redox chemistry.

Ground breaking studies by Gómez-Romero *et al.* (77) used Cs- $\text{PMo}_{12}$ /CNTs hybrid materials obtained by immobilizing Cs-containing POM anions on cationic, chitosan functionalized CNTs as composite electrodes in symmetric supercapacitors. The studies showed that the composites feature high capacitance (up to 285 F/g at  $I=200 \text{ mA/g}$ ), and good stability was observed over 500 charge–discharge cycles, suggesting that further development of this device configuration is promising.

Lian *et al.* (32,78) demonstrated that facile LbL assembly techniques can be used to get access to supercapacitors. And they used a three-layer LbL assembly based on MWNTs, PDDA, and two types of pseudocapacitive POMs,  $\text{SiMo}_{12}\text{O}_{40}^{4-}$  ( $\text{SiMo}_{12}$ ) and  $\text{PMo}_{12}\text{O}_{40}^{3-}$  ( $\text{PMo}_{12}$ ) (Fig. 14). The resultant composites exhibited continuous overlapping oxidation/reduction reactions and achieved an up to fourfold increase in specific capacitance when compared with the double-layer capacitance of pure MWNTs. The group subsequently extended their research by adding  $\text{PMo}_{10}\text{V}_2^{5-}$  ( $\text{PMo}_{10}\text{V}_2$ ) into the LbL deposition (79). The results revealed that a



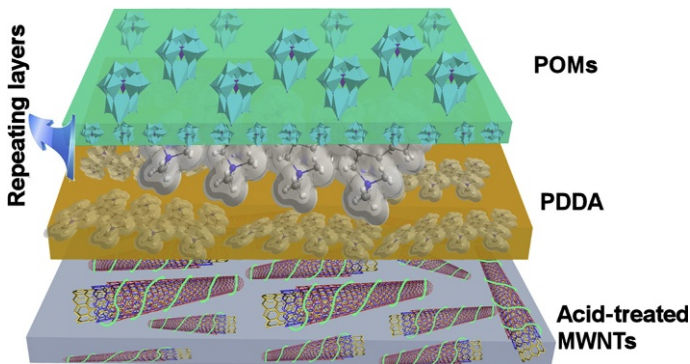


**Fig. 14** Schematic representation of the three-layer LbL deposition using MWNTs, PDDA, and POM (32). MWNTs are prepared as a thin film and acidized using nitric acid. A second layer of PDDA is dip-coated onto the MWNT film. Then, the POM layer is dip-coated onto the cationic PDDA film, giving the final composite.

dual-layer coating by  $\text{PMo}_{12}$  and  $\text{PMo}_{10}\text{V}_2$  on MWNTs showed a collective contribution of both active layers, increasing not only charge storage capacity but also the voltage window.

The LbL supercapacitor assembly was further extended by Kulesza *et al.* (80) who prepared a composite by depositing the Dawson POM  $[\text{P}_2\text{W}_{17}\text{VO}_{62}]^{8-}$  onto MWNTs. The materials feature a high specific capacitance parameter of  $82 \text{ F g}^{-1}$  (at the charging/discharging current of  $200 \text{ mA g}^{-1}$ ) compared with bare CNTs, where the specific capacitance under identical conditions was only  $50 \text{ F g}^{-1}$ . The results confirmed that the LbL technique is simple and effective for developing thin, nanoscale POM/CNT multilayers coatings to enhance the capacitance without sacrificing electric conductivity. Further, the studies show that significant changes in supercapacitor performance can be achieved by chemical modification of the POM components, highlighting the urgent need for more detailed studies, where other, nonprototype POMs are used in device fabrication.

### 3.2.3 Other Electrochemical Devices

The versatility of LbL-assembled POM/nanocarbon devices was further exploited by Müllen *et al.* (36) who reported that GO nanosheets and  $\text{H}_3\text{PW}_{12}\text{O}_{40}$  were assembled into multilayers films via electrostatic LbL assembly. Under UV irradiation, a POM-based photoreduction of GOs to rGOs was observed. The obtained films were used to fabricate field effect

transistors, which exhibited typical ambipolar features and good transport properties for both holes and electrons. The on/off ratios and the charge carrier mobility of the transistors depend on the number of deposited layers and can be easily controlled. Furthermore, efficient microelectrodes for photo-detector devices could be produced using photomasks to form conductive rGO patterns within the composite films.

A similar LbL approach allowed Xu *et al.* (81) to fabricate electrochromic nanocomposite film containing  $[P_2W_{18}O_{62}]^{6-}$ , CNTs, and chitosan. The electrochromic properties of the composite were improved by CNT incorporation, resulting in superior electrochromic performance compared to the nonhybridized reference, suggesting that the composite can offer longer operational lifetimes when used in electrochromic devices.

In summary, this section illustrates the broad versatility and wide application range of POM-modified nanocarbon materials. However, one striking feature of the results described is the fact that research is almost exclusively focused on the prototype Keggin and Dawson anions. Therefore, there is a tremendous opportunity for the use of the large number of other accessible POM anions which could easily be accessed and deposited on nanocarbons by close collaboration between researchers from both fields. As such, it can be envisaged that the coming years will provide significant leaps forward in developing materials, where selective chemical modification of the POMs is used to target specific redox activity or catalytic activity in a composite material.

### 3.3 Sensors and Environmental Pollutants

The ability of POMs to undergo reversible multielectron redox processes makes them interesting for amperometric sensor applications. Particularly, they can be used for the detection of redox-active industrial and agricultural pollutants such as nitrate (82), bromate (83), chlorate (84), iodate (85), and hydrogen peroxide (86–88). To read out the sensing information and to maximize amperometric response, the POMs need to be anchored or immobilized on conductive substrates while at the same time maintain molecular dispersion to reach low detection limits. Therefore, CNTs and graphene are ideal substrates for this purpose (89–91). Herein, a series of POM–CNTs and POM–graphene composites as sensor electrodes or devices are discussed, their limitations are highlighted and future research directions are proposed.

### 3.3.1 Hydrogen Peroxide Sensors

Hydrogen peroxide ( $\text{H}_2\text{O}_2$ ) is industrially used as antibacterial and sterilizing agent (92). In addition, peroxides are released from many other industrial processes, and their environmental release needs to be strictly controlled (93). In 2009, Salimi *et al.* (94) developed a three component electrochemical peroxide sensor. A simple procedure gave access to glassy carbon (GC) electrodes modified with SWNTs,  $\alpha - \text{SiMo}_{12}\text{O}_{40}^{4-}$  and the copper complex  $[\text{Cu}(\text{bpy})_2]\text{Br}_2$ . The copper complex and POM were irreversibly and strongly adsorbed onto GC electrode. Compared with a non-POM-functionalized reference electrode (based on a GC electrode modified with SWNTs and  $[\text{Cu}(\text{bpy})_2]\text{Br}_2$  only), the POM-modified system showed stable voltammetric response and gave excellent electrocatalytic activity toward  $\text{H}_2\text{O}_2$  reduction (bromate reduction was also reported) at low overpotential. The system was able to detect nanomolar concentrations of  $\text{H}_2\text{O}_2$  and bromate, highlighting the sensitivity which is associated with the highly dispersed POMs on the nanostructured conductive substrate.

Recently, Gorton *et al.* (95) assembled a robust and stable film composed of the ionic liquid  $[\text{C}_8\text{Py}][\text{PF}_6]$  and  $\text{PMo}_{12}$  on MWNT-modified GC electrodes using a simple dip-coating technique. Efficient  $\text{H}_2\text{O}_2$  and iodate detection at low overpotentials was found together with low detection limits, high sensitivity, short response time ( $< 2$  s) and satisfactory linear concentration range, illustrating that in principle the sensors can be assembled in the field and used for in situ pollutant benefits as their high conductivity presumably contributes to the electron transfer between POM and MWNT substrate.

### 3.3.2 Iodate and Bromate Sensors

Iodate and bromate are environmental pollutants and suspected carcinogen formed, e.g., in drinking water upon ozone treatment (96). In situ detection is therefore of high industrial interest. The problem was addressed by Chen *et al.* (83) who developed an amperometric bromate sensor based on a MWNTs/ $\text{PMo}_{12}$  composite film. The system showed a low detection limit of  $0.5 \mu\text{M}$ , high sensitivity of  $760.9 \mu\text{A mM}^{-1} \text{cm}^{-2}$ , short response times of less than 2 s, and wide linear range from  $5 \mu\text{M}$  to 15 mM. This research was expanded by Dong *et al.* (97) who proposed and developed a series of carbon nanotube paste (CNTP) electrodes based on purified MWNTs and methyl silicone oil. Keggin and Dawson POM anions were then assembled on the CNTP electrode surface using direct and indirect methods. The most

successful system was based on the Dawson-anion  $P_2Mo_{18}$  for which effective electrocatalytic reduction of bromate and iodate was observed. In an extension of this work, multilayer films of  $(P_2Mo_{18}/PDDA)_n$  were assembled on CNTP electrodes using the LbL technique and comparative studies showed higher electrocatalytic activity for the LbL-assembled composites compared with the composite materials that fabricated by the direct electrostatic assembly.

Work on Dawson-modified sensors was further expanded by Xu *et al.* (98) who reported a novel chemically modified electrode, where CNTs were dispersed in cationic chitosan films, which were used to electrostatically immobilize Dawson anions  $P_2W_{18}$ . Electrochemical studies demonstrated that the  $P_2W_{18}/CNT/chitosan$  electrode exhibits fast response and good electrocatalytic activity for the reduction of peroxodisulfate and iodate anions in acidic aqueous solution, and it was reported that the sensor works under acidic conditions also, broadening its applicability under industrial conditions.

In summary, the studies illustrate that the choice of cluster anion as well as assembly method is crucial and emphasizes that future electrode development needs to be driven by interdisciplinary research, ranging from molecular materials design to nano- and microstructure of the composites. In addition, it should be briefly noted that POM/nanocarbon composites have been used for the detection of a large number of other organic and inorganic analytes, including antimony (99), sulfite (100), glucose (101), dopamine (102), and ascorbic acid (103).

### 3.3.3 Future Developments and Applications

Future development of the POM/nanocarbon materials rests on several pillars. One obvious and highly promising approach is to investigate nonprototype POMs, where novel reactivity, higher stability, and different reactivity can be expected. To this end, an interdisciplinary approach is urgently required where target systems (i.e., electrocatalytic substrates, industrial pollutants, etc.) can be determined and POMs that can interact with these targets can be identified and combined with nanocarbons.

The importance of the electrode assembly has been discussed in several examples. One highly innovative approach to the POM/nanocarbon-layered electrodes which might be used for large scale has recently been presented by Shen *et al.* (104), who reported a combined

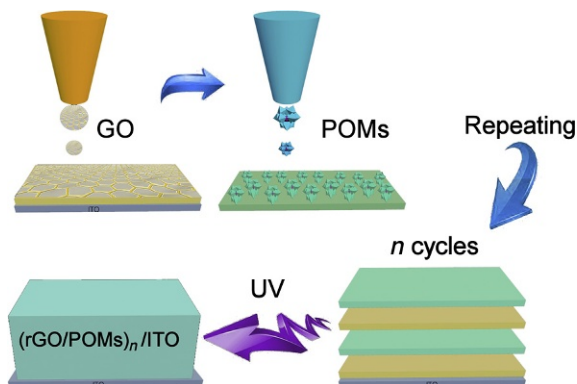


**Fig. 15** Scheme of  $(\text{rGO}/\text{POM})_n$  multilayer film production by LbL fabrication using inkjet printing (104). Repeated printing of GO and POM layers gives access to multilayer assemblies. Photoreduction of the film using UV irradiation gives the  $(\text{rGO}/\text{POM})_n$  multilayer film.

LbL-inkjet-printing approach to assemble layered  $\text{PW}_{12}/\text{rGO}$  composites (Fig. 15). The composite thin film showed linear, uniform, and regular LbL growth. Under UV irradiation, a POM-driven photoreduction led to the conversion of GO to rGO, and the materials were used as highly responsive dopamine sensors.

A further promising field is the development of photoactive electrodes for use in photocatalysis or photovoltaics (105). Initial work by Zhang *et al.* (106) showed the versatility of the approach, in which the authors assembled an Au NPs@POMs/CNTs tricomponent composite (Fig. 16). And the composite material was employed in photooxidative test reactions and showed significant enhancement on the photocatalytic degradation of Rhodamine B under visible light irradiation. The mechanism proposed is a visible light-induced electron transfer from Au NPs to CNTs resulting in oxidative degradation of organic pollutants. In contrast, significantly lower activity was observed for the bicomponent composite Au NPs@POMs, where fast charge recombination was observed due to the close proximity between POM and Au NPs. In the tricomponent Au NPs@POMs/CNTs composite, the charges can be transferred from the Au NPs to the CNTs, resulting in a remarkable synergistic enhancement of the photocatalytic activity. These initial studies clearly demonstrate the potential of using POMs not only as homogeneous photocatalysts but also as a component in composite materials with enhanced charge transfer properties.

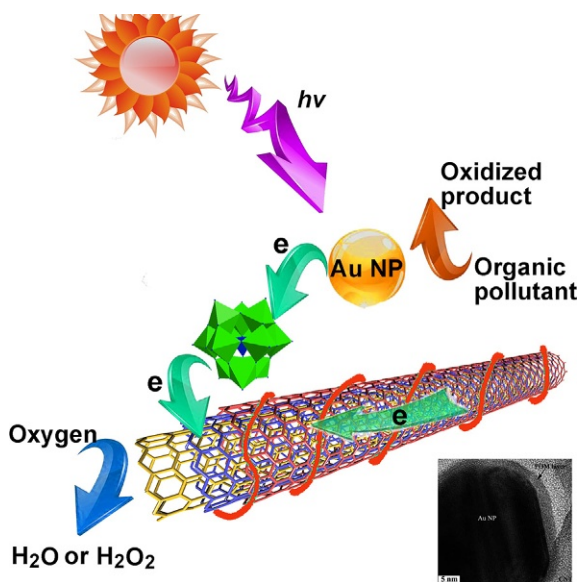


**Fig. 16** The photocatalytic mechanism of Au NPs@POMs/CNTs tricomponent nanocomposites. *Inset: HR-TEM image of Au NP attached on CNTs (106). Reproduced from Li, S.; Yu, X.; Zhang, G.; Ma, Y.; Yao, J.; Keita, B.; Louis, N.; Zhao, H. J. Mater. Chem. 2011, 21, 2282–2287 with permission of Royal Society of Chemistry Publishers.*

## 4. CONCLUSIONS

To summarize, the design, synthesis, and reactivity of novel POM/nanocarbon composite materials based on POM-functionalized CNTs or graphene have been discussed in detail. Their application as efficient electrocatalysts, electrodes for Li-ion batteries, supercapacitors, and sensors, etc. is highlighted, and particular focus is put on their improved performance compared with relevant state-of-the-art reference systems. Moreover, we have discussed the potential optimization methods including the covalent and noncovalent linkage modes between POMs and nanocarbons as well as the need to gain further understanding of the effects of different composite fabrication methods on the material properties. As the nanocarbons can be prepared in large scale at low cost, it can be envisaged that strongly coupled POMs/nanocarbon composites will find applications in technological electrochemical devices.

## REFERENCES

1. Dillon, A. C. *Chem. Rev.* **2010**, *110*, 6856–6872.
2. Whittingham, M. S. *Chem. Rev.* **2004**, *104*, 4271–4302.
3. Reddy, M. V.; Subba Rao, G. V.; Chowdari, B. V. R. *Chem. Rev.* **2013**, *113*, 5364–5457.
4. Su, D. S.; Perathoner, S.; Centi, G. *Chem. Rev.* **2013**, *113*, 5782–5816.
5. Lota, G.; Fic, K.; Frackowiak, E. *Energy Environ. Sci.* **2011**, *4*, 1592–1605.
6. Bamoharram, F. F. *Synth. React. Inorg. Met.-Org. Nano-Metal. Chem.* **2011**, *41*, 893–922.
7. Song, Y.-F.; Tsunashima, R. *Chem. Soc. Rev.* **2012**, *41*, 7384–7402.
8. Quintana, M.; López, A. M.; Rapino, S.; Toma, F. M.; Iurlo, M.; Carraro, M.; Sartorel, A.; Maccato, C.; Ke, X.; Bittencourt, C.; Da Ros, T.; Van Tendeloo, G.; Marcaccio, M.; Paolucci, F.; Prato, M.; Bonchio, M. *ACS Nano* **2012**, *7*, 811–817.
9. Müller, A.; Peters, F.; Pope, M. T.; Gatteschi, D. *Chem. Rev.* **1998**, *98*, 239–272.
10. Dolbecq, A.; Dumas, E.; Mayer, C. R.; Mialane, P. *Chem. Rev.* **2010**, *110*, 6009–6048.
11. Omwoma, S.; Chen, W.; Tsunashima, R.; Song, Y.-F. *Coord. Chem. Rev.* **2014**, *258–259*, 58–71.
12. McCreery, R. L. *Chem. Rev.* **2008**, *108*, 2646–2687.
13. Brownson, D. A. C.; Kampouris, D. K.; Banks, C. E. *Chem. Soc. Rev.* **2012**, *41*, 6944–6976.
14. Xu, C.; Xu, B.; Gu, Y.; Xiong, Z.; Sun, J.; Zhao, X. S. *Energy Environ. Sci.* **2013**, *6*, 1388–1414.
15. Andreiadis, E. S.; Jacques, P.-A.; Tran, P. D.; Leyris, A.; Chavarot-Kerlidou, M.; Jousselme, B.; Matheron, M.; Pecaut, J.; Palacin, S.; Fontecave, M.; Artero, V. *Nat. Chem.* **2013**, *5*, 6–7.
16. Liang, Y.; Li, Y.; Wang, H.; Dai, H. J. *Am. Chem. Soc.* **2013**, *135*, 2013–2036.
17. Pumera, M. *Chem. Rec.* **2009**, *9*, 211–223.
18. Tsunashima, R.; Iwamoto, Y.; Baba, Y.; Kato, C.; Ichihashi, K.; Nishihara, S.; Inoue, K.; Ishiguro, K.; Song, Y.-F.; Akutagawa, T. *Angew. Chem. Int. Ed.* **2014**, *53*, 11228–11231.
19. Tessonier, J. P.; Goubert-Renaudin, S.; Alia, S.; Yan, Y. S.; Barbeau, M. A. *Langmuir* **2013**, *29*, 393–402.
20. Toma, F. M.; Sartorel, A.; Iurlo, M.; Carraro, M.; Parisse, P.; Maccato, C.; Rapino, S.; Gonzalez, B. R.; Amenitsch, H.; Da Ros, T.; Casalis, L.; Goldoni, A.; Marcaccio, M.; Scorrano, G.; Scoles, G.; Paolucci, F.; Prato, M.; Bonchio, M. *Nat. Chem.* **2010**, *2*, 826–831.
21. Li, S.; Yu, X.; Zhang, G.; Ma, Y.; Yao, J.; de Oliveira, P. *Carbon* **2011**, *49*, 1906–1911.
22. Liu, R.; Li, S.; Yu, X.; Zhang, G.; Zhang, S.; Yao, J.; Zhi, L. J. *Mater. Chem.* **2012**, *22*, 3319–3322.
23. Liu, R.; Li, S.; Yu, X.; Zhang, G.; Zhang, S.; Yao, J.; Keita, B.; Nadjjo, L.; Zhi, L. *Small* **2012**, *8*, 1398–1406.
24. Proust, A.; Matt, B.; Villanneau, R.; Guillemot, G.; Gouzerh, P.; Izzet, G. *Chem. Soc. Rev.* **2012**, *41*, 7605–7622.
25. Proust, A.; Thouvenot, R.; Gouzerh, G. *Chem. Commun.* **2008**, 1837–1852.
26. Chen, W.; Huang, L.; Hu, J.; Li, T.; Jia, F.; Song, Y.-F. *Phys. Chem. Chem. Phys.* **2014**, *16*, 19668–19673.
27. Ji, Y.; Hu, J.; Huang, L.; Chen, W.; Streb, C.; Song, Y.-F. *Chem. Eur. J.* **2015**, *21*, 6469–6474.
28. Kawasaki, N.; Wang, H.; Nakanishi, R.; Hamanaka, S.; Kitaura, R.; Shinohara, H.; Yokoyama, T.; Yoshikawa, H.; Awaga, K. *Angew. Chem. Int. Ed.* **2011**, *50*, 3471–3474.

29. Toma, F. M.; Sartorel, A.; Iurlo, M.; Carraro, M.; Rapino, S.; Hooper-Burkhardt, L.; Da Ros, T.; Marcaccio, M.; Scorrano, G.; Paolucci, F.; Bonchio, M.; Prato, M. *ChemSusChem* **2011**, *4*, 1447–1451.
30. Ma, D.; Liang, L.; Chen, W.; Liu, H.; Song, Y.-F. *Adv. Funct. Mater.* **2013**, *23*, 6100–6105.
31. Huang, L.; Hu, J.; Ji, Y.; Streb, C.; Song, Y.-F. *Chem. Eur. J.* **2015**, *21*, 18799–18804.
32. Akter, T.; Hu, K.; Lian, K. *Electrochim. Acta* **2011**, *56*, 4966–4971.
33. Xiang, Y.; Lu, S.; Jiang, S. P. *Chem. Soc. Rev.* **2012**, *41*, 7291–7321.
34. Li, H.; Pang, S.; Feng, X.; Müllen, K.; Bubeck, C. *Chem. Commun.* **2010**, *46*, 6243–6245.
35. Wang, S.; Li, H.; Li, S.; Liu, F.; Wu, D.; Feng, X.; Wu, L. *Chem. Eur. J.* **2013**, *19*, 10895–10902.
36. Li, H.; Pang, S.; Wu, S.; Feng, X.; Müllen, K.; Bubeck, C. *J. Am. Chem. Soc.* **2011**, *133*, 9423–9429.
37. Koper, M. T. M. *Nat. Chem.* **2013**, *5*, 255–256.
38. Subbaraman, R.; Tripkovic, D.; Strmcnik, D.; Chang, K.-C.; Uchimura, M.; Paulikas, A. P.; Stamenkovic, V.; Markovic, N. M. *Science* **2011**, *334*, 1256–1260.
39. Bianchini, C.; Shen, P. K. *Chem. Rev.* **2009**, *109*, 4183–4206.
40. Simonsson, D. *Chem. Soc. Rev.* **1997**, *26*, 181–189.
41. Lv, H. J.; Geletii, Y. V.; Zhao, C. C.; Vickers, J. W.; Zhu, G. B.; Luo, Z.; Song, J.; Lian, T. Q.; Musaev, D. G.; Hill, C. L. *Chem. Soc. Rev.* **2012**, *41*, 7572–7589.
42. Sartorel, A.; Bonchio, M.; Campagna, S.; Scandola, F. *Chem. Soc. Rev.* **2013**, *42*, 2262–2280.
43. Kanan, M. W. N.; Daniel, G. *Science* **2008**, *321*, 1072–1075.
44. Ambrosi, A.; Chua, C. K.; Bonanni, A.; Pumera, M. *Chem. Rev.* **2014**, *114*, 7150–7188.
45. Guo, S.-X.; Liu, Y.; Lee, C.-Y.; Bond, A. M.; Zhang, J.; Geletii, Y. V.; Hill, C. L. *Energy Environ. Sci.* **2013**, *6*, 2654–2663.
46. Yin, Q. S.; Tan, J. M.; Besson, C.; Geletii, Y. V.; Musaev, D. G.; Kuznetsov, A. E.; Luo, Z.; Hardcastle, K. I.; Hill, C. L. *Science* **2010**, *328*, 342–345.
47. Liu, H.; Song, C.; Zhang, L.; Zhang, J.; Wang, H.; Wilkinson, D. P. *J. Power Sources* **2006**, *155*, 95–110.
48. Li, W.; Liang, C.; Zhou, W.; Qiu, J.; Zhou, Z.; Sun, G.; Xin, Q. *J. Phys. Chem. B* **2003**, *107*, 6292–6299.
49. Pan, D.; Chen, J.; Tao, W.; Nie, L.; Yao, S. *Langmuir* **2006**, *22*, 5872–5876.
50. Seo, M. H.; Choi, S. M.; Kim, H. J.; Kim, J. H.; Cho, B. K.; Kim, W. B. *J. Power Sources* **2008**, *179*, 81–86.
51. Han, D. M.; Guo, Z. P.; Zeng, R.; Kim, C. J.; Meng, Y. Z.; Liu, H. K. *Int. J. Hydrogen Energy* **2009**, *34*, 2426–2434.
52. Cui, Z.; Li, C. M.; Jiang, S. P. *Phys. Chem. Chem. Phys.* **2011**, *13*, 16349–16357.
53. Jin, X.; He, B.; Miao, J.; Yuan, J.; Zhang, Q.; Niu, L. *Carbon* **2012**, *50*, 3083–3091.
54. Adler, S. B. *Chem. Rev.* **2004**, *104*, 4791–4844.
55. Liu, Z.; Peng, F.; Wang, H.; Yu, H.; Zheng, W.; Yang, J. *Angew. Chem. Int. Ed.* **2011**, *50*, 3257–3261.
56. Kang, Y.; Ye, X.; Chen, J.; Cai, Y.; Diaz, R. E.; Adzic, R. R.; Stach, E. A.; Murray, C. B. *J. Am. Chem. Soc.* **2012**, *135*, 42–45.
57. Shao, M.; Shoemaker, K.; Peles, A.; Kaneko, K.; Protsailo, L. *J. Am. Chem. Soc.* **2010**, *132*, 9253–9255.
58. Wang, D.; Lu, S.; Jiang, S. P. *Chem. Commun.* **2010**, *46*, 2058–2060.
59. Suo, Y.; Zhuang, L.; Lu, J. *Angew. Chem. Int. Ed.* **2007**, *46*, 2862–2864.
60. Liu, R.; Li, S.; Yu, X.; Zhang, G.; Ma, Y.; Yao, J. *J. Mater. Chem.* **2011**, *21*, 14917–14924.



61. Liu, R.; Yu, X.; Zhang, G.; Zhang, S.; Cao, H.; Dolbecq, A.; Mialane, P.; Keita, B.; Zhi, L. *J. Mater. Chem. A* **2013**, *1*, 11961–11969.
62. Cui, Z.; Kulesza, P. J.; Li, C. M.; Xing, W.; Jiang, S. P. *Int. J. Hydrogen Energy* **2011**, *36*, 8508–8517.
63. Kim, Y.; Shanmugam, S. *ACS Appl. Mater. Interfaces* **2013**, *5*, 12197–12204.
64. Zhu, Y.; Murali, S.; Stoller, M. D.; Ganesh, K. J.; Cai, W.; Ferreira, P. J.; Pirkle, A.; Wallace, R. M.; Cychosz, K. A.; Thommes, M.; Su, D.; Stach, E. A.; Ruoff, R. S. *Science* **2011**, *332*, 1537–1541.
65. Ellis, B. L.; Knauth, P.; Djenizian, T. *Adv. Mater.* **2014**, *26*, 3368–3397.
66. Xie, K.; Wei, B. *Adv. Mater.* **2014**, *26*, 3592–3617.
67. Lu, Q.; Chen, J. F.; Xiao, J. Q. *Angew. Chem. Int. Ed.* **2013**, *52*, 1882–1889.
68. Poblet, J. M.; Lopez, X.; Bo, C. *Chem. Soc. Rev.* **2003**, *32*, 297–308.
69. Nishimoto, Y.; Yokogawa, D.; Yoshikawa, H.; Awaga, K.; Irle, S. *J. Am. Chem. Soc.* **2014**, *136*, 9042–9052.
70. Wang, H.; Hamanaka, S.; Nishimoto, Y.; Irle, S.; Yokoyama, T.; Yoshikawa, H.; Awaga, K. *J. Am. Chem. Soc.* **2012**, *134*, 4918–4924.
71. Chen, H.-Y.; Wee, G.; Al-Oweini, R.; Friedl, J.; Tan, K. S.; Wang, Y.; Wong, C. L.; Kortz, U.; Stimming, U.; Strinivasan, M. *ChemPhysChem* **2014**, *15*, 2162–2169.
72. Hu, J.; Ji, Y.; Chen, W.; Streb, C.; Song, Y.-F. *Energy Environ. Sci.* **2016**, *9*, 1095–1101.
73. Yeo, H. J.; Paik, Y.; Paek, S.-M.; Honama, I. *J. Phys. Chem. Solids* **2012**, *73*, 1417–1419.
74. De Volder, M. F. L.; Tawfick, S. H.; Baughman, B. H.; Hart, A. J. *Science* **2013**, *339*, 535–539.
75. Meng, Q.; Wu, H.; Meng, Y.; Xie, K.; Wei, Z.; Guo, Z. *Adv. Mater.* **2014**, *26*, 4100–4106.
76. Over, H. *Chem. Rev.* **2012**, *112*, 3356–3426.
77. Cuentas-Gallegos, A.; Martinez-Rosales, R.; Baibarac, M.; Gómez-Romero, P.; Rincon, M. E. *Electrochem. Commun.* **2007**, *9*, 2088–2092.
78. Bajwa, G.; Akter, T.; Lian, K. *ECS Trans.* **2011**, *35*, 31–37.
79. Bajwa, G.; Genovese, M.; Lian, K. *ECS J. Solid State Sci. Technol.* **2013**, *2*, M3046–M3050.
80. Sosnowska, M.; Goral-Kurbiel, M.; Skunik-Nuckowska, M.; Jurczakowski, R.; Kulesza, P. *J. Solid State Electrochem.* **2013**, *17*, 1631–1640.
81. Liu, S.; Xu, L.; Li, F.; Guo, W.; Xing, Y.; Sun, Z. *Electrochim. Acta* **2011**, *56*, 8256–8262.
82. Wang, P.; Wang, X.; Bi, L.; Zhu, G. *Analyst* **2000**, *125*, 1291–1294.
83. Li, Z.; Chen, J.; Pan, D.; Tao, W.; Nie, L.; Yao, S. *Electrochim. Acta* **2006**, *51*, 4255–4261.
84. Manivel, A.; Sivakumar, R.; Anandan, S.; Ashokkumar, M. *Electrocatalysis* **2012**, *3*, 22–29.
85. Li, Y.; Bu, W.; Wu, L.; Sun, C. *Sens. Actuators B* **2005**, *107*, 921–928.
86. Anwar, N.; Vagin, M.; Laffir, F.; Armstrong, G.; Dickinson, C.; McCormac, T. *Analyst* **2012**, *137*, 624–630.
87. Wang, X.; Zhang, H.; Wang, E.; Han, Z.; Hu, C. *Mater. Lett.* **2004**, *58*, 1661–1664.
88. Zhou, M.; Guo, L.; Lin, F.; Liu, H. *Anal. Chim. Acta* **2007**, *587*, 124–131.
89. Gooding, J. J. *Electrochim. Acta* **2005**, *50*, 3049–3060.
90. Dumitrescu, I.; Unwin, P. R.; Macpherson, J. V. *Chem. Commun.* **2009**, 6886–6901.
91. Pumera, M. *Chem. Eur. J.* **2009**, *15*, 4970–4978.
92. Charkoudian, L. K.; Pham, D. M.; Franz, K. J. *J. Am. Chem. Soc.* **2006**, *128*, 12424–12425.

93. Pryor, W. A.; Das, B.; Church, D. F. *Chem. Res. Toxicol.* **1991**, *4*, 341–348.
94. Salimi, A.; Komi, A.; Hallaj, R.; Khoshnavazi, R.; Hadadzadeh, H. *Anal. Chim. Acta* **2009**, *635*, 63–70.
95. Haghighi, B.; Hamidi, H.; Gorton, L. *Electrochim. Acta* **2010**, *55*, 4750–4757.
96. Zhang, Y.; Wen, F.; Jiang, Y.; Wang, L.; Zhou, C.; Wang, H. *Electrochim. Acta* **2014**, *115*, 504–510.
97. Qu, J.; Zou, X.; Liu, B.; Dong, S. *Anal. Chim. Acta* **2007**, *599*, 51–57.
98. Guo, W.; Xu, L.; Li, F.; Xu, B.; Yang, Y.; Liu, S.; Sun, Z. *Electrochim. Acta* **2010**, *55*, 1523–1527.
99. Salimi, A.; Korani, A.; Hallaj, R.; Khoshnavazi, R. *Electroanalysis* **2008**, *20*, 2509–2517.
100. Salimi, A.; Korani, A.; Hallaj, R.; Soltanian, S.; Hadadzadeh, H. *Thin Solid Films* **2010**, *518*, 5304–5310.
101. Li, X.; Zhu, Q. Y.; Tong, S. F.; Wang, W.; Song, W. B. *Sens. Actuators B* **2009**, *136*, 444–450.
102. Ling, Y.; Huang, Q.; Zhu, M.; Feng, D.; Li, X.; Wei, Y. J. *Electroanal. Chem.* **2013**, *693*, 9–15.
103. Zhang, W.; Du, D.; Gunaratne, D.; Colby, R.; Lin, Y.; Laskin, J. *Electroanalysis* **2014**, *26*, 178–183.
104. Zhang, H.; Xie, A.; Shen, Y.; Qiu, L.; Tian, X. *Phys. Chem. Chem. Phys.* **2012**, *14*, 12757–12763.
105. Streb, C. *Dalton Trans.* **2012**, *41*, 1651–1659.
106. Li, S.; Yu, X.; Zhang, G.; Ma, Y.; Yao, J.; Keita, B.; Louis, N.; Zhao, H. *J. Mater. Chem.* **2011**, *21*, 2282–2287.



# Design of Magnetic Polyoxometalates for Molecular Spintronics and as Spin Qubits

J.J. Baldoví, S. Cardona-Serra, A. Gaita-Ariño, E. Coronado<sup>1</sup>

Instituto de Ciencia Molecular (ICMol), Universidad de Valencia, Paterna, Spain

<sup>1</sup>Corresponding author: e-mail address: eugenio.coronado@uv.es

## Contents

1. Introduction	213
2. Relevant Precedent Studies of POMs in Molecular Magnetism	217
2.1 POMs as Magnetic Models and Single-Molecule Magnets: A Historical Perspective	217
2.2 Toward Rational Design and Processability of Magnetic POMs	224
3. Relevance of POMs in Molecular Spintronics	232
4. Recent Advances on the Use of POMs for Quantum Computing	236
4.1 Molecular Spin Qubits	236
4.2 POMs as Spin Qubits	239
4.3 POMs as Quantum Gates	242
5. Concluding Remarks	243
Acknowledgments	245
References	245

## Abstract

In the past decades, POMs have been used as minimal models in Molecular Magnetism, since they are a convenient playing ground to study fundamental phenomena such as anisotropic magnetic exchange and electron transfer. Now they have jumped to the stage of the rational design of single-ion magnets and are being considered as test subjects for simple experiments in Single-Molecule Spintronics and Molecular Quantum Computing. This chapter contains an overview of recent results that demonstrate the potential of POMs in these emerging fields.



## 1. INTRODUCTION

Spintronics (spin-based electronics) strives for the active manipulation of the electron spin to transmit and process information (1). The origin of this research field goes back to the discovery of the “giant

magnetoresistance” independently by Fert and Grünberg in the late 1980s (2,3). Compared with conventional electronic devices, which rely on the electron’s motion and charge, spintronic devices depend on the electron spin states as an additional degree of freedom, and thus have the potential to improve speeds and storage capacities. Indeed, spintronic systems based on inorganic metals and semiconductors have experienced a fast development. Considered as the first real application of nanotechnology, they are being used for a range of purposes, spanning from read-head devices and nonvolatile magnetic memories (4,5) to spin-transfer nanooscillators (6) and quantum bits (7).

The convergence of conventional spintronics with molecular electronics and molecular magnetism has led to the emergence of molecular spintronics (8,9), which combines the ideas and concepts developed in the former technology with the singular possibilities offered by these two molecular realms. This interdisciplinary field can be divided into two major areas: molecule-based spintronics (commonly known in the physics community as “organic spintronics”) and single-molecule spintronics (10). Molecule-based spintronics relies on the fabrication of novel devices that can replace inorganic metals and semiconductors by molecular-based materials with the aim of enhancing the properties of conventional spintronic devices and reducing their price. On the other hand, single-molecule spintronics intends to study individual magnetic molecules as main components of nanospintronic devices, including quantum information processing devices.

Commonly invoked advantages of molecular spintronics include: (1) the possibility of designing devices at a molecular-scale limit; (2) the use of molecular systems as spin collectors that can preserve spin information over times and distances much longer than in conventional semiconductor systems (11); (3) the formation of self-organized nanostructures based on molecules that had been designed to be easy to manipulate; (4) the use of magnetic molecules exhibiting exceptionally long spin–spin and spin–lattice relaxation times—milliseconds and seconds, respectively (12); and (5) the unique chemical and electronic features of the molecular world that provides flexible, low-density, transparent, and easy to process molecules and materials exhibiting novel added functionalities, including magnetic switching at the molecular level and emission of light.

More recently, the first steps in the manipulation in molecules of the electronic spin instead of its charge have been undertaken, revealing a tentative potential for memory or quantum information technology. This novel approach should enable the creation of electrically addressable

single-molecule magnetic qubits and molecular switches (13). However, as a solid foundation to fully tap on the resources of the molecular world, we need a deep understanding of the underlying mechanisms of molecular nanomagnetism, in particular, the behavior of isolated spins.

Since the early stages of spintronics, molecules have been used as model systems for studying the spin physics at a fundamental level (14). In this context, polyoxometalate (POM) chemistry has been shown to provide ideal systems (15). For example, mixed-valence (MV) POMs were investigated in order to understand the possibilities that these systems offer for electrical control of the spin state (16,17), including the possibility of designing electrically switchable magnetic POMs such as  $[\text{PMo}_{12}\text{O}_{40}(\text{VO})_2]^{q-}$  (18,19), and  $[\text{GeV}_{14}\text{O}_{40}]^{8-}$  (20–22), as will be discussed in this chapter. A significant theoretical effort has been devoted so far to explore these possibilities. This includes multiconfigurational studies, diagonalization of large matrices, DFT calculations, and also the consideration of vibronic coupling. These theoretical advances pave the way for developing experimental realizations of these proposals (23).

From the experimental point of view, an appealing class of magnetic molecules are the so-called single-molecule magnets (SMMs), i.e., magnetic molecules showing both slow relaxation of the macroscopic magnetization at low temperatures and unique quantum effects (24,25). The first generation of this kind of molecules was reported in the 1990s and was formed by clusters of exchange-coupled magnetic ions. The second generation is more recent (the first article was reported in 2003 (26), see Fig. 1, left) and is based on mononuclear metal complexes. In this case a single metal center—usually a lanthanide ion—has been shown to be sufficient to exhibit SMM properties; this class of systems is known as single-ion magnets (SIMs). Whereas SMMs were initially of interest only in Molecular Magnetism, with the discovery of SIMs they have also become of interest in Molecular Spintronics and Quantum Computing: with the spin located on a single atom, qubits based on SIMs tend to be better protected against noise. In fact, recent studies performed on these molecules have demonstrated the possibility to coherently manipulate the quantum state of spins, a first step toward molecular Quantum Computing. These results include the manipulation of the quantum state of nuclear spin in a  $\text{Tb}^{3+}$ -based phthalocyaninato complex using electrical current in a single-molecule experiment (27,28).

POMs based on lanthanoids are among the first examples of SIMs (see Fig. 1, right) (29). As we will discuss later, these mononuclear complexes have also shown to be of interest in Quantum Computing as they provide

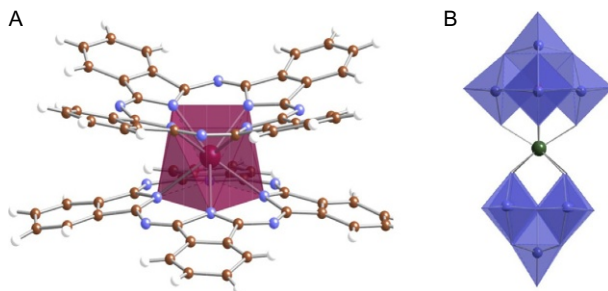


**Fig. 1** Representation of the first two families of SIMs: (A) phthalocyaninato-based SIMs  $[\text{LnPc}_2]^-$  (hydrogens are omitted for clarity) and (B) polyoxometalate-based SIMs of general formula  $[\text{Ln}(\text{W}_5\text{O}_{18})_2]^{9-}$ .

an ideal source of molecular spin qubits (30). In this context, it is important to note that the potential of POMs in Molecular Spintronics and Quantum Computing is remarkable compared with other coordination compounds, since these molecular-metal oxides present some advantageous chemical, structural, and electronic features (31):

- (i) They are robust molecules that maintain their integrity in solid state, in solution, and in some cases also on surfaces.
- (ii) They can accommodate magnetic ions or groups of magnetic ions at specific sites of the rigid POM structure, leading to magnetic molecules and large magnetic clusters with specific topologies and highly symmetric environments.
- (iii) Moreover, they can do so offering rigid, high-symmetry coordination environments, something of special interest when dealing with lanthanide ions (where magnetic and quantum properties depend crucially on their coordination environment).
- (iv) They can accept various numbers of electrons, while keeping their structure almost intact, leading to MV systems in which at least some of the electronic spins are extensively delocalized over the whole POM framework.

In this chapter, we will discuss the relevance of POM chemistry in molecular spintronics. In the next section, we will start describing the historical background of POMs in Molecular Magnetism, reaching up to the newest development in the design of processable SIMs. The relevance of POMs in Molecular Spintronics, in the narrow sense of spin manipulation by means of charge movement and electrical fields will be discussed in Section 3, which will include the presentation of recent results. The specific advantages of

POMs for Quantum Computing, in the sense of spin manipulation by means of microwave pulses, will be demonstrated in [Section 4](#).



## 2. RELEVANT PRECEDENT STUDIES OF POMs IN MOLECULAR MAGNETISM

### 2.1 POMs as Magnetic Models and Single-Molecule Magnets: A Historical Perspective

Historically, in order to understand two fundamental processes of extended metal-oxide systems—magnetic exchange and electron delocalization, POMs have been employed as model systems by the molecular magnetism community. Reviews on this topic distinguish between two classes of magnetic POMs for this purpose (15):

- (1) the spin-localized POMs, where each magnetic moment remains localized on a single 3d or 4f magnetic metal ion
- (2) the spin-delocalized MV POMs, where at least some of the electronic spins are delocalized over more than one metal center.

#### 2.1.1 Spin-Localized POMs

The possibilities that POM chemistry offers to encapsulate magnetic entities formed either by a single magnetic center, whether a 3d or a 4f ion, or by several magnetic centers linked by oxo-bridges (magnetic clusters) have extensively been exploited in the literature. This has led to a large set of complexes in which the magnetic ions may be replaced à la carte, while maintaining the structural characteristics of the system (32). For these purposes, lacunary POMs—obtained by removing part of the octahedral sites from the initial POM—have become ideal building blocks. The versatility of POM chemistry has permitted to use lacunary POMs as ligands to develop magnetic clusters of ever higher nuclearity, in which the experimentalist can control not only the number of magnetic ions but also the kind of magnetic interactions between them.

Such a chemical control over the magnetic exchange pathways has allowed stabilizing targeted ground states in different spin clusters. Since POMs permit the magnetic isolation of these spin clusters through the bulky diamagnetic POM shell, these complexes are considered as ideal model systems for the development of magnetic exchange theories (15). In particular, let us focus on clusters of cobalt cations encapsulated by POMs, which in the last decade has seen an enormous growth in the number of reported

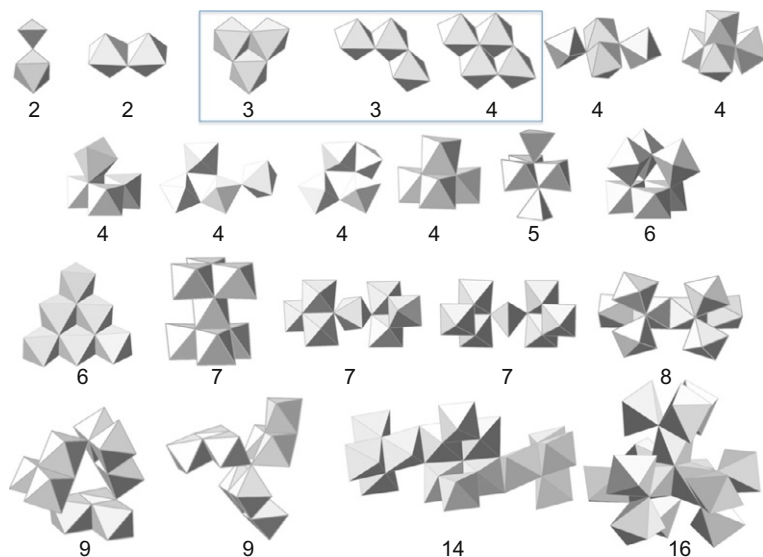


**Fig. 2** Cobalt(II) cores of polyoxometalates reported in the literature. The three examples discussed in this chapter are in the highlighted *blue frame*. Adapted from Ref. Duan, Y.; Clemente-Juan, J.M.; Giménez-Saiz, C.; Coronado, E. *Inorg. Chem.* **2016**, *55*, 925–938.

structures, with assorted connectivities and nuclearities ranging from  $n = 2$  to  $n = 16$  (see Fig. 2).

Indeed, a historically relevant example of the use of POMs to study magnetic exchange interactions was provided by cobalt(II) clusters. When a  $d^7$  ion is placed in an octahedral ligand field formed by POMs (weak crystal field ligands), the resulting complex presents high-spin  $S = 3/2$  with an unquenched orbital momentum, resulting in large spin anisotropy (33), whereas the first spin–orbit coupling state is a highly anisotropic spin doublet ( $S = 1/2$ ). The magnetic energy level structure of these Co(II) clusters can be determined by Inelastic Neutron Scattering (INS), providing a more accurate description than the one derived from thermodynamic measurements. Two decades ago, some of us started to apply this technique to describe Co(II)–Co(II) exchange anisotropy in a tetranuclear Co(II) cluster encapsulated by lacunary POMs of formula  $[\text{Co}_4(\text{H}_2\text{O})_2(\text{PW}_9\text{O}_{34})_2]^{10-}$  (see the tetranuclear  $\text{Co}_4$  magnetic core highlighted in the inset of Fig. 2, right) (34,35). For that, we took advantage of INS to determine the relative orientation of the exchange anisotropy axes by comparing two closely related trinuclear Co(II) clusters derived from the tetranuclear rhomb-like Co(II) cluster. The first one is an angular  $\text{Co}_3$  cluster obtained by replacement of a cobalt situated in the short diagonal of the rhomb by tungsten, leading



to a complex of general formula  $[\text{Co}_3\text{W}(\text{H}_2\text{O})(\text{ZnW}_9\text{O}_{34})_2]^{12-}$  (see the trinuclear  $\text{Co}_3$  magnetic core highlighted in the inset of Fig. 2, left). On the other hand, the second one is a triangular  $\text{Co}_3$  cluster obtained by replacement of a Co placed in the long diagonal of the rhomb by  $\text{Na}^+$   $[(\text{NaOH}_2)\text{Co}_3(\text{H}_2\text{O})(\text{P}_2\text{W}_{15}\text{O}_{56})_2]^{17-}$  (see the trinuclear  $\text{Co}_3$  magnetic core highlighted in the inset of Fig. 2, center). From the INS spectra of both clusters, one can deduce an energy splitting pattern formed by four doublets that arise from the three coupled effective spins  $S=1/2$ . These experimental observations could be reproduced by using a fully anisotropic exchange model, in which  $J_x \neq J_y \neq J_z$ . Such a model considers the symmetry of the molecule, which has permitted to describe the INS spectra using the following set of parameters: (1) the three components of the exchange parameters  $J^{13}_{(x,y,z)}$  associated with the side of the rhombus—similar for both clusters, and (2) the two components of the axial exchange  $J^{23}_{(x,y,z)}$  through the short diagonal ( $J^{23}_x = J^{23}_y$  due to the  $C_s$  symmetry). Thus, the anisotropic nature of the exchange interactions in magnetic clusters could be demonstrated for the first time in these Co clusters, taking advantage of the INS spectra (36).

### 2.1.2 Mixed-Valence POMs

The unique ability of POMs (mainly molybdates and vanadates) act as electron sponges hosting a variable number of “extra” electrons in their framework can provide an efficient way to tune the strength of the exchange coupling and, consequently, its spin state. Such a control can most easily be achieved by chemical means, during the synthesis of the POM (37). One needs to note here that, precisely because of the stability of the structures over many different oxidation states, the precise control and characterization of the final number of electrons is sometimes technically challenging.

As we will see later on, the possibility of achieving this control by physical means, in particular by applying an electrical bias in a single-molecule setup, will be quite interesting in spintronics, which of course presents its own array of experimental challenges. However, here, we need to start on the theoretical difficulties, which are also enormous in comparison with spin-localized systems. This is due to the fact that in MV systems several additional processes need to be taken into account in order to have a valid description of the spin states. First and foremost, there is electron transfer  $t$  between adjacent *occupied* and *empty* sites, i.e. between two metals with different oxidation states, e.g.,  $\text{W}(\text{V})-\text{W}(\text{VI})$ ,  $\text{Mo}(\text{V})-\text{Mo}(\text{VI})$ , or  $\text{V}(\text{IV})-\text{V}(\text{V})$ .

This process tends to delocalize the electron, commonly all over the cluster or at least along some electron transfer routes, and it is typically an order of magnitude more intense compared with magnetic super exchange. Of comparable importance is the Coulombic repulsion  $V$ , between every pair of electrons. This tends to place the electrons as far as possible to minimize its repulsion at any given time, but whether it will or not harm delocalization depends on the shape of the POM and its allowed electron transfer routes. Finally, although rarely taken into account because it requires going beyond Born–Oppenheimer approximation, there is also vibronic coupling,  $\lambda$ , that couples the “extra” electrons with the vibrational modes of the cluster. By binding the electron population of a metal site with the position of the ligands surrounding it, this effect tends to localize the electron on a given site, especially at low temperatures.

To illustrate these theoretical challenges, perhaps, the most classic example of MV POM is provided by the anion  $[\text{PW}_{12}\text{O}_{40}]^{5-}$ , reduced by two electrons that gives it, as happens with many MV POMs, a characteristic blue color. The diamagnetism of this Keggin “heteropolyblue,” originally attributed to a multiroute super-exchange mechanism, was eventually recognized to be due to the interplay between Coulombic repulsion and electron transfer, assuming the transfer routes have a certain relation in sign and magnitude (38,16). Indeed, while Coulombic repulsion ensures that states with two adjacent electrons are high in energy and thus triplets and singlets cannot be distinguished via super exchange, the different symmetry of triplet and singlet states mean their possible electron transfer routes are different and result in different energies, with a strong stabilization of the singlet. Later on, the effect of vibronic coupling on electron location was studied for the two electron reduced Keggin anion taking into account an adiabatic approximation (39). The effects of delocalization on the effective magnetic coupling are strongly affected by the vibronic interactions. While the details are complicated, effectively the vibronic interactions tend to localize the electrons, acting as if the transfer parameters were reduced. According to available theoretical results, for a strong vibronic coupling, spin-triplet states become partially or even fully localized, while fully delocalized states can be achieved only for spin-singlets. For weak vibronic coupling, in all cases, a fully delocalized configuration can be found. Recently, we have used this system to present a powerful theoretical approach to obtain an accurate solution of the dynamic vibronic problem in large-scale Jahn–Teller (JT) systems such as MV POMs. The approach uses a symmetry adapted vibronic basis to reduce the dimension of the problem (40). The application of this procedure

to Keggin anion is being developed and aims to give an accurate description of combined JT/pseudo-JT problems for the spin-singlet and spin-triplet states in this high-nuclearity system.

We can conclude that POMs are excellent model systems to study not just anisotropic exchange but also the interplay between electron delocalization and magnetic exchange in high-nuclearity clusters. Their highly symmetric structures facilitate the development of exact quantum-mechanical models in order to extract a clear picture of the local parameters that determine the magnetic properties.

### 2.1.3 Single-Molecule Magnets Based on POMs

In the last decade, the interest for magnetic POMs has evolved from their use as model systems in Molecular Magnetism toward the design of SMMs and their use as molecular spin qubits in nanospintronic devices. Thus, in this subsection, we will summarize the major breakthroughs achieved in the area of molecular nanomagnetism, while the aspects related with Molecular Spintronics and Quantum Computing will be presented in Sections 3 and 4.

By definition, an SMM is a molecule that displays magnetic bistability generated by an energy barrier to magnetization reversal. The magnetic behavior of SMMs is characterized by the presence of slow relaxation of the magnetization at low temperatures giving rise to a magnetic memory effect similar to that found in hard magnets, but accompanied by quantum phenomena like quantum tunneling of the magnetization (41), quantum coherence (42), or quantum interference (43). The first and most renowned example, which dates back to early 1990s, is  $[\text{Mn}_{12}\text{O}_{12}(\text{O}_2\text{CMe})_{16}(\text{H}_2\text{O})_4]$  (Fig. 3, left) (44), a molecule that combines a high axial anisotropy and a high-spin ground state (21). This molecule has been the subject of many magnetic and structural studies (45–47) and is composed by a group of eight ferromagnetically coupled  $\text{Mn}^{3+}$  ions with spins  $S=2$  resulting in  $S_{\text{Mn}^{3+}}=16$ , and a group of four  $\text{Mn}^{4+}$  ions with spins  $S=3/2$  resulting in  $S_{\text{Mn}^{4+}}=6$ . These two spin moieties are antiferromagnetically coupled to each other yielding a total ground state spin  $S=10$  that is itself split by magnetic anisotropy, creating an effective thermal barrier  $U=DS^2$  (Fig. 3, right). Spin reversal can occur either by passing through all those permitted states—thermally assisted—or by quantum tunneling between quasi-degenerate states placed on the opposite sides of the barrier (24).

Three years after the discovery of SMM behavior in  $\text{Mn}_{12}$ , an octanuclear iron complex  $[\text{Fe}_8\text{O}_2(\text{OH})_{12}(\text{tacn})_6]^{8+}$  (with tacn representing 1,4,7-triazacyclononane) (48) was also found to display SMM properties

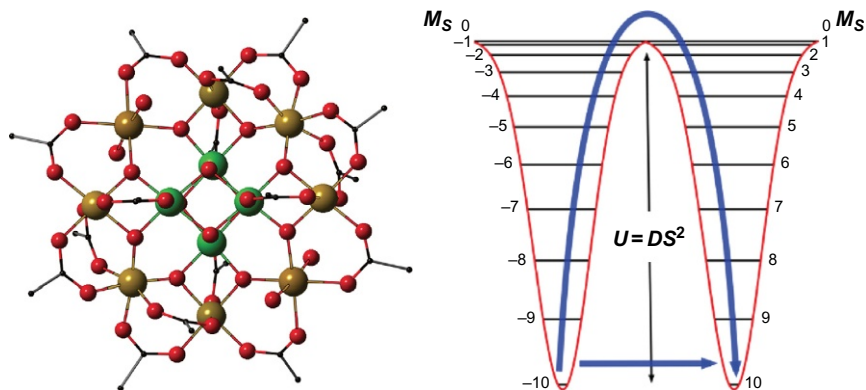


**Fig. 3** (Left) Molecular structure, Mn<sup>3+</sup> (gold) and Mn<sup>2+</sup> (green); (right) energy level scheme showing the two wells of [Mn<sub>12</sub>O<sub>12</sub>(O<sub>2</sub>CMe)<sub>16</sub>(H<sub>2</sub>O)<sub>4</sub>].

with more pronounced quantum effects (49, 50). Later, a rising number of lower nuclearity cluster systems were reported to behave as SMMs, for instance, the tetranuclear complex [Mn<sub>4</sub>(O<sub>2</sub>CMe)<sub>2</sub>(pdmH)<sub>6</sub>](ClO<sub>4</sub>)<sub>2</sub>, where pdmH<sub>2</sub> is pyridine-2,6-dimethanol (51). The major synthetic challenge in this field was to increase the energy barrier and, consequently, the blocking temperature  $T_B$ , by designing molecules having the maximum values of  $S$  and  $D$ . In this context, many examples of magnetic clusters with larger and larger nuclearities were reported (52–55) in an attempt to increase the spin state of the cluster and hence, the superparamagnetic barrier. However, the success of this approach has been very limited as demonstrated by the fact that Mn<sub>12</sub> is still among the transition metal clusters exhibiting the highest effective barriers (ca. 45–50 cm<sup>-1</sup>) and hysteresis (up to 4 K). In the POM area, some examples of magnetic clusters exhibiting SMM behavior were also described. For instance, a couple of iron(III) with hexa and nonanuclearity, [Fe<sub>4</sub>(H<sub>2</sub>O)<sub>2</sub>(FeW<sub>9</sub>O<sub>34</sub>)<sub>2</sub>]<sup>10-</sup> and [(Fe<sub>4</sub>W<sub>9</sub>O<sub>34</sub>(H<sub>2</sub>O))<sub>2</sub>(FeW<sub>6</sub>O<sub>26</sub>)]<sup>19-</sup>, respectively (56), a cobalt(II) with hexadecanuclearity, [{Co<sub>4</sub>(OH)<sub>3</sub>PO<sub>4</sub>}<sub>4</sub>(PW<sub>9</sub>O<sub>34</sub>)<sub>4</sub>]<sup>28-</sup> (57), and a heptanuclear manganese(III)–manganese(IV) cluster, [(α-P<sub>2</sub>W<sub>15</sub>O<sub>56</sub>)Mn<sub>3</sub><sup>III</sup>Mn<sup>IV</sup>O<sub>3</sub>(CH<sub>3</sub>COO)<sub>3</sub>]<sup>8-</sup> (58). Although these magnetic clusters add some new examples to the hundreds of already known SMMs, their novelty in the field of SMMs was very limited due to the low energy barriers that they present (10–12 cm<sup>-1</sup>) and to the lack of other interesting effects coming from the POM ligand.

These results contrast with the key role that POM chemistry is playing in the second generation of SMMs, usually called SIMs or mononuclear SMMs. This new way of thinking, proposed by Ishikawa and his coworkers

(59), consists in the development of minimalistic nanomagnets based on coordination complexes with a central lanthanide ion as the source of magnetic anisotropy. The first example of this kind was reported in 2003 in the lanthanoid complexes of general formula  $[\text{LnPc}_2]^-$ , with a “double-decker” structure and  $\text{Pc} = \text{phthalocyaninato}$  anions as ligands. In contrast to the first generation of SMMs, whose properties rely on the ability of exchange interactions to stabilize anisotropic high-spin states, the magnetic properties of SIMs depend primarily on the single-ion anisotropy resulting from the combination of spin-orbit coupling and ligand field (60). Hence, these two variables play a key role in the creation of a thermal barrier, which slows down the magnetization reversal (61).

In view that POM chemistry also provides lanthanoid complexes with antiprismatic  $D_{4d}$  symmetry, we decided to study the magnetic properties of the series  $[\text{Ln}(\text{W}_5\text{O}_{18})_2]^{9-}$  (Fig. 1B). As a consequence, we extended the concept of SIMs to ligands different from the phthalocyaninato ligands, leading to the second family of SIMs in 2008. This Lindqvist-type family has the general formula  $\text{Na}_9[\text{Ln}(\text{W}_5\text{O}_{18})_2]$  (in short,  $\text{LnW}_{10}$ ), displaying a square-antiprismatic  $D_{4d}$  symmetry (29). The most promising candidate for this series was the Er derivative ( $U_{\text{eff}} = 38.5 \text{ cm}^{-1}$ , close to that observed in  $\text{Mn}_{12}$ ,  $U_{\text{eff}} \approx 50 \text{ cm}^{-1}$ ), whereas in the preceding family such behavior was more remarkable in  $[\text{TbPc}_2]^-$ . The reason for this difference was assumed to lie on the different distortion of the square-antiprismatic site, which is compressed in the second family, in contrast with the axially elongated  $[\text{LnPc}_2]^-$  (Fig. 1A); this distortion affects different f-block metal ions in different ways. The interplanar distance of the  $\text{ErW}_{10}$  compound ( $d_{\text{pp}} = 2.47 \text{ \AA}$ ), which was calculated as the distance between the upper and lower planes containing the four oxygen atoms, is considerably smaller than the one of  $\text{TbPc}_2$  ( $d_{\text{pp}} = 2.76 \text{ \AA}$ ).

Since the discovery of SMM behaviour in  $\text{ErW}_{10}$ , the impact of this class of molecular nanomagnets has been dramatically increased and now hundreds of SIMs, having different coordination geometries and different types of ligands have been reported (62–64). It has been demonstrated that the SIM concept is quite general and can also be extended to other anisotropic metal ions in axial environments, such as mononuclear uranium complexes (65,66) and mononuclear *d*-transition metals (67,68).

The experimental studies of the first series of POM-based SIMs were extended to the Keggin-type series  $\text{K}_{13}[\text{Ln}(\beta_2\text{-SiW}_{11}\text{O}_{39})_2]$  (in short,  $\text{LnW}_{22}$ ). This permitted the analysis of the effects produced by a more distorted antiprismatic environment over the spin relaxation processes. A few

years later, a third family of mononuclear lanthanide SMMs based on POMs was also synthesized and characterized by our group. The molecule, which is based on the well-known Preyssler anion, is formulated as  $K_{12}[LnP_5W_{30}O_{110}] \cdot nH_2O$  and presents an unusual  $C_5$  axial symmetry. The fivefold geometry gives rise to large off-diagonal anisotropy parameters. The spin dynamics, mainly at low temperatures, is dominated by fast tunneling processes and strongly affected by hyperfine interactions.

## 2.2 Toward Rational Design and Processability of Magnetic POMs

As we have mentioned in [Section 2.1.2](#), the magnetic properties of SIMs mainly depend on the electronic spectrum resulting from the crystal field splitting and the anisotropy of the magnetic ion. As a consequence, a fairly complex crystal field Hamiltonian ( $H_{CF}$ ) must be properly defined for a full theoretical description. To rationalize the behavior of this growing collection of systems, we recently developed a general theoretical approach that estimates the effect of the CF on both the splitting of the  $J$  ground state and the mixing of the resulting magnetic levels, providing at the same time an indication of the leading anisotropy parameters that control such a splitting/mixture ([69](#)). A realistic description of the lowest energy sublevels and their wave functions may help to describe their magnetic properties and to rationalize which conditions are favorable for the discovery of new derivatives with interesting properties. Moreover, the description of spin eigenvectors will permit researchers to deal with the potential application of these systems as spin qubits in Quantum Computing ([70](#)).

The theoretical characterization of the magnetic properties of the first family of SIMs was based on a simultaneous fit of the temperature dependence of powder magnetic susceptibilities and  $^1H$  NMR spectra. This allowed the extraction of the CF parameters for the whole isomorphous series ([71](#)). Although a simultaneous adjustment is possible, overparametrization was a serious limitation of this kind of models and its predicting power was limited, as the parameters are not transferable to other compounds having the same kind of ligands. To overcome these limitations, a different approximation based on the real coordinates of the metal complex was developed by us through a computational package known as SIMPRE that uses the real geometries of the complexes to obtain the ground multiplet crystal field splitting and the static magnetic properties ([72](#)). As starting point, the point-charge electrostatic model was chosen due to its simplicity and versatility ([73](#)). The main advantage of this model is that it permits the

estimation of the CFPs using the chemical structure in an inexpensive way. An additional advantage is that it can be deeply improved by adding minor modifications, overcoming most limitations of the initial model, in order to provide an initial set of CFPs for further analysis using the full Hamiltonian. The simplified CF model that originally considered only equal charges at the nuclear positions of the atoms that coordinate the magnetic center was improved in 2012, distinguishing between different kinds of donor atoms. The model uses radial effective charges (REC) for those ligands that can be treated as spherical or that have the electron density of the donor atom pointing directly toward the metal. As we will see later, this model is perfectly suitable to reproduce and even predict the behavior of POMs as ligands coordinating through oxygen atoms. The REC model requires as parameters the effective charge and the effective distance (Fig. 4).

In 2014, both  $\text{LnW}_{10}$  and  $\text{LnW}_{22}$  POM-based SIM families were revisited by our group in order to describe their magnetic behavior according to the REC model (74). This magnetic theoretical characterization offered useful additional information about the Stark sublevels and ground multiplet wave functions with respect to the coordination environment. In our calculations, the coordinate system was referred aligned with the main symmetry axis of the square antiprism. Due to the fact that the eight oxygen atoms are chemically equivalent, a simultaneous fit of the magnetic susceptibility data of  $\text{LnW}_{10}$  and  $\text{LnW}_{22}$  ( $\text{Ln}=\text{Dy}, \text{Ho}, \text{Tb}, \text{Er}$ ) could be performed. This permitted to reduce the parameter space and allowed an interpretation of the ligand field effects of polyoxowolframates. The most satisfactory fitting of the temperature dependence of the magnetic susceptibility was obtained when  $D_r=0.895 \text{ \AA}$  and  $Z_i=0.105$ . The applicability of these two REC parameters was further tested by the prediction of the magnetic susceptibility of the related  $\text{TmW}_{22}$  and  $\text{YbW}_{22}$  derivatives. Their magnetic properties could be described successfully with the same two parameters as can be seen in Fig. 5 (right).

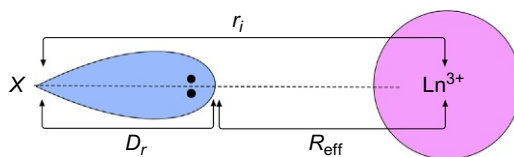


**Fig. 4** Electronic pair of a ligand X oriented toward the nucleus of a trivalent lanthanoid cation. The effective charge is located between the lanthanoid and the donor atom at  $R_{\text{eff}}=r_i - D_r$ .

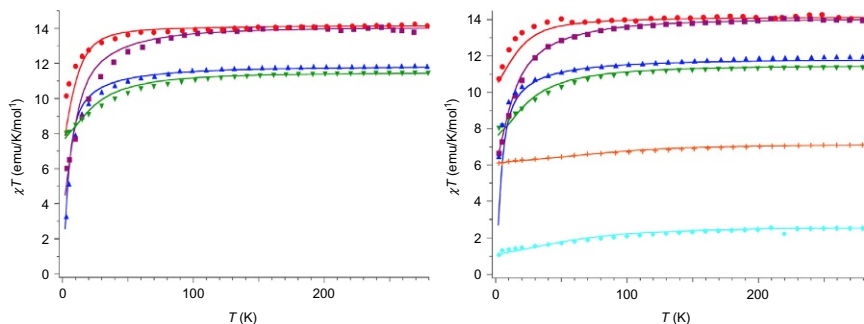


**Fig. 5** Fitting of the experimental  $\chi T$  product of the series of (left)  $[\text{Ln}(\text{W}_5\text{O}_{18})_2]^{9-}$  and (right)  $[\text{Ln}(\beta_2\text{-SiW}_{11}\text{O}_{39})_2]^{13-}$  using the REC model: Dy (●), Ho (■), Tb (▲), Er (▼), Tm (+), and Yb (◆). Markers: experimental data; solid line: theoretical fit for Dy–Er and prediction for Tm and Yb.

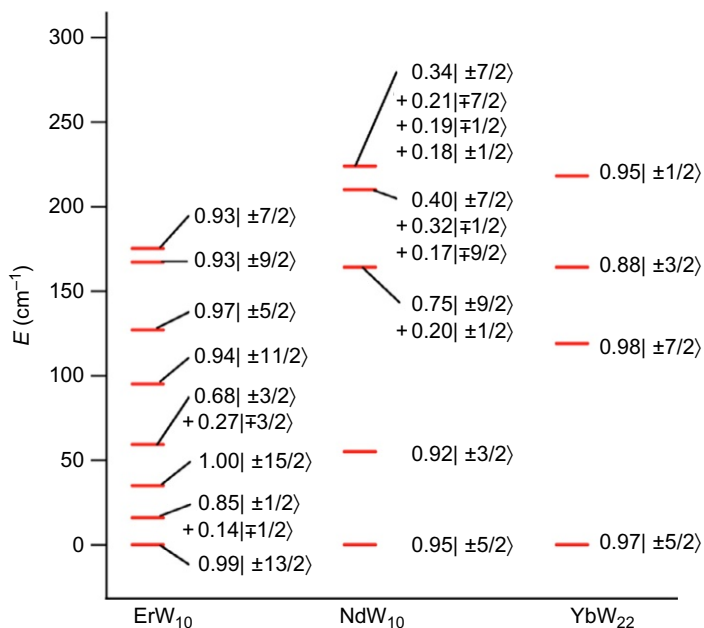


**Fig. 6** Energy level schemes and main  $M_J$  contributions for  $\text{ErW}_{10}$ ,  $\text{NdW}_{10}$ , and  $\text{YbW}_{22}$ . Note that all levels are Kramer's doublets.

The energy level schemes and ground state descriptions of the ten lanthanide-based polyoxowolframate derivatives are reported in Ref. (74). To have a closer look, the energy level schemes and main contributions to the wave functions of compounds  $\text{ErW}_{10}$  and  $\text{YbW}_{22}$  are shown in Fig. 6. One may observe the high contribution of a high  $M_J$  in both cases



(99% of  $\pm 13/2$  and 97% of  $\pm 5/2$  for  $\text{ErW}_{10}$  and  $\text{YbW}_{22}$ , respectively), which are compatible with the SMM behavior reported in the work of Aldamen *et al.* (29). It is worth to mention that in the case of  $\text{ErW}_{10}$  the calculated first excited state yields at  $16 \text{ cm}^{-1}$ , whereas the experimental one, which was determined by EPR and specific heat, is located at  $17 \text{ cm}^{-1}$  (75). This description has improved the previous description of the CF splitting of the  $\text{ErW}_{10}$  compound, where the first excited level (with a main contribution of  $\pm 1/2$ ) was placed at  $2 \text{ cm}^{-1}$ .

In a second step, the possibility of having novel SIMs in other derivatives of these two series was explored. The SIMPRE package was acting as a spy-glass and the most promising results were identified for  $\text{NdW}_{10}$  (74). Then, the real structure of the Nd derivative and the REC parameters obtained in the study of both polyoxowolframate families were combined to obtain a prediction of the energy level scheme and the contributions to the wave functions (Fig. 6). The theoretical calculations describe a ground state with 95% of contribution of  $M_J = \pm 5/2$ , which is very similar to the mononuclear SMM  $\text{YbW}_{22}$ . Furthermore, the main  $M_J$  contribution to the ground state wave function of  $\text{NdW}_{10}$  coincides with the one of the first Nd-based SIM reported by Rinehart and Long (76).

This encouraged us to prepare the sample and measure its magnetic properties. The compound exhibited the expected SMM behavior and the temperature dependence of the magnetic susceptibility was successfully predicted. The theoretical results regarding this thermodynamic property are plotted and compared with the experimental results in Fig. 7. As one may observe, there is an almost perfect agreement between the prediction and the experiment, showing the great possibilities that this strategy can provide to the community of POMs by checking new candidates with interesting magnetic properties. Analyses of the frequency dependence of the  $\chi''$  peaks through an Arrhenius plot allowed the estimation of the magnetization–relaxation parameters in this system. The best fitting affords a barrier height ( $U_{\text{eff}}$ ) of  $51.4 \text{ cm}^{-1}$  with a preexponential factor ( $\tau_0$ ) of  $3.55 \times 10^{-10} \text{ s}$ . Given the good insulation of the  $\text{Nd}^{3+}$  ions provided by the diamagnetic polyoxowolframate framework (the shortest Nd–Nd distance is  $11.221 \text{ \AA}$ ), the slow relaxation process exhibited by the complex should be considered as a single-molecule property.

All studies presented in this section so far have been on polyoxowolframates, but there is no fundamental limitation that impedes the use of polyoxomolybdates for the design of lanthanoid SIMs. In fact, among the advantages that polyoxomolybdates would present in comparison with

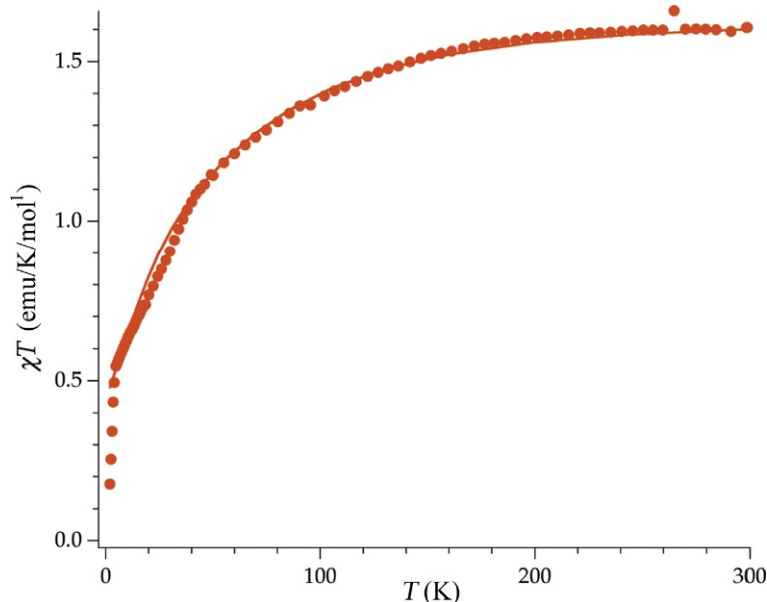


**Fig. 7**  $\chi T$  product of  $\text{NdW}_{10}$ . Circles, experimental data; solid line, theoretical prediction using the REC model.

the previous two families of SIMs based on polyoxowolframates is that they are in general more easily reducible by one or more electrons. This allows the coexistence of localized  $f$  electrons with a number of delocalized  $d$  electrons. As it has already been demonstrated with transition metal ions, these entities are unique model systems that favor the appearance of novel phenomena and possibilities in nanotechnology (19). Often, they can also be functionalized with more ease. Motivated by these perspectives and by the similar coordination environment with respect to the first two families of POM-based SIMs, we decided to proceed with the study of the magnetic properties of polyoxomolybdates encapsulating lanthanides (77).

We prepared and characterized two new families of POM-based mononuclear lanthanide complexes. The first family is formulated as  $[\text{Ln}(\beta\text{-Mo}_8\text{O}_{26})_2]^{5-}$  (in short,  $\text{LnMo}_{16}$ ),  $\{\text{Ln}^{\text{III}} = \text{Tb}, \text{Dy}, \text{Ho}, \text{Er}, \text{Tm}, \text{and Yb}\}$  and consists of a lanthanide ion trapped by two  $[\beta\text{-Mo}_8\text{O}_{26}]^{4-}$  moieties (78). The second family is formulated as  $[\text{Ln}\{\text{Mo}_5\text{O}_{13}(\text{OMe})_4\text{NNC}_6\text{H}_4\text{-}p\text{-NO}_2\}_2]^{3-}$  (in short,  $\text{LnMo}_{10}$ ),  $\{\text{Ln}^{\text{III}} = \text{Tb}, \text{Dy}, \text{Ho}, \text{Er}, \text{Yb}, \text{and Nd}\}$ . In these cases, the lanthanide ion is trapped by a functionalized POM based on a lacunary Lindqvist-type pentamolybdate (79). Despite the chemical differences (see Fig. 8), from the point of view of the lanthanoid, both systems

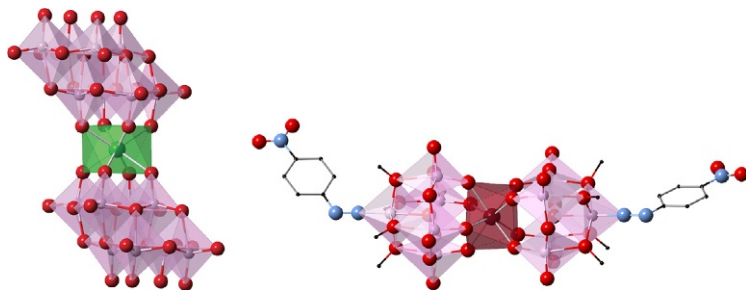


**Fig. 8** Molecular structures of (left)  $[\text{Er}(\text{Mo}_8\text{O}_{26})_2]^{5-}$  and (right)  $(\text{TBA})_3\{[\text{Mo}_5\text{O}_{13}(\text{OCH}_3)_4(\text{N}_2\text{C}_6\text{H}_4\text{-}p\text{-NO}_2)]_2\text{Tb}\}$ .

present a rigid square antiprism structure that is completely analogous to that of  $\text{LnW}_{10}$ .

While polyoxomolybdates present unique experimental challenges compared with polyoxowolframates, keeping in the topic of this chapter we will focus on the magnetostructural relations and its theoretical characterization. In the  $\text{LnMo}_{16}$  series, we carried out a simultaneous fit with SIMPRE of the four magnetic susceptibility curves of the  $\text{Tb}^{3+}$ ,  $\text{Dy}^{3+}$ ,  $\text{Ho}^{3+}$ , and  $\text{Er}^{3+}$  derivatives. The best agreement was reached using the REC parameters  $D_r = 0.72 \text{ \AA}$  and  $Z_i = 0.253$ . In this case the  $D_r$  value was slightly larger than the one obtained in  $\text{LnW}_{10}$  and  $\text{LnW}_{22}$ . This might be interpreted as the effective point charge needing a smaller covalent correction in this case. According to some *semiempirical* studies (80), this difference can be related to the different Pauling electronegativity of the Mo and W atoms. In this family, the larger difference in electronegativity between Mo (2.16) and O (3.44) enhances the ionic character of the Mo–O bonding and therefore also of the coordination bond Ln–O. The REC parameters were tested by applying them to the  $\text{Tm}^{3+}$  and  $\text{Yb}^{3+}$  derivatives, yielding a very good agreement with the experimental data (Fig. 9). The calculated energy levels can be found in Ref. (77). The slightly larger crystal field splitting for  $\text{LnMo}_{16}$  compared with  $\text{LnW}_{10}$  and  $\text{LnW}_{22}$  (according to our theoretical calculations) might be extrapolated to a trend of polyoxomolybdates producing a slightly stronger ligand field splitting compared with polyoxotungstates at a given metal–ligand distance.

Let us now focus on the second series of mono-lanthanide containing polyoxomolybdates of formula  $[\text{Ln}\{\text{Mo}_5\text{O}_{13}(\text{OMe})_4\text{NNC}_6\text{H}_4\text{-}p\text{-NO}_2\}_2]^{3-}$  species (from now on:  $\text{LnMo}_{10}$ , where  $\text{Ln} = \text{Tb}, \text{Dy}, \text{Ho}, \text{Er}, \text{Yb}$ , and  $\text{Nd}$ ), which are based on the hybrid lacunary Lindqvist-type pentamolybdate  $[\text{Mo}_5\text{O}_{13}(\text{OMe})_4(\text{NNC}_6\text{H}_4\text{-}p\text{-NO}_2)]^{3-}$  as a ligand (79) and synthesized by

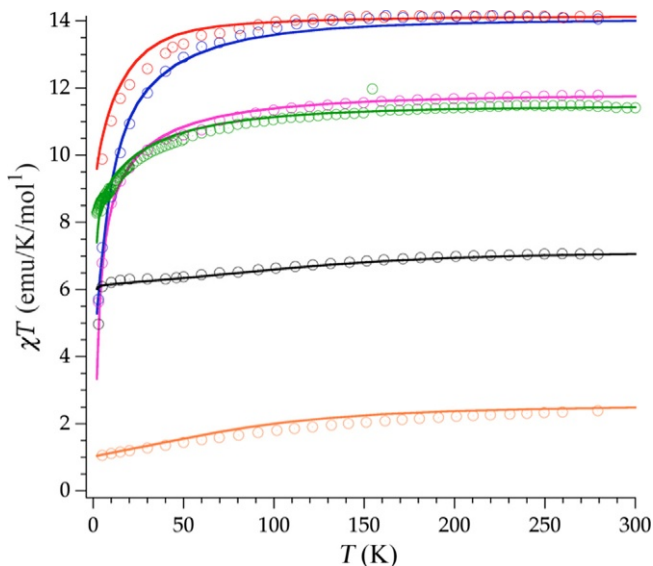


**Fig. 9** Fitting of the experimental product of the series  $[\text{Ln}(\text{Mo}_8\text{O}_{26})_2]^{5-}$  using the REC model: Dy (red), Ho (blue), Tb (blue), Er (green), Tm (black), and Yb (orange). Markers give experimental data, and the solid lines theoretical fits for Tb–Er and predictions for Tm and Yb.

the group of Prof. Proust in Paris. The key here is the substitution of organic ligands in the POM, which opens a path for chemical functionalization: a promising advance toward functional molecule-based nanostructures, a requirement for single-molecule experiments. In this case, the chemical structures of the Tb, Ho, and Er derivatives were determined by X-ray diffraction and show the lanthanoid ion coordinated by eight oxygen atoms that are bonded to molybdene atoms. Indeed, the coordination environment of the lanthanide is similar to the coordination environment of the series  $\text{LnW}_{10}$ . The POM complex is formed by two anionic  $[\text{Mo}_5\text{O}_{13}(\text{OMe})_4(\text{NNC}_6\text{H}_4\text{-}p\text{-NO}_2)]^{3-}$  moieties sandwiching the magnetic center in a slightly distorted square-antiprismatic geometry (Fig. 8 (right)). If we compare the structures with the families of polyoxowolframates exhibiting SMM behavior, the skew angle between the two anionic moieties in  $\text{TbMo}_{10}$ ,  $\text{DyMo}_{16}$ ,  $\text{HoMo}_{16}$ ,  $\text{ErMo}_{16}$ ,  $\text{TmMo}_{16}$ , and  $\text{TmMo}_{16}$  is comparable with the measured one for  $\text{ErW}_{10}$  (44.2 degree), whereas the Ho and Er derivatives of  $\text{LnMo}_{10}$ , as well as  $\text{TbMo}_{16}$ , are more distorted, being comparable with the  $\text{ErW}_{22}$  derivative (41.4 degree). So far we have no chemical control on the skew angle, which depends on a number of subtle crystal packing interactions.

Here we should note the different approaches one can take when applying the REC model, which range between (a) a quick prediction in the absence of any free parameters, which can be useful for the screening of known (or potential) structures in the search new SIMs, or (b) an individual fit of the magnetic and/or spectroscopic properties for each metal. The latter procedure has a descriptive, rather than predictive, goal. In the study of the  $\text{LnMo}_{10}$  family, we decided to apply an intermediate strategy, as follows. Because of the similarity with the coordination sphere of the  $\text{LnMo}_{16}$  series, the product of the parameters  $D_r=0.72 \text{ \AA}$  and  $Z_i=0.253$  was kept constant, thus reducing the number of free parameters to one for each metal. Within this constrains, the magnetic susceptibility curves of this series were fitted individually for each metal ion. Theoretical results, which show an excellent agreement with the experiment, are plotted in Fig. 10. The sharp decrease below 10 K that is observed in the  $\text{ErMo}_{10}$  derivative is reminiscent of a behavior observed in other complexes and is not yet well understood (81,82). We do have to note that, as happens in the current case, those systems present an Ising ground doublet ( $M_J=\pm 15/2$ ), which might favor a stronger dipolar interaction at low temperature.

Let us finally compare the calculated energy level schemes for  $\text{DyMo}_{10}$ ,  $\text{ErMo}_{10}$ , and  $\text{YbMo}_{10}$  (see Fig. 11). The calculated ground state of  $\text{DyMo}_{10}$  is dominated by  $M_J=\pm 11/2$  (86%), with an excited state at about  $11 \text{ cm}^{-1}$

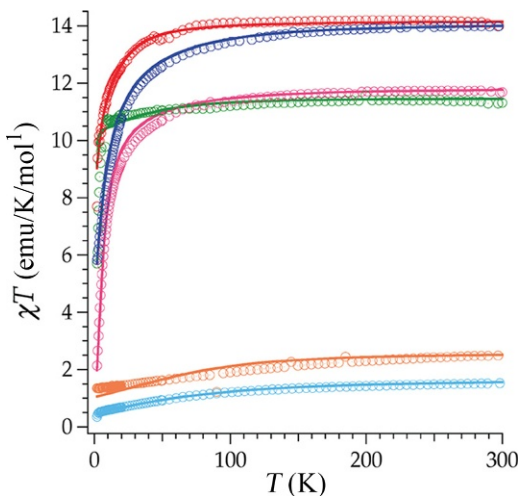


**Fig. 10** Experimental (circles) and predicted (solid lines)  $\chi T$  product of the series  $\text{LnMo}_{10}$  under a magnetic field of 1000 Oe:  $\text{Dy}^{3+}$  (red),  $\text{Ho}^{3+}$  (blue),  $\text{Tb}^{3+}$  (pink),  $\text{Er}^{3+}$  (green),  $\text{Yb}^{3+}$  (orange), and  $\text{Nd}^{3+}$  (clear blue) from 2 to 300 K.

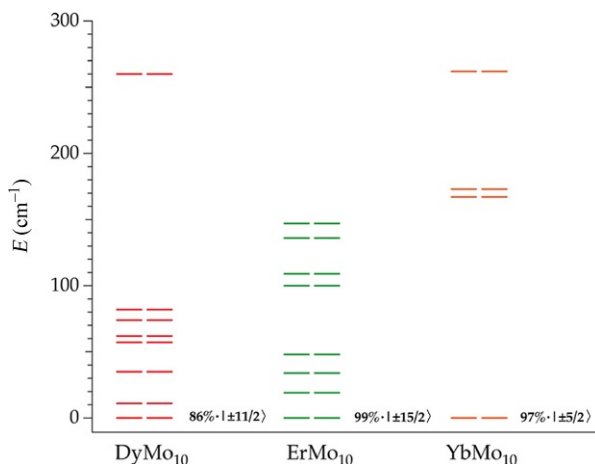


**Fig. 11** Energy level scheme and main contributions to the ground state wave function for  $\text{DyMo}_{10}$ ,  $\text{ErMo}_{10}$ , and  $\text{YbMo}_{10}$ .

characterized by  $M_J = 0.92|\pm 9/2\rangle$ , a scheme compatible with the observed SMM behavior. The situation is similar for  $\text{ErMo}_{10}$ , with the ground doublet calculated as 99% of  $M_J = 15/2$  and a first excited Kramers doublet placed at about  $19 \text{ cm}^{-1}$ . The calculated level scheme of  $\text{YbMo}_{10}$  also with an  $M_J = 97\%$  of  $|\pm 5/2\rangle$  is also compatible with SMM behavior a quasi-pure  $M_J$  function in the ground state without a clear thermal path for relaxation.

In sum, we have found that for POMs, the SIMPRE package using the REC model has so far resulted in good fits and/or satisfactory predictions using radial displacements in the range  $0.4 < D_r < 0.9$  and effective charges in a range  $0.1 < Z_i < 0.5$ , while at the same time maintaining the product in a range  $0.1 < D_r \cdot Z_i < 0.2$ . These kinds of calculations are expected to benefit from more detailed experimental information: recently, INS allowed to determine two distinct crystallographic phases in  $\text{TbW}_{10}$  with slightly different coordination environments (83).



### 3. RELEVANCE OF POMs IN MOLECULAR SPINTRONICS

Having just studied the relevance of POMs in molecular magnetism in the case of localized spin systems, let us now focus on the possibilities of MV POMs in Molecular Spintronics. As pointed out in Section 2.1.2, the possibility of considering the combined effects of electron transfer and magnetic exchange makes POM chemistry an exciting playground for theoretical proposals to advance our understanding of fundamental single-molecule spintronic processes. Furthermore, the chemical and mechanical robustness

of POMs combined with their ability to preserve their molecular structure intact, while a variable number of electrons are delocalized over its network of empty *d* orbitals makes them interesting candidates for single-molecular spintronic experiments.

Indeed, while the preparation of single-molecular nanodevices is now becoming commonplace, it is still extremely challenging to electrically manipulate the spin state of a single molecule. Originally, different families of electrically responsive magnetic molecules have been proposed for these experiments, namely spin-crossover metal complexes, valence-tautomeric metal complexes (84), MV metal complexes (85,86,19,87), and dipolar metal complexes, for example, molecular triangles formed by three antiferromagnetically coupled spins (88). In this section, we present some examples of MV POMs that present two possible spin states with different electronic properties so that they can change their ground spin state either by the application of an external electric field or by electric injection of extra electrons.

A first possibility for the electric switch of the spin state consists in altering the singlet-to-triplet gap in the two-electron reduced POMs. This can be achieved by approximating two electrons, which in absence of an electric stimulus and because of electron repulsion, reside at the most distant positions in the anion, resulting in two independent spin doublets. An example of this kind is provided by the dirreduced  $[\text{GeV}_{14}\text{O}_{40}]^{8-}$  (89). Magnetic susceptibility measurements in this MV POM are consistent with two independent electrons; this is surprising since it contradicts what is found in most dirreduced POMs, e.g., the Keggin anion or the decawolframate. *Ab initio* calculations on embedded fragments found that both the connectivity of the molecule and the magnitude of most parameters in the Hamiltonian are of the same order of magnitude to those of decawolframate, which is diamagnetic (90). The key difference lies in the central square ( $\text{GeV}_4$ ) of the cluster, which displays a higher orbital energy. Sandwiched between the two square pyramids ( $\text{V}_5$ ), this structural feature—which is absent in other MV POMs—acts as an effective barrier for electron transfer, separating the POM into two nearly independent wells. Indeed, the diagonalization of the  $t$ - $J$ - $V$  Hamiltonian for the whole molecule using the *ab initio* parameters resulted in two independent  $S = 1/2$  spins, in full agreement with the experimental result. This behavior could in principle be altered via the application of an electric field along the long axis of this POM that is forcing the two electrons to reside in the same well. Theoretical calculations estimate that, under an applied electric field of the order of 10 V/nm the electrons would be close enough for their spins to be strongly coupled (see Fig. 12) (20). In this case, the combination of *ab initio* calculations with an effective

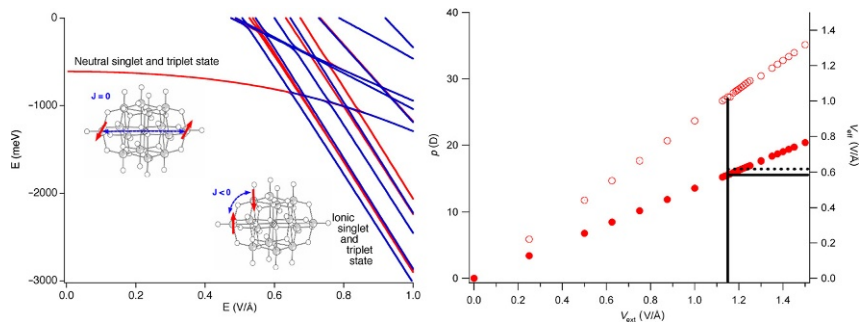


**Fig. 12** (Left) Energy arrangement of singlet and triplet states as a function of the intensity of the electric field along  $z$ . (Right) Molecular electrical dipole (left axis) and effective electrical potential (right axis) felt by  $[\text{GeV}_{14}\text{O}_{40}]^{8-}$  under an external electrical field applied along the molecular main axis.

Hamiltonian and an elementary dipolar model allowed to show that the polarization of the electron clouds, which creates a large molecular electrical dipole means that the electric field actually felt by the delocalized electrons was diminished by up to a factor of two compared with the external applied field, something to be taken into account when designing single-molecule experiments. Although in the present example the magnitude of the electric field is too strong, the sharp crossover from a paramagnetic state to an anti-ferromagnetic state under a relatively small increase of the magnetic field means that a more asymmetric POM would have promise to experimentally achieve this electrical switch.

A variation over the previous example was the one originally suggested for the MV POM  $[\text{PMo}_{12}\text{O}_{40}(\text{VO})_2]^{q-}$ . In this complex system a Keggin structure hosting a variable number of electrons is capped by two  $(\text{VO})^{2+}$ , each hosting one  $S=1/2$ . While the reduction state of the system can be altered by chemical synthesis, the proposal relies on the possibility on doing it on a single molecule contacted by electrodes which can inject electrons and remove them. The key for the switching behavior is that, according to theoretical calculations, an odd number of delocalized electrons originate a strong ferromagnetic coupling between the two distant spins located at the  $(\text{VO})^{2+}$  capping moieties, while an even number of delocalized electrons results in a very weak coupling. Hence, in this device, a control of the exchange interaction through injection of electrons can be achieved. Section 4.2 describes how this, if done with a precise time control, can be related with quantum logical gates between two qubits.

Moving on from the two theoretical possibilities outlined earlier, recently a proof-of-principle demonstration was presented for the



experimental fabrication of single-molecule nanorectifiers. This was achieved using the POM complex  $[\text{DyP}_5\text{W}_{30}\text{O}_{110}]^{12-}$  (in short,  $\text{DyW}_{30}$ ) deposited on gold that were individually contacted with a scanning tunneling microscope (STM) tip, meaning in conditions similar to those required for the implementation of the previous theoretical schemes (91). In this case it was possible to target a single molecule and to record  $I$ - $V$  curves by placing the STM tip above the POM and applying a voltage along it. Between  $-1.3$  and  $+1.3$  V, these  $I$ - $V$  curves showed a strongly rectifying behavior with a negligible current for negative voltages and an exponentially increasing current for positive voltages higher than 1 V. It was postulated that the rectification mechanism results from the combination of an asymmetry in the coupling of the molecule to the metal electrodes and an asymmetry in the electronic structure of the molecule, with either the HOMO or the LUMO located much closer in energy to the Fermi level of the electrodes than the other. Both conditions are likely met in  $\text{DyW}_{30}$ , since the crystal structure reveals that the trivalent cation resides in one of two possible pockets in the interior of the POM (Fig. 13). Thus, there are two very distinct electronic situations depending on whether the cation is closer to the tip or closer to the surface. A certain difficulty is predicted in tunneling between these situations, since a water molecule bound to the  $\text{Dy}^{3+}$  would also need to tunnel between two different positions. This enables thinking of a molecular diode, where the couplings of the molecule to the tip and to the substrate should be as different as possible, but taking into account that neither should be exceedingly small, since that would impede the current. Crucially, level broadening is diminished compared with  $\pi$ -conjugated organic systems, since in the POM the LUMO is localized in the  $d$  orbitals of the metal ions which are rather internal and thus isolated from the surface states of the substrate.

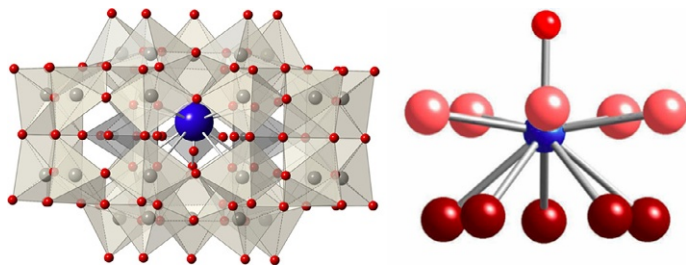


**Fig. 13** (Left) Chemical structure of  $[\text{DyP}_5\text{W}_{30}\text{O}_{110}]^{12-}$ , evidencing the lifting of the horizontal symmetry plane in the POM structure by the encapsulated  $\text{Dy}^{3+}$  cation. (Right) View of the fivefold coordination environment.



## 4. RECENT ADVANCES ON THE USE OF POMs FOR QUANTUM COMPUTING

### 4.1 Molecular Spin Qubits

The first hundred years of Quantum Mechanics have given us what is now known as the first quantum revolution, which involves a spectrum of quantum-supported technologies. These range from semiconductor electronics, lasers and giant-magnetoresistance-based hard drives to medical MRIs, superconducting quantum interference devices and quantum dots. Despite all these advances, or precisely thanks of them, society is still betting decidedly in favor of the future potential of this field, as attested by the recent announcement of a European Flagship on Quantum Technologies. The foreseeable technologies of the Second Quantum Revolution can be grouped in the following subfields: Quantum Computation including quantum simulation, quantum networks including quantum key distribution, and quantum metrology including quantum sensing and quantum imaging (92). Every technology of the Second Quantum Revolution, by definition, is explicitly based on highly nontrivial quantum-mechanical phenomena, such as quantum superposition or quantum entanglement, and they all stem from Quantum Information Technology, meaning they all will rely on the capability of coherently manipulate quantum systems. To be considered part of the Second Quantum Revolution, a given technology needs to have the capability of dealing with individual quantum bits, for example, individual spins, rather than with the average signal of an ensemble of quantum bits or spins. It is commonly noted that this capability will enable quantum information processing, commonly known as Quantum Computing.

The fundamental pieces in Quantum Computing are quantum bits and quantum logical gates, which are the quantum analogues to classical bits and Boolean logic gates: the elementary information unit and the elementary manipulation of information. A quantum bit or *qubit* is a quantum two-level system, e.g. a spin  $S=1/2$ , while a *quantum gate* is a logic operation between two or more of such qubits. Preparing quantum algorithms based on a series of quantum gates is qualitatively more efficient than classical information processing for a series of problems. This notably includes the physical simulation of quantum systems themselves and thus is of practical interest to physicists and chemists. While the potential benefits are enormous, two extremely challenging requisites needed for Quantum Computing are (a) sufficiently long quantum coherence times and (b) the possibility to

“scale up” the system to many hundreds of usable qubits. Neither has been satisfactorily met yet. The latter requirement, termed *scalability*, is mostly an engineering problem. While preparing an Avogadro number of identical spins is trivial in chemistry, preparing a compact array of hundreds (or millions) of spins that are physically distinguishable is very difficult. Indeed, the ability of chemists to obtain and combine molecular variations of a given system have a limit. Thus, from the point of view of chemistry, the problem of scalability is translated into achieving a magnetic molecule which can be efficiently coupled to a superconducting circuit, and then it is an engineering task to prepare a circuit that can be made complex enough by using relatively simple pieces (93). Additionally, as we will see with an example below, benefits are to be gained if the elected magnetic molecule has more than two accessible magnetic energy levels and thus can embody more than a single qubit.

In this chapter, we shall mostly concentrate on the problem of decoherence, which is a major obstacle for quantum applications (94). For chemists, it is easiest to think of decoherence as the spin–spin relaxation in NMR: an irreversible loss of information than cannot be recovered by spin echoes. It is in fact a rather analogous process, but taking into account that with magnetic molecules we care about the electronic spin rather than the nuclear spin. More properly, decoherence can be defined as the loss of the fragile quantum phase information because of an uncontrolled entanglement of the qubit with its environment: as the environment evolves in what is basically a classical way, the qubit is effectively “measured” and any quantum process is irreversibly perturbed. Here the environment is understood in a very general way, and, as we will mention later, notably includes electronic spins, nuclear spins, and lattice vibrations.

Decoherence is no trivial phenomenon; in fact, it is actually a fundamental physical problem, with deep philosophical consequences. Furthermore, in most solid-state systems, there is a chain of progressively weaker interactions that become relevant in the Hamiltonian as the temperature is lowered. This is a key obstacle in the quest of coherence, since this means that lowering the temperature does not in general mean entering a regime with no unwanted energy levels whose dynamics can destroy quantum effects.

One needs to note that we still lack general analyses of every relevant mechanism of decoherence, but much progress has been made in some areas such as the one represented by SMMs (95,96). The contributions of the so-called nuclear bath and electron spin baths have now been quantified and can be calculated (97) and the coupling with vibrations and the focus is currently on the coupling with phonons through local vibrations (98).

The most commonly used parameters to experimentally quantify the decoherence time in magnetic molecules are the spin–spin relaxation time  $T_2$  and the related phase memory  $T_m$ , which are analogous to the same parameters in NMR. In combination with the oscillation frequency, which characterizes the speed with which we are able to reverse a spin,  $T_2$  permits to estimate the average number of oscillations between the two states of the qubit that can happen before the system loses quantum phase information. Here it is interesting to note that symbols can be a source of confusion, since the same notation “ $T_2$ ” for a theoretician can represent a theoretical estimate, based on a handful of well-defined mechanisms, but for an experimentalist, it can instead represent an effective coefficient in an exponential equation that approximately reproduces a given experimental result, where the underlying mechanisms have perhaps not yet been well described. From a theoretical perspective, it is crucial to understand the mechanistic details behind decoherence, but from a practical standpoint, it suffices to guarantee that quantum coherence is maintained for a long enough time to “operate” the qubit, and often it is this criterion the one that determines whether a system is a suitable qubit. Practically, one commonly measures the so-called Rabi oscillations, which are coherent oscillations between the “up” and “down” orientations of a spin, or more generally between two energy levels representing the  $|0\rangle$  and  $|1\rangle$  states of the qubit. These are obtained by a nutation experiment in a pulsed-EPR setup, and the ability to measure at least a few Rabi oscillations in a given magnetic molecule is considered indicative of a good potential as a qubit.

As the above definition of qubit (a quantum two-level system) is rather general, of course very different physical, chemical, or even biological systems can embody a qubit. It turns out that, from the point of view of quantum coherence not all candidates are equally well suited, and it is at this point where chemical design may play a leading role. Indeed, the spectacular results reported in the last few years on the use of either Nitrogen-Vacancy (NV) defects in a diamond matrix, or Phosphorus impurities in a silicon matrix (99) have shown the potential of solid-state systems, which now rival optical systems. In the cases of NV defects and P impurities, record decoherence times of the order of milliseconds are regularly obtained for electronic spins. These reach multiple seconds in the case of nuclear spins (at low and even at room temperature), but with the downside that nuclear spins are harder and slower to couple to each other and to manipulate externally.

Recent relevant advances in molecular spin qubits designed through chemistry have shown that these systems can provide  $T_2$  times that are

competitive with those reported in the above solid-state systems. This can be seen in two relevant examples based on mononuclear transition metal complexes. The first case is Freedman's record of  $T_2 = 0.7$  ms for a fully deuterated salt of a Vanadium (IV) complex where the ligand carries no nuclear spins,  $(d^{20}\text{-Ph}_4\text{P})_2[\text{V}(\text{C}_8\text{S}_8)_3]$  in frozen  $\text{CS}_2$  solution (100). A careful design of the environment guarantees in this case a minimal presence of spins, not only in the complex but also in the solvent. Crucially, the ligands also lack methyl groups, where the free rotation can be a stronger component of decoherence, in addition to its contribution to the nuclear spin bath. Since the ligands are planar, there is also a certain rigidity of the environment.

The second study focuses precisely on vibrations, showing the crucial role of the rigid vanadyl stretching vibration, which is the only molecular movement that is strongly coupled to the qubit energy, allowing  $T_2 = 1$  ms at room temperature in a crystalline sample of  $[(\text{Ph})_4\text{P}]_2[(\text{VO})_{0.05}(\text{MoO})_{0.95}(\text{dmit})_2]$  (101). This example has shown the key role played by the spin-vibration coupling to understand and influence the relaxation mechanisms, underlying the relevance of the theory to predict the most relevant vibrational modes involved in these mechanisms (98,102).

Another aspect in which a molecular approach can be a suitable source of molecular spin qubits is that related with biophysics. In the last few years, the study of quantum effects in biological systems have also become a hot topic, as some natural biological processes—most notably, photosynthesis in plants and geolocation in birds—have been found to have a relation with quantum coherence. This shows that quantum coherent processes in molecules are not just beautiful theoretical constructs but may also be real-world solutions. In this context, the molecular self-organization processes, which are ubiquitous in biochemistry, may be an added value in the aim toward scalability (103).

## 4.2 POMs as Spin Qubits

A distinctive advantage of POMs is the possibility of combining a rich magnetochemistry with an environment that is relatively free of nuclear spins, which is in fact one of the main sources of decoherence for solid-state spin qubits. Of course, crystalline solids, such as simple oxides or ternary oxides, can also be free of nuclear spins, but these typically lack the flexibility of molecular chemistry. Typically it is not necessary to resort to isotopic purification, since the contribution to decoherence from oxygen, wolfram, molybdenum, and even phosphorus are in general negligible compared with other decoherence sources (97).

In the spin-localized POMs, the manipulation of quantum information can take place through time-dependent magnetic fields, i.e., EPR pulses. These coherently rotate the orientation of the magnetization of a macroscopic sample but can also be seen as coherently manipulating the quantum superposition between two or more spin states. In the spin-delocalized MV POMs, as we will discuss in the next section, the extra electrons enable a quantum manipulation through a precisely controlled time-dependent electric field.

Focusing on spin-localized POMs, let us start with the possibility of using as qubits cage complexes with an  $S = 1/2$  ground state. One example of this strategy is provided by the cluster  $[V_{15}As_6O_{42}(H_2O)]^{6-}$  SMM, which contains 15 antiferromagnetically coupled  $S = 1/2$  spins, leading to an  $S = 1/2$  collective ground state. When this system is placed into a resonant cavity, the microwave field induces oscillatory transitions between the ground and excited collective spin states (Rabi oscillations), indicative of long-lived quantum coherence (104). It has also been possible to distinguish between the Rabi oscillations of the ground state  $S = 1/2$  ( $T_2 = 149$  ns) and the first excited state  $S = 3/2$  ( $T_2 = 187.7$  ns) in a frozen trichloromethane solution at 2.4 K (105).

We shall now look at mononuclear lanthanoid POMs described in Section 2 as a source of spin qubits. Early studies of spin-lattice relaxation in  $ErW_{10}$  already indicated that these SIMs are promising candidates to act as the hardware for quantum information (75). More recently, it was possible to use single-crystals of  $Ho_xY_{(1-x)}W_{10}$ , to obtain unusually long decoherence times in relatively concentrated samples ( $T_2 \approx 8$   $\mu$ s at 5 K, regardless of whether  $x = 10^{-2}$  or  $x = 10^{-3}$ ). By operating at special values of the magnetic field in which the Ho energy levels are crossing, the corresponding transition energies (which are analogous to those reported in atomic clocks) have shown to be independent of the magnetic field up to the first order. This makes the nanomagnet invisible to the magnetic field at these points, therefore protecting the quantum process from magnetic noise, and thus making it resistant to fluctuations of neighboring spins. It was only possible to enter this regime because of the match between frequency of the EPR spectrometer and the unusually large tunneling splitting in this system, which in turns results from a  $C_4$  symmetry and a ground doublet mixing between  $M_J = +4$  and  $M_J = -4$ . The key advance here is the ability to ramp up concentration, since the usual operating conditions for maximum coherence time in studies on solid-state spin qubits has been to work with extremely dilute samples of the order of  $x = 10^{-4}$  to  $x = 10^{-5}$ .

Thus, the strategy of extreme dilution is a way to minimize unwanted interactions with nuclei or other qubits, which act as fluctuations in the magnetic field felt by each qubit and cause decoherence, but is undesirable since (a) for ensemble measurements, it decreases the signal; (b) for future single-molecule experiments, it evidences an extreme susceptibility to neighboring spins; and (c) it effectively impedes a setup that allows any kind of desired qubit–qubit communication such as two-qubit logical gates. It is envisioned that the use of clock transitions arising from a large tunneling splitting will help ease these problems.

Following on the idea of clock transitions, a theoretical study was presented on a different POM, in this case the Ho derivative of the  $[\text{LnPd}_{12}(\text{AsPh})_8\text{O}_{32}]^{5-}$  family of polyoxopalladates, in which the magnetic ion presents a cubic coordination environment (106). The lack of anisotropy, which makes these systems unsuitable as SMMs, generates an extraordinarily rich level structure at low energies. Lifting the strict cubic symmetry e.g. by an axial distortion of the cube or by applying an external magnetic field, it is possible to reach a regime where decoherence caused by the spin bath is expected to be quenched (see Fig. 14). This is achieved in the ground doublet when the two-qubit states have virtually identical spin expectation values, in a new kind of clock transition. In this regime the qubit states should be invisible to the spin bath, and vice versa.

Further exploration on decoherence minimization using POMs was performed using the  $\text{Gd}^{3+}$  analog of  $\text{DyW}_{30}^-$ , i.e.,  $[\text{GdP}_5\text{W}_{30}\text{O}_{110}]^{12-}$

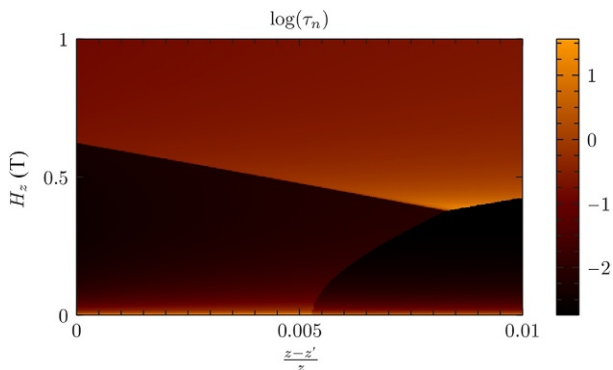


**Fig. 14** Logarithm of the variation of the decoherence time (in s) for a transition between the ground state and the first excited state, considering only the nuclear spin bath. The lines with sudden changes of decoherence time correspond to spin energy level crossings. *Vertical axis*: influence of a magnetic field. *Horizontal axis*: influence of an axial compression of up to 1% of the interatomic distances.

(in short, GdW<sub>30</sub>). There we experimentally proved that, if the pulse power can be set up in such a way that the Rabi oscillations is very close to the Larmor frequency of the proton (something known as the Hartmann–Hahn condition) a large number (>50) of Rabi-like coherent oscillations can be detected, about an order of magnitude higher compared with what is usual in other magnetic molecules. As a further alternative approach to highly coherent qubit storage in the same system, the influence of deuteration, diamagnetic dilution and microwave pulse power was tested on GdW<sub>30</sub>. Unexpectedly, high quantum coherence is maintained for longer times under high microwave power and moderate diamagnetic dilution compared with attenuated pulses and/or higher dilution. In the best conditions, strict coherence ( $0.999 > F > 0.99$ ) can be maintained for up to ( $0.6 < 2 < 1.1 \mu\text{s}$ ). The optimal regime involves a double stretched exponential decay with stretching parameters that are unprecedentedly high for molecular spin qubits.

### 4.3 POMs as Quantum Gates

In the previous section, we have seen that, among magnetic molecules, the magnetochemistry of POM makes them obvious candidates for the design of spin qubits. Since more than one spin qubit can be encapsulated in a single molecule, let us explore here the potential of POMs as hardware to implement quantum gates or even simple quantum processors.

The first proposal in this direction was made in the context of MV POMs, as outlined in [Section 3](#): in  $[\text{PMo}_{12}\text{O}_{40}(\text{VO})_2]^{q-}$  connected to an electric circuit through a STM set up, one can control the magnetic coupling between the two spins located at the  $(\text{VO})^{2+}$  sites through an electric tunneling current that injects a controlled number of electrons in the central MV Keggin cluster. An accurate time control to this spintronic switch permits the implementation of a  $\sqrt{\text{SWAP}}$  quantum gate, a fundamentally quantum operation that can leave the qubits in a superposition between two eigenstates. At the starting point of the process the Keggin cluster has an even number of electrons; this can be achieved with the help of a backgate potential. The quantum operation begins by changing the gate voltage so that an electron tunnels from the tip into the molecule, and ends at a certain time by reverting to the initial voltage so that the electron tunnels back out. The time needed to achieve a SWAP (or a  $\sqrt{\text{SWAP}}$ ) quantum gate between the left and right spin qubits, as well as the quantum fidelity of said operation, is a function of the effective exchange coupling parameters—which are characteristic of the molecule—and the tunnel coupling to the STM tip—which in



principle can be tuned. Several analogue POMs exist that could serve as extensions of this scheme, where the complexity of the qubit network is augmented either by either using  $\text{Ni}^{\text{II}}$  ( $S=1$ ) instead of  $\text{V}^{\text{IV}}$  ( $S=1/2$ ) or by having four magnetic sites instead of two.

More recently, a remarkable experimental advance has occurred with a proposal to integrate several electron spin qubits in a single magnetic ion, whose energy level scheme is tuned by a suitably chosen molecular environment (107). As in previous experimental implementations outlined in the previous section, this approach was illustrated with  $\text{GdW}_{30}$ , i.e., a nearly isotropic  $\text{Gd}^{3+}$  ion entrapped by a large POM molecule. This molecule was chosen because it provides an equatorial coordination environment that produces a very weak crystal field environment in  $\text{Gd}^{3+}$ , so that all required transitions can take place an energy window allowed by conventional pulsed-EPR technology, e.g., X-band (108). This is precisely the key ingredient that was missing in the proposal by Leuenberger and Loss to use  $\text{Mn}_{12}$  as a multiqubit system (109), a promising proposal that physicists have not been able to implement experimentally so far. By using microwave technologies, either three-dimensional cavities or quantum superconducting circuits, it was shown that the eight spin states corresponding to the ground  $S=7/2$  multiplet of  $\text{GdW}_{30}$  allow a set of coherently addressable transitions (with modest  $T_2$  times in the order of hundreds of nanoseconds, but allowing multiple Rabi oscillations) and thus allow a universal three-qubit processor (see Fig. 15). Given that all the transitions occur within a single ion, the problem of decoherence caused by dipolar interactions between neighboring qubits is not applicable, and it is possible to strongly couple three qubits while working with highly diluted magnetic samples. It constitutes a very efficient way (alternative to the atomic clock transitions) to minimize decoherence in these magnetic molecules. These results are especially interesting in the light of the recent proposal for a scalable architecture for Quantum Computation with molecular nanomagnets (93).



## 5. CONCLUDING REMARKS

After many years of being employed as minimal models in Molecular Magnetism and convenient playing ground to study fundamental phenomena, such as anisotropic magnetic exchange, electron transfer, and their intricate relation with Coulombic repulsion and vibronic coupling, POMs have now jumped to the stage of the rational design of SIMs and are being considered as test subjects for simple experiments in Single-Molecule

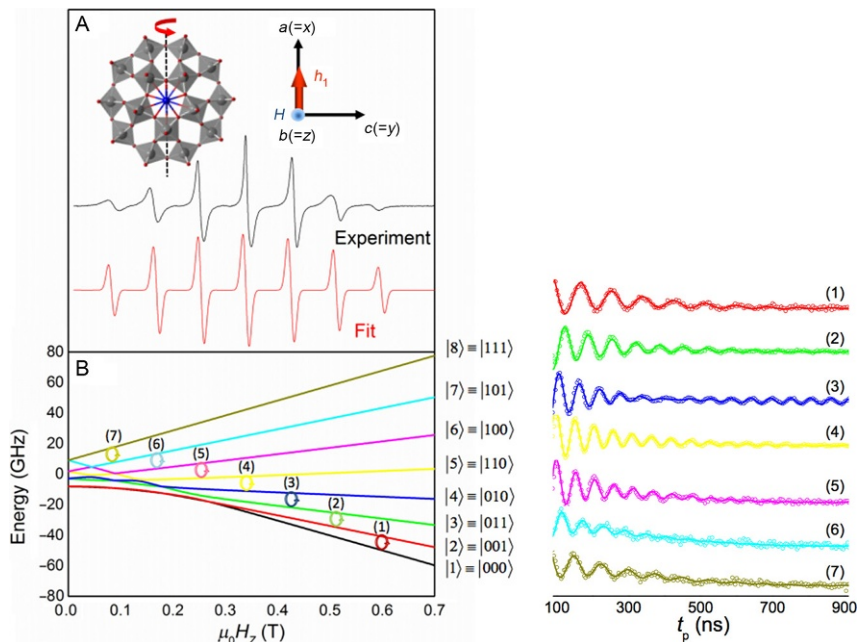


**Fig. 15** (Left) upper panel: Structure of  $GdW_{30}$ , orientation of the external magnetic field, continuous wave-EPR (experiment and simulation) (A) and theoretical energy level splitting displaying the eight energy levels and the seven transitions (B). (Right) Coherent Rabi oscillations for each of the seven transitions.

Spintronics and Molecular Quantum Computing. The two main features that made them attractive to be studied in Molecular Magnetism are still behind their current interest. These can be described as follows:

- (1) They are able to coordinate oxophilic magnetic cations and consist of fused regular polyhedra. Thus, they tend to encapsulate spins in very robust, highly symmetrical cages, on which multiple variations can be performed to study magnetostructural relations. This is equally interesting whether one is focused on magnetic exchange in polynuclear transition metal clusters or on the ligand field of mononuclear lanthanide complexes. Indeed, the theoretical characterization of families exhibiting similar coordination spheres from ligands of different natures has proven to be a useful path toward the design of new SIMs.
- (2) They are singular MV systems. The electron resides in essentially non-bonding  $d$  orbitals and as it can efficiently transfer via the pervasive network of oxo-bridges. This, combined with the previous characteristic, opens an infinite well of possibilities for the interaction of localized and

delocalized spins. With the current interest in Molecular Spintronics, the possibilities include the application of an electric field, which in the particular case of Quantum Computing needs to be time-dependent. Both in theory and in the experiment, it has been proven that POMs allow unique advancements in these fields.

Finally, one needs to note that certain characteristics which POMs have always displayed are now being found to be useful, in particular their rigidity and their low abundance of nuclear spins. In both cases, these properties facilitate the preservation of the quantum coherence (or quantum phase information) of encapsulated spins, which is a very desirable characteristic for Spintronics in general and for Quantum Computing in particular. This may be one of the reasons why several relevant advances in the field of molecular spin qubits have been led by POMs.

## ACKNOWLEDGMENTS

We wish to thank our colleagues, coworkers, and collaborators for the important contributions to the work reported herein. The present work has been funded by the EU (ERC Consolidator Grant DECRESIM, COST Actions CM1203 “Polyoxometalate Chemistry for Molecular Nanoscience, PoCheMon” and CA15128 Molecular Spintronics (MOLSPIN)), the Spanish MINECO (Grant MAT2014-56143-R, CTQ2014-52758-P, and Excellence Unit María de Maeztu MDM-2015-0538 granted to ICMol), and the Generalitat Valenciana (Prometeo Programme of Excellence). A.G.-A. acknowledges funding by the MINECO (Ramón y Cajal contract).

## REFERENCES

1. Wolf, S. A.; Awschalom, D. D.; Buhrman, R. A.; Daughton, J. M.; von Molnár, S.; Roukes, M. L.; Chtchelkanova, A. Y.; Treger, D. M. *Science* **2001**, *294*(5564), 1488–1495.
2. Baibich, M. N.; Broto, J. M.; Fertre, A.; Nguyen Van Dau, F.; Petroff, F.; Etienne, P.; Creuzet, G.; Friederich, A.; Chazelas, J. *Phys. Rev. Lett.* **1988**, *61*, 2472–2475.
3. Binasch, G.; Grünberg, P.; Saurenbach, F.; Zinn, W. *Phys. Rev. B* **1989**, *39*, 4828–4830.
4. Akerman, J. *Science* **2005**, *308*, 508–510.
5. Prejbeanu, I. L.; Kerekes, M.; Sousa, R. C.; Sibuet, H.; Redon, O.; Diény, B.; Nozières, J. P. *J. Phys. Condens. Matter* **2007**, *19*, 165218.
6. Georges, B.; Grollier, J.; Darques, M.; Cros, V.; Deranlot, C.; Marcilhac, B.; Faini, G.; Fert, A. *Phys. Rev. Lett.* **2008**, *101*, 017201.
7. Petta, J. R.; Johnson, A. C.; Taylor, J. M.; Laird, E. A.; Yacoby, A.; Lukin, M. D.; Marcus, C. M.; Hanson, M. P.; Gossard, A. C. *Science* **2005**, *309*, 2180–2184.
8. Rocha, A. R.; García-Suárez, V. M.; Bailey, S. W.; Lambert, C. J.; Ferrer, J.; Sanvito, S. *Nat. Mater.* **2005**, *4*, 335–339.
9. Sanvito, S.; Rocha, A. R. *J. Comput. Theor. Nanosci.* **2006**, *3*, 874–879.
10. Coronado, E.; Epsetin, A. J. *J. Mater. Chem.* **2009**, *19*, 1670–1671.
11. Sanvito, S.; Rocha, A. R. *J. Comput. Theor. Nanosci.* **2006**, *3*, 624–642.

12. Pramanik, S.; Stefanita, C. G.; Patibandla, S.; Bandyopadhyay, S.; Garre, K.; Harth, N.; Cahay, M. *Nat. Nanotechnol.* **2007**, *2*, 216–219.
13. Prins, F.; Monrabal-Capilla, M.; Osorio, E. A.; Coronado, E.; van der Zant, H. S. J. *Adv. Mater.* **2011**, *23*, 1545–1549.
14. Borrás-Almenar, J. J.; Clemente-Juan, J. M.; Coronado, E.; Tsukerblat, B. S. *Inorg. Chem.* **1999**, *38*, 6081–6088.
15. Clemente-Juan, J. M.; Coronado, E.; Gaita-Ariño, A. *Chem. Soc. Rev.* **2012**, *41*, 7464–7478.
16. Suaud, N.; Gaita-Ariño, A.; Clemente-Juan, J. M.; Coronado, E. *Chem. Eur. J.* **2004**, *10*, 4041–4053.
17. Borrás-Almenar, J. J.; Cardona-Serra, S.; Clemente-Juan, J. M.; Coronado, E.; Palií, A. V.; Tsukerblat, B. S. *J. Comput. Chem.* **2010**, *31*, 1321–1332.
18. Maestre, J. M.; Poblet, J. M.; Bo, C.; Casañ-Pastor, N.; Gómez-Romero, P. *Inorg. Chem.* **1998**, *37*, 3444–3446.
19. Lehmann, J.; Gaita-Ariño, A.; Coronado, E.; Loss, D. *Nat. Nanotechnol.* **2007**, *2*, 312–317.
20. Cardona-Serra, S.; Clemente-Juan, J. M.; Gaita-Ariño, A.; Suaud, N.; Svoboda, O.; Coronado, E. *Chem. Commun.* **2013**, *49*, 9621–9623.
21. Cardona-Serra, S.; Clemente-Juan, J. M.; Coronado, E.; Gaita-Ariño, A.; Suaud, N.; Svoboda, O.; Bastardis, R.; Guihéry, N.; Palacios, J. J. *Chem. Eur. J.* **2015**, *21*, 763–769.
22. Suaud, N.; Masaro, Y.; Coronado, E.; Clemente-Juan, J. M.; Guihéry, N. *Eur. J. Inorg. Chem.* **2009**, *2009*, 5109–5114.
23. Clemente-Juan, J. M.; Coronado, E.; Gaita-Ariño, A. In *World Scientific Series in Nanosciences and Nanotechnologies*; Secheresse, F., Ed.; World Scientific Publishing Co. Pte. Ltd: London, UK, 2013; pp. 155–172.
24. Gatteschi, D.; Sessoli, R. *Angew. Chem. Int. Ed. Engl.* **2003**, *42*, 268–297.
25. Bogani, L.; Wernsdorfer, W. *Nat. Mater.* **2008**, *7*, 179–186.
26. Ishikawa, N.; Sugita, M.; Ishikawa, T.; Koshihara, S. Y.; Kaizu, Y. *J. Am. Chem. Soc.* **2003**, *125*, 8694–8695.
27. Ganzhorn, M.; Klyatskaya, S.; Ruben, M.; Wernsdorfer, W. *Nat. Nanotechnol.* **2013**, *8*, 165–169.
28. Candini, A.; Klyatskaya, S.; Ruben, M.; Wernsdorfer, W.; Affronte, M. *Nano Lett.* **2011**, *11*, 2634–2639.
29. AlDamen, M. A.; Clemente-Juan, J. M.; Coronado, E.; Martí-Gastaldo, C.; Gaita-Ariño, A. *J. Am. Chem. Soc.* **2008**, *130*, 8874–8875.
30. Shiddiq, M.; Komijani, D.; Duan, Y.; Gaita-Ariño, A.; Coronado, E.; Hill, S. *Nature* **2016**, *531*, 348–351.
31. Clemente-Juan, J. M.; Coronado, E. *Coord. Chem. Rev.* **1999**, *193–195*, 361–394.
32. Long, D. L.; Burkholder, E.; Cronin, L. *Chem. Soc. Rev.* **2007**, *36*, 105–121.
33. Palií, A.; Tsukerblat, B.; Klokishner, S.; Dunbar, K. R.; Clemente-Juan, J. M.; Coronado, E. *Chem. Soc. Rev.* **2011**, *40*, 3130–3156.
34. Gómez-García, C. J.; Coronado, E.; Borrás-Almenar, J. J.; Aebersold, M.; Güdel, H. U.; Mutka, H. *Phys. B* **1992**, *181*, 238–240.
35. Andres, H.; Clemente-Juan, J. M.; Aebersold, M.; Güdel, H. U.; Coronado, E.; Büttner, H.; Kearly, G.; Melero, J.; Burriel, R. *J. Am. Chem. Soc.* **1999**, *121*, 10028–10034.
36. Clemente-Juan, J. M.; Coronado, E.; Gaita-Ariño, A.; Giménez-Saiz, C.; Güdel, H. U.; Sieber, A.; Bircher, R.; Mutka, H. *Inorg. Chem.* **2005**, *44*, 3389–3395.
37. Botar, B.; Ellern, A.; Hermann, R.; Kögerler, P. *Angew. Chem. Int. Ed. Engl.* **2009**, *48*, 9080–9083.

38. Borrás-Almenar, J. J.; Clemente, J. M.; Coronado, E.; Tsukerblat, B. S. *Chem. Phys.* **1995**, *195*, 1–15.
39. Borrás-Almenar, J. J.; Clemente, J. M.; Coronado, E.; Tsukerblat, B. S. *Chem. Phys.* **1995**, *195*, 29–47.
40. Tsukerblat, B.; Palií, A.; Clemente-Juan, J. M.; Gaita-Ariño, A.; Coronado, E. *Int. J. Quantum Chem.* **2012**, *112*(17), 2957–2964.
41. Wernsdorfer, W.; Aliaga-Alcalde, N.; Hendrickson, D. N.; Christou, G. *Nature* **2002**, *416*, 406–409.
42. Hill, S.; Edwards, R. S.; Aliaga-Alcalde, N.; Christou, G. *Science* **2003**, *302*, 1015–1018.
43. Wernsdorfer, W.; Chakov, N. E.; Christou, G. *Phys. Rev. Lett.* **2005**, *95*, 037203.
44. Sessoli, R.; Tsai, H. L.; Schake, A. R.; Wang, S.; Vincent, J. B.; Folting, K.; Gatteschi, D.; Christou, G.; Hendrickson, D. N. *J. Am. Chem. Soc.* **1993**, *115*, 1804–1816.
45. Friedman, J.; Sarachik, M.; Tejada, J.; Ziolo, R. *Phys. Rev. Lett.* **1996**, *76*, 3830.
46. Thomas, L.; Lioni, F.; Ballou, R.; Gatteschi, D.; Sessoli, R.; Barbara, B. *Nature* **1996**, *383*, 145–147.
47. Wernsdorfer, W.; Ohm, T.; Sangregorio, C.; Sessoli, R.; Mailly, D.; Paulsen, C. *Phys. Rev. Lett.* **1999**, *82*, 3903.
48. Barra, A. L.; Debrunner, P.; Gatteschi, D.; Schulz, C. E.; Sessoli, R. *Europhys. Lett.* **1996**, *35*, 133–138.
49. Wernsdorfer, W.; Caneschi, A.; Sessoli, R.; Gatteschi, D.; Cornia, A.; Villar, V.; Paulsen, C. *Phys. Rev. Lett.* **2000**, *84*, 2965.
50. Wernsdorfer, W.; Caneschi, A.; Sessoli, R.; Gatteschi, D.; Cornia, A. *Europhys. Lett.* **2000**, *50*, 552–558.
51. Yoo, J.; Brechin, E. K.; Yamaguchi, A.; Nakano, M.; Huffman, J. C.; Maniero, A. L.; Brunel, L. C.; Awaga, K.; Ishimoto, H.; Christou, G.; Hendrickson, D. N. *Inorg. Chem.* **2000**, *39*, 3615–3623.
52. Aubin, S. M. J.; Wemple, M. W.; Adams, D. M.; Tsai, H.-L.; Christou, G.; Hendrickson, D. N. *J. Am. Chem. Soc.* **1996**, *118*, 7746–7754.
53. King, P.; Wernsdorfer, W.; Abboud, K. A.; Christou, G. *Inorg. Chem.* **2004**, *43*, 7315–7323.
54. Tasiopoulos, A.; Vinslava, A.; Wernsdorfer, W.; Abboud, K. A.; Christou, G. *Angew. Chem. Int. Ed. Engl.* **2004**, *43*, 2117–2121.
55. Murugesu, M.; Takahashi, S.; Wilson, A.; Abboud, K. A.; Wernsdorfer, W.; Hill, S.; Christou, G. *Inorg. Chem.* **2008**, *47*, 9459–9470.
56. Compain, J.-D.; Mialane, P.; Dolbecq, A.; Mbomekallé, I. M.; Marrot, J.; Sécheresse, F.; Rivière, E.; Rogez, G.; Wernsdorfer, W. *Angew. Chem. Int. Ed. Engl.* **2009**, *48*, 3077–3081.
57. Ibrahim, M.; Lan, Y.; Bassil, B. S.; Xiang, Y.; Suchopar, A.; Powell, A. K.; Kortz, U. *Angew. Chem. Int. Ed. Engl.* **2011**, *50*, 4708–4711.
58. Fang, X.; Kögerler, P.; Speldrich, M.; Schilder, H.; Lubana, M. *Chem. Commun.* **2012**, *48*, 1218–1220.
59. Ishikawa, N.; Sugita, M.; Ishikawa, T.; Koshihara, S. Y.; Kaizu, Y. *J. Phys. Chem. B* **2004**, *108*, 11265–11271.
60. Sessoli, R.; Powell, A. K. *Coord. Chem. Rev.* **2009**, *253*, 2328–2341.
61. Campbell, V. E.; Bolvin, H.; Rivière, E.; Guillot, R.; Wernsdorfer, W.; Mallah, T. *Inorg. Chem.* **2014**, *53*(5), 2598–2605.
62. Jiang, S.; Sun, H.; Wang, Z.; Gao, S. *J. Am. Chem. Soc.* **2011**, *133*, 4730–4733.
63. Jiang, S.; Wang, B.; Su, G.; Wang, Z.; Gao, S. *Angew. Chem. Int. Ed. Engl.* **2010**, *49*, 7448–7451.

64. Cucinotta, G.; Perfetti, M.; Luzón, J.; Etienne, M.; Car, P. E.; Caneschi, A.; Calvez, G.; Bernot, K.; Sessoli, R. *Angew. Chem. Int. Ed. Engl.* **2012**, *51*, 1606–1610.
65. Rinehart, J. D.; Long, J. R. *J. Am. Chem. Soc.* **2009**, *131*, 12558–12559.
66. Rinehart, J. D.; Meihaus, K. R.; Long, J. R. *J. Am. Chem. Soc.* **2010**, *132*, 7572–7573.
67. Harman, W. H.; Harris, T. D.; Freedman, D. E.; Fong, H.; Chang, A.; Rinehart, J. D.; Ozarowski, A.; Sougrati, M. T.; Grandjean, F.; Long, G. J.; Long, J. R.; Chang, C. J. *J. Am. Chem. Soc.* **2010**, *132*, 18115.
68. Zadrozny, J. M.; Long, J. R. *J. Am. Chem. Soc.* **2011**, *133*, 20732.
69. Baldoví, J. J.; Cardona-Serra, S.; Clemente-Juan, J. M.; Coronado, E.; Gaita-Ariño, A.; Palií, A. *Inorg. Chem.* **2012**, *51*(22), 12565.
70. (a) Ardavan, A.; Blundell, S. J. *J. Mater. Chem.* **2009**, *19*, 1754; (b) Troiani, F.; Affronte, M. *Chem. Soc. Rev.* **2011**, *40*, 3119.
71. Ishikawa, N. *J. Phys. Chem. A* **2003**, *107*, 5831–5835.
72. (a) Baldoví, J. J.; Cardona-Serra, S.; Clemente-Juan, J. M.; Coronado, E.; Gaita-Ariño, A.; Palií, A. *J. Comput. Chem.* **2013**, *34*, 1961–1967; (b) Baldoví, J. J.; Clemente-Juan, J. M.; Coronado, E.; Gaita-Ariño, A.; Palií, A. *J. Comput. Chem.* **2014**, *35*(26), 1930–1934.
73. Bethe, H. A. *Ann. Phys.* **1929**, *3*, 133–206.
74. Baldoví, J. J.; Clemente-Juan, J. M.; Coronado, E.; Duan, Y.; Gaita-Ariño, A.; Giménez-Saiz, C. *Inorg. Chem.* **2014**, *53*(18), 9976–9980.
75. Luis, F.; Martínez-Pérez, M. J.; Montero, O.; Coronado, E.; Cardona-Serra, S.; Martí-Gastaldo, C.; Clemente-Juan, J. M.; Sesé, J.; Drung, D.; Schurig, T. *Phys. Rev. B* **2010**, *82*, 060403.
76. Rinehart, J. D.; Long, J. R. *Dalton Trans.* **2012**, *41*, 13572–13574.
77. Baldoví, J. J.; Duan, Y.; Bustos, C.; Cardona-Serra, S.; Gouzerh, P.; Villanneau, R.; Gontard, G.; Clemente-Juan, J. M.; Gaita-Ariño, A.; Giménez-Saiz, C.; Proust, A.; Coronado, E. *Dalton Trans.* **2016**, *45*, 16653–16660.
78. Kitamura, A.; Ozeki, T.; Yagasaki, A. *Inorg. Chem.* **1997**, *36*, 4275–4279.
79. Bustos, C.; Carey, D. M.-L.; Boubekeur, K.; Thouvenot, R.; Proust, A.; Gouzerh, P. *Inorg. Chim. Acta* **2010**, *363*, 4262–4268.
80. Baldoví, J. J.; Gaita-Ariño, A.; Coronado, E. *Dalton Trans.* **2015**, *44*, 12535–12538.
81. Meihaus, K. R.; Long, J. R. *J. Am. Chem. Soc.* **2013**, *135*, 17952–17957.
82. Singh, S. K.; Gupta, T.; Rajaraman, G. *Inorg. Chem.* **2014**, *53*, 10835–10845.
83. Vonci, M.; Giansiracusa, M. J.; Gable, R. W.; van den Heuvel, W.; Latham, K.; Moubaraki, B.; Murray, K. S.; Yu, D.; Mole, R. A.; Soncini, A.; Boskovic, C. *Chem. Commun.* **2016**, *52*, 2091–2094.
84. Droghetti, A.; Sanvito, S. *Phys. Rev. Lett.* **2011**, *107*, 047201.
85. Palií, A.; Tsukerblat, B.; Clemente-Juan, J. M.; Coronado, E. *J. Phys. Chem. C* **2012**, *116*, 4999.
86. Bosch-Serrano, C.; Clemente-Juan, J. M.; Coronado, E.; Gaita-Ariño, A.; Palií, A.; Tsukerblat, B. *ChemPhysChem* **2012**, *13*(11), 2662–2665.
87. Lehmann, J.; Gaita-Ariño, A.; Coronado, E.; Loss, D. *J. Mater. Chem.* **2009**, *19*(12), 1672–1677.
88. Trif, M.; Troiani, F.; Stepanenko, D.; Loss, D. *Phys. Rev. Lett.* **2008**, *101*, 217201.
89. Bi, L.-H.; Kortz, U.; Dickman, M. H.; Nellutla, S.; Dalal, N. S.; Keita, B.; Nadjo, L.; Prinz, M.; Neumann, M. *J. Cluster Sci.* **2006**, *17*, 143–165.
90. Clemente-Juan, J. M.; Coronado, E.; Gaita-Ariño, A.; Suaud, N. *J. Phys. Chem. A* **2007**, *111*, 9969.
91. Sherif, S.; Rubio-Bollinger, G.; Pinilla-Cienfuegos, E.; Coronado, E.; Cuevas, J. C.; Agraït, N. *Nanotechnology* **2015**, *26*, 291001.
92. Lewis, A.M.; Krämer, M.; Travagnin, M. Quantum Technologies: Implications for European Policy. EUR 27915 EN; DOI:10.2788/384376.

93. Jenkins, M. D.; Zueco, D.; Roubeau, O.; Aromí, G.; Majer, J.; Luis, F. *Dalton Trans.* **2016**, *45*, 16682.
94. Zagoskin, A. M. *Quantum Engineering*; Cambridge University Press: Cambridge, UK, 2011.
95. Takahashi, S.; Tupitsyn, I. S.; van Tol, J.; Beedle, C. C.; Hendrickson, D. N.; Stamp, P. C. E. *Nature* **2011**, *476*, 76–79.
96. Stamp, P. C. E.; Gaita-Ariño, A. *J. Mater. Chem.* **2009**, *19*, 1718–1730.
97. Cardona-Serra, S.; Escalera-Moreno, L.; Baldoví, J. J.; Gaita-Ariño, A.; Clemente-Juan, J. M.; Coronado, E. J. *Comput. Chem.* **2016**, *37*(13), 1238–1244.
98. Escalera-Moreno, L.; Suaud, N.; Gaita-Ariño, A.; Coronado, E. J. *Am. Chem. Soc.* **2016**, (under revision), arXiv:1512.05690v2.
99. Zwanenburg, F. A.; Dzurak, A. S.; Morello, A.; Simmons, M. Y.; Hollenberg, L. C. L.; Klimeck, G.; Rogge, S.; Coppersmith, S. N.; Eriksson, M. A. *Rev. Mod. Phys.* **2013**, *85*, 961.
100. Zadrozny, J. M.; Niklas, J.; Poluektov, O. G.; Freedman, D. E. *ACS Cent. Sci.* **2015**, *1*, 488–492.
101. Atzori, M.; Morra, E.; Tesi, L.; Albino, A.; Chiesa, M.; Sorace, L.; Sessoli, R. *J. Am. Chem. Soc.* **2016**, *138*, 11234–11244.
102. Tesi, L.; Lunghi, A.; Atzori, M.; Lucaccini, E.; Sorace, L.; Totti, F.; Sessoli, R. *Dalton Trans.* **2016**, *45*, 16635–16643.
103. Gaita-Ariño, A.; Prima-García, H.; Cardona-Serra, S.; Escalera-Moreno, L.; Rosaleny, L. E.; Baldoví, J. J. *Inorg. Chem. Front.* **2016**, *3*, 568–577.
104. Bertaina, S.; Gambarelli, S.; Mitra, T.; Tsukerblat, B.; Müller, A.; Barbara, B. *Nature* **2008**, *453*, 203–206.
105. Yang, J.; Wang, Y.; Wang, Z.; Rong, X.; Duan, C.-K.; Su, J.-H.; Du, J. *Phys. Rev. Lett.* **2012**, *108*, 230501.
106. Baldoví, J. J.; Rosaleny, L. E.; Ramachandran, V.; Christian, J.; Dalal, N. S.; Clemente-Juan, J. M.; Yang, P.; Kortz, U.; Gaita-Ariño, A.; Coronado, E. *Inorg. Chem. Front.* **2015**, *2*(10), 893–897.
107. Jenkins, M. D.; Duan, Y.; Diosdado, B.; García-Ripoll, J. J.; Gaita-Ariño, A.; Giménez-Saiz, C.; Alonso, P. J.; Coronado, E.; Luis, F. *Phys. Rev. Lett.* **2016**, (under revision), arXiv:1610.03994.
108. Martínez-Pérez, M. J.; Cardona-Serra, S.; Schlegel, C.; Moro, F.; Alonso, P. J.; Prima-García, H.; Clemente-Juan, J. M.; Evangelisti, M.; Gaita-Ariño, A.; Sesé, J.; van Slageren, J.; Coronado, E.; Luis, F. *Phys. Rev. Lett.* **2012**, *108*, 247213.
109. Leuenberger, M. N.; Loss, D. *Nature* **2012**, *410*, 789–793.

This page intentionally left blank





# Perspectives for Polyoxometalates in Single-Molecule Electronics and Spintronics

K.Y. Monakhov<sup>\*,†</sup>, M. Moors<sup>‡</sup>, P. Kögerler<sup>\*,†,1</sup>

<sup>\*</sup>Institute of Inorganic Chemistry, RWTH Aachen University, Aachen, Germany

<sup>†</sup>Peter Grünberg Institute (PGI-6), Research Centre Jülich, Jülich, Germany

<sup>‡</sup>Peter Grünberg Institute (PGI-7), Research Centre Jülich, Jülich, Germany

<sup>1</sup>Corresponding author: e-mail address: paul.koegerler@ac.rwth-aachen.de

## Contents

1. Introduction	252
2. Basics of Molecular Spin Electronics	255
3. Material Requirements for Molecular Spintronics	258
4. Advantages of Magnetic Polyoxometalates	260
4.1 Magnetically Functionalized Polyoxometalates Allow Studying the Effects of Anisotropic Environments on the Molecular Magnetic Properties	263
4.2 Hybrid Polyoxometalates Represent Potential Precursors for Controlled Molecule-Nanoelectrode Contacts	270
5. Polyoxometalates in Redox-Based Resistive Switching	277
6. Conclusions	282
Acknowledgments	283
References	283

## Abstract

Breakthroughs in future information technology mandate new materials. For the most pressing challenges in current information technology—i.e., a drastic decrease in energy dissipation and augmented device functionality beyond classical *von Neumann* computation architectures—several pathways have been proposed. A particularly promising direction is that of spintronics, where electronic spin state control complements electronic charge-state control (1). More recently, neuromorphic computing gained significant interest, characterized by a focus on synaptic functionality to realize neural networks and associative memory concepts. In the context of these developments, polyoxometalates, characterized by their unique structural versatility, their potential for functionalization and a highly versatile redox chemistry, provide several key advantages that motivate their exploration and use as single-molecule components of novel electronic and spintronic devices. As will be exemplified in this chapter, polyoxometalates provide near-perfect model systems to study the basic phenomena

associated with single-molecule electronics and spintronics. Given the infancy of this field, this chapter thus is intended not a classical review, but as a map of potential departure points for avenues to polyoxometalate-based single-molecule devices.



## 1. INTRODUCTION

Over 50 years ago, Gordon E. Moore predicted the continuous miniaturization of electronics to “lead to such wonders as home computers [...], automatic controls for automobiles, and personal portable communications equipment” (2). Moore’s foresight proved equally correct when he, in the same paper, conjectured an exponential increase with time of the number of transistors on a single integrated circuit. Although Moore expected the breakdown of this “law” to occur within 10 years, it has remained valid for five decades. However, with demonstrations of IBM of 7 nm node chips based on silicon-germanium transistors, the dimensions of the various elements of a CMOS (complementary metal oxide-semiconductor)-based transistor now approach those of single molecules. This anticipated evolution has sparked intense research in the field of molecular electronics (3–9), broadly defined as the study of charge transport at the molecular level. Since the first proposition of a molecular diode (10), molecular wires (11–13), switches (14), and transistors (15, 16), have been designed and characterized. Consequently the future development of information technology devices will be dominated by two major trends: first, a continuation of the exponential increase in performance and efficiency (an adjusted “Moore’s law”) by further down-scaling, new materials, and novel device fabrication concepts; second, added functionalities (“More than Moore”) stemming from the emergence of advanced concepts such as the implementation of neuromorphic concepts, in order to overcome the existing limits inherent to the classical concepts of binary logics and *von Neumann* architectures (i.e., a strict functional separation between information processing, information storage, etc.). Take, for example, what is considered a recent breakthrough in artificial intelligence: In 2011, IBM’s supercomputer Watson, trained to answer questions in natural language, for the first time beat human champions in the US quiz show “Jeopardy!.” (17) Winning this quiz show requires not only access to large amounts of factual data but also associative information processing. To beat the human brain, consuming less than 100 Watt for its 100 billion neurons, required the operation of 2880 POWER7 processors and 16 Terabytes RAM, while

consuming 2.3 MW of electrical power. This discrepancy to human “neurocomputing” or “cognitive computing” illustrates the necessity to reduce power dissipation by orders or magnitude and to introduce devices of synaptic functionality, in order to realize neural networks. This chapter will explore two emerging fields that promise significant advances into these directions and that are investigated in our research group on the basis of polyoxometalate chemistry. Note that several other concepts to utilize polyoxometalates in spintronics and information technology are being pursued, ranging from the electrostatic control of spin states in heterometal polyoxometalates (18) to the use of films of redox-active, switchable polyoxometalates as components in flash RAM (19).

The understanding and control of the correlation of molecular charge and molecular magnetic states and their combined exploitation are at the heart of single-molecule spintronics, a rapidly growing area at the intersection of molecular electronics, molecular magnetism, and condensed matter physics that aims to translate several concepts of classical, semiconductor-based spintronics (1) to the molecular level. The interest in charge transport mechanisms through individual molecules with magnetic ground states and the underlying physical phenomena is primarily triggered by several aspects of technological relevance. Among them are pronounced nonlinear charge transport effects which (in part) manifest the quantum nature of the molecular magnetic multiplet states, the low energy requirements to switch molecular spin states and the low-dissipation operation of molecular transistors at low-bias voltages, and the prospect of ultimate integration density. Next to nonlinear response modes and low-bias conductivity within the Coulomb blockade regions (see below), nontrivial functionalities such as negative differential resistivity (e.g., of interest for high-frequency logic circuits) can also emerge from single magnetic molecules (20), as will be detailed in Section 4.2. The ability to differentiate between and address not just two but multiple magnetic states in principle also implies that such systems allow for multilevel switching and signal processing and opens avenues to non-*von Neumann* logic devices such as a multilevel memristive device. As the immediate molecular environment also influences the molecular electronic states that are relevant to the molecular conductivity, molecular sensor applications are likely to be realized as well. Overall, a steady progress in theoretical modeling of the transport processes of both spin-polarized and nonpolarized currents points to a plethora of charge transport effects and intriguing physics yet to be experimentally confirmed. Finally, the predicted sensitivity even to very weak magnetic effects

(for example, Dzyaloshinskii–Moriya interactions in geometrically frustrated spin systems (21)), which is predicted to cause distinct features in the differential conduction maps, implies that low-temperature single-molecule charge transport measurements represent a single-molecule spectroscopy method.

However, the integration of individual molecules into nanoelectronic devices faces a severe discontinuity in process technologies, namely interfacing discrete molecules and macroscopic solid-state (metal and metal oxide) electrodes in a controlled fashion. Two-terminal molecular contacts can be realized in scanning tunneling microscopy (STM) setups and their spectroscopic variants (22,23) where charge transport involves a conducting surface, the molecule (chemisorbed or physisorbed on the surface), and the metallic STM tip. For a molecular analogue of a field-effect transistor (Fig. 1), a three-terminal-gated contact mode, essential to addressing specific molecular charge states via a gate voltage, is usually realized by embedding a molecule between the tips of a nanoscaled break junction, generated mechanically or via electromigration from an ultrathin gold (or Au-based alloy) layer on the top of a metal oxide-terminated substrate serving as the gate electrode (24,25). The deposition itself simply involves gas-phase transport or dipping the break junction into a solution of the molecule. To facilitate this deposition, the target molecule usually comprises chemisorptive groups, e.g., alkythiol chains, with a specific affinity toward the electrodes that define the source and drain terminals of the break junction. Unfortunately, the precise geometry of the nanogap cannot be controlled, and the straightforward but essentially statistical deposition method suffers from an inherent

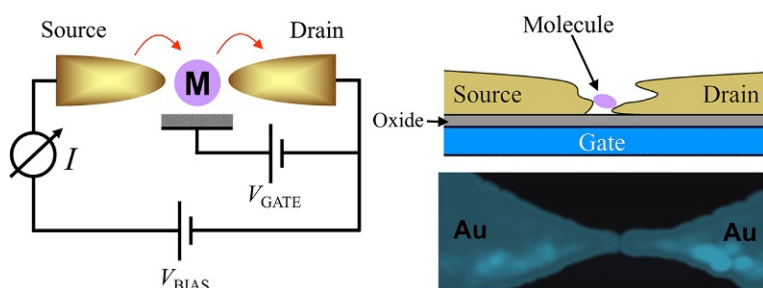


**Fig. 1** (Left) Schematic diagram of a single-molecule field-effect transistor. The molecule (M) is contacted by two metallic Source and Drain leads, while coupled to the field insulating (metal oxide-terminated) gate electrode. (Right, top) Schematic side view of a molecule bridging the nanogap of a break junction. (Right, bottom) Top-down scanning electron microscopy graph of a representative gold break junction nanogap, typically created by electromigration or mechanical strain.

lack of control and reproducibility. The desired arrangement of a single molecule in the break junction nanogap with respect to the source/drain and gate electrodes will thus be achieved only with a low probability. According to experimental groups active in this field, typically only less than 1% of experimental attempts result in conductivity data that are reproducible over several voltage sweeps. In the absence of imaging techniques able to locate and resolve the molecule within the nanogap, the resulting conductivity data frequently can be difficult to interpret. Other drawbacks are (1) the need to attach sulfur-terminated tether chains to the targeted magnetic molecules, as the introduction of such groups rules out molecular magnets that comprise transition metal centers too reactive toward such groups, and (2) the limited redox stability of classical magnetic molecules (commonly coordination complexes) upon contact with metal surfaces, which limits the choice of magnetic molecules to relatively few classes of compounds. Furthermore, the degree of electronic interaction between the metallic surface states and the molecular orbitals, which can in principle range from the weak to strong coupling regime (the latter implying vast hybridization with a loss of a clearly resolved molecular orbital structure), remains essentially uncontrollable in break junction environments.



## 2. BASICS OF MOLECULAR SPIN ELECTRONICS

When the spin of the electron, and not its charge, is the primary operative parameter, several limitations need to be taken into account: Because of the fast decoherence of spin in most materials, spin currents can only be observed over nanoscale distances. Spintronics thus experienced a fast development in commensurately scaled systems: giant magnetoresistance, the first spintronic effect discovered by the groups of A. Fert and P. Grünberg in 1988 (26,27), which was already commercially exploited in thin film-based devices in 1997. Paralleling the development of electronics, spintronics soon expanded from the use of metallic thin layers to semiconductors, nanoobjects (28,29), and molecules (30,31). So far, most examples of molecular spintronics have concentrated on diamagnetic molecules used as spin valves between ferromagnetic electrodes capable of producing a spin-polarized current. Systems incorporating magnetically active species (11,12,32–35), and in particular single-molecule magnets (SMMs) (36–42), have nevertheless attracted a great deal of attention, mostly from a theoretical point of view. In particular, this type of system seems also promising for quantum computing (43–45).

In order to explore the basic spintronics functionality of individual magnetic molecules, their single-molecule conductivity characteristics can be determined by utilizing the environment of a molecular transistor with source, drain, and gate terminals (Fig. 1).

Here, a single molecule is contacted by metallic source and drain electrodes, while it is capacitively coupled to the insulating (metal oxide-covered) gate electrode. In such a geometry, the current flowing from source to drain is measured as a function of both the bias and the gate voltage, and is most commonly represented as the differential conductivity ( $dI/dV$ ) in color-coded 2D ( $dI/dV$  vs  $V_{\text{BIAS}}$  vs  $V_{\text{GATE}}$ ) conductivity maps. The primary role of the gate field is to shift the molecular states relative to the Fermi levels of the source/drain electrodes. Note that the control offered by the gate field is of key importance, in particular when comparing to STM experiments where the charge or redox state of the molecule and the relative energy of its orbitals is not defined a priori and cannot be controlled directly. Since the magnetism and the conductivity of the molecule depend on its charge/redox state, this control is essential for systematic studies of spintronics functionality.

If the contact between the metallic source and drain electrodes is of an insulating nature, the molecular states are not significantly hybridized with the surface states of the metallic electrodes (the so-called weak coupling regime) and charge transport typically occurs via quantum tunneling processes. In this case, the predominant charge transport mechanism through single magnetic molecules (and, more generally, quantum dots) is sequential electron tunneling. This transport mechanism results in bias- and gate potential areas of finite differential conductivity  $dI/dV$  separated by rhombic Coulomb blockade regions (Fig. 2). The sequential tunneling of electrons from source to molecule to drain requires the molecular orbital levels to be in resonance (for zero-bias field) or to lie within the energetic “window” defined by the Fermi levels of the source and drain electrodes (for a finite bias field). The capacitive coupling of the molecule to a gate electrode shifts the molecular energy levels with respect to the source and drain Fermi levels, which can also change the charge state of the molecule. Excited (e.g., vibrational) states associated with a specific charge state of the molecule likewise translate into added differential conductivities and “pattern” the SET areas, leading to pronounced discontinuities in  $dI/dV$  and to the strong nonlinear  $I-V$  responses. A recent example demonstrated that vibrational excitations of a thioacetate-terminated oligophenylenevinylene could be derived from the  $dI/dV$  maps, with the excitation energies matching those determined from IR and Raman spectroscopy (Fig. 3) (46).

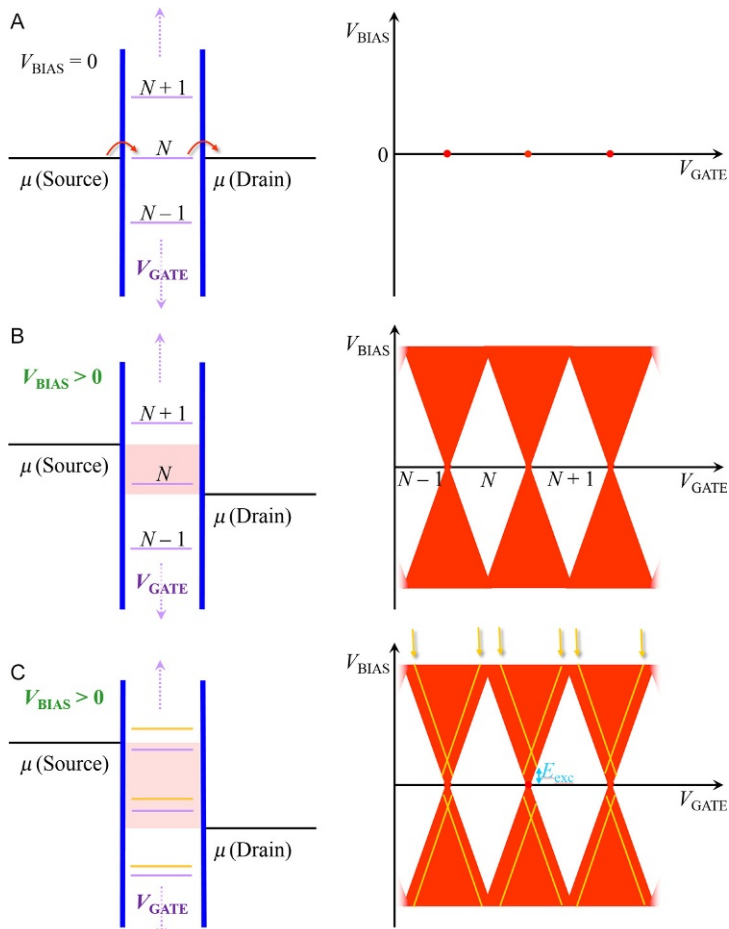


**Fig. 2** Schematic depiction of the origin of sequential electron tunneling (SET) in a molecular transistor in the weak coupling regime, here indicated by the *blue vertical lines* representing tunneling barriers. (A) In the absence of a bias field, the electrochemical potentials ( $\mu$ ) of the source and the drain electrodes (represented by the *horizontal black bars*) are identical, and SET is restricted to gate fields for which the molecular states are in resonance with the electrode Fermi levels, giving rise to finite conductivities for the  $V_{\text{GATE}}$  values for which the various charge states of the molecule (here specified by the number of electrons,  $N$ ) meet this criterion (*red dots* in the 2D  $dI/dV$  plot). (B) A bias field ( $V_{\text{BIAS}} > 0$ ) opens up an energy window (transparent *red area*), in which the presence of a molecular state can cause conductivity, commensurately broadening the  $V_{\text{GATE}}$  ranges for which SET is possible. In the 2D  $dI/dV$  plots, this results in SET regions that surround rhombic “Coulomb blockade” regions of zero conductivity. Each Coulomb diamond is connected to a specific number of electrons on the molecule. (C) Excited (e.g., vibrational) states that belong to the individual molecular charge states represented as *yellow horizontal lines* running parallel to the *diamond edges*, also contribute to the overall conductivity, giving rise to a distinct fine structure in the differential conductivity diagram, which also allows direct determination of the corresponding excitation energies ( $E_{\text{exc}}$ ).

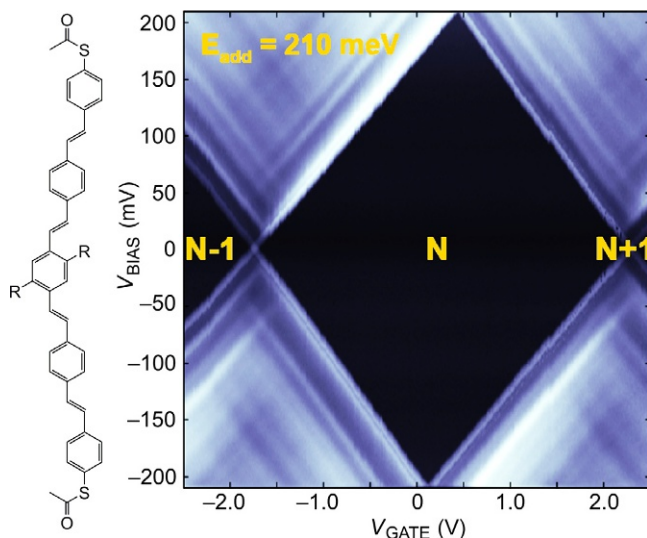


**Fig. 3** Color-coded differential conductivity diagram for an thioacetate-terminated oligophenylenevinylene (left,  $R = n\text{-C}_{12}\text{H}_{25}$ ) as derived from a three-terminal gold break junction measurement, highlighting the vibrational fine structure in the SET areas surrounding the central Coulomb blockade region (black). The SET areas here intersect at  $V_{\text{BIAS}} = 210$  mV, resulting in an addition energy of 210 meV. The color-coded  $dI/dV$  values range from approx. 1.5–2.5 nS. Adopted from Osorio, E. A.; O'Neill, K.; Stuhr-Hansen, N.; Nielsen, O. F.; Bjørnholm, T.; van der Zant, H. S. J., *Adv. Mater.* **2007**, 19, 281–285.

If the molecule at the heart of such a transistor is characterized by a magnetic ground state, the feature most commonly observed in correlation with electron transport is Kondo resonance spin flip tunneling, materialized by finite conductance of the system at zero bias and low temperatures (Fig. 4) (34,47). Magnetic molecules also exhibit several more exotic transport properties related to their exact magnetic structure, the underlying theory of which is only beginning to emerge (48).



### 3. MATERIAL REQUIREMENTS FOR MOLECULAR SPINTRONICS

From the molecular materials point of view, limited stability of numerous polynuclear coordination complexes remains a significant obstacle for charge transport experiments. Upon contact with a redox-active metallic surface, many well-known single-molecular magnets succumb to charge transfer-induced decomposition or rearrangement reactions. Because polynuclear complexes of transition metal usually present several readily



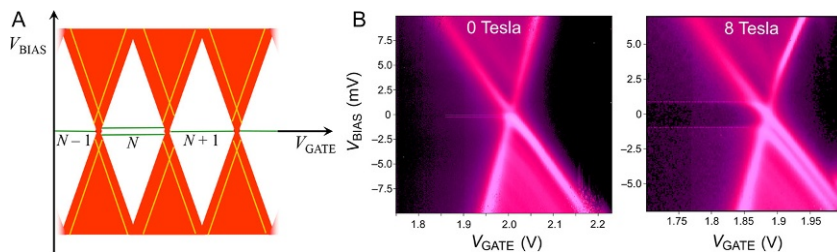


**Fig. 4** Signatures of spin states in single-molecule conductivity. (A) For a molecule exhibiting a high-spin ground state, Kondo resonance spin flip tunneling opens up additional transport channels, resulting in nonzero conductivities at (or near)  $V_{\text{BIAS}} = 0$  V. As such, this transport mechanism allows for single-molecule charge transport in the Coulomb blockade regions (represented by horizontal green lines). Zero-field splitting of the  $S$  ground state into its  $m_S$  substates results in additional transport channels (shown schematically by two horizontal lines for an arbitrary charge state  $N$ ). (B) Differential conductivity diagrams for the archetypal single-molecule magnet  $\{\text{Mn}_{12}\text{-OAcCl}_2\}$  (see Section 4.1) at 300 mK measured after solution deposition onto an electromigration-created Au break junction. The splitting is faintly visible (dotted pink lines serve as a guide to the eye) and symmetric with respect to the zero-bias line. Upon changing from  $B = 0$  (left) to 8 T (right), the Zeeman effect additionally separates the  $m_S$  substates. Adopted from Jo, M.-H.; Grose, J. E.; Baheti, K.; Deshmukh, M. M.; Sokol, J. J.; Rumberger, E. M.; Hendrickson, D. N.; Long, J. R.; Park, H.; Ralph, D. C. *Nano Lett.* **2006**, 6, 2014–2020.

accessible redox states, even surfaces usually considered as unreactive can induce catastrophic changes. For example, the deposition of the SMM  $[\text{Mn}^{\text{III}}_8\text{Mn}^{\text{IV}}_4\text{O}_{12}(\text{O}_2\text{CR})_{16}(\text{H}_2\text{O})_4]$  ( $\text{RCOOH} = 16\text{-acetylthiohexadecanoic acid}$  or  $4\text{-(methylthio)benzoic acid}$ ) on an Au(111) surface was investigated by Gatteschi and Cornia who determined from synchrotron XMCD and XAS measurements that a significant reduction of the manganese centers to  $\text{Mn}^{\text{II}}$  (and a potential decomposition of the  $\{\text{Mn}_{12}\}$  structure), with subsequent loss of the hysteretic properties characteristic of SMMs (49). Interestingly, this decomposition does not even require ultimate proximity between the  $\{\text{Mn}_{12}\}$  cluster and the Au(111) surface, since it was observed for both the long- and short-alkyl chain carboxylate groups. Several other redox reactions severely affecting the bulk magnetic properties of smaller coordination complexes have been studied in detail (50,51).

Molecular magnets with redox-active ligands, resulting in ligand-centered charge transfer, are one alternative to circumvent this problem. Lanthanide complexes, with their magnetic  $4f$  states usually impervious to redox reactions, based on macrocyclic tetrapyrrole ligands such as phthalocyanines (Pc), have recently been successfully attached to metallic or graphene-based

surfaces. Bulk magnetization measurements of a terbium(III) phthalocyanine double-decker complex in three different redox states ( $[\text{TbPc}_2]^{1-/0/1+}$ ) show that single-ion magnet properties due to an energy barrier formed by the single-ion  $m_J$  substates are retained in all states. However, the magnetization hysteresis loop changes significantly from one species to the other, indicating that the effect of the ligand field on the magnetic properties of the metal center cannot be ignored and that magnetic states can in principle be adjusted by switching between charge states (52). Additionally, the specific adsorption geometry, i.e., the exact positioning of the molecule on the surface, has consequences: In their STM studies of iron phthalocyanine of Au(111) surfaces, Gao *et al.* found that the strength of the observed Kondo resonance depends on whether the Fe(II) ion is situated on the top of an Au gold atom or between two Au atoms (53). If defect sites are taken into account in addition to the already significant number of possible coordination modes on an ideal surface, the variability of coordination modes, and therefore magnetic properties, can thus become a parameter of uncertainty. Stability issues exist even for lanthanide phthalocyanine complexes: In some cases, the coordination to the surface can compete with the loss of one of the Pc ligands. For example, when Tb(III) and Dy(III) double-decker phthalocyanines were deposited on an Au(111) surface, the formation of [MPc] complexes, nonexistent in the bulk, was observed. And while no Kondo resonance could be observed for  $[\text{TbPc}_2]$  under such conditions, it was detected for  $[\text{TbPc}]$  (38). Lanthanide 4f-centered states, on the other hand, could only be directly detected for  $[\text{NdPc}_2]$  in STM experiments, highlighting the importance of their correct energetic position with respect to the other molecular and surface states, in order to be energetically exposed for electrical access (54).

A typical strategy to avoid the perturbing influence of the metallic surface is the use of long tether groups, for example, the nonanethiol chain used by Sessoli *et al.* to anchor the SMM  $[\text{Fe}_4(\text{L})_2(\text{DPM})_6]$  ( $\text{H}_3\text{L} = 7\text{-(acetylthio)-2,2-bis(hydroxymethyl)heptan-1-ol}$ ; HDPM = dipivaloylmethane) to an Au surface (55,56). While the SMM character of the  $\{\text{Fe}_4\}$  molecule was successfully retained, the extreme sensitivity of coordination complex-based SMM to small geometric deformations and other environmental effects generally complicates the interpretation of magnetic data and calls for more rigid target molecules—a requirement that can in principle be met by molecular metal oxides.



#### 4. ADVANTAGES OF MAGNETIC POLYOXOMETALATES

Polyoxometalates, in particular polyoxovanadates, -molybdates, and -tungstates, are characterized by a range of materials properties that enable

us to circumvent the limitations listed above. As will be exemplified in this section, they represent ideal model systems for a systematic exploratory approach to single-molecule conductivity and spintronics. The exceptional and well-documented redox properties of POMs, combined with their high thermodynamic stability and vast array of nanosized architectures that allow for numerous magnetic functionalization strategies, results in a wide range of molecules that enable us to study the interplay of molecular charge and magnetic states and thus in theory offer significant potential as central elements of single-molecule spintronics devices. Furthermore, magnetically functionalized POMs have been shown to exhibit a wide variety of magnetic phenomena ranging from properties related to molecular spin frustration to electron delocalization-related properties and the magnetic metastability of SMMs (57–59). Compared to polynuclear coordination complexes, magnetic POMs can be carefully modified with respect to many parameters relevant to the molecular magnetic structure.

The magnetic functionalization of polyoxometalates has seen an extensive development over the past two decades, to the point where such systems can be fine-tuned to study the interplay between charge and magnetic states. In mixed-valent polyoxovanadate(IV/V) clusters, the vanadium centers themselves serve as spin ( $s = 1/2$ ) carriers and therefore any change in molecular charge can result in significant magnetic changes. On the other hand, polyoxomolybdates, including mixed-valent molybdate structures where Mo(4d) electrons are typically spin-paired, usually are diamagnetic. They are commonly magnetically functionalized by interlinking molybdate-based transferable building blocks of specific geometry and connectivity by magnetic transition metal or lanthanide ions. As redox-active building blocks, polyoxomolybdate substructures can be compared to the redox-active phthalocyanine ligands of LnPc<sub>2</sub> complexes. The versatility of polyoxomolybdate-based frameworks is exemplified by the thoroughly investigated polyoxomolybdate-based Keplerate cluster {Mo<sub>72</sub>Fe<sub>30</sub>}. In its charge-neutral, fully oxidized form, [ $\{\text{Mo}^{\text{VI}}_6\text{O}_{21}(\text{CH}_3\text{COO})\}_{12}(\text{Fe}^{\text{III}}_{30}(\text{H}_2\text{O})_2)_{30}\{\text{Mo}^{\text{VI}}_2\text{O}_7(\text{H}_2\text{O})\}_2\{\text{H}_2\text{Mo}^{\text{VI}}_2\text{O}_8(\text{H}_2\text{O})\}(\text{H}_2\text{O})_{31}$ ], this cluster incorporates 30 Fe(III) spin-5/2 centers that define the corners of icosidodecahedron, which represents a highly frustrated spin cluster that can in a first approximation be characterized by a uniform nearest-neighbor exchange energy  $J$ . A 16-fold reduced analogue of {Mo<sub>72</sub>Fe<sub>30</sub>} can be isolated with the composition [ $\{\text{Mo}^{\text{V/VI}}_6\text{O}_{21}(\text{H}_2\text{O})_3(\text{SO}_4)\}_{12}(\text{Fe}^{\text{III}}(\text{H}_2\text{O})_2)_{30}$ ]<sup>22-</sup> (60), which differs in its (diamagnetic) internal ligand groups due to differences in the synthesis

conditions but otherwise is virtually isostructural in terms of the overall spherical polyoxomolybdate shell structure. Importantly, despite the high degree of reduction and high  $\text{Mo}^{\text{V}}:\text{Mo}^{\text{VI}}$  ratio, the Fe centers remain in the formal oxidation state +III, as confirmed by Mößbauer spectroscopy. The apparent lack of structural reorganization upon uptake of multiple electrons is linked to a full delocalization of the added  $\text{Mo}(4d)$  electron density over the molybdate-based building blocks. Importantly, the minimal structural reorganization that accompanies the changes of the molecular redox state is an important to enable rapid charge-state switching. As the molybdate building blocks mediate the (antiferromagnetic) super-exchange interactions between the neighboring Fe(III) spin centers, the 16-electron reduction in this case causes a 50% change in exchange energy (vs the fully oxidized  $\{\text{Mo}^{\text{VI}}_{72}\text{Fe}^{\text{III}}_{30}\}$  species (61)), with the uniform nearest-neighbor exchange energy decreasing to  $J = -0.76$  K (vs  $-1.57$  K). Both the differences in redox states and the resulting changes in magnetic parameters are unprecedented when compared to redox-active conventional polynuclear coordination complexes.

This redox versatility, associated with only minimal structural reorganization, also extends to the class of polyoxovanadates (POVs). An instructive example concerns the archetypal spherical polyanion  $\{\text{V}_{18}\text{O}_{42}\}$  that can be isolated with various guest species (e.g.,  $\text{H}_2\text{O}$ , halides) and exists in various redox states, with  $\text{V}^{\text{IV}}:\text{V}^{\text{V}}$  ratios ranging from 18:0 (fully reduced) (62) to 10:8 (mixed valent) (63). A comparison of the cluster shell geometries of the 18:0 and the 10:8 derivatives shows only very small structural changes (Fig. 5).

On the other end of the spectrum, polyoxotungstate(VI) cluster structures are generally much more difficult to reduce to mixed-valent W(VI/V) or fully reduced W(V) species. As such, polyoxotungstate(VI) building blocks provide robust, redox-inert ligands that can form effective tunneling barriers, while they also form complexes with numerous magnetic ions.

Another advantage in using magnetic POMs concerns the fact that several of the magnetically functionalized polyoxomolybdates and -tungstates also exist as structurally similar nonmagnetic analogues in which, e.g., diamagnetic  $\text{Zn}^{2+}$ ,  $\text{La}^{3+}$ , or  $[\text{Mo}^{\text{VI}}=\text{O}]^{4+}$  groups replace some of the paramagnetic transition ions or in which the paramagnetic ions are not present. Therefore, one can elucidate the various magnetic contributions to a given molecular structure by comparison to diamagnetic derivatives.

Apart from these general features, the following sections will detail how magnetically functionalized polyoxometalates help to elucidate aspects that are relevant for their model character for molecular spintronics.

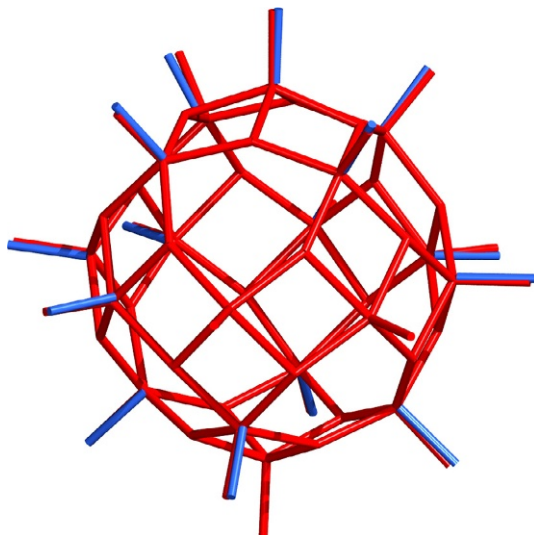


**Fig. 5** Superposition of the mixed-valent  $\{V^{IV}_{10}V^V_8O_{42}\}$  (red) and the fully reduced  $\{V^{IV}_{18}O_{42}\}$  (blue) cluster shells, highlighting the comparably small geometrical changes between the different redox states.

#### 4.1 Magnetically Functionalized Polyoxometalates Allow Studying the Effects of Anisotropic Environments on the Molecular Magnetic Properties

The influence of the electrostatically highly anisotropic environments of surfaces or break junction nanogaps on the magnetism of a single molecule has thus far—possibly naively—been ignored in the analysis of “magnetic signatures” in the conductivity features. Even in comparably symmetric and simple environments, e.g., a molecule physisorbed on a polarizable, flat surface, local fields result at the molecule–surface interface (mirror charges) that, in the case of polyoxometalates, can even induce reversible, temperature-controlled intramolecular redox reactions (64). Polyoxometalates, with their usually high charges, provide a reasonable testbed for such electrostatic effects, as exemplified by the following three scenarios:

- (1) A spin cluster of isotropic spin centers attached to a polyoxometalate

Back in 2008, we explored the possibility to utilize highly charged hard cations such as  $Zr^{4+}$  or  $Ce^{4+}$  in order to graft lacunary polyoxometalates to preformed molecular spin clusters. A first example employed was the charge-neutral manganese carboxylate cluster  $[Ce^{IV}Mn^{IV}_6O_9(CH_3COO)_9(NO_3)(H_2O)_2]$ , comprising a hexameric

planar ring of  $\mu_2$ -oxo-bridged, octahedrally coordinated isotropic spin-3/2 Mn(IV) centers, to which a central Ce(IV) ion is coordinated in a doming configuration (65). The Ce coordination environment here is completed by sufficiently labile, terminal water and nitrate ligands. The direct 1:1 stoichiometric reaction of this coordination cluster with the trilacunary  $[\alpha\text{-P}_2\text{W}_{15}\text{O}_{56}]^{12-}$  polyanion ( $=\{\text{P}_2\text{W}_{15}\}$  (66), derived from the  $\{\text{P}_2\text{W}_{18}\}$  Wells–Dawson archetype) and a dimethylammonium source at 70°C yielded the direct adduct  $[\{\alpha\text{-P}_2\text{W}_{16}\text{O}_{57}(\text{OH})_2\}\{\text{CeMn}_6\text{O}_9(\text{O}_2\text{CCH}_3)_8\}]^{8-}$ , exhibiting the anticipated linkage via the Ce(IV) site that now binds both to the  $\mu_2$ -O sites of the Mn<sub>6</sub> ring and several terminal oxo positions of the lacunary sites of the (now partially reconstructed  $\{\text{P}_2\text{W}_{16}\}$ ) Well–Dawson structure (Fig. 6) (67).

Importantly, although the formation of Ce–O–W bonds slightly elongates the distance between Ce and the Mn<sub>6</sub> ring, with Ce...Mn distances increased from 3.37 to 3.42 Å, the magnetically relevant geometry of the Mn<sub>6</sub> ring and its  $\mu_2$ -O/ $\mu_2$ -acetate-based

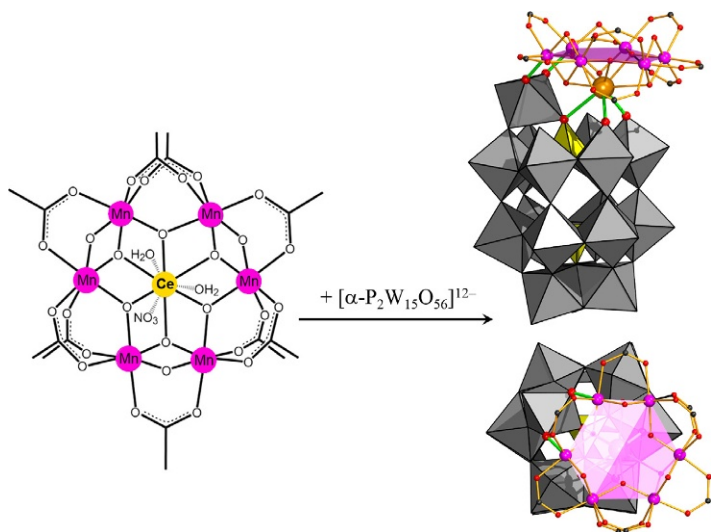


**Fig. 6** Structure of the acetate-supported  $\{\text{Ce}^{\text{IV}}\text{Mn}^{\text{IV}}_6\}$  spin ring (left) and its product upon reaction with the trilacunary  $\{\text{P}_2\text{W}_{15}\}$  polyoxotungstate, the adduct  $[\{\alpha\text{-P}_2\text{W}_{16}\text{O}_{57}(\text{OH})_2\}\{\text{CeMn}_6\text{O}_9(\text{O}_2\text{CCH}_3)_8\}]^{8-}$  (side view: top right, top view perpendicular to the hexagonal Mn<sub>6</sub> plane (transparent purple); bottom right). WO<sub>6</sub>, gray; PO<sub>4</sub>, yellow polyhedra; O, red; Mn<sup>IV</sup>, purple; Ce<sup>IV</sup>, yellow spheres. Green lines highlight the coordinative bonds between the  $\{\text{CeMn}_6\}$  cluster and the polyoxotungstate. Methyl groups on the bridging acetates are omitted for clarity.

nearest-neighbor exchange pathways is nearly unaffected. However, one Mn–O–C–O–Mn carboxylate bridge in the  $\{\text{CeMn}_6\}$  precursor is replaced by an Mn–O–W–O–Mn bridge, and in contrast to  $\{\text{CeMn}_6\}$ , where two Mn...Mn bridging modes alternate within the  $\text{Mn}_6$  ring, three nearest-neighbor Mn...Mn exchange coupling energies (and furthermore a uniform weak next-nearest-neighbor coupling energy) are necessary to reproduce the magnetic susceptibility data for the  $[\{\alpha\text{-P}_2\text{W}_{16}\text{O}_{57}(\text{OH})_2\}\{\text{CeMn}_6\text{O}_9(\text{O}_2\text{CCH}_3)_8\}]^{8-}$  aggregate. In any case, its low-field (0.1 T) magnetic susceptibility data (1.8–290 K) is virtually identical compared to that of the  $\{\text{CeMn}_6\}$  precursor compound. This is in line with the fact that the dominating  $\mu_2$ -oxo-mediated super-exchange pathways have not been significantly altered by the addition of the  $[\alpha\text{-P}_2\text{W}_{15}\text{O}_{56}]^{12-}$  polyoxotungstate. In summary, as the octahedrally coordinated Mn(IV) ions here represent pure isotropic spin centers, the changes to the magnetism of the  $\text{Mn}_6$  spin cluster upon attachment of the  $[\alpha\text{-P}_2\text{W}_{15}\text{O}_{56}]^{12-}$  polyanions are commensurate with the minor geometric changes induced by this reaction, and no further effects are observed.

(2) A magnetically anisotropic spin cluster grafted to a polyoxometalate

Significant effort has been focused to combine the seminal SMM  $[\text{Mn}^{\text{IV}}_4\text{Mn}^{\text{III}}_8\text{O}_{12}(\text{CH}_3\text{COO})_{16}(\text{H}_2\text{O})_4]$  ( $=\{\text{Mn}_{12}\text{-OAc}\}$ , usually isolated as  $\{\text{Mn}_{12}\text{-OAc}\} \cdot 4\text{H}_2\text{O} \cdot 2\text{CH}_3\text{COOH}$  (68)) with polyoxometalate clusters. In (distorted) octahedral environments, the Mn(III) sites represent  $S=2$  centers ( ${}^5\text{B}_{1g}$ ), the Mn(IV) centers represent  $S=3/2$  centers ( ${}^4\text{A}_2$ ); in the numerous  $\{\text{Mn}_{12}\}$  derivatives, ferromagnetic  $\text{Mn}^{\text{III}}\dots\text{Mn}^{\text{III}}$  and  $\text{Mn}^{\text{IV}}\dots\text{Mn}^{\text{IV}}$  as well as antiferromagnetic  $\text{Mn}^{\text{III}}\dots\text{Mn}^{\text{IV}}$  coupling produces an  $S=10$  ground state (69). Coronado and coworkers have reported that polycationic  $\{\text{Mn}_{12}\}$  derivatives, where acetate groups are replaced by carboxylate-substituted alkylammonium groups, produce stable salts with various polyoxotungstates; however, because of the weak ionic interactions, structural and magnetic influences on the  $\{\text{Mn}_{12}\}$ -type cluster imposed by the polyoxometalates are negligible (70). Nevertheless, the  $\{\text{Mn}_{12}\text{-OAc}\}$  complex can be employed as a precursor for reacting with polyoxotungstates. Although the  $\{\text{Mn}^{\text{IV}}_4\text{Mn}^{\text{III}}_8\}$  core itself could not yet be retained in reactions with polyanions in aqueous solutions, the slow decomposition of  $\{\text{Mn}_{12}\text{-OAc}\}$  in the presence of various lacunary POTs can lead to a number of polyanions with Mn(III) and Mn(IV) centers (71).

Using this approach, in 2010, we were able to condense a decomposition product of  $\{\text{Mn}_{12}\text{-OAc}\}$ , namely the cubane-type  $\{\text{Mn}^{\text{III}}_3\text{Mn}^{\text{IV}}\text{O}_4\}$  cluster on the lacunary plane of  $[\alpha\text{-P}_2\text{W}_{15}\text{O}_{56}]^{12-}$ , resulting in an  $[\text{Mn}^{\text{III}}_3\text{Mn}^{\text{IV}}\text{O}_3(\text{CH}_3\text{COO})_3(\alpha\text{-P}_2\text{W}_{15}\text{O}_{56})]^{8-}$  polyanion ( $=\{\text{Mn}_4\text{P}_2\text{W}_{15}\}$ , isolated as  $[\text{Me}_2\text{NH}_2]_{5.33}\text{H}_2\text{Mn}^{\text{II}}_{0.33}\{\text{Mn}_4\text{P}_2\text{W}_{15}\} \cdot 16\text{H}_2\text{O}$  (72)). The  $\{\text{Mn}^{\text{III}}_3\text{Mn}^{\text{IV}}(\mu_3\text{-O})_3(\mu_3\text{-X})\}$  ( $\text{X}=\text{halides}, \text{MeO}^-, \text{MeCO}_2^-, \text{NO}_3^-, \text{etc.}$ ) cubane-type assemblies, supported by various organic bridging ligands, constitute a well-known family of SMMs that in the “effective spin” approach are described by a  $S=9/2$  ground state and a zero-field splitting energy (characterized by the empirical parameter  $D$ ) ranging from  $-0.3$  to  $-0.6 \text{ cm}^{-1}$  (73). Of particular interest for us was the fact that the next excited multiplet ( $S=7/2$ ) is energetically well separated (by ca.  $180 \text{ cm}^{-1}$ ) from the  $S=9/2$  ground state, meaning that the ground state properties are dominating the low-temperature magnetism. In the structure of  $\{\text{Mn}_4\text{P}_2\text{W}_{15}\}$  (Fig. 7), all three Mn(III) centers are coordinated by the  $\{\text{P}_2\text{W}_{15}\}$  units. Here, the Mn(III) centers experience typical Jahn–Teller distortion, with the O atom of the adjacent  $\text{PO}_4$  group in  $\{\text{P}_2\text{W}_{15}\}$  acting as one vertex of the  $\text{Mn}_4\text{O}_4$  cubane and defining the orientation of the Jahn–Teller elongation.

The Mn(IV) ion forms the apex of the  $\{\text{Mn}^{\text{III}}_3\text{Mn}^{\text{IV}}\}$  trigonal pyramid and is linked to the Mn(III) centers by three  $\mu_3$ -oxo ligands each connecting the Mn(IV) and two Mn(III) ions, and  $\mu_2$ -acetate groups bridging the every Mn(III)/Mn(IV) pair. Importantly, the geometry of the magnetically relevant exchange pathways in the  $\text{Mn}_4\text{O}_4$  cubane substructure is very similar to that in a typical example for a  $\{\text{Mn}_4\text{O}_4\}$  coordination cluster,  $[\text{Mn}_4\text{O}_3(\text{AcO})_4(\text{dbm})_3]$  (where dbm represents the monoanion of dibenzoylmethane), for which  $D=-0.39 \text{ cm}^{-1}$  has been reported (74), with the usual SMM characteristics and the typical onset of a finite  $\chi''$  component of the ac susceptibility below 3 K (for 1000 Hz).

The static (dc) magnetic susceptibility data for  $\{\text{Mn}_4\text{P}_2\text{W}_{15}\}$  is fully in line with that of the numerous published  $\{\text{Mn}^{\text{III}}_3\text{Mn}^{\text{IV}}\text{O}_3\text{X}\}$ -based SMMs. This includes a  $S=9/2$  ground state due to antiferromagnetic coupling (and thus ferrimagnetic arrangement) of the  $\text{Mn}^{\text{IV}}$  and  $\text{Mn}^{\text{III}}$  spin centers ( $J=-31.3 \text{ cm}^{-1}$ ) and ferromagnetic coupling between the  $\text{Mn}^{\text{III}}$  spin centers ( $J=+10.2 \text{ cm}^{-1}$ ). The field-dependent magnetization curves at low temperatures (1.8–5 K) reflect strong zero-field



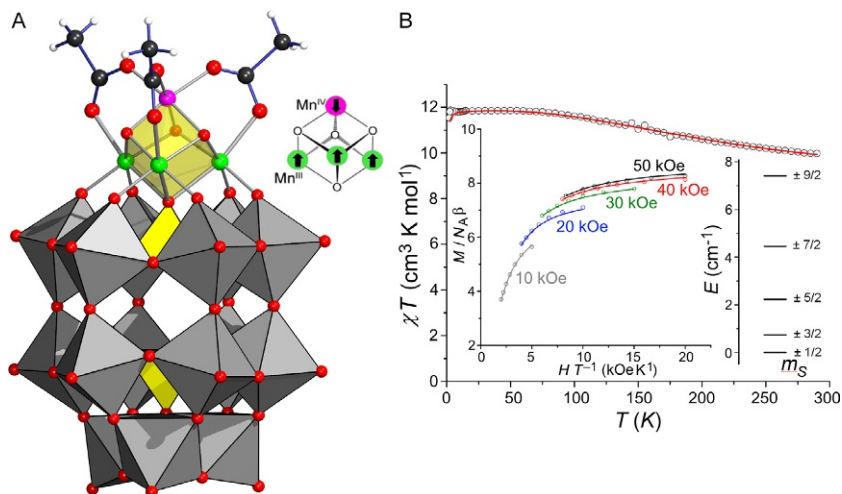


**Fig. 7** (A) Molecular structure of the  $\{\text{Mn}^{\text{III}}_3\text{Mn}^{\text{IV}}\text{O}_4\} - \{\text{P}_2\text{W}_{15}\}$  adduct  $[(\alpha - \text{P}_2\text{W}_{15}\text{O}_{56})\text{Mn}^{\text{III}}_3\text{Mn}^{\text{IV}}\text{O}_3(\text{CH}_3\text{COO})_3]^{8-}$ . Note that the  $\{\text{Mn}^{\text{III}}_3\text{Mn}^{\text{IV}}\text{O}_4\}^{4+}$  cubane fragment (highlighted in *transparent yellow*) coordinates to all oxo positions of the lacunary face of  $\{\text{P}_2\text{W}_{15}\}$ . Mn<sup>III</sup>, green; Mn<sup>IV</sup>, purple spheres; O, red; C, black; H, white;  $\text{WO}_6$ , gray;  $\text{PO}_4$ , yellow polyhedra. Inset: Simplified illustration of the coupling of the Mn(III) ( $S=2$ ) and the Mn(IV) ( $S=3/2$ ) spin centers, resulting in the  $S=9/2$  ground state. (B) Temperature dependence of  $\chi_m T$  at 0.1 T and field-dependent reduced magnetization at low temperatures (*inset*), indicating a clear deviation from the isotropic Brillouin-type behavior due to significant zero-field splitting. *Open circles*: experimental data, solid graphs: least-squares fit resulting from a CONDON simulation. The level diagram shows the energetic ordering of the  $m_S$  substates emerging from the  $S=9/2$  ground state, as derived from the same CONDON-fitting procedure. Note that, in contrast to all other known  $\{\text{Mn}^{\text{III}}_3\text{Mn}^{\text{IV}}\text{O}_3\text{X}\}$  - type SMMs, the  $m_S = +1/2$  and  $-1/2$  substates here are lowest in energy.

splitting due to ligand field effects associated with the Jahn–Teller-distorted Mn<sup>III</sup> sites (Fig. 7B). However, the polyanions surprisingly do not exhibit any slowing down of the magnetization relaxation toward lower temperatures (Fig. 8), a hallmark of SMMs, and no out-of-phase  $\chi''$  component can be detected in the *ac* susceptibility down to 1.8 K and an ac frequency of up to 1500 Hz. This observation was explained by the fact that the simulated ZFS parameter  $D = +0.36 \text{ cm}^{-1}$  appeared to be positive, resulting in an inversion of the energetic ordering of the zero-field split  $m_S = +9/2, +7/2, \dots, -7/2, -9/2$  substates belonging to the  $S=9/2$  ground state. This is in stark contrast with the situation in all known SMMs with the

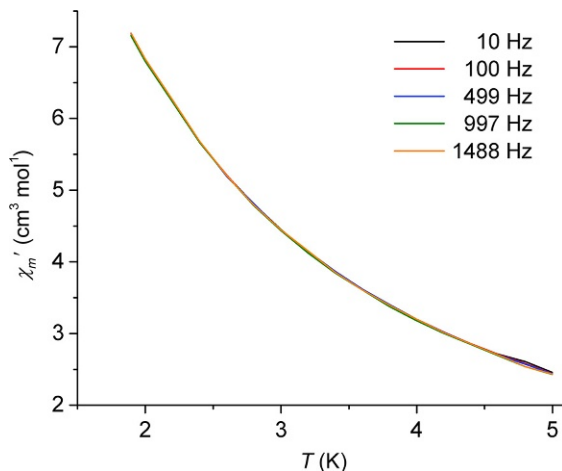


**Fig. 8** Temperature dependence of the in-phase ac molar susceptibility ( $\chi'_m$ ) for several ac frequencies for the adduct  $\{\text{Mn}_4\text{P}_2\text{W}_{15}\}$ . No frequency dependence, and thus no significant (nonzero) out-of-phase component  $\chi''$ , is observed down to 1.8 K.

cubane-like  $\{\text{Mn}^{\text{III}}_3\text{Mn}^{\text{IV}}\text{O}_3\text{X}\}$  core, where these  $m_S$  states define a parabolic energy barrier between the energetically lowest  $m_S = +9/2$  and  $-9/2$  substates in their  $E$  vs  $m_S$  plots due to the negative sign of  $D$ , and where this energy barrier causes the observed slow magnetization relaxation at lower temperatures, concomitant out-of-phase  $\chi''$  components in the ac susceptibility and, usually at much lower temperatures, magnetization hysteresis akin to that of a ferromagnet. Why did this barrier, crucial for SMM behavior, vanish in the  $\{\text{Mn}_4\text{P}_2\text{W}_{15}\}$  cluster aggregate?

- (3) A magnetically anisotropic spin cluster symmetrically sandwiched between two polyoxometalates

Performing the reaction between the same reagents,  $\{\text{Mn}_{12}\text{-OAc}\}$  and  $\{\text{P}_2\text{W}_{15}\}$ , in  $\text{H}_2\text{O}$  instead of diluted acetic acid led to  $[(\alpha - \text{P}_2\text{W}_{15}\text{O}_{56})_2\text{Mn}^{\text{III}}_6\text{Mn}^{\text{IV}}\text{O}_6(\text{H}_2\text{O})_6]^{14-}$  ( $=\{\text{Mn}_7(\text{P}_2\text{W}_{15})_2\}$ ), isolated as  $\text{Na}_{14}\{\text{Mn}_7(\text{P}_2\text{W}_{15})_2\} \cdot 68\text{H}_2\text{O}$  where the  $\{\text{Mn}^{\text{III}}_6\text{Mn}^{\text{IV}}\text{O}_6(\text{H}_2\text{O})_6\}$  magnetic cluster is sandwiched between the two identical  $\{\text{P}_2\text{W}_{15}\}$  units (75). The structure of the central  $\{\text{Mn}^{\text{III}}_6\text{Mn}^{\text{IV}}\text{O}_6(\text{H}_2\text{O})_6\}$  core can be viewed as two  $\{\text{Mn}^{\text{III}}_3\text{Mn}^{\text{IV}}\text{O}_3(\text{H}_2\text{O})_3\}$  cubane-like assemblies sharing a common  $\text{Mn}^{\text{IV}}$  vertex (Fig. 9). The analysis of the dc magnetic susceptibility data supports the  $S=21/2$  ground state that results from the straightforward coupling diagram:

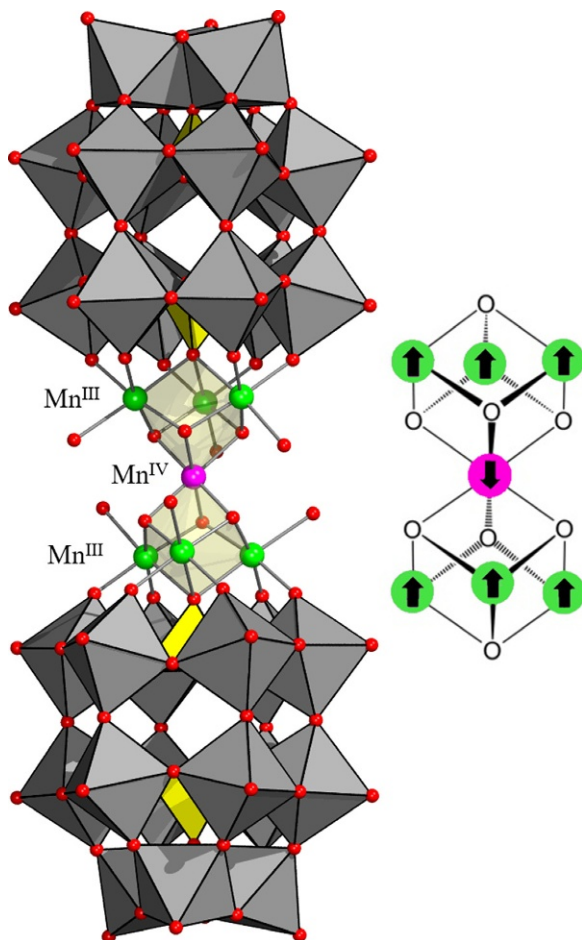


**Fig. 9** Structure of the polyanion  $\{\text{Mn}_7(\text{P}_2\text{W}_{15})_2\}$  and simplified coupling scheme. Mn(IV), purple; Mn(III), green spheres, O, red;  $\text{WO}_6$ , gray;  $\text{PO}_4$ , yellow. The two  $\text{Mn}_4\text{O}_4$  cubanes are highlighted in transparent yellow. Hydrogens omitted for clarity.

antiferromagnetic exchange interaction between the  $\text{Mn}^{\text{III}}$  and  $\text{Mn}^{\text{IV}}$  ions ( $J = -18.75 \text{ cm}^{-1}$ ) and ferromagnetic  $\text{Mn}^{\text{III}}\text{--Mn}^{\text{III}}$  coupling ( $J = +12.5 \text{ cm}^{-1}$ ). This implies a similar situation compared to  $\{\text{Mn}_4\text{P}_2\text{W}_{15}\}$ , but with the  $\text{Mn}^{\text{III}}\text{--Mn}^{\text{IV}}$  coupling significantly weakened in  $\{\text{Mn}_7(\text{P}_2\text{W}_{15})_2\}$  compared to  $\{\text{Mn}_4\text{P}_2\text{W}_{15}\}$ , a consequence of the missing acetate exchange pathways. In particular, the relative orientation of the Jahn–Teller axes of the Mn(III) ions in each  $\text{Mn}^{\text{III}}_3\text{Mn}^{\text{IV}}$  substructure is nearly unchanged compared to the situation in  $\{\text{Mn}_4\text{P}_2\text{W}_{15}\}$ . The most pronounced difference in its coordination

environment concerns the single Mn(IV) center that itself represents an isotropic spin center. Despite the similarities, the frequency-dependent ac susceptibility measurements showed the characteristic onset of a slowing down of the magnetization relaxation below 3 K—the SMM barrier has re-appeared. A CONDON analysis yielded a total zero-field splitting of  $15.7 \text{ cm}^{-1}$  and confirmed a negative ZFS  $D$  value ( $-0.143 \text{ cm}^{-1}$ ; Fig. 10).

This surprising resurgence of the energy barrier between the energetically lowest  $m_S$  states ( $m_S = +21/2$  and  $-21/2$ ) was tentatively linked to the fact that the inversion-symmetric  $\{\text{Mn}_7(\text{P}_2\text{W}_{15})_2\}$  polyoxometalate cluster does not exhibit a molecular dipole moment—in contrast to the situation in  $\{\text{Mn}_4\text{P}_2\text{W}_{15}\}$ , where an  $[\text{Mn}^{\text{III}}_3\text{Mn}^{\text{IV}}\text{O}_3(\text{CH}_3\text{COO})_3]$  group with a formal charge of +4 is attached to a polyoxotungstate with a formal charge of  $-12$  (Fig. 11).

Given that spin-orbit coupling, which factors into the molecular magnetic anisotropy, depends on the presence of a local electric field gradient (76), we suggest that the electrostatic environment of the spin structures within such a magnetically functionalized polyoxometalate can in principle affect its magnetic anisotropy, at least within the conceptual boundaries discussed above. On the other hand, for *isotropic* spin clusters (see the  $\{\text{CeMn}_6\}$ - $\{\text{P}_2\text{W}_{15}\}$  aggregate, a structure with a molecular dipole moment), the changes upon introducing a local electrical field gradient appear insignificant and are in line with the observed small geometric changes. This, in turn, also generally implies that the magnetic properties of magnetically anisotropic molecules deposited on surfaces (or are situated within other electrostatically anisotropic environments) cannot be assumed to be identical to the symmetric environment of a solid-state crystal lattice.

## 4.2 Hybrid Polyoxometalates Represent Potential Precursors for Controlled Molecule-Nanoelectrode Contacts

As detailed earlier, the development of single-molecule electronics (and spintronics) is currently limited by the experimental problems associated with break junction-based measurements, i.e., the state-of-the-art method to realize single-molecule conductivity studies in gated environments. One postulated (and still speculative) bottom-up alternative to the break junction approach is based on recent developments in polyoxometalate synthesis that allow us to (1) interlink distinct, intact polyoxometalate archetypes and to (2)

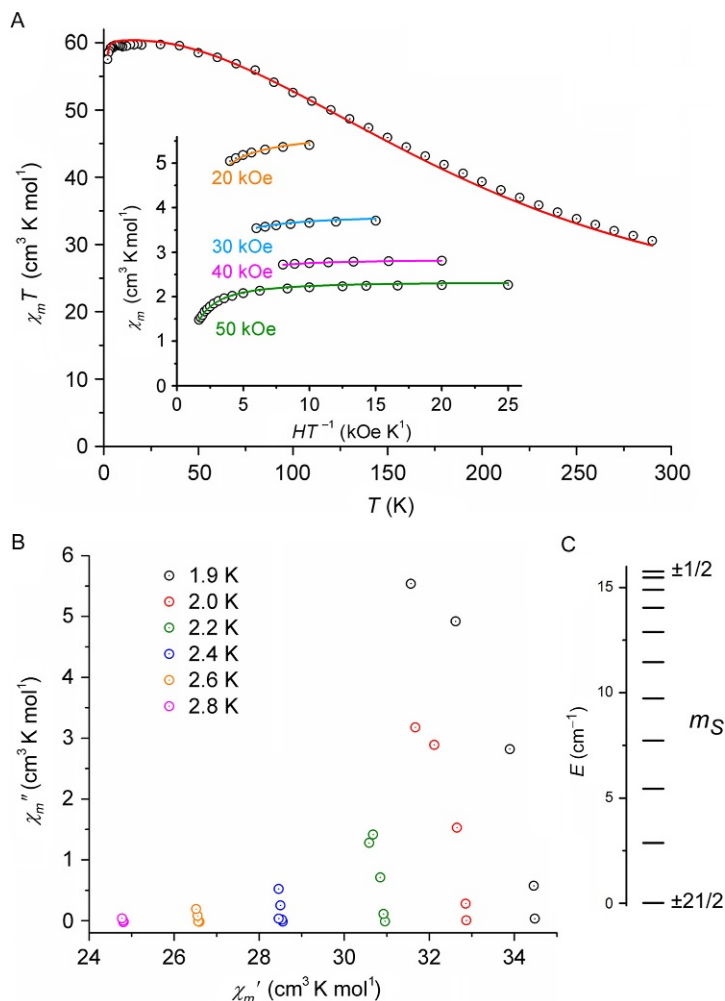


**Fig. 10** (A) Temperature and field dependence of  $\chi_m T$  (at 0.1 T) and  $\chi_m$  (inset). Circles: experimental data; solid color graphs: results of least-squares CONDON fit. (B) Cole–Cole plot showing the divergence of the in-phase and out-of-phase molar ac susceptibility components ( $\chi''$  vs  $\chi'$ ); zero-bias field, 3 G ac amplitude. (C) Zero-field splitting of the  $S=21/2$  ground state multiplet resulting from CONDON simulations.

generate hybrid cluster structures from both “classical” polyoxometalates (based on early transition metal addenda atoms) and “nonclassical” polyoxometalates (based on late transition metal addenda atoms (77)). The rationale behind these strategies to marry different polyoxometalates is to create polyoxometalates that are augmented by peripheral metal oxide cluster

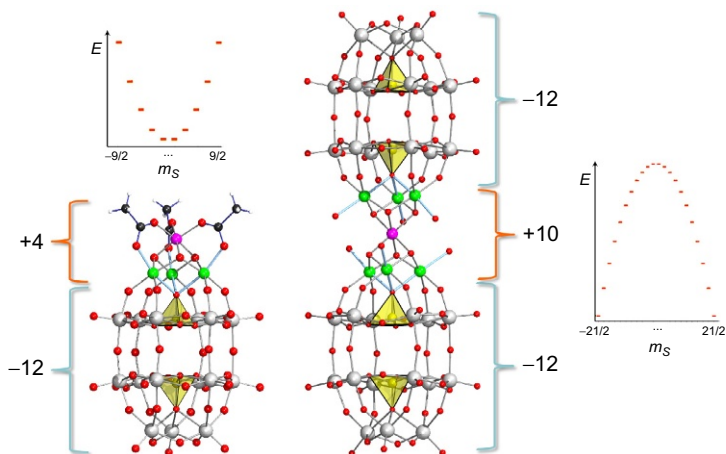


**Fig. 11** Side-by-side comparison of the  $\{\text{Mn}_4\text{P}_2\text{W}_{15}\}$  and  $\{\text{Mn}_7(\text{P}_2\text{W}_{15})_2\}$  cluster anions and the formal partial charges of their manganese- and polyoxotungstate-based building blocks. *Blue lines* indicate the Jahn–Teller elongated  $\text{Mn}^{\text{III}}\text{—O}$  bonds in both structures (color codes as in [Figs. 7 and 9](#)). The zero-field splitting of their ground state multiplet (substate energy vs  $m_S$ ) showcases the inversion of the parabola upon changing from the polar  $\{\text{Mn}_4\text{P}_2\text{W}_{15}\}$  to the  $\{\text{Mn}_7(\text{P}_2\text{W}_{15})_2\}$  structure with no net dipole moment.

groups of distinctively different reactivity, which potentially can be transformed into metallic nanoparticles. If these metallic nanoclusters can be kept attached to the polyoxometalate core structure, eventually representing the single molecule accessible to charge transport experiments, they can serve as precursors for source and drain electrodes, e.g., in multitip STM experiments where a minimal distance between the individual STM tips (typically several dozen nanometers) precludes direct multiterminal conductivity measurements on individual molecules. Our group thus explores the possibilities to augment the (magnetically functionalized) molecule of choice by preformed auxiliary metal nanoparticles, which could in turn enable multi-terminal charge transport measurements using commercial STM setups ([Fig. 12](#)).

A first example of a super-cluster structure that exclusively comprises nonlacunary polyoxometalate constituents is given by  $[\text{Mn}_{40}^{\text{III}}\text{P}_{32}\text{W}_{224}^{\text{VI}}\text{O}_{888}]^{152-}$  ( $=\{\text{Mn}_{40}\text{W}_{224}\}$ ), isolated as  $\text{K}_{56}\text{Li}_{74}\text{H}_{22}\{\text{Mn}_{40}\text{W}_{224}\} \cdot \text{ca. } 680\text{H}_2\text{O}$ , a core-shell structure consisting of a central  $\{\text{P}_8\text{W}_{48}\}$  wheel-shaped cluster, to the outer surface of which 12 Wells–Dawson-type  $\{\text{P}_2\text{W}_{14/15}\text{Mn}_{4/3}^{\text{III}}\}$  are attached ([Fig. 13](#)) (79). The  $\{\text{P}_2\text{W}_{14/15}\text{Mn}_{4/3}^{\text{III}}\}$  units themselves are organized in trimers. Each cluster constituent is linked

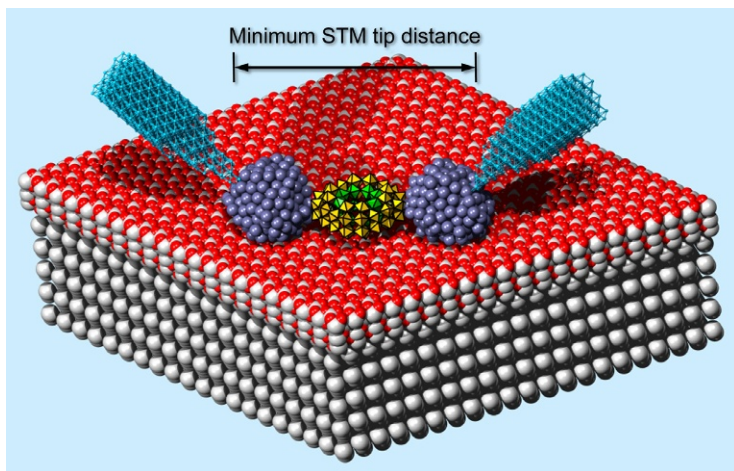


**Fig. 12** Hypothetical scenario of a three-terminal molecular transistor architecture realized in a two-tip STM experiment: an arbitrary magnetic molecule (here: a  $\{\text{Fe}^{\text{III}}_{16}\text{W}^{\text{VI}}_{48}\}$  cluster; (78) Fe, green; W, yellow) is deposited on the top of a metal oxide-terminated gate electrode. Two metal clusters (blue-gray spheres) are attached to this molecule and act as “contact pads” (or extensions) to the two STM tips (light blue) that have to retain a minimal distance. Upon contact, these tips then assume the functions of source and drain electrodes. Note that in this given scenario, the fully oxidized  $\{\text{P}_8\text{W}_{48}\}$  wheel cluster would serve as insulating tunneling barrier between the metallic nanoparticles and the inner Fe(III) sites, preventing hybridization of the magnetically relevant 3d orbitals with the metallic states.

via two Mn–O–W bridges to its neighbor cluster units. Note that the inter-cluster condensation mode is highly unusual, also because the outer oxo positions of intact archetypal polyoxometalates typically exhibit a decreased electron density due to their  $\pi$  donor bonding to the fully oxidized metal centers, and coordination to them often is too labile for the isolation of aggregates. The formation of  $\{\text{Mn}_{40}\text{W}_{224}\}$  has been scrutinized in terms of the various (slow) elementary reactions, for which a scheme of kinetically controlled cocondensation has been proposed (Fig. 14). We conjecture that this key finding can be translated to other archetypal polyoxometalates, including magnetically functionalized derivatives.

First proof-of-concept examples for classical/nonclassical polyoxometalate hybrid structures have been reported recently, in which polyoxotungstates and polyoxopalladates are directly conjoined with no further bridging groups (Fig. 15) (80). The polyanions  $[\text{Se}^{\text{IV}}_2\text{Pd}^{\text{II}}_4\text{W}^{\text{VI}}_{14}\text{O}_{56}]^{12-}$  form by cocondensation of  $\text{Pd}^{\text{II}}$  ions with tungstoselenites in aqueous acetate medium (pH 6.4) and comprise an  $\{\alpha\text{-Se}_2\text{W}_{14}\text{O}_{52}\}$  polyoxotungstate

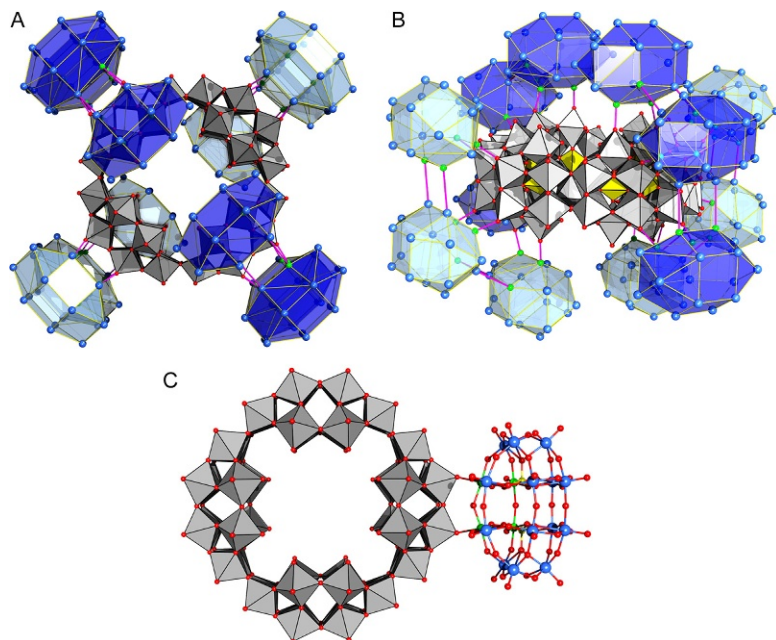


**Fig. 13** Simplified structure of the  $\{\text{Mn}_{40}\text{W}_{224}\}$  polyanions in a view perpendicular (A) and parallel (B) to the central  $\{\text{P}_8\text{W}_{48}\}$  ring (shown in polyhedral representation,  $\text{WO}_6$ , gray;  $\text{PO}_4$ , yellow), with only the metal skeletons of the 12 attached Wells–Dawson-type  $\{\text{P}_2\text{W}_{14}\text{Mn}_4\}/\{\text{P}_2\text{W}_{15}\text{Mn}_3\}$  clusters shown. The four  $\{\text{P}_2\text{W}_{14}\text{Mn}_4\}$   $\{\text{P}_2\text{W}_{15}\text{Mn}_3\}_2$  triads are shown in light and dark transparent blue. Purple lines indicate the W–O–Mn bridges that form the primary link between the individual clusters. Mn, light green spheres. (C) A segment of the  $\{\text{Mn}_{40}\text{W}_{224}\}$  structure showing the two Mn–O–W links with which a  $\{\text{P}_2\text{W}_{14}\text{Mn}_4\}$  cluster (shown as ball-and-stick model) here is attached to the outer surface of the archetypal  $\{\text{P}_8\text{W}_{48}\}$  wheel (yellow octahedra).

moiety supporting an isotetraoxopalladate fragment  $\{\text{Pd}_4\text{O}_4\}$  (Fig. 15A). The direct connection between the  $\text{Pd}^{\text{II}}$  centers by oxo ligands as well as the complete integration of the polyoxopalladate  $\{\text{Pd}_4\text{O}_4\}$  unit in the polyoxometalate framework allows us to consider  $[\text{Se}^{\text{IV}}_2\text{Pd}^{\text{II}}_4\text{W}^{\text{VI}}_{14}\text{O}_{56}]^{12-}$  as a *bona fide* hybrid polyoxopalladatotungstate. The  $\mu_2$ -O bridging the  $\text{Pd}^{\text{II}}$  centers in  $[\text{Se}^{\text{IV}}_2\text{Pd}^{\text{II}}_4\text{W}^{\text{VI}}_{14}\text{O}_{56}]^{12-}$  are rather nucleophilic and can bind to heterometal ions as proved by coordination of a  $\{\text{Na}(\text{OH}_2)_3\}$  moiety to the  $\{\text{Pd}_4\text{O}_4\}$  site of the polyanion in  $\text{Cs}_4\text{Na}_3\text{H}_4[\text{Se}_2\text{Pd}_4\text{W}_{14}\text{O}_{56}\text{H}] \cdot 18\text{H}_2\text{O} \cdot 0.3\text{CsOAc} \cdot 0.2\text{NaOAc}$  crystals (Fig. 15B). In principle, it lanthanide(III), Zr(IV), or Ce(IV) ions should potentially replace  $\text{Na}^+$  in such architectures. Hence, they can act as direct link between the magnetic polyoxometalates and polyoxopalladatotungstate hybrids in architectures



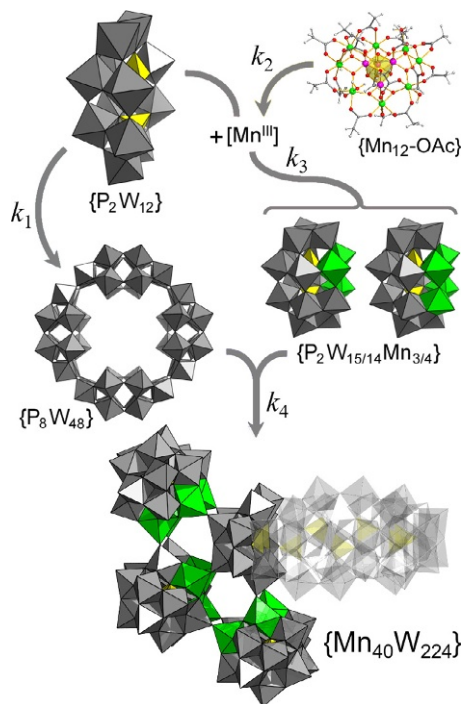


**Fig. 14** The principle of kinetically controlled conformation/cocondensation postulated for the self-assembly of  $\{\text{Mn}_{40}\text{W}_{224}\}$ . The hexalacunary and highly nucleophilic  $\{\text{P}_2\text{W}_{12}\}$  precursor (formally derived from the intact  $\{\text{P}_2\text{W}_{18}\}$  Wells–Dawson structure) oligomerizes to  $\{\text{P}_8\text{W}_{48}\}$  under the chosen reaction conditions (an aqueous 1:1 HOAc/LiOAc buffer solution), its tetramer and reacts with  $\text{Mn}^{\text{III}}$  species that are slowly produced by decomposition of the  $\{\text{Mn}_{12}\text{-OAc}\}$  precursor ( $\text{Mn}^{\text{III}}$ , green;  $\text{Mn}^{\text{IV}}$ , purple spheres). Note that  $\text{Mn}^{\text{III}}$  ions would otherwise disproportionate in the absence of suitable reactants. A smaller fraction also partially decomposes and provides a source of low-nuclearity tungstate that reconstitute the Wells–Dawson structure, resulting in heterometal  $\{\text{P}_2\text{W}_{14}\text{Mn}_4\}$  and  $\{\text{P}_2\text{W}_{15}\text{Mn}_3\}$  intermediates. In a final step, these then cocondense with the  $\{\text{P}_2\text{W}_{12}\}$  constituents of the  $\{\text{P}_8\text{W}_{48}\}$  rings via their outward-oriented terminal oxo groups to form the  $\{\text{Mn}_{40}\text{W}_{224}\}$  polyanions (only one  $\{\text{P}_2\text{W}_{14}\text{Mn}_4\}\{\text{P}_2\text{W}_{15}\text{Mn}_3\}_2\{\text{P}_2\text{W}_{12}\}$  unit is shown; the adjoined three  $\{\text{P}_2\text{W}_{12}\}$  groups of the central  $\{\text{P}_8\text{W}_{48}\}$  ring are shown in transparent).  $\text{WO}_6$ , gray;  $\text{MnO}_6$ , green;  $\text{PO}_4$ , yellow polyhedra.

schematically shown in Fig. 15C. There is also a possibility is to assemble larger polyoxopalladatotungstate structures with potential active sites on the polyoxotungstate side as exemplified by formation of another classical/nonclassical polyoxometalate hybrid  $[\text{Se}^{\text{IV}}_4\text{Pd}^{\text{II}}_4\text{W}^{\text{VI}}_{28}\text{O}_{108}\text{H}_{12}]^{12-}$  representing a dimer of two  $\{(\text{H}_2\text{O})(\text{OH})_2\text{Pd}^{\text{II}}_2\text{Se}^{\text{IV}}_2\text{W}_{13}\text{O}_{49}\}$  units connected by two *trans*- $\{\text{O}=\text{W}(\text{H}_2\text{O})\}$  groups (80). The hybrid

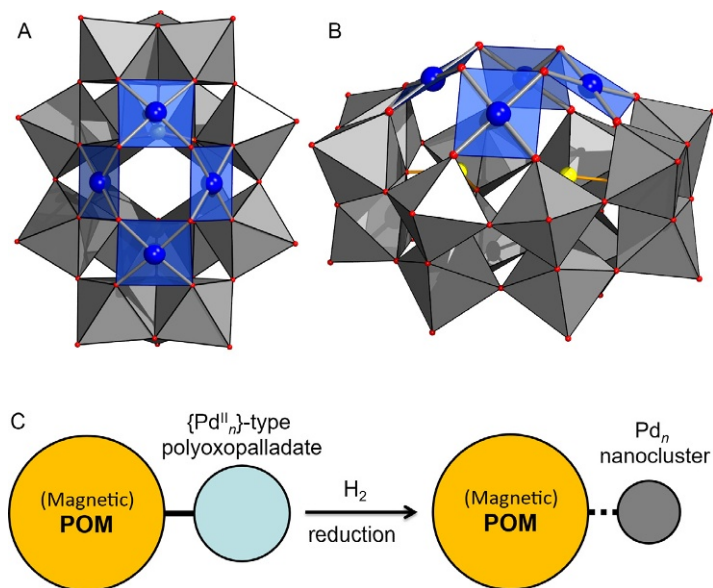


**Fig. 15** Structure of  $[\text{Se}^{\text{IV}}_2\text{Pd}^{\text{II}}_4\text{W}^{\text{VI}}_{14}\text{O}_{56}\text{H}]^{11-}$  in a top-down (A) and a side (B) view of the polyanions. The polyoxopalladate parts are highlighted in *transparent blue*. Pd, *blue*; O, *red*; Se, *yellow spheres*;  $\text{WO}_6$ , *gray octahedra*. (C) Schematic illustration of the prospect of hybrid polyoxotungstate–polyoxopalladate clusters to act as precursors for metal oxide cluster–metal nanocluster aggregates. Element-selective reduction of the polyoxopalladate, e.g., with  $\text{H}_2$ , is predicted to yield Pd (or Pd-based alloy) nanoparticles.

palladatungstate structures are of particular interest as they should in principle be amenable to subsequent reduction reactions in which the polyoxopalladate constituent is transformed into a metallic Pd nanocluster or, depending on the reaction conditions, a Pd-based alloy nanoparticle. For example, in the presence of  $[\text{Fe}(\text{CO})_5]$ , nanoparticles of the hard ferromagnetic PdFe phases (81) can be formed; these structures might become relevant for spin-polarized charge transport experiments. Some  $\text{Pd}_x\text{Se}$  phases ( $x > 1.5$ ), on the other hand, are superconducting up to 2.66 K (82).

It will remain to be seen if the Pd or PdFe nanoparticles, formed upon reduction of the polyoxopalladate constituents, will remain attached to the neighboring “classical” polyoxotungstate. At the same time, initial experiments with polyoxotungstate-stabilized, ultrasmall ( $< 3$  nm in diameter)  $\text{PtFe}_2$  nanoclusters, which are known to be chemically very similar to PdFe-type clusters, display a strong nanocluster–POM interaction (83). Polyoxometalates here are able to readily supplant typical organic surfactant

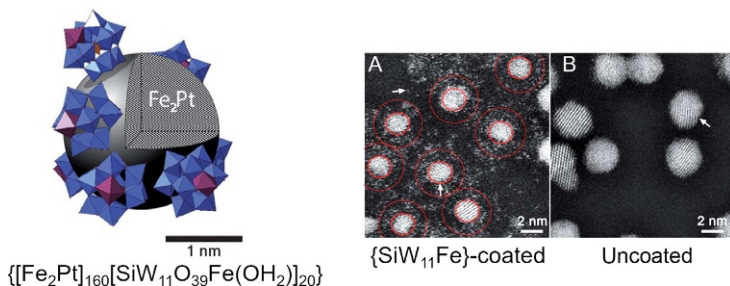


**Fig. 16** Will a paramagnetic Pd or a ferromagnetic PdFe nanoparticle, formed as sketched up in Fig. 15C, remain attached to a polyoxotungstate cluster? The stabilization of ultrasmall PtFe<sub>2</sub> nanoclusters (approx. composition: [PtFe<sub>2</sub>]<sub>160</sub>) by ca. 20 {SiW<sub>11</sub>Fe} Keggin-type polyoxotungstates points toward this scenario. Transmission electron microscopy graphs show that stabilization by {SiW<sub>11</sub>Fe} yields significantly smaller and nonagglomerated PtFe<sub>2</sub> nanoparticles (A) compared to the particles that are formed in the presence of only organic surfactants (B). *Reproduced from Seemann, K. M.; Bauer, A.; Kindervater, J.; Meyer, M.; Besson, C.; Luysberg, M.; Durkin, P.; Pyckhout-Hintzen, W.; Budisa, N.; Georgii, R.; Schneider, C. M.; Kögerler, P. Nanoscale* **2013**, 5, 2511–2519 with permission from the Royal Society of Chemistry.

groups such as oleylamine or oleic acid that are commonly used to stabilize late transition metal nanoclusters; POM-protected PtFe<sub>2</sub> nanoclusters are even soluble and stable in water (Fig. 16). This bolsters the assumption that the polyoxotungstate–Pd nanoparticle binding might be sufficiently strong to prevent further, uncontrolled Pd nanoparticle agglomeration—a key requirement for their use as source/drain electrode precursors.



## 5. POLYOXOMETALATES IN REDOX-BASED RESISTIVE SWITCHING

As motivated in Section 1, significant potential has been predicted for memristor devices, i.e., multiple-state resistive switching devices (84) that can mimic key synaptic features. Reversal switching between different redox states by an applied external electric field has been shown for a wide range of transition metal oxides (SrZrO<sub>3</sub>, SrTiO<sub>3</sub>, TiO<sub>2</sub>, MnO<sub>2</sub>, Ta<sub>2</sub>O<sub>5</sub>, HfO<sub>2</sub>, ZrO<sub>x</sub>, etc.) (85) and is the physical basis of data storage in Resistive Random Access Memory (ReRAM) devices (86). This new class of computer memories is regarded as promising successor of flash memories. The simple Metal–Insulator–Metal (MIM) structure of ReRAM cells allows fast and highly dense packed nonvolatile memories, which can be operated at very low voltages, resulting in a very high energy efficiency. In general,

classical ReRAM cells consisting of oxide or chalcogenide switching layers can be arranged in three different classes (electrochemical metallization, valence change, and thermochemical memories (TCM)) (87).

The electrochemical metallization memories (ECM) are characterized by a good ion conducting material as switching layer, which is sandwiched between an electrochemically active electrode (e.g., Ag, Ni, or Cu) and an electrochemically inert counter electrode (e.g., Pt, Ir, or W). Especially amorphous metal oxides, selenides, and sulfides are suited as switching layer due to their high mobility for metal cations. By applying a positive voltage to the active electrode, metal ions are dissolved, migrate through the switching layer, and recrystallize at the inactive electrode until a galvanic contact between both electrodes is established through a metallic filament in the switching layer (see Fig. 17B). Reversing the switching polarity leads to the disruption of the conducting filament and an increase of the cell resistance.

It could be shown that many transition metal oxides exhibit such a bipolar switching behavior even in the absence of an electrochemically active electrode. In these so-called valence change memory (VCM) cells, the switching process is realized by the electromigration of oxygen vacancies. In many transition metal oxides such oxygen related defects are much more mobile than the metal cations. In an initial forming step an n-conducting

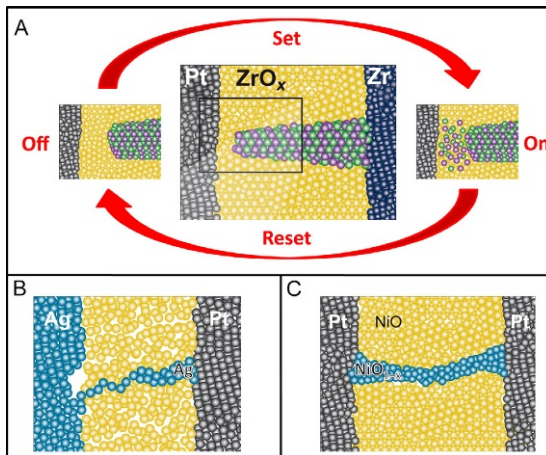


**Fig. 17** Schematic drawings of the composition and structure of conducting filaments in exemplary chosen solid-state material systems for classical VCM (A), ECM (B), and TCM (C) resistive switching cells.

region consisting of oxygen vacancy-enriched and thus reduced oxide is formed at the cathode and propagates toward the anode (see Fig. 17A). When this so-called virtual cathode almost touches the anode, the cell resistance decreases significantly. After this electroforming step, switching between the ON and OFF state can be realized with much lower voltages because only a small amount of vacancies has to be moved in order to close or open the remaining gap in the conductive filament.

Several transition metal oxides, which exhibit a rather large difference between the high and low resistance state, show a unipolar switching behavior, i.e., SET and RESET processes occur at the same voltage polarity. In some systems even a change between bipolar and unipolar switching was observed depending on layer thickness and temperature. These unipolar switching cells belong to the class of TCM. Here, resistive switching is triggered by a thermally induced breakdown of a rather thin and highly reduced oxide filament (see Fig. 17C). This mechanism is often referred to as the fuse-antifuse type. Because of the rather high switching voltages due to the necessary local heating TCM cells are usually seen as less attractive than ECM or VCM systems. The concept of resistive switching, known for various aforementioned solid-state structures, can in fact be translated to the level of assembled and individual polyoxometalates that display several well-defined redox states. For some polyoxometalates, preliminary studies point to the fact that their various redox states significantly differ in their molecular conductivity, which represents a crucial requirement for their use in resistive switching. However, from the mechanistic point of view, such systems would probably be most closely related to the classical VCM cells. As such, we are exploring redox-active polyoxometalates, in particular, POVs that often exhibit a rich redox chemistry (88), as prototypes for thermodynamically stable single-molecule resistive memory and memristor devices, the functional principles of which are illustrated in Fig. 18.

Research in this direction is at a very beginning. A first proof-of-concept example concerns the stoichiometric  $W_3O_9$  nanocluster, which can easily be formed by thermal evaporation of  $WO_3$  powder under UHV conditions and which displays parallels to the envisioned use of POMs for resistive switching. Mass spectrometric studies indicated that the trimeric compound is the main component of tungsten trioxide vapor (89,90), which renders this  $W_3O_9$  cluster easily available for fundamental surface science studies. DFT calculations indicated that the most stable structure of the nanocluster is a six-membered ring with  $D_{3h}$ -symmetry consisting of oxygen-bridged

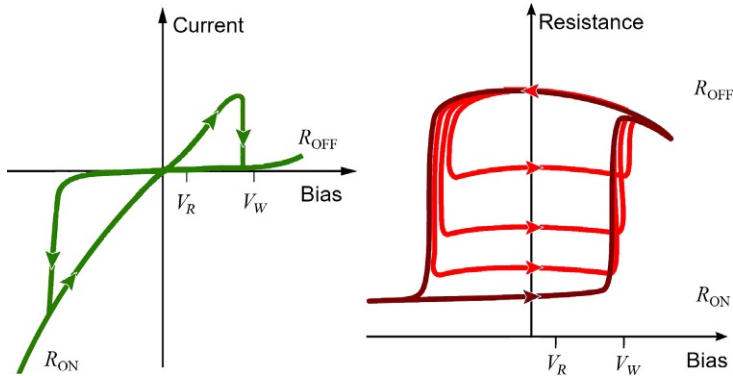


**Fig. 18** Idealized hysteretic current ( $I$ , green graph) vs bias voltage curve for a resistive switching device (left) and schematic state-dependent resistance curves (red graphs) for a memristive device (right).  $V_R$  and  $V_W$  indicate read bias voltages for read and write operations. The memristive functionality implies switching between the different resistivity states by bias pulse sequences, comparable to the conditioning of synaptic connections between biological neurons via multiple potential pulses.

tungsten atoms with two additional terminating oxygen atoms at each of the tetrahedrally coordinated tungsten atoms (91). Its large energy gap of 3.4 eV nearly reaches the value for bulk  $WO_3$ , which exhibits a direct band gap of 3.5 eV (92). Thus,  $W_3O_9$  can be viewed as smallest molecular model for bulk  $WO_3$ . Besides the neutral stoichiometric cluster also the corresponding anions and oxygen-deficient clusters have been objects of theoretical investigation. It was shown that both the  $[W_3O_9]^-$  and  $[W_3O_9]^{2-}$  clusters are highly stabilized by d-orbital aromaticity (93), so that these anions might be accessible via charge injection into the neutral cluster. Removing a terminal oxygen atom from a  $W_3O_9$  cluster results in the formation of the under-stoichiometric  $W_3O_8$  cluster with  $C_S$  symmetry, which contains a tricoordinated tungsten site. Calculations revealed that this tungsten atom possesses a localized 5d electron pair and represents a localized  $W^{4+}$  defect site. As a consequence,  $W_3O_8$  exhibits a very high adsorption energy for  $O_2$  of  $-78$  kcal/mol. Therefore, this  $W_3O_8$  cluster can be viewed as a molecular model for an oxygen-deficient site in tungsten oxides. The wide range of stable ionic and neutral relatives of the  $W_3O_9$  cluster raises hope to establish a stable switching between different molecular redox states.

In our preliminary prototypal experiment, the electrically conducting STM tip could be utilized for changing the electronic structure of an immobilized  $W_3O_9$  nanocluster (94). Hereby, the metallic STM tip acts

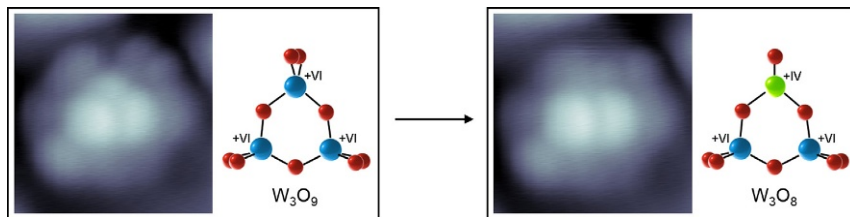


**Fig. 19** STM images of a  $W_3O_9$  cluster (*left*) and a possible  $W_3O_8$  cluster (*right*) adsorbed on an ultrathin titanium oxide film. The latter has been formed by charge injection through a metallic STM tip.

as the top electrode of an exemplary switching cell with the oxide cluster as active component and the substrate as bottom electrode. The typical trimeric structure in the STM depiction of  $W_3O_9$  is caused by the  $W^{6+}$  atoms of the cluster ring. By inducing a charge transfer process through the STM tip, its threefold symmetry could be irreversibly transformed into a twofold one (Fig. 19). This may be due to an oxygen removal from one of the tungsten centers in the cluster ring leading to a partial reduction.

The unique combination of chemical and physical properties of reduced and mixed-valent POMs (Robin–Day class II or III) such as the pronounced correlation between the electron (de)localization (see, as an example,  $V^{IV}:V^V$  ratios in the  $\{V_{18}O_{42}\}$  cluster: 18:0, 16:2, and 10:8) (63,95), magnetic state, Kondo resonance, redox state, and electrical single-molecule conductance may have great benefits in the exploitation in molecular layer-based and single-molecule charge transport experiments that pave the way for the eventual integration of POM species into nanoelectronic and nanospintronic devices. In particular, POVs whose redox states can be adjusted with no or only minimal structural changes (see earlier) attract great attention (96). Interestingly, we showcased that the POV's magnetochemical behavior is governed not only by distinct redox states but can also be significantly influenced by the different nature of supramolecular guest species within the POV host structures, as exemplified by the quasi-isostructural, mixed-valence  $[X@HV^{IV}_8V^V_{14}O_{54}]^{6-}$  encapsulating diamagnetic template anions  $X = VO_2F_2^-$  ( $C_{2v}$ ),  $SCN^-$  ( $C_{\infty v}$ ), or  $ClO_4^-$  ( $T_d$ ) (97).

As an outlook, a first promising result was obtained on  $\{V_{18}O_{42}\}$  clusters that were deposited on gold (by heating the tetraethylammonium salt of  $[V_{18}O_{42}(I)]^{5-}$  under UHV conditions). Although a fraction of the cluster anions decomposed on the metal substrate, these decomposition products

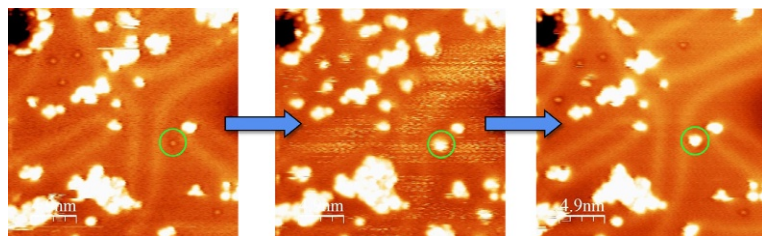


**Fig. 20** Preliminary STM graphs of bias voltage-induced conductance change of a discrete  $\{V_{18}O_{42}\}$ -derived POM (*encircled*) deposited on Au(111). The pronounced change in molecular conductivity upon switching from a negative bias voltage (*left*) to a positive voltage (*middle*) is retained when switching back to a negative voltage. Scale bar: 4.9 nm.

(likely representing smaller cluster fragments) exhibit a tip-induced change of their electronic conductance that might even be hysteretic (Fig. 20) (94).

## 6. CONCLUSIONS

Today's level of development of polyoxometalate chemistry—in particular with regard to magnetic functionalization, the POM's surface chemistry and organizational tendencies on surfaces and other substrates (graphene, carbon nanotubes, etc.), control of charge and redox characteristics, and the ability to interlink different cluster archetypes—opens pathways toward their integration in CMOS devices. We are currently exploring how their unique materials properties can be translated into single-molecule (spin) transistors and memristors, as these targets promise especially beneficial for future information technology (98). The current interest in artificial intelligence and complex neural networks for “deep learning” will certainly boost the search for molecular memristors, which can also be used for content-addressable memory that enables parallel searching functionality within the memory devices, i.e., a departure from the *von Neumann* computing architecture.

The biggest obstacle remains the full understanding of polyoxometalates on surfaces, near surface defects, etc., where the experimental methodology reaches its limits, e.g., in time-resolved studies. At the same time, the molecule–surface interface is exactly the area where numerous novel physical phenomena (including technologically relevant ones) are predicted to occur. To quote Wolfgang Pauli: “God made the bulk; surfaces were invented by the devil.” As such, the study of POMs in this context will remain a challenging yet highly rewarding frontier.



## ACKNOWLEDGMENTS

We thank Natalya V. Izarova, Claire Besson, and Jeff S. Rawson for highly valuable input and discussions. We thank Moon-Ho Jo for providing the conductance data shown in Fig. 4. K.Y.M. thanks the Deutsche Forschungsgemeinschaft (DFG) for an Emmy Noether Fellowship. K.Y.M. and M.M. are grateful to the Jülich-Aachen Research Alliance—Future Information Technology (JARAFIT) for a Seed Fund grant. P.K. acknowledges funding by the European Research Council (ERC StG no. 308051—MOLSPINTRON).

## REFERENCES

1. (a) Schäpers, T. *Semiconductor Spintronics*, De Gruyter: Berlin, 2016; (b) Sato, K., Saitoh, E., Eds. *Spintronics for Next Generation Innovative Devices*; Wiley: Chichester, 2015; (c) Felsler, C., Fecher, G. H., Eds. *Spintronics: From Materials to Devices*; Springer: Dordrecht, 2013; (d) Bandyopadhyay, S.; Cahay, M. *Introduction to Spintronics*, 2nd ed.; CRC Press: Boca Raton, 2015.
2. Moore, G. E. *Electronics* **1965**, *38*, 114–117.
3. Vuillaume, D. *C. R. Phys.* **2008**, *9*, 78–94.
4. Heath, J. R. *Annu. Rev. Mater. Res.* **2009**, *39*, 1–23.
5. Metzger, R. M. *J. Mater. Chem.* **2008**, *18*, 4364–4396.
6. Moth-Poulsen, K.; Bjornholm, T. *Nat. Nanotechnol.* **2009**, *4*, 551–556.
7. Del Nero, J.; de Souza, F. M.; Capaz, R. B. *J. Comput. Theor. Nanosci.* **2010**, *7*, 503–516.
8. Shen, Q.; Guo, X.; Steigerwald, M. L.; Nuckolls, C. *Chem. Asian J.* **2010**, *5*, 1040–1057.
9. Cuevas, J. C.; Scheer, E. *Molecular Electronics: An Introduction to Theory and Experiment*; World Scientific Publishing Co.: Singapore, 2010.
10. Aviram, A.; Ratner, M. A. *Chem. Phys. Lett.* **1974**, *29*, 277–283.
11. Park, J.; Pasupathy, A. N.; Goldsmith, J. I.; Chang, C.; Yaish, Y.; Petta, J. R.; Rinkoski, M.; Sethna, J. P.; Abruna, H. D.; McEuen, P. L.; Ralph, D. C. *Nature* **2002**, *417*, 722–725.
12. Liang, W.; Shores, M. P.; Bockrath, M.; Long, J. R.; Park, H. *Nature* **2002**, *417*, 725–729.
13. de Cola, L. *Top. Curr. Chem.* **2005**, *257*, 1–133.
14. van der Molen, S. J.; Liljeroth, P. *J. Phys. Condens. Matter* **2010**, *22*, 133001.
15. Jäckel, F.; Watson, M. D.; Müllen, K.; Rabe, J. P. *Phys. Rev. Lett.* **2004**, *92*, 188303.
16. Song, H.; Kim, Y.; Jang, Y. H.; Jeong, H.; Reed, M. A.; Lee, T. *Nature* **2009**, *462*, 1039–1043.
17. Ferrucci, D.; Levas, A.; Bagchi, S.; Gondek, D.; Mueller, E. T. *Artif. Intell.* **2013**, *199–200*, 93–105.
18. Clemente-Juan, J. M.; Coronado, E.; Gaita-Ariño, A. *Chem. Soc. Rev.* **2012**, *41*, 7464–7478.
19. Busche, C.; Vila-Nadal, L.; Yan, J.; Miras, H. N.; Long, D.-L.; Georgiev, V. P.; Asenov, A.; Pedersen, R. H.; Gadegaard, N.; Mirza, M. M.; Paul, D. J.; Poblet, J. M.; Cronin, L. *Nature* **2014**, *515*, 545–549.
20. Xue, H.-B.; Liang, J.-Q.; Liu, W.-M. *Sci. Rep.* **2015**, *5*, 8730/1–8730/11.
21. Herzog, S.; Wegewijs, M. R. *Nanotechnology* **2010**, *21*, 274010.
22. Zandvliet, H. J. W.; van Houselt, A. *Annu. Rev. Anal. Chem.* **2009**, *2*, 37–55.
23. Li, B.; Li, Z.; Yang, J.; Hou, J. G. *Chem. Commun.* **2011**, *47*, 2747–2762.
24. Li, T.; Hu, W.; Zhu, D. *Adv. Mater.* **2010**, *22*, 286–300.
25. Osorio, E. A.; Bjørnholm, T.; Lehn, J. M.; Ruben, M.; van der Zant, H. S. J. *J. Phys. Condens. Matter* **2008**, *20*, 374121.
26. Baibich, M. N.; Broto, J. M.; Fert, A.; Van Dau, F. N.; Petroff, F.; Etienne, P.; Creuzet, G.; Friederich, A.; Chazelas, J. *Phys. Rev. Lett.* **1988**, *61*, 2472–2475.

27. Binasch, G.; Grünberg, P.; Saurenbach, F.; Zinn, W. *Phys. Rev. B* **1989**, *39*, 4828–4830.
28. Seneor, P.; Bernand-Mantel, A.; Petroff, F. *J. Phys. Condens. Matter* **2007**, *19*, 165222.
29. Barnaš, J.; Weymann, I. *J. Phys. Condens. Matter* **2008**, *20*, 423202.
30. Rocha, A. R.; Garcia-Suarez, V. M.; Bailey, S. W.; Lambert, C. J.; Ferrer, J.; Sanvito, S. *Nat. Mater.* **2005**, *4*, 335–339.
31. Ferrer, J.; Garcia-Suarez, V. M. *J. Mater. Chem.* **2009**, *19*, 1696–1717.
32. Andergassen, S.; Meden, V.; Schoeller, H.; Splettstoesser, J.; Wegewijs, M. R. *Nanotechnology* **2010**, *21*, 272001.
33. May, F.; Wegewijs, M. R.; Hofstetter, W. *Beilstein J. Nanotechnol.* **2011**, *2*, 693–698.
34. Scott, G. D.; Natelson, D. *ACS Nano* **2010**, *4*, 3560–3579.
35. Yu, L. H.; Natelson, D. *Nanotechnology* **2004**, *15*, S517.
36. Bogani, L.; Wernsdorfer, W. *Nat. Mater.* **2008**, *7*, 179–186.
37. Voss, S.; Zander, O.; Fonin, M.; Rüdiger, U.; Burgert, M.; Groth, U. *Phys. Rev. B* **2008**, *78*, 155403.
38. Katoh, K.; Yoshida, Y.; Yamashita, M.; Miyasaka, H.; Breedlove, B. K.; Kajiwara, T.; Takaishi, S.; Ishikawa, N.; Isshiki, H.; Zhang, Y. F.; Komeda, T.; Yamagishi, M.; Takeya, J. *J. Am. Chem. Soc.* **2009**, *131*, 9967–9976.
39. Katoh, K.; Komeda, T.; Yamashita, M. *Dalton Trans.* **2010**, *39*, 4708–4723.
40. Wernsdorfer, W. *Int. J. Nanotechnol.* **2010**, *7*, 497–522.
41. Komeda, T.; Isshiki, H.; Liu, J.; Zhang, Y.-F.; Lorente, N.; Katoh, K.; Breedlove, B. K.; Yamashita, M. *Nat. Commun.* **2011**, *2*, 217.
42. Urdampilleta, M.; Klyatskaya, S.; Cleuziou, J. P.; Ruben, M.; Wernsdorfer, W. *Nat. Mater.* **2011**, *10*, 502–506.
43. Leuenberger, M. N.; Loss, D. *Nature* **2001**, *410*, 789–793.
44. Cerletti, V.; Coish, W. A.; Gywat, O.; Loss, D. *Nanotechnology* **2005**, *16*, R27.
45. Ardavan, A.; Blundell, S. J. *J. Mater. Chem.* **2009**, *19*, 1754–1760.
46. Osorio, E. A.; O'Neill, K.; Stuhr-Hansen, N.; Nielsen, O. F.; Bjørnholm, T.; van der Zant, H. S. J. *Adv. Mater.* **2007**, *19*, 281–285.
47. Romeike, C.; Wegewijs, M. R.; Hofstetter, W.; Schoeller, H. *Phys. Rev. Lett.* **2006**, *97*, 206601.
48. Wegewijs, M. R.; Romeike, C.; Schoeller, H.; Hofstetter, W. *New J. Phys.* **2007**, *9*, 344. Corrigendum: *New J. Phys.* **2011**, *13*, 079501.
49. Mannini, M.; Sainctavit, P.; Sessoli, R.; Cartier dit Moulin, C.; Pineider, F.; Arrio, M.-A.; Cornia, A.; Gatteschi, D. *Chem. Eur. J.* **2008**, *14*, 7530–7535.
50. Freedman, D. E.; Jenkins, D. M.; Iavarone, A. T.; Long, J. R. *J. Am. Chem. Soc.* **2008**, *130*, 2884–2885.
51. Dul, M.-C.; Pardo, E.; Lescouëzec, R.; Chamoreau, L.-M.; Villain, F.; Journaux, Y.; Ruiz-García, R.; Cano, J.; Julve, M.; Lloret, F.; Pasán, J.; Ruiz-Pérez, C. *J. Am. Chem. Soc.* **2009**, *131*, 14614–14615.
52. Gonidec, M.; Davies, E. S.; McMaster, J.; Amabilino, D. B.; Veciana, J. *J. Am. Chem. Soc.* **2010**, *132*, 1756–1757.
53. Gao, L.; Ji, W.; Hu, Y. B.; Cheng, Z. H.; Deng, Z. T.; Liu, Q.; Jiang, N.; Lin, X.; Guo, W.; Du, S. X.; Hofer, W. A.; Xie, X. C.; Gao, H. J. *Phys. Rev. Lett.* **2007**, *99*, 106402.
54. Fahrenndorf, S.; Atodiresi, N.; Besson, C.; Caciuc, V.; Matthes, F.; Blügel, S.; Kögerler, P.; Bürgler, D. E.; Schneider, C. M. *Nat. Commun.* **2013**, *4*, 2425.
55. Mannini, M.; Pineider, F.; Sainctavit, P.; Danieli, C.; Otero, E.; Sciancalepore, C.; Talarico, A. M.; Arrio, M.-A.; Cornia, A.; Gatteschi, D.; Sessoli, R. *Nat. Mater.* **2009**, *8*, 194–197.
56. Mannini, M.; Pineider, F.; Danieli, C.; Totti, F.; Sorace, L.; Sainctavit, P.; Arrio, M. A.; Otero, E.; Joly, L.; Cezar, J. C.; Cornia, A.; Sessoli, R. *Nature* **2010**, *468*, 417–421.
57. Clemente-Juan, J. M.; Coronado, E. *Coord. Chem. Rev.* **1999**, *193–195*, 361–394.
58. Kögerler, P.; Tsukerblat, B.; Müller, A. *Dalton Trans.* **2010**, *39*, 21–36.

59. Kortz, U.; Müller, A.; van Slageren, J.; Schnack, J.; Dalal, N. S.; Dressel, M. *Coord. Chem. Rev.* **2009**, *253*, 2315–2327.
60. Botar, B.; Ellern, A.; Hermann, R.; Kögerler, P. *Angew. Chem. Int. Ed. Engl.* **2009**, *48*, 9080–9083.
61. Müller, A.; Luban, M.; Schröder, C.; Modler, R.; Kögerler, P.; Axenovich, M.; Schnack, J.; Canfield, P.; Bud'ko, S.; Harrison, N. *ChemPhysChem* **2001**, *2*, 517–521.
62. Johnson, G. K.; Schlemper, E. O. *J. Am. Chem. Soc.* **1978**, *100*, 3645–3646.
63. Müller, A.; Sessoli, R.; Krickemeyer, E.; Bögge, H.; Meyer, J.; Gatteschi, D.; Pardi, L.; Westphal, J.; Hovemeier, K.; Rohlfing, R.; Döring, J.; Hellweg, F.; Beugholt, C.; Schmidtman, M. *Inorg. Chem.* **1997**, *36*, 5239–5250.
64. (a) Tasiopoulos, A. J.; O'Brien, T. A.; Abboud, K. A.; Christou, G. *Angew. Chem. Int. Ed. Engl.* **2004**, *43*, 345–349; (b) Tasiopoulos, A. J.; Milligan, P. L., Jr.; Abboud, K. A.; O'Brien, T. A.; Christou, G. *Inorg. Chem.* **2007**, *46*, 9678–9691.
65. Contant, R.; Herve, G. *Rev. Inorg. Chem.* **2002**, *22*, 63–111.
66. Fang, X.; Kögerler, P. *Chem. Commun.* **2008**, 3396–3398.
67. Sessoli, R.; Gatteschi, D.; Caneschi, A.; Novak, M. A. *Nature* **1993**, *365*, 141–143.
68. Gatteschi, D.; Sessoli, R.; Villain, J. *Molecular Nanomagnets*; Oxford University Press: Oxford, 2006.
69. Forment-Aliaga, A.; Coronado, E.; Feliz, M.; Gaita-Ariño, A.; Llusar, R.; Romero, F. M. *Inorg. Chem.* **2003**, *42*, 8019–8027.
70. (a) Wu, Q.; Li, Y.-G.; Wang, Y.-H.; Wang, E.-B.; Zhang, Z.-M.; Clérac, R. *Inorg. Chem.* **2009**, *48*, 1606–1612; (b) Fang, X.; McCallum, K.; Pratt, H. D., III; Anderson, T. M.; Dennis, K.; Luban, M. *Dalton Trans.* **2012**, *41*, 9867–9870; (c) Al-Oweini, R.; Bassil, B. S.; Friedl, J.; Kottisch, V.; Ibrahim, M.; Asano, M.; Keita, B.; Novitchi, G.; Lan, Y.; Powell, A.; Stimming, U.; Kortz, U. *Inorg. Chem.* **2014**, *53*, 5663–5673.
71. Fang, X.; Speldrich, M.; Schilder, H.; Cao, R.; O'Halloran, K. P.; Hill, C. L.; Kögerler, P. *Chem. Commun.* **2010**, *46*, 2760–2762.
72. (a) Andres, H.; Basler, R.; Güdel, H.-U.; Aromí, G.; Christou, G.; Büttner, H.; Rufflé, B. *J. Am. Chem. Soc.* **2000**, *122*, 12469–12477; (b) Aromí, G.; Brechin, E. K. *Struct. Bonding* **2006**, *122*, 1–67.
73. Aubin, S. M. J.; Wemple, M. W.; Adams, D. M.; Tsai, H.-L.; Christou, G.; Hendrickson, D. N. *J. Am. Chem. Soc.* **1996**, *118*, 7746–7754.
74. Fang, X.; Kögerler, P.; Speldrich, M.; Schilder, H.; Luban, M. *Chem. Commun.* **2012**, *48*, 1218–1220.
75. Messiah, A. *Quantum Mechanics*, Vol. 2; Dover Publications: Mineola, 1999. chapter 20.
76. See e.g. (a) Scullion, R. A.; Surman, A. J.; Xu, F.; Mathieson, J. S.; Long, D.-L.; Haso, F.; Liu, T.; Cronin, L. *Angew. Chem. Int. Ed. Engl.* **2014**, *53*, 10032–10037. (b) Izarova, N. V.; Lin, Z.; Yang, P.; Kondinski, A.; Vankova, N.; Heine, T.; Kortz, U. *Dalton Trans.* **2016**, *45*, 2394–2398.
77. Mal, S. S.; Dickman, M. H.; Kortz, U.; Todea, A. M.; Merca, A.; Bögge, H.; Glaser, T.; Müller, A.; Nelluta, S.; Kaur, N.; van Tol, J.; Dalal, N. S.; Keita, B.; Nadjo, L. *Chem. Eur. J.* **2008**, *14*, 1186–1195.
78. Fang, X.; Kögerler, P.; Furukawa, Y.; Speldrich, M.; Luban, M. *Angew. Chem. Int. Ed. Engl.* **2011**, *50*, 5212–5216.
79. Izarova, N. V.; Santiago-Schübel, B.; Willbold, S.; Heß, V.; Kögerler, P. *Chem. Eur. J.* **2016**, *22*, 16052–16056.
80. Sun, S. *Adv. Mater.* **2006**, *18*, 393–403.
81. Takabatake, T.; Ishikawa, M.; Junod, A. *J. Phys. Soc. Jpn.* **1988**, *57*, 2763–2767.
82. Seemann, K. M.; Bauer, A.; Kindervater, J.; Meyer, M.; Besson, C.; Luysberg, M.; Durkin, P.; Pyckhout-Hintzen, W.; Budisa, N.; Georgii, R.; Schneider, C. M.; Kögerler, P. *Nanoscale* **2013**, *5*, 2511–2519.

83. Fleming, C.; Long, D.-L.; McMillan, N.; Johnston, J.; Bovet, N.; Dhanak, V.; Gadegaard, N.; Kögerler, P.; Cronin, L.; Kadodwala, M. *Nat. Nanotechnol.* **2008**, *3*, 233–289.
84. Ielmini, D., Waser, R., Eds. *Resistive Switching*; Wiley-VCH: Weinheim, 2016.
85. Pagnia, H.; Sotnik, N. *Phys. Status Solidi A* **1988**, *108*, 11–65.
86. Waser, R.; Aono, M. *Nat. Mater.* **2007**, *6*, 833–840.
87. Waser, R.; Dittmann, R.; Staikov, G.; Szot, K. *Adv. Mater.* **2009**, *21*, 2632–2663.
88. (a) Daniel, C.; Hartl, H. J. *Am. Chem. Soc.* **2009**, *131*, 5101–5114; (b) Keene, T. D.; D’Alessandro, D. M.; Krämer, K. W.; Price, J. R.; Price, D. J.; Decurtins, S.; Kepert, C. J. *Inorg. Chem.* **2012**, *51*, 9192–9199.
89. Berkowitz, J.; Chupka, W. A.; Inghram, M. G. *J. Chem. Phys.* **1957**, *27*, 87–90.
90. Azens, A.; Kitenbergs, M.; Kanders, U. *Vacuum* **1995**, *46*, 745–747.
91. Huang, X.; Zhai, H.-J.; Li, J.; Wang, L.-S. *J. Phys. Chem. A* **2006**, *110*, 85–92.
92. Koffyberg, F. P.; Dwight, K.; Wold, A. *Solid State Commun.* **1979**, *30*, 433–437.
93. Huang, X.; Zhai, H.-J.; Kiran, B.; Wang, L.-S. *Angew. Chem. Int. Ed. Engl.* **2005**, *44*, 7251–7254.
94. R. Waser et al., Unpublished results.
95. Calzado, C. J.; Clemente-Juan, J. M.; Coronado, E.; Gaita-Arino, A.; Suaud, N. *Inorg. Chem.* **2008**, *47*, 5889–5901.
96. Monakhov, K. Y.; Bensch, W.; Kögerler, P. *Chem. Soc. Rev.* **2015**, *44*, 8443–8483.
97. Monakhov, K. Y.; Linnenberg, O.; Kozłowski, P.; van Leusen, J.; Besson, C.; Secker, T.; Ellem, A.; López, X.; Poblet, J. M.; Kögerler, P. *Chem. Eur. J.* **2015**, *21*, 2387–2397.
98. Waser, R., Ed. *Nanoelectronics and Information Technology*, 3rd ed.; Wiley-VCH: Weinheim, 2012.



# Nonaqueous Polyoxometalate Synthesis for Systematic Studies of Hydrolysis, Protonation, and Reduction

R.J. Errington<sup>1</sup>

School of Chemistry, Newcastle University, Newcastle upon Tyne, United Kingdom

<sup>1</sup>Corresponding author: e-mail address: John.Errington@newcastle.ac.uk

## Contents

1. Introduction	288
2. Synthesis of Lindqvist-Type Heterometalates	289
2.1 A Ditungsten-Substituted <i>cis</i> -{Ti <sub>2</sub> W <sub>4</sub> } Derivative	289
2.2 Tin-Substituted {SnW <sub>5</sub> } Derivatives	291
2.3 Cobalt-Substituted {CoW <sub>5</sub> } Derivatives	294
2.4 The Hydrolytic Assembly Process	298
3. Synthesis of Keggin-Type Heterometalates	299
3.1 Titanium(IV)- and Tin(IV)-Substituted {MPW <sub>11</sub> } Derivatives	301
3.2 Tin(II)- and Lead(II)-Substituted {MPW <sub>11</sub> } Derivatives	303
3.3 A Platinum(IV)-Substituted {PtSiW <sub>11</sub> } Anion	303
4. Protonolysis of M–OR Bonds and Condensation	303
4.1 Hydrolysis of {(MeO)MW <sub>5</sub> } Lindqvist Anions	305
4.2 Hydrolysis of {(MeO)MPW <sub>11</sub> } Keggin Anions	309
4.3 Alcohol Interchange	310
4.4 Alkoxido Metathesis	311
4.5 Theoretical Studies	313
5. Synthesis and Reactivity of Chlorido {ClMW <sub>5</sub> } Lindqvist Anions	315
6. Studies of {MW <sub>5</sub> } Lindqvist Anion Protonation	319
6.1 Protonation of (TBA) <sub>3</sub> [(MeO)TiW <sub>5</sub> O <sub>18</sub> ]	319
6.2 Protonation of (TBA) <sub>3</sub> [(HO)SnW <sub>5</sub> O <sub>18</sub> ]	320
6.3 Protonation of (TBA) <sub>6</sub> [( $\mu$ -O)(TiW <sub>5</sub> O <sub>18</sub> ) <sub>2</sub> ]	322
6.4 Protonation Arising From the Reaction Between (TBA) <sub>3</sub> [(MeO)TiW <sub>5</sub> O <sub>18</sub> ] and H <sub>2</sub> O <sub>2</sub>	323
7. Ligand Behavior of [( $\mu$ -O)(TiW <sub>5</sub> O <sub>18</sub> ) <sub>2</sub> ] <sup>6-</sup>	324
8. Reductive Transformations	327
9. Summary	332
Acknowledgments	333
References	333

## Abstract

Dynamic aspects of polyoxometalate chemistry are often overlooked because of difficulties in monitoring subtle structural and/or speciation changes in solution. This chapter features the nonaqueous approaches to polyoxometalate synthesis being developed in our laboratory as a platform for detailed and systematic reactivity studies. Methods based on metal alkoxide hydrolysis are described that provide access to a range of substituted  $\{M_2W_4\}$  and  $\{MW_5\}$  Lindqvist-type polyoxometalates containing reactive  $\{MX\}^{n+}$  heterometal sites, and examples are given that highlight the importance of  $^{17}\text{O}$  NMR as a tool for monitoring solution reactivity. Lindqvist-type  $\{\text{XTiW}_5\}$  and  $\{\text{XSnW}_5\}$  and related Keggin-type  $\{\text{XMPW}_{11}\}$  anions are compared, and significant differences in their hydrolysis and condensation behaviors are discussed in relation to DFT studies. The solution reactivity observed upon halide abstraction from  $\{\text{ClTiW}_5\}$  or protonation of  $\{\text{(RO)TiW}_5\}$  species is rationalized in terms of a common difunctional reactive intermediate  $[\text{TiW}_5\text{O}_{18}]^{2-}$ , which has been characterized in its dimeric form. Following the identification of diprotonated  $[(\mu\text{-O})(\text{TiW}_5\text{O}_{18}\text{H})_2]^{4-}$  a new type of polyoxometalate ligand behavior is proposed, based on the characterization of  $[(\mu\text{-O})(\text{TiW}_5\text{O}_{18})_2(\text{SnMe}_2)]^{4-}$ ,  $^{17}\text{O}$  NMR studies of reactions with electrophiles, and DFT studies of  $[(\mu\text{-O})(\text{TiW}_5\text{O}_{18})_2(\text{AuCl})]^{4-}$ . The final section describes nonaqueous reductive aggregation reactions of  $(\text{TBA})_3[\text{PMo}_{12}\text{O}_{40}]$  that have produced a family of electron-rich anions of the type  $\alpha\text{-[PMo}_{12}\text{O}_{40}(\text{ML}_n)_2]^{x-}$ , and the reductive degradation of  $(\text{TBA})_2[\text{Mo}_6\text{O}_{19}]$  to give the tetra-capped  $\epsilon\text{-[Mo}_{13}\text{O}_{40}\text{H}_4\{\text{Mg}(\text{DMSO})_3\}_4]^{2+}$ .

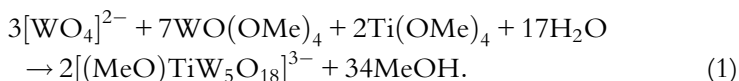


## 1. INTRODUCTION

Despite their comparatively simple compositions (in many cases only metal and oxygen atoms), the spontaneous assembly from simple starting materials of polyoxometalates with structures ranging from the reassuringly symmetric Lindqvist-type hexametalates  $[\text{M}_6\text{O}_{19}]^{n-}$  to giant rings and spheres has fascinated chemists for many years (1). Given their rich variety of properties and their similarity to fragments of extended metal oxide structures, it is easy to appreciate why this is a fertile area of chemistry and materials science (2).

A new era for POM chemistry emerged with the use of organic solvents for their synthesis and subsequent reactivity studies (3). This led to the establishment of  $^{17}\text{O}$  NMR as a powerful technique for POM characterization, despite the low natural abundance (0.0373%) of this nucleus (4), bringing detailed studies of solution reactivity within reach for  $^{17}\text{O}$ -enriched compounds. Organic solubility may be achieved by suitable choice of cation, most commonly tetra-alkyl ammonium, and the simplest approach has generally been to precipitate preformed POMs from aqueous solution by

addition of a tetra-alkyl ammonium salt. In an alternative approach, Jahr and Fuchs demonstrated that POMs can be synthesized in organic solvents by taking advantage of the hydrolytic sensitivity of metal alkoxides, and obtained  $(\text{TBA})_2[\text{W}_6\text{O}_{19}]$  by alkaline hydrolysis of  $\text{WO}(\text{OMe})_4$  (5). We adapted this approach to prepare mixed-metal Lindqvist derivatives containing terminal alkoxido ligands  $[(\text{RO})\text{M}'\text{M}_5\text{O}_{18}]^{n-}$ , thereby introducing metal sites that are more reactive than the  $\text{M}=\text{O}$  centers of the parent isopolymetalates (6). For example, the titanium-substituted tungstate  $(\text{TBA})_3[(\text{MeO})\text{TiW}_5\text{O}_{18}]$  was obtained from  $(\text{TBA})_2\text{WO}_4$ ,  $\text{WO}(\text{OMe})_4$ , and  $\text{Ti}(\text{OMe})_4$  by the reaction shown in Eq. (1), and subsequent substitution of the alkoxido ligands provided systematic access to a wide range of hybrid POMs (7)



An important feature of this approach is that  $^{17}\text{O}$ -enriched POMs can be synthesized using the minimum amount of  $^{17}\text{O}$ -enriched water, which reduces the expense of routine  $^{17}\text{O}$  NMR spectroscopy for detailed solution reactivity studies.

Reliable methods for POM synthesis coupled with a detailed understanding of electronic properties and chemical reactivity are fundamental requirements for advances in POM-based catalysis and advanced materials based on POM functional components. This chapter describes recent work in our laboratory on platform development for rational POM synthesis and manipulation, specifically for the elaboration of Lindqvist- and Keggin-type structural families, and includes insights gained from  $^{17}\text{O}$  NMR spectroscopic studies of proton-transfer reactions and recent successes in the targeted synthesis of electron-rich POMs by chemical reduction.

## 2. SYNTHESIS OF LINDQVIST-TYPE HETEROMETALATES

### 2.1 A Ditungsten-Substituted *cis*- $\{\text{Ti}_2\text{W}_4\}$ Derivative

By adjusting the relative amounts of titanium and tungsten precursors from those in Eq. (1) to those in Eq. (2) we were able to obtain the first ditungsten-substituted hexametalate  $(\text{TBA})_3[(\text{MeO})_3\text{Ti}_2\text{W}_4\text{O}_{16}]$  from its constituent metal alkoxides (8). A single-crystal X-ray structure determination showed the anion to have two terminal methoxido ligands and one bridging the two titanium atoms (Fig. 1), which was consistent with the

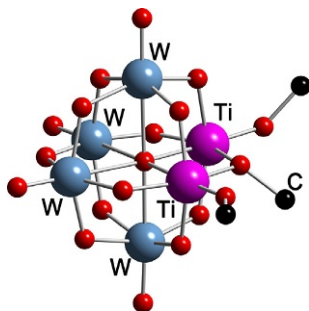


Fig. 1 Structure of the anion  $[(\text{MeO})_3\text{Ti}_2\text{W}_4\text{O}_{16}]^{3-}$ .

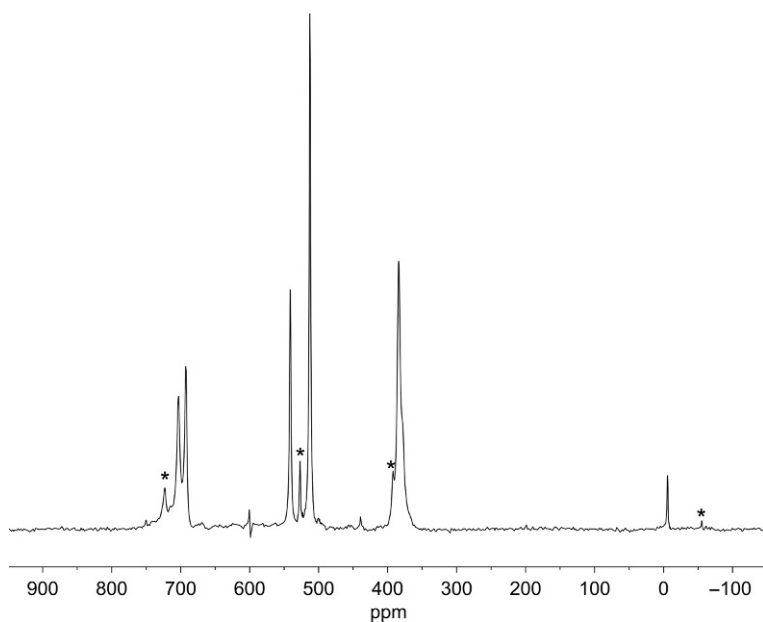
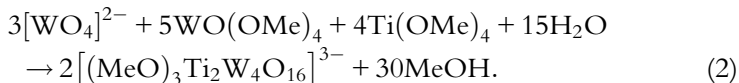


Fig. 2  $^{17}\text{O}$  NMR spectrum of  $(\text{TBA})_3[(\text{MeO})_3\text{Ti}_2\text{W}_4\text{O}_{16}]$ . Peaks marked with an *asterisk* are due to  $(\text{TBA})_3[(\text{MeO})\text{TiW}_5\text{O}_{18}]$ .

presence of OMe peaks in the  $^1\text{H}$  NMR spectrum at 4.09 ppm for the terminal TiOMe groups and 3.80 ppm for  $\text{Ti}(\mu\text{-OMe})\text{Ti}$ . The  $^{17}\text{O}$  NMR spectrum corresponded to a  $C_{2v}$  metal oxide framework, with two peaks for  $\text{W}=\text{O}$ , two peaks for  $\text{TiOW}$ , a single peak with a shoulder for  $\text{WOW}$ , and one peak for the central oxygen. The expected intensities for this structure are 2:2 ( $\text{W}=\text{O}$ ), 2:4 ( $\text{TiOW}$ ), 4:1 ( $\text{WOW}$ ), and 1 ( $\mu_6\text{-O}$ ). The minor impurity peaks in the spectrum shown in Fig. 2 can be assigned to the mono-substituted anion  $[(\text{MeO})\text{TiW}_5\text{O}_{18}]^{3-}$ . It is worth noting that this  $\{\text{Ti}_2\text{W}_4\}$



POM was initially obtained from a reaction with a different stoichiometry that was intended to produce the anion  $[(\text{MeO})_2\text{Ti}_2\text{W}_4\text{O}_{17}]^{4-}$  with two terminal  $\text{Ti}(\text{OMe})$  groups, which would seem to indicate that the  $\text{TiOTi}$  bridging oxygen in this putative anion is strongly basic and the bridging methoxido ligand is preferred in the presence of methanol. This is not unexpected in the light of previous  $^{17}\text{O}$  NMR studies of *cis*- $[\text{V}_2\text{W}_4\text{O}_{19}]^{4-}$  acidification, which established that the bridging VOV was protonated (9)



## 2.2 Tin-Substituted $\{\text{SnW}_5\}$ Derivatives

In order to explore the effects of substituting the transition metal heteroatom in the  $\{\text{TiW}_5\}$  Lindqvist anions for a main group metal, we extended our alkoxide-based hydrolytic approach to the synthesis of Lindqvist-type  $(\text{TBA})_3[(\text{MeO})\text{SnW}_5\text{O}_{18}]$  (10). The reaction between  $(\text{TBA})_2\text{WO}_4$  and  $\text{Sn}(\text{O}^i\text{Bu})_4$  in dry acetonitrile gave a complex mixture of oxoalkoxido species, which simplified upon addition of  $\text{WO}(\text{OMe})_4$ . Stoichiometric hydrolysis of this mixture according to Eq. (3), followed by a final treatment with an excess of methanol to ensure complete exchange of alkoxido ligands, gave a high yield of the desired methoxido species. In the crystal structure, the  $\text{SnOMe}$  group was disordered over two *trans* sites, but the anion was fully characterized by  $^1\text{H}$ ,  $^{13}\text{C}$ ,  $^{17}\text{O}$ ,  $^{119}\text{Sn}$ , and  $^{183}\text{W}$  NMR spectroscopy. Satellite peaks for the  $\text{SnOMe}$  resonance at 3.64 ppm in the  $^1\text{H}$  NMR spectrum gave  $^3J$  couplings to  $^{119}\text{Sn}$ ,  $^{117}\text{Sn}$ , and  $^{115}\text{Sn}$  of 77, 72, and 66 Hz, respectively, while satellite peaks associated with the  $\text{OMe}$  resonance at 53 ppm in the  $^{13}\text{C}\{^1\text{H}\}$  NMR spectrum showed  $^2J(^{119}\text{Sn}^{13}\text{C})$  of 35 Hz. In the  $^{17}\text{O}$  NMR spectrum (Fig. 3) the peak at 395 ppm was assigned to  $\text{SnOW}$ , which is significantly upfield of the analogous  $\text{TiOW}$  peak for  $[(\text{MeO})\text{TiW}_5\text{O}_{18}]^{3-}$  at 525 ppm. In the  $^{119}\text{Sn}\{^1\text{H}\}$  NMR spectrum, the peak for  $[(\text{MeO})\text{SnW}_5\text{O}_{18}]^{3-}$  was observed at  $-647$  ppm, and  $^2J(^{119}\text{Sn}^{183}\text{W})$  couplings of 38 and 12 Hz to equatorial and axial tungstens, respectively, were resolved in a  $^{119}\text{Sn}\{^1\text{H}\}$  NMR spectrum obtained from a  $^{119}\text{Sn}$  INEPT experiment (Fig. 4). The  $^{183}\text{W}$  NMR spectrum of this anion is remarkably different from that of  $[(\text{MeO})\text{TiW}_5\text{O}_{18}]^{3-}$ , with resonances at 77 ppm for  $W_{\text{eq}}$  and  $-128$  ppm for  $W_{\text{ax}}$  compared to the analogous  $\{\text{TiW}_5\}$  peaks at 32 and 65 ppm, respectively. A reversible one-electron reduction was observed at  $-1.84$  V vs  $\text{Ag}/\text{AgCl}$  in the cyclic voltammogram of

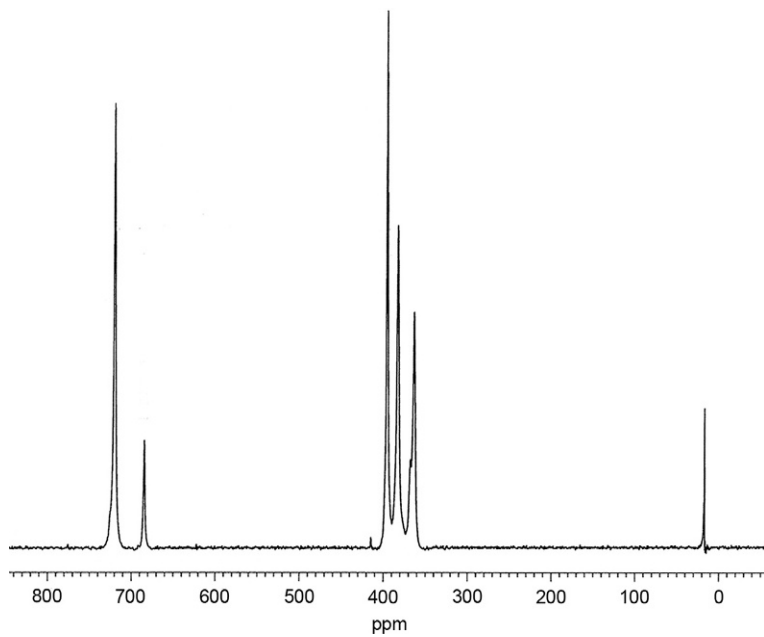


Fig. 3  $^{17}\text{O}$  NMR spectrum of  $(\text{TBA})_3[(\text{MeO})\text{SnW}_5\text{O}_{18}]$ .

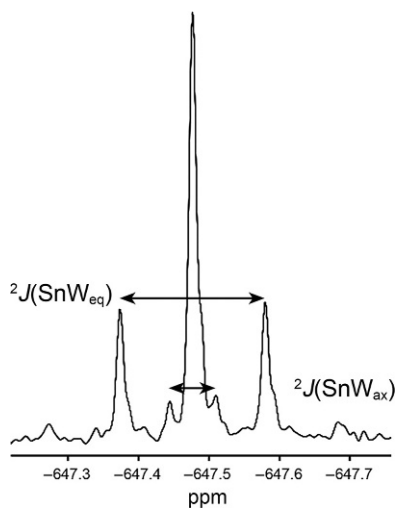
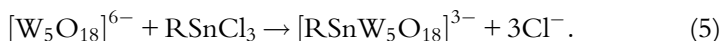
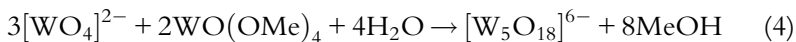
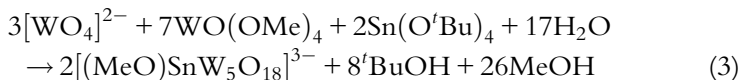


Fig. 4  $^{119}\text{Sn}$  INEPT NMR spectrum of  $(\text{TBA})_3[(\text{MeO})\text{SnW}_5\text{O}_{18}]$ .

(TBA)<sub>3</sub>[(MeO)SnW<sub>5</sub>O<sub>18</sub>], which is more negative than the second reversible wave for (TBA)<sub>2</sub>[W<sub>6</sub>O<sub>19</sub>] in MeCN, i.e., [W<sub>6</sub>O<sub>19</sub>]<sup>3-</sup>/[W<sub>6</sub>O<sub>19</sub>]<sup>4-</sup>, which we observed at -1.64 V



A modified hydrolytic approach was adopted for the synthesis of alkyltin Lindqvist derivatives, based on our attempts to synthesize the lacunary species [W<sub>5</sub>O<sub>18</sub>]<sup>6-</sup> from (TBA)<sub>2</sub>WO<sub>4</sub> and WO(OMe)<sub>4</sub> by the reaction shown in Eq. (4). Our strategy was to generate this pentadentate lacunary POM ligand and then insert {LM}<sup>n+</sup> moieties by treatment with labile precursors LMX<sub>n</sub> (11). Although the {W<sub>5</sub>} lacunary species could not be identified in spectroscopic studies of the product from the hydrolytic reaction in Eq. (4), when this was treated with RSnCl<sub>3</sub> we obtained high yields of the organo-tin species (TBA)<sub>3</sub>[RSnW<sub>5</sub>O<sub>18</sub>] (R = Me, Ph, and 4-IC<sub>6</sub>H<sub>4</sub>) (Eq. 5) (12). We were able to obtain crystal structures for (TBA)<sub>3</sub>[PhSnW<sub>5</sub>O<sub>18</sub>] and (TBA)<sub>3</sub>[(4-IC<sub>6</sub>H<sub>4</sub>)SnW<sub>5</sub>O<sub>18</sub>], and the anion in the latter compound is shown in Fig. 5. The incorporation of an iodophenyl group provides a reactive site for further organic functionalization via Sonogashira coupling, as demonstrated by Proust and coworkers for related tin-substituted Keggin anions (13). <sup>1</sup>H, <sup>17</sup>O, <sup>119</sup>Sn, and <sup>183</sup>W NMR spectra

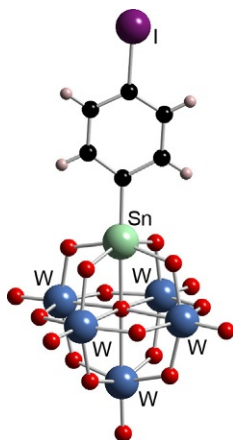


Fig. 5 Structure of the anion [(4-IC<sub>6</sub>H<sub>4</sub>)SnW<sub>5</sub>O<sub>18</sub>]<sup>3-</sup>.

for  $(\text{TBA})_3[\text{MeSnW}_5\text{O}_{18}]$  are shown in Fig. 6, and NMR data for all three organo-tin compounds are compared with those of the alkoxido anions and their derivatives in Table 1. A previous brief report of  $(\text{TBA})_3[\text{PhSnW}_5\text{O}_{18}]$ , obtained by acidification of  $(\text{TBA})_2\text{WO}_4$  in the presence of  $\text{PhSnCl}_3$ , included a picture of the anion structure and mentioned the  $^{17}\text{O}$  NMR spectrum but no data were given (14), while the product obtained from a reaction between  $\text{K}_9[\text{Ce}(\text{W}_5\text{O}_{18})_2]$  and  $\text{MeSnCl}_3$  that was proposed to be  $(\text{TBA})_3[\text{MeSnW}_5\text{O}_{18}]$  showed peaks at  $-20.3$  ppm for  $W_{\text{eq}}$  and  $-16.0$  ppm for  $W_{\text{ax}}$  in its  $^{183}\text{W}$  NMR spectrum, which are markedly different from the chemical shifts of 58 ppm for  $W_{\text{eq}}$  and  $-155$  ppm for  $W_{\text{ax}}$  that we observed for this methyltin anion (15).

A characteristic feature in the  $^{183}\text{W}$  NMR spectra of all of the  $\{\text{SnW}_5\}$  Lindqvist anions is the large difference between the chemical shifts for  $W_{\text{eq}}$  and  $W_{\text{ax}}$  and the large upfield shifts for  $W_{\text{ax}}$  in comparison to the group 4 transition metal analogs. DFT calculations of  $^{183}\text{W}$  NMR chemical shifts and  $^2J(^{119}\text{Sn}^{183}\text{W})$  coupling constants for  $[(\text{MeO})\text{SnW}_5\text{O}_{18}]^{3-}$  were carried out by the group of Poblet at IRV Tarragona to investigate this feature (16). Calculations for two conformations of the anion with  $C_s$  symmetry and  $\text{OSnOC}$  torsion angles of either 0 degree (eclipsed) or 60 degree (staggered) to simulate rotation of the  $\text{CH}_3$  group around the  $\text{Sn}-\text{O}$  bond gave the values shown in Table 2. Although the absolute errors in the prediction of the shifts are not negligible ( $-88$  vs  $-128$  ppm for  $W_{\text{ax}}$  and 105 vs 70 ppm for the  $W_{\text{eq}}$ ), the experimentally observed trend in chemical shifts is reproduced well and, moreover, the large separation between the two predicted peaks (193 ppm) is close to the experimental value (205 ppm). Calculations showed that the large negative chemical shift observed for  $W_{\text{ax}}$  ( $-128$  ppm) has an electronic origin, and the  $^{183}\text{W}$  NMR chemical shifts computed for the Ti analog were +80 ppm ( $W_{\text{ax}}$ ) and +61 ppm ( $W_{\text{eq}}$ ), which are close to the observed shifts of +65 and +32 ppm, respectively. With regard to the coupling constants, the average magnitudes of  $^2J(^{119}\text{Sn}^{183}\text{W})$  for the two conformers also provide very good estimates of the experimental values, i.e., 9.3 vs 12 Hz for  $^2J(^{119}\text{Sn}^{183}\text{W}_{\text{ax}})$  and 39.7 vs 38 Hz for  $^2J(^{119}\text{Sn}^{183}\text{W}_{\text{eq}})$ .

### 2.3 Cobalt-Substituted $\{\text{CoW}_5\}$ Derivatives

The “virtual” pentatungstate precursor described above was also used to prepare the first  $\{\text{CoW}_5\}$  Lindqvist-type heterometalates by treatment of this material with  $\text{Co}^{2+}$  precursors (17). Addition of  $[\text{Co}(\text{MeCN})_4(\text{H}_2\text{O})_2](\text{BF}_4)_2$  or  $\text{CoCl}_2$  to the hydrolysis product from Eq. (4) did not give the

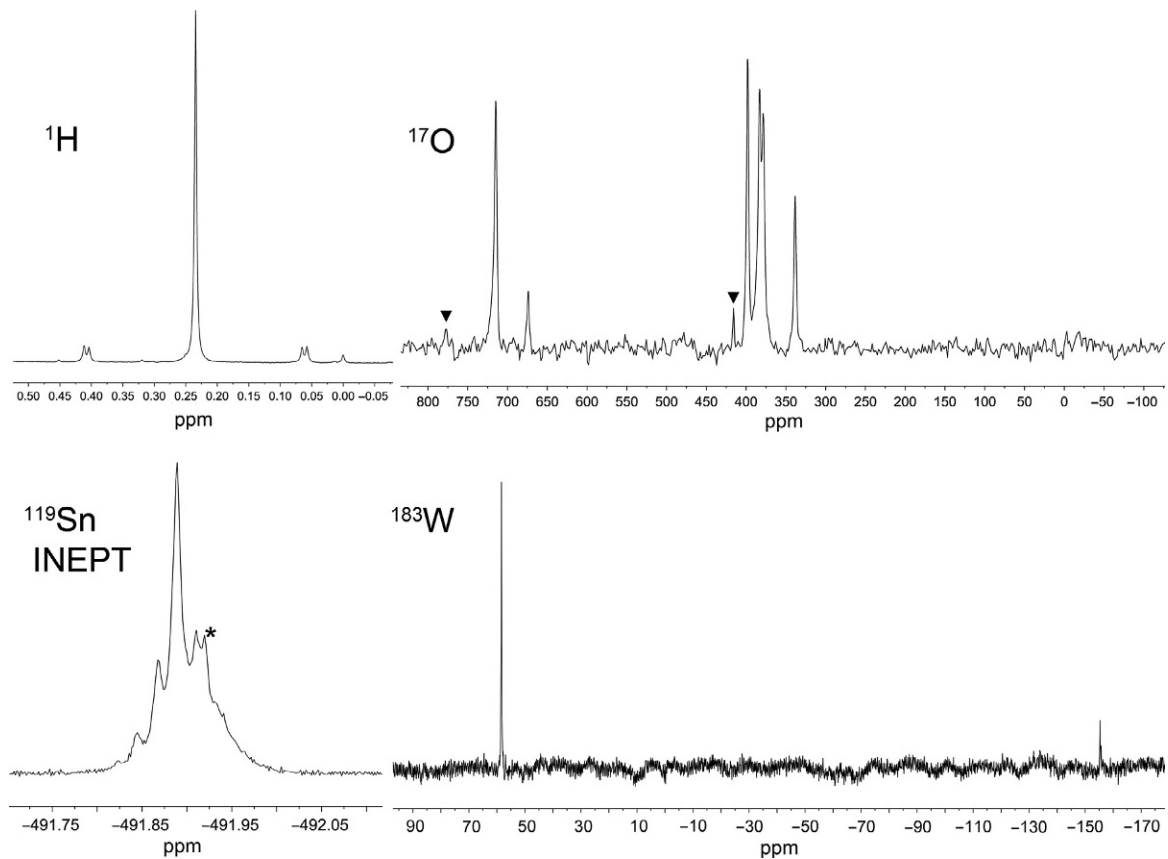


**Fig. 6**  $^1\text{H}$ ,  $^{17}\text{O}$ ,  $^{119}\text{Sn}$ , and  $^{183}\text{W}$  NMR spectra of  $(\text{TBA})_3[\text{MeSnW}_5\text{O}_{18}]$ . Peaks in the  $^{17}\text{O}$  NMR spectrum marked with  $\blacktriangledown$  are due to  $[\text{W}_6\text{O}_{19}]^{2-}$  and the peak marked with an *asterisk* in the  $^{119}\text{Sn}$  NMR spectrum is due to an uncharacterized tin impurity.

**Table 1**  $^{119}\text{Sn}$ ,  $^{183}\text{W}$ , and  $^{17}\text{O}$  NMR Data for  $\{\text{SnW}_5\}$  Lindqvist-Type Anions<sup>a</sup>

Anion	$^{119}\text{Sn}$ Chemical Shift/ppm	$^{183}\text{W}$ Chemical Shift/ppm		$^{17}\text{O}$ Chemical Shift/ppm			
	( $^2J\{^{119}\text{Sn}^{183}\text{W}_{\text{eq}}\}/\text{Hz}$ )	$W_{\text{eq}}$	$W_{\text{ax}}$	$W=\text{O}$	$\text{SnOW}$	$\text{WOW}$	$\mu_6\text{-O}$
$[(\text{HO})\text{SnW}_5\text{O}_{18}]^{3-}$	−633 (37.4)	72.2	−121.2	719, 683	395	382, 367	17
$[(\text{MeO})\text{SnW}_5\text{O}_{18}]^{3-}$	−647 (38.4)	76.9	−128.1	720, 684	395	383, 363	17
$[(\text{EtO})\text{SnW}_5\text{O}_{18}]^{3-}$	−651 (39.8)	74.7	−129.6	725, 684	395	382, 365	17
$[(^i\text{PrO})\text{SnW}_5\text{O}_{18}]^{3-}$	−654 (29.9)	74.5	−128.3	726, 684	396	383, 367	18
$[(^t\text{BuO})\text{SnW}_5\text{O}_{18}]^{3-}$	−663 (40.3)	71.8	−126.7	725, 683	396	382, 368	18
$[(\text{C}_6\text{H}_5\text{O})\text{SnW}_5\text{O}_{18}]^{3-}$	−673 (45.6)	77.4	−124.1	723, 689	397	385, 361	16
$[(4\text{-MeC}_6\text{H}_4\text{O})\text{SnW}_5\text{O}_{18}]^{3-}$	−674 (47.5)	78.9	−122.8	722, 688	396	385, 361	16
$(4\text{-}^t\text{BuC}_6\text{H}_4\text{O})\text{SnW}_5\text{O}_{18}]^{3-}$	−673 (45.6)	76.7	−121.6	723, 689	396	386, 362	17
$[(4\text{-HOC}_6\text{H}_4\text{O})\text{SnW}_5\text{O}_{18}]^{3-}$	−674 (51.2)	76.4	−122.8	723, 689	398	386, 363	17
$[\{2\text{-(CHO)C}_6\text{H}_4\text{O}\}\text{SnW}_5\text{O}_{18}]^{3-}$	−672 (48.9)	79.1	−120.6	725, 691	399	387, 365	15
$[\text{MeSnW}_5\text{O}_{18}]^{3-}$	−492 (7.5)	58.4	−155.0	713, 669	397	383, 378	<sup>b</sup>
$[(\text{C}_6\text{H}_5)\text{SnW}_5\text{O}_{18}]^{3-}$	−572 <sup>b</sup>	66.2	−153.9	716, 675	398	379, 376	20
$[(4\text{-IC}_6\text{H}_4)\text{SnW}_5\text{O}_{18}]^{3-}$	−566 <sup>b</sup>	<sup>c</sup>	<sup>c</sup>	717, 677	398	380, 374	<sup>b</sup>

<sup>a</sup>As  $^t\text{Bu}_4\text{N}^+$  salts.

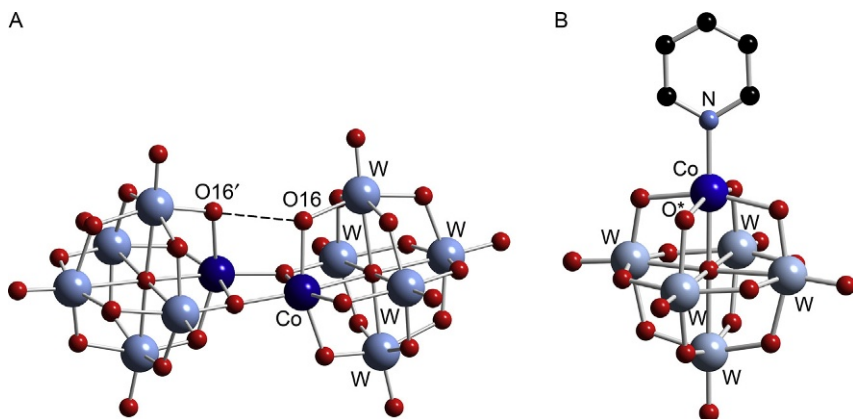
<sup>b</sup>Not observed.

<sup>c</sup>Not measured.

**Table 2** Calculated NMR Parameters for  $[(\text{MeO})\text{TiW}_5\text{O}_{18}]^{3-}$  and  $[(\text{MeO})\text{SnW}_5\text{O}_{18}]^{3-a}$   
 $[(\text{MeO})\text{SnW}_5\text{O}_{18}]^{3-}$   $[(\text{MeO})\text{TiW}_5\text{O}_{18}]^{3-}$ 

	Calculated	Experimental	Calculated	Experimental
$\delta(\text{W}_{\text{eq}})/\text{ppm}$	104.1	76.9	61	32
$\delta(\text{W}_{\text{ax}})/\text{ppm}$	-90.5	-128.1	80	65
$ \Delta\delta\text{W} /\text{ppm}$	195	205	19	33
${}^2J(^{119}\text{Sn}^{183}\text{W}_{\text{eq}})/\text{Hz}$	-38.9	38	—	—
${}^2J(^{119}\text{Sn}^{183}\text{W}_{\text{ax}})/\text{Hz}$	-9.0	12	—	—

<sup>a</sup>DFT calculations were performed with the ADF2009 package (ADF 2009.01. Department of Theoretical Chemistry, Vrije Universiteit, Amsterdam).


**Fig. 7** Structures of the anions (A)  $[\text{Co}(\text{W}_5\text{O}_{18}\text{H})_2]^{6-}$  and (B)  $[(\text{py})\text{CoW}_5\text{O}_{18}\text{H}]^{3-}$ .

expected solvated monomeric anion  $[(\text{MeCN})\text{CoW}_5\text{O}_{18}]^{4-}$  but rather the protonated dimer  $[(\text{CoW}_5\text{O}_{18}\text{H})_2]^{6-}$  with the structure shown in Fig. 7A. The protons associated with the anion were not located directly, but the short distance between O16 and O16' (2.735 Å) suggested a hydrogen-bonded O–H–O interaction, while the other proton is disordered over the other CoOW bridging atoms. Further support for the protonated formulation was obtained from the crystal structure of the monomeric adduct  $[(\text{py})\text{CoW}_5\text{O}_{18}\text{H}]^{3-}$  which was obtained by treatment of the dimer with pyridine (Fig. 7B). In this case, the longer W–O\*(Co) distance of 2.000(9) Å and a bond valence sum of 1.13 for O\* (averages for the three independent anions in the crystal structure) clearly indicated localized protonation at a single CoOW site, reflecting the strongly basic nature of these oxygens in the  $[(\text{L})\text{CoW}_5\text{O}_{18}]^{4-}$  anion.

It is worth noting that on some occasions when using the reaction in Eq. (4) we observed hydrolysis of the MeCN solvent and in several cases crystals of  $\text{CH}_3\text{C}(\text{O})\text{NH}_2 \cdot (\text{TBA})\text{Cl}$  were isolated upon attempted preparation of  $(\text{TBA})_4[\text{M}^{\text{II}}\text{W}_5\text{O}_{18}]$  first-row transition metal derivatives from the metal chlorides. In one instance, a reaction with  $\text{CoCl}_2$  produced the acetamide adduct  $(\text{TBA})_3[\{\text{CH}_3\text{C}(\text{O})\text{NH}_2\}\text{CoW}_5\text{O}_{17}(\text{OMe})]$ , and the X-ray crystal structure showed the acetamide ligand in the anion to be hydrogen-bonded to a CoOW bridging oxygen (Fig. 8), while the presence of the bridging methoxido ligand is reminiscent of the protonated CoOW in  $[(\text{py})\text{CoW}_5\text{O}_{18}\text{H}]^{3-}$  and of the bridging  $\text{Ti}(\mu\text{-OMe})\text{Ti}$  in  $[(\text{MeO})_3\text{Ti}_2\text{W}_4\text{O}_{16}]^{3-}$ . These  $\{\text{CoW}_5\}$  structures serve to illustrate the dual functionality of  $[\text{MW}_5\text{O}_{18}]^{n-}$  POMs, which contain a Lewis acidic heterometal site flanked by basic MOW oxygens, a feature which is likely to have implications for the reactivity of these anions. This situation is reminiscent of Lewis acidic, oxide-supported metal sites in heterogeneous catalysts (18).

## 2.4 The Hydrolytic Assembly Process

In an attempt to shed light onto the aggregation processes occurring during these nonaqueous hydrolytic routes to hexametalates, we monitored the simplest tungstate system by  $^{17}\text{O}$  NMR spectroscopy, i.e., the formation of  $[\text{W}_6\text{O}_{19}]^{2-}$  from  $[\text{WO}_4]^{2-}$  and  $\text{WO}(\text{OMe})_4$  via the reaction shown in Eq. (6) (12):

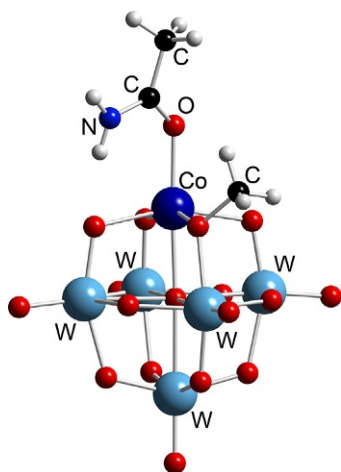
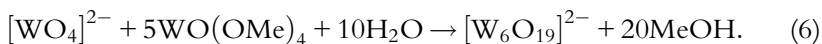


Fig. 8 Structure of the anion  $[\{\text{CH}_3\text{C}(\text{O})\text{NH}_2\}\text{CoW}_5\text{O}_{17}(\text{OMe})]^{3-}$ .



The room temperature  $^{17}\text{O}$  NMR spectrum recorded soon after addition of  $^{17}\text{O}$ -enriched water (Fig. 9A) shows  $\text{W}=\text{O}$  and  $\text{WOW}$  peaks characteristic of  $[\text{W}_6\text{O}_{19}]^{2-}$  at 776 and 415 ppm (the peak for central  $\mu_6\text{-O}$  at  $-78$  ppm is much less intense due to a low level of enrichment at this site) along with broad peaks in the region of 750 and 525 and 400 ppm, which sharpen somewhat after a day (Fig. 9B). Heating to  $60^\circ\text{C}$  has a marked effect (Fig. 9C), and after heating overnight the spectrum is dominated by the peaks for  $[\text{W}_6\text{O}_{19}]^{2-}$  (Fig. 9D). After removal of crystalline  $(\text{TBA})_2[\text{W}_6\text{O}_{19}]$  (Fig. 9E), the spectrum of the mother liquor revealed peaks due to intermediate species that further diminish over several days at room temperature and with subsequent heating to give essentially complete conversion to  $[\text{W}_6\text{O}_{19}]^{2-}$  (Fig. 9F–H). The broad features observed during the initial stages of this reaction are probably associated with oxoalkoxido species resulting from ligand redistribution between  $(\text{TBA})_2[\text{WO}_4]$  and  $\text{WO}(\text{OMe})_4$ , as previously observed for a 1:1 mixture of these compounds (19), and possibly transient hydroxido complexes resulting from their hydrolysis. It is worth noting that the sharper peaks associated with intermediate species do not correspond to any reported values for known isopolytungstates (4,20). This study of POM self-assembly serves to demonstrate the special stability of the hexanuclear Lindqvist structure in nonaqueous solutions, and investigations are now being extended to the  $\{\text{MW}_5\}$  heterometallic systems described above, in which speciation is expected to be more complex, not least because of differential hydrolysis rates for the  $\text{W-OR}$  and  $\text{M-OR}$  bonds.



### 3. SYNTHESIS OF KEGGIN-TYPE HETEROMETALATES

One of the longest-established rational approaches to heterometallic POM synthesis is the treatment of monolacunary  $\{\text{EW}_{11}\}$  Keggin species with suitable labile heterometal compounds. Many substituted derivatives of the type  $[(\text{L})\text{MPW}_{11}\text{O}_{39}]^{n-}$  have been obtained from aqueous reactions of alkali metal salts of  $[\text{PW}_{11}\text{O}_{39}]^{7-}$ , while the organic-soluble  $(\text{TBA})_4[\text{H}_3\text{PW}_{11}\text{O}_{39}]$  has been employed in nonaqueous reactions (21). We previously reported the highly soluble monosodium salt  $(\text{TBA})_6[\text{NaPW}_{11}\text{O}_{39}]$  as a convenient alternative precursor for nonaqueous reactions (11), and we have found this can readily be enriched in  $^{17}\text{O}$  by stirring an acetonitrile solution with  $^{17}\text{O}$ -enriched water, although the less accessible central  $\text{PO}_4$  oxygen atoms are not enriched by this method, as shown by the absence of a resonance at about 60 ppm in the  $^{17}\text{O}$  NMR spectrum (Fig. 10) (22). X-ray crystal

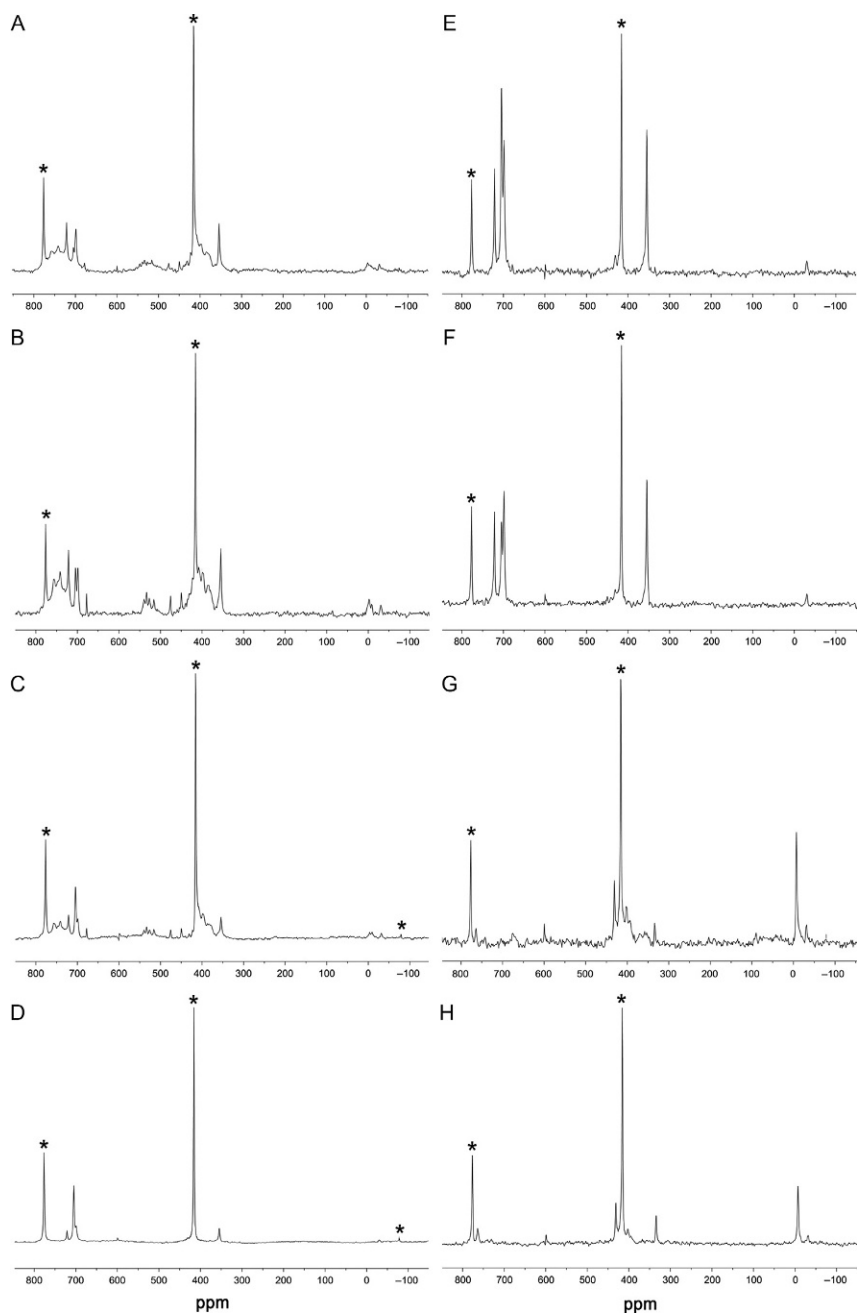


**Fig. 9**  $^{17}\text{O}$  NMR spectra of the hydrolytic reaction shown in Eq. (6): (A) immediately after addition of water; (B) after 1 day; (C) after heating to  $60^\circ\text{C}$ ; (D) after overnight heating at  $60^\circ\text{C}$ ; (E) mother liquor after removal of crystalline  $(\text{TBA})_2[\text{W}_6\text{O}_{19}]$ ; (F) mother liquor after several days at room temperature; (G) mother liquor after heating to  $60^\circ\text{C}$ ; (H) mother liquor after heating overnight at  $60^\circ\text{C}$ . Peaks for  $[\text{W}_6\text{O}_{19}]^{2-}$  are marked with an *asterisk*.

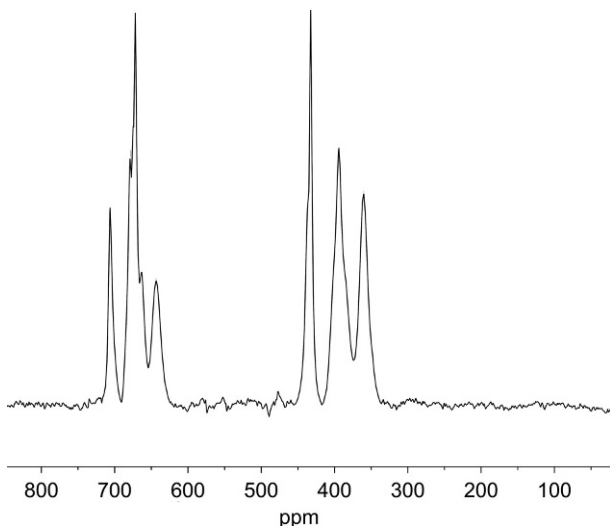


**Fig. 10**  $^{17}\text{O}$  NMR spectrum of  $(\text{TBA})_6[\text{NaPW}_{11}\text{O}_{39}]$ .

structure determinations showed the sodium ion to be bound within the vacant site of the lacunary Keggin anion, although the site was disordered over several metal positions. The peaks for the two nonequivalent NaOW oxygens expected from this structure are barely resolved at 438 and 432 ppm in Fig. 11, although separate peaks are observed when smaller line-broadening values are used during processing. This route to  $^{17}\text{O}$ -enriched  $\{\text{MPW}_{11}\}$  derivatives provides a convenient alternative to the methods described in the pioneering work of Klemperer (4), and some specific applications of this approach are described below.

### 3.1 Titanium(IV)- and Tin(IV)-Substituted $\{\text{MPW}_{11}\}$ Derivatives

The chlorido derivatives  $(\text{TBA})_4[\text{ClTiPW}_{11}\text{O}_{39}]$  and  $(\text{TBA})_4[\text{ClSnPW}_{11}\text{O}_{39}]$  were first prepared by Knoth from  $(\text{TBA})_4[\text{H}_3\text{PW}_{11}\text{O}_{39}]$  (23). We found that  $^{17}\text{O}$ -enriched samples of these compounds could be obtained in quantitative yields from enriched  $(\text{TBA})_6[\text{NaPW}_{11}\text{O}_{39}]$  by treatment with  $\text{TiCl}_4$  or  $\text{SnCl}_4$ , respectively, and subsequent halide exchange reactions with NaOMe afforded  $^{17}\text{O}$ -enriched  $(\text{TBA})_4[(\text{MeO})\text{TiPW}_{11}\text{O}_{39}]$  and  $(\text{TBA})_4[(\text{MeO})\text{SnPW}_{11}\text{O}_{39}]$  for protonolysis studies (see Section 4). The  $^{17}\text{O}$  NMR spectra of the  $\{\text{TiPW}_{11}\}$  compounds contain two distinct TiOW peaks at 585 and 565 ppm ( $\text{X} = \text{Cl}$ ) or 560 and 535 ppm ( $\text{X} = \text{OMe}$ ), while the SnOW peaks in the  $^{17}\text{O}$  NMR spectra of  $\{\text{Sn}^{\text{IV}}\text{PW}_{11}\}$  anions have not been assigned unambiguously, as these peaks are shifted upfield into the region

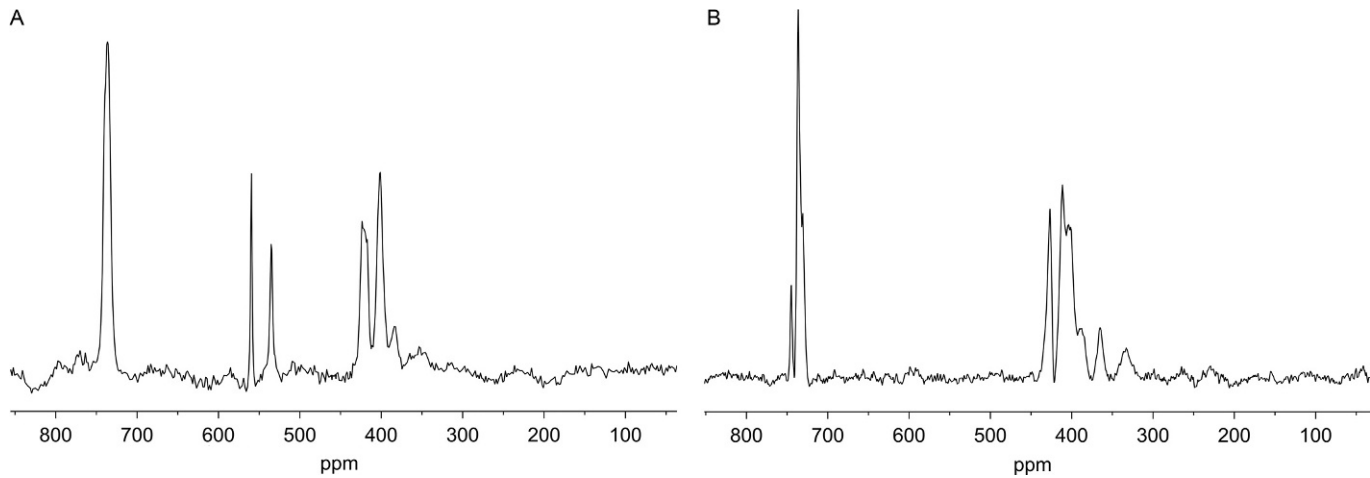


**Fig. 11**  $^{17}\text{O}$  NMR spectra of (A)  $(\text{TBA})_4[(\text{MeO})\text{TiPW}_{11}\text{O}_{39}]$  and (B)  $(\text{TBA})_4[(\text{MeO})\text{SnPW}_{11}\text{O}_{39}]$ .

associated with bridging WOW (Fig. 11), in a similar fashion to the upfield shifts of SnOW peaks in the  $^{17}\text{O}$  NMR spectra of  $\{\text{XSnW}_5\}$  anions (Table 1) compared to TiOW in  $\{\text{XTiW}_5\}$  anions (7).

### 3.2 Tin(II)- and Lead(II)-Substituted $\{\text{MPW}_{11}\}$ Derivatives

$^{17}\text{O}$ -enriched  $(\text{TBA})_5[\text{SnPW}_{11}\text{O}_{39}]$  and  $(\text{TBA})_5[\text{PbPW}_{11}\text{O}_{39}]$  were similarly obtained by treatment of  $(\text{TBA})_6[\text{NaPW}_{11}\text{O}_{39}]$  with  $\text{SnCl}_2$  or  $\text{Pb}(\text{O}_2\text{CCH}_3)_2 \cdot 3\text{H}_2\text{O}$ , respectively, and broadened peaks at 527 and 566 ppm in the respective  $^{17}\text{O}$  NMR spectra were assigned to unresolved  $\text{Sn}^{\text{II}}\text{OW}$  and  $\text{Pb}^{\text{II}}\text{OW}$  resonances for each anion (Fig. 12) (22). The downfield shift of  $\text{Sn}^{\text{II}}\text{OW}$  compared to  $\text{Sn}^{\text{IV}}\text{OW}$  in  $[\text{XSnPW}_{11}\text{O}_{39}]^{4-}$  ( $\text{X} = \text{Cl}, \text{OMe}$ ) is due to the less electrophilic nature of  $\text{Sn}^{2+}$  in  $[\text{SnPW}_{11}\text{O}_{39}]^{5-}$ . As observed previously, no  $^2J(^{31}\text{P}^{119}\text{Sn})$  coupling was evident for the Sn(II) compound (24), indicating that Sn is not bound to the central P–O oxygen of the lacunary pocket, which is also the case for Pb in the crystallographically characterized  $[\text{PbGaW}_{11}\text{O}_{39}]^{7-}$  (25).  $^{17}\text{O}$  NMR data for this series of  $\{\text{MPW}_{11}\}$  Keggin anions are collected in Table 3.

### 3.3 A Platinum(IV)-Substituted $\{\text{PtSiW}_{11}\}$ Anion

Our efforts to synthesize a Pt(IV)-substituted Keggin anion from  $(\text{TBA})_6[\text{NaPW}_{11}\text{O}_{39}]$  and Pt(IV) salts in nonaqueous media have to date proved inconclusive, but the first characterized Pt(IV)-substituted Keggin species  $(\text{TBA})_4[\text{H}_2\text{PtSiW}_{11}\text{O}_{40}]$  was obtained by addition of  $(\text{TBA})\text{Br}$  to an aqueous solution of  $\text{K}_8\text{SiW}_{11}\text{O}_{39} \cdot 13\text{H}_2\text{O}$  and  $\text{K}_2[\text{Pt}(\text{OH})_6]$  that had been acidified to pH 4, although isolation of the pure compound free from plenary  $[\text{SiW}_{12}\text{O}_{40}]^{4-}$  required additional purification steps (26). The compound was characterized by  $^{183}\text{W}$  and  $^{195}\text{Pt}$  NMR spectroscopy in addition to FTIR spectroscopy and elemental microanalysis, although the nature of the terminal ligand bonded to platinum could not be determined unambiguously to be either water or hydroxide. Initial reactivity studies indicate that this ligand may be substituted, e.g., by  $\text{NO}_3^-$  and that the platinum can be reduced to Pt(II) and reoxidized to Pt(IV), raising the possibility of catalytic chemistry for this anion.



## 4. PROTONOLYSIS OF M–OR BONDS AND CONDENSATION

A general feature of metal alkoxido complexes is their susceptibility to ligand exchange via protonolysis with elimination of alcohol. This tendency

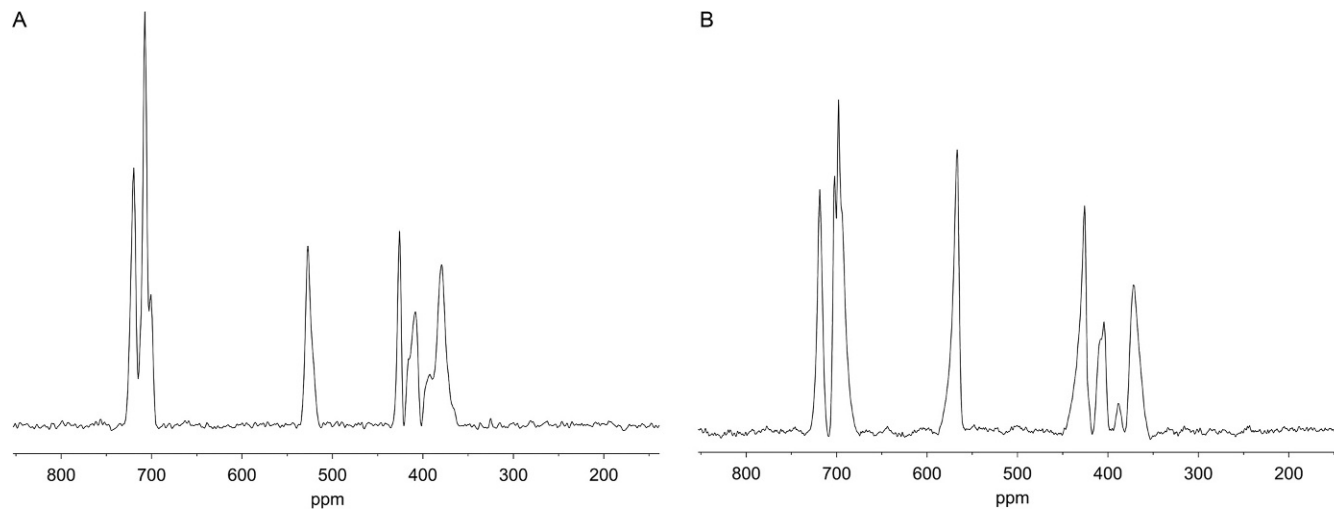


**Fig. 12**  $^{17}\text{O}$  NMR spectra for Keggin-type anions (A)  $(\text{TBA})_5[\text{SnPW}_{11}\text{O}_{39}]$  and (B)  $(\text{TBA})_5[\text{PbPW}_{11}\text{O}_{39}]$ .

**Table 3**  $^{17}\text{O}$  NMR Data for {MPW<sub>11</sub>} Keggin Anions<sup>a</sup>

Anion	$^{17}\text{O}$ Chemical Shift/ppm			
	W=O	MOM	MOW	WOW
[NaPW <sub>11</sub> O <sub>39</sub> ] <sup>6-</sup>	707–646	—	438, 432	401–360
[Sn <sup>II</sup> PW <sub>11</sub> O <sub>39</sub> ] <sup>5-</sup>	720–701	—	527, 522	426–372
[Pb <sup>II</sup> PW <sub>11</sub> O <sub>39</sub> ] <sup>5-</sup>	718–693	—	566	426–372
[ClTiPW <sub>11</sub> O <sub>39</sub> ] <sup>4-</sup>	747–743	—	585, 565	427–386
[(MeO)TiPW <sub>11</sub> O <sub>39</sub> ] <sup>4-</sup>	739–735	—	559, 535	423–401
[(HO)TiPW <sub>11</sub> O <sub>39</sub> ] <sup>4-</sup>	739–736	—	559, 536	433–384
[( $\mu$ -O)(TiPW <sub>11</sub> O <sub>39</sub> ) <sub>2</sub> ] <sup>8-</sup>	741–722	713	571, 541	424–398
[ClSn <sup>IV</sup> PW <sub>11</sub> O <sub>39</sub> ] <sup>4-</sup>	749–737	—	429–373	
[(MeO)Sn <sup>IV</sup> PW <sub>11</sub> O <sub>39</sub> ] <sup>4-</sup>	745–731	—	427–333	
[(HO)Sn <sup>IV</sup> PW <sub>11</sub> O <sub>39</sub> ] <sup>4-</sup>	746–733	—	427–374	
[( $\mu$ -O)(Sn <sup>IV</sup> PW <sub>11</sub> O <sub>39</sub> ) <sub>2</sub> ] <sup>8-</sup>	747–732	<sup>b</sup>	429–374	
[PW <sub>12</sub> O <sub>40</sub> ] <sup>3-</sup>	770	—	—	432, 405

<sup>a</sup>As <sup>n</sup>Bu<sub>4</sub>N<sup>+</sup> salts.<sup>b</sup>Not observed.

has been exploited extensively in the preparation of metal oxide materials via the sol-gel process, but the complexity of the solution speciation during hydrolysis of homoleptic metal alkoxides, where there is more than one M-OR bond per metal, makes it difficult to identify the intermediate stages in reactions leading to large polynuclear species, such as those identified in Klemperer's pivotal NMR studies of Ti(OR)<sub>4</sub> alkoxide hydrolysis (27). The incorporation of single {MOR}<sup>3+</sup> fragments (M = Ti, Sn) into the Lindqvist [(RO)MW<sub>5</sub>O<sub>18</sub>]<sup>3-</sup> and Keggin [(RO)MPW<sub>11</sub>O<sub>39</sub>]<sup>4-</sup> anions provided the opportunity to study and compare the reactivity at these structurally related sites and consider the factors affecting the underlying mechanisms.

#### 4.1 Hydrolysis of {(MeO)MW<sub>5</sub>} Lindqvist Anions

We previously noted that the hydrolysis of (TBA)<sub>3</sub>[(MeO)TiW<sub>5</sub>O<sub>18</sub>] is slow and at higher temperatures proceeds to the condensation product (TBA)<sub>6</sub>[( $\mu$ -O)(TiW<sub>5</sub>O<sub>18</sub>)<sub>2</sub>] rather than the hydroxide (TBA)<sub>3</sub>[(HO)TiW<sub>5</sub>O<sub>18</sub>] (7). In an attempt to isolate the hydroxido species we therefore employed repeated cycles of mild hydrolysis with subsequent removal of all

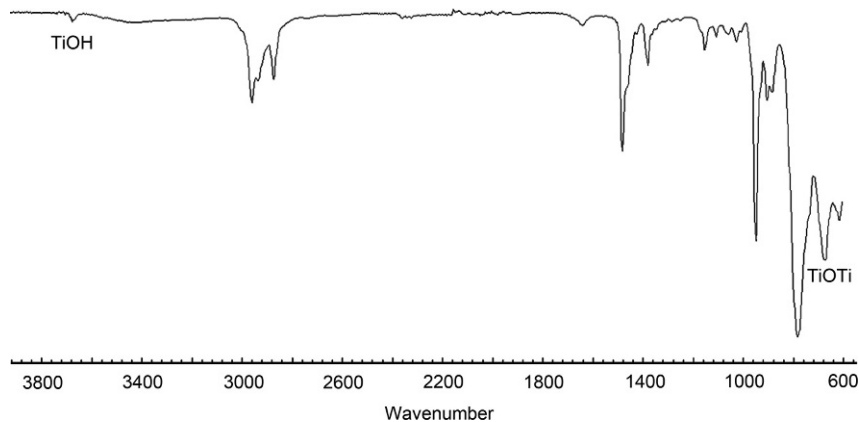


**Fig. 13** ATR FTIR spectrum of the product from  $(\text{TBA})_3[(\text{MeO})\text{TiW}_5\text{O}_{18}]$  hydrolysis.

volatiles in an effort to drive the reaction toward  $[(\text{HO})\text{TiW}_5\text{O}_{18}]^{3-}$  and minimize condensation. The FTIR spectrum of the resulting product did indeed show a band for  $\nu(\text{TiOH})$  at  $3676\text{ cm}^{-1}$ , but there was also a band at  $673\text{ cm}^{-1}$  due to  $\nu_{\text{as}}(\text{Ti}-\text{O})$  of the  $\text{TiOTi}$  bridge, indicating that condensation occurs even under mild conditions (Fig. 13) (12).

The hydrolysis of  $(\text{TBA})_3[(\text{MeO})\text{SnW}_5\text{O}_{18}]$  proceeded much more quickly than the titanium analog. In this case, the hydroxide derivative  $(\text{TBA})_3[(\text{HO})\text{SnW}_5\text{O}_{18}]$  was formed cleanly at ambient temperature and the subsequent condensation was less favorable than for titanium. Although the  $\text{SnOH}$  group could not be distinguished in the single-crystal X-ray structure of  $(\text{TBA})_3[(\text{HO})\text{SnW}_5\text{O}_{18}]$  because of disorder over all six metal positions, the presence of  $\text{SnOH}$  was established by the observation of  $\nu(\text{SnOH})$  at  $3648\text{ cm}^{-1}$  in the IR spectrum and by the presence of  ${}^2J(^1\text{H}^{119}\text{Sn})$  coupling of 47.7 Hz in the  $^{119}\text{Sn}$  NMR spectrum for the resonance at  $-633\text{ ppm}$  when the spectrum was measured without proton decoupling (Fig. 14) (28). Tungsten satellites are also present with  ${}^2J(^{119}\text{Sn}^{183}\text{W}_{\text{eq}})$  of 37 Hz. In  $d_6$ -DMSO the  $\text{SnOH}$  group was observed directly by  ${}^1\text{H}$  NMR as a broadened singlet at 3.42 ppm. Separate satellites for  ${}^2J(^1\text{H}^{119}\text{Sn})$  and  ${}^2J(^1\text{H}^{117}\text{Sn})$  were not resolved, but the coupling constant for the broadened satellites was ca. 44 Hz.

In the  $^{119}\text{Sn}$  NMR spectrum of  $(\text{TBA})_3[(\text{HO})\text{SnW}_5\text{O}_{18}]$ , in addition to the main peak at  $-633\text{ ppm}$  a small peak at  $-666\text{ ppm}$  appeared over several days at ambient temperature due to the formation of  $(\text{TBA})_6[(\mu-\text{O})(\text{SnW}_5\text{O}_{18})_2]$ . In order to drive the condensation equilibrium toward the oxo-bridged species, volatiles were removed periodically from a heated



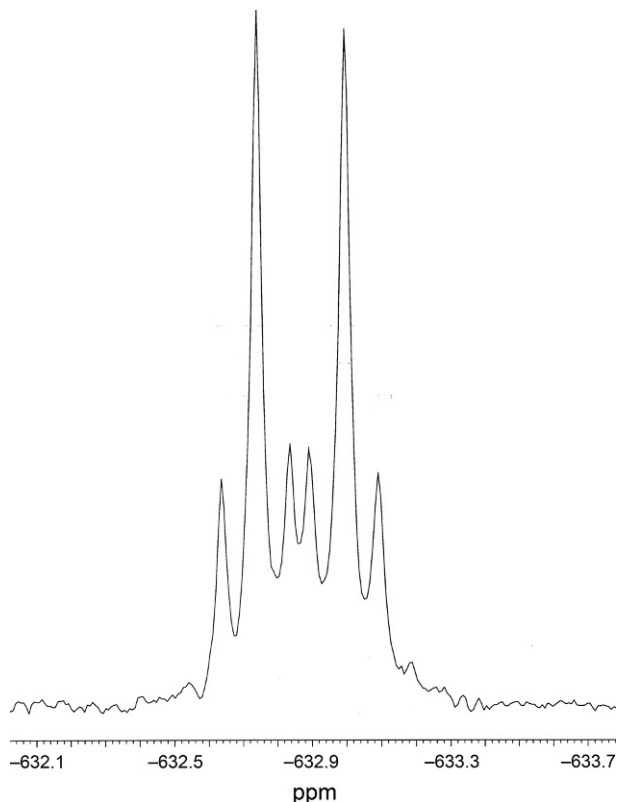


**Fig. 14**  $^{119}\text{Sn}$  NMR spectrum of  $(\text{TBA})_3[(\text{HO})\text{SnW}_5\text{O}_{18}]$  without  $^1\text{H}$  decoupling.

solution of  $(\text{TBA})_3[(\text{HO})\text{SnW}_5\text{O}_{18}]$  while monitoring the conversion by  $^{119}\text{Sn}$  NMR as shown in Fig. 15. Evidence for the formation of the SnOSn bridge was obtained by recording the  $^{119}\text{Sn}$  NMR spectrum without  $^1\text{H}$  decoupling, which showed no  $^2J(^1\text{H}^{119}\text{Sn})$  coupling and extra satellite peaks due to a  $^2J(^{117}\text{Sn}^{119}\text{Sn})$  coupling of 333 Hz in addition to  $^2J(^{119}\text{Sn}^{183}\text{W})$  coupling of 46 Hz (Fig. 16). Interestingly, condensation did not occur when  $(\text{TBA})_3[(\text{HO})\text{SnW}_5\text{O}_{18}]$  was heated in DMSO instead of MeCN, suggesting that DMSO is a sufficiently good ligand to interact with the Sn centers and prevent the formation of Sn(OH)Sn bridging interactions and the subsequent H migration and elimination of water. Attempts to obtain single crystals for X-ray structure determination have to date been unsuccessful, but the anion was characterized in a hydrogen-bonded structure with  $^i\text{Pr}_2\text{NH}_2^+$  cations (Section 5; Fig. 25).

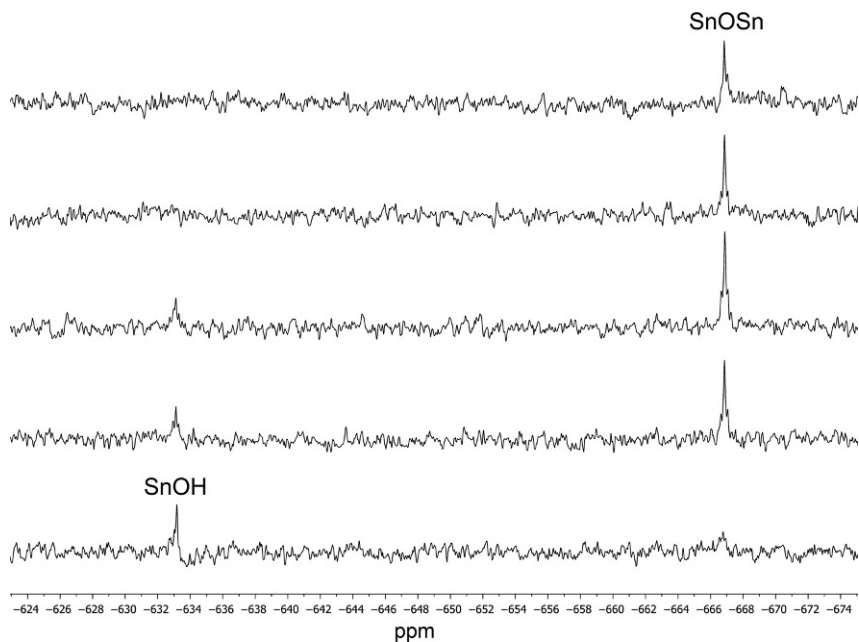


**Fig. 15**  $^{119}\text{Sn}(^1\text{H})$  NMR spectra of successive cycles of heat treatment with removal of volatiles showing conversion of  $(\text{TBA})_3[(\text{HO})\text{SnW}_5\text{O}_{18}]$  (bottom) to  $(\text{TBA})_6[(\mu\text{-O})(\text{SnW}_5\text{O}_{18})_2]$  (top).

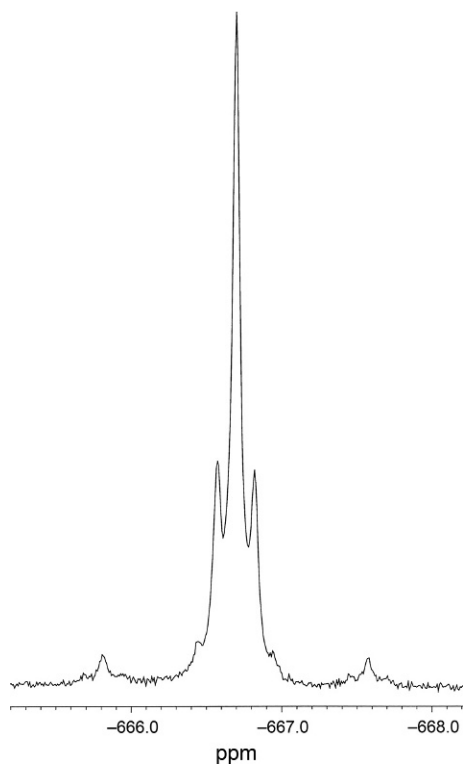


**Fig. 16**  $^{119}\text{Sn}$  NMR spectrum of  $(\text{TBA})_6[(\mu\text{-O})(\text{SnW}_5\text{O}_{18})_2]$  without  $^1\text{H}$  decoupling.

## 4.2 Hydrolysis of {(MeO)MPW<sub>11</sub>} Keggin Anions

In a series of papers, Kholdeeva and coworkers have discussed the chemistry associated with POMs based on the {TiPW<sub>11</sub>} framework, including the interconversion of monomeric [XTiPW<sub>11</sub>O<sub>39</sub>]<sup>4-</sup> and dimeric [(μ-O)(TiPW<sub>11</sub>O<sub>39</sub>)<sub>2</sub>]<sup>8-</sup> anions (29), and the crystal structure and solution chemistry of [Et<sub>2</sub>NH<sub>2</sub>]<sub>8</sub>[(μ-O)(TiPW<sub>11</sub>O<sub>39</sub>)<sub>2</sub>] have also been reported by Nomiya and coworkers (30). We were interested to establish whether substitution of Ti for Sn would cause differences in the hydrolysis and condensation behavior of the [(MeO)MPW<sub>11</sub>O<sub>39</sub>]<sup>4-</sup> anions in the same way as observed for [(MeO)MW<sub>5</sub>O<sub>18</sub>]<sup>3-</sup> anions. Our studies of (TBA)<sub>4</sub>[(MeO)TiPW<sub>11</sub>O<sub>39</sub>] confirmed that hydrolysis is comparatively slow. <sup>31</sup>P NMR spectra revealed that with a 100-fold excess of water, [(MeO)TiPW<sub>11</sub>O<sub>39</sub>]<sup>4-</sup> was converted to [(HO)TiPW<sub>11</sub>O<sub>39</sub>]<sup>4-</sup> after 10 min and the subsequent slow formation of [(μ-O)(TiPW<sub>11</sub>O<sub>39</sub>)<sub>2</sub>]<sup>8-</sup> at ambient temperature could then be followed over the course of several days (Fig. 17) (22). The intermediate hydroxide species is notably longer lived than the analogous

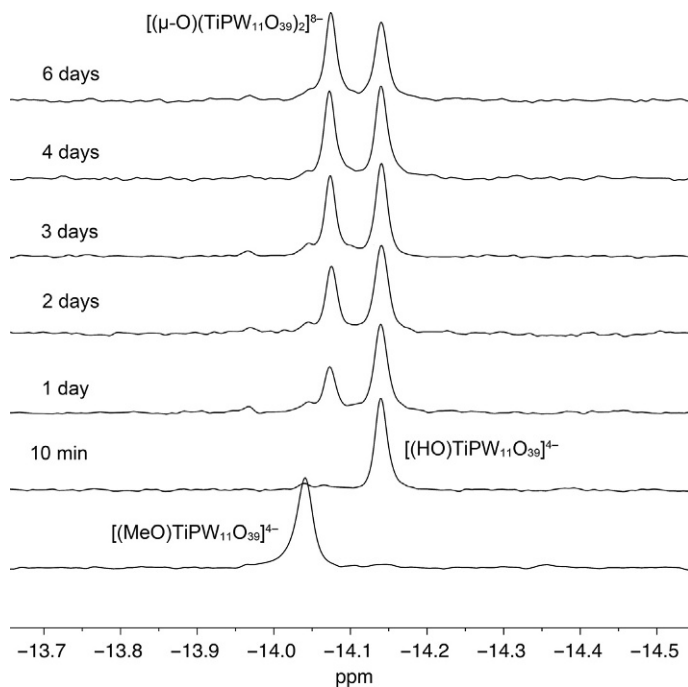


**Fig. 17** <sup>31</sup>P NMR spectra of [(MeO)TiPW<sub>11</sub>O<sub>39</sub>]<sup>4-</sup> hydrolysis (100-fold excess of water; 25°C).

Lindqvist species, so that it was possible to isolate  $(\text{TBA})_4[(\text{HO})\text{TiPW}_{11}\text{O}_{39}]$  in high yield by carrying out the hydrolysis with a large excess of water, then removing all volatiles after about 30 min, and repeating the process several times. The product shows  $\nu(\text{OH})$  at  $3633\text{ cm}^{-1}$ , and the  $^{17}\text{O}$  NMR data for the enriched anion are given in Table 3. Pure oxo-bridged  $(\text{TBA})_8[(\mu\text{-O})(\text{TiPW}_{11}\text{O}_{39})_2]$  was obtained by stirring a solution of  $(\text{TBA})_4[(\text{MeO})\text{TiPW}_{11}\text{O}_{39}]$  with a slight excess of water for several hours to give a mixture of  $(\text{TBA})_4[(\text{HO})\text{TiPW}_{11}\text{O}_{39}]$  and  $(\text{TBA})_8[(\mu\text{-O})(\text{TiPW}_{11}\text{O}_{39})_2]$  from which the volatiles were removed. The residual solid was then dissolved in acetonitrile and treated with 3A molecular sieves until the condensation reaction was complete. This hydrolysis–condensation process enabled the TiOTi site to be selectively enriched in  $^{17}\text{O}$  by using  $^{17}\text{O}$ -enriched water, giving a single peak at 713 ppm in the  $^{17}\text{O}$  NMR spectrum.

As in the case for the Lindqvist hexametalates, the tin-substituted Keggin species  $(\text{TBA})_4[(\text{MeO})\text{SnPW}_{11}\text{O}_{39}]$  hydrolyzed much more rapidly than its titanium analog to give the hydroxido derivative  $(\text{TBA})_4[(\text{HO})\text{SnPW}_{11}\text{O}_{39}]$ , and in an attempt to quantify the rate by  $^1\text{H}$  NMR, the reaction proceeded almost to equilibrium by the time the first spectrum had been recorded. The FTIR spectrum of  $(\text{TBA})_4[(\text{HO})\text{SnPW}_{11}\text{O}_{39}]$  contains a band for  $\nu(\text{OH})$  at  $3639\text{ cm}^{-1}$ , close to that for  $[(\text{HO})\text{TiPW}_{11}\text{O}_{39}]^{4-}$  at  $3633\text{ cm}^{-1}$ . Condensation to  $(\text{TBA})_8[(\mu\text{-O})(\text{SnPW}_{11}\text{O}_{39})_2]$  was more difficult than for the titanium system, but was achieved by repeatedly heating a solution of  $(\text{TBA})_4[(\text{HO})\text{SnPW}_{11}\text{O}_{39}]$  with regular partial removal of the volatiles.  $^{183}\text{W}$  NMR spectra for these two  $\{\text{SnPW}_{11}\}$  anions shown in Fig. 18 are consistent with the proposed monosubstituted  $\alpha$ -Keggin structures. In each spectrum, the extreme peaks can be assigned to the tungsten atoms adjacent to tin, where the size of  $^2J(^{119}\text{Sn}^{183}\text{W})$  increases with the SnOW angle in the structure. For  $[(\text{HO})\text{SnPW}_{11}\text{O}_{39}]^{4-}$  the couplings are 53.5 and 144.1 Hz for the peaks at  $-76.4$  and  $-175.2$  ppm, respectively, and for  $[(\mu\text{-O})(\text{SnPW}_{11}\text{O}_{39})_2]^{8-}$  the couplings are 68.3 and 163.5 Hz for the peaks at  $-82.5$  and  $-182.2$  ppm, respectively, enabling assignment of the downfield peaks in each case to the tungsten atoms in the  $\text{SnW}_2$  “triads” with the smaller SnOW bond angles. By comparison,  $[(\text{HO})\text{SnW}_5\text{O}_{18}]^{3-}$  and  $[(\mu\text{-O})(\text{SnW}_5\text{O}_{18})_2]^{6-}$  have  $^2J(^{119}\text{Sn}^{183}\text{W}_{\text{eq}})$  values of 37 and 46 Hz, respectively.

### 4.3 Alcohol Interchange

Addition of alcohol  $\text{R}'\text{OH}$  to  $[(\text{RO})\text{M}'\text{M}_5\text{O}_{18}]^{3-}$  was expected to result in alkoxido exchange but, surprisingly, the  $^1\text{H}$  NMR spectra after addition of

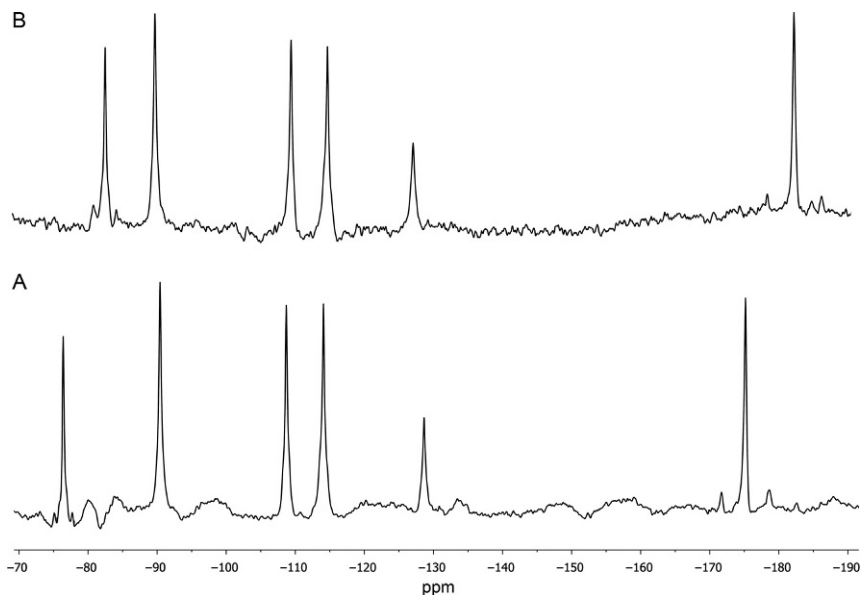


**Fig. 18**  $^{183}\text{W}$  NMR spectra for (A)  $[(\text{HO})\text{SnPW}_{11}\text{O}_{39}]^{4-}$ ; (B)  $[(\mu\text{-O})(\text{SnPW}_{11}\text{O}_{39})_2]^{8-}$ .

MeOH to  $(\text{TBA})_3[(\text{MeO})\text{TiW}_5\text{O}_{18}]$  showed separate sharp peaks for MeOH and  $(\text{MeO})\text{Ti}$ , even at elevated temperatures ( $70^\circ\text{C}$ ) indicative of slow exchange on the NMR time scale. We previously reported off-diagonal exchange peaks in a 2D  $^1\text{H}$  EXSY NMR experiment for a mixture of MeOH and  $[(\text{MeO})\text{TiW}_5\text{O}_{18}]^{3-}$  (7). However, we have now repeated this experiment several times for both MeOH/ $[(\text{MeO})\text{TiW}_5\text{O}_{18}]^{3-}$  and MeOH/ $[(\text{MeO})\text{TiPW}_{11}\text{O}_{39}]^{4-}$  mixtures and did not observe any  $\text{TiOMe}/\text{MeOH}$  exchange peaks, even after addition of water at  $60^\circ\text{C}$ , although small peaks did appear upon addition of small amounts of  $\text{HBF}_4$ . In contrast, off-diagonal  $\text{SnOMe}/\text{MeOH}$  cross peaks were observed for MeOH/ $[(\text{MeO})\text{SnW}_5\text{O}_{18}]^{3-}$  and MeOH/ $[(\text{MeO})\text{SnPW}_{11}\text{O}_{39}]^{4-}$  mixtures as shown in Fig. 19. These observations are consistent with our general observation that alkoxido-tin(IV)-substituted POMs are much more moisture sensitive than their titanium analogs.

#### 4.4 Alkoxido Metathesis

Despite the relatively slow alcohol exchange rates for  $(\text{TBA})_3[(\text{MeO})\text{TiW}_5\text{O}_{18}]$ , we were able previously to obtain a range of  $(\text{TBA})_3[\text{XTiW}_5\text{O}_{18}]$  derivatives with oxygen-donor ligands X from reactions at elevated temperatures (7). Protonolysis reactions of  $(\text{TBA})_3[(\text{MeO})$

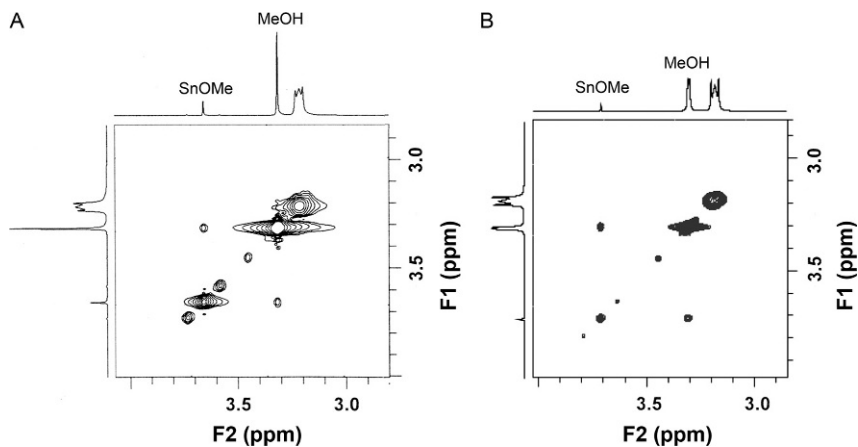


**Fig. 19** 2D  $^1\text{H}$  EXSY NMR spectra for mixtures of (A)  $(\text{TBA})_3[(\text{MeO})\text{SnW}_5\text{O}_{18}]$  and MeOH; (B)  $(\text{TBA})_4[(\text{MeO})\text{SnPW}_{11}\text{O}_{39}]$  and MeOH.

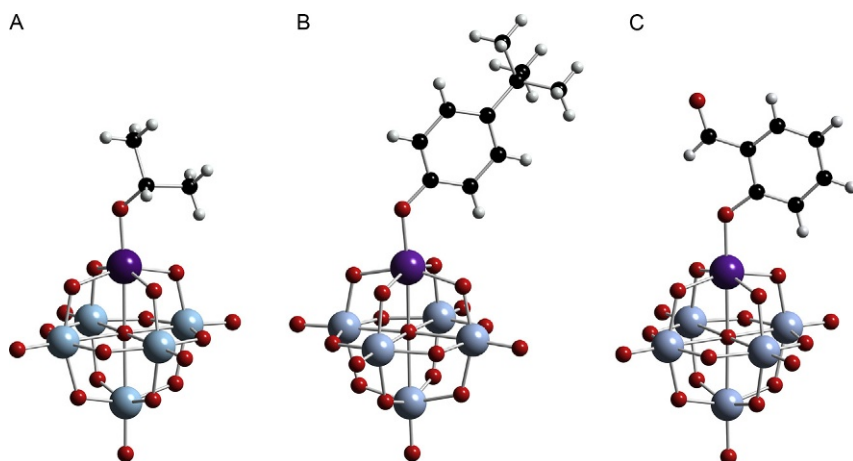


**Fig. 20** Structures of Lindqvist-type anions (A)  $[(^t\text{PrO})\text{SnW}_5\text{O}_{18}]^{3-}$ ; (B)  $[(^t\text{BuO})\text{SnW}_5\text{O}_{18}]^{3-}$ ; (C)  $[\{2\text{-(CHO)C}_6\text{H}_4\text{O}\}\text{SnW}_5\text{O}_{18}]^{3-}$ .

$\text{SnW}_5\text{O}_{18}$ ], although faster, were also facilitated by heating and provided access to a series of exchange products  $(\text{TBA})_3[(\text{RO})\text{SnW}_5\text{O}_{18}]$  including  $\text{R}=\text{Et}$ ,  $^t\text{Pr}$ ,  $^t\text{Bu}$ ,  $\text{C}_6\text{H}_5$ ,  $4\text{-MeC}_6\text{H}_4$ ,  $4\text{-}^t\text{BuC}_6\text{H}_4$ ,  $4\text{-HOC}_6\text{H}_4$ , and  $2\text{-(CHO)C}_6\text{H}_4$ , which have all been characterized by single-crystal X-ray crystallography, although disorder was problematic for  $\text{R}=\text{Et}$  and  $4\text{-HOC}_6\text{H}_4$ . A selection of these  $\{\text{SnW}_5\}$  structures is shown in Fig. 20, and NMR data are included in Table 1 (28).

## 4.5 Theoretical Studies

DFT calculations on methanol exchange and hydrolysis reactions for Lindqvist  $[(\text{MeO})\text{MW}_5\text{O}_{18}]^{3-}$  and Keggin  $[(\text{MeO})\text{MPW}_{11}\text{O}_{39}]^{4-}$  anions ( $\text{M}=\text{Ti}, \text{Sn}$ ) were carried out in collaboration with the Poblet group at URV, Tarragona (16). The results suggested that methanol exchange occurs via attack of  $\text{MeOH}$  at  $\text{M}$  and the formation of a symmetrical transition state with a seven-coordinate heteroatom and hydrogen bridging between the two  $\text{OMe}$  groups, followed by proton transfer and elimination of methanol. The activation energies for this concerted process were calculated to be higher for  $\{\text{TiW}_5\}$  than for  $\{\text{SnW}_5\}$ , which is consistent with results from EXSY NMR experiments, where exchange cross peaks were observed for  $\{\text{SnW}_5\}$  but not for  $\{\text{TiW}_5\}$ . Calculations on the hydrolysis of  $[(\text{MeO})\text{MW}_5\text{O}_{18}]^{3-}$  anions predicted a similar concerted mechanism for reactions leading to hydroxido derivatives, with a lower activation energy for the tin anion and greater stability for  $[(\text{HO})\text{SnW}_5\text{O}_{18}]^{3-}$  (Fig. 21), which is consistent with the faster hydrolysis rate observed for

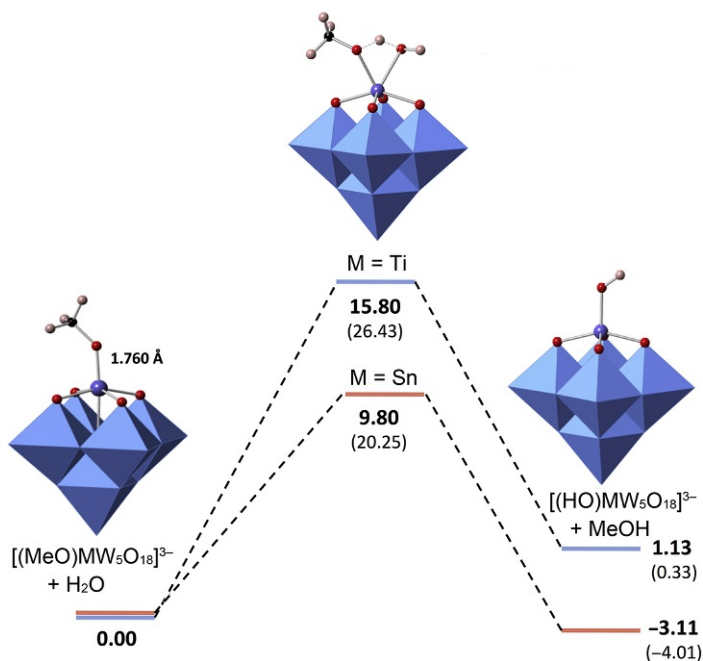


**Fig. 21** Reaction profiles for hydrolysis of  $[(\text{MeO})\text{TiW}_5\text{O}_{18}]^{3-}$  and  $[(\text{MeO})\text{SnW}_5\text{O}_{18}]^{3-}$  Lindqvist-type anions. Electronic energies are shown in *bold*, and  $\Delta\text{G}$  values are given in *brackets* (kcal mol<sup>-1</sup>).

the tin compound and the facile isolation of  $(\text{TBA})_3[(\text{HO})\text{SnW}_5\text{O}_{18}]$ . The preferred condensation reaction pathways for both hydroxido anions involve nucleophilic attack by the OH group of one  $[(\text{HO})\text{MW}_5\text{O}_{18}]^{3-}$  anion at the heterometal M of an adjacent anion with subsequent hydrogen transfer and elimination of a water molecule. However, the pathways for Ti and Sn differ slightly in that an extra transition state for the initial Sn–O bond formation was found in the case of the  $\{\text{SnW}_5\}$  anion, while hydrogen transfer and loss of water were found to occur in a second step (Fig. 22). This

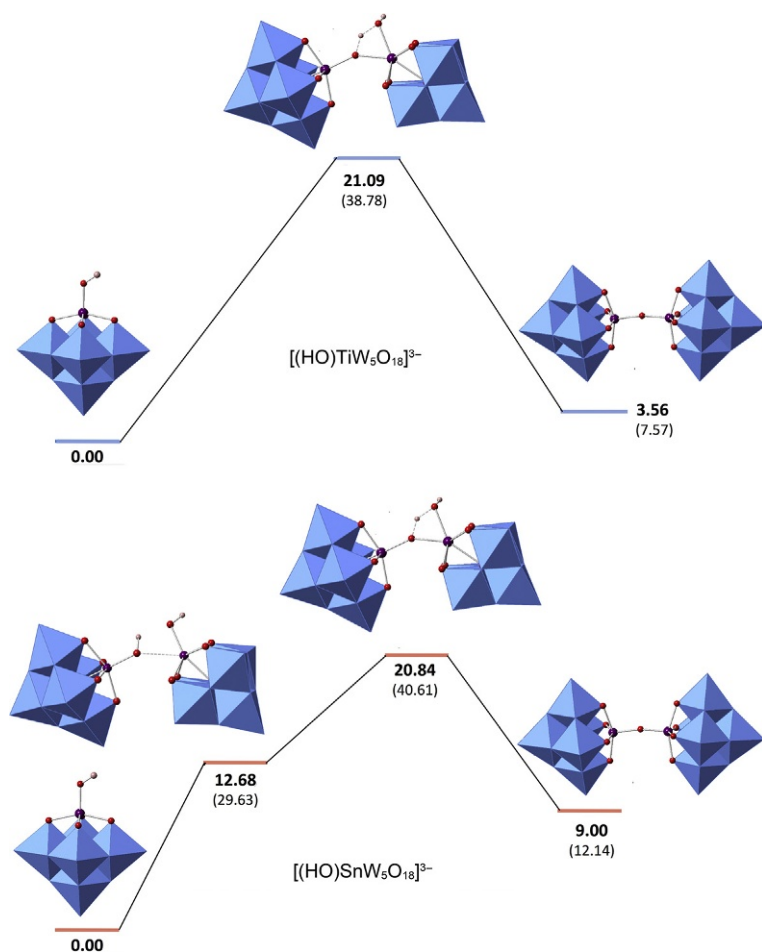


**Fig. 22** Reaction profiles for condensation of  $[(\text{HO})\text{TiW}_5\text{O}_{18}]^{3-}$  and  $[(\text{HO})\text{SnW}_5\text{O}_{18}]^{4-}$  Lindqvist-type anions. Electronic energies are shown in *bold*, and  $\Delta G$  values are given in *brackets* ( $\text{kcal mol}^{-1}$ ).



may explain why DMSO was observed to inhibit the condensation of  $[(\text{HO})\text{SnW}_5\text{O}_{18}]^{3-}$ . Similar values were obtained for the highest energy transition state in each of these condensation reactions, but the titanium oxo-bridged product  $[(\mu\text{-O})(\text{TiW}_5\text{O}_{18})_2]^{6-}$  was predicted to be significantly more stable than the tin analog. Again, this is consistent with the experimental observations, where it was significantly more difficult to prepare pure samples of  $(\text{TBA})_6[(\mu\text{-O})(\text{SnW}_5\text{O}_{18})_2]$ .

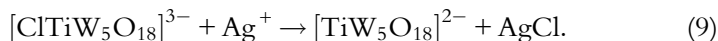
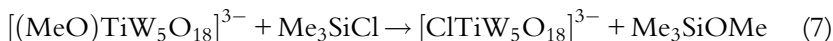
Calculations on the Keggin anions  $[(\text{MeO})\text{MPW}_{11}\text{O}_{39}]^{4-}$  ( $\text{M} = \text{Ti}, \text{Sn}$ ) gave similar results to the corresponding Lindqvist anions, and predicted that  $[(\text{MeO})\text{SnPW}_{11}\text{O}_{39}]^{4-}$  should hydrolyze more readily than  $[(\text{MeO})\text{TiPW}_{11}\text{O}_{39}]^{4-}$ , as observed experimentally. As in the case of the Lindqvist anions, separate steps were predicted for Sn–O bond formation and water elimination in the  $\{\text{SnPW}_{11}\}$  condensation reaction but not for  $\{\text{TiPW}_{11}\}$ . Comparison of the Lindqvist  $\{\text{MW}_5\}$  and Keggin  $\{\text{MPW}_{11}\}$  hydrolysis reaction profiles shows that the highest energy barrier is for  $\{\text{TiPW}_{11}\}$  and the lowest for  $\{\text{SnPW}_{11}\}$ , and the most stable products are the tin-substituted hydroxido anions in each family. A similar comparison of condensation reaction profiles shows that the highest energy barrier is for the  $\{\text{SnPW}_{11}\}$  Keggin anion and the lowest is for the  $\{\text{SnW}_5\}$  Lindqvist anion (which is only slightly lower than that for the  $\{\text{TiW}_5\}$  anion). The most stable oxo-bridged product is  $[(\mu\text{-O})(\text{TiW}_5\text{O}_{18})_2]^{6-}$  and the least stable is  $[(\mu\text{-O})(\text{SnPW}_{11}\text{O}_{39})_2]^{8-}$ . This reflects the observed extreme moisture sensitivity of  $(\text{TBA})_8[(\mu\text{-O})(\text{SnPW}_{11}\text{O}_{39})_2]$ , which readily reverts to  $(\text{TBA})_4[(\text{HO})\text{SnPW}_{11}\text{O}_{39}]$  in the presence of traces of water.



## 5. SYNTHESIS AND REACTIVITY OF CHLORIDO $\{\text{CLMW}_5\}$ LINDQVIST ANIONS

POMs containing embedded heterometal  $\{\text{MCl}\}$  groups are attractive because they should provide access to the range of chemical transformations that are the mainstay of organometallic and metalorganic chemistry, e.g., ligand metathesis, reduction, and halide abstraction, thereby expanding the range of POM reactivity platforms. While the Keggin-type anions  $(\text{TBA})_4[\text{ClTiPW}_{11}\text{O}_{39}]$ ,  $(\text{TBA})_4[\text{ClSnPW}_{11}\text{O}_{39}]$ , and  $(\text{TBA})_4[\text{ClAlPW}_{11}\text{O}_{39}\text{H}]$  were described some time ago (23), similar Lindqvist derivatives have not been reported. We have previously used the “virtual”  $[\text{W}_5\text{O}_{18}]^{6-}$  precursor to access the chlorido species  $(\text{TBA})_3[\text{ClTiW}_5\text{O}_{18}]$  (11), but we subsequently found that chlorination of  $[(\text{MeO})\text{TiW}_5\text{O}_{18}]^{3-}$  with  $\text{Me}_3\text{SiCl}$  is a cleaner reaction and gives better

yields (Eq. 7), while attempts to use HCl for chlorination resulted in significant decomposition and formation of  $(\text{TBA})_2[\text{W}_6\text{O}_{19}]$ .  $(\text{TBA})_3[(\text{MeO})\text{SnW}_5\text{O}_{18}]$  reacted similarly with  $\text{Me}_3\text{SiCl}$  to give  $(\text{TBA})_3[\text{ClSnW}_5\text{O}_{18}]$ , but in this case clean conversion to the chlorido anion is readily achieved by treatment with aqueous HCl without decomposition (Eq. 8) (28)



In an attempt to create a coordinatively unsaturated heteroatom within a molecular metal oxide that might mimic the reactivity of surface sites in a solid metal oxide, we treated  $(\text{TBA})_3[\text{ClTiW}_5\text{O}_{18}]$  with  $\text{AgBF}_4$  in order to abstract  $\text{Cl}^-$  (Eq. 9) in anticipation that this might result in coordination of MeCN to the unsaturated titanium site (31). The peak for  $\nu(\text{W}=\text{O})$  at  $966\text{ cm}^{-1}$  in the FTIR spectrum of the product was at higher wavenumber than that for  $[\text{ClTiW}_5\text{O}_{18}]^{3-}$  at  $954\text{ cm}^{-1}$ , suggesting that chloride abstraction had occurred to give an anion with a lower charge. In the  $^{17}\text{O}$  NMR spectrum, the downfield shift of the broadened  $\text{W}=\text{O}$  peak to 762 ppm was also consistent with a lower anion charge and can be compared with the peaks at 734 and 721 ppm for  $[\text{ClTiW}_5\text{O}_{18}]^{3-}$  and 721 and 713 ppm for  $[(\text{MeO})\text{TiW}_5\text{O}_{18}]^{3-}$ . A single-crystal X-ray structure confirmed this deduction, but the compound was shown to be the dimeric  $(\text{TBA})_4[(\text{TiW}_5\text{O}_{18})_2]$  rather than a monomeric  $[(\text{L})\text{TiW}_5\text{O}_{18}]^{2-}$  Lindqvist unit, and the structure of the anion is shown in Fig. 23. The formation of

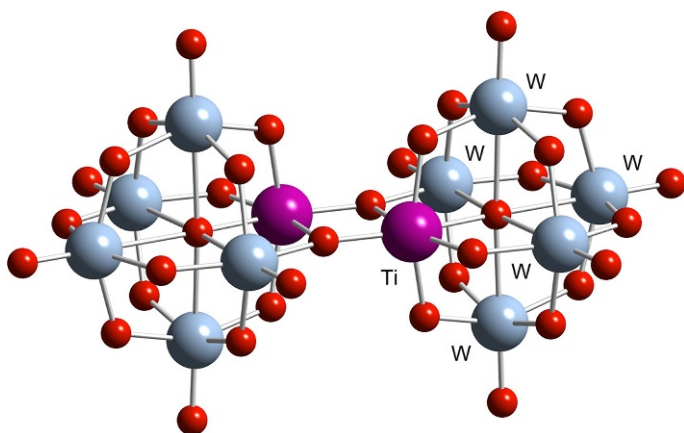
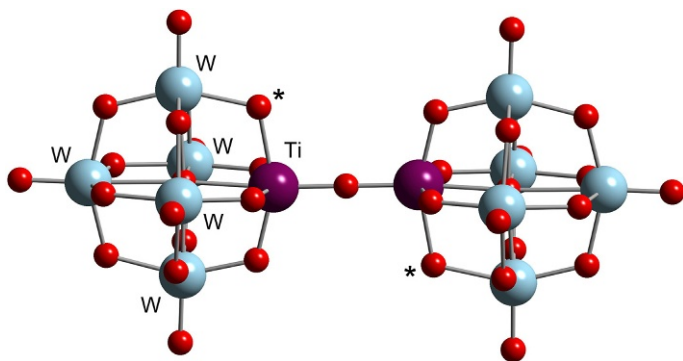


Fig. 23 Structure of the dimeric anion  $[(\text{TiW}_5\text{O}_{18})_2]^{4-}$ .

this dimeric structure shows that halide abstraction generates a strongly Lewis acidic titanium center that prefers to bond to a basic TiOW bridging oxygen of another  $[\text{TiW}_5\text{O}_{18}]^{2-}$  anion rather than the solvent MeCN, which is a comparatively weak ligand. The dimeric structure is reminiscent of the cobalt-substituted  $[(\text{CoW}_5\text{O}_{18}\text{H})_2]^{6-}$  shown in Fig. 7A where each of the Co(II) centers is bonded to a basic CoW oxygen from another hexametallate rather than the MeCN solvent (17).

While this dimerization might at first appear to defeat the objective of generating a reactive titanium site, it became apparent that  $[(\text{TiW}_5\text{O}_{18})_2]^{4-}$  is reactive toward water, as the first attempt to crystallize  $(\text{TBA})_4[(\text{TiW}_5\text{O}_{18})_2]$  by slow diffusion of diethyl ether into a solution in MeCN resulted instead in the formation of  $(\text{TBA})_4[(\text{TiW}_5\text{O}_{18}\text{H})_2]$  (Fig. 24). This reaction may be viewed as the heterolytic cleavage of  $\text{H}_2\text{O}$  by two “masked” Lewis acidic Ti sites and their adjacent basic TiOW oxygen sites. It is interesting that the reaction occurs with retention of the  $\{\text{TiW}_5\}$  structural units, despite the fact that in the planar  $\text{Ti}_2\text{O}_2$  unit that links the two halves of the  $[(\text{TiW}_5\text{O}_{18})_2]^{4-}$  anion, the bridging Ti–O distance (1.864 Å) is shorter than the Ti–O bond within the  $\{\text{TiW}_5\}$  Lindqvist unit (2.130 Å). The characterization of the protonated oxo-bridged anion  $[(\mu\text{-O})(\text{TiW}_5\text{O}_{18}\text{H})_2]^{4-}$  prompted a detailed investigation into the controlled protonation of  $[(\mu\text{-O})(\text{TiW}_5\text{O}_{18})_2]^{6-}$ , as described in Section 6, and led to the discovery of new POM ligand behavior highlighted in Section 7.

Metathesis of the Sn–Cl bond in  $(\text{TBA})_3[\text{ClSnW}_5\text{O}_{18}]$  by treatment with NaOMe proceeded as expected to give  $[(\text{MeO})\text{SnW}_5\text{O}_{18}]^{3-}$ , but an attempt



**Fig. 24** Structure of the protonated anion  $[(\mu\text{-O})(\text{TiW}_5\text{O}_{18}\text{H})_2]^{4-}$ . The proton is located at the TiOW oxygens marked with *asterisks*.

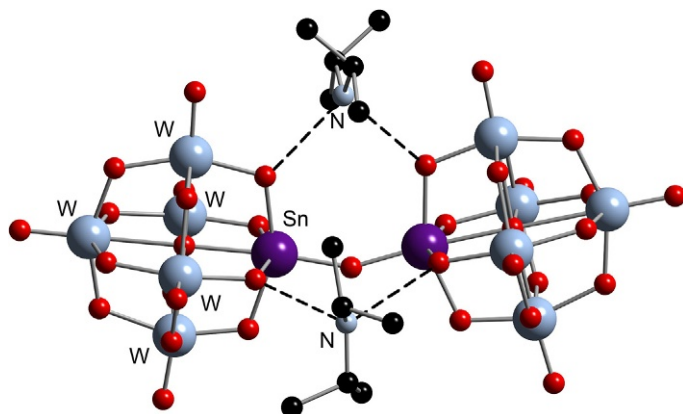


**Fig. 25** Structure of the anion  $[(\mu\text{-O})(\text{SnW}_5\text{O}_{18})_2(\text{H}_2\text{N}^i\text{Pr}_2)_2]^{4-}$ . Hydrogen bonds are indicated by dashed lines.

to generate a tin dialkylamido derivative by treating  $(\text{TBA})_3[\text{ClSnW}_5\text{O}_{18}]$  with  ${}^i\text{Pr}_2\text{NH}$  was less straightforward and resulted instead in the isolation of  $(\text{TBA})_4[(\mu\text{-O})(\text{SnW}_5\text{O}_{18})_2(\text{H}_2\text{N}^i\text{Pr}_2)_2]$ , the structure of which is shown in Fig. 25 (28). The two  ${}^i\text{Pr}_2\text{N}$  fragments occupy the cleft in the oxo-bridged anion structure with  $\text{N}\cdots\text{O}$  distances for each nitrogen (2.688, 2.784 Å and 2.919, 2.769 Å) that are indicative of H bonding. The four hydrogens involved were not located so it is not possible to define exactly the nature of the bonding in this region. The formula of this compound as written indicates that it may be viewed as a mixed-cation salt of the oxo-bridged  $[(\mu\text{-O})(\text{SnW}_5\text{O}_{18})_2]^{6-}$  in which the  ${}^i\text{Pr}_2\text{NH}_2^+$  cations are hydrogen-bonded to four of the basic SnOW sites. However, an alternative formulation might be  $(\text{TBA})_4[(\mu\text{-O})(\text{SnW}_5\text{O}_{18}\text{H})_2(\text{HN}^i\text{Pr}_2)_2]$ , where the diprotonated anion  $[(\mu\text{-O})(\text{SnW}_5\text{O}_{18}\text{H})_2]^{4-}$  is hydrogen-bonded to two  ${}^i\text{Pr}_2\text{NH}$  molecules. The latter mode is related to characterized structures where the diprotonated, oxo-bridged titanotungstate  $[(\mu\text{-O})(\text{TiW}_5\text{O}_{18}\text{H})_2]^{4-}$  forms two hydrogen bonds to an acceptor molecule such as THF or DMSO (Figs. 27 and 30). It is interesting that the addition of  ${}^i\text{Pr}_2\text{NH}$  to  $(\text{TBA})_3[\text{ClSnW}_5\text{O}_{18}]$  appears to promote hydrolysis of the Sn–Cl bond, whereas the chlorido anion does not readily hydrolyze when treated with water alone. This may suggest that the dialkylamido species  $[({}^i\text{Pr}_2\text{N})\text{SnW}_5\text{O}_{18}]^{3-}$  was indeed formed in this reaction but, because of its sensitivity toward hydrolysis, it reacted with traces of moisture to give the oxo-bridged anion.



## 6. STUDIES OF {MW<sub>5</sub>} LINDQVIST ANION PROTONATION

Section 4 described protonolysis of M–OR bonds in [(MeO)MW<sub>5</sub>O<sub>18</sub>]<sup>3−</sup> and [(MeO)MPW<sub>11</sub>O<sub>39</sub>]<sup>4−</sup> anions by HOR where RO<sup>−</sup> binds to M (M = Ti, Sn) upon loss of methanol. In order to probe further the relative basicities of the oxido and X sites in [XMW<sub>5</sub>O<sub>18</sub>]<sup>3−</sup>, [(μ-O)(TiW<sub>5</sub>O<sub>18</sub>)<sub>2</sub>]<sup>6−</sup>, and [(μ-O)(TiPW<sub>11</sub>O<sub>39</sub>)<sub>2</sub>]<sup>8−</sup> <sup>17</sup>O NMR spectroscopy was used to investigate protonation by HBF<sub>4</sub>·Et<sub>2</sub>O where [BF<sub>4</sub>]<sup>−</sup> was expected to act as a noncoordinating anion. Protonation of an oxygen causes its <sup>17</sup>O chemical shift to decrease, but the magnitude of the change in chemical shift is reduced if the proton is delocalized across several equivalent sites (32). In the metal oxide framework of {MW<sub>5</sub>} Lindqvist anions, the MOW sites are expected to be the most basic, but for alkoxido derivatives the MOR group is expected to be protonated because of the significant ionic nature of M–OR bonds (33). It was hoped that nonaqueous acidification studies might be able to show whether any competitive protonation occurs at MOW sites when acid is added to [(MeO)MW<sub>5</sub>O<sub>18</sub>]<sup>3−</sup> or whether the methoxido group is exclusively protonated and lost as methanol. Note that alkoxido sites are not enriched by the hydrolytic synthetic route. Another useful feature of polyoxometalate <sup>17</sup>O NMR spectra is that when the anionic charge is reduced the peaks generally move to higher chemical shifts (and vice versa) (4). Protonation is therefore expected to move all peaks to higher chemical shift *except* for the oxygen sites that are protonated, which will be moved to lower chemical shift. The results of several studies are summarized below (12).

### 6.1 Protonation of (TBA)<sub>3</sub>[(MeO)TiW<sub>5</sub>O<sub>18</sub>]

Addition of 0.5 mole equivalents of a solution of HBF<sub>4</sub>·Et<sub>2</sub>O to (TBA)<sub>3</sub>[(MeO)TiW<sub>5</sub>O<sub>18</sub>] resulted in a general increase in the chemical shifts of peaks in the <sup>17</sup>O NMR spectrum, consistent with the expected decrease in anion charge. Apart from the slight downfield shift from 525 to 532 ppm, no significant change in the TiOW peak was observed until at least 1 mole equivalent of acid had been added, at which point this peak diminished and eventually disappeared to be replaced by a broader peak at about 460 ppm (Fig. 26). This suggests that the addition of 1.0 mole equivalent of acid produces [(MeOH)TiW<sub>5</sub>O<sub>18</sub>]<sup>2−</sup>, which may lose methanol to give [(TiW<sub>5</sub>O<sub>18</sub>)<sub>2</sub>]<sup>4−</sup> (see Section 5). A reaction between (TBA)<sub>3</sub>[(MeO)TiW<sub>5</sub>O<sub>18</sub>] and a THF solution of HBF<sub>4</sub> gave a crystalline product that

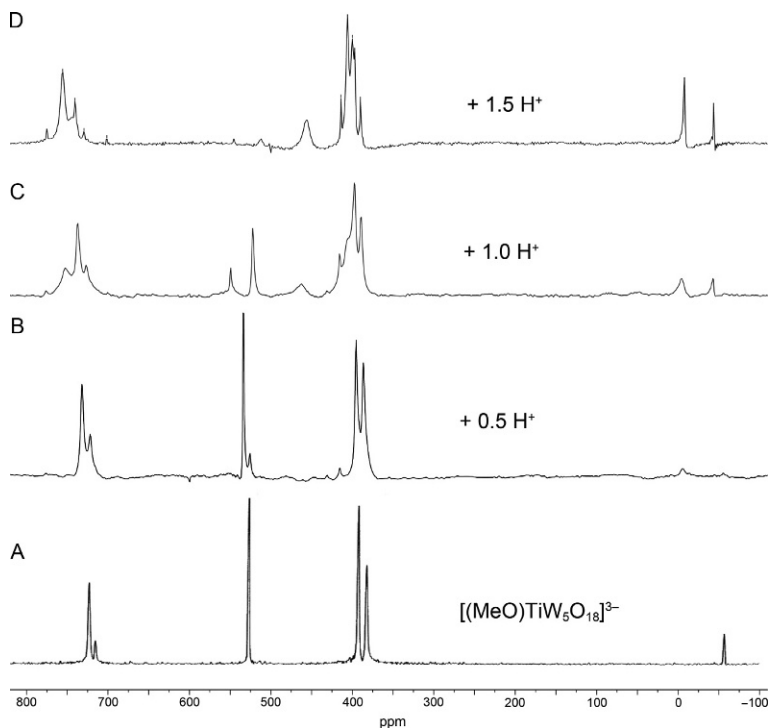


**Fig. 26** (A)  $^{17}\text{O}$  NMR spectrum of  $(\text{TBA})_3[(\text{MeO})\text{TiW}_5\text{O}_{18}]$ ; (B–D) spectra after addition of increasing amounts of  $\text{HBF}_4 \cdot \text{Et}_2\text{O}$ .

contained  $[(\mu\text{-O})(\text{TiW}_5\text{O}_{18}\text{H})_2(\text{THF})]^{4-}$  (Fig. 27), in which THF is doubly hydrogen-bonded to the diprotonated anion. The hydrogen-bonded  $\text{O}\cdots\text{O}$  distances between  $\text{TiOW}$  and THF are 2.676 and 2.716 Å, and the formation of this species may be explained by the initial formation of  $[(\text{TiW}_5\text{O}_{18})_2]^{4-}$ , which then reacts with traces of water as discussed in the previous section. Some decomposition of the  $\{\text{TiW}_5\}$  Lindqvist unit had evidently also occurred, as the anions  $[\text{W}_6\text{O}_{19}]^{2-}$  and  $[\text{W}_{10}\text{O}_{32}]^{4-}$  were also present in the crystal structure.

## 6.2 Protonation of $(\text{TBA})_3[(\text{HO})\text{SnW}_5\text{O}_{18}]$

$^{17}\text{O}$  NMR spectra of the reaction between  $(\text{TBA})_3[(\text{HO})\text{SnW}_5\text{O}_{18}]$  and  $\text{HBF}_4 \cdot \text{Et}_2\text{O}$  were consistent with protonation at the hydroxido group rather than  $\text{SnOW}$  sites. In addition,  $^{119}\text{Sn}$  NMR spectra showed the major product of the reaction to be  $(\text{TBA})_3[\text{FSnW}_5\text{O}_{18}]$ , possibly formed via

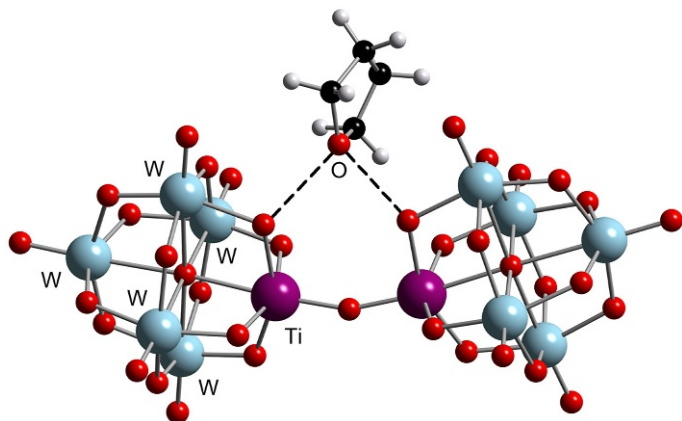


**Fig. 27** Structure of the anion  $[(\mu\text{-O})(\text{TiW}_5\text{O}_{18}\text{H})_2(\text{THF})]^{4-}$ . Hydrogen bonds are indicated by *dashed lines*.

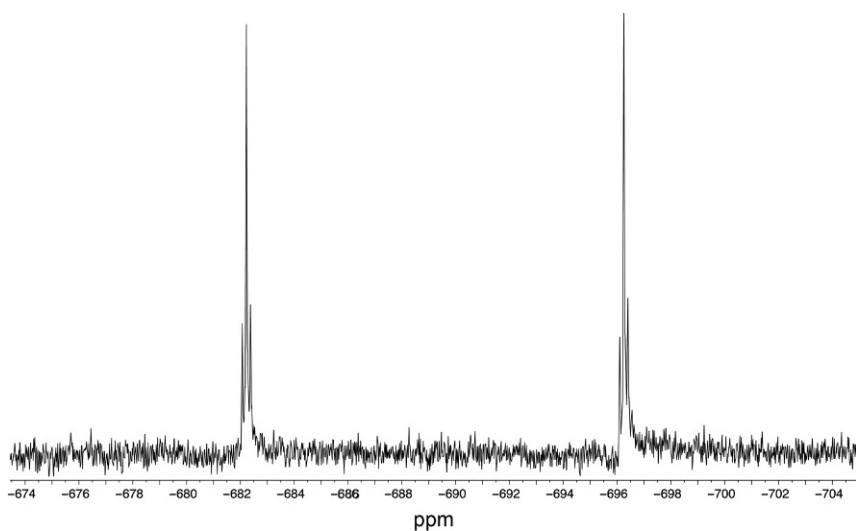


**Fig. 28**  $^{119}\text{Sn}$  NMR spectrum of  $(\text{TBA})_3[\text{FSnW}_5\text{O}_{18}]$ .

fluoride abstraction from  $\text{BF}_4^-$  by the Lewis acidic  $\text{Sn}(\text{IV})$  in  $[\text{SnW}_5\text{O}_{18}]^{2-}$ , the species that would result from protonation of  $[(\text{HO})\text{SnW}_5\text{O}_{18}]^{3-}$  with subsequent loss of water. The  $^{119}\text{Sn}$  chemical shift of  $[\text{FSnW}_5\text{O}_{18}]^{3-}$  is  $-689$  ppm with  $^1J(^{19}\text{F}^{119}\text{Sn})$  and  $^2J(^{119}\text{Sn}^{183}\text{W})$  coupling constants of 2613 and 56 Hz, respectively (Fig. 28).

### 6.3 Protonation of $(\text{TBA})_6[(\mu\text{-O})(\text{TiW}_5\text{O}_{18})_2]$

The serendipitous isolation of diprotonated  $[(\mu\text{-O})(\text{TiW}_5\text{O}_{18}\text{H})_2]^{4-}$  and  $[(\mu\text{-O})(\text{TiW}_5\text{O}_{18}\text{H})_2(\text{THF})]^{4-}$  from reactions involving  $[\text{ClTiW}_5\text{O}_{18}]^{3-}$  and  $[(\text{MeO})\text{TiW}_5\text{O}_{18}]^{3-}$ , respectively, prompted  $^{17}\text{O}$  NMR studies of the protonation of  $(\text{TBA})_6[(\mu\text{-O})(\text{TiW}_5\text{O}_{18})_2]$ . In contrast to the  $^{17}\text{O}$  NMR spectra obtained during the stepwise acidification of  $(\text{TBA})_3[(\text{MeO})\text{TiW}_5\text{O}_{18}]$  and  $(\text{TBA})_3[(\text{HO})\text{SnW}_5\text{O}_{18}]$ , the peak for TiOW 534 ppm in the  $^{17}\text{O}$  NMR spectrum of  $(\text{TBA})_6[(\mu\text{-O})(\text{TiW}_5\text{O}_{18})_2]$  moved upfield immediately upon addition of acid until, after addition of 2 mole equivalents per oxo-bridged dimer, a new TiOW peak was present at 490 ppm (Fig. 29). At the same time, W=O peaks moved from 721 and 713 ppm to 742 and 732 ppm, WOW peaks from 389 and 381 ppm to 401, 395, and 387 ppm, and the peak for the central oxygen from  $-64$  to  $-49$  ppm. These changes were consistent with protonation of the TiOW bridging sites to give an anion with overall lower charge. This reaction appears to be quite clean with very little sign of decomposition to  $[\text{W}_6\text{O}_{19}]^{2-}$  and provides a rational synthesis of the diprotonated derivative directly from the oxo-bridged dimer. Crystals isolated from a reaction carried out in DMSO were characterized by X-ray

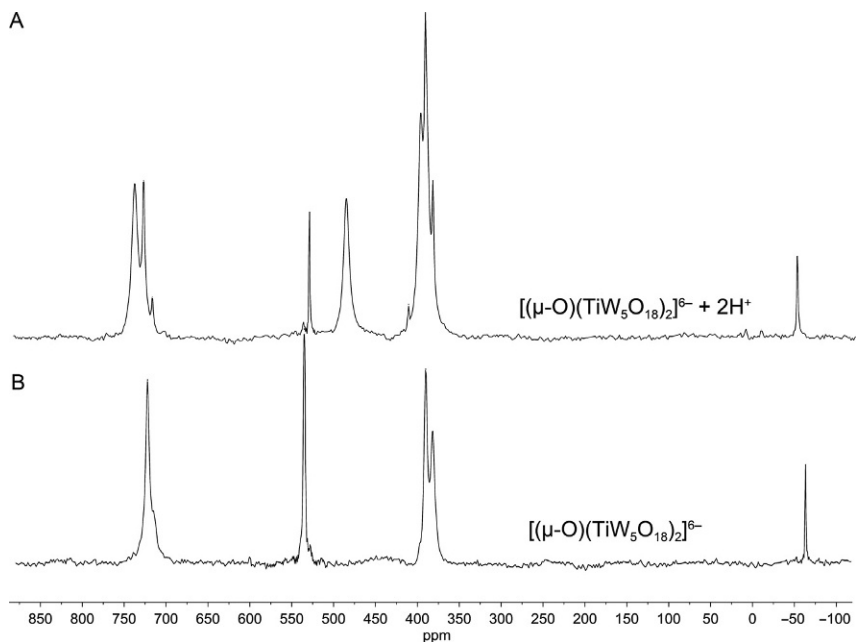


**Fig. 29** (A)  $^{17}\text{O}$  NMR spectrum of  $(\text{TBA})_6[(\mu\text{-O})(\text{TiW}_5\text{O}_{18})_2]$ ; (B) after treatment with 2 mole equivalents of  $\text{HBF}_4 \cdot \text{Et}_2\text{O}$ .



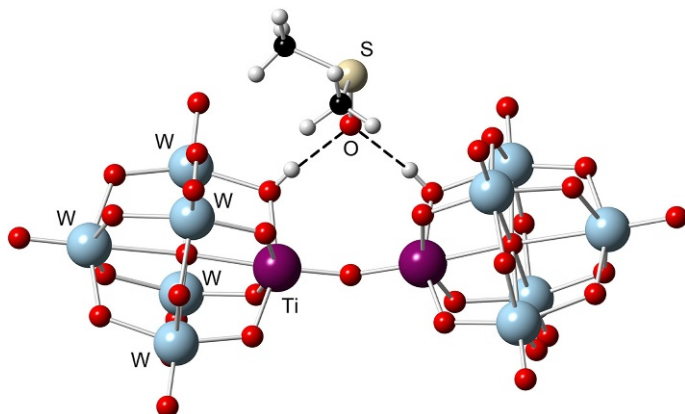
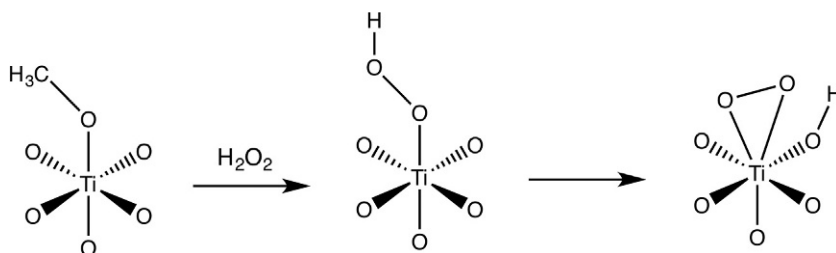


**Fig. 30** Structure of the anion  $[(\mu\text{-O})(\text{TiW}_5\text{O}_{18}\text{H})_2(\text{DMSO})]^{4-}$ . Hydrogen bonds are indicated by *dashed lines*.



**Scheme 1** Reactivity of the Ti–OMe bond in  $(\text{TBA})_3[(\text{MeO})\text{TiW}_5\text{O}_{18}]$  toward  $\text{H}_2\text{O}_2$ .

crystallography, and the structure showed DMSO to be hydrogen-bonded in the cleft of the diprotonated anion in a similar fashion to the THF adduct described above, with hydrogen-bonded  $\text{O}\cdots\text{O}$  distances between  $\text{TiOW}$  and DMSO of 2.615 and 2.674 Å (Fig. 30).

#### 6.4 Protonation Arising From the Reaction Between $(\text{TBA})_3[(\text{MeO})\text{TiW}_5\text{O}_{18}]$ and $\text{H}_2\text{O}_2$

The role of protonation in catalytic alkene epoxidation with  $\text{H}_2\text{O}_2$  and titanium-substituted polyoxometalates has been discussed by Kholdeeva and coworkers (29). The reaction between  $(\text{TBA})_3[(\text{MeO})\text{TiW}_5\text{O}_{18}]$  and aqueous  $\text{H}_2\text{O}_2$  was therefore studied by  $^{17}\text{O}$  NMR in order to establish whether the product from this reaction was a hydroperoxo or peroxo species (Scheme 1) (34). The notable feature of  $^{17}\text{O}$  NMR spectra of the reaction mixture is that the  $\text{TiOW}$  peak is seen to move upfield,

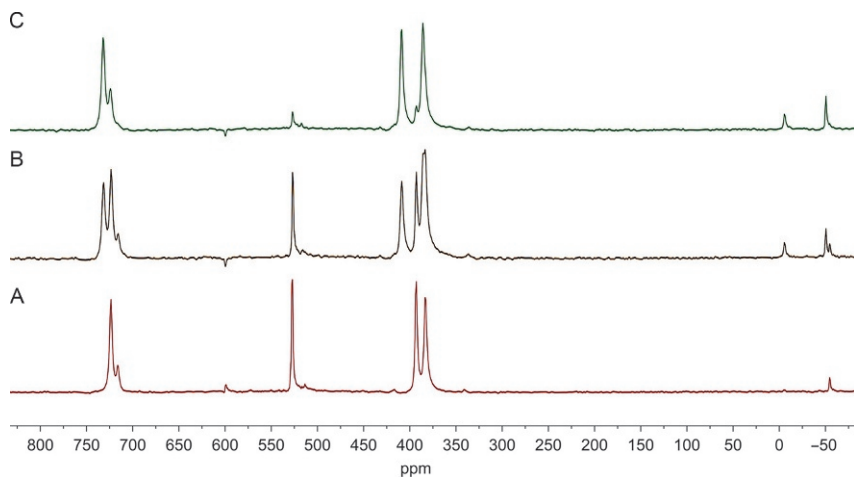


**Fig. 31** (A)  $^{17}\text{O}$  NMR spectrum of  $(\text{TBA})_3[(\text{MeO})\text{TiW}_5\text{O}_{18}]$ ; (B) immediately after addition of 2 mole equivalents of  $\text{H}_2\text{O}_2$ ; (C) 15 min after addition of 2 mole equivalents of  $\text{H}_2\text{O}_2$ .

indicating proton migration from the initially generated hydroperoxy group to TiOW (Fig. 31), which appears to confirm the formation of  $[(\eta^2\text{-O}_2)\text{TiW}_5\text{O}_{18}\text{H}]^{3-}$  in this reaction. This system has been shown to be active for catalytic alkene epoxidation, and results will be published elsewhere.



## 7. LIGAND BEHAVIOR OF $[(\mu\text{-O})(\text{TiW}_5\text{O}_{18})_2]^{6-}$

The apparently clean protonation of  $(\text{TBA})_6[(\mu\text{-O})(\text{TiW}_5\text{O}_{18})_2]$  revealed by  $^{17}\text{O}$  NMR studies and the crystallographic characterization of the diprotonated form  $(\text{TBA})_4[(\mu\text{-O})(\text{TiW}_5\text{O}_{18}\text{H})_2]$  as well as the hydrogen-bonded adducts  $(\text{TBA})_4[(\mu\text{-O})(\text{TiW}_5\text{O}_{18}\text{H})_2(\text{THF})]$  and  $(\text{TBA})_4[(\mu\text{-O})(\text{TiW}_5\text{O}_{18}\text{H})_2(\text{DMSO})]$  prompted us to contemplate the possibility that other electrophiles might bind to the basic TiOW sites of  $[(\mu\text{-O})(\text{TiW}_5\text{O}_{18})_2]^{6-}$  and bridge the central cleft in the oxo-bridged anion. We speculated that it might be possible for a metal to also bond to the TiOTi bridging oxygen, such that the  $[(\mu\text{-O})(\text{TiW}_5\text{O}_{18})_2]^{6-}$  anion would then act as an inorganic  $\text{OOO}^{6-}$  “pincer” ligand. Given the fascinating chemistry of complexes derived from pincer ligands, which has undergone remarkable expansion since the early examples from the Shaw group (35), and the expected noninnocent behavior of POMs when acting as ligands it seemed possible that this system might provide a platform for a host of new metalorganic and organometallic chemistry based on this bi- or

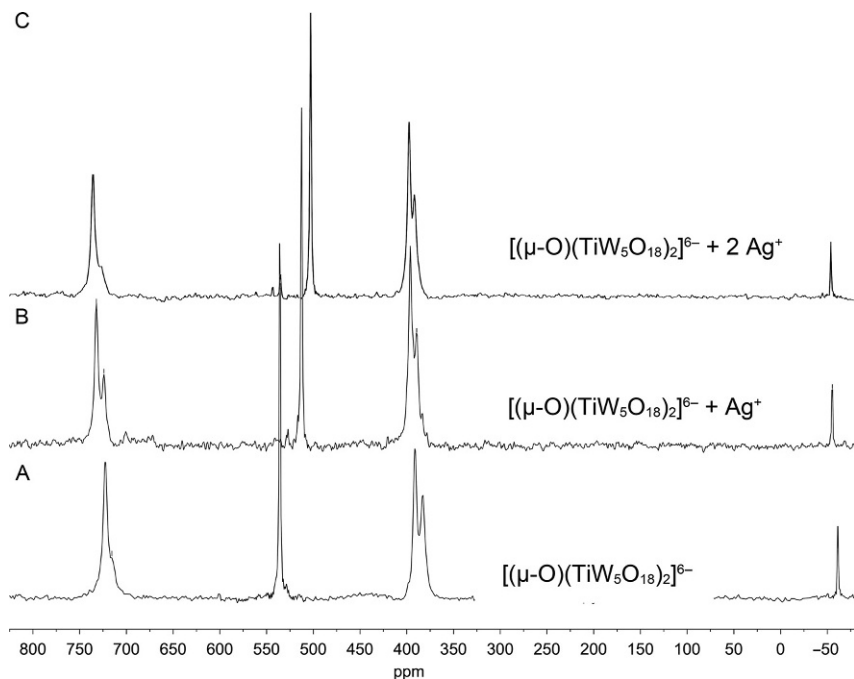


**Fig. 32** (A)  $^{17}\text{O}$  NMR spectrum of  $(\text{TBA})_6[(\mu\text{-O})(\text{TiW}_5\text{O}_{18})_2]$ ; (B) after treatment with 1 mole equivalent of  $\text{AgBF}_4$ ; (C) after treatment with 2 mole equivalents of  $\text{AgBF}_4$ .

tridentate POM ligand. With this in mind we monitored the reactivity of  $(\text{TBA})_6[(\mu\text{-O})(\text{TiW}_5\text{O}_{18})_2]$  toward a range of electrophiles by  $^{17}\text{O}$  NMR spectroscopy (12).

Addition of 1 or 2 mole equivalents of  $\text{AgBF}_4$  to  $(\text{TBA})_6[(\mu\text{-O})(\text{TiW}_5\text{O}_{18})_2]$  caused upfield shifts in the TiOW resonances, showing that  $\text{Ag}^+$  interacts with TiOW sites of the POM (Fig. 32). The observation of a single peak for TiOW suggests that the adducts are dynamic in solution.

Greater upfield shifts were observed upon addition of  $\text{Me}_2\text{SnCl}_2$  to  $(\text{TBA})_6[(\mu\text{-O})(\text{TiW}_5\text{O}_{18})_2]$ , as shown in Fig. 33B, and a peak at 695 ppm was assigned to TiOTi, which is downfield of the TiOTi peak in the  $^{17}\text{O}$  NMR spectrum of  $[(\mu\text{-O})(\text{TiW}_5\text{O}_{18})_2]^{6-}$  (679 ppm). Note that the  $^{17}\text{O}$  enrichment at the TiOTi site, and hence the observed intensity of this peak, is variable. An X-ray crystal structure of the product showed that  $\{\text{Me}_2\text{Sn}\}^{2+}$  had indeed added across the center of the anion, but there was no interaction with the bridging TiOTi (Fig. 34). We reasoned that a suitably electrophilic metal center with a preference for square-planar coordination geometry might also bind to TiOTi within the central cleft,

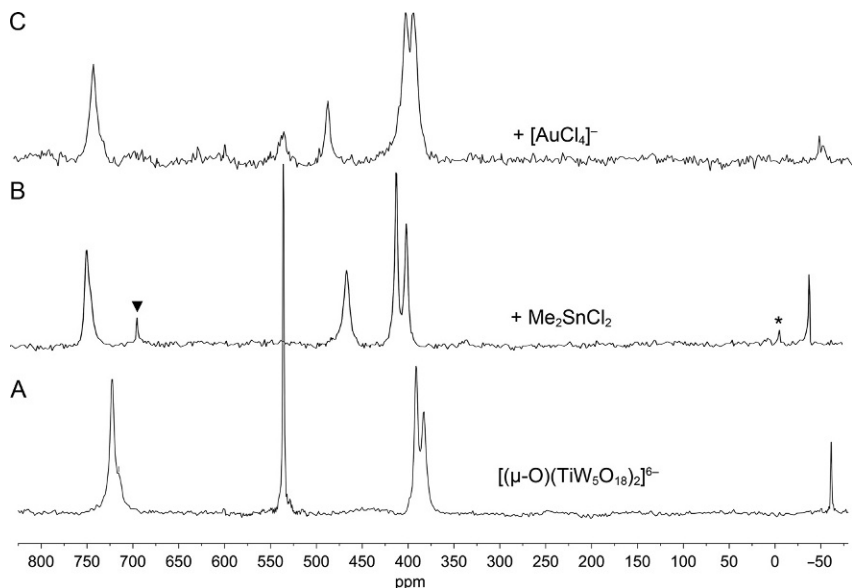


**Fig. 33** (A)  $^{17}\text{O}$  NMR spectrum of  $(\text{TBA})_6[(\mu\text{-O})(\text{TiW}_5\text{O}_{18})_2]$ ; (B) after treatment with  $\text{Me}_2\text{SnCl}_2$ ; (C) after treatment with  $\text{Cs}[\text{AuCl}_4]$ . Peaks marked with  $\blacktriangledown$  or an *asterisk* are assigned to  $\text{TiOTi}$  and  $\text{H}_2\text{O}$ , respectively.

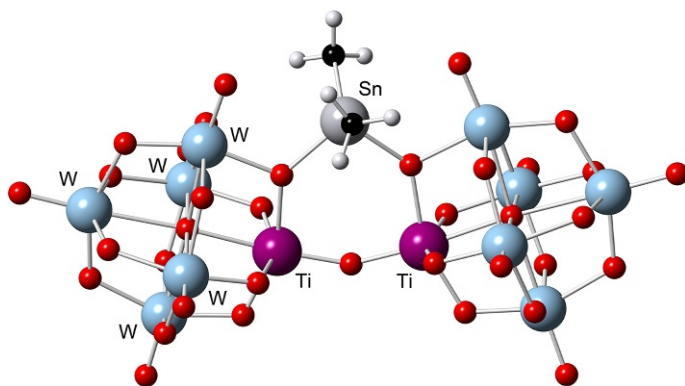


**Fig. 34** Structure of the anion  $[(\mu\text{-O})(\text{TiW}_5\text{O}_{18})_2(\text{SnMe}_2)]^{4-}$ .

and the  $^{17}\text{O}$  NMR spectrum after addition of  $\text{CsAuCl}_4$  to  $(\text{TBA})_6[(\mu\text{-O})(\text{TiW}_5\text{O}_{18})_2]$  showed similar upfield shifts for the  $\text{TiOW}$  resonance to those observed in reactions with two protons or  $\{\text{Me}_2\text{Sn}\}^{2+}$  (Fig. 33C). Calculations by the Poblet group at URV, Tarragona produced a minimum energy configuration for incorporation of  $\{\text{AuCl}\}^{2+}$  into  $[(\mu\text{-O})(\text{TiW}_5\text{O}_{18})_2]^{6-}$  in

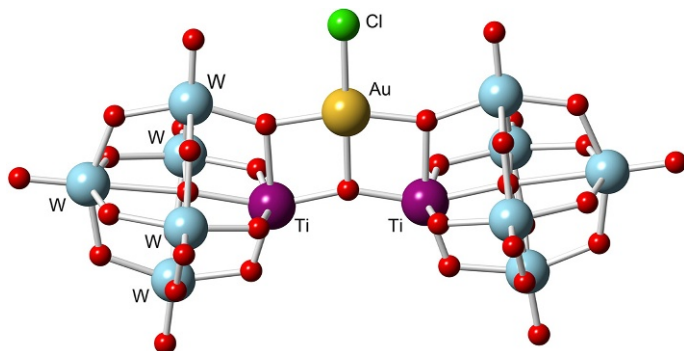


**Fig. 35** Minimum energy structure calculated for  $[(\mu\text{-O})(\text{TiW}_5\text{O}_{18})_2(\text{AuCl})]^{4-}$ .

which square-planar Au(III) is coordinated to two TiOW and the central TiOTi oxygens from the POM (Fig. 35), although the crystal structure of this compound has yet to be determined (16). These  $^{17}\text{O}$  NMR results suggest that the oxo-bridged anion  $[(\mu\text{-O})(\text{TiW}_5\text{O}_{18})_2]^{6-}$  has a general capacity to capture further metal centers in either a chelating or “pincer” fashion. This is a new binding mode for POMs acting as ligands and, unlike the adducts obtained by inserting metal ions into lacunary POMs such as  $[\text{PW}_{11}\text{O}_{39}]^{7-}$ , the oxo-bridged POM occupies only two or three coordination sites, which leaves more sites available for reactivity at the bound metal.

## 8. REDUCTIVE TRANSFORMATIONS

The widespread use of hydrothermal and solvothermal reactions has generated a plethora of new polyoxometalate structures, although it is generally recognized that these methods do not usually provide much control over the course of the reaction and the products. The role of the various components of reaction mixtures is often not understood, and metal salts added as a source of heterometals are frequently found to be crucial for the formation of a specific product, even though the metal itself may not be incorporated into the product. Despite this, products from these reactions can reveal interesting features that might be targeted by design in more controlled reactions.

Reduction is a recurring feature of hydro/solvothermal reactions, and POMs in which electrophilic capping groups are attached to reduced core structures are emerging as building blocks for advanced materials or as components for molecular devices. Inorganic and metalorganic

frameworks based on capped  $\epsilon$ -isomers of reduced Keggin structures are being explored as battery and catalyst materials (36), while bicapped anions  $[\text{PMo}_{12}\text{O}_{40}(\text{V}^{\text{IV}}\text{O})_2]^{n-}$  have been proposed as qubits for molecular spintronics (37). The phosphomolybdate Keggin anion  $[\text{PMo}_{12}\text{O}_{40}]^{3-}$  has a long-established electrochemistry that is being exploited in energy-transfer and -storage applications (38), and superreduction by up to 24 electrons has been proposed to explain the large capacities of batteries containing 10%  $(\text{TBA})_3[\text{PMo}_{12}\text{O}_{40}]$  in the cathode material (39), although such a high degree of reduction has yet to be achieved in solution by chemical rather than electrochemical means.

We therefore set out to investigate rational and reliable methods for the targeted synthesis of capped, electron-rich POMs via controlled reductive aggregation, with the aim of developing a general strategy for the rational assembly of electron-rich POMs. We reasoned that nonaqueous reduction in MeCN in the absence of other ligands would maximize the chance that cations added to the reaction might bind to the surface of the reduced phosphomolybdate, whereas solvation of the cation might compete in aqueous reactions. In addition, direct POM-cation interactions should facilitate reduction of the phosphomolybdate core. Hence, we established that mild, nonaqueous reduction of  $[\text{PMo}_{12}\text{O}_{40}]^{3-}$  with sodium-mercury amalgam as a stoichiometric reducing agent in the presence of  $\text{CoCl}_2$ ,  $\text{VOCl}_3$ , or  $\text{SbCl}_3$  provided access to capped Keggin-type POMs with one or two caps and varying degrees of reduction as in Eqs. (10)–(12) and Fig. 36 (40). The binding of  $\text{Co}^{\text{II}}$  in the two-electron-reduced  $(\text{TBA})_3[\text{PMo}_{12}\text{O}_{40}\{\text{Co}^{\text{II}}(\text{MeCN})_2\}]$  was monitored by the paramagnetically shifted peak for the central phosphorus in the  $^{31}\text{P}$  NMR, and this revealed that  $\text{Co}^{2+}$  dissociates upon reoxidation by one electron. For the vanadyl-capped species, further reduction of the four-electron-reduced core in  $(\text{TBA})_3[\text{PMo}_{12}\text{O}_{40}(\text{V}^{\text{IV}}\text{O})_2]$  to five- and six-electron-reduced derivatives  $[\text{PMo}_{12}\text{O}_{40}(\text{V}^{\text{IV}}\text{O})_2]^{4-}$  and  $[\text{PMo}_{12}\text{O}_{40}(\text{V}^{\text{IV}}\text{O})_2]^{5-}$  was achieved in reactions with sodium-mercury amalgam, which is relevant to the proposal that the  $[\text{PMo}_{12}\text{O}_{40}(\text{V}^{\text{IV}}\text{O})_2]^{x-}$  structure might behave as a molecular spin qubit because of the theoretical magnetism switch involved in the transition from the state with  $x=3$  to states with  $x=4$  or 5 (37). In the antimony-capped compound  $(\text{TBA})_3[\text{PMo}_{12}\text{O}_{40}\text{Sb}_2]$ , no ligands were bound to the capping Sb(III), although long  $\text{Sb}\cdots\text{O}=\text{Mo}$  contacts of 3.21 Å in the crystal structure link the anions into chains (Fig. 36C). In parallel aqueous studies of the diantimony-capped  $[\text{SiMo}_{12}\text{O}_{40}\text{Sb}_2]^{4-}$ , synthesized by a hydrothermal route, it has been shown that the capping Sb(III)

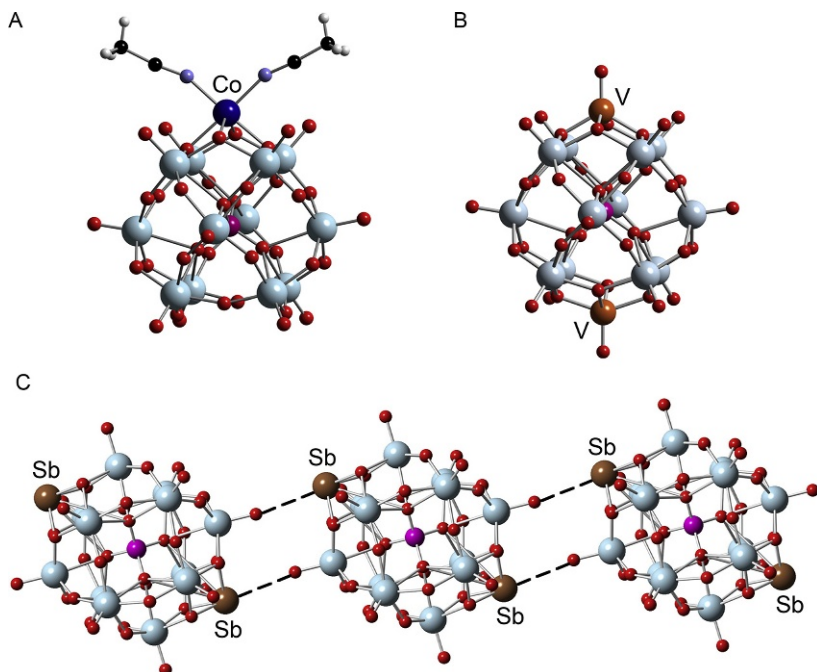
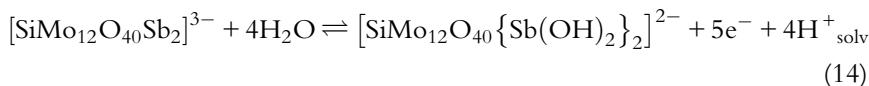
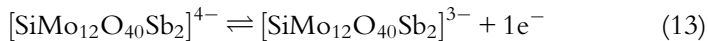
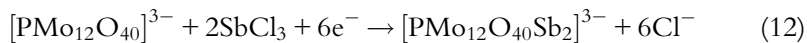
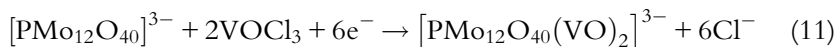
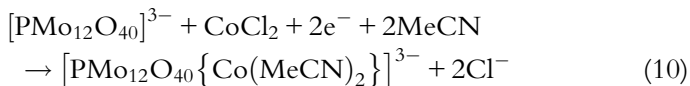


**Fig. 36** Structures of the capped Keggin anions (A)  $[\text{PMo}_{12}\text{O}_{40}\{\text{Co}(\text{MeCN})_2\}]^{3-}$ , (B)  $[\text{PMo}_{12}\text{O}_{40}(\text{VO})_2]^{3-}$ , and (C)  $[\text{PMo}_{12}\text{O}_{40}\text{Sb}_2]^{3-}$ . *Dashed lines* indicate weaker Sb–O interactions leading to an extended 1-D structure.

plays an important role in the electron-transfer properties of the anion, such that oxidation is accompanied by hydrolysis of the Sb(III) during the transfer of six electrons over a narrow potential window via a pH-independent one-electron step (13) followed by a pH-dependent step involving five electrons (14) (41)



In the attempted synthesis of iron-capped derivatives  $[\text{PMo}_{12}\text{O}_{40}(\text{FeL}_2)_2]^{3-}$  by reduction with sodium–mercury amalgam (Eq. 15), the addition of  $\{\text{FeL}_n\}^{x+}$  capping groups was found to be solvent dependent. In acetonitrile, treatment of  $(\text{TBA})_3[\text{PMo}_{12}\text{O}_{40}]$  with 2 mole equivalents of  $\text{FeCl}_2$  and 4 mole equivalents of sodium–mercury amalgam gave the crystallographically characterized  $(\text{TBA})_4[\text{PMo}_{12}\text{O}_{40}\{(\text{FeCl})_2\}]$ , while in DMSO the isolated product was found to be  $(\text{TBA})[\text{PMo}_{12}\text{O}_{40}\{\text{Fe}(\text{DMSO})_2\}_2]$  (Fig. 37) (42). Bond valence sum calculations were indicative of Fe(III) rather than Fe(II) caps in each case, implying that the core had been reduced by five electrons in the case of  $[\text{PMo}_{12}\text{O}_{40}\{(\text{Fe}^{\text{III}}\text{Cl})_2\}]^{4-}$  and four electrons in  $[\text{PMo}_{12}\text{O}_{40}\{\text{Fe}^{\text{III}}(\text{DMSO})_2\}_2]^-$ , although a mixed Fe(II)/Fe(III) formulation with a four-electron-reduced core has yet to be ruled out for the  $\{\text{FeCl}\}$ -capped anion. It appears that the stabilities of the different overall reduction states as well as the distribution of electrons within diiron-capped  $[\text{PMo}_{12}\text{O}_{40}(\text{FeL}_n)_2]^{x-}$  anions are delicately balanced.

Other compatible reducing agent and solvent combinations were explored as alternatives to mercury amalgam reducing agents, and it was found that reduction with metallic magnesium proceeded cleanly to

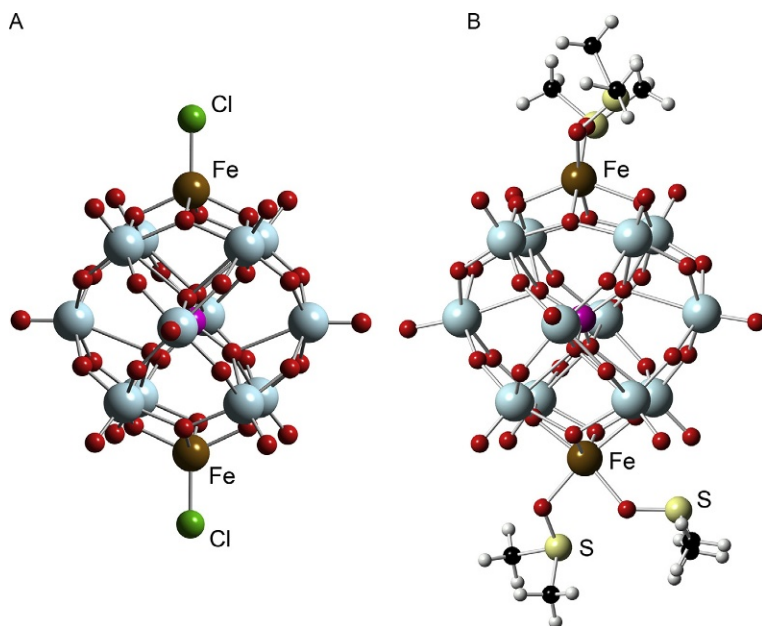


**Fig. 37** Structures of capped Keggin anions (A)  $[\text{PMo}_{12}\text{O}_{40}(\text{FeCl})_2]^{4-}$  and (B)  $[\text{PMo}_{12}\text{O}_{40}\{\text{Fe}(\text{DMSO})_2\}_2]^-$ .



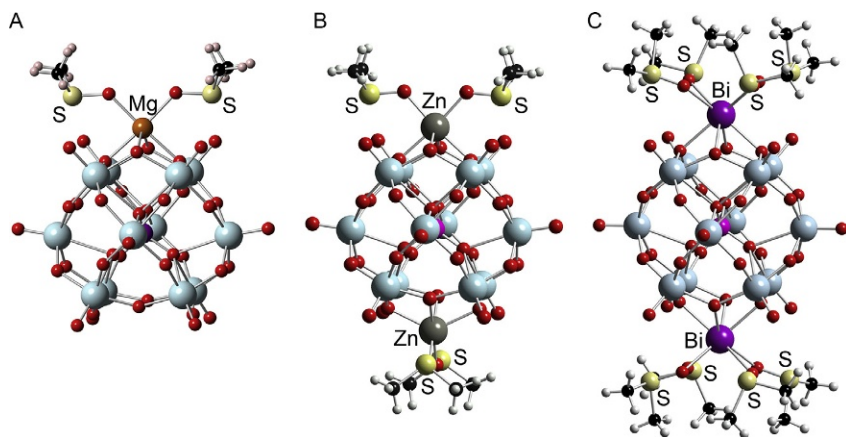


**Fig. 38** Structures of capped Keggin anions: (A)  $[\text{PMo}_{12}\text{O}_{40}\{\text{Mg}(\text{MeCN})_2\}]^{3-}$ ; (B)  $[\text{PMo}_{12}\text{O}_{40}\{\text{Zn}(\text{DMSO})_2\}_2]^{3-}$ ; (C)  $[\text{PMo}_{12}\text{O}_{40}\{\text{Bi}(\text{DMSO})_4\}_2]^{3-}$ .

the two-electron-reduced  $(\text{TBA})_3[\text{PMo}_{12}\text{O}_{40}\{\text{Mg}(\text{DMSO})_2\}]$  in DMSO but not in MeCN (43). In similar reactions, the four-electron-reduced  $(\text{TBA})_3[\text{PMo}_{12}\text{O}_{40}\{\text{Zn}(\text{DMSO})_2\}_2]$  was obtained with zinc in DMSO and the six-electron-reduced  $(\text{TBA})_3[\text{PMo}_{12}\text{O}_{40}\{\text{Bi}(\text{DMSO})_4\}_2]$  was isolated from the reaction with bismuth in DMSO (Fig. 38) (44). Interestingly, only mono- or bicapped anions  $[\text{PMo}_{12}\text{O}_{40}(\text{ML}_n)_z]^{x-}$  ( $z = 1$  or  $2$ ) with a maximum of six-electron reduction of the phosphomolybdate core have been obtained to date, although NMR studies suggest that other species might be accessible if conditions can be optimized.

While the hexamolybdate Lindqvist anion  $[\text{Mo}_6\text{O}_{19}]^{2-}$  has a less extensive redox chemistry than the Keggin anion  $[\text{PMo}_{12}\text{O}_{40}]^{3-}$ , we were interested to explore its nonaqueous chemical reduction. The cyclic voltammogram of  $(\text{TBA})_2[\text{Mo}_6\text{O}_{19}]$  in MeCN shows two reduction waves, the second of which is not reversible (Fig. 39A). The brown one-electron-reduced anion  $[\text{Mo}_6\text{O}_{19}]^{3-}$  has been isolated from electrochemically reduced solutions in organic solvents (45), while in acidified mixed water/acetone solutions,  $\{\text{Mo}^{\text{V}}_2\text{O}_4\}^{2+}$  species have been identified spectroscopically (46). With these observations in mind, we found that the targeted two-electron reduction with magnesium in DMSO produced red-brown solutions upon heating, from which crystals of  $[\text{Mo}_{13}\text{O}_{40}\text{H}_4\{\text{Mg}(\text{DMSO})_3\}_4]_2[\text{Mo}_8\text{O}_{26}]$  were isolated and characterized by X-ray crystallography (43). The cation  $[\text{Mo}_{13}\text{O}_{40}\text{H}_4\{\text{Mg}(\text{DMSO})_3\}_4]^{2+}$  has the  $\epsilon$ - $\{\text{Mo}_{13}\text{O}_{40}\}$  Keggin structure (Fig. 39B), containing eight localized Mo(V) sites with four relatively short  $\text{Mo}^{\text{V}}\cdots\text{Mo}^{\text{V}}$  distances averaging 2.6212(7) Å and four bridging OH groups

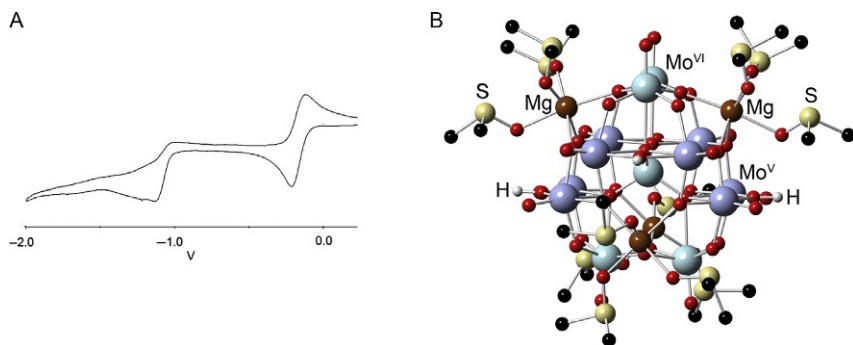


**Fig. 39** (A) Cyclic voltammogram of a  $5 \times 10^{-3}$  M MeCN solution of  $(\text{TBA})_2[\text{Mo}_6\text{O}_{19}]$  with 0.1 M  $(n\text{Bu}_4\text{N})\text{BF}_4$  as supporting electrolyte; glassy carbon working electrode, Pt counter electrode, and Ag/AgCl quasi reference electrode, scan rate  $100 \text{ mV s}^{-1}$ ; (B) structure of the cation  $\epsilon\text{-}[\text{Mo}_{13}\text{O}_{40}\text{H}_4\{\text{Mg}(\text{DMSO})_3\}_4]^{2+}$ .

between the four  $\{\text{Mo}^{\text{V}}_2\}$  units (as revealed by bond valence sums for the bridging oxygen atoms). The formation of  $[\text{Mo}_{13}\text{O}_{40}\text{H}_4\{\text{Mg}(\text{DMSO})_3\}_4]^{2+}$  in this reaction is consistent with the previous detection of  $\{\text{Mo}^{\text{V}}_2\text{O}_4\}^{2+}$  in the electrochemical reduction of acidified solutions of  $[\text{Mo}_6\text{O}_{19}]^{2-}$  as well as the generation of  $\epsilon$ -Keggin structures in hydro/solvothermal reactions of molybdates in the presence of reducing agents. While this nonaqueous approach to the reduction of  $(\text{TBA})_2[\text{Mo}_6\text{O}_{19}]$  is more disruptive than the mild reductive aggregation reactions involving  $[\text{PMo}_{12}\text{O}_{40}]^{3-}$  described above, the approach is being explored as a route to soluble  $\epsilon$ -Keggin building blocks for tailored synthesis of polyoxometalate organic framework (POMOF) materials of the type being explored by researchers at the Institut Lavoisier de Versailles, UVSQ, Versailles (47).



## 9. SUMMARY

This chapter describes how nonaqueous synthesis of substituted polyoxometalates via hydrolytic aggregation from metal alkoxides provides reactive species that are readily enriched in  $^{17}\text{O}$  for detailed solution studies. The methods presented are sufficiently flexible to enable preparation of a family of  $\{\text{XMW}_5\}$  Lindqvist anions for comparative studies and have also been extended to disubstituted  $[(\text{MeO})_3\text{Ti}_2\text{W}_4\text{O}_{16}]^{3-}$ . Through experimental and theoretical DFT studies, the hydrolysis of alkoxido-substituted anions  $[(\text{MeO})\text{MW}_5\text{O}_{18}]^{3-}$  and  $[(\text{MeO})\text{MPW}_{11}\text{O}_{39}]^{4-}$  for  $\text{M} = \text{Ti}$  and  $\text{Sn}$  has led to an full appreciation of the relative stabilities of the various hydroxido

derivatives and oxido-bridged condensation products  $[(\mu\text{-O})(\text{MW}_5\text{O}_{18})_2]^{6-}$  and  $[(\mu\text{-O})(\text{MPW}_{11}\text{O}_{39})_2]^{8-}$ . Halide abstraction from  $\{\text{ClTiW}_5\}$  or protonation of  $\{(\text{MeO})\text{TiW}_5\}$  anions resulted in enhanced Lewis acidity of titanium, and the dimerization and hydrolysis of the resulting  $[\text{TiW}_5\text{O}_{18}]^{2-}$  species serve to highlight the dual Lewis acid–Lewis base reactivity. Nonaqueous protonation studies also led to the discovery of chelating and potential pincer-type ligand properties of the oxo-bridged  $[(\mu\text{-O})(\text{TiW}_5\text{O}_{18})_2]^{6-}$ .

The search for mild, reliable methods for the synthesis of electron-rich polyoxometalates has led to the preparation of a series of mono- and bicapped Keggin anions  $[\text{PMo}_{12}\text{O}_{40}(\text{ML}_n)_z]^{x-}$  having central oxometalate cores with variable degrees of reduction, thus providing a platform for magnetic and electronic investigations and the preparation of functional oxide materials. The degradation of  $(\text{TBA})_2[\text{Mo}_6\text{O}_{19}]$  during reduction with magnesium in DMSO to give  $\varepsilon\text{-}[\text{Mo}_{13}\text{O}_{40}\text{H}_4\{\text{Mg}(\text{DMSO})_3\}_4]^{2+}$  suggests that the rational synthesis of soluble  $\varepsilon$ -Keggin structures may be possible, and might provide mild routes to electron-rich metal oxide framework materials based on these building blocks.

The work described here demonstrates the benefits of nonaqueous methods for the study of molecular metal oxides, where proton-transfer reactions must be considered and redox reactivity may be coupled with hydrolytic processes in the presence of water.

## ACKNOWLEDGMENTS

This chapter is testament to the efforts of current and former PhD students Balamurugan Kandasamy, Thompson Izuagie, Daniel Lebbie, and Gavin Harle, former undergraduate students Eleanor Balme and Leticia Prince, COST Short Term Scientific Mission visitors Magda Pascual Borrás (URV, Tarragona), William Salomon (Institut Lavoisier, UVSQ, Versailles) Yan Duan (ICMol, Univ. of Valencia), Sergey Adonin (Nikolaev Institute of Inorganic Chemistry, Novosibirsk), and Nataliya Maksimchuk (Borekov Institute of Catalysis, Novosibirsk). I am grateful to COST Action CM1203 (Polyoxometalate Chemistry for Molecular Nanoscience, PoCheMoN) for the award of funds for STSMs supported by COST (European Collaboration in Science and Technology) and to Dr. Corinne Wills and Prof. William McFarlane for assistance with NMR experiments.

## REFERENCES

1. (a) Pope, M. T.; Müller, A. *Angew. Chem. Int. Ed.* **1991**, *30*, 34–48; (b) Müller, A.; Polarz, S.; Das, S. K.; Krickmeyer, E.; Bögge, H.; Schmidtmann, M.; Hauptfleisch, B. *Angew. Chem. Int. Ed.* **1999**, *38*, 3241–3245; (c) Schäffer, C.; Todea, A. M.; Gouzerh, P.; Müller, A. *Chem. Commun.* **2012**, *48*, 350–352; (d) Zhan, C.-H.; Winter, R. S.; Zheng, Q.; Yan, J.; Cameron, J. M.; Long, D.-L.; Cronin, L. *Angew. Chem. Int. Ed.* **2015**, *54*, 14308–14312; (e) Minato, T.; Suzuki, K.; Yamaguchi, K.; Mizuno, N. *Angew. Chem. Int. Ed.* **2016**, *55*, 9630–9633.

2. (a) Pope, M. T. *Heteropoly and Isopoly Oxometalates*; Springer-Verlag: Berlin, 1983; (b) Secheresse, F., Ed. *World Series in Nanoscience and Nanotechnology*, Vol. 8; *Polyoxometalate Chemistry: Some Recent Trends*; World Scientific: Singapore, 2013; (c) Ruhlmann, L., Schaming, D., Eds. *Trends in Polyoxometalates Research*; Nova Science Publishers, Inc.: United States, 2015.
3. (a) Meiklejohn, P. T.; Pope, M. T.; Prados, R. A. *J. Am. Chem. Soc.* **1974**, *96*, 6779–6781; (b) Ho, R. K. C.; Klemperer, W. G. *J. Am. Chem. Soc.* **1978**, *100*, 6772–6774; (c) Katsoulis, D. E.; Pope, M. T. *J. Am. Chem. Soc.* **1984**, *106*, 2737–2738; (d) Day, V. W.; Klemperer, W. G. *Science* **1985**, *228*, 533–541.
4. (a) English, A. D.; Jesson, J. P.; Klemperer, W. G.; Mamouneas, T.; Messerle, L.; Shum, W.; Tramontano, A. *J. Am. Chem. Soc.* **1975**, *97*, 4785–4786; (b) Filowitz, M.; Klemperer, W. G. *J. Chem. Soc. Chem. Commun.* **1976**, 233–234; (c) Filowitz, M.; Klemperer, W. G.; Messerle, L.; Shum, W. *J. Am. Chem. Soc.* **1976**, *98*, 2345–2346; (d) Filowitz, M.; Ho, R. K. C.; Klemperer, W. G.; Shum, W. *Inorg. Chem.* **1979**, *18*, 93–103; (e) Besecker, C. J.; Klemperer, W. G.; Maltbie, D. J.; Wright, D. A. *Inorg. Chem.* **1985**, *24*, 1027–1032.
5. Jahr, K. F.; Fuchs, J.; Oberhauser, R. *Chem. Ber.* **1968**, *101*, 477–481.
6. Clegg, W.; Elsegood, M. R. J.; Errington, R. J.; Havelock, J. J. *Chem. Soc. Dalton Trans.* **1996**, 681–690.
7. (a) Errington, R. J.; Petkar, S. S.; Middleton, P. S.; McFarlane, W.; Clegg, W.; Coxall, R. A.; Harrington, R. W. *J. Am. Chem. Soc.* **2007**, *129*, 12181–12196; (b) Errington, R. J.; Petkar, S. S.; Middleton, P. S.; McFarlane, W.; Clegg, W.; Coxall, R. A.; Harrington, R. W. *Dalton Trans.* **2007**, 5211–5222; (c) Coyle, L.; Middleton, P. S.; Murphy, C. J.; Clegg, W.; Harrington, R. W.; Errington, R. J. *Dalton Trans.* **2012**, *41*, 971–981.
8. Coquentif, A.; Maksimchuk, N.; Errington, R.J. unpublished results.
9. Klemperer, W. G.; Shum, W. *J. Am. Chem. Soc.* **1978**, *100*, 4891–4893.
10. Kandasamy, B.; Wills, C.; McFarlane, W.; Clegg, W.; Harrington, R. W.; Rodriguez-Fortea, A.; Poblet, J. M.; Bruce, P. G.; Errington, R. J. *Chem. Eur. J.* **2012**, *18*, 59–62.
11. (a) Errington, R. J. In *Comprehensive Coordination Chemistry II*, Vol. 2, Elsevier: Amsterdam, 2003; pp 759–773; (b) Errington, R. J. In *Polyoxometalate Molecular Science*; Borrás-Almenar, J. J., Coronado, E., Müller, A., Pope, M. T., Eds.; Kluwer: Dordrecht, 2003; pp 55–77; (c) Errington, R. J. In *Polyoxometalate Chemistry: From Topology via Self-Assembly to Applications*; Pope, M. T., Müller, A., Eds.; Kluwer: Dordrecht, 2001; pp 1–22.
12. Lebbie, D.; Errington, R.J. unpublished results.
13. (a) Rinfrey, C.; Brasiliense, V.; Izzet, G.; Volatron, F.; Alves, S.; Combellas, C.; Kanoufi, F.; Proust, A. *Inorg. Chem.* **2016**, *55*, 6929–6937; (b) Yaqub, M.; Walsh, J. J.; Keyes, T. E.; Proust, A.; Rinfrey, C.; Izzet, G.; McCormac, T.; Forster, R. *Langmuir* **2014**, *30*, 4509–4516.
14. Krebs, B.; Klein, R. In *Polyoxometalates: From Platonic Solids to Anti-Retroviral Activity*; Pope, M. T., Müller, A., Eds.; Kluwer: Dordrecht, The Netherlands, 1994; p 41.
15. Belai, N.; Pope, M. T. *Polyhedron* **2006**, *25*, 2015–2020.
16. Pascual-Borrás, M.; Poblet, J.M.; Errington, R.J. unpublished results.
17. Errington, R. J.; Harle, G.; Clegg, W.; Harrington, R. W. *Eur. J. Inorg. Chem.* **2009**, 5240–5246.
18. (a) Delley, M. F.; Nunez-Zarur, F.; Conley, M. P.; Comas-Vives, A.; Siddiqi, G.; Norsic, S.; Monteil, V.; Safonova, O. V.; Copéret, C. *Proc. Natl. Acad. Sci. U.S.A.* **2014**, *111*, 11624–11629; (b) Conley, M. P.; Delley, M. F.; Nunez-Zarur, F.; Comas-Vives, A.; Copéret, C. *Inorg. Chem.* **2015**, *54*, 5065–5078.

19. Clegg, W.; Errington, R. J.; Fraser, K. A.; Richards, D. G. *J. Chem. Soc. Chem. Commun.* **1993**, 1105–1107.
20. (a) Maksimovskaya, R. I.; Burtseva, K. G. *Polyhedron* **1985**, *4*, 1559–1562; (b) Hastings, J. J.; Howarth, O. W. *J. Chem. Soc. Dalton Trans.* **1992**, 209–215.
21. (a) Tourné, C. C. R. *Hebd. Seanc. Acad. Sci. Ser. C* **1968**, *266*, 702; (b) Tourné, C.; Tourné, G. *Bull. Soc. Chim. Fr.* **1969**, *4*, 1124; (c) Ho, R.K.C., PhD Thesis, Columbia University, 1979; (d) Radkov, E.; Beer, R. H. *Polyhedron* **1995**, *14*, 2139–2143.
22. Izuagie, T.; Errington, R.J. unpublished results.
23. Knoth, W. H.; Domaille, P. J.; Roe, D. C. *Inorg. Chem.* **1983**, *22*, 198–201.
24. Chorghade, G. S.; Pope, M. T. *J. Am. Chem. Soc.* **1987**, *109*, 5134–5138.
25. Tourné, G. F.; Tourné, C. M.; Schouten, A. *Acta Cryst.* **1982**, *B38*, 1414–1418.
26. Klonowski, P.; Goloboy, J. C.; Uribe-Romo, F. J.; Sun, F.; Zhu, L.; Gandara, F.; Wills, C.; Errington, R. J.; Yaghi, O. M.; Klemperer, W. G. *Inorg. Chem.* **2014**, *53*, 13239–13246.
27. (a) Day, V. W.; Eberspacher, T. A.; Klemperer, W. G.; Park, C. W.; Rosenberg, F. S. *J. Am. Chem. Soc.* **1991**, *113*, 8190–8192; (b) Day, V. W.; Eberspacher, T. A.; Klemperer, W. G.; Park, C. W. *J. Am. Chem. Soc.* **1993**, *115*, 8469–8470.
28. Kandasamy, B.; Errington, R.J. unpublished results.
29. (a) Kholdeeva, O. A.; Maksimov, G. M.; Maksimovskaya, R. I.; Kovaleva, L. A.; Fedotov, M. A.; Grigoriev, V. A.; Hill, C. L. *Inorg. Chem.* **2000**, *39*, 3828–3837; (b) Kholdeeva, O. A.; Trubitsina, T. A.; Maksimovskaya, R. I.; Golovin, A. V.; Neiwert, W. A.; Kolesov, B. A.; Lopez, X.; Poblet, J. M. *Inorg. Chem.* **2004**, *43*, 2284–2292; (c) Kholdeeva, O. A.; Trubitsina, T. A.; Maksimov, G. M.; Golovin, A. V.; Maksimovskaya, R. I. *Inorg. Chem.* **2005**, *44*, 1635–1642; (d) Maksimov, G. M.; Maksimovskaya, R. I.; Kholdeeva, O. A.; Fedotov, M. A.; Zaikovskii, V. I.; Vasil'ev, V. G.; Arzumanov, S. S. *J. Struct. Chem.* **2009**, *50*, 618–627; (e) Kholdeeva, O. A. *Eur. J. Inorg. Chem.* **2013**, 1595–1605.
30. Matsuki, Y.; Mouri, Y.; Sakai, Y.; Matsunaga, S.; Nomija, K. *Eur. J. Inorg. Chem.* **2013**, 1754–1761.
31. Balme, E.; Errington, R.J. unpublished results.
32. Pascual-Borràs, M.; Rodríguez-Forteza, A.; Errington, R. J.; Poblet, J. M. *Chem. Sci.* **2014**, *5*, 2031–2042.
33. (a) Bradley, D. C.; Mehrotra, R. C.; Gaur, D. P. *Metal Alkoxides*; Academic Press: London, 1978; (b) Bradley, D. C.; Mehrotra, R. C.; Rothwell, I. P.; Singh, A. *Alkoxo and Aryloxo Derivatives of Metals*; Academic Press: London, 2001.
34. Maksimchuk, N.; Errington, R.J. unpublished results.
35. (a) Moulton, C. J.; Shaw, B. L. *J. Chem. Soc. Dalton Trans.* **1976**, 1020–1024; (b) Crocker, C.; Errington, R. J.; McDonald, W. S.; Odell, K. J.; Shaw, B. L.; Goodfellow, R. J. *J. Chem. Soc. Chem. Commun.* **1979**, 498–499; (c) Errington, R. J.; McDonald, W. S.; Shaw, B. L. *J. Chem. Soc. Dalton Trans.* **1980**, 2312–2314.
36. (a) Mialane, P.; Dolbecq, A.; Lisnard, L.; Mallard, A.; Marrot, J.; Sécheresse, F. *Angew. Chem. Int. Ed.* **2002**, *41*, 2398–2401; (b) Dolbecq, A.; Mialane, P.; Lisnard, L.; Marrot, J.; Sécheresse, F. *Chem. Eur. J.* **2003**, *9*, 2914–2920; (c) Zhang, Z.; Sadakane, M.; Murayama, T.; Izumi, S.; Yasuda, N.; Sagaguchi, N.; Ueda, W. *Inorg. Chem.* **2014**, *53*, 903–911; (d) Zhang, Z.; Ishikawa, S.; Tsuboi, Y.; Sadakane, S.; Murayama, T.; Ueda, W. *Farad. Discuss.* **2016**, *188*, 81–98; (e) Zhang, Z.; Yoshikawa, H.; Zhang, Z.; Murayama, T.; Sadakane, M.; Inoue, Y.; Ueda, W.; Awaga, K.; Hara, M. *Eur. J. Inorg. Chem.* **2016**, 1242–1250.
37. (a) Lehmann, J.; Gaita-Arino, A.; Coronado, E.; Loss, D. *J. Mater. Chem.* **2009**, *19*, 1672–1677; (b) Lehmann, J.; Gaita-Arino, A.; Coronado, E.; Loss, D. *Nat. Nanotechnol.* **2007**, *2*, 312–317.

38. (a) Yamada, A.; Goodenough, J. B. *J. Electrochem. Soc.* **1998**, *145*, 737–743; (b) Sonoyama, N.; Suganuma, Y.; Kume, T.; Quan, Z. *J. Power Sources* **2011**, *196*, 6822–6827; (c) Zhao, X.; Zhu, J. Y. *ChemSusChem* **2016**, *9*, 197–207.
39. (a) Nishimoto, Y.; Yokogawa, D.; Yoshikawa, H.; Awaga, K.; Irle, S. *J. Am. Chem. Soc.* **2014**, *136*, 9042–9052; (b) Wang, H.; Hamanaka, S.; Nishimoto, Y.; Irle, S.; Yokoyama, T.; Yoshikawa, H.; Awaga, K. *J. Am. Chem. Soc.* **2012**, *134*, 4918–4924.
40. Bakri, R.; Booth, A.; Harle, G.; Middleton, P. S.; Wills, C.; Clegg, W.; Harrington, R. W.; Errington, R. J. *Chem. Commun.* **2012**, *48*, 2279–2781.
41. Canioni, R.; Cadot, E.; Errington, R.J.; Leclerc-Laronze, N.; Roche-Marchal, C. *Curr. Inorg. Chem.* submitted.
42. Harle, G.; Yildiz, C.; Errington, R.J. unpublished results.
43. Prince, L.B.; Errington, R.J. unpublished results.
44. Adonin, S.; Yidiz, C.; Errington, R.J. unpublished results.
45. Che, M.; Fournier, M.; Launay, J. P. *J. Chem. Phys.* **1979**, *71*, 1954.
46. Osakai, T.; Himeno, S.; Saito, A.; Hori, T. *J. Electroanal. Chem.* **1990**, *285*, 209–221.
47. (a) Dolbecq, A.; Mellot-Draznieks, C.; Mialane, P.; Marrot, J.; Férey, G.; Sécheresse, F. *Eur. J. Inorg. Chem.* **2005**, 3009–3018; (b) Nohra, B.; El Moll, H.; Rodriguez Albelo, L. M.; Mialane, P.; Marrot, J.; Mellot-Draznieks, C.; O’Keefe, M.; Ngo Bilboum, R.; Lemaire, J.; Keita, B.; Nadjo, L.; Dolbecq, A. *J. Am. Chem. Soc.* **2011**, *133*, 13363–13374.

# INDEX

Note: Page numbers followed by “*f*” indicate figures, “*t*” indicate tables, and “*s*” indicate schemes.

## A

- Aerobic oxidation
  - molecular oxygen, 68–69
  - of organic compounds, 68–70
  - oxygen donors, 68–69
  - peroxides, 68–69
  - Wacker-type reactions, 69–70
- Alcohol interchange, 310–311
- Alkali counterions, in POM macroions, 47–49
- Alkoxido metathesis, 311–312
- Amino-functionalized Keggin-type cluster, 199–200
- Anisotropic surface charge density distribution, 41–42
- Artificial photosynthesis. *See* Solar fuel production

## B

- Benzothiophene polymerization, 76s
- Blackberry membrane, POM macroions
  - cation transportation, 49–50, 50f
  - driving force for, 35–37, 36f
  - self-assembly into, 33–35
- Blackberry moieties, 19–20
- Born-Oppenheimer approximation, 219–220
- Bromate sensors, 205–206

## C

- Capped Keggin anions, 329–331f
- Carbon-metal bond, oxygen insertion, 84–85
- Carbon nanotubes (CNTs)
  - functionalization of, 193f
  - and graphene, 182–183, 186–188
- Cation transportation, blackberry membrane, 49–50, 50f
- Chlorido {ClMW<sub>5</sub>} lindqvist anion, synthesis and reactivity, 315–318

- $[\text{Co}_9(\text{H}_2\text{O})_6(\text{OH})_3(\text{HPO}_4)_2(\text{PW}_9\text{O}_{34})_3]16^-$  catalysts
  - characterization with NACLO, 161–165 and cobalt oxide, 174–175
  - homogeneous electrocatalytic water oxidation activity, 158–161
  - long-term stability, 164–165, 165t
  - molecular representation, 158f
  - speciation
    - carbon paste electrodes, 171–176, 173f
    - catalytic oxygen evolution conditions, 169–171
    - on pH, 168, 169t
    - in water and phosphate buffer, 166–168
- Cobalt-substituted {CoW<sub>5</sub>} derivatives, 294–298, 297f
- Coulombic repulsion, 220–221
- Counterion-mediated self-assembly, POM macroions
  - anisotropic surface charge density distribution, 41–42
  - blackberry formation, driving force for, 35–37, 36f
  - distance distribution functions, 38f
  - distribution, 37–39
  - exchange, 37–39
  - human papilloma virus, 44–45
  - hydrogen bonding effect, 42
- Counterions
  - alkali counterions in POM macroions, 47–49
  - POM-counterion ion pairing, 45–47, 46f

## D

- Dawson-based clusters, 16
- Debye-Huckel theory, 30, 35
- Density functional theory (DFT), 80–82
- Derjaguin-Landau-Verwey-Overbeek (DLVO) theory, 30
- Dibenzothiophene polymerization, 76s

- Direct methanol fuel cells (DMFCs), 188–190
- Dititanium-substituted *as*-{Ti<sub>2</sub>W<sub>4</sub>} derivative, 289–291, 290*f*
- Dynamic light scattering (DLS) measurements  
[Co<sub>9</sub>(H<sub>2</sub>O)<sub>6</sub>(OH)<sub>3</sub>(HPO<sub>4</sub>)<sub>2</sub>(PW<sub>9</sub>O<sub>34</sub>)<sub>3</sub>]<sup>16-</sup> catalysts, 164  
CONTIN analysis, 33–35  
discrete anionic clusters by, 19–20  
POM macroions, 33–35  
self-assembly, 56–57
- E**
- Electrocatalysis  
electrochemical methanol oxidation tests, 193–194  
electrochemical reactions, 191*f*  
methanol oxidation, 188–194, 193*f*  
oxygen reduction, 194–196  
water oxidation, 186–188, 187*f*
- Electrochemical metallization memories (ECM), 278
- Electron-coupled proton buffer (ECPB), 120–121
- Electron transfer oxidations,  
H<sub>5</sub>PV<sub>2</sub>Mo<sub>10</sub>O<sub>40</sub> polyoxometalate and, 70–71
- Electron transfer-oxygen transfer, catalyzed by H<sub>5</sub>PV<sub>2</sub>Mo<sub>10</sub>O<sub>40</sub>, 72–73
- Energy storage  
lithium ion batteries, 197–202, 201*f*  
supercapacitors, 202–203, 203*f*
- F**
- First quantum revolution, 236
- G**
- Graphene  
carbon nanotubes and, 182–183, 186–188  
with organic cations, 189*f*
- H**
- Heteropolyoxoniobate, 134–136
- H<sub>5</sub>PV<sub>2</sub>Mo<sub>10</sub>O<sub>40</sub> polyoxometalate  
aerobic oxidative dehydrogenation, 71*s*  
benzothiophene polymerization catalyzed by, 76*s*  
dibenzothiophene polymerization catalyzed by, 76*s*  
and electron transfer oxidations, 70–71  
electron transfer-oxygen transfer catalyzed by, 72–73  
isomers, 71*f*  
oxidation  
of primary and vicinal alcohols, 76–79  
of sulfides, 73–75, 75*f*  
via activation of C–H bonds revisited, 79–84  
redox potential of, 81*f*  
structure during catalytic reaction, 85–87  
vanadium atoms, 70–71, 86
- Hydration layer in of U<sub>60</sub>, 51–53, 52*f*
- Hydrocarbons, 69–70
- Hydrogen peroxide sensors, 205
- Hydrolysis  
{(MeO)MPW<sub>11</sub>} Keggin anions, 309–310, 309*f*  
{(MeO)MW<sub>5</sub>} lindqvist anions, 305–308  
(TBA)<sub>3</sub> [(MeO)SnW<sub>5</sub>O<sub>18</sub>], 306
- Hydrolytic assembly process, 298–299, 300*f*
- I**
- Inelastic Neutron Scattering (INS), 218–219
- Inorganic chemical cells (iCHELLs), 22–24
- Iodate sensors, 205–206
- Ion selectivity of U<sub>60</sub>, 53–56
- J**
- Jahn-Teller (JT) systems, 220–221
- K**
- Keggin anions, capped, 329–331*f*
- Keggin-type heterometalates  
<sup>17</sup>O NMR spectrum, 301–302*f*  
platinum(IV)-substituted PtSiW<sub>11</sub> anion, 303  
tin(II)- and lead(II)-substituted MPW<sub>11</sub> derivatives, 303  
titanium(IV)- and tin(IV)-substituted MPW<sub>11</sub> derivatives, 301–303



**L**

Lanthanoids, 215–216

Lindqvist-type heterometalates

cobalt-substituted  $\{\text{CoW}_5\}$  derivatives,  
294–298

dititanium-substituted cis- $\{\text{Ti}_2\text{W}_4\}$   
derivative, 289–291

hydrolytic assembly process, 298–299

tin-substituted  $\{\text{SnW}_5\}$  derivatives,  
291–294

Lithium ion batteries, 197–202, 201*f*

**M**

Magnetic polyoxometalates

acetate-supported spin ring, 264*f*

advantages, 260–277

anisotropic environment effects, 263–270

anisotropic spin cluster, 265

classical/nonclassical polyoxometalate

hybrid structures, 273–276

CONDON analysis, 268–270

controlled molecule–nanoelectrode

contacts, 270–277

in-phase ac molar susceptibility, 268*f*

isotropic spin cluster, 263, 270

magnetically anisotropic spin cluster, 268

$\{\text{Mn}^{\text{III}}3\text{Mn}^{\text{IV}}\text{O}_4\text{-P}_2\text{W}_{15}\}$  molecular  
structure, 266, 267*f*

$\{\text{Mn}_{40}\text{W}_{224}\}$  polyanions structure, 274*f*

$\{\text{Mn}_{40}\text{W}_{224}\}$  self-assembly, 275*f*

polyanion structure, 269*f*

rational design and processability, 224–232

redox-based resistive switching, 277–282

spin-orbit coupling, 270

static magnetic susceptibility data for,  
266–268

super-cluster structure, 272–273

temperature and field dependence, 271*f*

three-terminal molecular transistor  
architecture, 273*f*

MAI<sub>2</sub> cations

metastable intermediates, 105–112,  
106–107*f*, 109*f*

now-undercoordinated metal, 110–111*f*

partly detached structure in, 102–104, 103*t*

Metal alkoxides, 288–289, 303–305

Metal-catalyzed oxidation, 68*s*

Methanol oxidation, 188–194, 193*f*

Mixed-valence POMs, 219–221

Molecular cluster batteries (MCBs), 198, 198*f*

Molecular conductivity, 253–254, 279, 282*f*

Molecular oxygen, 68–69

Molecular spintronics

basics of, 255–258

material requirements for, 258–260

POMs relevance in, 232–235

and Quantum Computing, 215–216

SET in, 257*f*

thioacetate-terminated

oligophenylenevinylene, 258*f*

Molecular transistor

SET in, 257*f*

three-terminal architecture, 273*f*

Molybdenum, 17–18, 17*f*

M–OR bonds and condensation,

protonolysis

alcohol interchange, 310–311

alkoxido metathesis, 311–312

$\{(\text{MeO})\text{MPW}_{11}\}$  Keggin anions,

hydrolysis, 309–310

$\{(\text{MeO})\text{MW}_5\}$  lindqvist anions,

hydrolysis, 305–308

theoretical studies, 313–315

$\{(\text{MeO})\text{MPW}_{11}\}$  Keggin anions, hydrolysis,  
309–310, 309*f*

$\{\text{MW}_5\}$  lindqvist anion protonation

$(\text{TBA})_3 [(\text{HO})\text{SnW}_5\text{O}_{18}]$  protonation,  
320–321

$(\text{TBA})_3 [(\text{MeO})\text{TiW}_5\text{O}_{18}]$  and  $\text{H}_2\text{O}_2$

reaction, protonation from, 323–324

$(\text{TBA})_3 [(\text{MeO})\text{TiW}_5\text{O}_{18}]$  protonation,

319–320

$(\text{TBA})_6 [(\mu\text{-O})(\text{TiW}_5\text{O}_{18})_2]$  protonation,  
322–323

$\{(\text{MeO})\text{MW}_5\}$  lindqvist anions, hydrolysis,  
305–308

**N**

Nanocarbon composites, POM

covalent functionalization methods,

182–184

direct functionalization, 184

postfunctionalization, 184

electrocatalysis

methanol oxidation, 188–194, 193*f*

- Nanocarbon composites, POM (*Continued*)
- oxygen reduction, 194–196
  - water oxidation, 186–188, 187*f*
  - energy storage
    - electrochemical/photochemical reduction, 201*f*
    - lithium ion batteries, 197–202, 201*f*
    - supercapacitors, 202–203, 203*f*
    - ultrasonication-driven periodic patterning, 201*f*
  - noncovalent functionalization methods, 184–185
    - electro-assisted/photo-assisted assembly, 185
    - electrostatic interactions, 184
    - layer-by-layer assembly, 185, 203
    - $\pi$ - $\pi$  interactions, 184
  - sensors and environmental pollutants
    - developments and applications, 206–207
    - hydrogen peroxide sensors, 205
    - iodate and bromate sensors, 205–206
- Nernstian potentials, 156
- Niobates, acid-base chemistry and reactivity in, 98–102
- Nitrogen-Vacancy (NV) defects, 238
- Normal hydrogen electrode (NHE) reference, 119–120
- O**
- <sup>17</sup>O-NMR
- diminution, 101
  - (TBA)<sub>3</sub>[(MeO)<sub>3</sub>Ti<sub>2</sub>W<sub>4</sub>O<sub>16</sub>], 290*f*
  - oxygen-exchange rates, 104*f*
  - for oxygen sites, 99–100, 99*f*
  - for POM characterization, 288–289
  - water molecules exchange, 103*t*
  - [( $\mu$ -O)(TiW<sub>3</sub>O<sub>18</sub>)<sub>2</sub>]<sup>6-</sup>, ligand behavior, 324–327, 325–327*f*
- Oxidation
- photochemical generation of, 121–123
  - of primary and vicinal alcohols, 76–79
  - of sulfides, 73–75, 75*f*
  - via activation of C-H bonds revisited, 79–84
- Oxygen donors, 68–69
- Oxygen reduction reaction (ORR), 194–196, 196*f*
- Oxygen-stuffing reactions, 108–109
- P**
- Peroxides, 68–69
- Photochemical generation, of oxidant/reductant, 121–123
- Platinum(IV)-substituted {PtSiW<sub>11</sub>} anion, 303
- [PMo<sub>12</sub>O<sub>40</sub>(VO)<sub>2</sub>]<sup>3-</sup> structures, 329*f*
- [PMo<sub>12</sub>O<sub>40</sub>{Bi(DMSO)<sub>4</sub>]<sub>2</sub>]<sup>3-</sup> structure, 331*f*
- [PMo<sub>12</sub>O<sub>40</sub>(FeCl)<sub>2</sub>]<sup>4-</sup> structures, 330*f*
- [PMo<sub>12</sub>O<sub>40</sub>{Co(MeCN)<sub>2</sub>]<sub>2</sub>]<sup>3-</sup> structures, 329*f*
- [PMo<sub>12</sub>O<sub>40</sub>{Fe(DMSO)<sub>2</sub>]<sub>2</sub>]<sup>-</sup> structures, 330*f*
- [PMo<sub>12</sub>O<sub>40</sub>{Mg(MeCN)<sub>2</sub>]<sub>2</sub>]<sup>3-</sup> structure, 331*f*
- [PMo<sub>12</sub>O<sub>40</sub>Sb<sub>2</sub>]<sup>3-</sup> structures, 329*f*
- [PMo<sub>12</sub>O<sub>40</sub>{Zn(DMSO)<sub>2</sub>]<sub>2</sub>]<sup>3-</sup> structure, 331*f*
- Polyoxoanions. *See* Polyoxometalates (POMs)
- Polyoxometalates (POMs), 2
- acid-base chemistry and reactivity in niobates, 98–102
  - amphoteric variation in rates, 98*f*
  - blackberry formations, 19, 19*f*
  - building blocks, 5–6
  - classification, 2–4, 3*f*
  - CF parameters, 224–225
  - cobalt(II) cores of, 218*f*
  - counterion-directed self-assembly approach, 6–7
  - Dawson-based clusters, 16
  - dissolution rates, 95*f*, 97*f*
  - experimental models, 92–94, 93*f*
  - fully controlled assembly process, 5–6
  - gigantic structures, 12, 12*f*
  - heteropolyoxoniobate, 134–136
  - inorganic-organic-inorganic hybrid molecules, 20–21
  - isopolyanions, 4
  - ligands, 6–10
  - MAI<sub>12</sub> cations, partly detached structure in, 102–104, 103*t*
  - magnetic POMs, 224–232
  - metal cations, 6–10
  - mixed-valence POMs, 219–221
  - Mo-brown species, 4

- nanostructures, 18–21
- nested membranous system, 23*f*
- one-pot synthesis, 7*f*, 8–9
- organic solubility, 288–289
- oxidant/reductant, photochemical
  - generation, 121–123
- oxygen-exchange rates, 104*f*
- oxygen-isotope exchange, 100–101*f*
- pH ranges, 118
- polyhedral representation, 17*f*
- polyoxoniobates, 136
- for Quantum Computing
  - decoherence time, 241*f*
  - lack of anisotropy, 241
  - molecular spin qubits, 236–239
  - NV defects, 238
  - oscillation frequency, 238
  - quantum gate, 236–237, 242–243
  - qubit, 236–237
  - Rabi oscillations, 238, 241–242
  - scalability, 236–237
  - spin qubits, 239–242
- reactivity trends, 94–98
- reductively triggered assembly, 17–18
- reductive transformations, 327–332
- relevance in molecular spintronics, 232–235
- ring-shaped species, 12
- sandwich-type, 133, 136–137
- self-assembled to self-organizing cluster systems, 21–24
- self-assembly process, 4–5
- serendipity to directed assembly, 4–6
- single molecule magnet and, 10, 11*f*, 221–224
- spin-localized POMs, 217–219
- spin-triplet states, 220–221
- solar fuel production, 118–119
- stability, 119
- sulfite anion, 13–15, 13–14*f*
- templated assembly, 10–16
- tetrahedral inorganic anions, 12
- tetraruthenium(IV)-POM-based
  - homogeneous catalyst, 11
- turnover conditions, 130, 140, 145, 147
- water oxidation catalysts, 125–128*t*
  - Co-substitution, 129–132
  - immobilization, 137–143
  - iron-containment, 133
  - Ir-substitution, 133
  - Ni-substitution, 132–133
  - Ru-substitution, 124–129
  - X-ray crystal structures, 124*f*
- water reduction catalysts, 134–137, 135*t*
- water splitting
  - catalytic activity, 123–124
  - experimental approaches, 123
  - reaction thermodynamics of, 119–121
  - water reduction, 119–120
- W-only framework, 8*f*
- Polyoxoniobates, 136
- POM-counterion ion pairing, 45–47, 46*f*
- POM macroions
  - alkali counterions in, 47–49
  - counterion-mediated self-assembly
    - anisotropic surface charge density distribution, 41–42
    - blackberry formation, driving force for, 35–37, 36*f*
    - counterion distribution, 37–39
    - counterion exchange, 37–39
    - distance distribution functions, 38*f*
  - formulas, 31–32*t*
  - kinetic properties and lag phase, 42–45
  - self-assembly
    - into blackberry structures, 33–35
    - Chaumont and Wipff study, 60
    - coarse-grained model, 61*f*
    - CONTIN analysis, 58*f*
    - Liu study, 61
    - self-recognition behaviors, 56–60
    - SLS results, 59*f*
    - TEM image, 59*f*
    - Verhoeff study, 60–61
  - size of, 30
  - uranyl peroxide nanocage, selective permeability
    - change of assembly sizes, 54*f*
    - hydration layer in, 51–53, 52*f*
    - ion selectivity, controlling, 53–56
  - variable-temperature solution, 48–49*f*
- POM/nanocarbon composites
  - covalent functionalization methods, 182–184
  - direct functionalization, 184
  - postfunctionalization, 184

POM/nanocarbon composites (*Continued*)

- electrocatalysis
  - methanol oxidation, 188–194, 193*f*
  - oxygen reduction, 194–196
  - water oxidation, 186–188, 187*f*
- energy storage
  - electrochemical/photochemical reduction, 201*f*
  - lithium ion batteries, 197–202, 201*f*
  - supercapacitors, 202–203, 203*f*
  - ultrasonication-driven periodic patterning, 201*f*
- noncovalent functionalization methods, 184–185
  - electro-assisted/photo-assisted assembly, 185
  - electrostatic interactions, 184
  - layer-by-layer assembly, 185, 203
  - $\pi$ - $\pi$  interactions, 184
- sensors and environmental pollutants
  - developments and applications, 206–207
  - hydrogen peroxide sensors, 205
  - iodate and bromate sensors, 205–206
- POMs. *See* Polyoxometalates (POMs)
- Primary alcohols, oxidation of, 76–79
- Proton-coupled electron transfer (PCET), 69–70
- Protonolysis of M-OR bonds and condensation
  - alcohol interchange, 310–311
  - alkoxido metathesis, 311–312
  - {(MeO)MPW<sub>11</sub>} Keggin anions, hydrolysis, 309–310
  - {(MeO)MW<sub>5</sub>} Lindqvist anions, hydrolysis, 305–308
  - theoretical studies, 313–315
- Proton transfer, 289, 313–315

**R**

- Rabi oscillations, 238
- Radial effective charges (REC), 224–225
- Reaction thermodynamics, of water
  - splitting, 119–121
- Redox-based resistive switching, 277–282
- Reductive transformations, POMs, 327–332

**S**

- Scanning tunneling microscopy (STM), 254–255, 282*f*
- Second Quantum Revolution, 236
- Sensors and environmental pollutants
  - developments and applications, 206–207, 207*f*
  - hydrogen peroxide sensors, 205
  - iodate and bromate sensors, 205–206
- Sequential electron tunneling (SET), in molecular transistor, 257*f*
- Silicate fabric, 96
- SIMPRE package, 224–225, 227, 232
- Single-ion magnets (SIMs), 215
  - phthalocyaninato-based SIMs, 216*f*
  - polyoxometalate-based SIMs, 216*f*
- Single-molecule conductivity, spin states in, 259*f*
- Single-molecule field-effect transistor, 254*f*
- Single-molecule magnets (SMMs), 215, 255
  - based on POMs, 221–224
  - polyanion, 10, 11*f*
- Small-angle X-ray scattering (SAXS), 37–39
- Solar fuel production, 118–119. *See also* Polyoxometalates (POMs)
- Spin-localized POMs, 217–219, 239–242
- Spin qubits
  - molecular spin qubits, 236–239
  - POMs as, 239–242
- Spintronics, 255. *See also* Molecular spintronics
  - application, 213–214
  - convergence, 214
  - molecule-based spintronics, 214
  - single-molecule spintronics, 214–215
- Standard reference hydrogen electrode (SHE), 119–120
- Static light scattering (SLS), POM macroions, 33–35
- Sulfides, oxidation of, 73–75, 75*f*
- Sulfite anion POMs, 13–15, 13–14*f*
- Supercapacitors, 202–203, 203*f*

**T**

- (TBA)<sub>3</sub> [(HO)SnW<sub>5</sub>O<sub>18</sub>] protonation, 320–321
- <sup>119</sup>Sn NMR spectrum, 306–307, 307–308*f*

- (TBA)<sub>6</sub> [( $\mu$ -O)(TiW<sub>5</sub>O<sub>18</sub>)<sub>2</sub>] protonation, 322–323
- (TBA)<sub>3</sub> [(MeO)SnW<sub>5</sub>O<sub>18</sub>] hydrolysis, 306
- (TBA)<sub>3</sub> [(MeO)TiW<sub>5</sub>O<sub>18</sub>] and H<sub>2</sub>O<sub>2</sub> reaction, protonation from, 323–324
- (TBA)<sub>3</sub> [(MeO)TiW<sub>5</sub>O<sub>18</sub>] protonation, 319–320
- Thermochemical memories (TCM), 279
- Tin(II)- and lead(II)-substituted MPW<sub>11</sub> derivatives, 303, 304*f*, 305*t*
- Tin-substituted SnW<sub>5</sub> derivatives, 291–294, 292*f*, 295*f*, 296–297*t*
- Titanium(IV)- and tin(IV)-substituted MPW<sub>11</sub> derivatives, 301–303
- Transmission electron microscopy (TEM) images
- POM macroions, 33, 34*f*
  - POM/SWNT hybrid materials, 198*f*
- Tungsten, 18
- Turnover frequency (TOF), 123–124
- Turnover number (TON), 123–124
- U**
- Uranyl peroxide nanocage (U<sub>60</sub>)
- change of assembly sizes, 54*f*
  - hydration layer in, 51–53, 52*f*
  - ion selectivity, controlling, 53–56
- V**
- Valence change memory (VCM) cells, 278–279
- Vanadium, 17–18
- Vicinal alcohols, oxidation of, 76–79
- W**
- Water electrolyzers, 156–157
- Water oxidation, 186–188
- Water oxidation catalysis (WOC), 156
- artificial leaf concept, 157
  - assessment
  - acid/base properties, 144–145
  - light-driven systems stability, 143–144
  - purity, 145
- [Co<sub>9</sub>(H<sub>2</sub>O)<sub>6</sub>(OH)<sub>3</sub>(HPO<sub>4</sub>)<sub>2</sub>(PW<sub>9</sub>O<sub>34</sub>)<sub>3</sub>]<sup>16-</sup>
- carbon paste electrodes, speciation, 171–176, 173*f*
  - catalytic oxygen evolution conditions, speciation, 169–171
  - characterization with naclO, 161–165
  - and cobalt oxide, comparison, 174–175
  - homogeneous electrocatalytic water oxidation activity, 158–161
  - long-term stability, 164–165, 165*t*
  - molecular representation, 158*f*
  - speciation in water and phosphate buffer, 166–168
  - speciation on pH, 168, 169*t*
- Co-substitution, 129–132
- evaluation, 123
  - four-electron oxidation, 156
  - homogeneous WOCs, 157
  - immobilization, 137, 141–142*t*
    - carbon nanotubes, 138
    - characterizing, 140–143
    - graphene, 138–139
    - metal oxides, 139–140
    - methods, 138–140  - iron-containment, 133
  - Ir-substitution, 133
  - Ni-substitution, 132–133
  - oxidative stability, 147
  - Ru-substitution, 124–129
  - stability, 145–148
  - thermodynamic stability, 147
  - X-ray crystal structures, 124*f*
- Water reduction catalysts, POMs, 134–137, 135*t*
- WOC. *See* Water oxidation catalyst (WOC)

This page intentionally left blank

# Errata: Catalytic Hydrogenation of Carbon Dioxide to Formic Acid

**Correction** of the experimental data in Behr, A.; Nowakowski, K., Catalytic hydrogenation of carbon dioxide to formic acid, Chapter 7 in *CO<sub>2</sub> Chemistry, Advances in Inorganic Chemistry*, Vol. 66, van Eldik, R.; Aresta, M. (Eds.) Academic Press: London, 2014; pp 223–258.

In Section 2 “Hydrogenation of carbon dioxide” the SI unit for the standard molar entropy ( $\Delta S^0$ ) in Figure 7.3 is incorrect. The correct unit is [J/mol·K].

All experimentally determined TONs (turn over numbers) with the catalyst ruthenium(III)tris(acetylacetonate) (Ru(acac)<sub>3</sub>) in the laboratory and on mini-plant scale (Table 7.6; Figures 7.12, 7.15, and 7.16) in Section 3 “Continuous hydrogenation of carbon dioxide in mini-plant scale” are erroneous due to an incorrect interpretation of the chromatographic analyses of the reaction solutions.

The analyses of the following results were performed by HPLC analysis analogous to Himeda et al. (1). The liquid–liquid multiphase concept (water and triethylamine) to recycle the catalyst was maintained due to the clearly better solubility of the catalyst in triethylamine.

As shown in Table 1, the homogenous hydrogenation of carbon dioxide with Ru(acac)<sub>3</sub> and triphenylphosphine (TPP) as ligand was performed at 60 °C and 120 °C. At 60 °C the reaction does not take place and the coloration of the reaction solution is red. By increasing the temperature up to 120 °C, a TON of 279 is achieved and the reaction solution is light yellow. Therefore, higher reaction temperatures are necessary to activate the catalyst. Without the ligand TPP the hydrogenation of carbon dioxide occurred

**Table 1** Results of the Carbon Dioxide Hydrogenation with Ru(acac)<sub>3</sub>

Ligand	Temperature [°C]	TON [-]	TOF <sub>total</sub> [h <sup>-1</sup> ]	Metal leaching [ppm]	Phosphorus leaching [ppm]
<b>TPP</b>	60	0	0	10	5
<b>TPP</b>	120	279	56	5	9
<b>Without</b>	120	494	99	43	–

Conditions: V(total) = 30 ml, V(solvent) = 7.5 ml, p(total) = 40 bar, p(H<sub>2</sub>):p(CO<sub>2</sub>) = 1:1, c(cat.) = 0.5 mmol/l, solvent = water, base = triethylamine, c(base) = 5 mol/l, M:P = 1:2, t = 5 h, D = 700 rpm, TPP = triphenylphosphine

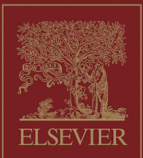
with a TON of 494 but with a higher metal leaching (43 ppm). The maximum  $\text{TOF}_{\text{total}}$  of  $220 \text{ h}^{-1}$  is reached at 0.75 h. It is assumed that triethylamine coordinated specifically to the catalyst. Triethylamine acts as a ligand in the hydrogenation of carbon dioxide by using  $\text{Ru}(\text{acac})_3$ .

In the continuously operated mini-plant the ligand-free system was analyzed over 30 h. The maximum  $\text{TON}_{\text{total}}$  of 160 is achieved at 10.5-h reaction time. The catalyst leaching is the content of ruthenium in the liquid-product phase. It has been determined by ICP analysis (inductively coupled plasma). During the mini-plant experiment, the catalyst leaching of ruthenium fluctuates; at a reaction time of 8.5 h the leaching amounts to 21 ppm and at 11.5 h to 8 ppm. Thus, the catalyst leaching is considerably below the investigation in laboratory scale (43 ppm). This is due to the liquid-liquid separation under reaction pressure. The reaction terminated after 30-h reaction time. This result can be explained by the impoverishment of carbon dioxide in the gas phase.

## REFERENCE

1. Himeda, Y.; Onozawa-Komatsuzaki, N.; Sugihara, H.; Kasuga, K. Simultaneous Tuning of Activity and Water Solubility of Complex Catalysts by Acid-Base Equilibrium of Ligands for Conversion of Carbon Dioxide. *Organometallics* **2007**, *26*(3), 702–712.





**ACADEMIC PRESS**

An imprint of Elsevier  
[elsevier.com/books-and-journals](http://elsevier.com/books-and-journals)

ISBN 978-0-12-811105-5



9 780128 111055